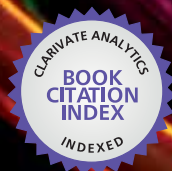


IntechOpen

Infrared Spectroscopy

Materials Science, Engineering
and Technology

Edited by Theophile Theophanides



WEB OF SCIENCE™

INFRARED SPECTROSCOPY— MATERIALS SCIENCE, ENGINEERING AND TECHNOLOGY

Edited by **Theophile Theophanides**

Infrared Spectroscopy - Materials Science, Engineering and Technology

<http://dx.doi.org/10.5772/2055>

Edited by Theophile Theophanides

Contributors

Bayar Hexig, Alata Hexig, Daniel Macedo, Moisés Romolos Cesário, Grazielle Souza, Beatriz Cela, Carlos Paskocimas, Antonio Martinelli, Dulce Melo, Rubens Maribondo Do Nascimento, Eugen Sheregii, Perla E. García Casillas, Carlos A. Martínez Pérez, Claudia A. Rodriguez Gonzalez, Anggoro Tri Mursito, Tsuyoshi Hirajima, Suedina Maria De Lima Silva, Carla Lima R. C. Braga, Marcus Vinícius Lia Fook, Claudia Maria De Oliveira Raposo, Laura Hecker De Carvalho, Eduardo Luis Canedo, Jun-Ichi Fukuda, Tadej Rojac, Primož Segeđin, Marija Kosec, Liberata Guadagno, Vladimir Alonso Escobar Barrios, Jose Rene Rangel-Mendez, Guillermo Andrade-Espinosa, José Luis Dávila-Rodríguez, Nancy Verónica Pérez-Aguilar, Tarik Chafik, Lucia J Fernández, Olga Belskaya, Irina Danilova, Maxim Kazakov, Roman Mikhailovich Mironenko, Alexander Lavrenov, Vladimir Likholobov, Jose Luis Rivera Armenta, Cynthia Graciela Flores-Hernández, Ruth Zurisadai Del Angel Aldana, Carlos Velasco-Santos, Ana Maria Mendoza-Martínez, Ana Laura Martinez-Hernandez, Juan Baselga, María González, Juan C. Cabanelas, Simona Carmen Litescu, Eugenia D. Teodor, Gabriel-Lucian Radu, Georgiana-Ileana Badea, Andreia Tache, Johannes Lützenkirchen, Gregory Lefevre, Tajana Preocanin, Somayeh Mohamadi, Christian Braunschier, Daniel Lumpi, Takaomi Kobayashi, Liga Berzina-Cimdina, Natalija Borodajenko, Zahra Monsef Khoshhesab, Chris Aldrich, Hansie Knoetze, Corne Marais, Spiros Tzavalas, Marco Sangermano, Patrick Meier, Yankun Peng, Yongyu Li, Jingjing Chen, Eugen Culea, Simona Rada, Theophanides Theophile

© The Editor(s) and the Author(s) 2012

The moral rights of the and the author(s) have been asserted.

All rights to the book as a whole are reserved by INTECH. The book as a whole (compilation) cannot be reproduced, distributed or used for commercial or non-commercial purposes without INTECH's written permission.

Enquiries concerning the use of the book should be directed to INTECH rights and permissions department (permissions@intechopen.com).

Violations are liable to prosecution under the governing Copyright Law.



Individual chapters of this publication are distributed under the terms of the Creative Commons Attribution 3.0 Unported License which permits commercial use, distribution and reproduction of the individual chapters, provided the original author(s) and source publication are appropriately acknowledged. If so indicated, certain images may not be included under the Creative Commons license. In such cases users will need to obtain permission from the license holder to reproduce the material. More details and guidelines concerning content reuse and adaptation can be found at <http://www.intechopen.com/copyright-policy.html>.

Notice

Statements and opinions expressed in the chapters are these of the individual contributors and not necessarily those of the editors or publisher. No responsibility is accepted for the accuracy of information contained in the published chapters. The publisher assumes no responsibility for any damage or injury to persons or property arising out of the use of any materials, instructions, methods or ideas contained in the book.

First published in Croatia, 2012 by INTECH d.o.o.

eBook (PDF) Published by IN TECH d.o.o.

Place and year of publication of eBook (PDF): Rijeka, 2019.

IntechOpen is the global imprint of IN TECH d.o.o.

Printed in Croatia

Legal deposit, Croatia: National and University Library in Zagreb

Additional hard and PDF copies can be obtained from orders@intechopen.com

Infrared Spectroscopy - Materials Science, Engineering and Technology

Edited by Theophile Theophanides

p. cm.

ISBN 978-953-51-0537-4

eBook (PDF) ISBN 978-953-51-4300-0

We are IntechOpen, the first native scientific publisher of Open Access books

3,400+

Open access books available

109,000+

International authors and editors

115M+

Downloads

151

Countries delivered to

Our authors are among the
Top 1%

most cited scientists

12.2%

Contributors from top 500 universities



WEB OF SCIENCE™

Selection of our books indexed in the Book Citation Index
in Web of Science™ Core Collection (BKCI)

Interested in publishing with us?
Contact book.department@intechopen.com

Numbers displayed above are based on latest data collected.
For more information visit www.intechopen.com



Meet the editor



Professor Theophile Theophanides was born in Platamon, Kavala, Greece and is known from his ground-breaking research in the field of Metal Coordination Chemistry and Infrared Spectroscopy. In particular his research focus has been in the areas of life metal ions, bioinorganic chemistry and in his pioneering work in anti-tumor drugs, such as cis-Platinum, commonly employed in chemotherapy. He has authored over 250 peer-reviewed scientific publications in international journals, penned numerous articles and book chapters and served on the board of many Scientific Associations and Committees. He has been honored many times for his research. He is an Honorary Professor of the University of Montreal and the National Technical University of Athens, Doctor Honoris Causa of the University of Reims and Silver Medalist of the National French Academy of Medicine for his outstanding work on magnesium research. Additionally, he has received medals from Universities, Media and other Associations for his research and communications on Environmental and Public Health issues.

Contents

Preface XIII

- Introductory Chapter **Introduction to Infrared Spectroscopy 1**
Theophile Theophanides
- Section 1 Minerals and Glasses 11**
- Chapter 1 **Using Infrared Spectroscopy to Identify New Amorphous Phases – A Case Study of Carbonato Complex Formed by Mechanochemical Processing 13**
Tadej Rojac, Primož Šegedin and Marija Kosec
- Chapter 2 **Application of Infrared Spectroscopy to Analysis of Chitosan/Clay Nanocomposites 43**
Suédina M.L. Silva, Carla R.C. Braga, Marcus V.L. Fook, Claudia M.O. Raposo, Laura H. Carvalho and Eduardo L. Canedo
- Chapter 3 **Structural and Optical Behavior of Vanadate-Tellurate Glasses Containing PbO or Sm₂O₃ 63**
E. Culea, S. Rada, M. Culea and M. Rada
- Chapter 4 **Water in Rocks and Minerals – Species, Distributions, and Temperature Dependences 77**
Jun-ichi Fukuda
- Chapter 5 **Attenuated Total Reflection – Infrared Spectroscopy Applied to the Study of Mineral – Aqueous Electrolyte Solution Interfaces: A General Overview and a Case Study 97**
Grégory Lefèvre, Tajana Preočanin and Johannes Lützenkirchen
- Chapter 6 **Research of Calcium Phosphates Using Fourier Transform Infrared Spectroscopy 123**
Liga Berzina-Cimdina and Natalija Borodajenko

- Chapter 7 **FTIR Spectroscopy of Adsorbed Probe Molecules for Analyzing the Surface Properties of Supported Pt (Pd) Catalysts** 149
Olga B. Belskaya, Irina G. Danilova, Maxim O. Kazakov, Roman M. Mironenko, Alexander V. Lavrenov and Vladimir A. Likholobov
- Chapter 8 **Hydrothermal Treatment of Hokkaido Peat – An Application of FTIR and ¹³C NMR Spectroscopy on Examining of Artificial Coalification Process and Development** 179
Anggoro Tri Mursito and Tsuyoshi Hirajima
- Section 2 Polymers and Biopolymers** 193
- Chapter 9 **FTIR – An Essential Characterization Technique for Polymeric Materials** 195
Vladimir A. Escobar Barrios, José R. Rangel Méndez, Nancy V. Pérez Aguilar, Guillermo Andrade Espinosa and José L. Dávila Rodríguez
- Chapter 10 **Preparation and Characterization of PVDF/PMMA/Graphene Polymer Blend Nanocomposites by Using ATR-FTIR Technique** 213
Somayeh Mohamadi
- Chapter 11 **Reflectance IR Spectroscopy** 233
Zahra Monsef Khoshhesab
- Chapter 12 **Evaluation of Graft Copolymerization of Acrylic Monomers Onto Natural Polymers by Means Infrared Spectroscopy** 245
José Luis Rivera-Armenta, Cynthia Graciela Flores-Hernández, Ruth Zurisadai Del Angel-Aldana, Ana María Mendoza-Martínez, Carlos Velasco-Santos and Ana Laura Martínez-Hernández
- Chapter 13 **Applications of FTIR on Epoxy Resins – Identification, Monitoring the Curing Process, Phase Separation and Water Uptake** 261
María González González, Juan Carlos Cabanelas and Juan Baselga
- Chapter 14 **Use of FTIR Analysis to Control the Self-Healing Functionality of Epoxy Resins** 285
Liberata Guadagno and Marialuigia Raimondo
- Chapter 15 **Infrared Analysis of Electrostatic Layer-By-Layer Polymer Membranes Having Characteristics of Heavy Metal Ion Desalination** 301
Weimin Zhou, Huitan Fu and Takaomi Kobayashi

- Chapter 16 **Infrared Spectroscopy as a Tool to Monitor Radiation Curing** 325
Marco Sangermano, Patrick Meier and Spiros Tzavalas
- Section 3 Materials Technology** 337
- Chapter 17 **Characterization of Compositional Gradient Structure of Polymeric Materials by FTIR Technology** 339
Alata Hexig and Bayar Hexig
- Chapter 18 **Fourier Transform Infrared Spectroscopy – Useful Analytical Tool for Non-Destructive Analysis** 353
Simona-Carmen Litescu, Eugenia D. Teodor, Georgiana-Ileana Truica, Andreia Tache and Gabriel-Lucian Radu
- Chapter 19 **Infrared Spectroscopy in the Analysis of Building and Construction Materials** 369
Lucía Fernández-Carrasco, D. Torrens-Martín, L.M. Morales and Sagrario Martínez-Ramírez
- Chapter 20 **Infrared Spectroscopy Techniques in the Characterization of SOFC Functional Ceramics** 383
Daniel A. Macedo, Moisés R. Cesário, Grazielle L. Souza, Beatriz Cela, Carlos A. Paskocimas, Antonio E. Martinelli, Dulce M. A. Melo and Rubens M. Nascimento
- Chapter 21 **Infrared Spectroscopy of Functionalized Magnetic Nanoparticles** 405
Perla E. García Casillas, Claudia A. Rodriguez Gonzalez and Carlos A. Martínez Pérez
- Chapter 22 **Determination of Adsorption Characteristics of Volatile Organic Compounds Using Gas Phase FTIR Spectroscopy Flow Analysis** 421
Tarik Chafik
- Chapter 23 **Identification of Rocket Motor Characteristics from Infrared Emission Spectra** 433
N. Hamp, J.H. Knoetze, C. Aldrich and C. Marais
- Chapter 24 **Optical Technologies for Determination of Pesticide Residue** 453
Yankun Peng, Yongyu Li and Jingjing Chen
- Chapter 25 **High Resolution Far Infrared Spectra of the Semiconductor Alloys Obtained Using the Synchrotron Radiation as Source** 467
E.M. Sheregii

Chapter 26	Effective Reaction Monitoring of Intermediates by ATR-IR Spectroscopy Utilizing Fibre Optic Probes	493
	Daniel Lumpi and Christian Braunschier	

Preface

This book has been written in response to a need for the edition of a book to support the advances that have been made in Infrared Spectroscopy. It aims to provide a comprehensive review of the most up-to-date knowledge on the advances of infrared spectroscopy in the materials science.

50 years have passed since I have been dealing with the first infrared spectrum when working on my PhD thesis at the University of Toronto. Infrared spectroscopy has developed since into a major field of study with far reaching scientific implications. Topics such as brain activity, chemical research and spectral analyses on cereals, plants and fruits which haven't been discussed 50 years ago, now present major fields in the discipline. More traditional topics such as infrared spectra of gases and materials have also been placed on firmer foundations.

The method of infrared (IR) spectroscopy, discovered in 1835 has so far produced a wealth of information on the architecture of matter in our planet and even in the far away stars. Infrared spectroscopy is a powerful technique that allows us to learn more about the structure of materials and their identification and characterization. This study is based on the interaction of electromagnetic (EM) radiation with matter. The EM radiation has energy states comparable to the vibrational energy states of the molecules. These states are included in the energy region between 14000 cm^{-1} and 100 cm^{-1} of the Electromagnetic Radiation, which is divided in three sub-regions called 1) NEAR-IR, or NIRS 2) MID-IR or MIRS and 3) FAR-IR, or FIRS:

The book contains 3 sections, which regroup the 26 chapters covering Infrared spectroscopy applied in all the above three regions. Section 1: **Minerals and Glasses** contains 8 chapters, which describe the applications of IR in identifying amorphous phases of materials, glasses, rocks and minerals, catalysts, as well as peat and in reaction processes. Section 2: **Polymers and Biopolymers** deals especially with the characterization and evaluation of polymers and biopolymers using as a tool the IR technique. Finally, the last section 3: **Materials Technology** is concerned with research in FT-IR studies, in particular for characterization purposes and coupled with ATR and fiber optic probes in monitoring reaction intermediates.

The interaction of EM with the vibrational energy states of the molecules gives birth to the IR-spectra in the above three regions. The IR spectra are really the "finger prints"

of the materials and the absorption or transmission bands are the “signature bands” that characterize such materials (see Introduction to Infrared Spectroscopy). NIRS has been used also extensively in the food and agriculture industry as well as in pharmaceutical industry and medicine for the past 30 years. Recent technological advances have made NIRS an attractive analytical method to use in several other disciplines as well.

This book may be a useful survey for those who would like to advance their knowledge in the application of FT-IR for the characterization and structural information of materials in materials science and technology.

Theophile Theophanides

National Technical University of Athens, Chemical Engineering Department,
Radiation Chemistry and Biospectroscopy, Zografou Campus, Zografou, Athens
Greece

Introductory Chapter

Introduction to Infrared Spectroscopy

Theophile Theophanides

National Technical University of Athens, Chemical Engineering Department,
Radiation Chemistry and Biospectroscopy, Zografou Campus, Zografou, Athens
Greece

1. Introduction

1.1 Short history of the technique

Infrared radiation was discovered by Sir William Herschel in 1800 [1]. Herschel was investigating the energy levels associated with the wavelengths of light in the visible spectrum. Sunlight was directed through a prism and showed the well known visible spectrum of the *rainbow colors*, i.e, the visible spectrum from blue to red with the analogous wavelengths or frequencies [2, 3] (see Fig.1).

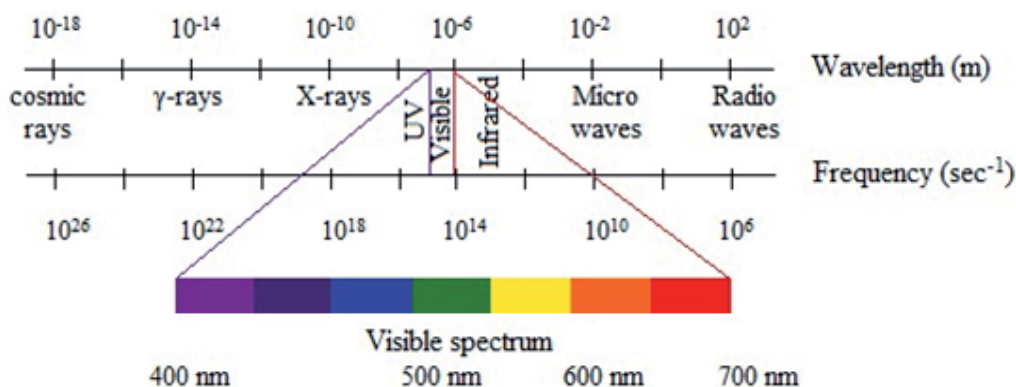


Fig. 1. The electromagnetic spectrum.

Spectroscopy is the study of interaction of electromagnetic waves (EM) with matter. The wavelengths of the colors correspond to the energy levels of the rainbow colors. Herschel by slowly moving the thermometer through the visible spectrum from the blue color to the red and measuring the temperatures through the spectrum, he noticed that the temperature increased from blue to red part of the spectrum. Herschel then decided to measure the temperature just below the red portion thinking that the increase of temperature would stop outside the visible spectrum, but to his surprise he found that the temperature was even higher. He called these rays, which were below the red rays “non colorific rays” or invisible rays, which were called later “infrared rays” or IR light. This light is not visible to human eye. A typical human eye will respond to wavelengths from 390 to 750 nm. The IR spectrum starts at 0.75 nm. One nanometer (nm) is 10⁻⁹ m The Infrared spectrum is divided into, Near Infrared (NIRS), Mid Infrared (MIRS) and Far Infrared (FIRS) [4-6].

1.2 The three Infra red regions of interest in the electromagnetic spectrum

In terms of wavelengths the three regions in micrometers (μm) are the following:

- i. NIRS, (0.7 μm to 2,5 μm)
- ii. MIRS (2,5 μm to 25 μm)
- iii. FIRS (25 μm to 300 μm).

In terms of wavenumbers the three regions in cm^{-1} are:

1. (NIRS), 14000-4000 cm^{-1}
2. (MIRS), 4000-400 cm^{-1}
3. (FIRS), 400-10 cm^{-1}

The first region (NIRS) allows the study of overtones and harmonic or combination vibrations. The MIRS region is to study the fundamental vibrations and the rotation-vibration structure of small molecules, whereas the FIRS region is for the low heavy atom vibrations (metal-ligand or the lattice vibrations). Infrared (IR) light is electromagnetic (EM) radiation with a wavelength longer than that of visible light: $\leq 0.7\mu\text{m}$. One micrometer (μm) is 10^{-6}m .

Experiments continued with the use of these infrared rays in spectroscopy called, Infrared Spectroscopy and the first infrared spectrometer was built in 1835. IR Spectroscopy expanded rapidly in the study of materials and for the chemical characterization of materials that are in our planet as well as beyond the planets and the stars. The renowned spectroscopists, Hertzberg, Coblenz and Angstrom in the years that followed had advanced greatly the cause of Infrared spectroscopy. By 1900 IR spectroscopy became an important tool for identification and characterization of chemical compounds and materials. For example, the carboxylic acids, R-COOH , show two characteristic bands at 1700 cm^{-1} and near 3500 cm^{-1} , which correspond to the C=O and O-H stretching vibrations of the carboxyl group, $-\text{COOH}$. Ketones, R-CO-R absorb at 1730-40 cm^{-1} . Saturated carboxylic acids absorb at 1710 cm^{-1} , whereas saturated/aromatic carboxylic acids absorb at 1680-1690 cm^{-1} and carboxylic salts or metal carboxylates absorb at 1550-1610 cm^{-1} . By 1950 IR spectroscopy was applied to more complicated molecules such as proteins by Elliot and Ambrose [2]. These later studies showed that IR spectroscopy could also be used to study biological molecules, such as proteins, DNA and membranes and could be used in biosciences, in general [2-8].

Physicochemical techniques, especially infrared spectroscopic methods are non destructive and may be the ones that can extract information concerning molecular structure and characterization of many materials at a variety of levels. Spectroscopic techniques those based upon the interaction of light with matter have for long time been used to study materials both *in vivo* and *in ex vivo* or *in vitro*. Infrared spectroscopy can provide information on isolated materials, biomaterials, such as biopolymers as well as biological materials, connective tissues, single cells and in general biological fluids to give only a few examples. Such varied information may be obtained in a single experiment from very small samples. Clearly then infrared spectroscopy is providing information on the energy levels of the molecules in wavenumbers(cm^{-1}) in the region of electromagnetic spectrum by studying the vibrations of the molecules, which are also given in wavelengths (μm).

Thus, infrared spectroscopy is the study of the interaction of matter with light radiation when waves travel through the medium (matter). The waves are electromagnetic in nature and interact with the polarity of the chemical bonds of the molecules [3]. If there is no

polarity (dipole moment) in the molecule then the infrared interaction is inactive and the molecule does not produce any IR spectrum.

1.3 Degrees of freedom of vibrations

The forces that hold the atoms in a molecule are the chemical bonds. In a diatomic molecule, such as hydrochloric acid (H-Cl), the chemical bond is between hydrogen (H) and chlorine (Cl). The chemical forces that hold these two atoms together are considered to be similar to those exerted by massless springs. Each mass requires three coordinates, in order to define the molecule's position in space, with coordinate axes x, y, z in a Cartesian coordinate system. Therefore, the molecule has three independent **degrees of freedom** of motion. If there are N atoms in a molecule there will be a total of **$3N$ degrees of freedom** of motion for all the atoms in the molecule. After subtracting the translational and rotational degrees of freedom from the $3N$ degrees of freedom, we are left with $3N-6$ internal motions for a non linear molecule and $3N-5$ for a linear molecule, since the rotation in a linear molecule, such as H-Cl the motion around the axis of the bond does not change the energy of the molecule. These internal vibrations are called the normal modes of vibration. Thus, in the example of H-Cl we have one vibration, $(3 \times 2) - 5 = 1$, i.e. only one vibration along the H-Cl axis or along the chemical bond of the molecule. For a non linear molecule as H_2O we have $(3 \times 3) - 6 = 3$ vibrations, the two vibrations along the chemical bonds O-H symmetrical (ν_s) and antisymmetrical (ν_{as}) O-H bonds and the bending vibration (δ) of changing the angle H-O-H of the two bonds [3,4]. In this way we can interpret the IR-spectra of small inorganic compounds, such as, SO_2 , CO_2 and NH_3 quite reasonably. For the more complicated organic molecules the IR spectrum will give more vibrations as calculated from the $3N-6$ vibrations, since the number of atoms in the molecule increases, however the spectrum is interpreted on the basis of characteristic bands.

2. Theory

2.1 Interaction of light waves with molecules

The interaction of light and molecules forms the basis of IR spectroscopy. Here it will be given a short description of the Electromagnetic Radiation, the energy levels of a molecule and the way the Electromagnetic Radiation interacts with molecules and their structure [5, 6].

2.2 Electromagnetic radiation

The EM radiation is a combination of periodically changing or oscillating electric field (EF) and magnetic field (MF) oscillating at the same frequency, but perpendicular to the electrical field [7] (see Fig.2).

The wavelength is represented by λ [6], which is the wavelength, the distance between two positions in the same phase and frequency (ν) is the number of oscillations per unit time of the EM wave per sec or vibrations/unit time. The wavenumber is the number of waves/unit length [7]. It can be easily seen [3] that c is given by equation 1:

$$c = \lambda\nu \quad (1)$$

where, c is the velocity of light of EM waves, or light waves, which is a constant for a medium in which the waves are propagating, $c = 3 \times 10^8 \text{ m/s}$

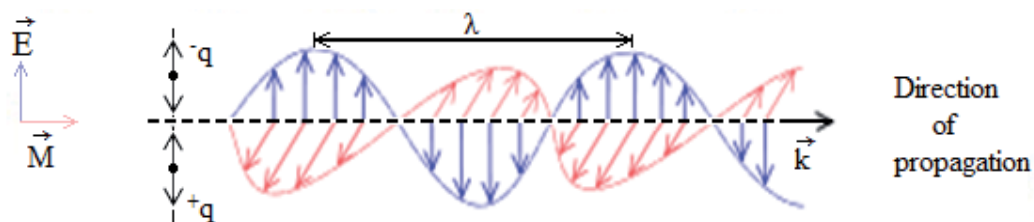


Fig. 2. An Illustration of Electromagnetic Radiation can be imagined as a self-propagating transverse oscillating wave of electric and magnetic fields. This diagram shows a plane linearly polarized wave propagating from left to right. The electric field is in a vertical plane (E) blue and the magnetic field in a horizontal plane (M) red

The wavelength (λ) is inversely proportional to the frequency, $1/\nu$. The Energy in quantum terms [8]: is given by Planck's equation:

$$E = h\nu \quad (2)$$

Which was deduced later also by Einstein, where, E is the energy of the photon of frequency ν and h is Max Planck's constant [8], $h=6.62606896 \times 10^{-34}$ Js or $h = 4.13566733 \times 10^{-15}$ eV. Wave number and frequency are related by the equation

$$\nu = c\tilde{\nu} \quad (3)$$

The EM spectrum can be divided as we have seen into several regions differing in frequency or wavelength. The relationship between the frequency (ν) the wavelength (λ) and the speed of light (c) is given below:

$$\nu = \frac{c}{\lambda} \quad \nu = \frac{E}{h} \quad E = \frac{hc}{\lambda} \quad (4)$$

The frequency in wavenumbers is given by the equation:

$$\tilde{\nu} = \frac{1}{2\pi c} \sqrt{\frac{k}{\mu}} \quad (\text{cm}^{-1}) \quad (5)$$

Where, k=bond spring constant, μ = reduced mass, c=velocity of light (cm/sec),

μ is the reduced mass of the AB bond system of masses and m= mass of the atoms, m_A =mass of A and m_B = mass of B. The isotope effect can also be calculated using the reduced mass and substituting the isotopic mass in the equation of the frequency in wavenumbers.

Example, the H-Cl molecule

$$\mu = \frac{m_H m_{Cl}}{m_H + m_{Cl}}$$

m_H and m_{Cl} are the atomic masses of H and Cl atoms.

2.3 Energy of a molecule

The name *atom* was coined by Democritus [9] from the Greek, α-τέμνω, meaning in Greek it cannot be cut any more or it is indivisible. This is the first time that it was postulated that the atom is the smallest particle of matter with its characteristics and it is the building block of all materials in the universe. Combinations of atoms form molecules.

The energy of a molecule is the sum of 4 types of energies [3]:

$$E = E_{\text{ele}} + E_{\text{vib}} + E_{\text{rot}} + E_{\text{tra}} + E_{\text{nuc}} \quad (6)$$

E_{ele} : is the electronic energy of all the electrons of the molecule

E_{vib} : is the vibrational energy of the molecule, i.e., the sum of the vibrations of the atoms in the molecule

E_{rot} : is the rotational energy of the molecule, which can rotate along the three axes, x, y, z

E_{tra} : is the translational energy of the molecule, which is due to the movement of the molecule as a whole along the three cartesian axes, x, y, z .

E_{nuc} : is the nuclear energy

Energy level electronic transitions (see Figs 3A, 3B):

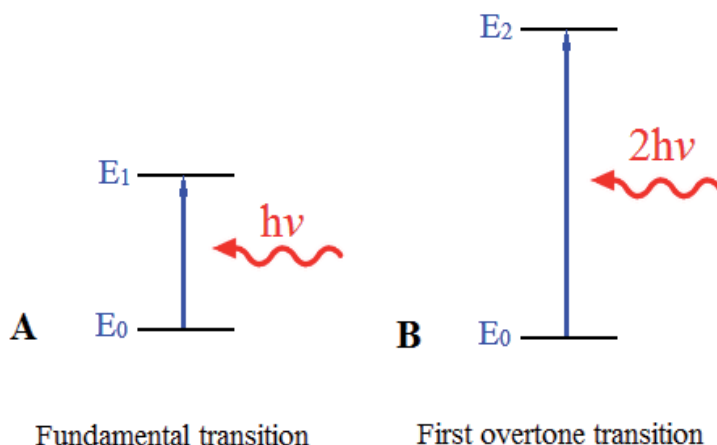


Fig. 3. A: Increasing the energy level from E_0 to E_1 with the wave energy $h\nu$, which results in the fundamental transition, B: Increasing the energy level from E_0 to E_2 leads to the first overtone transition or first harmonic.

3. The techniques of infrared spectroscopy

We have two types of IR spectrophotometers: The classical and the Fourier Transform spectrophotometers with the interferometer

3.1 The classical IR spectrometers [3, 4]

The main elements of the standard IR classical instrumentation consist of 4 parts (see Fig.4)

1. A light source of irradiation
2. A dispersing element, diffraction grating or a prism

3. A detector
4. Optical system of mirrors

Schematics of a two-beam absorption spectrometer are shown in in. Fig. 4.

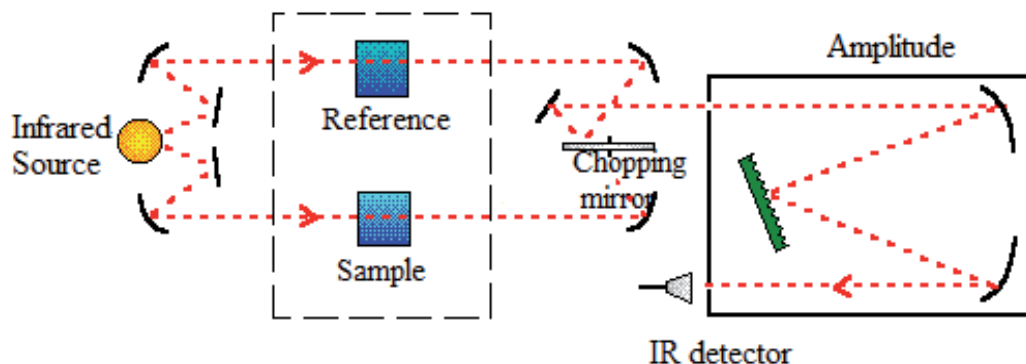


Fig. 4. A schematic diagram of the classical dispersive IR spectrophotometer.

The infrared radiation from the source by reflecting to a flat mirror passes through the sample and reference monochromator then through the sample. The beams are reflected on a rotating mirror, which alternates passing the sample and reference beams to the dispersing element and finally to detector to give the spectrum (see Fig 4). As the beams alternate the mirror rotates slowly and different frequencies of infrared radiation pass to detector.

3.2 Fourier Transform IR spectrometers

The modern spectrometers [7] came with the development of the high performance Fourier Transform Infrared Spectroscopy (FT-IR) with the application of a Michelson Interferometer [10]. Both IR spectrometers classical and modern give the same information the main difference is the use of Michelson interferometer, which allows all the frequencies to reach the detector at once and not one at the time/

In the 1870's A.A. Michelson [11] was measuring light and its speed with great precision(3) and reported the speed of light with the greatest precision to be 299,940 km/s and for this he was awarded the Nobel Prize in 1907. However, even though the experiments in interferometry by Michelson and Morley [12] were performed in 1887 the interferograms obtained with this spectrometer were very complex and could not be analyzed at that time because the mathematical formulae of Jean Baptiste Fourier series in 1882 could not be solved [13]. We had to wait until the invention of Lasers and the high performance of electronic computers in order to solve the mathematical formulae of Fourier to transform a number of points into waves and finally into the spectra [14]

The addition, of the lasers to the Michelson interferometer provided an accurate method (see Figs. 5A & 5B) of monitoring displacements of a moving mirror in the interferometer with a high performance computer, which allowed the complex interferogram to be analyzed and to be converted *via* Fourier transform to give spectra.



Fig. 5A. Michelson FT-IR Spectrometer has the following main parts:

1. Light source
2. Beam splitter (half silvered mirror)
3. Translating mirror
4. Detector
5. Optical System (fixed mirror)

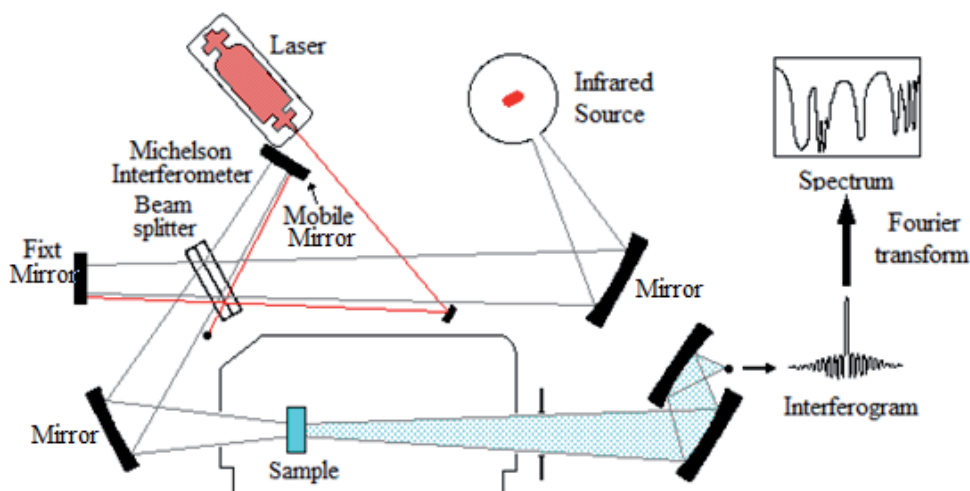


Fig. 5B. Schematic illustration of a modern FTIR Spectrophotometer.

Infrared spectroscopy underwent tremendous advances after the second world war and after 1950 with improvements in instrumentation and electronics, which put the technique at the center of chemical research and later in the 80's in the biosciences in general with new sample handling techniques, the attenuated total reflection method (ATR) and of course the interferometer [13]. The Fourier Transform IR spectrophotometry is now widely used in both research and industry as a routine method and as a reliable technique for quality control,

molecular structure determination and kinetics [14-16] in biosciences(see Fig. 6). Here the spectrum of a very complex matter , such as an atheromatic plaque is given and interpreted.

In practice today modern techniques are used and these are the FT-methods. The non- FT methods are the classical IR techniques of dispersion of light with a prism or a diffraction grating. The FT-technique determines the absorption spectra more precisely. A Michelson interferometer should be used today to obtain the IR spectra [17]. The advantage of FT-method is that it detects a broad band of radiation all the time (the multiplex or Fellget advantage) and the greater proportion of the source radiation passes through the instrument because of the circular aperture (Jacquinot advantage) rather than the narrow slit used for prisms or diffraction gratings in the classical instrument.

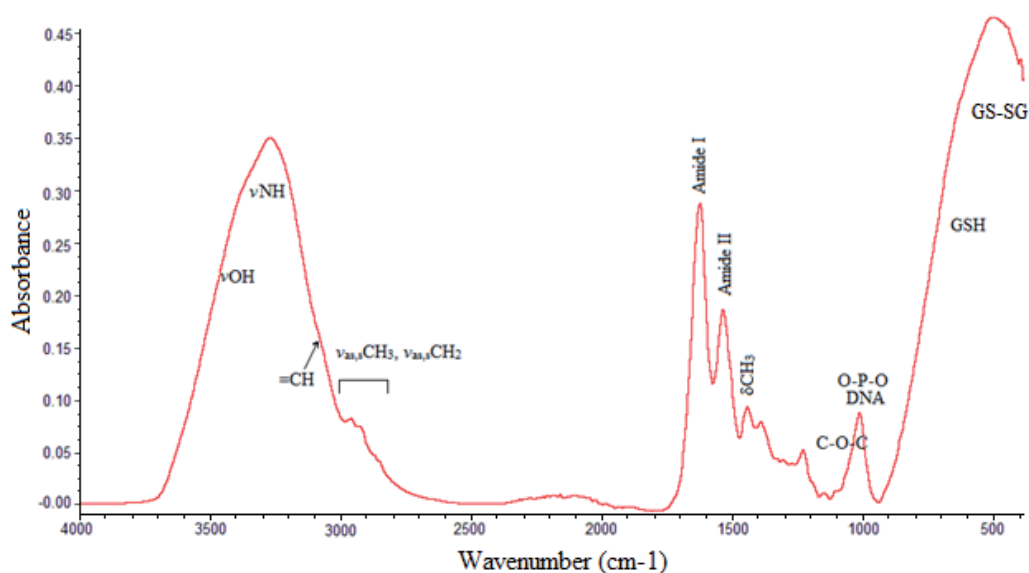


Fig. 6. FT-IR spectrum of a coronary atheromatic plaque is shown with the characteristic absorption bands of proteins, amide bands, O-P-O of DNA or phospholipids, disulfide groups, etc.

3.3 Micro-FT-IR spectrometers

The addition of a reflecting microscope to the IR spectrometer permits to obtain IR spectra of small molecules, crystals and tissues cells, thus we can apply the IR spectroscopy to biological systems, such as connective tissues, blood samples and bones, in pathology in medicine [15, 26-27]. In Fig. 7 is shown the microscope imaging of cancerous breast tissues and its spectrum.

4. Applications

Infrared spectroscopy is used in chemistry and industry for identification and characterization of molecules. Since an IR spectrum is the “fingerprint” of each molecule IR is used to characterize substances [16, 17]. Infrared spectroscopy is a non destructive method and as such it is useful to study the secondary structure of more complicated systems such

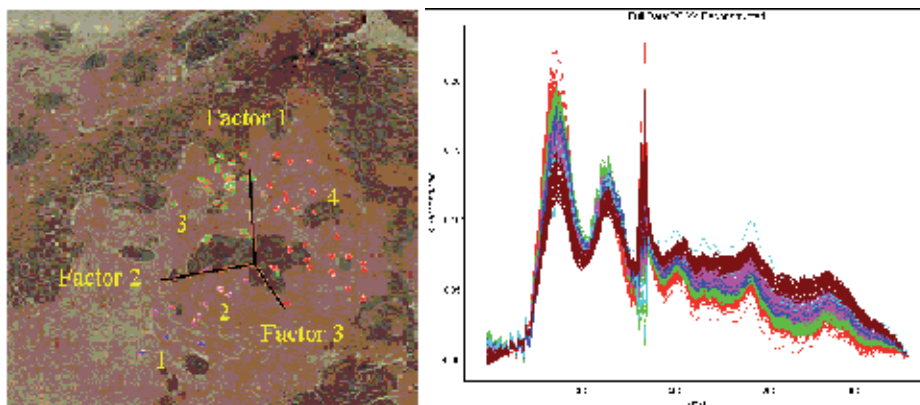


Fig. 7. Breast tissue: a 3-axis diagram and the mean spectral components are shown [25].

as biological molecules proteins, DNA and membranes. In the last decade infrared spectroscopy started to be used to characterize healthy and non healthy human tissues in medical sciences.

IR spectroscopy is used in both research and industry for measurement and quality control. The instruments are now small and portable to be transported, even for use in field trials. Samples in solution can also be measured accurately. The spectra of substances can be compared with a store of thousands of reference spectra [18]. Some samples of specific applications of IR spectroscopy are the following:

IR spectroscopy has been highly successful in measuring the degree of polymerization in polymer manufacture [18]. IR spectroscopy is useful for identifying and characterizing substances and confirming their identity since the IR spectrum is the “fingerprint” of a substance. Therefore, IR also has a forensic purpose and IR spectroscopy is used to analyze substances, such as, alcohol, drugs, fibers, blood and paints [19-28]. In the several sections that are given in the book the reader will find numerous examples of such applications.

5. References

- [1] W. Herschel, Phil. Trans.R.Soc.London, 90, 284 (1800)
- [2] Elliot and E. Ambrose, Nature, Structure of Synthetic Polypeptides 165, 921 (1950);
D.L.Woernley, Infrared Absorption Curves for Normal and Neoplastic Tissues and Related Biological Substances, Current Research, Vol. 12, , 1950 , 516p
- [3] T. Theophanides, In Greek, National Technical University of Athens, Chapter in “Properties of Materials”, NTUA, Athens (1990); 67p
- [4] J. Anastasopoulou and Th. Theophanides, Chemistry and Symmetry”, In Greek National Technical University of Athens, NTUA, (1997), 94p
- [5] G.Herzberg, Atomic spectra and atomic structure, Dover Books, New York,Academic press, 1969, 472 p
- [6] Maas, J.H. van der (1972) *Basic Infrared Spectroscopy*.2nd edition. London: Heyden & Son Ltd. 105p
- [7] Colthup, N.B., Daly, L.H., and Wiberley, S.E.(1990).*Introduction to Infrared and Raman Spectroscopy*.Third Edition. London: Academic press Ltd, 547 p.

- [8] Fowles, G.R. (1975). *Introduction to Modern Optics*. Second Edition. New York: Dover publications Inc., 336 p
- [9] Democritos, Avdera, Thrace, Greece, 460-370 BC
- [10] Hecht, E. *Optics*. Fourth edition. San Francisco: Pearson Education Inc. (2002)
- [11] A.A. Michelson, *Studies in Optics*, University of Chicago, Press, Chicago (1962), 208 p
- [12] A.A Michelson and Morley, "on the Relative Motion of the Earth and the luminiferous Ether" *Am. J. of Science*, 333-335(1887); F.Gires and P.Toumois, " L'interférométrie utilisable pour la compression lumineuse module en fréquence " *Comptes Rendus de l'Académie des Sciences de Paris*, 258, 6112-6115(1964)
- [13] Jean Baptiste Joseph Fourier, *Oeuvres de Fourier*, (1888); Idem *Annals de Chimie et de Physique*, 27, Paris, *Annals of Chemistry and Physics*, (1824) 236-281p
- [14] S. Tolansky, *An Introduction to Interferometry*, William Clowes and Sons Ltd.(1966), 253 p
- [15] J. Anastassopoulou, E. Boukaki, C. Conti, P. Ferraris, E.Giorgini, C. Rubini, S. Sabbatini, T. Theophanides, G. Tosi, *Microimaging FT-IR spectroscopy on pathological breast tissues, Vibrational Spectroscopy*, 51 (2009)270-275
- [16] Melissa A. Page and W. Tandy Grubbs, *J. Educ.*, 76(5), p.666 (1999)
- [17] *Modern Spectroscopy*, 2nd Edition, J.Michael Hollas, ISBN: 471-93076-8.
- [18] Wikipedia, the free encyclopedia. *Infrared spectroscopy* <http://en.wikipedia.org> (July 28, 2007).
- [19] Mount Holyoke College, South Hadley, Massachusetts. *Forensic applications of IR* <http://www.mtholyoke.edu> (July 28, 2007)
- [20] T. Theophanides, *Infrared and Raman Spectra of Biological Molecules*, NATO Advanced Study Institute, D. Reidel Publishing Co. Dodrecht, 1978,372p.
- [21] T. Theophanides, C. Sandorfy) *Spectroscopy of Biological Molecules*, NATO Advanced Study Institute, D. Reidel Publishing Co. Dodrecht, 1984 , 646p
- [22] T. Theophanides *Fourier Transform Infrared Spectroscopy*, D. Reidel Publishing Co. Dodrecht, 1984.
- [23] T. Theophanides, *Inorganic Bioactivators*, NATO Advanced Study Institute, D. Reidel Publishing Co. Dodrecht, 1989,415p
- [24] G. Vergoten and T. Theophanides, *Biomolecular Structure and Dynamics: Recent experimental and Theoretical Advances*, NATO Advanced Study Institute, Kluwer Academic Publishers, The Netherlands, 1997, 327p
- [25] C. Conti, P. Ferraris, E. Giorgini, C. Rubini, S. Sabbatini, G. Tosi, J. Anastassopoulou, P. Arapantoni, E. Boukaki, S FT-IR, T. Theophanides, C. Valavanis, FT-IR Microimaging Spectroscopy:Discrimination between healthy and neoplastic human colon tissues , *J. Mol Struc.* 881 (2008) 46-51.
- [26] M. Petra, J. Anastassopoulou, T. Theologis & T. Theophanides, Synchrotron micro-FT-IR spectroscopic evaluation of normal paediatric human bone, *J. Mol Structure*, 78 (2005) 101
- [27] P. Kolovou and J. Anastassopoulou, "Synchrotron FT-IR spectroscopy of human bones. The effect of aging". *Brilliant Light in Life and Material Sciences*, Eds. V. Tsakanov and H. Wiedemann, Springer, 2007 267-272p.
- [28] T. Theophanides, J. Anastassopoulou and N. Fotopoulos, *Fifth International Conference on the Spectroscopy of Biological Molecules*, Kluwer Academic Publishers, Dodrecht, 1991,409p

Section 1

Minerals and Glasses

Using Infrared Spectroscopy to Identify New Amorphous Phases – A Case Study of Carbonato Complex Formed by Mechanochemical Processing

Tadej Rojac¹, Primož Šegedin² and Marija Kosec¹

¹Jožef Stefan Institute

*²Faculty of Chemistry and Chemical Technology,
University of Ljubljana
Slovenia*

1. Introduction

1.1 Mechanochemistry and high-energy milling

Since the first laboratory experiments of M. Carey Lea and the original definition by F. W. Ostwald at the end of the 19th century, mechanochemistry, a field treating chemical changes induced in substances as a result of applied mechanical stress, has been evolved as an important area of chemistry from the viewpoint of both the fundamental research and applications (Takacs, 2004; Boldyrev & Tkačova, 2000). Whereas the fundamentals of mechanochemistry are still being extensively explored, the mechanical alloying, a powder metallurgy process involving ball milling of particles under high-energy impact conditions, met the commercial ground as early as in 1966 and was used to produce improved nickel- and iron-based alloys for aerospace industry (Suryanarayana et al., 2001). In addition to metallurgy, the science and technology of mechanochemical processes are continuously developing within various other fields, including ceramics processing, processing of minerals, catalysis, pharmaceuticals, and many others.

Due to simplicity and technological reasons, the most common way to apply mechanical stress to a solid is via ball-particle collisions in a milling device. This is often referred to as the “high-energy milling” technique. What distinguishes this method from the classical “wet ball-milling”, used primarily for reducing particle size and/or mixing components, is that a powder or mixture of powders is typically milled in liquid-free conditions; under such circumstances, a larger amount of the kinetic energy of a moving ball inside a grinding bowl is transferred to the powder particles during collisions; this is also the origin of the term “high-energy” milling. Owing to the feasibility to conduct chemical reactions by high-energy milling, an often used term in the literature is “mechanochemical synthesis”.

To carry out mechanochemical processes, various types of milling devices are used, including shaker, planetary, horizontal, attrition mill, etc. (Lu & Lai, 1998). One of the most

used, in particular for research purposes, is the planetary ball mill (Fig. 1a). A schematic view of the ball motion inside a grinding bowl of a planetary mill is illustrated in Fig. 1b. This characteristic ball motion results from two types of rotations: i) rotation of the grinding bowl around its center and ii) rotation of the supporting disc to which the bowls are attached; the two rotational senses are opposite (see Fig. 1b). In such a rotational geometry, the forces acting on the milling balls result into a periodical ball movement, illustrated by arrows in Fig. 1b, during which, when certain conditions are met, the balls are detached from the bowl's internal surface, colliding onto the powder particles on the opposite side. Even if simplified, the mathematical model derived from such an idealized ball movement agreed well with the experimental measurements of power consumption during milling (Burgio et al., 1991; Iasonna & Magini, 1996). In addition, this periodical movement was confirmed by numerical simulations (Watanabe et al., 1995a) and high-speed video camera recordings (Le Brun et al., 1993).

The high energy released during ball-powder collisions leads to various phenomena in the solid; this includes creation of a large amount of defects in the crystal structure, amorphization or complete loss of long-range structural periodicity, plastic and elastic deformation of particles, decrease of particle size down to the nanometer scale, increase of specific surface area of the powders, polymorphic transitions and even chemical reactions (Fig. 1c). Such changes result in distinct powder properties. The so-called mechanochemical reactions, which take place directly during the milling process without any external supply of thermal energy, make the method particularly interesting and distinguished from other conventional synthesis methods, which are typically based upon thermally driven reactions.

Due to their complexity, understanding mechanochemical reactions and the underlying mechanisms is a difficult task. In addition to local heating, provided by the high-energy collisions, modelling of the high-energy milling process revealed a large increase of pressure at the contact area between two colliding milling balls, which can reach levels of up to several GPa. It should be noted that both temperature and pressure rise are realized in tenths of microseconds, an estimated duration of a collision, illustrating the non-equilibrium nature of the mechanochemical process (Maurice & Courtney, 1990). Actually, during high-energy collisions the powder particles are subjected to a combination of hydrostatic and shear stress components, which further complicate the overall picture, even in apparently simple cases, such as polymorphic phase transitions. It was shown, for example, that conventional thermodynamic phase diagrams cannot be applied for polymorphic phase transitions realized during high-energy milling (Lin & Nativ, 1979). In fact, the classical hydrostatic-pressure-temperature (p - T) phase diagram, e.g., in the case of a polymorphic transition between litharge and massicot forms of PbO, is considerably altered by introducing the shear component into the calculations; a two-phase field region appears in the phase diagram, suggesting co-existence of the two polymorphs, rather than a sharp transition line characteristic for the conventional PbO p - T diagram. This might explain the often observed co-existence of two polymorphic modifications upon prolonged milling when "steady-state" milling conditions are reached (Lin & Nativ, 1979; Iguchi & Senna, 1985). The influence of shear stress and local temperature rise on more complex mechanochemical reactions are still subject of intensive discussions.

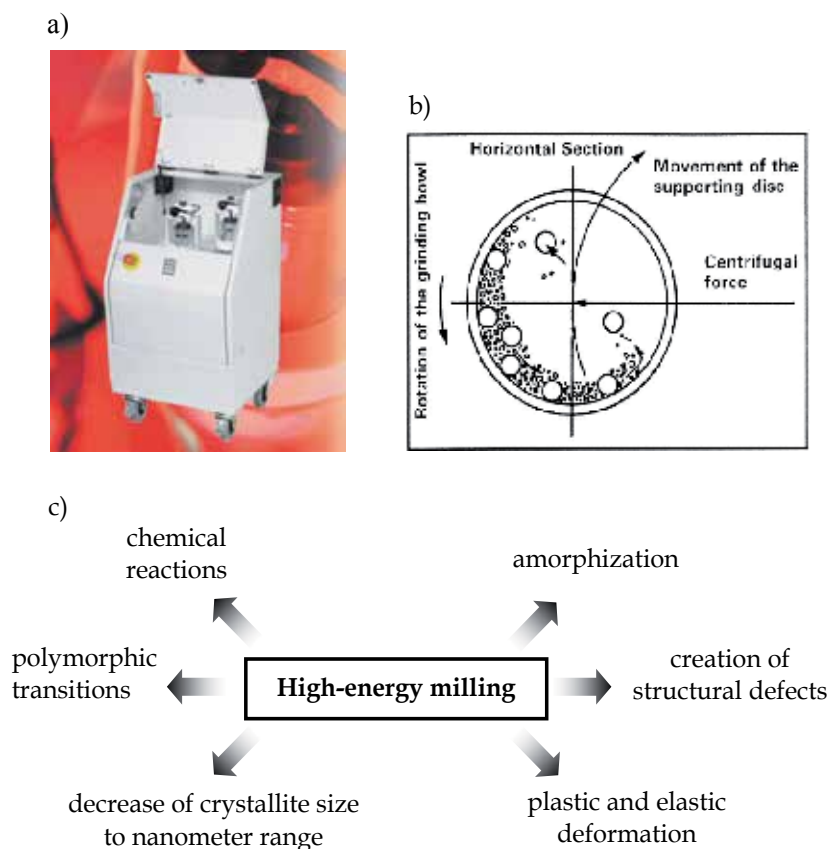


Fig. 1. a) Laboratory-scale planetary mill Fritsch Pulverisette 4, b) schematic representation of the movement of milling balls in a planetary mill (from Suryanarayana, 2001) and c) characteristic phenomena taking place in the solids as a result of high-energy collisions.

1.2 Mechanochemical synthesis of complex ceramic oxides and underlying reaction mechanisms

Mechanochemical synthesis (or high-energy milling assisted synthesis) has been found particularly useful for the synthesis of ceramic oxides with complex chemical composition, ranging from ferroelectric, magnetic and multiferroic oxides to oxides exhibiting semiconducting and catalytic properties. For an overview of the research activity in this field the reader should consult Kong et al. (2008) and Sopicka-Lizer (2010).

Whereas, in general, extensive literature data can be found on the mechanochemical synthesis of complex oxides, only limited studies are devoted to the understanding of mechanochemical reaction mechanisms. Primarily driven by the need to enrich our fundamental knowledge of mechanochemistry, the studies of reaction mechanisms have also been found to be essential in order to efficiently design a mechanochemical process, which includes the selection of milling parameters, milling regime, etc. (Rojac et al., 2010).

One of the main difficulties in analyzing the complex mechanisms of mechanochemical reactions is the identification of amorphous phases, which are metastable and appear often transitional with respect to the course of the reaction. To illustrate an example, we present in Fig. 2 the mechanochemical synthesis of KNbO_3 from a powder mixture of K_2CO_3 and Nb_2O_5 (Rojac et al., 2009). In the first 90 hours of milling, the initial crystalline K_2CO_3 and Nb_2O_5 (Fig. 2a, 0 h) are transformed into an amorphous phase, characterized by two broad “humps” centred at around 29° and 54° 2-theta (Fig. 2a, 90 h). The formation of the amorphous phase was confirmed by transmission electron microscopy (TEM), i.e., an amorphous matrix was observed with embedded nanocrystalline particles of Nb_2O_5 (Fig. 2b), which is consistent with the X-ray diffraction (XRD) pattern (Fig. 2a, 90 h). Further milling from 90 to 350 hours resulted in the crystallization from the amorphous phase; this is evident from the appearance of new peaks after 150 and 350 hours of milling, which were assigned to various potassium niobate phases with different K/Nb molar ratio (Fig. 2a, 150 and 350 h). Therefore, the amorphous phase represents a transitional phase of the reaction. In addition, comparison of the 90-hours milled K_2CO_3 - Nb_2O_5 mixture (Fig. 2a, 90 h) with the

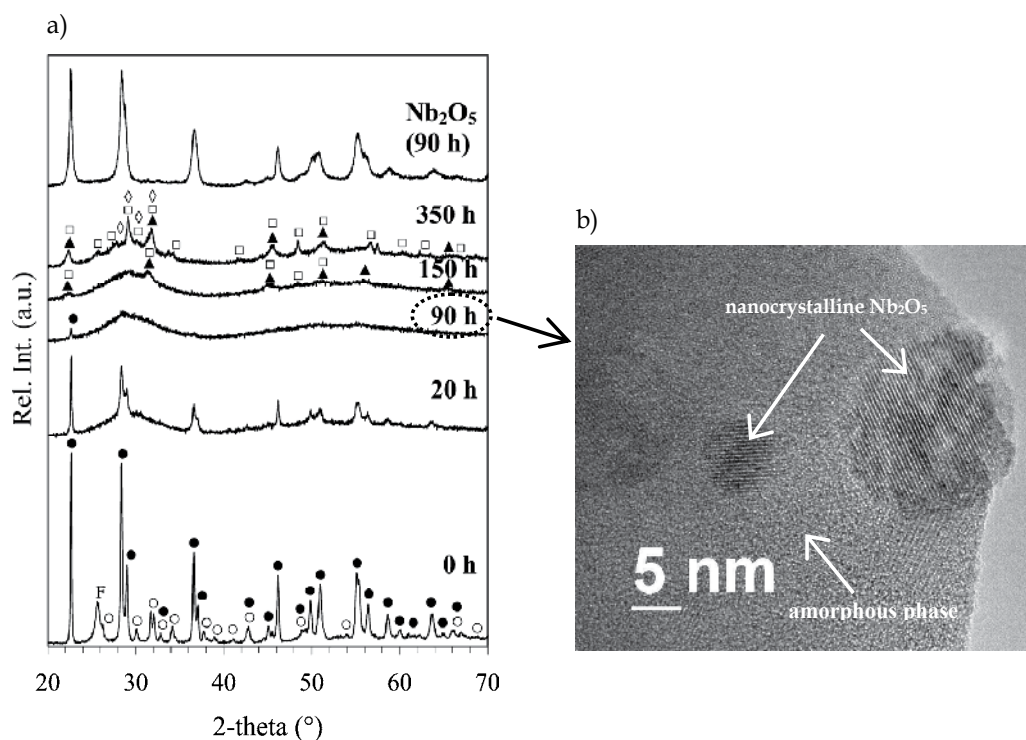


Fig. 2. a) XRD patterns of K_2CO_3 - Nb_2O_5 powder mixture after high-energy milling for 20, 90, 150 and 350 hours. The non-milled mixture is denoted as “0 h”. The pattern of the 90-hours-separately-milled Nb_2O_5 is added for comparison. In order to prevent adsorption of water during XRD measurements, a polymeric foil was used to cover the non-milled powder mixture. b) TEM image of the K_2CO_3 - Nb_2O_5 powder mixture after high-energy milling for 90 hours. Notations: K_2CO_3 (\circ , PDF 71-1466), Nb_2O_5 (\bullet , PDF 30-0873), KNbO_3 (\blacktriangle , PDF 71-0946), $\text{K}_6\text{Nb}_{10.88}\text{O}_{30}$ (\square , PDF 87-1856), $\text{K}_8\text{Nb}_{18}\text{O}_{49}$ (\diamond , PDF 31-1065), polymeric foil (F); “h” denotes milling hours (from Rojac et al., 2009).

90-hours separately milled Nb_2O_5 (Fig. 2a, Nb_2O_5 90 h), revealed a much larger degree of amorphization of Nb_2O_5 when co-milled with K_2CO_3 ; note the considerably weaker Nb_2O_5 peaks and higher XRD background in the case of the mixture as compared to separately milled Nb_2O_5 . This suggests that the amorphization of Nb_2O_5 is not a consequence of the high-energy impacts only, but has its origin in the mechanochemical interaction with the carbonate. It should be emphasized that this is not an isolated case; examples involving transitional amorphous phases can also be found during mechanical alloying of mixture of metals (El-Eskandarany et al., 1997). Finally, a nucleation-and-growth mechanism from amorphous phase was recently proposed as a general concept to explain the mechanochemical synthesis of a variety of complex oxides, such as $\text{Pb}(\text{Zr}_{0.52}\text{Ti}_{0.48})\text{O}_3$, $\text{Pb}(\text{Mg}_{1/3}\text{Nb}_{2/3})\text{O}_3$, $\text{Pb}(\text{Zn}_{1/3}\text{Nb}_{2/3})\text{O}_3$, etc. (Wang et al., 2000a, 2000b; Kuscer et al., 2006). In order to understand mechanochemical reactions, it is thus indispensable to analyze more closely the transitional amorphous phase.

It is clear from the above considerations that the most often used and widely reported XRD analysis becomes insufficient to provide detailed information about amorphous phases. The benefits of in-depth studies of mechanochemical reaction mechanisms by selection of appropriate analytical tools, able to provide data on a short-range (local) structural scale, such as nuclear magnetic resonance (NMR), X-ray photoelectron spectroscopy (XPS), electron paramagnetic resonance (EPR) spectroscopy, infrared spectroscopy (IR), Raman spectroscopy, etc., were demonstrated by the pioneering work of Senna, Watanabe and co-workers (Watanabe et al., 1996, 1997; Senna, 1997). In those cases, the synthesis of selected complex oxide systems have been studied from starting mixtures comprising typically hydroxide and oxide compounds; extensive data on these studies can be found in Avvakumov et al. (2001).

Mechanochemical processing has recently provided important improvements in the synthesis of ceramic materials in the family of alkaline niobates tantalates, a rich group of materials exhibiting wide applicability; this includes KTaO_3 and $(\text{K,Na,Li})(\text{Nb,Ta})\text{O}_3$ (KNLNT), which are considered as promising materials for dielectric (microwave) and piezoelectric applications, respectively (Glinsek et al., 2011; Tchernychova et al., 2011; Rojac et al., 2008a, 2010). Since alkali carbonates are the most frequently used as starting alkali compounds, it naturally became of interest to understand in more details the mechanochemical reaction mechanisms in which carbonate ions (CO_3^{2-}) are involved. The results of these studies carry important practical consequences. For example, in the case of the synthesis of the complex KNLNT solid solution, it was demonstrated that the identification of the reaction mechanism during mechanochemical processing is a key step leading to highly homogeneous KNLNT ceramics with excellent piezoelectric response. After identifying an intermediate amorphous carbonato complex, to which the present chapter is particularly devoted, it was found that a homogeneous KNLNT can only be obtained by providing the formation of this complex during the high-energy milling step. In other words, milling conditions that did not lead to the formation of the carbonato complex, e.g., milling in the “friction” mode instead of the “friction+impact” mode, resulted into considerable Ta-inhomogeneities and, consequently, to a reduced piezoelectric response (Rojac et al., 2010).

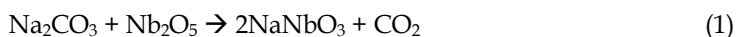
In this chapter we present an overview of the studies of reaction mechanisms in systems comprising CO_3^{2-} ions. The chapter aims primarily at showing the importance of combining various analytical methods, including quantitative XRD analysis, thermal analysis and

infrared spectroscopy, to obtain an overall picture of a complex reaction mechanism, such as the one encountered during mechanochemical processing. The first part of the chapter is devoted to the synthesis of NaNbO_3 from a mixture of Na_2CO_3 and Nb_2O_5 . After demonstrating the feasibility of synthesizing NaNbO_3 directly by high-energy milling, we show systematically how a mechanism can be revealed by a built-up of data from various analytical methods. The focus is to gain insight into the amorphous phase, which represents a transitional phase in the synthesis of NaNbO_3 . In the second part of the chapter we will extend the studies to other systems based on sodium carbonate, i.e., $\text{Na}_2\text{CO}_3\text{-M}_2\text{O}_5$ ($M = \text{V, Nb, Ta}$). The transition-metal oxides were selected through the 5th group of the periodic table to allow systematic comparisons and propose potentially a general reaction mechanism.

2. Mechanochemical reaction mechanism in the $\text{Na}_2\text{CO}_3\text{-Nb}_2\text{O}_5$ system studied by a combination of quantitative X-ray diffraction, thermal and infrared spectroscopy analysis

2.1 Quantitative X-ray diffraction analysis

The mechanochemical synthesis of NaNbO_3 from a $\text{Na}_2\text{CO}_3\text{-Nb}_2\text{O}_5$ mixture was followed by XRD analysis. Fig. 3 shows the XRD patterns of the $\text{Na}_2\text{CO}_3\text{-Nb}_2\text{O}_5$ mixture after selected milling times. The pattern of the non-milled mixture (Fig. 3, 0 h), which is a homogenized mixture of Na_2CO_3 and Nb_2O_5 powders just before mechanochemical treatment, can be fully indexed with the initial monoclinic Na_2CO_3 and orthorhombic Nb_2O_5 (Fig. 3, 0 h). The first 5 hours of high-energy milling are characterized by broaden peaks of the two reagents together with reduced peak intensity (Fig. 3, 5 h). After 40 hours of milling Na_2CO_3 was not observed anymore in the mixture, whereas traces of the newly formed NaNbO_3 were first detected (Fig. 3, 40 h). Further milling from 40 to 400 h led to a progressive disappearance of Nb_2O_5 from the mixture at the expense of the growing NaNbO_3 . Note the long milling time, i.e., 400 hours, needed to obtain the final NaNbO_3 free of any reagents (Fig. 3, 400 h). The low rate of the reaction between Na_2CO_3 and Nb_2O_5 resulted from the mild milling conditions, which were applied intentionally in order to enable a careful analysis of the individual reaction stages. It should be noted, however, that more intensive milling, resulting into NaNbO_3 after 32 hours of milling, did not change qualitatively the course of the reaction (for details see Rojac et al., 2008b). The results of the XRD analysis from Fig. 3 confirm the mechanochemical formation of NaNbO_3 according to the following reaction:



In order to obtain a more quantitative picture of the mechanochemical reaction, we performed a quantitative XRD phase analysis using the Rietveld refinement method. In addition to the amount of the crystalline phases, i.e., Na_2CO_3 , Nb_2O_5 and NaNbO_3 , we determined also the contribution from the XRD background, which we denoted as “XRD-amorphous” phase. This was done using an internal standard method; details of the method can be found in Kuscer et al. (2006) and Rojac et al. (2008b).

The results of the refinement analysis in terms of the amounts of Na_2CO_3 , Nb_2O_5 , NaNbO_3 and XRD-amorphous phase as a function of milling time are shown in Fig. 4. The amounts

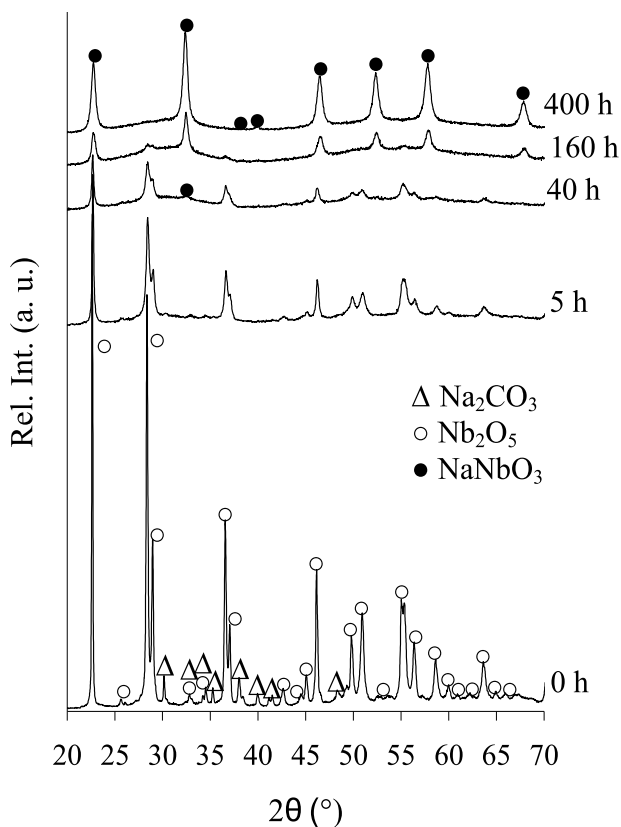


Fig. 3. XRD patterns of Na_2CO_3 - Nb_2O_5 powder mixture after high-energy milling for 5, 40, 160 and 400 hours. The non-milled mixture is denoted as "0 h". Notations: Na_2CO_3 (Δ , PDF 19-1130), Nb_2O_5 (\circ , PDF 30-0873) and NaNbO_3 (\bullet , PDF 33-1270); "h" denotes milling hours (from Rojac et al., 2008b).

of both Na_2CO_3 and Nb_2O_5 decrease with milling time (Fig. 4a). While Nb_2O_5 persists in the mixture up to 280 hours (Fig. 4a, closed rectangular), Na_2CO_3 is no longer detected after 20 hours of milling (Fig. 4a, open rectangular). The amount of the XRD-amorphous phase rapidly increases in the initial part of the reaction, reaching a maximum of 91% after 110 hours of milling, after which it decreases with further milling. Note the constant amount of the XRD-amorphous phase after reaching 600 hours of milling. The formation of NaNbO_3 follows a sigmoidal trend: at the beginning of the reaction the formation rate is low, after which it increases and slows down again in the final part of the reaction (Fig. 4b, open circles). Similarly like the XRD-amorphous phase, no differences in the amount of NaNbO_3 are observed with milling from 600 to 700 hours, suggesting a constant NaNbO_3 -to-amorphous-phase mass ratio upon prolonged milling.

From the quantitative analysis, shown in Fig. 4, an important observation can be derived by looking more closely at the initial stage of the reaction. An enlarged view of this part of the reaction is shown as inset in Fig. 4b. Here, we can see that in the initial 20 hours of milling, during which no NaNbO_3 was detected, a large amount, i.e., 73%, of the amorphous phase was formed. Only subsequently, i.e., after 40 hours of milling, NaNbO_3 was firstly detected.

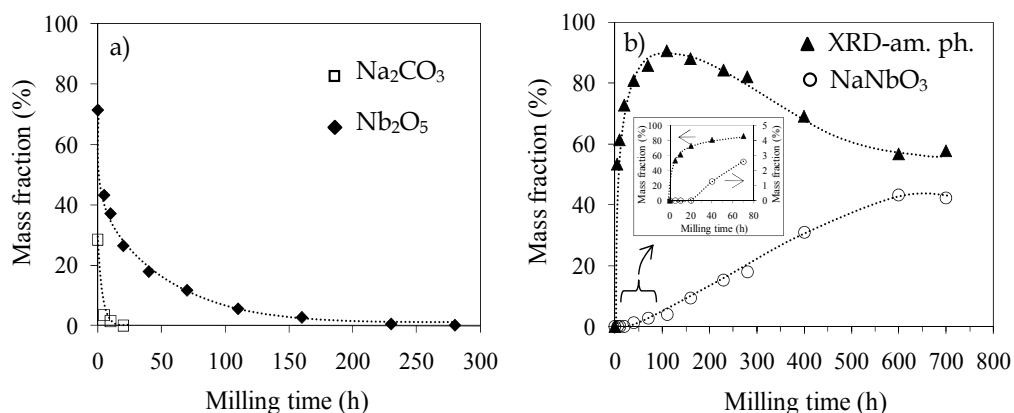


Fig. 4. Fractions of crystalline phases (Na_2CO_3 , Nb_2O_5 and NaNbO_3) and XRD-amorphous phase, determined by Rietveld refinement analysis, as a function of milling time. a) Na_2CO_3 and Nb_2O_5 , b) NaNbO_3 and XRD-amorphous phase. The inset of b) shows an enlarged view of the curves in the initial 80 hours of milling. The lines are drawn as a guide for the eye (from Rojac et al., 2008b).

From this simple observation we can infer that NaNbO_3 is not formed directly, like assumed by equation 1, but through an intermediate amorphous phase. The transitional nature of the amorphous phase is further confirmed by the maximum in its amount after 110 hours of milling. Moreover, literature data go in favour of our conclusions. In fact, based on studies of the kinetics, the sigmoidal trend, like that observed in the case of NaNbO_3 (Fig. 4b, open circles), is characteristic for multistep mechanochemical processes, such as the amorphization of a mixture of metals, where the phase transformation requires two or more impacts on the same powder fraction. In contrast, continuously decelerating processes, described by asymptotic kinetics, are typical for the amorphization of single-phase compounds, such as intermetallics, where the structure is already altered after the first impact (Delogu & Cocco, 2000; Cocco et al., 2000; Delogu et al., 2004). Therefore, independently of the analysis on the XRD-amorphous phase, the sigmoidal-like trend in the formation of NaNbO_3 (Fig. 4b, open circles) suggests that the niobate is formed via a transitional phase.

In addition to the XRD-amorphous phase, we shall look at the changes induced in the Na_2CO_3 in the initial part of milling. Fig. 5 compares the XRD patterns of the Na_2CO_3 - Nb_2O_5 mixture in the first 40 hours of milling (Fig. 5a) with the XRD patterns of Na_2CO_3 (Fig. 5b), which was high-energy milled alone, without Nb_2O_5 , with exactly the same milling conditions as the mixture. While the peaks of Na_2CO_3 when milled together with Nb_2O_5 completely disappeared after 20 hours of milling (see open triangles in Fig. 5a), this is clearly not the case even after 40 hours if Na_2CO_3 was milled alone (see Fig. 5b). The broader peaks of Na_2CO_3 after 40 hours of separate milling (Fig. 5b, 40 h) are most probably a consequence of reduced crystallite size and increase in microstrains due to creation of structural disorder. The disappearance of the original crystalline Na_2CO_3 from the mixture, suggesting amorphization, is therefore an effect triggered by the presence of Nb_2O_5 rather than a pure effect of the high-energy collisions. In relation to this mechanochemical

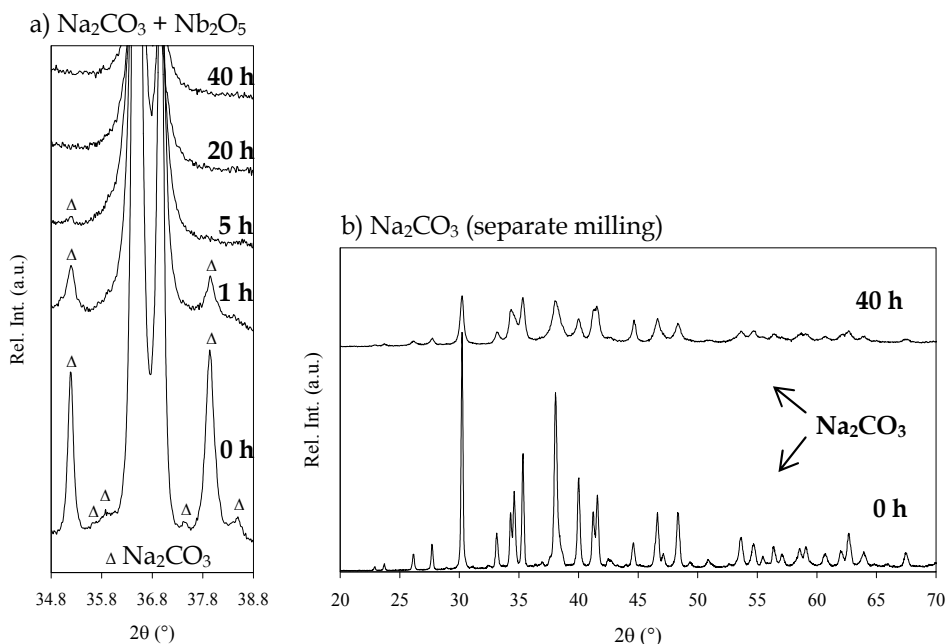


Fig. 5. XRD patterns of a) Na₂CO₃-Nb₂O₅ mixture and b) Na₂CO₃ after high-energy milling for up to 40 hours. The pattern in a) shows a narrow 2-theta region, i.e., from 34.8 to 38.8°, to highlight the changes upon milling in the peaks corresponding to Na₂CO₃. Note that all the peaks on the patterns of non-milled and 40-hours-separately-milled Na₂CO₃ in b) are indexed with monoclinic Na₂CO₃. Notation: Na₂CO₃ (Δ, PDF 19-1130); "h" denotes milling hours (from Rojac et al., 2006).

interaction between Na₂CO₃ and Nb₂O₅, a question that arises at this point is whether this interaction resulted into the carbonate decomposition. This is also relevant with respect to the nature of the amorphous phase. Obviously, further information could be obtained by following the decomposition of the carbonate during milling. This can be done using thermogravimetric (TG) analysis; the results of TG coupled with differential thermal analysis (DTA) and evolved-gas analysis (EGA) are presented in the following section.

2.2 Thermal analysis

In order to explore the origin of the reaction-induced amorphization and/or possible decomposition of Na₂CO₃ (Fig. 5) we were further focused on the initial part of milling, i.e., results are presented for the samples treated in the first 40 hours of milling.

Fig. 6 presents the thermogravimetric (TG), derivative thermogravimetric (DTG), differential thermal analysis (DTA) and evolved-gas analysis (EGA) curves of the Na₂CO₃-Nb₂O₅ powder mixture in the first 40 hours of high-energy milling. The non-milled Na₂CO₃-Nb₂O₅ mixture loses mass in several steps in a broad temperature range from 400 °C to 800 °C (Fig. 6a and b, 0 h). The total mass loss of this mixture upon annealing to 900 °C amounts to 11.7%, which agrees well with the theoretical mass loss of 11.8%, calculated according to equation 1 for the complete decomposition of Na₂CO₃ in an

equimolar mixture with Nb_2O_5 . The carbonate decomposition is further confirmed by EGA, which shows a release of CO_2 in the temperature range 400–800 °C (Fig. 6d, 0 h, full line). Note also that the DTG peaks (Fig. 6b, 0 h) coincide with the EGA(CO_2) peaks (Fig. 6d, 0 h, full line), showing that the measured mass loss in this sample is indeed entirely related to the decomposition of Na_2CO_3 , which is triggered by the reaction with Nb_2O_5 , like represented by equation 1.

High-energy milling resulted into several changes in the thermal behaviour of the Na_2CO_3 - Nb_2O_5 mixture. Firstly, by inspecting the TG curves, a mass loss appears in the milled samples in the temperature range 25–300 °C, which was not observed prior milling (Fig. 6a, compare milled samples with the non-milled). According to the DTA curves (Fig. 6c), these mass losses between room temperature and 300 °C are accompanied by endothermic heat effects, which first manifest as a sharp endothermic peak at around 100 °C (Fig. 6c, 1 h), progressively evolving with milling into a broader endothermic peak, which expands from 80 °C to 250 °C (see for example Fig. 6c, 40 h). According to EGA(H_2O), the mass losses in this low temperature range correspond to the removal of H_2O (Fig. 6d, milled samples, dashed lines). The amounts of H_2O removed from the samples milled for 0, 1, 5, 20, 40 hours, as determined from the TG curves (Fig. 6a, milled samples, 25–300 °C), are 0%, 2.5%, 4.0%, 4.8% and 5.1%, respectively. This suggests gradual adsorption of H_2O on the powder with increasing milling time; taking into account that the milling was performed in open air and also considering the hygroscopic nature of Na_2CO_3 , the adsorption of H_2O is not surprising. We note that the H_2O removal from the samples milled for longer periods, i.e., 5, 20 and 40 hours, takes place at temperatures higher than 100 °C (Fig. 6d, dashed lines), which might suggest water chemisorption rather than physical adsorption.

In addition to water adsorption, high-energy milling induced considerable changes in the thermal decomposition of the carbonate. This is best seen by inspecting the DTG and EGA (CO_2) curves of the milled samples (Fig. 6b and 6d, milled samples). Firstly, it should be noted that in the temperature range between 350 °C and 500 °C the DTG peaks of the milled mixtures (Fig. 6b, milled samples) coincide with those of EGA(CO_2) (Fig. 6d, milled samples, full lines), which means that the mass loss in this temperature range is related to the CO_2 removal, i.e., to the carbonate decomposition. For the sake of discussion, we consider in the following only the EGA(CO_2) curves (Fig. 6d, full lines). In contrast to the carbonate decomposition in the non-milled mixture (Fig. 6d, 0 h, 400–800 °C), occurring in several steps and in a broad temperature range, which is characteristic for a physical mixture of Na_2CO_3 and Nb_2O_5 particles (Jenko, 2006), the mixture milled for only 1 hour releases CO_2 in a much narrower temperature range, i.e., 400–500 °C (Fig. 6d, 1 h). We attribute this effect to the smaller particle size after 1 hour of milling, which is known to decrease considerably the decomposition temperature of Na_2CO_3 in the Na_2CO_3 - Nb_2O_5 mixture due to reduced diffusion paths (Jenko, 2006). In comparison with the 1-hour milled sample, upon milling for 5 hours only small changes are observed in the shape of the EGA(CO_2) peak (Fig. 6d, 5 h, 400–500 °C). After 20 hours of milling a new, weak EGA(CO_2) peak appears at 370 °C (Fig. 6d, 20 h), suggesting two-step carbonate decomposition; this peak then shifts to 400 °C upon 40 hours of milling (Fig. 6d, 40 h). Note that after 40 hours of milling the intense EGA(CO_2) peak at 420 °C becomes sharper in comparison with shorter milling times, i.e., 1, 5 and 20 hours, indicating a more uniform decomposition of the carbonate.

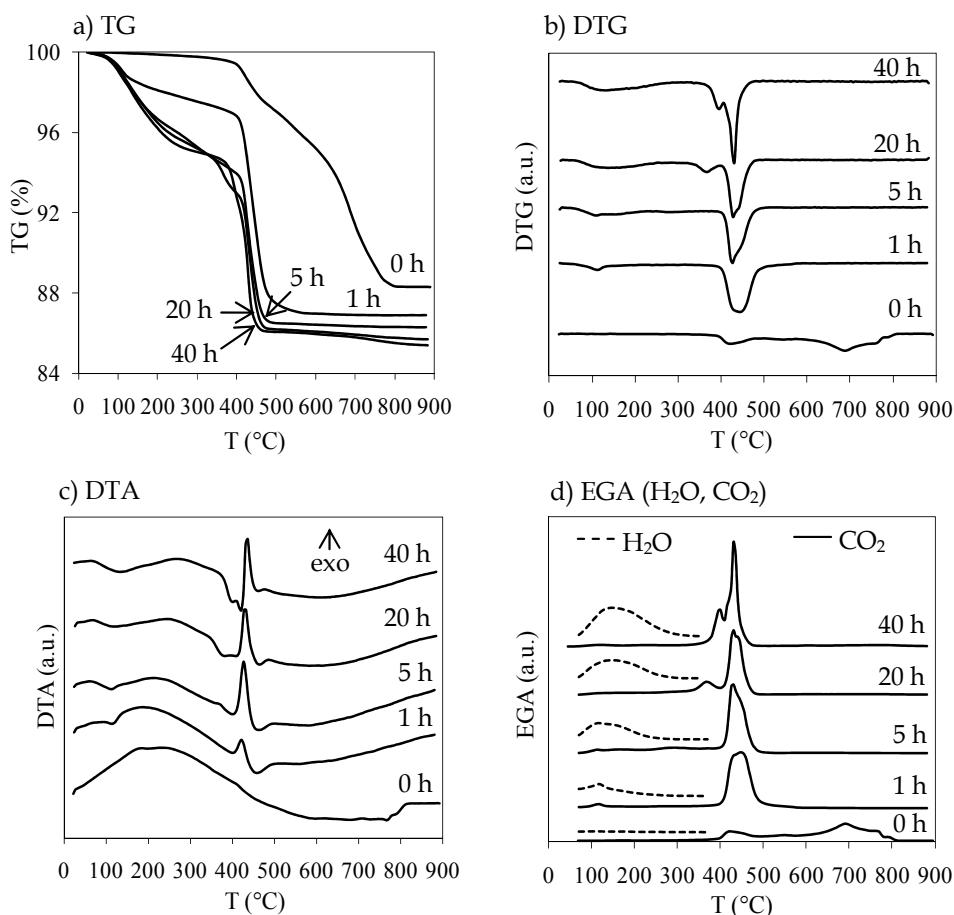


Fig. 6. a) TG, b) DTG, c) DTA and d) EGA(H_2O , CO_2) curves of the $\text{Na}_2\text{CO}_3\text{-Nb}_2\text{O}_5$ powder mixture after high-energy milling for 1, 5, 20 and 40 hours. The non-milled mixture is denoted as "0 h". Since the main EGA(H_2O) signal was observed in the temperature range 25–350 $^\circ\text{C}$ the data are plotted accordingly. "h" denotes milling hours (from Rojac et al., 2006).

According to DTA, the decomposition of the carbonate in the milled samples is accompanied by an exothermic heat effect (Fig. 6c, milled samples). This is seen from the sharp and intense exothermic peaks appearing in all the milled samples in the temperature range where the CO_2 is released, i.e., 400–500 $^\circ\text{C}$ (compare Fig. 6c with Fig. 6d).

To summarize, the DTA and EGA(CO_2) analyses on the milled samples (Fig. 6c and d, milled samples) suggest a rather defined carbonate decomposition occurring in a narrow temperature range, which is not typical for a physical mixture of Na_2CO_3 and Nb_2O_5 (compare 0 h with milled samples in Fig. 6c and 6d; see also Jenko, 2006); this indicates a change in the chemical state of the carbonate upon milling and formation of a new phase.

According to the mass loss related to the CO_2 release, which can be separated from the loss of H_2O by combining EGA and TG curves, we can calculate the amount of the residual

carbonate in the mixture, i.e., the amount of the carbonate that did not decompose during high-energy milling. The total CO_2 loss from the sample milled for 40 hours is 9.6%, corresponding to 85.0% of residual carbonate. Therefore, in the first 40 hours of milling, a minor amount of the carbonate decomposed, whereas the major part, according to XRD analysis (Fig. 5a), became amorphous. As mentioned in the previous section, the Na_2CO_3 amorphization is stimulated by the mechanochemical interaction with Nb_2O_5 . This observation, together with the characteristic changes in the decomposition of the carbonate upon milling (Fig. 6), indicates a formation of a new carbonate compound. As a next step, it seems reasonable to explore the symmetry of the CO_3^{2-} ions, which was done using infrared spectroscopy.

2.3 Infrared spectroscopy analysis

The IR spectra of the $\text{Na}_2\text{CO}_3\text{-Nb}_2\text{O}_5$ mixture before and after milling for various periods are shown in Fig. 7a. The two separate graphs in Fig. 7a show two different wavenumber regions, i.e., 950–1150 cm^{-1} and 1280–1880 cm^{-1} . The spectrum of the non-milled mixture is composed of a weak band at 1775 cm^{-1} and a strong one at 1445 cm^{-1} ; no bands are observed in the lower wavenumber region between 950 and 1150 cm^{-1} (Fig. 7a, 0 h). Based on the literature data, the spectrum of the non-milled mixture can be entirely indexed with

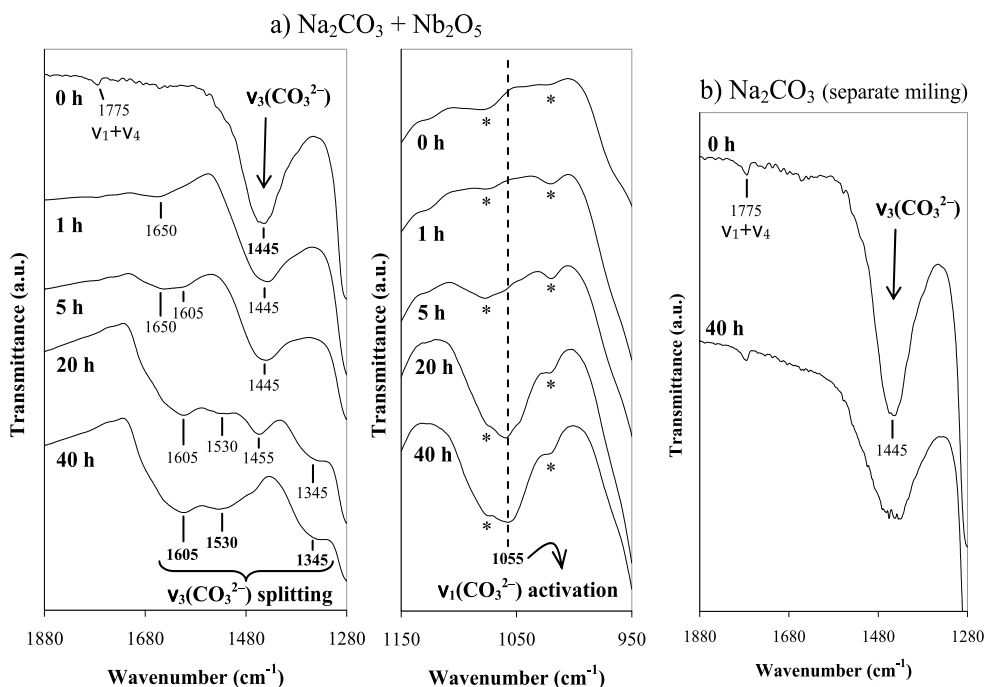


Fig. 7. FT-IR spectra of a) $\text{Na}_2\text{CO}_3\text{-Nb}_2\text{O}_5$ powder mixture after high-energy milling for 1, 5, 20 and 40 hours and (b) Na_2CO_3 subjected to separate high-energy milling for 40 hours. The non-milled powders are denoted as "0 h". Note that, in contrast to the $\text{Na}_2\text{CO}_3\text{-Nb}_2\text{O}_5$ mixture (a), no splitting of $\nu_3(\text{CO}_3^{2-})$ is observed in the case of the separately milled Na_2CO_3 (b). Notation: * Nujol, for bands assignment refer to Table 1; "h" denotes milling hours. (from Rojac et al., 2006).

vibrational bands of the CO_3^{2-} ions, present in the initial Na_2CO_3 (Harris & Salje, 1992; Gatehouse et al., 1958). This is consistent with the fact that Nb_2O_5 , which is also a part of the mixture, did not show any IR bands in the two examined wavenumber regions (the IR spectrum of Nb_2O_5 is not shown).

The IR vibrations of the free CO_3^{2-} ion having D_{3h} point group symmetry are listed in Table 1. The CO_3^{2-} ion possesses two stretching and two bending vibrational modes. The symmetrical C–O stretching vibration, denoted as ν_1 , is IR-inactive, while the ν_2 , ν_3 and ν_4 are IR-active. According to Harris & Salje (1992), and Table 1, the strongest band of the non-milled sample at 1445 cm^{-1} (Fig. 7a, 0 h) belongs to the asymmetrical C–O stretching vibration of CO_3^{2-} (ν_3), while the weak band at 1775 cm^{-1} can be assigned to the combinational band of the type $\nu_1+\nu_4$. No bands are observed in the $950\text{--}1150\text{ cm}^{-1}$ region (Fig. 7a, 0 h), consistent with absence of the IR-inactive ν_1 vibration. With the exception of some differences in the position, the bands of the non-milled mixture, which belong to Na_2CO_3 , are consistent with vibrations characteristic for the free CO_3^{2-} ion with D_{3h} symmetry. This is in agreement with the literature data and was explained as being a consequence of the small effect of the crystal field of Na^+ ions on the symmetry of the CO_3^{2-} in the Na_2CO_3 structure. This is somewhat different, for example, in Li_2CO_3 , where a stronger interaction between crystal lattice and CO_3^{2-} ions leads to lowered CO_3^{2-} symmetry and, consequently, to a more complex IR spectrum (Buijs & Schutte, 1961; Brooker & Bates, 1971).

Type of vibration	Notation	Wavenumber (cm^{-1})
C–O symmetrical stretching	$\nu_1 (A_1')$	1063
Out-of-plane CO_3^{2-} bending	$\nu_2 (A_2'')$	879
C–O asymmetrical stretching	$\nu_3 (E')$	1415
In-plane CO_3^{2-} bending	$\nu_4 (E')$	680

Table 1. Fundamental IR vibrations of carbonate (CO_3^{2-}) ion with D_{3h} symmetry. ν_2 , ν_3 and ν_4 are IR-active vibrations, while ν_1 is IR-inactive (Gatehouse et al., 1958; Nakamoto, 1997).

Upon milling the $\text{Na}_2\text{CO}_3\text{--Nb}_2\text{O}_5$ mixture, considerable changes can be observed in the IR spectra (Fig. 7a, milled samples). After 1 hour of milling a new weak band appears at 1650 cm^{-1} . The position of this band coincides with one of the strongest HCO_3^- bands typical for alkaline hydrogencarbonates (Watters, 2005). This is in agreement with the simultaneous loss of H_2O and CO_2 upon annealing this sample (Fig. 6d, 1 h), which is characteristic for the hydrogencarbonate decomposition. Furthermore, we should not eliminate the possibility of having the in-plane bending vibration of H_2O , which also appears near 1650 cm^{-1} (Veniaminov & Prendergast, 1997).

By further milling from 1 hour to 40 hours related and simultaneous trends can be noted: i) the $\nu_3(\text{CO}_3^{2-})$ vibration shifts from 1445 cm^{-1} (Fig. 7a, 1 and 5 h) to 1455 cm^{-1} (Fig. 7a, 20 h) and decreases in intensity until it completely disappears after 40 h of milling, ii) the ν_3 vibration is gradually replaced by new absorption bands appearing at 1605 , 1530 and 1345 cm^{-1} (Fig. 7a, 40 h), and iii) a new band arises during milling, located at 1055 cm^{-1} , which belongs to the symmetrical C–O stretching vibration of the CO_3^{2-} ions (ν_1) (Fig. 7a, see region $950\text{--}1150\text{ cm}^{-1}$). We can conclude from these results that milling induced a splitting of ν_3 and activation of ν_1 vibrations, suggesting a change of the CO_3^{2-} symmetry from the

original D_{3h} . We shall come back to this point after examining the fundamental relation between symmetry and IR vibrations of the carbonate ion.

An extensive review on the IR spectroscopic identification of different species arising from the reactive adsorption of CO_2 on metal oxide surfaces can be found in Busca & Lorenzelli, 1982. In principle, the carbonate ion is a highly versatile ligand, which gives rise not only to simple mono- or bidentate structures, but also to a number of more complicated bidentate bridged structures. Some examples of CO_3^{2-} coordinated configurations are schematically illustrated in Fig. 8.

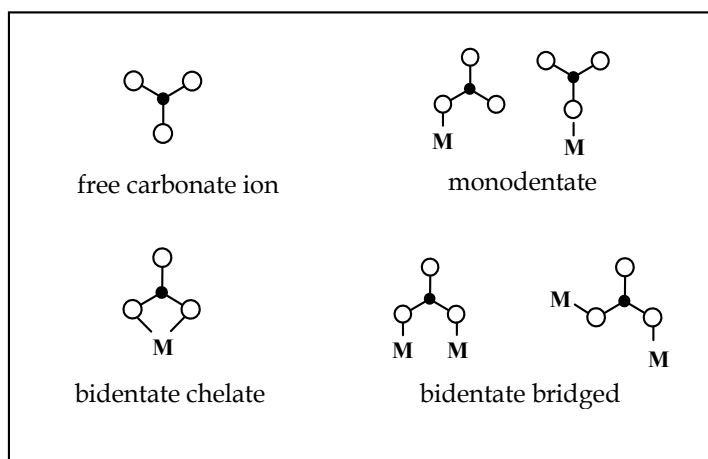


Fig. 8. Schematic view of free (non-coordinated) and various types of coordinated CO_3^{2-} ions.

When the CO_3^{2-} ion is bound, through one or more of its oxygens, to a metal cation (denoted as "M" in Fig. 8), its point group symmetry is lowered. It is well known from the literature that the lowering of the CO_3^{2-} symmetry, resulting from the coordination of the carbonate ion in a carbonato complex, causes the following changes in the IR vibrational modes of the free carbonate ion (Gatehouse et al., 1958; Hester & Grossman, 1966; Brintzinger & Hester, 1966; Goldsmith & Ross, 1967; Jolivet et al., 1980; Busca & Lorenzelli, 1982; Nakamoto, 1997):

1. Activation of IR-inactive ν_1 vibration
2. Shift of ν_2 vibration
3. Splitting of ν_3 vibration
4. Splitting of ν_4 vibration

The most characteristic of the above IR spectroscopic changes upon CO_3^{2-} coordination is the infrared activation of the ν_1 , i.e., the symmetrical C-O stretching vibration. This vibration, as mentioned earlier, is IR-inactive for the free carbonate ion, but also for most alkali, alkaline-earth and heavy-metal carbonates; it appears as a weak band only in certain carbonates of the aragonite type (Gatehouse et al., 1958). To derive the relation between symmetry and IR vibrations, we shall first look at the details of the ν_1 vibration. According to the IR selection rule, which states that *the vibration is IR-active if the dipole moment is changed during vibration*, we can understand that there will be no net change in the dipole moment during symmetrical C-O stretching vibration (ν_1) of the CO_3^{2-} ion with D_{3h}

symmetry; this comes from the equivalence of the three C–O bonds, which is schematically illustrated in Fig. 9 (bottom-left quadrant). The equivalence of these three C–O bonds is lost upon coordination, so that typically the C–O bond coordinated to the metal cation becomes weaker, while the C–O bonds not involved in metal binding becomes stronger with respect to the C–O bond in the free, non-coordinated, CO_3^{2-} ion (Fig. 9, upper-right quadrant) (Fujita et al., 1962; Brintzinger & Hester, 1966). This in turn leads to lowered CO_3^{2-} symmetry, e.g., from D_{3h} to C_{2v} , and to the activation of the ν_1 vibration (Fig. 9, bottom-right quadrant). In the case of monodentate coordination, also the C_s symmetry is possible and arises when the M–O–C bond is not collinear (Fig. 9, upper-right quadrant); same IR spectroscopic changes also apply for this case (Fujita et al., 1962; Nakamoto, 1997).

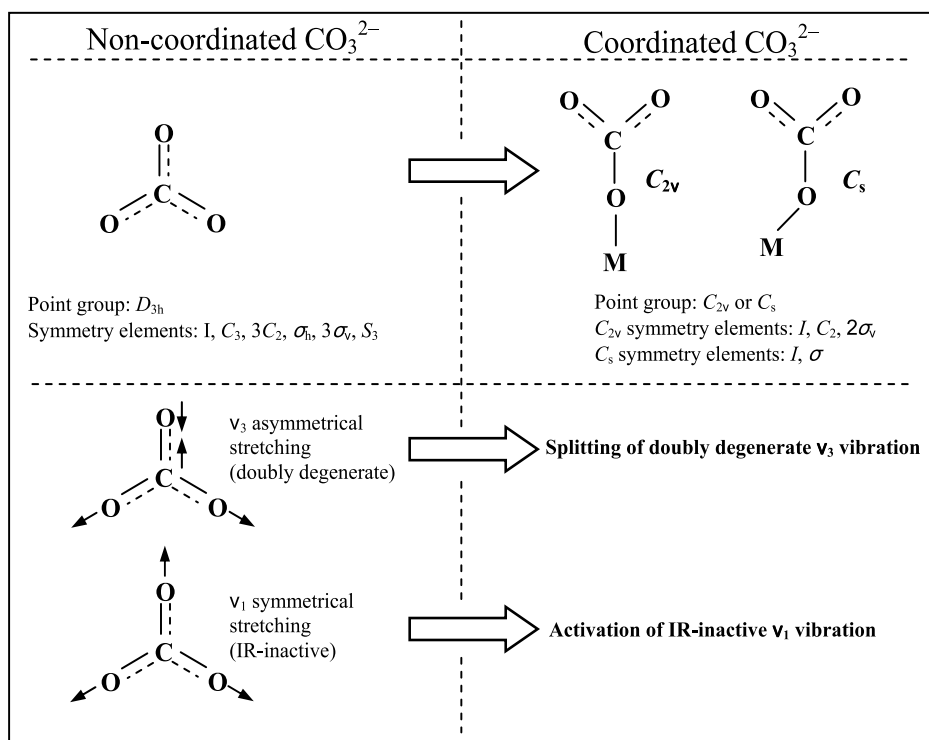


Fig. 9. Schematic representation of non-coordinated and coordinated CO_3^{2-} ion and the corresponding point group symmetry elements. The changes in the ν_1 and ν_3 IR vibrations of the CO_3^{2-} ion upon coordination are also shown. For simplicity, only monodentate coordination is presented. Notations: I – identity, C_n – n -fold axis of rotation, σ_h, σ_v – mirror planes perpendicular and parallel to the principal axis, respectively, S_n – n -fold rotation-reflection operation. The number preceding the symmetry operation symbol refers to number of such symmetry elements that the molecule possesses. For further details consult Nakamoto, 1997.

In parallel with the ν_1 activation, also the splitting of the ν_3 vibration occurs upon coordination. In the free CO_3^{2-} ion, the ν_3 vibration is doubly degenerate (Fig. 9, bottom-left quadrant). Doubly degenerate vibrations occur only in molecules possessing an axis higher than twofold, which is the case of the D_{3h} symmetry, having a three-fold rotational axis (see

Fig. 9, upper-left quadrant; C_3 – three-fold axis) (Nakamoto, 1997). The lowering of the symmetry of the carbonate ion from D_{3h} to either C_{2v} or C_s , which means loss of the equivalence of the three C–O bonds in the CO_3^{2-} and, therefore, loss of the three-fold rotational axis, leads to the separation (splitting) of the doubly degenerate vibrations (Fig. 9, bottom-right quadrant).

With respect to the changes upon coordination in the other two vibrational modes, i.e., ν_2 and ν_4 , it should be noted that the splitting of the ν_4 vibration has been studied to a lesser extent in comparison with the characteristic ν_3 splitting. In addition, the shift of the ν_2 vibration upon coordination is typically small and the values for complexes do not differ greatly in comparison with those of simple carbonates (Gatehouse et al., 1958).

Coming back to our case from Fig. 7a, we can interpret the ν_3 splitting and ν_1 activation of the CO_3^{2-} vibrations during milling of the Na_2CO_3 - Nb_2O_5 mixture as characteristic of lowered CO_3^{2-} symmetry, which is related to the mechanochemical formation of a carbonato complex. For comparison, we compiled in Table 2 the data of a number of carbonato complexes, with metals such as Cu and Co, provided from the literature. According to the notation of the coordinated C_{2v} symmetry, the ν_3 vibration of the D_{3h} symmetry is now split into two components, which are denoted as ν_1 and ν_4 (second and third column in Table 2); the activated ν_1 vibration becomes ν_2 (fourth column in Table 2). The regions in which the carbonato complex absorption bands appear are 1623-1500 cm^{-1} , 1362-1265 cm^{-1} (ν_3 splitting) and 1080-1026 cm^{-1} (ν_1 activation) (Table 2). By comparing these data with our case, we can observe that the ν_3 split bands at 1605, 1530 and 1345 cm^{-1} , and the ν_1 activated band at 1055 cm^{-1} from Fig. 7a (40 h) fall entirely within the wavenumber regions of carbonato complexes from Table 2.

Carbonato complex	$\nu_4(B_2)$ (cm^{-1})	$\nu_1(A_1)$ (cm^{-1})	$\nu_2(A_1)$ (cm^{-1})
$Na_2Cu(CO_3)_2$	1500	1362	1058
$Na_2Cu(CO_3)_2 \cdot 3H_2O$	1529	1326	1066, 1050
$K_3Co(CO_3)_3 \cdot 3H_2O$	1527	1330	1080, 1037
$KCo(NH_3)_2(CO_3)_2$	1623, 1597	1265	1026
$Co(NH_3)_6Co(CO_3)_3$	1523	1285	1073, 1031
$Co(NH_3)_4CO_3Cl$	1593	1265	1030
$Co(NH_3)_4CO_3ClO_4$	1602	1284	not reported

Table 2. Some copper and cobalt carbonato complexes and the corresponding IR absorption bands related to CO_3^{2-} vibrations. ν_1 , ν_2 and ν_4 correspond to vibrations of CO_3^{2-} in the C_{2v} symmetry notation; according to this notation, the doubly degenerate ν_3 vibration of the free CO_3^{2-} ion, which splits into two components, is denoted as ν_1 and ν_4 , whereas the activated ν_1 vibration is denoted as ν_2 (data compiled from Gatehouse et al., 1958; Fujita et al., 1962; Jolivet et al., 1982; Healy & White, 1972).

It is important to note that, in contrast to the Na_2CO_3 - Nb_2O_5 mixture, the ν_3 vibration did not split when Na_2CO_3 was milled alone, i.e., without Nb_2O_5 . This is seen in Fig. 7b, which shows the IR spectra of Na_2CO_3 before and after separate milling. Except for the reduced intensity, which might be related to the decreased crystallite size and structural disordering

induced by milling, the ν_3 band at 1445 cm^{-1} is still present after 40 hours of separate milling. We emphasize that for this separate Na_2CO_3 milling the same milling conditions and same milling time, i.e., 40 hours, were applied as for the $\text{Na}_2\text{CO}_3\text{-Nb}_2\text{O}_5$ mixture. Therefore, the lowering of the CO_3^{2-} symmetry and the corresponding coordination of the CO_3^{2-} ions can only be explained by the presence of Nb_2O_5 or, in other words, by the participation of Nb^{5+} as central cation.

The mechanochemical formation of the carbonato complex is further supported by XRD analysis. By comparing XRD and IR data, we find that the ν_3 splitting and ν_1 activation, which took place progressively from 5 to 40 hours of milling (Fig. 7a), coincide with the amorphization of Na_2CO_3 (Fig. 5a). For example, after 20 hours of milling, when the split ν_3 bands are resolved for the first time and intense ν_1 band appeared (Fig. 7a, 20 h), the XRD peaks of Na_2CO_3 could not be detected anymore (Fig. 5a, 20 h). From this comparison we can conclude that the amorphization of Na_2CO_3 is closely related to the formation of the complex. The conclusion seems reasonable if we consider that the formation of the complex requires a reconstruction, i.e., coordination, of the CO_3^{2-} ions; such reconstruction can eventually ruin the original Na_2CO_3 structure over the long range, make it undetectable to X-ray diffraction. The relation between amorphization and coordination is further supported by the fact that neither the amorphization of Na_2CO_3 nor the ν_3 splitting were observed during separate milling of Na_2CO_3 (see Fig. 5b and Fig. 7b).

We finally note that after 40 hours of milling the powder mixture contains 81% of XRD-amorphous phase (inset of Fig. 4b). According to this large amount and based on the fact that we did not detect any new crystalline phase during 40 hours of milling we can conclude that the carbonato complex is amorphous or eventually nanocrystalline to an extent that is undetectable with X-ray diffraction methods. This example illustrates that enriched information on a local structural scale can only be achieved by appropriate selection of analytical tools. The amorphous carbonato complex has recently been confirmed using Raman and nuclear magnetic resonance (NMR) spectroscopies (Rojac et al., to be published).

Another important aspect to discuss is the possible role of water on of the formation of the complex. Jolivet et al. (1982) emphasized the influence of the water molecules on the ν_3 splitting, which can be significant, depending on whether they can interact via hydrogen bonding with the carbonate group. This was demonstrated through various examples of lanthanide carbonates, where the hydrated forms showed different ν_3 splitting with respect to their dehydrated analogues. As an example, the hydrated form of the $\text{Na}_2\text{Cu}(\text{CO}_3)_2$ complex, that is $\text{Na}_2\text{Cu}(\text{CO}_3)_2\cdot 3\text{H}_2\text{O}$, showed larger $\Delta\nu_3$ splitting, i.e., 203 cm^{-1} , in comparison with its dehydrated form, i.e., 138 cm^{-1} (see also Table 2, first two examples).

In our case, the possible influence of water molecules on the carbonate ion should be considered. In fact, we showed in section 2.2 (Fig. 6) that an amount of water was introduced in the sample from the air during the milling. Therefore, we have to examine more carefully the possible influence of water adsorption on the ν_3 splitting. This was done by quenching the 40-hours-treated sample in air from different temperatures so that controlled amounts of water were released; the quenched samples were then analyzed using IR spectroscopy. The IR spectra together with the TG and EGA curves are shown in Fig. 10. The mass losses after quenching at $100\text{ }^\circ\text{C}$, $170\text{ }^\circ\text{C}$ and $300\text{ }^\circ\text{C}$ were 0.8 %, 3.1 % and 5.0 %, respectively.

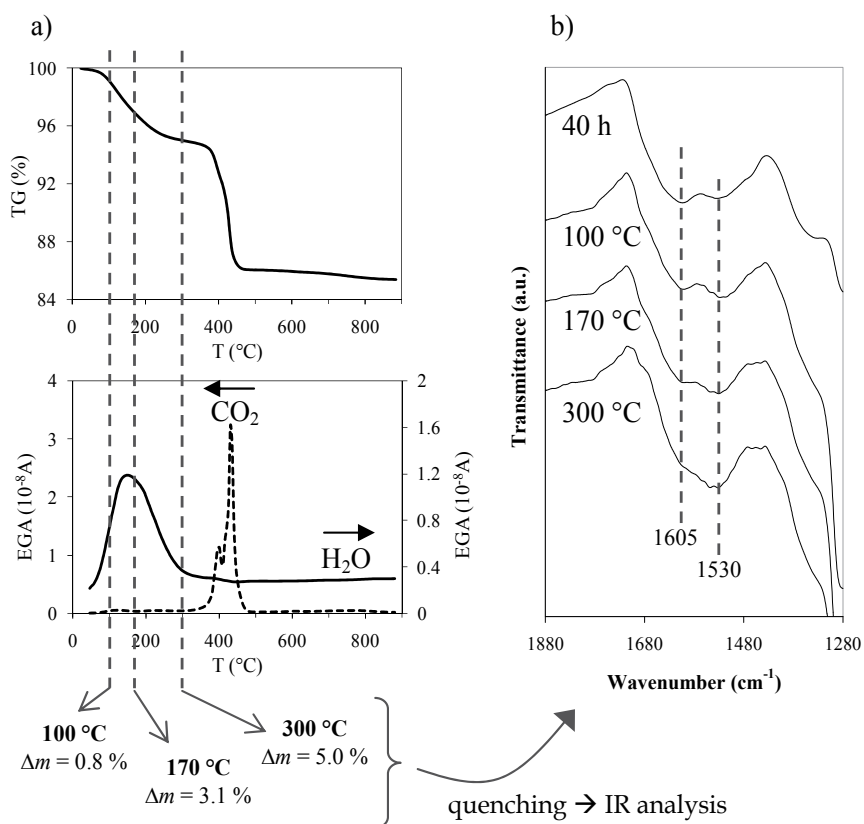


Fig. 10. a) TG and EGA(H_2O, CO_2) curves of the 40-hours high-energy milled $Na_2CO_3-Nb_2O_5$ powder mixture. The dashed lines on the graphs represent the temperatures at which the 40-hours milled sample was air-quenched. b) FT-IR spectra of the 40-hours high-energy milled $Na_2CO_3-Nb_2O_5$ powder mixture air-quenched from various temperatures (from Rojac et al., 2006).

respectively. According to EGA, these mass losses correspond entirely to the removal of water (Fig. 10a, see dashed lines). From Fig. 10b we can see that with increasing amount of released H_2O the band at 1605 cm^{-1} gradually decreases at the expense of the band at 1530 cm^{-1} . Note that the intensity of the band at 1345 cm^{-1} decreases, too. The results confirm the influence of H_2O on the splitting of the ν_3 vibration.

There are some cases of carbonato complexes, as pointed out by Jolivet et al. (1982), in which water molecules can even modify the coordination state of the carbonate ion. This is also the case of the $Na_2Cu(CO_3)_2 \cdot 3H_2O$ complex, which contains both bidentate chelate and bridged carbonate ions, whereas its dehydrated form is exclusively a bridged structured (see also Fig. 8). Concerning our carbonato complex, it would be interesting to get more information about the actual influence of H_2O on the CO_3^{2-} coordination. Since apparently the H_2O has an active role in the mechanochemical formation of the complex, namely, it affects the ν_3 splitting, and taking into account that this complex represents an intermediate phase from which the $NaNbO_3$ is formed, it would also be interesting to find out whether milling in

humid-free conditions will affect the formation of the niobate. These questions will be left for further investigations.

3. Mechanochemical reaction rate in $\text{Na}_2\text{CO}_3\text{-M}_2\text{O}_5$ ($\text{M} = \text{V, Nb, Ta}$) powder mixtures

3.1 Quantitative X-ray diffraction, infrared spectroscopy and thermogravimetric analysis

In-depth study of reaction mechanism limited to one system is often insufficient if fundamental characteristics governing certain type of mechanochemical reaction are to be determined. Following the results from the previous section, in which we identified an amorphous carbonato complex as a transitional stage of the reaction between Na_2CO_3 and Nb_2O_5 , it is the next step to find out i) whether this mechanism is general for mechanochemical reactions involving CO_3^{2-} ions and ii) which parameters control the decomposition of the carbonato complex. The latter is particularly important as the decomposition of the complex is a necessary step for the formation of the final binary oxide.

In order to study systematically the mechanochemical interaction between CO_3^{2-} ions and various metal cations, which could possibly lead to the formation of the carbonato complex, we explored the reactions involving Na_2CO_3 , as one reaction counterpart, and various 5th group transition-metal oxides, including V_2O_5 , Nb_2O_5 and Ta_2O_5 . The aim of the study was to determine the influence of the transition-metal oxide on i) the mechanochemical decomposition of Na_2CO_3 and ii) the rate of formation of the target binary oxides, i.e., NaVO_3 , NaTaO_3 and NaNbO_3 .

The mechanochemical formation of NaMO_3 ($\text{M} = \text{V, Nb, Ta}$) from respective $\text{Na}_2\text{CO}_3\text{-M}_2\text{O}_5$ ($\text{M} = \text{V, Nb, Ta}$) mixtures was followed by quantitative X-ray diffraction phase analysis using Rietveld refinement method. The fractions of NaMO_3 ($\text{M} = \text{V, Nb, Ta}$) as a function of milling time are shown in Fig. 11. The rate of formation of the final oxides follows the order $\text{NaVO}_3 > \text{NaTaO}_3 > \text{NaNbO}_3$. Note that the vanadate was formed within 4 hours, while the

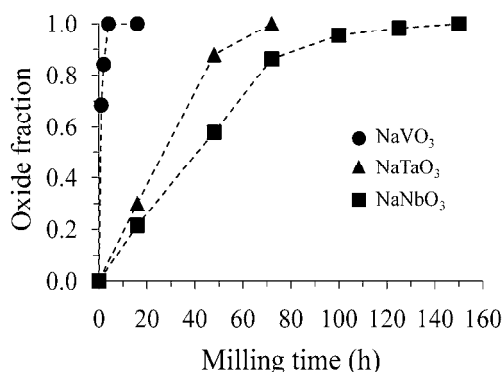


Fig. 11. Fraction of NaMO_3 ($\text{M} = \text{V, Nb, Ta}$), determined by Rietveld refinement analysis, as a function of milling time. The lines are drawn as a guide for the eye (from Rojac et al., 2011).

tantalate and niobate required much longer milling times to be the only crystalline phase detected in the mixtures, i.e., 72 and 150 hours, respectively. The results show that the type of the transition-metal oxide plays an important role in the formation kinetics of NaMO_3 ($M = \text{V}, \text{Nb}, \text{Ta}$).

In order to verify whether the amorphous carbonato complex appears as a transitional phase in the three examined reactions, we performed an IR spectroscopy analysis. The results are presented in Fig. 12. In all the systems, a common trend, characteristic for the lowering of the CO_3^{2-} symmetry, is observed during milling: i) the $\nu_3(\text{CO}_3^{2-})$ vibration shifts gradually to higher wavenumbers and decreases in intensity until it disappears after certain milling time, ii) the ν_3 vibration is replaced by new bands in the region 1650–1250 cm^{-1} , showing ν_3 splitting (see 4 h, 72 h, 150 h in Fig. 12 a, b and c, respectively) and iii) the ν_1 vibration is activated. Note that the ν_1 activation in the case of the $\text{Na}_2\text{CO}_3\text{-V}_2\text{O}_5$ mixture could not be ascertained due to overlapping with the band at 1025 cm^{-1} , related to the stretching vibration of the double vanadyl $\text{V}=\text{O}$ bonds of V_2O_5 (Fig. 12a). According to the relation between symmetry and IR vibrational spectroscopy of the CO_3^{2-} ion, described in detail in the previous section, the formation of the carbonato complex is confirmed in all the examined systems.

We note that the milling conditions for the mechanochemical synthesis of NaNbO_3 presented in the previous section were different from the ones that we applied for the study presented here. This is seen from the different kinetics of the formation of NaNbO_3 , i.e., by comparing the timescale of the NaNbO_3 fraction-versus-time curves from Fig. 11 (closed rectangular) and Fig. 4b (open circles). Therefore, the mechanism of the mechanochemical interaction between Na_2CO_3 and Nb_2O_5 , in terms of the transitional carbonato complex, is qualitatively unaffected by the milling intensity.

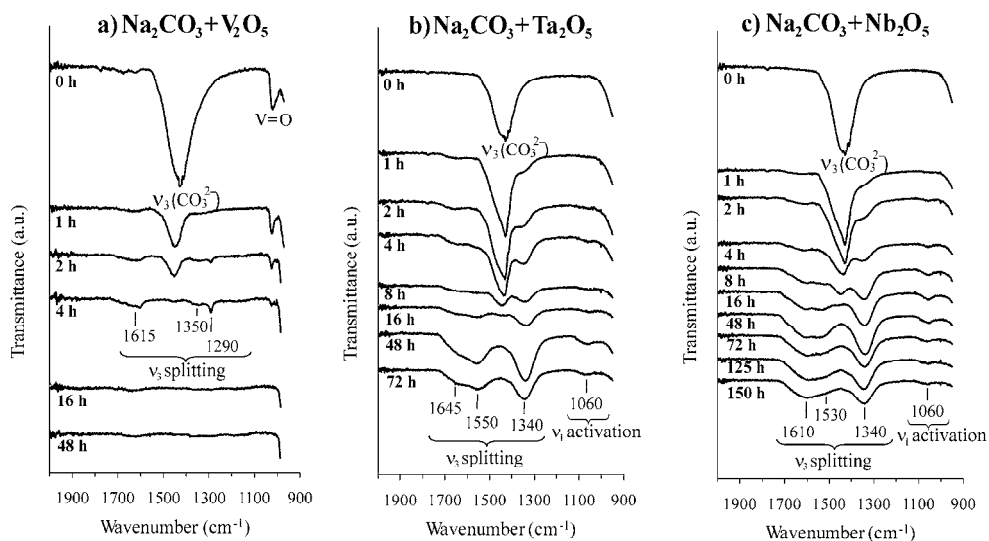


Fig. 12. FT-IR spectra of $\text{Na}_2\text{CO}_3\text{-M}_2\text{O}_5$ ($M = \text{V}, \text{Nb}, \text{Ta}$) powder mixtures after different milling times (from Rojac et al., 2011).

The results from Fig. 12 suggest a general reaction mechanism in mixtures involving CO_3^{2-} ions; in fact, in addition to the systems presented in this chapter, the carbonato complex was identified in a number of other alkaline-carbonate-transition-metal oxide mixtures, including the following:

- $\text{Li}_2\text{CO}_3\text{-Nb}_2\text{O}_5$ (unpublished work)
- $\text{K}_2\text{CO}_3\text{-Nb}_2\text{O}_5$ (Rojac et al., 2009)
- $\text{Rb}_2\text{CO}_3\text{-Nb}_2\text{O}_5$ (unpublished work)
- $\text{K}_2\text{CO}_3\text{-Ta}_2\text{O}_5$ (Glinsek et al., 2011)
- $\text{Na}_2\text{CO}_3\text{-K}_2\text{CO}_3\text{-Nb}_2\text{O}_5$ (unpublished work)
- $\text{Na}_2\text{CO}_3\text{-K}_2\text{CO}_3\text{-Nb}_2\text{O}_5\text{-Ta}_2\text{O}_5$ (Rojac et al., 2010)
- $\text{Na}_2\text{CO}_3\text{-K}_2\text{CO}_3\text{-Li}_2\text{C}_2\text{O}_4\text{-Nb}_2\text{O}_5\text{-Ta}_2\text{O}_5$ (Rojac et al., 2010)

A closer inspection of Fig. 12 reveals several differences between the three reaction systems. First of all, the degree of the ν_3 splitting is different depending on the metal cation, i.e., V^{5+} , Nb^{5+} or Ta^{5+} , to which the CO_3^{2-} coordinate. The maximum splitting of ν_3 from the spectra of the $\text{Na}_2\text{CO}_3\text{-M}_2\text{O}_5$ ($\text{M} = \text{V}, \text{Ta}, \text{Nb}$) mixtures after 4, 72 and 150 hours of milling, respectively (Fig. 12), is collected in Table 3. The maximum $\Delta\nu_3$ splitting is largest in the case of V_2O_5 (325 cm^{-1}), followed by Ta_2O_5 (305 cm^{-1}) and Nb_2O_5 (270 cm^{-1}).

Mixture	Max $\Delta\nu_3$ splitting (cm^{-1})
$\text{Na}_2\text{CO}_3\text{-V}_2\text{O}_5$	325
$\text{Na}_2\text{CO}_3\text{-Ta}_2\text{O}_5$	305
$\text{Na}_2\text{CO}_3\text{-Nb}_2\text{O}_5$	270

Table 3. Maximum splitting of $\nu_3(\text{CO}_3^{2-})$ vibration in $\text{Na}_2\text{CO}_3\text{-M}_2\text{O}_5$ ($\text{M} = \text{V}, \text{Nb}, \text{Ta}$) powder mixtures (from Rojac et al., 2011).

Nakamoto et al. (1957) were the first to propose the degree of ν_3 splitting ($\Delta\nu_3$) as a criterion to distinguish between mono- and bidentate coordination in carbonato complexes. Their results showed that some bidentate cobalt carbonato complexes have $\Delta\nu_3$ splitting of about 300 cm^{-1} , while monodentate complexes of analogous chemical composition exhibit about 80 cm^{-1} of $\Delta\nu_3$. Calculations based on models of XO_3 ($\text{X} = \text{C}, \text{N}$) groups coordinated to a metal cation confirmed the larger splitting in the case of bidentate coordination, as compared to the monodentate coordination (Britzinger & Hester, 1966; Hester & Grossman, 1966). A general relationship between the type of coordination and $\Delta\nu_3$ splitting, which we updated according to the critical review by Busca & Lorenzelli (1982), is shown schematically in Fig. 13a. While monodentate configurations show splitting of around 100 cm^{-1} or lower, larger $\Delta\nu_3$ splitting can be expected for bidentate chelate and bidentate bridged coordinations.

In addition to the type of coordination, other factors influence the degree of the ν_3 splitting. As explained in the previous section, the coordination of the CO_3^{2-} ion causes a rearrangement of the C–O bonds, i.e., the C–O bond coordinated to the metal cation is typically weakened, while the others, non-coordinated, are strengthened. Calculations showed that, for a given type of coordination, this CO_3^{2-} polarization is more pronounced if the polarizing power of the central cation is high as it can attract electrons more strongly (Britzinger & Hester, 1966). The $\Delta\nu_3$ splitting, which reflects the CO_3^{2-} polarization, should

therefore depend on the polarizing power of the central cation. This was indeed confirmed experimentally by Jolivet et al. (1982), which identified a linear increase of $\Delta\nu_3$ splitting with the polarizing power of the central cation for numerous carbonato complexes having the same bidentate coordination (Fig. 13b). For those cases, the polarizing power of the cation was assumed to be proportional to e/r^2 , where e and r are cation charge and radius, respectively. Therefore, the $\Delta\nu_3$ splitting criterion for distinguishing between different types of coordination (Fig. 13a) should only be applied if the polarizing power of the cation is taken into account (Fig. 13b). As pointed out by Busca & Lorenzelli (1982), low values of $\Delta\nu_3$ splitting, e.g., $\sim 100\text{ cm}^{-1}$, do not unequivocally indicate the presence of monodentate structure, particularly in cases of metals having low polarizing power (see also Fig. 13b).

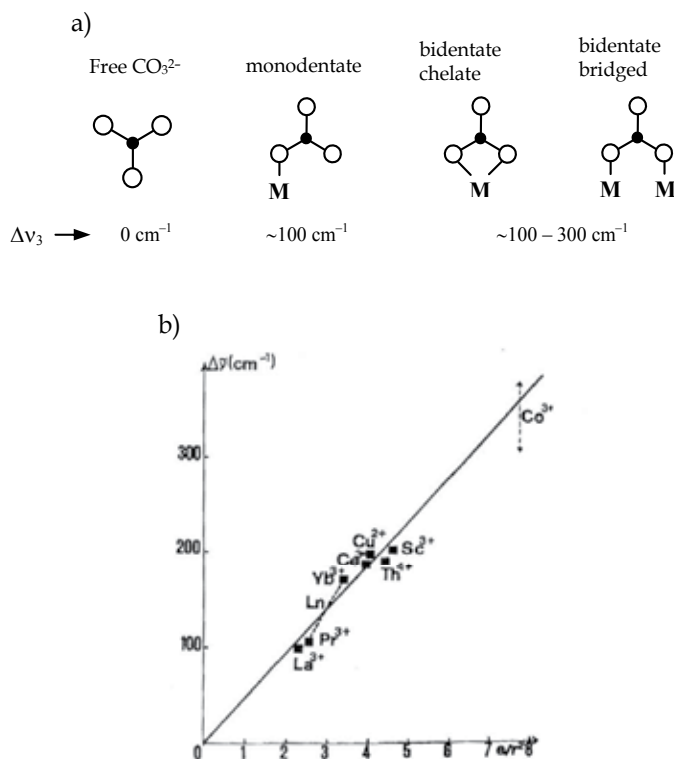


Fig. 13. a) Schematic view of the influence of the type of coordination on splitting of $\nu_3(\text{CO}_3^{2-})$ vibration (from Busca & Lorenzelli, 1982) and b) correlation between splitting of $\nu_3(\text{CO}_3^{2-})$ vibration and polarizing power (e/r^2) of the central cation for bidentate carbonato complexes. “ e ” and “ r ” denote cation charge and radius, respectively (from Jolivet et al., 1982).

By comparing with the literature data and considering the relationship shown in Fig. 13a, the maximum $\Delta\nu_3$ splitting in the three mixtures from Table 3, being larger than 100 cm^{-1} , might suggest bidentate chelate and/or bridged coordination. The increasing $\Delta\nu_3$ from the system with niobium, having the smallest $\Delta\nu_3$ of 270 cm^{-1} , to that with vanadium, with the largest $\Delta\nu_3$ of 325 cm^{-1} (Table 3), correlates with the increasing cation acidity, appearing in

the order $\text{Nb}^{5+} < \text{Ta}^{5+} < \text{V}^{5+}$ (see X_z/CN values in Table 5 and refer to the next section for details). Since it is generally accepted that the acidity scales with the cation charge density, i.e., e/r (Avvakumov et al., 2001), our correlation, in principle, agrees with the one of Jolivet et al. (1982) from Fig. 13b. However, even if a correlation exists, it should be interpreted carefully since in addition to the polarizing ability of the central cation, we should not neglect other influences on the $\Delta\nu_3$ splitting, such as, for example, incorporation of water molecules, as demonstrated in previous section (Fig. 10), which might differ between the three examined systems.

In addition to the ν_3 splitting, another difference between the three reactions that should be noted is the much faster formation of the complex in the case of V^{5+} as central cation in comparison with Nb^{5+} and Ta^{5+} (Fig. 12). This can be seen by comparing the characteristic ν_3 splitting among the three systems taking into consideration the point of the transition of the original ν_3 vibration into split bands as a criterion for the CO_3^{2-} coordination (Fig. 12). Whereas in the case of V_2O_5 the ν_3 vibration almost completely disappeared after 4 hours of milling, giving rise to split bands (Fig. 12a), at least 16 hours were needed in the case of Nb_2O_5 and Ta_2O_5 (Fig. 12b and c). This is in agreement with the kinetics of NaMO_3 formation ($M = \text{V}, \text{Nb}, \text{Ta}$), shown in Fig. 11.

In contrast to the $\text{Na}_2\text{CO}_3\text{-Ta}_2\text{O}_5$ and $\text{Na}_2\text{CO}_3\text{-Nb}_2\text{O}_5$ systems, where the IR absorption bands of the carbonato complex are still clearly resolved after 72 and 150 hours of milling (Fig. 12b and c), these bands completely disappeared after only 16 h of milling in the case of the $\text{Na}_2\text{CO}_3\text{-V}_2\text{O}_5$ mixture (Fig. 12a). A reasonable explanation for the absence of the IR bands related to the complex is its decomposition. If this is the case, it suggests that the transition-metal oxide plays a role in the decomposition of the carbonato complex.

We can compare quantitatively the carbonate decomposition in the three studied systems by using thermogravimetric analysis. Similarly like explained in the previous section, by separating the mass loss related to the H_2O release from the one that is due to the CO_2 release, we can estimate the amount of the residual carbonate in the powder mixtures. The results of this analysis are shown in Fig. 14. As expected, in all the mixtures the carbonate fraction decreases with increasing milling time; this is associated with the mechanochemically driven carbonate decomposition. We can summarize the reaction as follows: after being formed (Fig. 12), the carbonato complex decomposes (Fig. 14), leading to the formation of the final NaMO_3 oxides (Fig. 11). Note that, in terms of the reaction timescale, these three stages are not clearly separated, instead, they are overlapped.

The results of TG analysis (Fig. 14) reveal a substantial difference in the decomposition rate of the carbonate between the three systems: the fastest is in the case of V_2O_5 , followed by Ta_2O_5 and Nb_2O_5 . Note also that the carbonate fraction reaches a plateau after prolonged milling, which we denote here as the “steady-state” milling condition. The amount of the carbonate in this “steady-state” condition depends strongly on the type of the transition-metal oxides participating in the reaction. Whereas the carbonato complex decomposed nearly completely in the case of vanadium, i.e., only 0.5% of residual carbonate was determined in the “steady-state” milling condition, 29% and 39% remained in the mixture in the case of Ta and Nb, respectively (Fig. 14 and Table 4). This is in agreement with the IR spectra from Fig 12, i.e., in contrast to the cases with Nb and Ta, no IR bands related to the carbonato complex are observed after prolonged milling of the $\text{Na}_2\text{CO}_3\text{-V}_2\text{O}_5$ mixture (Fig.

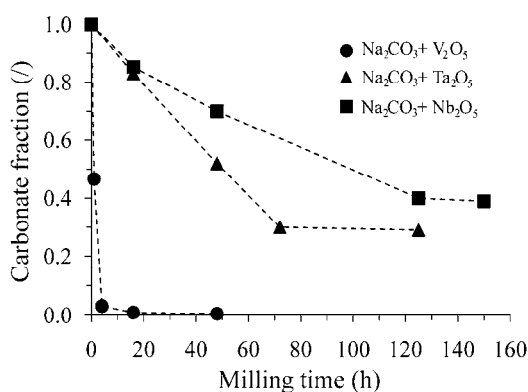


Fig. 14. Fraction of carbonate, determined by TG analysis, as a function of milling time in $\text{Na}_2\text{CO}_3\text{-M}_2\text{O}_5$ ($M = \text{V, Nb, Ta}$) powder mixtures. The lines are drawn as a guide for the eye (from Rojac et al., 2011).

Mixture	Carbonate fraction (%)
$\text{Na}_2\text{CO}_3\text{-V}_2\text{O}_5$	0.5
$\text{Na}_2\text{CO}_3\text{-Ta}_2\text{O}_5$	29
$\text{Na}_2\text{CO}_3\text{-Nb}_2\text{O}_5$	39

Table 4. Fraction of residual carbonate in $\text{Na}_2\text{CO}_3\text{-M}_2\text{O}_5$ ($M = \text{V, Nb, Ta}$) powder mixtures in the “steady-state” milling conditions (see carbonate fraction after prolonged milling in Fig. 14) (from Rojac et al., 2011).

12a, see 16 and 48 hours). Finally, it is important to stress that the complex is amorphous and could not be analyzed using Rietveld analysis (Fig. 11); instead, we were able to follow its formation and decomposition using IR and TG analyses, respectively (Fig. 12 and 14).

From the presented results we can infer that a common mechanism, characterized by the formation of an intermediate amorphous carbonato complex, link the reactions between Na_2CO_3 and M_2O_5 ($M = \text{V, Nb, Ta}$); however, considerable differences exist in the rate of the formation and decomposition of this carbonato complex and, consequently, in the crystallization of the final binary compounds. The sequence of the rates of these reactions, i.e., $\text{Na}_2\text{CO}_3\text{-V}_2\text{O}_5 > \text{Na}_2\text{CO}_3\text{-Ta}_2\text{O}_5 > \text{Na}_2\text{CO}_3\text{-Nb}_2\text{O}_5$, can be interpreted by considering the acid-base properties of the reagents involved.

3.2 Acid-base mechanochemical reaction mechanism

In their extensive work on the mechanochemical reactions involving hydroxide-oxide mixtures, Senna and co-workers (Liao & Senna, 1992, 1993; Watanabe et al., 1995b, 1996, Avvakumov et al., 2001) showed that the mechanism in these mixtures is governed by an acid-base reaction between different hydroxyl groups on the solid surface. The driving force for these reactions is the acid-base potential, i.e., the difference in the acid-base properties between an acidic and basic surface -OH group, which is determined by the type of metal on which it is bound, and therefore, on the strength of the M-OH bond (M denotes the

metal). For example, in the case of the $M(OH)_2-SiO_2$ ($M = Ca, Mg$) mixtures, they showed experimentally that a larger acid-base potential between $Ca(OH)_2$ and SiO_2 brought a faster mechanochemical interaction (Liao & Senna, 1993).

The acid-base reaction mechanism is not confined to the hydroxyl groups only. Thermodynamic calculations showed that a correlation exists between the Gibbs free energies of a variety of reactions between oxide compounds and the acid-base potential between the participating oxide reagents for two-component systems: the larger the potential, the more negative the value of the Gibbs energy and, thus, the faster and more complete the reaction (Avvakumov et al., 2001).

In order to fully consider the acid-base properties of oxide compounds, one should take into account that the acidity of a cation, incorporated into a certain oxide compound, depends on the oxidation state and the coordination number. For example, when the oxidation degree of the manganese ion increases by unity, the acidity increases by 2-3 times; same trend is observed when the coordination number of Si^{4+} decreases from 6 to 4. For correct comparisons, the influence of these parameters on the acid-base properties of cations should be taken into account. This can be done by introducing the electronegativity of a cation, divided by the coordination number, which defines the cation-ligand force per one bond in a coordination polyhedron; the larger the force, the larger the acidity of the cation, i.e., the stronger is the ability to attract electron pairs forming covalent bonds (Avvakumov et al., 2001).

To address the acid-base properties of the transition-metal cations, we adopted the electronegativity scale for cations derived by Zhang (1982). Table 5 shows the electronegativities X_z for V^{5+} , Ta^{5+} and Nb^{5+} . The ratio X_z/CN , where CN refers to the coordination number of the cation, taken as being indicative of the acidity of the cations in their respective oxides, is the highest for V^{5+} , followed by Ta^{5+} and Nb^{5+} .

Cation	X_z	X_z/CN
V^{5+}	2.02	0.40
Ta^{5+}	1.88	0.29
Nb^{5+}	1.77	0.27

Table 5. Electronegativity values X_z and X_z/CN ratios for V^{5+} , Nb^{5+} and Ta^{5+} . X_z and CN denote cation electronegativity defined by Zhang and coordination number, respectively. The X_z/CN ratio is taken as a parameter proportional to cation acidity (from Rojac et al., 2011).

The order of the cation acidity, i.e., $V^{5+}>Ta^{5+}>Nb^{5+}$ (Table 5) correlates with our experimental results; in fact, the reaction rate follows the same order, i.e., $Na_2CO_3-V_2O_5>Na_2CO_3-Ta_2O_5>Na_2CO_3-Nb_2O_5$ (see Fig. 11). This means that the higher is the acidity of the cation involved, the faster is the reaction, including the formation and decomposition of the carbonato complex (Fig. 12 and 14), and the crystallization of the final oxides (Fig. 11). The agreement between the reaction rate sequence and the cation acidity or acid-base potential, where Na_2CO_3 is taken as basic and transition-metal oxides as acidic compound, suggests that the mechanochemical reactions studied here suit the concept of an acid-base interaction mechanism. Similar correlations between the acid-base properties and the mechanochemical reaction rate can also be found in other systems comprising CaO , as one reagent, and Al_2O_3 , SiO_2 , TiO_2 , V_2O_5 or WO_3 , as the other reagent (Avvakumov et al. 1994).

We showed in the previous section that after reaching a specific milling time (“steady-state” milling condition), the fraction of the residual carbonate did not change any longer if further milling was applied (Fig. 14). These carbonate fractions correlate with the acidity of the cations as well (compare Table 4 with Table 5). Note that the small carbonate fraction in the $\text{Na}_2\text{CO}_3\text{-V}_2\text{O}_5$ system, i.e., 0.5 % (Table 4), is consistent with the much larger acidity of V^{5+} as compared to Ta^{5+} or Nb^{5+} (see X_Z/CN values in Table 5). The results seem reasonable considering the relation that was found between the acid-base potential and the reaction Gibbs free energy; however, insufficient thermodynamic data for the systems presented here prevent us from making further steps in this direction. We note that these results carry practical consequences, i.e., they suggest that attempting to eliminate the carbonate from a mixture, characterized by a low acid-base potential, by intensifying the milling might not be successful. In fact, the residual carbonate fraction seems to be dependent on the acid-base potential, which is a characteristic of a system, rather than on the milling conditions (Rojac et al., 2008b).

Even if the rate of the three examined reactions apparently agrees with the acid-base reaction concept, we shall not neglect other parameters that could influence the course of the reaction, such as, e.g., adsorption of H_2O during milling, which might differ from one system to another. In order to directly verify this possibility, we plot in Fig. 15 the reaction rate constant versus X_Z/CN . The reaction rate constant was obtained by fitting the curves from Fig. 11 with a kinetic model proposed for mechanochemical transformations in binary mixtures (Cocco et al., 2000). A linear relationship would be expected if the reaction rate will be largely dominated by the cation acidity. While the sequence of the reaction rate constants, i.e., $\text{V} > \text{Ta} > \text{Nb}$, agrees with the acid-base reaction mechanism, the non-linear relationship between the rate constant and X_Z/CN from Fig. 15 suggests that, in addition to the cation acidity, probably other factors influence the reaction rate. The origin of these additional influences will be left open for further studies.

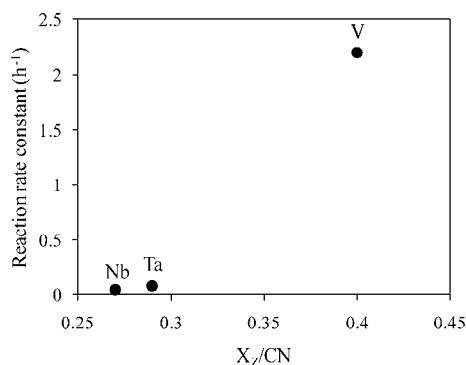


Fig. 15. Reaction rate constant versus X_Z/CN for the reactions between Na_2CO_3 and M_2O_5 ($\text{M} = \text{V}, \text{Nb}, \text{Ta}$) (from Rojac et al., 2011).

4. Conclusions

A systematic study of the reaction mechanism during high-energy milling of a $\text{Na}_2\text{CO}_3\text{-Nb}_2\text{O}_5$ mixture, presented in the first part of the chapter, revealed that the synthesis of NaNbO_3 takes place through an intermediate amorphous stage. Quantitative phase analysis using XRD diffraction and Rietveld refinement method showed indeed a large amount of

the amorphous phase, i.e., of up of 91%, formed in the initial part of the reaction. The amount of this amorphous phase then decreased by subsequent milling, leading to the crystallization of the final NaNbO_3 . Only limited information, including mainly the identification of the transitional nature of the amorphous phase, was obtained using quantitative XRD phase analysis.

The decomposition of the carbonate in the $\text{Na}_2\text{CO}_3\text{-Nb}_2\text{O}_5$ mixtures was analyzed using TG analysis coupled with DTA and EGA. By following the carbonate decomposition upon annealing the mixtures milled for various periods we were able to infer about the changes occurring in the carbonate during high-energy milling. Characteristic changes in the carbonate decomposition upon increasing the milling time suggested a formation of an intermediate carbonate compound with rather defined decomposition temperature occurring in a narrow temperature range; such decomposition was found to be atypical for physical mixtures of Na_2CO_3 and Nb_2O_5 powders.

A more accurate identification of the amorphous phase was made possible using IR spectroscopy analysis. Characteristic IR vibrational changes during milling, including splitting of ν_3 and activation of ν_1 C–O stretching vibrations of the CO_3^{2-} ion, suggested lowered CO_3^{2-} symmetry, which was interpreted as being a consequence of CO_3^{2-} coordination and formation of an amorphous carbonato complex.

Expanding the study of the $\text{Na}_2\text{CO}_3\text{-Nb}_2\text{O}_5$ to other systems, we showed in the second part of the chapter that the mechanism involving the transitional amorphous carbonato complex is common for several alkaline-carbonate-transition-metal oxide mixtures, including $\text{Na}_2\text{CO}_3\text{-M}_2\text{O}_5$ ($M = \text{V, Nb, Ta}$). The sequence of the reaction rate in these three systems, including the formation of the complex, its decomposition and crystallization of the final NaMO_3 ($M = \text{V, Nb, Ta}$), was interpreted by considering the acid-base reaction mechanism. The largest the acid-base potential, i.e., the difference between acidic and basic properties of the reagents involved, the faster the mechanochemical reaction.

5. Acknowledgments

The work was supported by the Slovenian Research Agency within the framework of the research program “Electronic Ceramics, Nano, 2D and 3D Structures” (P2-0105) and postdoctoral project “Mechanochemical Synthesis of Complex Ceramic Oxides” (Z2-1195). For the financial support, additional acknowledgements go to Network of Excellence MIND, COST Actions 528 and 539, and bilateral project PROTEUS BI-FR/03-001. For valuable discussions on the topic we thank Barbara Malič and Janez Holc. For the help with various analytical methods, Jana Cilenšek, Bojan Kozlevčar, Edi Krajnc, Anton Meden, Andreja Benčan, Goran Dražič and Bojan Budič are sincerely acknowledged. A special thank is given for the help in the laboratory to Sebastjan Glinšek, Mojca Lončnar, Tanja Urh, Živa Trtnik and Silvo Drnovšek. Collaborations from abroad include Olivier Masson and René Guinebretière from SPCTS, University of Limoges, France, and Bozena Hilczer and Maria Polomska from the Institute of Molecular Physics, Polish Academy of Sciences, Poznan, Poland.

6. References

Avvakumov, E. G.; Devyatkina, E. T. & Kosova, N. V. (1994). Mechanochemical Reactions of Hydrated Oxides. *Journal of Solid State Chemistry*, Vol.113, No.2, pp. 379–383.

- Avvakumov, E.; Senna, M. & Kosova, N. (2001). *Soft Mechanochemical Synthesis*, Kluwer Academic Publisher, Boston, USA.
- Boldyrev, B. B. & Tkacova, K. (2000). Mechanochemistry of Solids: Past, Present, and Prospects. *Journal of Materials Synthesis and Processing*, Vol.8, No.3-4, pp. 121-132.
- Brintzinger, H. & Hester, R. E. (1966). Vibrational Analysis of Some Oxyanion-Metal Complexes. *Inorganic Chemistry*, Vol.5, No.6, pp. 980-985.
- Brooker, M. H. & Bates, J. B. (1971). Raman and Infrared Spectral Studies of Anhydrous Li_2CO_3 and Na_2CO_3 . *The Journal of Chemical Physics*, Vol.54, No.11, pp. 4788-4796.
- Buijs, K. & Schutte, C. J. H. (1961). The Infra-red Spectra and Structures of Li_2CO_3 and Anhydrous Na_2CO_3 . *Spectrochimica Acta B*, Vol.17, No.9-10, pp. 927-932.
- Burgio, N.; Iasonna, A; Magini, M.; Martelli, S. & Padella, F. (1991). Mechanical Alloying of the Fe-Zr System: Correlation between Input Energy and End Products. *Il Nuovo Cimento*, Vol.13D, No.4, pp. 459-476.
- Busca, G. & Lorenzelli, V. (1982). Infrared Spectroscopic Identification of Species Arising from Reactive Adsorption of Carbon Oxides on Metal Oxide Surfaces. *Materials Chemistry*, Vol.7, No.1, pp. 89-126.
- Cocco, G.; Delogu, F. & Schiffrini, L. (2000). Toward a Quantitative Understanding of the Mechanical Alloying Process. *Journal of Materials Synthesis and Processing*, Vol.8, No.3-4, pp. 167-180.
- Delogu, F. & Cocco, G. (2000). Relating Single-Impact Events to Macrokinetic Features in Mechanical Alloying Processes. *Journal of Materials Synthesis and Processing*, Vol.8, No.5-6, pp. 271-277.
- Delogu, F.; Mulas, G.; Schiffrini L. & Cocco, G. (2004). Mechanical Work and Conversion Degree in Mechanically Induced Processes. *Materials Science and Engineering A*, Vol.382, No.1-2, pp. 280-287.
- El-Eskandarany, M. S.; Akoi, K.; Sumiyama, K. & Suzuki, K. (1997). Cyclic Crystalline-Amorphous Transformations of Mechanically Alloyed $\text{Co}_{75}\text{Ti}_{25}$. *Applied Physics Letters*, Vol.70, No.13, pp. 1679-1681.
- Fujita, J.; Martell, A. E. & Nakamoto, K. (1962). Infrared Spectra of Metal Chelate Compounds. VIII. Infrared Spectra of Co(III) Carbonato Complexes. *The Journal of Chemical Physics*, Vol.36, No.2, pp. 339-345.
- Gatehouse, B. M.; Livingstone, S. E. & Nyholm, R. S. (1958). The Infrared Spectra of Some Simple and Complex Carbonates. *Journal of the Chemical Society*, pp. 3137-3142.
- Glinšek, S.; Malič, B.; Rojac, T.; Filipič, C.; Budič, B. & Kosec, M. (2011). KTaO_3 Ceramics Prepared by the Mechanochemically Activated Solid-State Synthesis. *Journal of the American Ceramic Society*, Vol.94, No.5, pp. 1368-1373.
- Goldsmith, J. A. & Ross, S. D. (1967). Factors Affecting the Infra-Red Spectra of Planar Anions with D_{3h} Symmetry - IV. The Vibrational Spectra of Some Complex Carbonates in the Region 4000-400 cm^{-1} . *Spectrochimica Acta A*, Vol.24, No.8, pp. 993-998.
- Haris, M. J. & Salje, E. K. H. (1992). The Incommensurate Phase of Sodium Carbonates: An Infrared Absorption Study. *Journal of Physics: Condensed Matter*, Vol.4, No.18, pp. 4399-4408.
- Healy, P. C. & White, A. H. (1972). Crystal Structure and Physical Properties of Anhydrous Sodium Copper Carbonate. *Journal of the Chemical Society, Dalton Transactions*, pp. 1913-1917.
- Hester, R. E. & Grossman, W. E. L. (1966). Vibrational Analysis of Bidentate Nitrate and Carbonate Complexes. *Inorganic Chemistry*, Vol.5, No.8, pp. 1308-1312.

- Iasonna, A. & Magini, M. (1996). Power Measurements during Mechanical Milling: An Experimental Way to Investigate the Energy Transfer Phenomena. *Acta Materialia*, Vol.44, No.3, pp. 1109–1117.
- Iguchi, Y. & Senna, M. (1985). Mechanochemical Polymorphic Transformation and Its Stationary State between Aragonite and Calcite. I. Effects of Preliminary Annealing. *Powder Technology*, Vol.43, No.2, pp. 155–162.
- Jenko, D. (2006). *Synthesis of (K,Na)NbO₃ Ceramics*, PhD Thesis, University of Ljubljana, Ljubljana, Slovenia.
- Jolivet, J. P.; Thomas, Y. & Taravel, B. (1980). Vibrational Study of Coordinated CO₃²⁻ Ions. *Journal of Molecular Structure*, Vol.60, pp. 93–98.
- Jolivet, J. P.; Thomas, Y. & Taravel, B. (1982). Infrared Spectra of Cerium and Thorium Pentacarbonate Complexes. *Journal of Molecular Structure*, Vol.79, pp. 403–408.
- Kong, L. B.; Zhang, T. S.; Ma, J. & Boey, F. (2008). Progress in Synthesis of Ferroelectric Ceramic Materials Via High-Energy Mechanochemical Technique. *Progress in Materials Science*, Vol.53, No.2, pp. 207–322.
- Kuscser, D.; Holc, J. & Kosec, M. (2006). Mechano-Synthesis of Lead-Magnesium-Niobate Ceramics. *Journal of the American Ceramic Society*, Vol.89, No.10, pp. 3081–3088.
- Le Brun, P.; Froyen, L. & Delaey, L. (1993). The Modeling of the Mechanical Alloying Process in a Planetary Ball Mill: Comparison between Theory and In-situ Observations. *Materials Science and Engineering A*, Vol. 161, No.1, pp. 75–82.
- Liao, J. & Senna, M. (1992). Enhanced Dehydration and Amorphization of Mg(OH)₂ in the Presence of Ultrafine SiO₂ Under Mechanochemical Conditions. *Thermochemica Acta*, Vol.210, pp. 89–102.
- Liao, J. & Senna, M. (1993). Mechanochemical Dehydration and Amorphization of Hydroxides of Ca, Mg and Al on Grinding With and Without SiO₂. *Solid State Ionics*, Vol.66, No.3-4, pp. 313–319.
- Lin, I. J. & Nadiv, S. (1979). Review of the Phase Transformation and Synthesis of Inorganic Solids Obtained by Mechanical Treatment (Mechanochemical Reactions). *Materials Science and Engineering*, Vol.39, No.2, pp. 193–209.
- Lu, L. & Lai, M. O. (1998). *Mechanical Alloying*, Kluwer Academic Publisher, Boston, USA.
- Maurice, D. R. & Courtney, T. H. (1990). The Physics of Mechanical Alloying. *Metallurgical Transactions A*, Vol.21, No.1, pp. 289–303.
- Nakamoto, K.; Fujita, J.; Tanaka, S. & Kobayashi, M. (1957). Infrared Spectra of Metallic Complexes. IV. Comparison of the Infrared Spectra of Unidentate and Bidentate Complexes. *Journal of the American Chemical Society*, Vol.79, No.18, pp. 4904–4908.
- Nakamoto, K. (1997). *Infrared and Raman Spectra of Inorganic and Coordination Compounds. Part A: Theory and Applications in Inorganic Chemistry*, Kluwer Academic Publisher, Boston, USA.
- Rojac, T.; Kosec, M.; Šegedin, P.; Malič, B. & Holc, J. (2006). The Formation of a Carbonato Complex during the Mechanochemical Treatment of a Na₂CO₃–Nb₂O₅ Mixture. *Solid State Ionics*, Vol.177, No.33-34, pp. 2987–2995.
- Rojac, T.; Benčan, A.; Uršič, H.; Malič, B. & Kosec, M. (2008a). Synthesis of a Li- and Ta-Modified (K,Na)NbO₃ Solid Solution by Mechanochemical Activation. *Journal of the American Ceramic Society*, Vol.91, No.11, pp. 3789–3791.
- Rojac, T.; Kosec, M.; Malič, B. & Holc, J. (2008b). The Mechanochemical Synthesis of NaNbO₃ Using Different Ball-Impact Energies. *Journal of the American Ceramic Society*, Vol.91, No.5, pp. 1559–1565.

- Rojac, T.; Kosec, M.; Polomska, M.; Hilczer, B.; Šegedin, P. & Benčan, A. (2009). Mechanochemical Reaction in the K_2CO_3 - Nb_2O_5 System. *Journal of the European Ceramic Society*, Vol.29, No.14, pp. 2999–3006.
- Rojac, T.; Benčan, A. & Kosec, M. (2010). Mechanism and Role of Mechanochemical Activation in the Synthesis of $(K,Na,Li)(Nb,Ta)O_3$ Ceramics. *Journal of the American Ceramic Society*, Vol.93, No.6, pp. 1619–1625.
- Rojac, T.; Trtnik, Ž. & Kosec, M. (2011). Mechanochemical Reactions in Na_2CO_3 - M_2O_5 (M = V, Nb, Ta) Powder Mixtures: Influence of Transition-Metal Oxide on Reaction Rate. *Solid State Ionics*, Vol.190, No.1, pp. 1–7.
- Senna, M. & Isobe, T. (1997). NMR and EPR Studies on the Charge Transfer and Formation of Complexes through Incompletely Coordinated States. *Solid State Ionics*, Vol.101-103, No.1, pp. 387–392.
- Sopicka-Lizer, M. (2010). *High-Energy Ball Milling: Mechanochemical Processing of Nanopowders*, Woodhead Publishing, Boston, USA.
- Suryanarayana, C. (2001). Mechanical Alloying and Milling. *Progress in Materials Science*, Vol.46, No.3-4, pp. 1–184.
- Tacaks, L. (2004). M. Carey Lea, The First Mechanochemist. *Journal of Materials Science*, Vol.39, No.16-17, pp. 4987–4993.
- Tchernychova, E.; Glinšek, S.; Malič, B. & Kosec, M. (2011). Combined Analytical Transmission Electron Microscopy Approach to Reliable Composition Evaluation of $KTaO_3$. *Journal of the American Ceramic Society*, Vol.94, No.5, pp. 1611–1618.
- Venyaminov, S. Y. & Pendergast, F. G. (1997). Water (H_2O and D_2O) Molar Absorptivity in the 1000–4000 cm^{-1} Range and Quantitative Infrared Spectroscopy of Aqueous Solutions. *Analytical Biochemistry*, Vol.248, No.2, pp. 234–245.
- Wang, J.; Xue, J. M.; Wan, D. M. & Gan, B. K. (2000a). Mechanically Activating Nucleation and Growth of Complex Perovskites. *Journal of Solid State Chemistry*, Vol.154, No.2, pp. 321–328.
- Wang, J.; Xue, J. M. & Wan, D. (2000b). How Different is Mechanical Activation from Thermal Activation? A Case Study with PZN and PZN-Based Relaxors. *Solid State Ionics*, Vol.127, No.1-2, pp. 169–175.
- Watanabe, R.; Hashimoto, H. & Lee, G. G. (1995a). Computer Simulation of Milling Ball Motion in Mechanical Alloying (Overview). *Materials Transactions JIM*, Vol.36, No.2, pp. 102–109.
- Watanabe, T.; Liao, J. & Senna, M. (1995b). Changes in the Basicity and Species on the Surface of $Me(OH)_2$ - SiO_2 (Me=Ca, Mg, Sr) Mixtures Due to Mechanical Activation. *Journal of Solid State Chemistry*, Vol.115, No.2, pp. 390–394.
- Watanabe, T.; Isobe, T. & Senna, M. (1996). Mechanisms of Incipient Chemical Reaction between $Ca(OH)_2$ and SiO_2 under Moderate Mechanical Stressing. I. A Solid State Acid-Base Reaction and Charge Transfer Due to Complex Formation. *Journal of Solid State Chemistry*, Vol.122, No.1, pp. 74–80.
- Watanabe, T.; Isobe, T. & Senna, M. (1997). Mechanisms of Incipient Chemical Reaction between $Ca(OH)_2$ and SiO_2 under Moderate Mechanical Stressing. III. Changes in the Short-Range Ordering throughout the Mechanical and Thermal Processes. *Journal of Solid State Chemistry*, Vol.130, No.2, pp. 248–289.
- Watters, R. L. (2005). NIST Standard Reference Database N°69, United States, June 2005 Release (robert.watters@nist.gov).
- Zhang, Y. (1982). Electronegativities of Elements in Valence States and Their Applications. 1. Electronegativities of Elements in Valence States. *Inorganic Chemistry*, Vol.21, No.11, pp. 3886–3889.

Application of Infrared Spectroscopy to Analysis of Chitosan/Clay Nanocomposites

Suédina M.L. Silva, Carla R.C. Braga, Marcus V.L. Fook,
Claudia M.O. Raposo, Laura H. Carvalho and Eduardo L. Canedo
*Federal University of Campina Grande, Department of Materials Engineering
Brazil*

1. Introduction

In recent years, polymer/clay nanocomposites have attracted considerable interest because they combine the structure and physical and chemical properties of inorganic and organic materials. Most work with polymer/clay nanocomposites has concentrated on synthetic polymers, including thermosets such as epoxy polymers, and thermoplastics, such as polyethylene, polypropylene, nylon and poly(ethylene terephthalate) (Pandey & Mishra, 2011). Comparatively little attention has been paid to natural polymer/clay nanocomposites. However, the opportunity to combine at nanometric level clays and natural polymers (biopolymers), such as chitosan, appears as an attractive way to modify some of the properties of this polysaccharide including its mechanical and thermal behavior, solubility and swelling properties, antimicrobial activity, bioadhesion, etc. (Han et al., 2010). Chitosan/clay nanocomposites are economically interesting because they are easy to prepare and involve inexpensive chemical reagents. Chitosan, obtained from chitin, is a relatively inexpensive material because chitin is the second most abundant polymer in nature, next to cellulose (Chang & Juang, 2004). In the same way, clays are abundant and low-cost natural materials. Although chitosan/clay nanocomposites are very attractive, they were not extensively investigated, with relatively small number of scientific publications. In addition, the successful preparation of the nanocomposites still encounters problems, mainly related to the proper dispersion of nano-fillers within the polymer matrix. In this chapter, in addition to discussing the synthesis and characterisation by infrared spectroscopy of chitosan/clay nanocomposites, data of x-ray diffraction and mechanical properties are also considered.

1.1 Chitosan

Chitosan is a naturally occurring linear polysaccharide, closely related to chitin, a polymer widely distributed in the animal kingdom. The discovery of chitosan is ascribed to Rouget in 1859 when he found that boiling chitin in potassium hydroxide rendered the polymer soluble in organic acids. In 1894 Hoppe-Seyler named this material chitosan. Only in 1950 was the structure of chitosan finally resolved (Dodane & Vilivalam, 1998, as cited in Dash et al., 2011). Chitin can be extracted from crustacean shells, insects, fungi, insects and other biological materials (Wan Ngah et al., 2011). The main commercial sources of chitin are the

shell waste of shrimps, lobsters, krills, and crabs. Several millions tons of chitin are harvested annually in the world, making this biopolymer an inexpensive and readily available resource (Dash et al., 2011). Chitosan is found naturally only in certain fungi (Mucoraceae), but it is easily obtained by the thermochemical deacetylation of chitin in the presence of alkali (Darder et al., 2003). Several methods have been proposed, most of them involving the hydrolysis of the acetylated residue using sodium or potassium hydroxide solutions, as well as a mixture of anhydrous hydrazine and hydrazine sulfate. The conditions used for deacetylation determines the polymer molecular weight and the degree of deacetylation (DD) (Dash et al., 2011; Lavorgna et al., 2010).

Chitosan is a copolymer whose chemical structure is shown in Fig. 1. The numbers on the extreme left ring are conventionally assigned to the six carbons in the glucopyranose ring, from C-1 to C-6. Substitution at C-2 may be an acetamido or amino group. Chitosan contains more than 50% (commonly 70 to 90%) of acetamido residues on the C-2 of the structural unit, while amino groups predominate in chitin. The degree of deacetylation (DD) serves as a diagnostic to classify the biopolymer as chitin or chitosan (Dash et al., 2011; Rinaudo, 2006). Notice that $DD + DA = 1$.

The DD is the key property that affects the physical and chemical properties of chitosan, such as solubility, chemical reactivity and biodegradability and, consequently their applications. A quick test to differentiate between chitin and chitosan is based on solubility and nitrogen content. Chitin is soluble in 5% lithium chloride/*N,N*-dimethylacetamide solvent [LiCl/DMAc] and insoluble in aqueous acetic acid while the opposite is true of chitosan. The nitrogen content in purified samples is less than 7% for chitin and more than 7% for chitosan (Dash et al., 2011; Rinaudo, 2006).

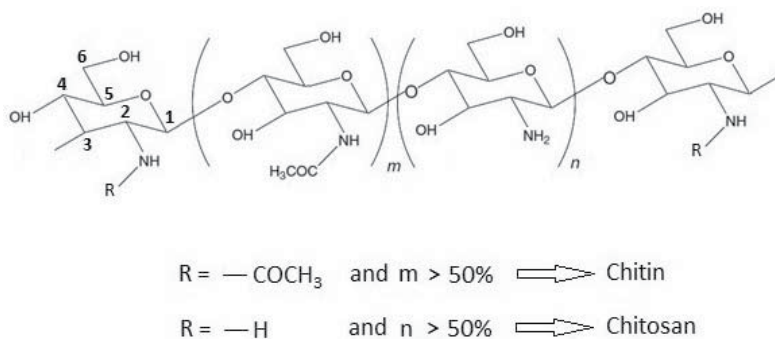


Fig. 1. Chemical structure of chitin and chitosan.

In the solid state, chitosan is a semicrystalline polymer. Its morphology has been investigated and many polymorphs are mentioned in the literature. Single crystals of chitosan were obtained using fully deacetylated chitin of low molecular weight. The dimensions the orthorhombic unit cell of the most common form were determined as $a = 0,807$ nm, $b = 0,844$ nm, $c = 1,034$ nm; the unit cell contains two antiparallel chitosan chains, but no water molecules (Dash et al., 2011).

The degree of acetylation (DA) and the crystallinity of chitin molecules affect the solubility in common solvents. Reducing the acetylation level in chitosan ensures the presence of free amino groups, which can be easily protonated in an acid environment, making chitosan

water soluble below pH about 6.5 (Krajewska, 2004; Lavorgna et al., 2010). In acid conditions, when the amino groups are protonated (Fig. 2), chitosan becomes a soluble polycation (Chivrac et al., 2009). The presence of amino groups make chitosan a cationic polyelectrolyte ($pK_a \approx 6.5$), one of the few found in nature. Soluble chitosan is heavily charged on the NH_3^+ groups, it adheres to negatively charged surfaces, aggregates with polyanionic compounds, and chelates heavy metal ions. These characteristics offer extraordinary potential in a broad spectrum of chitosan applications.

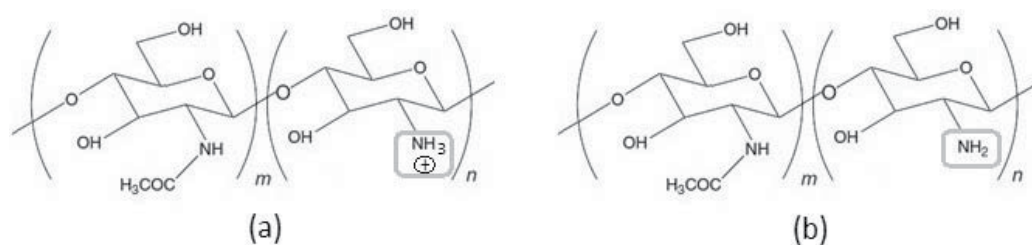


Fig. 2. Schematic illustration of chitosan: (a) at low pH (less than about 6.5), chitosan's amine groups become protonated (polycation); (b) at higher pH (above about 6.5), chitosan's aminogroups are deprotonated and reactive.

Increasingly over the last decade chitosan-based materials have been examined and a number of potential products have been developed for areas such as wastewater treatment (removal of heavy metal ions, flocculation/coagulation of dyes and proteins, membrane purification processes), the food industry (anticholesterol and fat binding, preservative, packaging material, animal feed additive), agriculture (seed and fertilizer coating, controlled agrochemical release), pulp and paper industry (surface treatment, photographic paper), cosmetic and toiletries (moisturizer, body creams, bath lotion) (No et al., 2000). Owing to the unparalleled biological properties, the most exciting uses of chitosan-based materials are in the area of medicine and biotechnology. Medicine takes advantage of its biocompatibility, biodegradability to harmless products, nontoxicity, physiological inertness, remarkable affinity to proteins, hemostatic, fungistatic, antitumoral and anticholesteremic properties; it may be in drug delivery vehicles, drug controlled release systems, artificial cells, wound healing ointments and dressings, haemodialysis membranes, contact lenses, artificial skin, surgical sutures and for tissue engineering. In biotechnology they may find application as chromatographic matrices, membranes for membrane separations, and notably as enzyme/cell immobilization supports (Felt et al., 2000; Krajewska, 2004). The current interest in medical applications of chitosan is easily understood.

Even though a number of potential products have been developed using chitosan-based materials, the tensile properties of pristine chitosan films are poor (due to its crystallinity). Thermal stability, hardness, gas barrier properties and bacteriostatic activity frequently are not good enough to meet the wide ranges of demanding applications. Thus, modification (chemical modification, blending and graft copolymerization) of chitosan has gained importance as means of tailoring the material to the desired properties. In this context, synthesis of nanocomposites with layered silicate loadings was proposed as a novel approach to modify some of the properties of chitosan, including mechanical and thermal behavior (Wang et al., 2005; Wu and Wu, 2006), solubility and swelling properties in acidic media (Pongjanyakul et al., 2005), antimicrobial activity (Han et al., 2010; Wang et al., 2006)

and bioadhesion (Pongjanyakul and Suksri, 2009). Chemical structure of chitosan containing multiple functional groups (hydroxyl, carbonyl, carboxyl, amine, amide) creates new possibilities for bonding chitosan to clays.

1.2 Clays

Clays are fine-grained, sedimentary rocks originated from the hydrothermal weathering volcanic volcanic ashes in alkaline lakes and seas. As such, clays are classified based on their stratigraphic position, location, and mineral content. Clays contain minerals of definite crystalline structure and elementary composition, some as main components, many as impurities, which usually include organic matter in the form of humic acids. Notwithstanding the fundamental difference between clay and clay mineral, both terms are sometimes used as indistinctly, especially in the frequent occasions in which the clay has a single principal mineral component; in this sense, the clay is considered as the impure mineral and the mineral as the purified clay (Utracki, 2004).

Clays are classified on the basis of their crystal structure and the amount and locations of electric charge (deficit or excess) per unit cell. Crystalline clays range from kaolins, which are relatively uniform in chemical composition, to smectites, which vary in their composition, cation exchange properties, and ability to expand. The most commonly employed smectite clay for the preparation of polymeric nanocomposites is bentonite, whose main mineral component is montmorillonite (Utracki, 2004).

Montmorillonite is the name given to clay found near Montmorillon in France, where it was identified by Knight in 1896 (Utracki, 2004). Montmorillonite is a 2:1 layered hydrated aluminosilicate, with a triple-sheet sandwich structure consisting of a central, hydrous alumina octahedral sheet, bonded to two silica tetrahedral sheets by shared oxygen ions (Fig. 3). The unit cell of this ideal structure has a composition $[Al_2(OH)_2(Si_2O_5)_2]_2$ with a molar

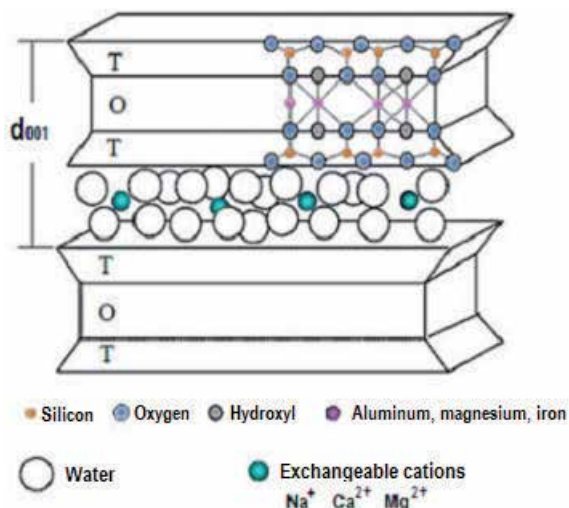


Fig. 3. Schematic of a montmorillonite, layered clay mineral with a triple-sheet sandwich structure consisting of a central, hydrous alumina octahedral sheet (O), bonded to two silica tetrahedral sheets (T) by shared oxygens.

mass of 720 g/mol. Isomorphic substitution of Al^{3+} in the octahedral sheets by Mg^{2+} (less commonly Fe^{2+} , Mn^{2+} , and other) and, less frequently, of Si^{4+} by Al^{3+} in the tetrahedral sheet, results in a net negative charge on the crystalline layer, which is compensated by the presence of cations, such as Na^+ , K^+ , Ca^{2+} , or Mg^{2+} , sorbed between the layers and surrounding the edges. An idealised montmorillonite has 0.67 units of negative charge per unit cell, in other words, it behaves as a weak acid. These loosely held cations do not belong to the crystal structure and can be readily exchanged by other cations, organic or inorganic. The cation exchange capacity (CEC) of montmorillonite ranges from 0.8 to 1.2 meq/g of air-dried clay, resulting in 0.6–0.9 exchangeable cations per unit cell. The layers organize themselves to form stacks with a regular gap between them, the interlayer space or gallery. The electrostatic and Van der Waals forces holding the layers together are relatively weak, and the interlayer distance varies depending on the radius of the cation present and its degree of hydration. In general, the smaller the cation and the lower its charge, the higher the clay swells in water or alcohols. For montmorillonite, the swelling capacity decreases depending on the cation chemical type according to the following trend: $\text{Li}^+ > \text{Na}^+ > \text{Ca}^{2+} > \text{Fe}^{2+} > \text{K}^+$ (Powell et al., 1998; Tettenhorst et al., 1962, as cited in Chivrac et al., 2009). The distance between two platelets of the primary particle, called inter-layer spacing or d-spacing (d_{001}), depends on the silicate type, on the type of the counter-cation, and on the hydration state. For instance, $d_{001} = 0.96$ nm for anhydrous sodium montmorillonite, but $d_{001} = 1.2$ – 1.4 nm in usual, partially hydrated conditions, as determined by x-ray diffraction techniques (Utracki, 2004).

Commercial montmorillonite is available as a powder of about 8 μm particle size, each particle containing about 3000 platelets. Montmorillonite exhibits enhanced gel strength, mucoadhesive capability to cross the gastrointestinal barrier and adsorb bacterial and metabolic toxins such as steroidal metabolites. Because of these advantages in biomedical applications, it is sometimes called a medical clay. Bentonite (named after Ford Benton, Wyoming) is rich in montmorillonite (usually more than 80%) (Utracki, 2004; Wei et al., 2009; Holzer et al., 2010; Li et al., 2010). Its color varies from white to yellow, to olive green, to brown. The names bentonite and montmorillonite are often used interchangeably. However, the terms represent materials with different degrees of purity. Bentonite is the ore that comprises montmorillonite, inessential minerals and other impurities. Beyond quartz, kaolinite, and many other minerals often present in minute proportions (feldspar, calcite, dolomite, muscovite, chlorite, hematite, etc), organic matter is present in bentonites as intrinsic impurities composed predominantly of humic substances (Bolto et al., 2001). Since competitive reactions can take place between the organic matter present in the bentonite and the chitosan, the extent of intercalation and polymer/clay interactions can be affected. Purification capable of removing of organic matter from bentonites before intercalation is fundamental.

As mentioned previously, because of the polycationic nature of chitosan in acidic media, the biopolymer may be intercalated in sodium montmorillonite through cation exchange and hydrogen-bonding processes, the resulting nanocomposites showing interesting structural and functional properties.

Chitosan/clay nanocomposites represent an innovative and promising class of materials. Potential biomedical applications of chitosan/clay nanocomposites include: the intercalation of cationic chitosan in the expandable aluminosilicate structure of the clay is expected to affect the binding of cationic drugs by anionic clay; the solubility of chitosan at the low pH of gastric fluid may decrease the premature release of drugs in the gastric environment;

cationic chitosan may result in the efficient transport of negatively charged drugs; the presence of reactive amine groups on chitosan may provide ligand attachment sites for targeted drug delivery; etc. The limited solubility of a chitosan/clay nanocomposite drug carriers at gastric pH offers significant advantages for colon-specific delivery of drugs that may be destroyed in the acidic gastric environment or by the presence of gastric digestive enzymes. Furthermore, the mucoadhesive properties of chitosan may enhance the bioavailability of drugs in the gastrointestinal tract.

Many actual applications of chitosan/clay nanocomposites are reported in the literature. Darder et al., 2005 prepared chitosan/montmorillonite nanocomposites and used them in potentiometric sensors for anion detection. Gecol et al., 2006 investigated the removal of tungsten from water using chitosan coated montmorillonite biosorbents. Chang and Juang, 2004 studied the adsorption of tannic acid, humic acid, and dyes from water using chitosan/activated clay composites. An and Dultz, 2007 reported the adsorption of tannic acid on chitosan–montmorillonite as well Pongjanyakul et al., 2005; Wang et al., 2005; Wu and Wu, 2006; Günister et al., 2007; Khunawattanakul et al., 2008; Pongjanyakul & Suksri, 2009. Darder et al. , 2005 synthesized functional chitosan/MMT nanocomposites, successfully used in the development of bulk modified electrodes. Wang et al., 2005 reported the effect of acetic acid residue and MMT loading in the nanocomposites.

However, there are few reports on chitosan/bentonite nanocomposites (Yang & Chen, 2007; Zhang et al., 2009; Wan Ngah et al., 2010). The physical properties and biological response of chitosan strongly depend on the starting materials and nanocomposite preparation conditions. In the present study chitosan/clay nanocomposites were prepared using two kinds of clay and different chitosan/clay ratios, to evaluate how these variables affect the dispersion of clay particles into the chitosan matrix. The samples obtained were characterized by infrared spectroscopy, x-ray diffraction, and mechanical (tensile) properties.

2. Experimental

2.1 Materials

Chitosan was supplied by Polymar (Fortaleza, CE, Brazil) and used without purification. The chitosan was obtained by deacetylation of chitin from crab shells, with a degree of deacetylation of 86.7%. Sodium bentonite (Argel 35) was provided by Bentonit União Nordeste (Campina Grande, PB, Brazil). The clay, coded BNT, was purified according to procedure reported elsewhere (Araujo et al., 2007); the cation exchange capacity (CEC) of the purified bentonite was 0.92 meq/g (Leite et al., 2010). Sodium montmorillonite (Cloisite Na⁺), coded MMT, with a CEC of 0.90 meq/g was supplied by Southern Clay Products (Gonzalez, TX, USA). Both of the clays, purified sodium bentonite (BNT) and sodium montmorillonite (MMT), were screened to 200 mesh size before mixed with chitosan.

2.2 Preparation of chitosan films

Chitosan solutions were prepared by dissolving chitosan in a 1% aqueous acetic acid solution at a concentration of 1 wt% under continuous stirring at 45°C for 2 h followed by vacuum filtering to remove the insoluble residue. This solution was cast into Petri dishes (radius ~ 12 cm) and dried at 50°C for 20 h to evaporate the solvent and form the films. The

dried films were soaked with an aqueous solution of 1 M NaOH for 30 min to remove residual acetic acid, followed by rinsing with distilled water to neutralize, and then dried at room temperature. The chitosan films were coded CS.

2.3 Preparation of the chitosan/clay films

Chitosan/clay films were prepared by a casting/solvent evaporation technique. Firstly, 1% chitosan solutions were adjusted to pH = 4.9 by addition a 1M sodium hydroxide solution to form the NH_3^+ groups in the chitosan structure. Given that the primary amine group in the structure of the chitosan has a pKa = 6.3, 95% of the groups amine will be protonated at the final pH = 5. of the chitosan/clay mixture (Darder et al., 2005). After, the chitosan solution was slowly added to a 1 wt% clay suspension followed by stirring at $53 \pm 2^\circ\text{C}$ for 4 h to obtain the films with chitosan/clay mass ratios of 1:1, 5:1 and 10:1. This chitosan/clay solution was cast into Petri dishes and dried at 50°C for 20 h to evaporate the solvent and form the films. Following the same procedure used for chitosan films, the dried films were soaked into an aqueous solution of 1 M NaOH for 30 min to remove residual acetic acid, followed by rinsing in distilled water to neutral and then dried at room temperature. The chitosan/purified sodium bentonite and chitosan/sodium montmorillonite films prepared from chitosan/clay mass ratio of the 1:1, 5:1 and 10:1 were denoted CS1:BNT1; CS5:BNT1; CS10/BNT1 and CS1:MMT1; CS5:MMT1; CS10:MMT1, respectively.

2.4 Characterization

Although the clay dispersion process is usually followed by x-ray diffraction and transmission electron microscopy, infrared spectroscopic techniques may shed light into the complex chemical and physical interactions involved, helping scientists and technologists to understand the mechanisms of nanocomposite formation, and leading to better products and production methods in the laboratory and the industrial plant. Furthermore, infrared spectroscopic is relatively rapid, is a common instrument found in most research laboratories, sample purity is not as critical and the method can be used with insoluble samples. This gives infrared spectroscopic methods an advantage over other methods, which require elaborate and time-consuming sample preparation.

Fourier transform infrared spectra of the chitosan films and the chitosan/clay films were collected using a Spectrum 400 Perkin Elmer operating in the range of $400\text{-}4000\text{ cm}^{-1}$ at a resolution of 4 cm^{-1} .

XRD patterns were obtained using a Shimadzu XRD-6000 diffractometer with $\text{Cu}_{\text{K}\alpha}$ radiation ($\lambda = 0.154\text{ nm}$, 40 kV, 30 mA) at room temperature. XRD scans were performed on sodium montmorillonite and purified sodium bentonite, chitosan films and chitosan/clay films with a 2θ range between 1.5° and 12.0° , at a scanning rate of $1^\circ/\text{min}$ and a scanning step of 0.02° . The basal spacing (d_{001}) value of the layered silicates and the chitosan/layer silicate films were computed using Bragg's law.

Mechanical properties of chitosan films and chitosan/clay films were measured following ASTM D882 standard procedures. The films were cut in rectangular strips ($80 \times 10\text{ mm}$) and the thickness of each sample was measured at three different locations and averaged. The tensile strength (TS), elastic modulus (EM) and elongation at break (E) of the samples were determined using a universal testing machine (EMIC, model DL1000) fitted with a load cell

of 50 N, with initial gauge separation of 50 mm and a stretching speed of 5 mm/min. Reported results were the average of five independent measurements.

3. Results and discussion

3.1 Infrared spectroscopy (FTIR)

Fig. 4 shows FTIR spectra in the 4000–400 cm^{-1} wave number range for sodium montmorillonite (MMT), purified sodium bentonite (BNT), chitosan film (CS),

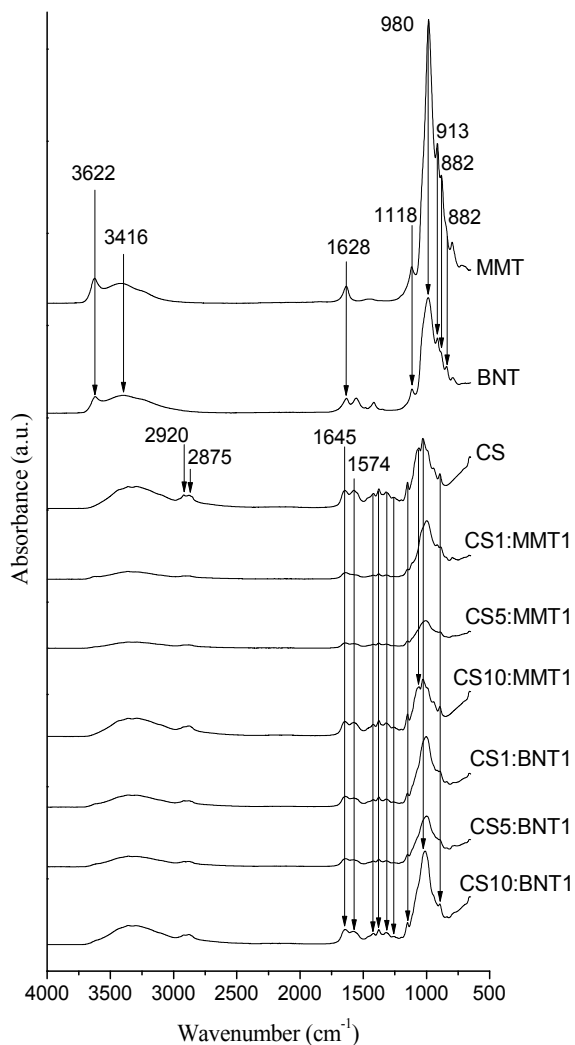


Fig. 4. FTIR spectra in the 4000–400 cm^{-1} wave number range for sodium montmorillonite (MMT), purified sodium bentonite (BNT), chitosan film (CS), chitosan/MMT and chitosan/BNT films with 1:1, 5:1 and 10:1 chitosan/clay ratios, respectively (CS1:MMT1; CS5:MMT1; CS10:MMT1 and CS1:BNT1; CS5:BNT1; CS10:BNT1).

chitosan/MMT and chitosan/BNT films with 1:1, 5:1 and 10:1 chitosan/clay ratios, respectively (CS1:MMT1; CS5:MMT1; CS10:MMT1 and CS1:BNT1; CS5:BNT1; CS10:BNT1).

In the clay spectra (MMT and BNT), the characteristic absorption band at $\sim 3622\text{ cm}^{-1}$ [ν_{OH}] is assigned to the stretching vibration of AlOH and SiOH; at $\sim 3416\text{ cm}^{-1}$ [ν_{OH}] to the stretching vibration of H_2O ; at $\sim 1628\text{ cm}^{-1}$ [δ_{HOH}] to the bending vibration of H_2O ; at $\sim 1118\text{ cm}^{-1}$ and at $\sim 980\text{ cm}^{-1}$ [$\nu_{\text{Si-O}}$] to the stretching vibration of SiO; at $\sim 913\text{ cm}^{-1}$ [$\delta_{\text{Al-Al-OH}}$] to the bending vibration of AlAlOH; at $\sim 882\text{ cm}^{-1}$ [$\delta_{\text{Al-Fe-OH}}$] to the bending vibration of AlFeOH; and at $\sim 841\text{ cm}^{-1}$ [$\delta_{\text{Al-Mg-OH}}$] to the bending vibration of AlMgOH (Awad et al., 2004; Bora et al., 2000; Leite et al., 2010; Madejová, 2003; Xu et al., 2009).

In order to fully characterize the starting materials, a spectrum of pure chitosan was also recorded. The main bands appearing in that spectrum were due to stretching vibrations of OH groups in the range from 3750 cm^{-1} to 3000 cm^{-1} , which are overlapped to the stretching vibration of N-H; and C-H bond in $-\text{CH}_2$ ($\nu_1 = 2920\text{ cm}^{-1}$) and $-\text{CH}_3$ ($\nu_2 = 2875\text{ cm}^{-1}$) groups, respectively. Bending vibrations of methylene and methyl groups were also visible at $\nu = 1375\text{ cm}^{-1}$ and $\nu = 1426\text{ cm}^{-1}$, respectively (Mano et al., 2003). Absorption in the range of $1680\text{--}1480\text{ cm}^{-1}$ was related to the vibrations of carbonyl bonds (C=O) of the amide group CONHR (secondary amide, $\nu_1 = 1645\text{ cm}^{-1}$) and to the vibrations of protonated amine group ($\delta_{\text{NH}_3^+}$, $\nu_2 = 1574\text{ cm}^{-1}$) (Marchessault et al., 2006). Absorption in the range from 1160 cm^{-1} to 1000 cm^{-1} has been attributed to vibrations of CO group (Xu et al., 2005). The band located near $\nu = 1150\text{ cm}^{-1}$ is related to asymmetric vibrations of CO in the oxygen bridge resulting from deacetylation of chitosan. The bands near $1080\text{--}1025\text{ cm}^{-1}$ are attributed to ν_{CO} of the ring COH, COC and CH_2OH . The small peak at $\sim 890\text{ cm}^{-1}$ corresponds to wagging of the saccharide structure of chitosan (Darder et al., 2003; Paluszkiwicz et al., 2011; Yuan et al., 2010). The assigned characteristic FTIR absorption bands of clay (MMT and BNT) and chitosan film (CS) derived from Fig. 4 are summarized in Table 1.

FTIR was also used to study the polymer/clay interaction, since a shift in the $\delta_{\text{NH}_3^+}$ vibration may be expected when $-\text{NH}_3^+$ groups interact electrostatically with the negatively charged sites of the clay. In fact, a shift of the $\delta_{\text{NH}_3^+}$ band towards a lower frequency is observed in all the chitosan/clay films (CS1:MMT1; CS5:MMT1; CS10:MMT1 and CS1:BNT1; CS5:BNT1; CS10:BNT1) as show in Fig. 5 (spectra of Fig. 4 in the $1800\text{--}1400\text{ cm}^{-1}$ wavenumber range) and Table 2. Nevertheless, this shift is higher for chitosan/clay films with the lowest amounts of chitosan (CS1:MMT1; CS5:MMT1 and CS1:BNT1; CS5:BNT1), while the chitosan/clay films with the highest amounts of biopolymer (CS10:MMT1 and CS10:BNT1) show a frequency value that trends to that observed in the films of pure chitosan (CS). This fact may be related to the $-\text{NH}_3^+$ groups that do not interact electrostatically with the clay substrate (Fig.6). Besides, the intensity of the $\delta_{\text{NH}_3^+}$ band also increases for higher amounts of intercalated chitosan (CS10:MMT1 and CS10:BNT1) (Fig.5). The secondary amide band (ν_1) at 1645 cm^{-1} of chitosan is overlapped with the δ_{HOH} bending vibration band at 1628 cm^{-1} of the water molecules associated to the chitosan/clay films, which are present as in the starting clay, as expected for a biopolymer with high water retention capability (Darder et al., 2003; Darder et al., 2005; Han et al., 2010; Paluszkiwicz et al., 2011; Tan et al., 2007; Wang & Wang, 2007). Comparing the spectra of chitosan/MMT with the spectra of chitosan/BNT we can observe that the interaction of the chitosan with both clays (MMT and BNT) is similar.

Sample	IR band (cm ⁻¹)	Description*
Clay (MMT and BNT)	3622	v(O-H) for Al-OH and Si-OH
	3416	v(O-H) for H-O-H
	1628	δ(HOH) for H-O-H
	1118 and 980	v(Si-O) out of plane
	913	δ(AlAlOH)
	882	δ(AlFeOH)
	841	δ(AlMgOH)
	Chitosan film (CS)	3750-3000
2920		v _{as} (C-H)
2875		v _s (C-H)
1645		v(-C=O) secondaryamide
1574		v(-C=O)protonated amine
1426, 1375		δ(C-H)
1313		v _s (-CH ₃) tertiary amide
1261		v(C-O-H)
1150, 1065, 1024		v _{as} (C-O-C) and v _s (C-O-C)
890		ω(C-H)

*v = stretching vibration; v_s = symmetric stretching vibration; v_{as} = asymmetric stretching vibration; ω = wagging.

Table 1. Assignment of FTIR spectra of clays and chitosan derived from Fig. 4.

Sample	δ _{HOH} (cm ⁻¹)	δ _{NH₃} (cm ⁻¹)
Clay (MMT and BNT)	1628*	-
Chitosan film (CS)	1645	1574
Chitosan/MMT (CS1:MMT1)	1638	1555
Chitosan/MMT (CS5:MMT1)	1640	1558
Chitosan/MMT (CS10:MMT1)	1645	1570
Chitosan/BNT (CS1:BNT1)	1640	1557
Chitosan/BNT (CS5:BNT1)	1641	1558
Chitosan/BNT (CS10:BNT1)	1643	1570

*stretching band of secondary amide v(-C=O).

Table 2. Frequency values of vibrational bands corresponding to the water molecules associated with the clay (MMT and BNT) and with the protonated amine group in the chitosan chain.

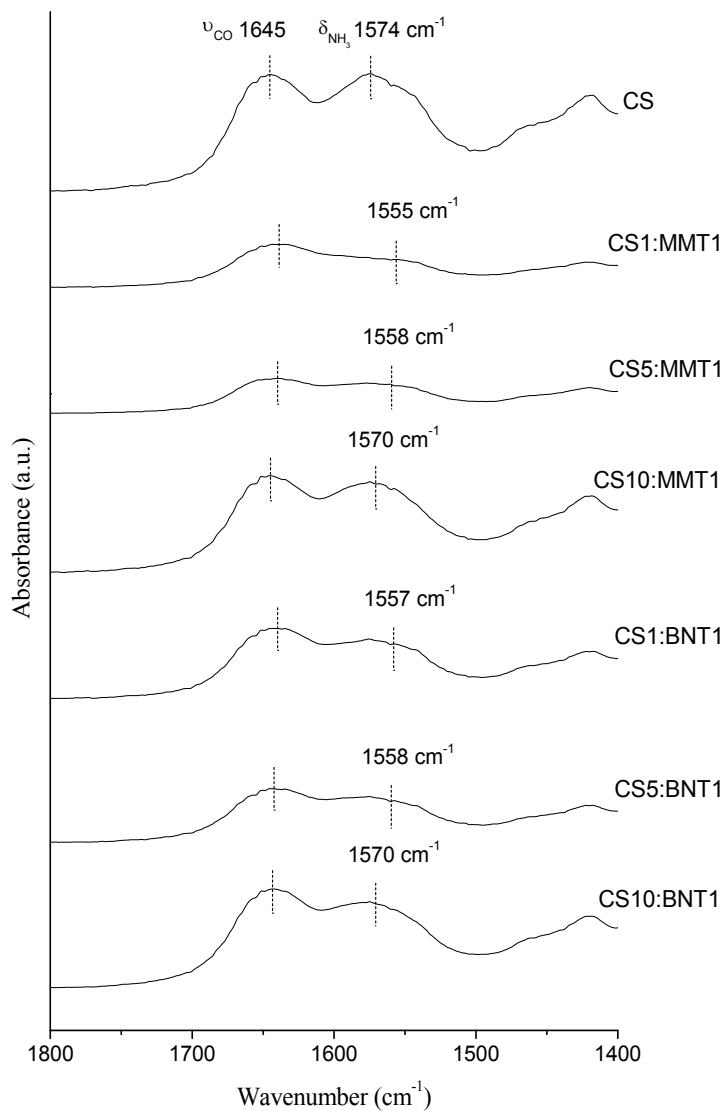


Fig. 5. IR spectra of Fig. 4 in the 1800–1400 cm⁻¹ wavenumber range of chitosan film (CS), chitosan/MMT and chitosan/BNT films prepared from 1:1, 5:1 and 10:1 chitosan–clay ratios (CS1:MMT1; CS5:MMT1; CS10:MMT1 and CS1:BNT1; CS5:BNT1; CS10:BNT1).

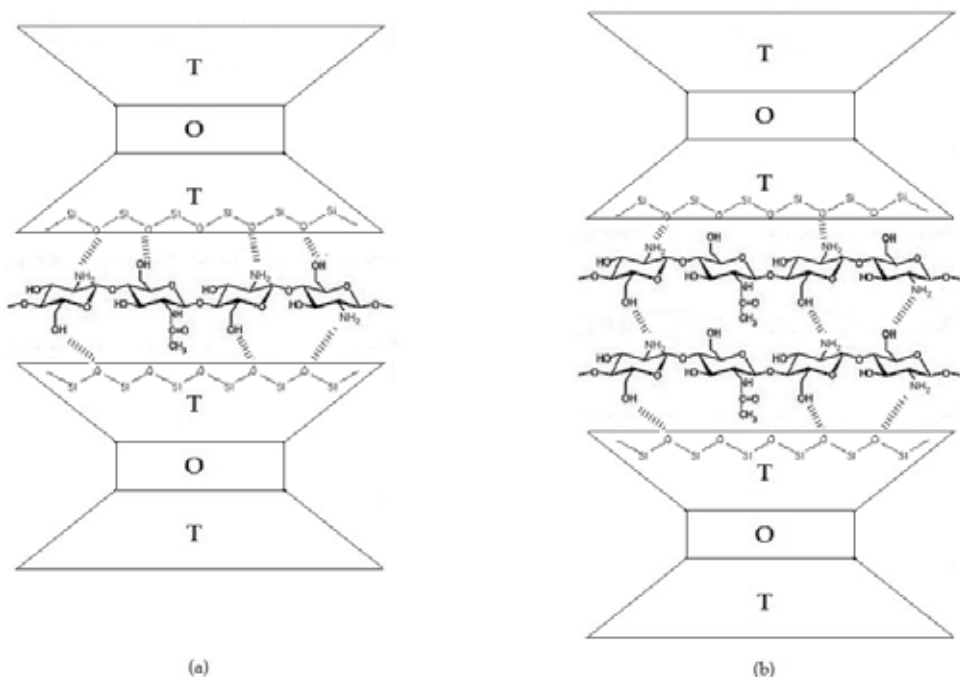


Fig. 6. Schematic illustration of the intercalation of chitosan layers into the clay inter-layer spacing for films (a) with the lowest amounts of chitosan (CS1:MMT1 and CS1:BNT1) and (b) with the highest amounts of biopolymer (CS10:MMT1, CS5:MMT1 and CS10:BNT1, CS5:BNT1).

3.2 X ray diffraction analysis (XRD)

XRD is the principal method that has been used to examine the distribution/dispersion of the clay platelet stacks in the polymer matrix (Utracki, 2004). Depending on the relative distribution/dispersion of the stacks, three types of nanocomposites can be described: *intercalated nanocomposites*, where polymer chains are interleaved with silicate layers, resulting in a well ordered multilayer morphology built up with alternating polymer and inorganic sheets; *flocculated nanocomposites*, where intercalated clay layers are sometimes bonded by hydroxylated edge-edge interactions, and *exfoliated/delaminated nanocomposites*, where individual clay layers are completely and homogeneously dispersed in the polymer matrix (Wang et al., 2005).

FTIR data indicate that chitosan was intercalated into the MMT and BNT interlayers. However, to confirm the FTIR results, the MMT and BNT clays, as well as, chitosan/MMT and chitosan/BNT films prepared from 1:1, 5:1 and 10:1 chitosan/clay ratios, respectively (CS1:MMT1; CS5:MMT1; CS10:MMT1 and CS1:BNT1; CS5:BNT1; CS10:BNT1) were analyzed by XRD and the results are shown in Figs. 7-9.

The XRD patterns of the MMT (Fig. 7) shows a reflection peak at about $2\theta = 5.9^\circ$, corresponding to a basal spacing (d_{001}) of 1.50 nm. After incorporating MMT within CS, with CS/MMT 1:1 ratio, the basal plane of MMT at $2\theta = 5.9^\circ$ disappears, substituted by a new weakened broad peak at around $2\theta = 2.8^\circ - 3.7^\circ$ [CS1:MMT1 (1), CS1:MMT1 (2) and

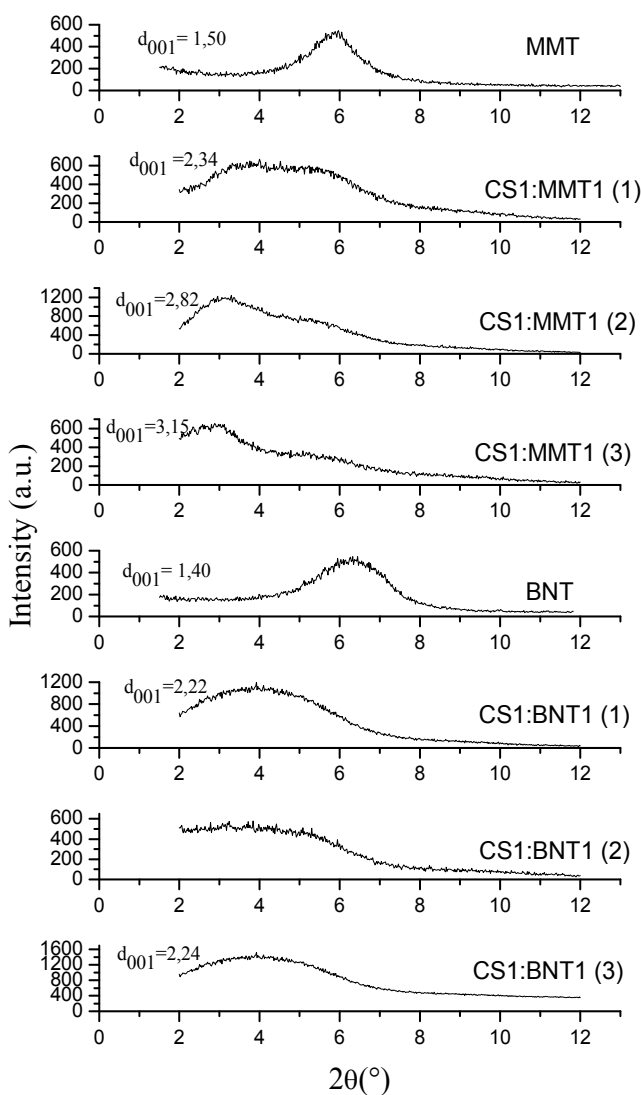


Fig. 7. XRD pattern of sodium montmorillonite (MMT), purified sodium bentonite (BNT), chitosan/MMT and chitosan/BNT films prepared from 1:1 chitosan/clay ratios in triplicate [CS1:MMT1 (1), CS1:MMT1 (2), CS1:MMT1 (3) and CS1:BNT1 (1), CS1:BNT1 (2), CS1:BNT1 (3)].

CS1:MMT1 (3)]. The shift of the basal reflection of MMT to lower angle indicates the formation of an intercalated nanostructure, while the peak broadening and intensity decreases most likely indicate the disordered intercalated or exfoliated structure (Utracki, 2004; Wang et al., 2005). Similar behavior was observed for CS/BNT (Fig. 7), i.e. the basal plane of BNT at $2\theta = 6.3^\circ$ disappears, substituted by a new weakened broad peak at around $2\theta = 3.0^\circ - 3.9^\circ$ [CS1:BNT1 (1), CS1:BNT1 (2) and CS1:BNT1 (3)]. It is suggested that the MMT and the BNT form intercalated and flocculated structures.

Fig. 8 shows the XRD patterns of the MMT, BNT, chitosan/MMT and chitosan/BNT films prepared from 5:1 chitosan/clay ratios in triplicate [CS5:MMT1 (1), CS5:MMT1 (2), CS5:MMT1 (3) and CS5:BNT1 (1), CS5:BNT1 (2), CS5:BNT1 (3)]. After incorporating MMT within CS, with CS/MMT 5:1 ratio, the basal plane of MMT at $2\theta = 5.9^\circ$ disappears, substituted by a new weakened broad peak at around $2\theta = 2.0^\circ - 3.8^\circ$ [CS5:MMT1 (1), CS5:MMT1 (2) and CS5:MMT1 (3)]. In this case the 2θ values were smaller than the values observed for chitosan/MMT prepared from 1:1 ratio (Fig. 7), indicating that exfoliated/delaminated nanocomposites were probably obtained. In the same way exfoliated/delaminated nanocomposites are probably obtained for Chitosan/BNT [CS5:BNT1 (1), CS5:BNT1 (2) and CS5:BNT1 (3)].

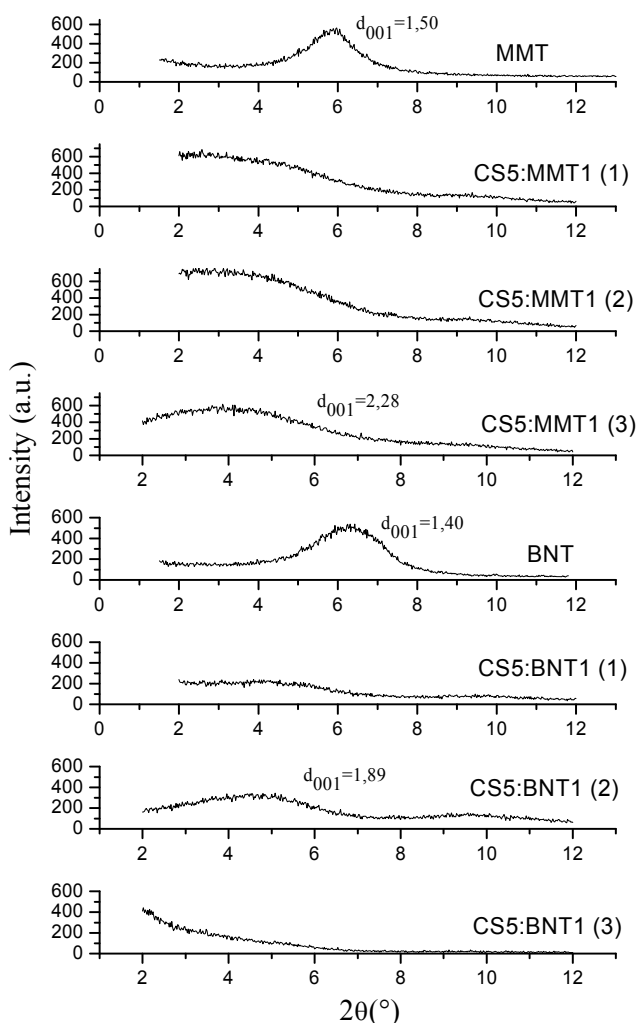


Fig. 8. XRD pattern of MMT, BNT, chitosan/MMT and chitosan/BNT films prepared from 5:1 chitosan/clay ratios in triplicate [CS5:MMT1 (1), CS5:MMT1 (2), CS5:MMT1 (3) and CS5:BNT1 (1), CS5:BNT1 (2), CS5:BNT1 (3)].

Fig. 9 shows the XRD patterns of the MMT, BNT, chitosan/MMT and chitosan/BNT films prepared from 10:1 chitosan/clay ratios in triplicate [CS10:MMT1 (1), CS10:MMT1 (2), CS10:MMT1 (3) and CS10:BNT1 (1), CS10:BNT1 (2), CS10:BNT1 (3)]. With increasing CS content, the 2θ of (001) peak becomes lower and it is not possible to calculate the interlayer distance for each nanocomposite in the broad peaks, indicating that the MMT and the BNT forms intercalated and exfoliated structures. In all probability, exfoliated/delaminated structures were obtained in this case.

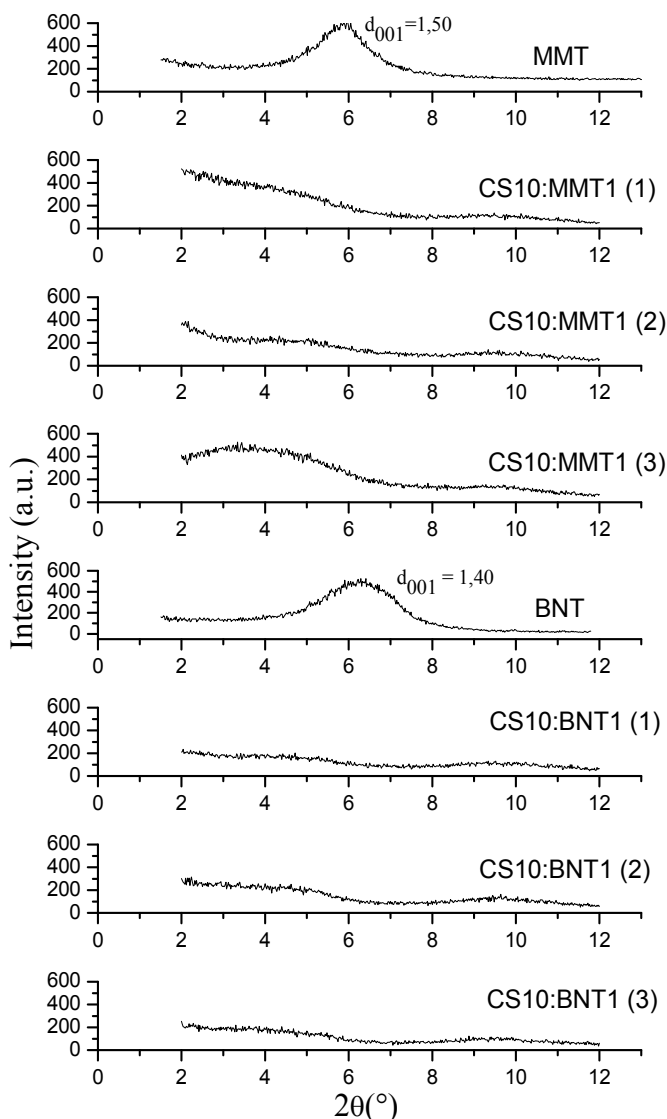


Fig. 9. XRD pattern of MMT, BNT, chitosan/MMT and chitosan/BNT films prepared from 10:1 chitosan/clay ratios in triplicate [CS10:MMT1 (1), CS10:MMT1 (2), CS10:MMT1 (3) and CS10:BNT1 (1), CS10:BNT1 (2), CS10:BNT1 (3)].

In summary, the morphology of the nanocomposites was affected by chitosan/clay ratios. On the base of XRD patterns, it is suggested that the MMT and the BNT forms intercalated and exfoliated structures at higher CS content (CS10:MMT1, CS5:MMT1 and CS10:BNT1, CS5:BNT1), while decreasing the CS content (CS1:MMT1 and CS1:BNT1), clay layers (MMT and BNT) form intercalated and flocculated structures. According Wang et al., 2005, the formation of flocculated structure in CS/clay nanocomposites can be due to the hydroxylated edge-edge interactions of the clay layers. Since one chitosan unit possesses one amino and two hydroxyl functional groups, these groups can form hydrogen bonds with the clay hydroxyl edge groups, which leads to the strong interactions between matrix and clay layers (Fig.6a) and corroborate FTIR results. This strong interaction is believed to be the main driving force for the assembly of MMT and BNT in the CS matrix to form flocculated structures.

3.3 Mechanical properties

Tensile properties of the chitosan film (CS) and chitosan/clay films prepared from 1:1, 5:1 and 10:1 chitosan/clay ratios, respectively (CS1:MMT1; CS5:MMT1; CS10:MMT1 and CS1:BNT1; CS5:BNT1; CS10:BNT1) are collected in Table 3. The tensile strength (TS) and elastic modulus (EM) of chitosan films increase by the formation of nanocomposites, particularly for chitosan/clay prepared from 5:1 ratios. The increase in the TS and EM of such nanocomposite films can be attributed to the high rigidity and aspect ratio of the nano-clay as well as the high affinity between the biopolymer and the clay. On the other hand, the chitosan/clay nanocomposites have shown significant decrease in elongation at break (EB). This reduction can be attributed to the restricted mobility of macromolecular chains.

Sample	TS (MPa)	EM (MPa)	EB (%)
Chitosan film (CS)	44.5 ± 4.5	1774 ± 63	7.7 ± 0.5
Chitosan/MMT (CS1:MMT1)	84.9 ± 3.7	5214 ± 112	3.3 ± 0.5
Chitosan/MMT (CS5:MMT1)	79.1 ± 1.1	4449 ± 329	4.6 ± 0.7
Chitosan/MMT (CS10:MMT1)	68.5 ± 1.4	3536 ± 180	4.6 ± 0.8
Chitosan/BNT (CS1:BNT1)	49.6 ± 4.9	4075 ± 73	2.4 ± 0.9
Chitosan/BNT (CS5:BNT1)	62.1 ± 4.5	3106 ± 50	6.8 ± 0.8
Chitosan/BNT (CS10:BNT1)	40.4 ± 1.8	2421 ± 87	5.9 ± 0.8

(TS = tensile strength, EM = elastic modulus (EM), EB = elongation at break)

Table 3. Tensile properties of chitosan and chitosan/clay films.

4. Conclusions

In this study chitosan/clay nanocomposites were successfully prepared by the solution intercalation process. It was found that clay dispersion is affected by the kind of clay and the chitosan/clay ratio. Since the nanocomposites prepared with purified bentonite (BNT) showed similar behavior to that prepared with montmorillonite, less expensive bentonite may be employed in the preparation of chitosan/clay nanocomposites.

The intercalation of the cationic biopolymer chitosan into layered silicate clays (montmorillonite and bentonite) through a cation exchange process results in nanocomposites with interesting structural and functional properties. The clay reduces the film-forming capability of chitosan leading to compact, robust, and handy three-dimensional nanocomposites. The techniques employed in the characterization of the nanocomposites, infrared spectroscopy, x-ray diffraction, and mechanical properties in tension, confirm the high affinity between the clay substrate and the biopolymer, as well as the special arrangement of chitosan as a bilayer when the biopolymer amount exceeds the cation exchange capacity of the clay. The intercalation of the first layer of chitosan takes place mainly by electrostatic interactions between positive ammonium groups in the chitosan chain and negative sites in the clay. In contrast, hydrogen bonds between amino and hydroxyl groups of chitosan and the clay substrate are established in the adsorption of the second layer.

5. Acknowledgments

This research was financially supported by CAPES, CNPq and INAMI (Brazil). We thank Prof. Heber Carlos Ferreira (Department of Materials Engineering, Federal University of Campina Grande) for graciously providing sodium montmorillonite (Cloisite Na⁺) samples.

6. References

- An JH., Dultz S. (2007). Adsorption of tannic acid on chitosan-montmorillonite as a function of pH and surface charge properties. *Applied Clay Science*. Vol. 36, pp. 256-64.
- Araujo, P. E. R.; Araújo, S. S.; Raposo, C. M. O.; Silva, S. M. L. (2007). 23th Polymer Processing Society Annual Meeting. Vol. 23, pp.1.
- Awad, W. H.; Gilman, J. W.; Nyden, M.; Harris, R. H.; Sutto, T. E.; Callahan, J.; Trulove, P. C.; Delong, H. C.; Fox, D. M. (2004). Thermal degradation studies of alkyl-imidazolium salts and their application in nanocomposites. *Thermochimica Acta*. Vol. 409, p. 3-11.
- Bolto, B.; Dixon, D.; Eldridge, R.; King, S. (2001). Cationic polymer and clay or metal oxide combinations for natural organic matter removal. *Water Research*. Vol. 35, p. 2669-2676.
- Bora, M.; Ganguli, J. N.; Dutta, D. K. (2000). Thermal and spectroscopic studies on the decomposition of [Ni{di(2-aminoethyl)amine}2]- and [Ni(2,2':6'',2''-terpyridine)2]-Montmorillonite intercalated composites *Thermochimica Acta*. Vol. 346, p.169-175.
- Chang, M. Y.; Juang, R. S. (2004). Adsorption of tannic acid, humic acid and dyes from water using the composite of chitosan and activated clay. *Journal of Colloid and Interface Science*. Vol. 278, pp.18-25.
- Chivrac, F.; Pollet, E.; Avérous, L. (2009). Progress in nano biocomposites based on polysaccharides and nanoclays. *Materials Science and Engineering R*. Vol. 67, pp. 1-17.
- Darder, M.; Colilla, M.; Ruiz-hitzky, E. (2003). Biopolymer-Clay Nanocomposites Based on Chitosan Intercalated in Montmorillonite. *Chemical Materials*. vol. 15, pp. 3774-3780.
- Darder, M.; Colilla, M.; Ruiz-Hitzky, E. (2005). Chitosan clay nanocomposites: application as Electrochemical sensors. *Applied Clay Science*. Vol.28, pp.199-208.

- Dash, M.; Chiellini, F.; Ottenbrite, R.M.; Chiellini E. (2011). Chitosan—A versatile semi-synthetic polymer in biomedical applications. *Progress in Polymer Science*, Vol. 36, pp. 981–1014.
- E. S. Costa; H. S. Mansur. (2008). Preparação e caracterização de blendas de quitosana/poli (álcool vinílico) reticuladas quimicamente com glutaraldeído para aplicação em engenharia de tecido. *Química Nova*. Vol.31, pp.1460–1466.
- Felt, O.; Carrel, A.; Baehni, P.; Buri, P.; Gurny, R. (2000) Chitosan as tear substitute: a wetting agent endowed with antimicrobial efficacy. *Journal of Ocular Pharmacology and Therapeutics*. Vol. 16, pp. 261–270.
- Gecol, H.; Miakatsindila, P.; Ergican, E.; Hiibel, S. R. (2006). Biopolymer coated clay particles for the adsorption of tungsten from water. *Desalination*. Vol. 197, pp. 165–78.
- Günister, E., Pestreli, D., Ünlü, C.H.; Güngör, N. (2007). Synthesis and characterization of chitosan-MMT biocomposite systems. *Carbohydrate Polymers*. Vol. 67, pp.358-365.
- Han, Y.; Lee, S.; Choi, K. H. (2010). Preparation and characterization of chitosan-clay nanocomposites with antimicrobial activity. *Journal of Physics and Chemistry of Solids*. Vol. 71, pp. 464–467.
- Holzer, L.; Münch, B.; Rizzi, M.; Wepf, R.; Marschall, P.; Graule, T. (2010). 3D-microstructure analysis of hydrated bentonite with cryo-stabilized pore water. *Applied Clay Science*. Vol. 47, pp. 330–342.
- Khunawattanakul, W.; Puttipipatkachorn, S.; Rades, T.; Pongjanyakul, T. (2008). Chitosan-magnesium aluminum silicate composite dispersions: characterization of rheology, flocculate size and zeta potential. *International Journal of Pharmaceutics*. Vol.351, pp. 227–235.
- Krajewska, B. (2004). Application of chitin and chitosan-based materials for enzyme immobilizations: a review. *Enzyme and Microbial Technology*. Vol. 35, pp. 126–134.
- Lavorgna, M.; Piscitelli, F.; Mangiacapra, P.; Buonocore, G. (2010). Study of the combined effect of both clay and glycerol plasticizer on the properties of chitosan films. *Carbohydrate Polymers*. Vol. 82, pp. 291–298.
- Leite, I. F.; Soares, A. P. S.; Carvalho, L.H.; Malta, O. M. L.; Raposo, C. M. O.; Silva, S. M. S. (2010). Characterization of pristine and purified organobentonites. *Journal of Thermal Analysis and Calorimetry*. Vol. 100, pp.563.
- Li, Q.; Yue, Q. Y.; Sun, H. J.; Su, Y.; Gao, B. Y. (2010). A comparative study on the properties, mechanism and process designs for the adsorption of non-ionic or anionic dyes onto cationic-polymer/bentonite. *Journal of Environmental Management*. Vol. 91, pp.1601–1611.
- Madejová, J. (2003). FTIR techniques in clay mineral studies. *Vibrational Spectroscopy*. Vol.31, pp.1-10.
- Mano, J.F.; Koniarova, D.; Reis, R.L. (2003). *Journal of Materials Science: Materials in Medicine*. Vol. 14, pp.127–135.
- Marchessault, R.H.; Ravenelle, F.; Zhu, X.X. (2006). Polysaccharides for drug delivery and pharmaceutical applications, *American Chemical Society*.
- No, H. K.; Lee, K. S.; Meyers, S. P. (2000). Correlation between physicochemical characteristics and binding capacities of chitosan products. *Journal Food Science*. Vol. 65, pp. 1134–1137.

- Pandey, S. Mishra S. B., (2011). Organic-inorganic hybrid of chitosan/organoclay bionanocomposites for hexavalent chromium uptake, *Journal of Colloid and Interface Science*. Vol. 361, pp. 509-520.
- Paluszkiwicz, C.; Stodolak, E.; Hasik, M.; Blazewicz, M. (2011). FT-IR study of montmorillonite - chitosan nanocomposite materials, *Spectrochimica Acta Part A*. Vol. 79, pp. 784-788.
- Pongjanyakul, T.; Priprem, A.; Puttipipatkachorn, S. (2005). Investigation of novel alginate-magnesium aluminum silicate microcomposite films for modified-release tablets. *Journal Control. Release*. Vol. 107, pp. 343-356.
- Pongjanyakul, T.; Suksri, H. (2009). Alginate -magnesium aluminum silicate films for buccal delivery of nicotine. *Colloids and Surfaces B: Biointerfaces*. Vol. 74, pp. 103-113.
- Rinaudo, M. (2006). Chitin and chitosan: Properties and applications. *Progress in Polymer Science*. Vol. 31, pp. 603-632.
- Tan, W.; Zhang, Y.; Szeto, Y.; Liao, L. (2007). A novel method to prepare chitosan/montmorillonite nanocomposites in the presence of hydroxyl-aluminum oligomeric cations. *Composites Science and Technology*.
- Utracki, L. A. (2004). Basic Elements of Polymeric Nanocomposite Technology, In: *Clay-Containing Polymeric Nanocomposites*, pp. 73-96, Rapra Technology Limited, England.
- Wan Ngah, W. S.; Ariff, N. F. M.; Hanafiah, M. A. K. M. (2010). Preparation, characterization, and environmental application of crosslinked chitosan-coated bentonite for tartrazine adsorption from aqueous solutions. *Water, Air and Soil Pollution*. Vol. 206, pp. 225-236.
- Wan Ngah, W. S.; Teong, L. C.; Hanafiah, M. A. K. M. (2011). Adsorption of dyes and heavy metal ions by chitosan composites: A review. *Carbohydrate Polymers*. Vol. 83, pp. 1446-1456.
- Wang, L.; Wang, A. (2007). Adsorption characteristics of Congo Red onto the chitosan/montmorillonite nanocomposite. *Journal of Hazardous Materials*. Vol. 147, pp. 979-985.
- Wang, S. F.; Shen, L.; Tong, Y. J.; Chen, L.; Phang, I. Y.; Lim, P. Q. (2005). Biopolymer chitosan/montmorillonite nanocomposites: Preparation and characterization. *Polymer Degradation and Stability*. Vol. 90, pp. 123-131.
- Wang, X.; Du, Y.; Yang, J.; Wang, X.; Shi, X.; Hu Y. (2006). Preparation, characterization and antimicrobial activity of chitosan/layered silicate nanocomposites. *Polymer*. Vol. 47, pp. 6738-6744.
- Wei, J. M.; Zhu, R. L.; Zhu, J. X.; Ge, F.; Yuan, P.; He, H. P. (2009). Simultaneous sorption of crystal violet and 2-naphthol to bentonite with different CECs. *Journal of Hazardous Materials*. Vol. 166, pp. 195-199.
- Wu, T. M.; Wu, C. Y. (2006). Biodegradable poly (lactic acid)/chitosan-modified montmorillonite nanocomposites: preparation and characterization. *Polymer Degradation and Stability*. Vol. 91, pp. 2198-2204.
- Xu, X.; Ding, Y.; Qian, Z.; Wang, F.; Wen, B.; Zhou, H.; Zhang, S.; Yang, M. (2009). Degradation of poly(ethylene terephthalate)/clay nanocomposites during melt extrusion: Effect of clay catalysis and chain extension. *Polymer Degradation and Stability*. Vol. 94, pp. 113-123.

- Xu, Y.; Kim, K.; Hanna, M.; Nag, D. (2005). Industrial Crops and Products. Vol. 21, pp. 185-192.
- Yang, Y. Q.; Chen, H. J. (2007). Study on the intercalation organic bentonite and its adsorption. Journal of Xinyang Normal University. Vol. 20, pp. 338-340.
- Yuan, Q.; Shah, J.; Hein, S.; Misra, R.D.K. (2010). Controlled and extended drug release behavior of chitosan-based nanoparticle carrier. *Acta Biomaterialia*. Vol. 6, pp. 1140-1148.
- Zhang, A. C.; Sun, L. S.; Xiang, J.; Hu, S.; Fu, P; Su, S. (2009). Removal of elemental mercury from coal combustion flue gas by bentonite-chitosan and their modifier. *Journal of Fuel Chemistry and Technology*. Vol. 37, pp. 489-495.

Structural and Optical Behavior of Vanadate-Tellurate Glasses Containing PbO or Sm₂O₃

E. Culea¹, S. Rada¹, M. Culea² and M. Rada³

¹*Department of Physics and Chemistry, Technical University of Cluj-Napoca, Cluj-Napoca*

²*Faculty of Physics, Babes-Bolyai University of Cluj-Napoca, Cluj-Napoca*

³*National Institute for R&D of Isotopic and Molecular Technologies, Cluj-Napoca
Romania*

1. Introduction

Tellurium oxide based glasses are of scientific and technological interest due to their unique properties such as chemical durability, electrical conductivity, transmission capability, high refractive indices, high dielectric constant and low melting points [1-3].

Tellurate glasses have recently gained wide attention because of their potential as hosts of rare earth elements for the development of fibres and lasers covering all the main telecommunication bands and promising materials for optical switching devices [4, 5]. Recently, tellurate glasses doped with heavy metal oxides or rare earth oxides have received great scientific interest because these oxides can change the optical and physical properties of the tellurate glasses [5].

Vanadium tellurate glasses showed better mechanical and electrical properties due to the V₂O₅ incorporated into the tellurate glass matrix. In the case of V₂O₅ contents below 20mol%, the three-dimensional tellurate network is partially broken by the formation of [TeO₃] trigonal pyramidal units, which in turn reduce the glass rigidity and. When the V₂O₅ concentration is above 20mol%, the glass structure changes from the continuous tellurate network to the continuous vanadate network [6].

Due to the large atomic mass and high polarizability of the Pb²⁺ ions, heavy metal oxide glasses with PbO possess high refractive index, wide infrared transmittance, and hence they are considered to be promising glass hosts for photonic devices [7, 8]. The special significance of PbO is that it contributes to form stable glasses over a wide range of concentrations due to its dual role as glass modifier and glass former.

Rare-earth ions doped glasses have been prepared and characterized to understand their commercial applications as glass lasers and also in the production of wide variety of other types of optical components [9].

The luminescence spectral properties of rare earth ions such as Eu⁺³ (4f⁶) and Tb⁺³ (4f⁸), Sm⁺³ (4f⁵) and Dy⁺³ (4f⁹) in the heavy-metal borate glasses have shown interesting and encouraging results [10, 11]. Eu⁺³ and Tb⁺³ ions have shown prominent emissions (red and green) in the visible wavelength region, while Sm⁺³ and Dy⁺³ show strong absorption bands

in the NIR range (800–2200 nm) and intense emission bands in the visible region (550–730 nm) [11].

The present work deals with the role of lead and samarium ions in the short-range structural order of the vanadate-tellurate glass network. Lead and samarium-activated vanadate-tellurate glasses have been investigated using infrared spectroscopy and ultraviolet-visible spectroscopy. The main goal is to obtain information about the influence of the radii and concentration of lead and samarium ions on the $\text{TeO}_4/\text{TeO}_3$ and VO_5/VO_4 conversion in vanadate-tellurate glasses and especially to illuminate aspects of the vanadate glass network using DFT calculations.

2. Experimental procedure

Glasses were prepared by mixing and melting of appropriate amounts of lead (IV) oxide, tellurium oxide (IV), lead (II) oxide or samarium (III) oxide of high purity (99,99%, Aldrich Chemical Co.). Reagents were melted at 875°C for 10 minutes and quenched by pouring the melts on stainless steel plates.

The samples were analyzed by means of X-ray diffraction using a XRD-6000 Shimadzu diffractometer, with a monochromator of graphite for the Cu-K α radiation ($\lambda=1.54\text{\AA}$) at room temperature.

The FT-IR absorption spectra of the glasses in the 370-1100 cm^{-1} spectral range were obtained with a JASCO FTIR 6200 spectrometer using the standard KBr pellet disc technique. The spectra were carried out with a standard resolution of 2 cm^{-1} .

UV-Visible absorption spectra measurements in the wavelength range of 250-1050nm were performed at room temperature using a Perkin-Elmer Lambda 45 UV/VIS spectrometer equipped with an integrating sphere. These measurements were made on glass powder dispersed in KBr pellets. The optical absorption coefficient, α , was calculated from the absorbance, A , using the equation:

$$\alpha = 2.303 A/d$$

where d is the thickness of the sample.

The starting structures have been built using the graphical interface of Spartan'04 [12] and preoptimized by molecular mechanics. Optimizations were continued at DFT level (B3LYP/CEP-4G/ECP) using the Gaussian'03 package of programs [13].

It should be noticed that only the broken bonds at the model boundary were terminated by hydrogen atoms. The positions of boundary atoms were frozen during the calculation and the coordinates of internal atoms were optimized in order to model the active fragment flexibility and its incorporation into the bulk.

3. Results and discussion

The vitreous or/and crystalline nature of the $x\text{PbO}\cdot(100-x)(3\text{TeO}_2\cdot 2\text{V}_2\text{O}_5)$ and $x\text{Sm}_2\text{O}_3\cdot(100-x)(3\text{TeO}_2\cdot 2\text{V}_2\text{O}_5)$ samples with various contents of lead or samarium oxide ($0\leq x\leq 50\text{mol}\%$) was tested by X-ray diffraction. The X-ray diffraction patterns of the studied samples are shown in Fig. 1. The X-ray diffraction patterns did not reveal the crystalline phases in the

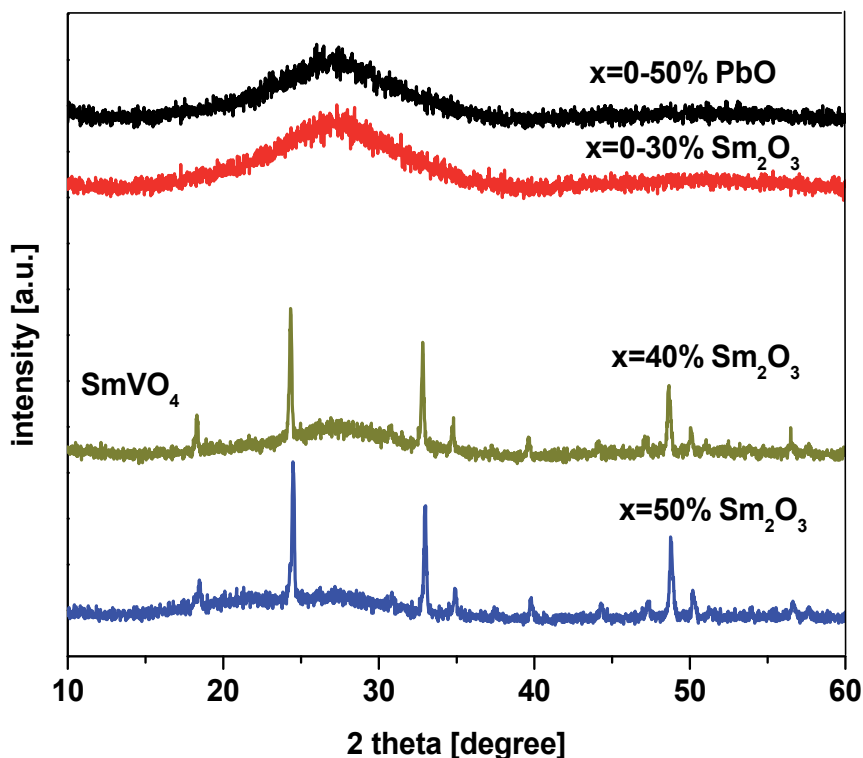


Fig. 1. X-ray diffraction patterns for $x\text{PbO}$ (or $x\text{Sm}_2\text{O}_3$)· $(100-x)[3\text{TeO}_2\cdot 2\text{V}_2\text{O}_5]$ samples where $0 \leq x \leq 50\text{mol}\%$.

samples with $0 \leq x \leq 50\text{mol}\%$ PbO while in the samples with $x \geq 40\text{mol}\%$ Sm₂O₃ the presence of the SmVO₄ crystalline phase was detected.

3.1 FTIR spectroscopy

The absorption bands located around 460cm^{-1} , $610\text{-}680$ and 720 to 780cm^{-1} are assigned to the bending mode of Te-O-Te or O-Te-O linkages, the stretching mode of $[\text{TeO}_4]$ trigonal pyramids with bridging oxygen and the stretching mode of $[\text{TeO}_3]$ trigonal pyramids with non-bridging oxygen, respectively [14-18].

The IR spectrum of the pure crystalline and amorphous V₂O₅ is characterized by the intense band in the $1000\text{-}1020\text{cm}^{-1}$ range which is related to vibrations of isolated V=O vanadyl groups in $[\text{VO}_5]$ trigonal bipyramids. The band located at $950\text{-}970\text{cm}^{-1}$ was attributed to the $[\text{VO}_4]$ units [19-21].

The examination of the FTIR spectra of the $x\text{M}_a\text{O}_b \cdot (100-x)[3\text{TeO}_2 \cdot 2\text{V}_2\text{O}_5]$ where $\text{M}_a\text{O}_b = \text{PbO}$ or Sm₂O₃ glasses and glass ceramics shows some changes in the characteristic bands corresponding to the structural units of the glass network (Fig. 2). These modifications can be summarized as follows:

1. $x = 10\text{mol}\%$ M_aO_b (1)

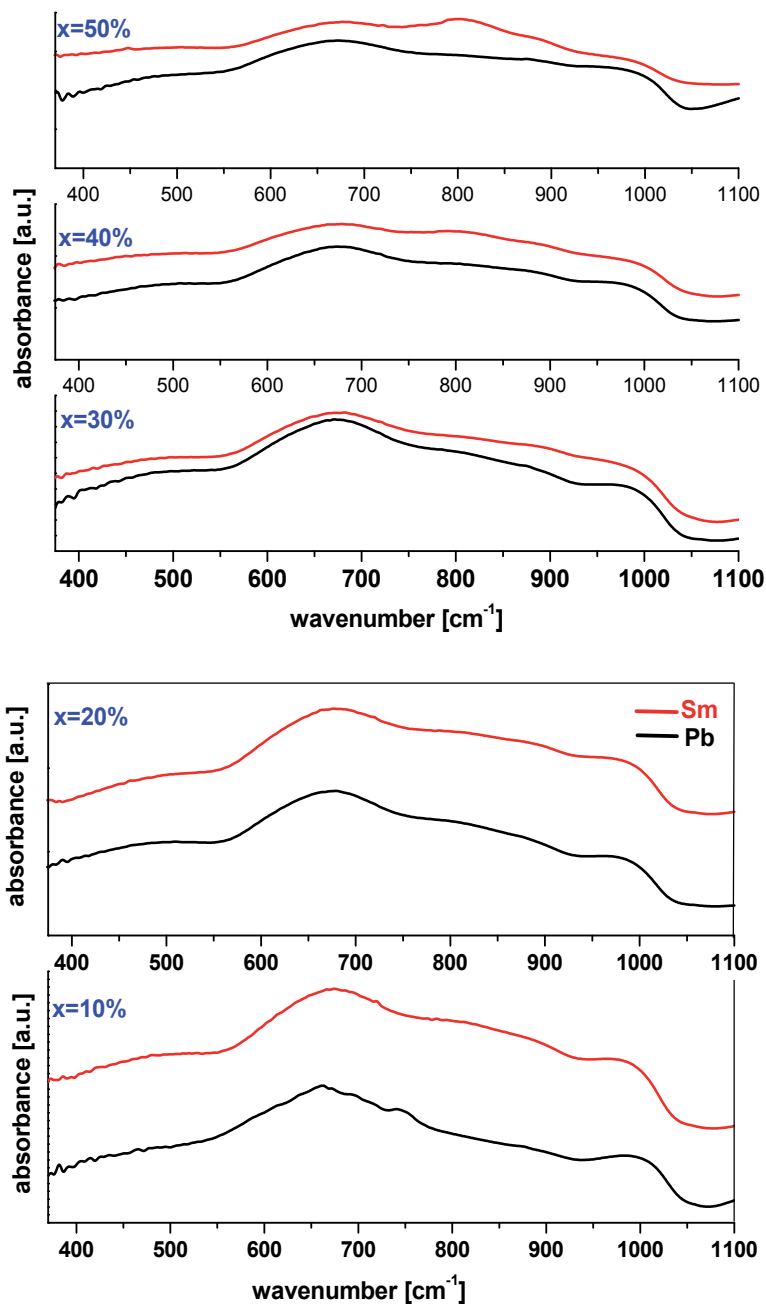


Fig. 2. FTIR spectra of $x\text{PbO}$ (or $x\text{Sm}_2\text{O}_3$)- $(100-x)[3\text{TeO}_2 \cdot 2\text{V}_2\text{O}_5]$ samples where $0 \leq x \leq 50\text{mol}\%$.

The incorporation of network modifier lead ions into the vanadate-tellurate glasses enhances the breaking of axial Te-O-Te linkages in the $[\text{TeO}_4]$ trigonal bipyramidal structural units. As a consequence, three-coordination tellurium is formed and accumulated. The band centered at about 750cm^{-1} indicates the presence of the $[\text{TeO}_3]$ structural units [17,

18]. The [TeO₃] structural units are expected to participate in the depolymerization of the glass network because they create more bonding defects and non-bonding oxygens.

The intensity of the band corresponding to the [TeO₃] units (located at about ~750cm⁻¹) decreases and a new band located at about 800cm⁻¹ appears with the adding of the Sm₂O₃ content. In detail, the band situated at about 800cm⁻¹ is due to the asymmetric stretching of VO₄⁻³ entity from orthovanadate species [22, 23].

2. 10 ≤ x ≤ 30 mol% M_aO_b (2)

An increasing trend was observed in the strength of the bands centered at ~1020cm⁻¹. The feature of the band located at about 875cm⁻¹ comes up in intensity. This effect is more pronounced when adding of samarium ions in the matrix network. This band is attributed to the vibrations of the V-O bonds from the pyrovanadate structural units.

The gradual addition of the samarium (III) oxide leads not only to a simple incorporation of these ions in the host glass matrix but also generates changes of the basic structural units of the glass matrix. Structural changes reveal that the samarium ions causes a change from the continuous vanadate-tellurate network to a continuous samarium-vanadate-tellurate network interconnected through Sm-O-V and Te-O-Sm bridges. Then, the surplus of non-bridging oxygens is be converted to bridging ones leading to the decrease of the connectivity of the network.

3. x ≥ 40mol% M_aO_b (3)

By increasing the Sm₂O₃ content up to 40mol%, the evolution of the structure can be explained considering the higher capacity of migration of the samarium ions inside the glass network and the formation of the SmVO₄ crystalline phase, in agreement with XRD data. The accumulation of oxygen atoms in the glass network can be supported by the formation of ortho- and pyro-vanadate structural units.

On the other hand, the lead oxide generates the rapid deformation of the Te-O-Te linkages yielding the formation of [TeO₃] structural units. Further, the excess of oxygen can be accommodated in the host matrix by conversion of some [VO₄] structural units into [VO₅] structural units.

The broader band centered at ~ 670-850cm⁻¹ can be attributed to the Pb-O bonds vibrations from the [PbO₄] and [PbO₃] structural units. The absorption band centered at about 470cm⁻¹ may be correlated with the Pb-O stretching vibration in [PbO₄] structural units [24-26]. The increase in the intensity of the bands situated between 650 and 850cm⁻¹ show that the excess of oxygen in the glass network can be supported by the increase of [PbO_n] structural units (with n=3 and 4).

In brief, the variations observed in the FTIR spectra suggest a gradual inclusion of the lead ions in the host vitreous matrix with increasing of the PbO content up to 50mol%, while progressive adding of samarium oxide determines the increase in the intensity of the bands due to the ortho- and pyrovanadate structural units. The mechanisms of incorporation of the lead and samarium ions in the host matrices can be summarized as following:

- i. For the samples with lead oxide, the Pb^{+2} ions can occupy a position in the chain itself and their influence on the $\text{V}=\text{O}$ bonds is limited. Since the $\text{V}=\text{O}$ mode position from about 1020cm^{-1} is preserved it can be concluded that the $\text{V}=\text{O}$ bond is not directly influenced and the coordination number and symmetry of the $[\text{VO}_4]$ and $[\text{VO}_5]$ structural units do not change significantly. The increase in the intensity of the bands situated at 650 and 850cm^{-1} show that the PbO acts as a network former with a moderate effect on the vanadate-tellurate network.
- ii. By increasing the samarium oxide content up to $30\text{mol}\%$, Sm^{+3} ions located between the vanadate chains may affect the isolated $\text{V}=\text{O}$ bonds yielding to the depolymerization of the vanadate network in shorter and isolated chains formed of ortho- and pyrovanadate structural units. As a result they are markedly elongated and the vibrations frequency shifts toward lower wavenumbers. The increase of the content of samarium ions produces a strong depolymerization of the network leading to formation of SmVO_4 crystalline phase, in agreement with the XRD data. The combined XRD and IR spectroscopy data show that the Sm_2O_3 acts as a network modifier with a strong effect about vanadate network.

3.2 UV-VIS spectroscopy

Optical absorption in solids occurs by various mechanisms, in all of which the phonon energy will be absorbed by either the lattice or by electrons where the transferred energy is covered. The lattice (or phonon) absorption will give information about atomic vibrations involved and this absorption of radiation normally occurs in the infrared region of the spectrum. Optical absorption is a useful method for investigating optically induced transitions and getting information about the energy gap of non-crystalline materials and the band structure. The principle of this technique is that a photon with energy greater than the band gap energy will be absorbed [27].

One of the most important concerns in rare earth doped glasses is to define the dopant environment. Hypersensitive transitions are observed in the spectra of all rare earth ions having more than one f electrons. Hypersensitive transitions of rare earth ions manifest an anomalous sensitivity of line strength to the character of the dopant environment [28, 29].

The measured UV-VIS absorption spectra of the lead and samarium-vanadate-tellurate glasses are shown in Fig. 3. The spectra show that the maxima of the absorption are located in the UV region for all investigated glasses containing PbO or Sm_2O_3 .

The Pb^{+2} ions absorb strongly in the ultraviolet (310nm) and yield broad emission bands in the ultraviolet and blue spectral area [30]. The Sm^{+3} ions have five electrons in the f shell. The absorption bands due to the electron jump from the ${}^6\text{H}_{5/2}$ ground state to the ${}^6\text{P}_{5/2}$ (365nm), ${}^6\text{P}_{7/2}$ (375nm), ${}^6\text{P}_{3/2}$ (400nm), ${}^4\text{K}_{11/2}$ (415nm), ${}^4\text{F}_{15/2}$ (460nm) and ${}^4\text{F}_{13/2}$ (475nm) excited states were observed [31].

The stronger transitions in the UV region can be due to the presence of the $\text{Te}=\text{O}$ bonds from the $[\text{TeO}_3]$ structural units, the $\text{Pb}=\text{O}$ bonds from $[\text{PbO}_3]$ structural units and the $\text{V}=\text{O}$ bonds from $[\text{VO}_4]$ structural units which allow $n-\pi^*$ transitions. The intensity of these bands slightly increases and shifts towards higher wavelengths with increasing the concentration of PbO and Sm_2O_3 . This may be due to the increase of the number of the $\text{V}=\text{O}$ bonds from

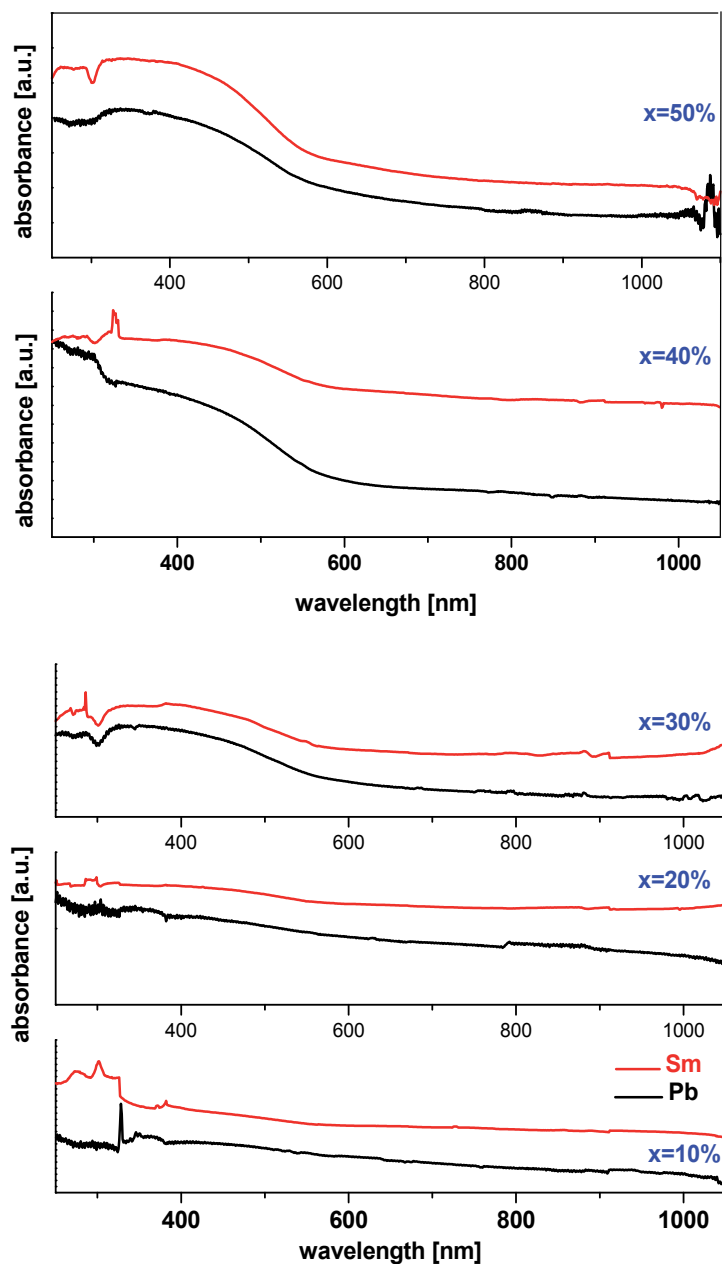


Fig. 3. UV-VIS absorption spectra of $x\text{PbO}$ (or $x\text{Sm}_2\text{O}_3$)· $(100-x)[3\text{TeO}_2\cdot 2\text{V}_2\text{O}_5]$ samples where $0 \leq x \leq 50\text{mol}\%$ in function of lead (II) or samarium (III) oxide content.

orthovanadate structural units for the samples with Sm₂O₃ content and the increase of the number of [PbO₃] structural units in the samples with PbO.

The measurements of optical absorption and the absorption edge are important especially in connection with the theory of electronic structure of amorphous materials. The energy gap,

E_g is an important feature of semiconductors which determines their applications in optoelectronics [32]. Observations of the variation of E_g with increase in the modifier content can be attributed to the changes in the bonding that takes place in the glass

The nature of the optical transition involved in the network can be determined on the basis of the dependence of absorption coefficient (α) on photon energy ($h\nu$). The total absorption could be due to the optical transition which is fitted to the relation:

$$\alpha h\nu = \alpha_0 (h\nu - E_g)^n$$

where E_g is the optical energy gap between the bottom of the conduction band and the top of the valence band at the same value of wavenumber, α_0 is a constant related to the extent of the band tailing and the exponent n is an index which can have any values between $\frac{1}{2}$ and 2 depending on the nature of the interband electronic transitions.

Extrapolating the linear portion of the graph $(\alpha h\nu)^2 \rightarrow 0$ to $h\nu$ axis, the optical band gaps, E_g are determined with increasing PbO and Sm_2O_3 content (Figs. 4 and 5). The optical band gap increases gradually from 1.84eV to 2.09eV and 2.21eV, respectively, by adding of PbO and Sm_2O_3 . In either case the values are systematically increasing with the increase of x . It is to be noted that the curves are characterized by the presence of an exponential decay tail at low energy. These results indicate the presence of a well defined $\pi \rightarrow \pi^*$ transition associated with the formation of conjugated electronic structure [33].

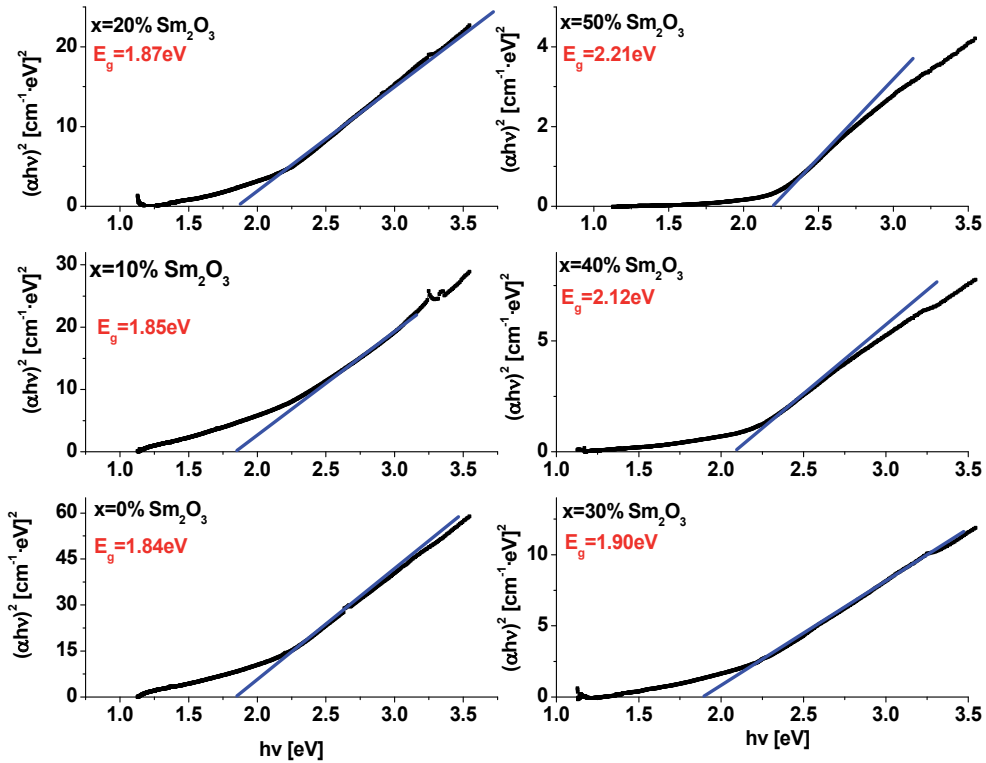


Fig. 4. Plots of $(\alpha h\nu)^2$ versus $h\nu$ for $x\text{PbO} \cdot (100-x)[3\text{TeO}_2 \cdot 2\text{V}_2\text{O}_5]$ glasses where $0 \leq x \leq 50\text{mol}\%$

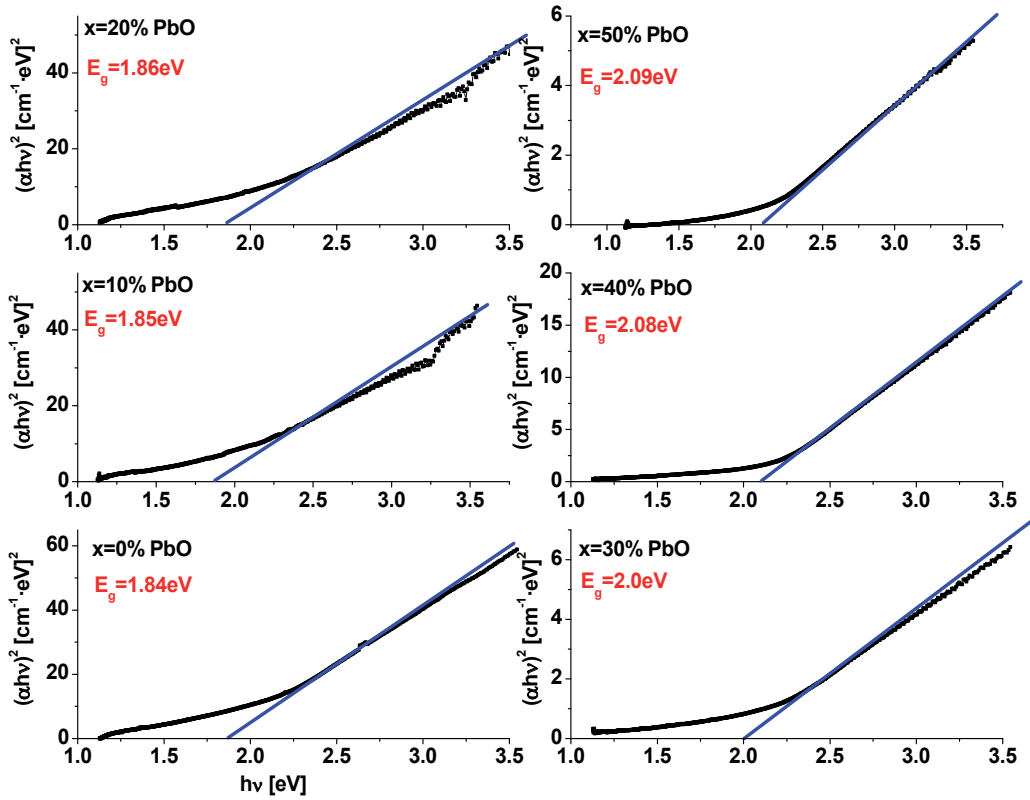


Fig. 5. Plots of $(\alpha h\nu)^2$ versus $h\nu$ for $x\text{Sm}_2\text{O}_3\cdot(100-x)[3\text{TeO}_2\cdot 2\text{V}_2\text{O}_5]$ samples where $0\leq x\leq 50\text{mol}\%$.

The increase of the band gap may occur due to variation in non-bridging oxygen ion concentrations. In metal oxides, the valence band maximum mainly consists of 2p orbital of the oxygen atom and the conduction band minimum mainly consists of ns orbital of the metal atom. The non-bridging oxygen ions contribute to the valence band maximum. The non-bridging orbitals have higher energies than bonding orbitals. When a metal-oxygen bond is broken, the bond energy is released. The increase in concentration of the non-bridging oxygen ions results in the shift of the valence band maximum to higher energies and the reduction of the band gap. Thus, the enlarging of band gap energy due to increase in the PbO or Sm₂O₃ content suggests that non-bridging oxygen ion concentration decreases with increasing the PbO or Sm₂O₃ content that expands the band gap energy. In the glasses doped with Sm₂O₃, the non-bridging oxygen ions concentration decreases due to the formation of orthovanadate structural units. In the glasses doped with PbO, the non-bridging oxygen ions concentration decreases also because the lead atoms act as network formers and the accommodation with the excess of oxygen ions is possible by the increase of the polymerization degree of the network by Pb-O-Te and Pb-O-V linkages.

The existence and variation of optical energy gap may be also explained by invoking the occurrence of local cross linking within the amorphous phase of the matrix network, in such a way as to increase the degree of ordering in these parts.

Refractive index is one of the most important properties in optical glasses. A large number of researchers have carried out investigations to ascertain the relation between refractive index and glass composition. It is generally recognized that the refractive index, n , of many common glasses can be varied by changing the base glass composition [34].

The observed decrease in the refractive index of the studied glasses accompanying to the addition of PbO or Sm₂O₃ content presented in the Fig. 6 can be considered as an indication of a decrease in number of non-bridging oxygen ions.

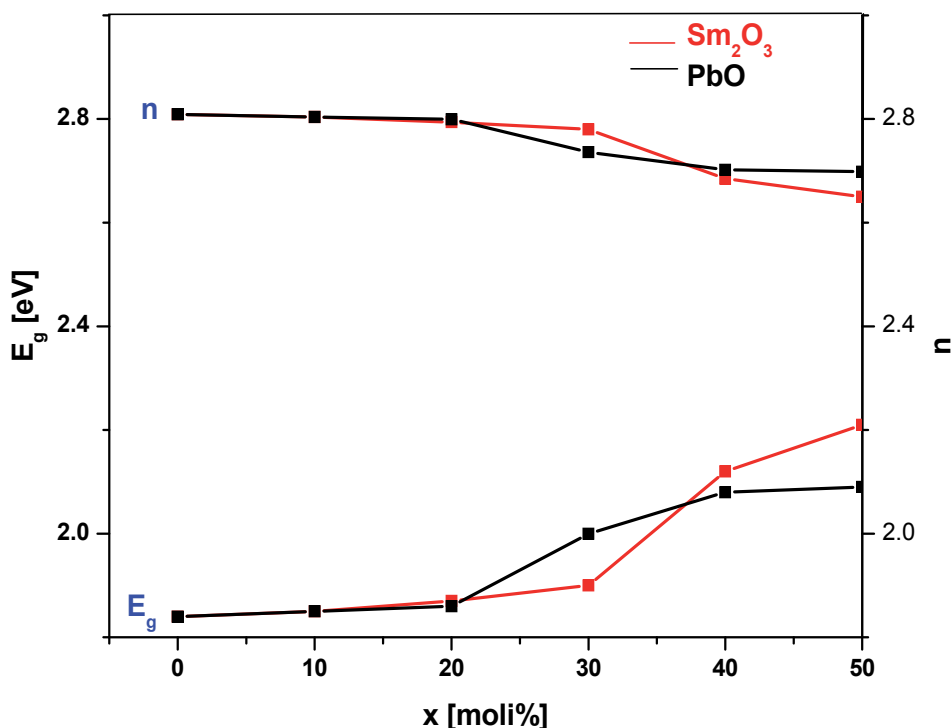


Fig. 6. The relationship between the optic gap, E_g , and refractive index, n , and the and the PbO or Sm₂O₃ contents (the line is only a guide for the eye).

In brief, we can conclude that the optical band gap increases with increasing the PbO or Sm₂O₃ content of the glass. Since the basic structural units of the vanadate-tellurate glasses are known to be the [TeO₃] and [VO₄] structural units and the internal vibrations of these molecular units take part in the transitions. In this work, the increase of the optical band gap, E_g , to larger energies with increasing the PbO or Sm₂O₃ content is probably related to the progressive decrease in the concentration of non-bridging oxygen. This decrease in turn gives rise to a possible decrease in the bridging Te-O-Te and V-O-V linkages. The shift is attributed to structural changes which are the result of the different (interstitial or substitutional) site occupations of the Pb⁺² or Sm⁺³ ions which are added to the vanadate-tellurate matrix and modify the network.

We assume that as the cation concentration increases, the Te-O-Te and V-O-V linkages develop bonds with Pb⁺² or Sm⁺³ ions, which in turn leads to the gradual breakdown of the

glass network. This effect seems more pronounced in doping of the network with the Sm⁺³ ions. These results are in agreement with XRD data which indicate the higher affinity of the samarium ions to attract structural units with negative charge yielding the formation of the SmVO₄ crystalline phase for samples with x>30mol%.

3.3 DFT calculations

In this section, the purpose of the present paper was to continue the investigation of the structure of the vanadate-tellurate network and especially to illuminate structural aspects of the vanadate network using quantum-chemical calculations because the coordination state of vanadium atoms is not well understood. Figure 7 shows the optimized structure proposed to the 3TeO₂·2V₂O₅ glass network.

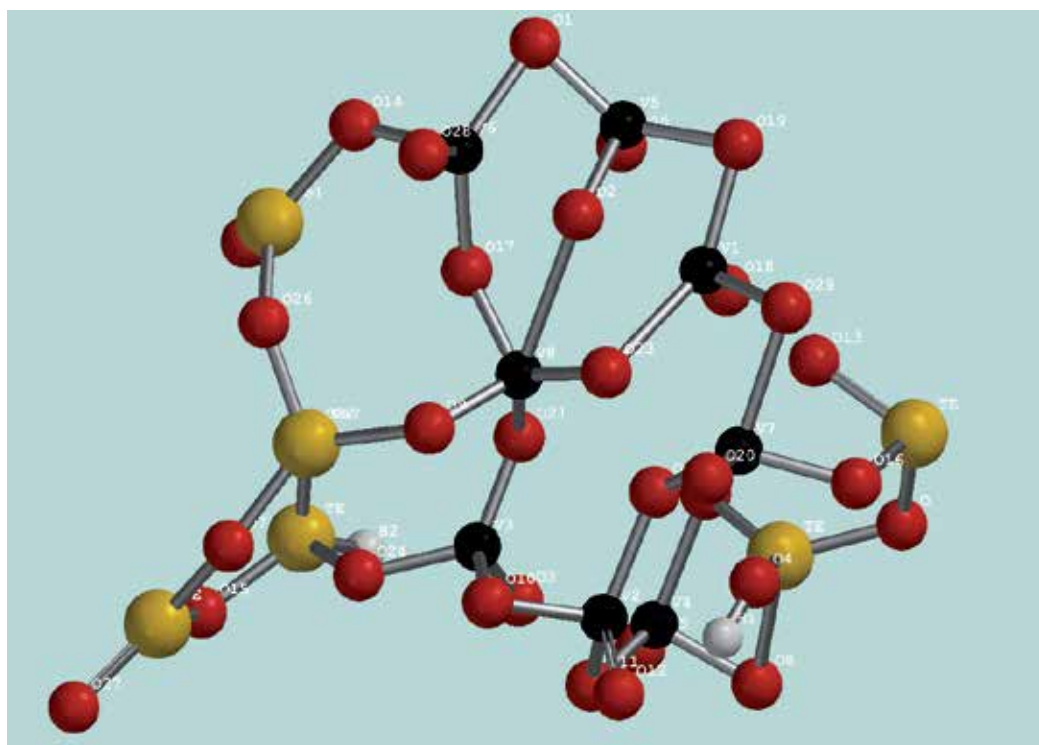


Fig. 7. Optimized structure of the model for binary 3TeO₂·2V₂O₅ glassy.

Analyzing the structural changes resulted from the geometry optimization of our model, we found that the vanadium ions are distributed into two crystallographic sites: the [VO₄] tetrahedral and [VO₅] square pyramidal units. The vanadium tetrahedrons are very regular with vanadium-oxygen distances ranging from 1.57 to 1.82Å and O-V-O angles ranging from 104° to 110° (with a mean value (109.5°) very close to the ideal value (109.28°) corresponding to the tetrahedral geometry). In our model, the V-O interatomic bond distances are ranging from 1.60 to 1.65Å, 1.75 to 1.80Å (the average V-O distance is 1.72Å) and O-V-O angles values are ranging from 101 to 112°. This result show that the [VO₄] tetrahedrons are easy distorted around the vanadium center.

The [VO₅] square pyramidal units are considerably distorted around the vanadium center and the V-O bond distances are ranging from 1.65 to 2.30Å. Such a behavior was reported for the two-dimensional layered vanadate compounds [35, 36]. This shows that there is instability in the nonequivalent V-O bonds in the polyhedron. In essence, this is due to the displacement of the vanadium atom from the centre of the polyhedron, whose asymmetry strongly depends on the manner of connection with the surrounding polyhedron. This deformation will be expressed more clearly in the formation of the vitreous matrix.

This structural model shows a very complex behavior of the vanadium atoms and their stabilization can be achieved by the formation of orthovanadate structural units or by the intercalation of [PbO₃] structural units in the immediate vicinity of these units.

4. Conclusions

The X-ray diffraction patterns reveal the SmVO₄ crystalline phase in the samples with $x > 30\text{mol}\%$ Sm₂O₃ indicating that the samarium ions have an pronounced affinity towards the vanadate structural units. By adding of Sm₂O₃ content in the host matrix, the FTIR spectra suggests that the glass network modification has taken place mainly in the vanadate part whereas by adding of PbO, the network is transformed from a vanadate-tellurate network into a continuous lead-vanadate-tellurate network by Te-O-Pb and V-O-Pb linkages.

The UV-VIS absorption spectra of the studied samples reveal the additional absorptions in the 250-1050nm range due to the generation of $n \rightarrow \pi^*$ transitions and the presence of the transition or rare earth metallic ions. By increasing the metal oxide content up to 50mol%, the optical band gap energy increases. This suggests a decrease of the non-bridging oxygens due to the formation of orthovanadate (for adding Sm₂O₃) and [PbO₃] (for adding PbO) structural units, respectively. The band gap energy was changed due to structural modifications of the network.

Our DFT investigations show that the penta-coordinated vanadium atoms show a unique influence on the structural properties of the glasses.

5. Acknowledgments

The financial support of the Ministry of Education and Research of Romania-National University Research Council (CNCSIS, PN II-IDEI 183/2008, contract number 476/2009) is gratefully acknowledged by the authors.

6. References

- [1] S. Tanaba, K. Hirao, N. Soga, J. Non-Cryst. Solids 122 (1990) 79.
- [2] H. Nasu, O. Matsusita, K. Kamiya, H. Kobayashi, K. Kubodera, J. Non-Cryst. Solids 124 (1990) 275.
- [3] B. Eraiah, Bull. Mater. Sci. 29(4) (2006) 375.
- [4] G. Nunziconti, S. Bemeschi, M. Bettinelli, M. Brei, B. Chen, S. Pelli, A. Speghini, G. C. Righini, J. Non-Cryst. Solids 345&346 (2004) 343.
- [5] M. Ganguli, M. Bhat Harish, K. J. Rao, Phys. Chem. Glasses 40 (1999) 297.

- [6] S. Jayaseelan, P. Muralidharan, M. Venkateswarlu, N. Satyanarayana, *Mater. Chem. Phys.* 87 (2004) 370.
- [7] G. A. Kumar, A. Martinez, A. Mejia, C. G. Eden, *J. Alloys Compd.* 365 (2004) 117.
- [8] J. Yang, S. Dai, Y. Zhou, L. Wen, L. Hu, Z. H. Jiang, *J. Appl. Phys.* 93 (2003) 977.
- [9] W. A. Pisarski, T. Goryczka, B. Wodecka-Dus, M. Plonska, J. Pisarska, *Mater. Sci. Eng.* 122 (2005) 94.
- [10] G. Lakshminarayana, S. Buddhudu, *Mater. Chem. Phys.* 102 (2007) 181.
- [11] Thulasiramudu, S. Buddhudu, *Spectrochim Acta A* 67 (2007) 802.
- [12] Spartan'04, Wavefunction Inc., 18401 Von Karman Avenue, Suite 370 Irvine, CA 92612.
- [13] M. J. Frisch, G. W. Trucks, H. B. Schlegel, G. E. Scuseria, M. A. Robb, J. R. Cheeseman, J. A. Montgomery, Jr., T. Vreven, K. N. Kudin, J. C. Burant, J. M. Millam, S. S. Iyengar, J. Tomasi, V. Barone, B. Mennucci, M. Cossi, G. Scalmani, N. Rega, G. A. Petersson, H. Nakatsuji, M. Hada, M. Ehara, K. Toyota, R. Fukuda, J. Hasegawa, M. Ishida, T. Nakajima, Y. Honda, O. Kitao, H. Nakai, M. Klene, X. Li, J. E. Knox, H. P. Hratchian, J. B. Cross, C. Adamo, J. Jaramillo, R. Gomperts, R. E. Stratmann, O. Yazyev, A. J. Austin, R. Cammi, C. Pomelli, J. W. Ochterski, P. Y. Ayala, K. Morokuma, G. A. Voth, P. Salvador, J. J. Dannenberg, V. G. Zakrzewski, S. Dapprich, A. D. Daniels, M. C. Strain, O. Farkas, D. K. Malick, A. D. Rabuck, K. Raghavachari, J. B. Foresman, J. V. Ortiz, Q. Cui, A. G. Baboul, S. Clifford, J. Cioslowski, B. B. Stefanov, G. Liu, A. Liashenko, P. Piskorz, I. Komaromi, R. L. Martin, D. J. Fox, T. Keith, M. A. Al-Laham, C. Y. Peng, A. Nanayakkara, M. Challacombe, P. M. W. Gill, B. Johnson, W. Chen, M. W. Wong, C. Gonzalez, and J. A. Pople, *Gaussian 03, Revision A.1*, Gaussian, Inc., Pittsburgh PA, 2003.
- [14] S. Rada, M. Culea, E. Culea, *J. Phys. Chem. A* 112(44) (2008) 11251.
- [15] S. Rada, M. Neumann, E. Culea, *Solid State Ionics* 181 (2010) 1164.
- [16] S. Rada, E. Culea, M. Rada, *Mater. Chem. Phys.* 128(3) (2011) 464.
- [17] S. Rada, E. Culea, M. Culea, *Borate-Tellurate Glasses: An Alternative of Immobilization of the Hazardous Wastes*, Nova Science Publishers INC., New York, 2010.
- [18] S. Rada, E. Culea, *J. Molec. Struct.* 929 (2009) 141.
- [19] M. Rada, V. Maties, S. Rada, E. Culea, *J. Non-Cryst. Solids* 356 (2010) 1267.
- [20] S. Rada, R. Chelcea, E. Culea, *J. Molec. Model.* 17 (2011) 165.
- [21] S. Rada, E. Culea, M. Culea, *J. Mater. Sci.* 43(19) (2008) 6480.
- [22] K. V. Ramesh, D. L. Sastry, *J. Non-Cryst. Solids* 352 (2006) 5421.
- [23] K. Gatterer, G. Pucker, H. P. Fritzer, *Phys. Chem. Glasses* 38 (1997) 293.
- [24] S. Rada, M. Culea, E. Culea, *J. Non-Cryst. Solids* 354(52-54) (2008) 5491.
- [25] S. Rada, M. Culea, M. Neumann, E. Culea, *Chem. Phys. Letters* 460 (2008) 196.
- [26] M. Rada, V. Maties, M. Culea, S. Rada, E. Culea, *Spectrochim. Acta A* 75 (2010) 507.
- [27] M. T. Abd El-Ati, A. A. Higazy, *J. Mater. Sci.* 35 (2000) 6175.
- [28] S. N. Misra, S. O. Sommerer, *Appl. Spectrosc. Rev.* 26 (1991) 151.
- [29] V. K. Tikhomirov, M. Naftaly, A. Jha, *J. Appl. Phys.* 86 (1999) 351.
- [30] D. Ehrhart, *J. Non-Cryst. Solids* 348 (2004) 22.
- [31] A. M. Nassar, N. A. Ghoneim, *J. Non-Cryst. Solids* 46 (1981) 181.
- [32] T. Aoki, Y. Hatanaka, D.C. Look, *Appl. Phys. Lett.* 76 (2000) 3257.
- [33] W. R. Salaneck, C. R. Wu, J. L. Bredas, J. J. Ritsko, *Chem. Phys. Lett.* 127 (1986) 88.
- [34] R. El-Mallawany, *J. Appl. Phys.* 72 (1992) 1774.

[35] Sun, E. Wang, D. Xiao, H. An, L. Xu, J. *Molec. Struct.* 840 (2007) 53.

[36] Y. Zhou, H. Qiao, *Inorg. Chem. Comm.* 10 (2007) 1318.

Water in Rocks and Minerals – Species, Distributions, and Temperature Dependences

Jun-ichi Fukuda
Tohoku University
Japan

1. Introduction

Water is ubiquitously distributed in the interior of the earth, as various forms in rocks and minerals: In rocks, aggregates of minerals, fluid water in which molecular H₂O is clustered, is trapped at intergranular regions and as fluid inclusions (e.g., Hiraga et al., 2001). In minerals, water is located as the form of -OH in their crystal structures as impurities. Surprisingly, such water species are distributed over five times in the earth's interior than ocean water (e.g., Jacobsen & Van der Lee, 2006), and play very important roles on earth dynamics such as deformation and reactions of minerals and rocks (e.g., Thompson & Rubie, 1985; Dysthe & Wogelius, 2006). In the field of earth sciences therefore, people are trying to measure properties of water in rocks and minerals such as species, contents, distribution, thermal behaviour, migration rate, etc.

Infrared (IR) spectroscopy is a powerful tool to quantitatively measure these properties of water in rocks and minerals (See Aines & Rossman, 1984; Keppler & Smyth, 2006 for IR spectra of various rocks and minerals). In this chapter, for an advanced IR spectroscopic measurement, I introduce in-situ high temperature IR spectroscopy to investigate above matters. First, I use chalcedonic quartz, which contains fluid water at intergranular regions and -OH in quartz crystal structures. Next, I use beryl, a typical cyclosilicate which contains isolated (not clustered) H₂O molecules in open cavities of the crystal structure. Changes of the states of water in chalcedonic quartz and beryl by temperature changes and dehydration will be discussed. Finally, I perform two-dimensional IR mappings for naturally deformed rocks to investigate water distribution in polyminerale mixtures, and discuss possible water transportation during rock deformation.

2. Methods

Transmitted IR spectra for rocks and minerals are generally measured by making thin sections of samples with thicknesses of from 20 to 200 μm, which depend on concentrations and absorption coefficients based on Beer-Lambert law. A Fourier Transform IR microspectrometer totally used in this study is equipped with a silicon carbide (globar) IR source and a Ge-coated KBr beamsplitter. IR light through a sample is measured using a mercury-cadmium-telluride detector.

In-situ high temperature IR spectra were measured for a sample on a heating stage which was inserted into the IR path. The sample was heated at 100 °C/minute to desired

temperature, and spectra were collected at about 1 minute. Mapping measurements were carried out using an auto XY-stage under atmospheric condition.

3. Water in rocks: As an example of chalcedonic quartz

Fluid water and -OH are trapped in chalcedonic quartz, an aggregate of microcrystalline quartz (SiO_2) grains (sometimes called as chalcedony or agate which has different transparency and is treated as a gem). Fluid water in chalcedonic quartz is dominantly trapped at intergranular regions such as grain boundaries and triple junctions of grains. IR spectra of chalcedonic quartz have been measured at room temperature (RT) (Frondel, 1982; Graetsch et al., 1985). In this section, I measure in-situ high temperature IR spectra for chalcedonic quartz as a representative material that abundantly contains fluid water and structurally-trapped -OH.

3.1 Typical IR spectrum at RT and water species

Figure 1 is a typical IR spectrum at RT for a thin section (ca. 100 μm thickness) of chalcedonic quartz. The band due to fluid water shows an asymmetric broad band ranging from 2750 to 3800 cm^{-1} with a shoulder around 3260 cm^{-1} : this band feature is the same with that of simple fluid water which exists everywhere around us (e.g., Eisenberg & Kauzman, 1969). -OH in chalcedonic quartz is mainly trapped as Si-OH by breaking the network of SiO_2 bonds (Kronenberg & Wolf, 1990), and the OH stretching band is sharp (3585 cm^{-1} at RT). The bending mode of fluid water, which should be seen at around 1600 cm^{-1} , is hindered by many sharp Si-O stretching bands. Combination modes of the stretching and bending modes of fluid water and Si-OH are clearly seen for a thicker sample (1 mm in Fig. 1), and they are detected at 5200 cm^{-1} and 4500 cm^{-1} respectively. Contents of fluid water and Si-OH can be calculated from these bands' heights using their molar absorption coefficients of 0.761 and 1.141 $\text{L mol}^{-1} \text{cm}^{-1}$, respectively (Scholze, 1960; Graetsch et al., 1985); in this case 0.32 wt % H_2O and 0.28 wt % Si-OH, respectively (Fukuda et al., 2009a).

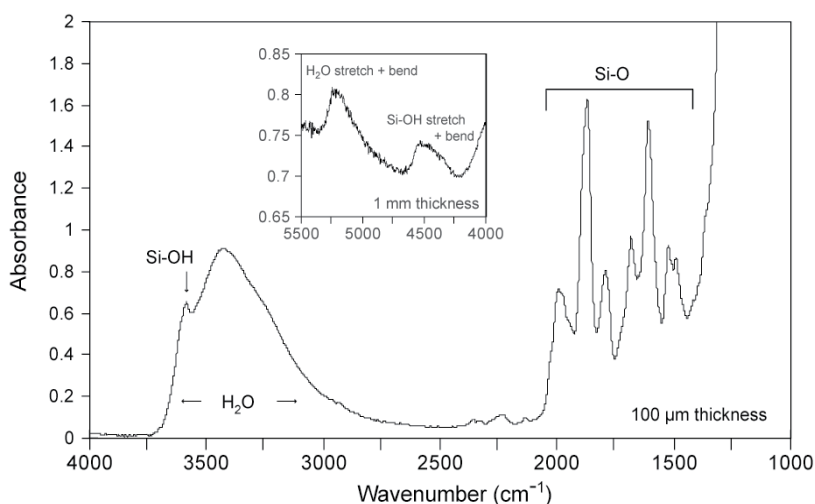


Fig. 1. Typical IR spectrum of chalcedonic quartz at RT. The sample thickness of 100 μm for 4000–1000 cm^{-1} and 1 mm for 5500–4000 cm^{-1} (combination modes of the stretching and bending modes of fluid water and Si-OH).

3.2 Water vibrations at high temperatures

High temperature IR spectra were measured for the sample set on the heating stage (Fig. 2). With increasing temperature up to 400 °C, the broad band due to fluid water dominantly and asymmetrically shifts to high wavenumbers. Contrary to this, the band due to Si-OH slightly shifts to high wavenumbers. After quenching to RT from high temperatures, these water bands do not change from those before heating, indicating that vibrational states of fluid water and Si-OH are changed at high temperatures without dehydration. The following is discussion for changes in the vibrational states of water.

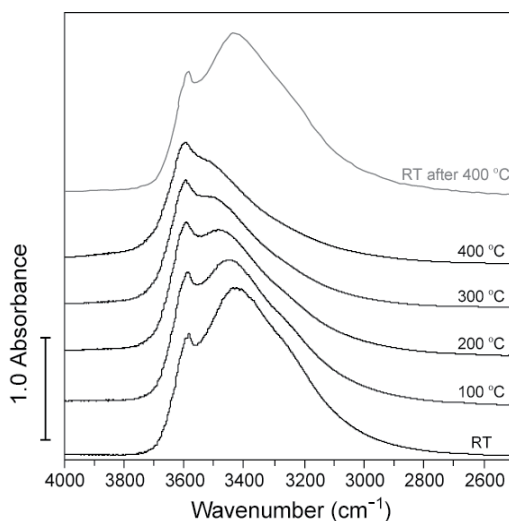


Fig. 2. In-situ high temperature IR spectra of a chalcedonic quartz (black lines) in the water stretching region (Replotted from Fukuda et al., 2009c). The spectrum at RT after heating at 400 °C is shown as gray line on the top, showing no significant change from the spectrum before heating.

Since vibrational energy of OH stretching of Si-OH is structurally limited within quartz crystal structures, the band is sharp even at high temperatures. The deviation of the wavenumber from free -OH stretching (around 3650 cm^{-1} ; summarized in Libowitzky, 1999) can be explained by the work of hydrogen bond in Si-OH...O-Si in quartz crystal structures, which weaken OH vibrational energy. With increasing temperature, the hydrogen bond distance is extended due to thermal expansion of quartz crystal structure (e.g., Kihara, 2001). Resultantly, the band due to Si-OH slightly shifts to high wavenumber and the band height is not so decreased (3599 cm^{-1} at 400 °C; Fukuda & Nakashima, 2008).

In fluid water, H_2O is clustered and networked by various hydrogen bond strengths (e.g., Brubach et al., 2005). Therefore, fluid water shows the broad band. With increasing temperatures, the average coordination numbers of a H_2O molecule to adjacent H_2O molecules at confined intergranular regions of chalcedonic quartz are reduced due to increases of vibrational energies without dehydration. The average coordination number of a single H_2O molecule in fluid water is 2–3 molecules at RT (Brubach et al., 2005), and 1–2 above supercritical temperature (Nakahara et al., 2001). This leads to significant shifts of wavenumbers to higher. Also, band heights of fluid water are decreased with increasing

temperatures. For example, the maximum band height at 400 °C is approximately 50 % of that at RT. This is also because of decreases of average numbers of H₂O in areas that IR light captures (i.e., density; Schwarzer et al., 2005).

3.3 Dehydration behaviour

When the sample is kept at high temperatures, dehydration occurs. High temperature IR spectra were continuously measured to monitor dehydration. Figure 3 shows dehydration behaviour measured at 500 °C (Fig. 3a) and 400 °C (Fig. 3b). Both of the experiments were performed by heating during 500 minutes in total. Broad bands around 3800-3000 cm⁻¹ in both spectra decrease with keeping at high temperatures, and the wavenumbers of the broad bands are not changed during heating. IR spectra at RT after heating (gray spectra in Fig. 3) also show decreases of fluid water. This indicates that fluid water was dehydrated through intergranular regions which are fast paths for mass transfers (See Ingrin et al., 1995; Okumura and Nakashima, 2004; Fukuda et al., 2009c for estimation of water diffusivity). Over 50 % of the band areas are decreased during the heating in 84 minutes at 500 °C. Band areas of 80 % are decreased in 250 minutes, and the features of the spectra are not changed after that. The RT temperature spectrum after 500 minutes heating at 500 °C also shows significant reduction of board band due to fluid water. This remained band due to fluid water may reflect fluid inclusions, which is tightly trapped at open spaces in crystal structures. On the other hand, 60 % of the band areas are preserved after heating in 500 minutes at 400 °C, and the RT spectrum after 500 minutes heating at 400 °C still shows a strong signal of fluid water.

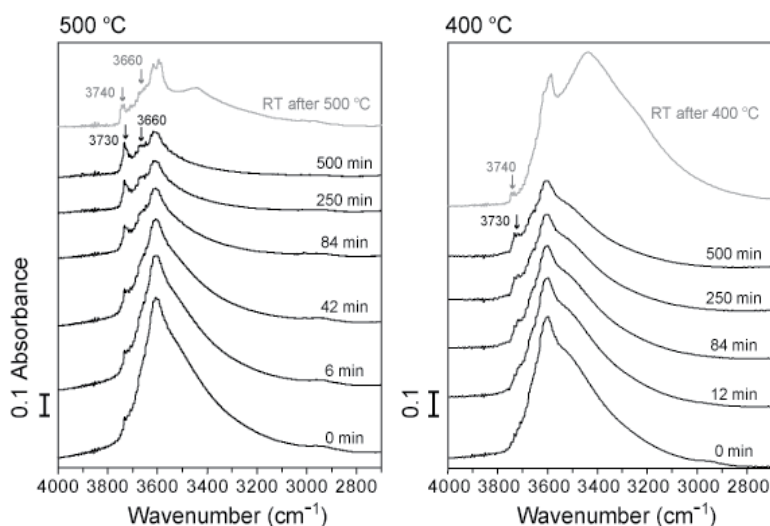


Fig. 3. Dehydration behaviour at 500 °C (left) and 400 °C (right) in the water stretching region (after Fukuda et al., 2009c). The spectra at RT after heatings are also shown as gray lines. The integrated heating times are shown at the right of each spectrum.

Since contents of fluid water are reduced by dehydration, different degrees of hydrogen bonds of Si-OH at intergranular regions (surface silanol) to fluid water are formed. This leads to the appearances of several -OH bands (3660 and 3730 cm⁻¹ at 500 °C, and possibly

the split of the band at 3585 cm^{-1} at RT (Yamagishi et al., 1997). The appearance of the band at 3730 cm^{-1} at 0 minute heating at $500\text{ }^{\circ}\text{C}$ is due to slight dehydration during heating from RT to $500\text{ }^{\circ}\text{C}$ at $100\text{ }^{\circ}\text{C}/\text{minute}$. The wavenumbers of these new $-\text{OH}$ bands at high temperature are slightly different from those at RT, presumably due to thermal expansions of crystals and changes of hydrogen bond distances at high temperature.

4. H_2O molecules in minerals: As an example of beryl

In addition to fluid water in rocks and $-\text{OH}$ in mineral crystal structures as described above, isolated (not clustered) H_2O molecules are incorporated in open cavities of crystal structures, and they are sometimes coupled with cations. H_2O in open cavities has well been studied for beryl, a typical cyclosilicate (after Wood & Nassau, 1967). Ideal chemical formula of beryl is $\text{Be}_3\text{Al}_2\text{Si}_6\text{O}_{18}$, and six-membered SiO_4 rings are stacked along the crystallographic c -axis and make a pipe-like cavity called a channel (Fig. 4) (Gibbs et al., 1968). Isolated H_2O is trapped in the channel, and forms two kinds of orientations, depending on whether it coordinates to a cation (called type II) or not (called type I) (after Wood & Nassau, 1967). Such cations are trapped in the channels to compensate the electrical charge balances caused by Be^{2+} - Li^+ and Si^{4+} - Al^{3+} substitutions and lacks of Be^{2+} in the crystal structure of beryl. The cations in the channels are assumed to be mainly Na^+ , and some other alkali cations may be incorporated (Hawthorne and Černý, 1977; Aurisicchio et al., 1988; Artioli et al., 1993; Andersson, 2006). In this section, I introduce polarized IR spectra of beryl, and discuss changes of the states of type I/II H_2O in the channels by temperature changes and dehydration.

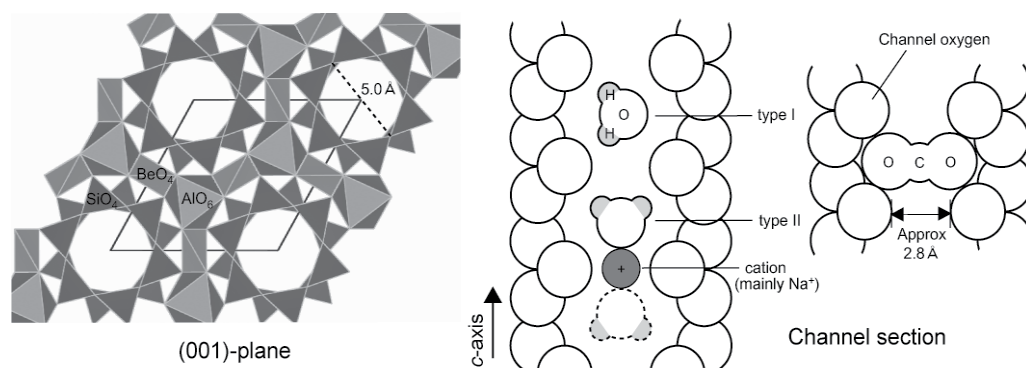


Fig. 4. Crystal structure of beryl. The (001)-plane (i.e., viewed down from the c -axis) and the channel section. Positions of type I/II H_2O , a cation, and CO_2 are also shown. Modified after Fukuda & Shinoda (2011).

4.1 Chemical composition of the sample

The chemical composition of the natural beryl sample used in this study was analyzed by X-ray wavelength dispersive spectroscopy for major atomic contents, inductivity coupled plasma-atomic emission spectroscopy for Be content, and atomic absorption spectroscopy for Li and Rb contents (Table 1). The type I/II H_2O contents were determined from intensities of IR bands due to the asymmetric stretching of type I and the symmetric stretching of type II in a polarized IR spectrum at RT (See the spectrum in the next section), using their molar absorption coefficients of $206\text{ L mol}^{-1}\text{ cm}^{-1}$ and $256\text{ L mol}^{-1}\text{ cm}^{-1}$,

respectively (Goldman et al., 1977). The CO₂ content was also calculated for the band at 2360 cm⁻¹ from 800 L mol⁻¹ cm⁻¹ in Della Ventura et al. (2009). In the chemical composition, the Li and Na contents are relatively high in addition to the Si, Al and Be contents of major atoms. Be content (2.893 in 18 oxygen), which is lower than the ideal composition of beryl (Be₃Al₂Si₆O₁₈), must be replaced by Li, and Na must be incorporated as Na⁺ in the channels to compensate the electrical charge balance. However, Li⁺ may be also incorporated in the channels, since the Li content is not completely explained by Be²⁺-Li⁺ substitution (e.g., Hawthorne and Černý, 1977).

wt%		18O base	
SiO ₂	64.45	Si	5.961
Al ₂ O ₃	18.01	Al	2.006
BeO	13.08	Be	2.893
MgO	0.01	Mg	0.002
FeO	0.16	Fe	0.013
TiO ₂	–	Ti	–
MnO	0.02	Mn	0.002
CaO	0.01	Ca	0.001
NiO	0.01	Ni	0.001
Cr ₂ O ₃	–	Cr	–
ZnO	0.17	Zn	0.012
Li ₂ O	0.50	Li	0.185
Na ₂ O	0.54	Na	0.097
K ₂ O	0.04	K	0.004
Rb ₂ O	0.02	Rb	0.001
H ₂ O			
type I	1.80		
type II	1.24		
CO ₂			
	0.01		
total	100.08		

Table 1. Chemical composition of the beryl sample used in this study.

4.2 Typical polarized IR spectra of beryl at RT and types of H₂O

Polarized IR spectra were measured by inserting a wire grid IR polarizer to IR light through the sample. Electric vector of IR light, *E* to the *c*-axis (i.e., the direction of the arrangements of the channels) were gradually changed and spectra were obtained (Fig. 5). Fundamental vibrations of type I/II H₂O (asymmetric stretching; *v*₃, symmetric stretching; *v*₁, and bending modes; *v*₂) can be detected under different polarized conditions, which correspond to the orientations of type I/II H₂O in the channels (Fig. 4) and IR active orientations of their vibrational modes: In a sample section of the (100)-plane (i.e., the section including the alignment of channels), the bands due to the *v*₃ mode of type I (referred to as *v*₃-I hereafter), *v*₁-II, and *v*₂-II are dominantly detected under *E*//*c*-axis (Fig. 5a). Their wavenumbers are 3698, 3597, and 1628 cm⁻¹, respectively.

Under *E*⊥*c*-axis in the (100)-section (bottom spectra in Fig. 5a) or in the (001)-section (Fig. 5b), the bands due to *v*₃-II (3661 cm⁻¹), *v*₁-I (3605 cm⁻¹), and *v*₂-I are dominant. The *v*₂-I

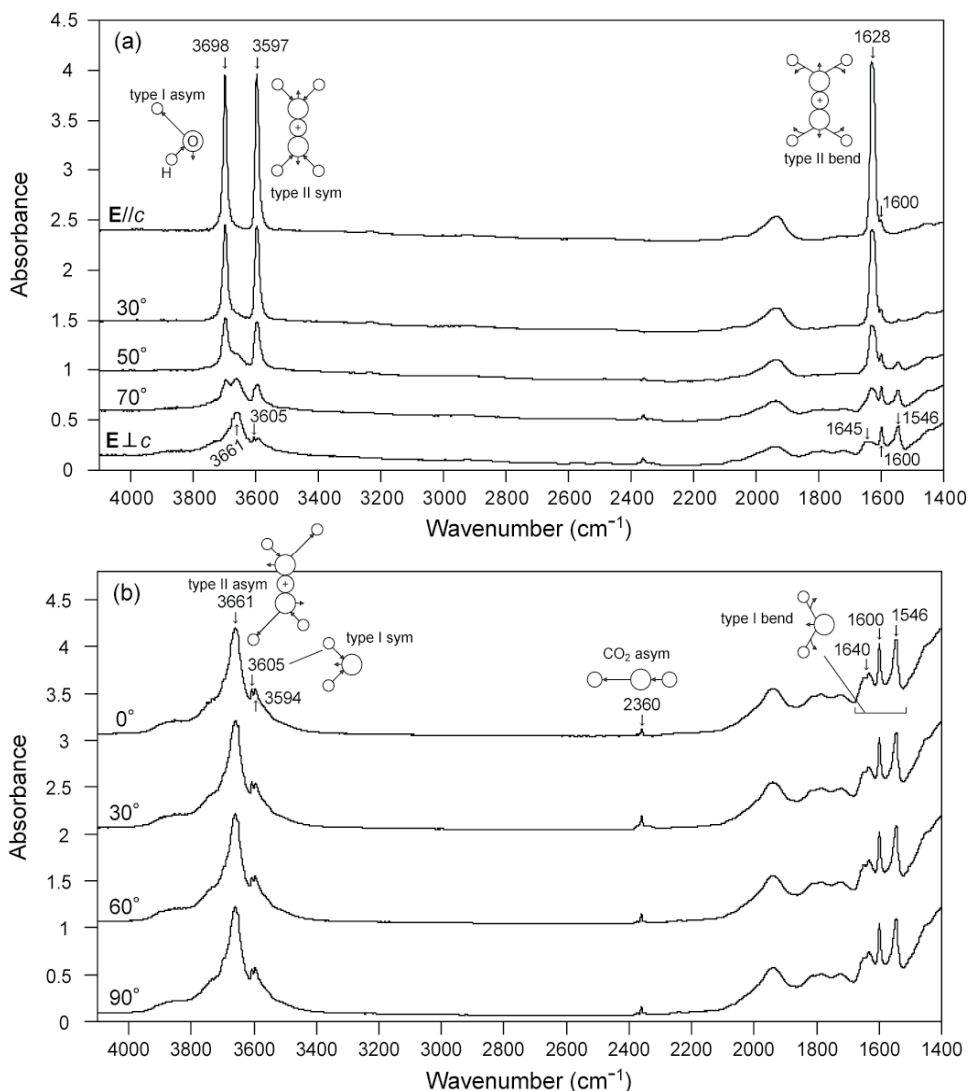


Fig. 5. Polarized IR spectra for natural beryl under different polarized conditions at RT. (a) From $E//c$ -axis to $E \perp c$ -axis in the (100)-section (the sample thickness of 20 μm). The angle of the c -axis (i.e., the direction of the channels) respective to E is shown on the left of each spectrum. (b) Under $E \perp c$ -axis in the (001)-section (the sample thickness of 120 μm).

somewhat shows three bands at 1640, 1600, and 1546 cm^{-1} (e.g., Wood & Nassau 1967; Charoy et al., 1996; Łodziński et al., 2005), and I refer these three bands to the ν_2 -I related bands. The asymmetric stretching mode of CO_2 molecules is detected at 2360 cm^{-1} under $E \perp c$ -axis. These H_2O and CO_2 bands are not changed at any angles of E to the sample in the (001)-plane, corresponding to that these molecules are isotropically distributed due to the hexagonal symmetry of beryl. There are other unassigned bands; for example the sharp band at 3594 cm^{-1} can be seen. This band has been argued and might be due to Na^+ -OH in the channels.

Ideally, the ν_3 , ν_1 , and ν_2 modes of isolated free H_2O are detected at 3756, 3657, and 1595 cm^{-1} , respectively at RT (Eisenberg & Kauzman, 1969). That the fundamental vibrations of type I/II H_2O in beryl are deviated from those for ideal value, is due to interaction of type I/II H_2O with channel oxygens and cations (Fig. 5). The wavenumbers of the stretching modes of type I/II H_2O at RT are lower than those of free H_2O , while those of the bending modes are higher. Falk (1984) experimentally demonstrated reverse correlations of band shifts between stretching and bending modes. The lower wavenumbers of the stretching modes than those of isolated water molecules are due to weak hydrogen bonds between type I/II and channel oxygens, similarly to the case for chalcedonic quartz. The reverse wavenumber shifts from ideal H_2O between stretching and bending modes is mainly explained by changes in H-H repulsion constants in a simple spring model (Fukuda & Shinoda, 2008).

4.3 Water vibrations at high temperatures

Significant dehydration does not occur during short time heating from RT to 800 °C (temperature raise of 100 °C/minute and 1 minute for the measurements at each temperature; see Section 2). Figure 6 shows high temperature behaviour of type I/II H_2O in

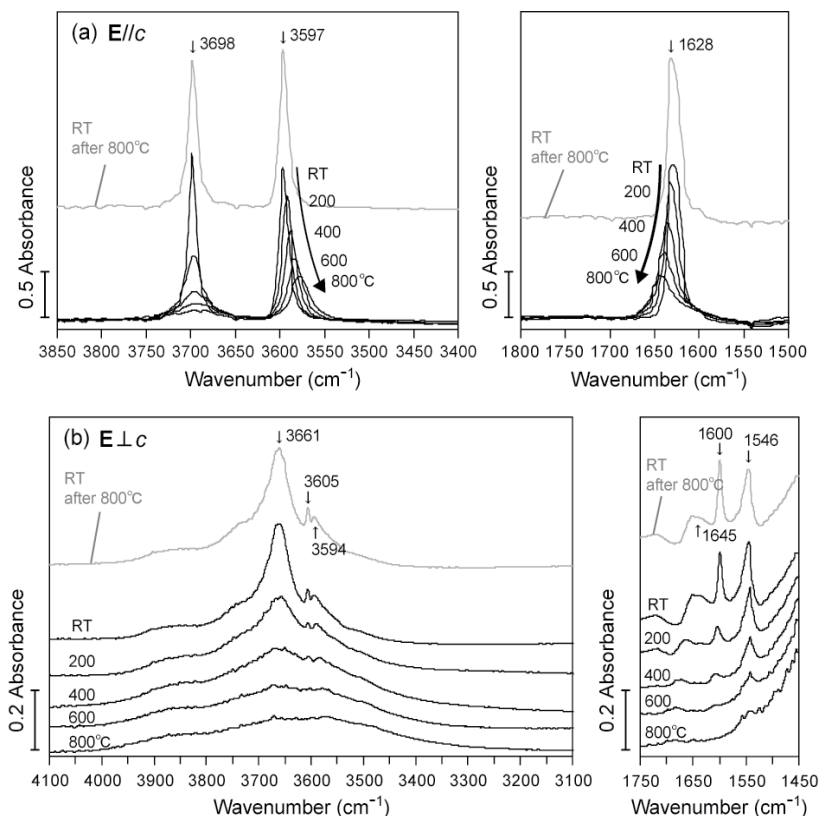


Fig. 6. High temperature behaviour of beryl from RT to 800 °C for the samples in Fig. 5 (Replotted from Fukuda & Shinoda, 2011). (a) under $E//c$ -axis. (b) under $E\perp c$ -axis. The RT spectra after heating at 800 °C are shown as gray lines, showing no significant dehydration occurred during heating.

beryl under $E//c$ -axis (Fig. 6a) and $E\perp c$ -axis (Fig. 6b) in the water stretching and bending regions. Spectral changes are different for each vibrational mode of type I/II H_2O : Under $E//c$ -axis at RT, the ν_3 -I and ν_1 -II bands are clearly seen at 3698 and 3597 cm^{-1} , respectively. The ν_3 -I band is rapidly decreased in its height with increasing temperature; for example 60 % of the band height decreases at 200 °C, compared with that at RT (Fig. 7). The rapid decreases of the type I band are also seen for the ν_1 -I band and the ν_2 -I related bands under $E\perp c$ -axis (Fig. 6b). Contrary to the case for the type I bands, only 20 % of the ν_1 -II and ν_2 -II bands are decreased at 200 °C. Alternatively, wavenumber shifts dominantly occur for these bands. The wavenumber of the former (3597 cm^{-1} at RT) and latter bands (1628 cm^{-1} at RT) linearly shift to lower and higher, with increasing temperature (Fig. 7). The changes of the ν_3 -II band (3661 cm^{-1} at RT) under $E\perp c$ -axis are difficult to monitor because of overlapping with other bands at high temperatures. Since these changes are reversible upon heating and cooling, they are not due to dehydration but changes of the states of type I/II H_2O in the channels. Discussion is as follows.

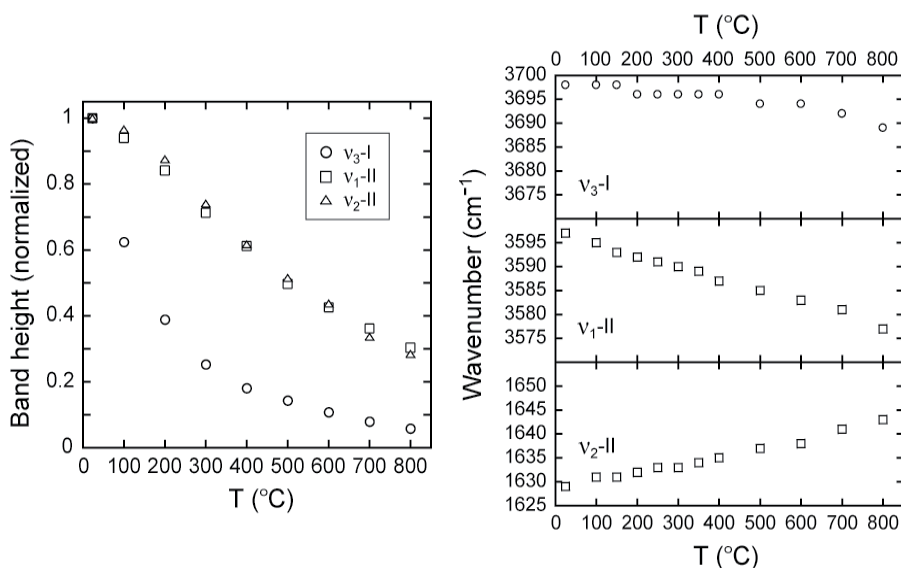


Fig. 7. Changes of band heights (left) and wavenumbers (right) of the ν_3 -I, ν_1 -II, and ν_2 -II bands with increasing temperature (Modified after Fukuda & Shinoda, 2011). Values are determined from the spectra in Fig. 6a.

These changes in band heights and wavenumbers of type I/II H_2O are interpreted mainly due to the presence (type I) or absence of cations (type II) in the beryl channels (Fig. 4). Since type I H_2O is not coupled with a cation, its position in the channels is easy lost with increasing temperature, resulting the rapid decreases of band heights. On the other hand, since the position of type II H_2O is fixed by a cation (mainly Na^+), the decreases in band heights with increasing temperature do not significantly occur, compared with those for type I bands. Alternatively, the wavenumber shifts occur. The inverse wavenumber shifts of type II bands in stretching and bending modes would be due to modifications in vibrational constants in the thermally-expanded beryl channels (Fukuda et al., 2009b), as similar to the deviations of wavenumbers from ideal H_2O molecule in RT spectra (Section 4.2).

4.4 Dehydration behaviour

The beryl sample was heated on the heating stage at 850 °C where dehydration is enhanced (Fukuda & Shinoda, 2008). Polarized IR spectra are shown only at RT quenched from 850 °C (Fig. 8), since in-situ high temperature IR spectra at 850 °C show broadened water bands (Fig. 6) and changes of each bands are not clearly monitored. Under $E//c$ -axis, the ν_3 -I band at 3698 cm^{-1} disappeared at heating of 12 hours, without any wavenumber changes (Fig. 8a). This trend is same with the band at 3605 cm^{-1} (ν_1 -I) and three ν_2 -I-related bands under $E\perp c$ -axis (Fig. 8b). Some bands remain in the water bending region under $E\perp c$ -axis, and they would be due to structural vibrations of beryl. The dehydration behaviour of type II bands are different with that of type I: Since the position of type II H_2O is fixed by a cation, its dehydration is obviously slower than type I H_2O . Under $E//c$ -axis, new bands develop at 3587 and 1638 cm^{-1} with decreasing of the initial bands at 3597 (ν_1 -II) and 1628 cm^{-1} (ν_2 -II). The band at 3661 cm^{-1} (ν_3 -II) under $E\perp c$ -axis also shows the wavenumber shifts to the lower with decreasing its intensity. These bands are stable after 24 hours heating. The appearances of these bands are explained as follows.

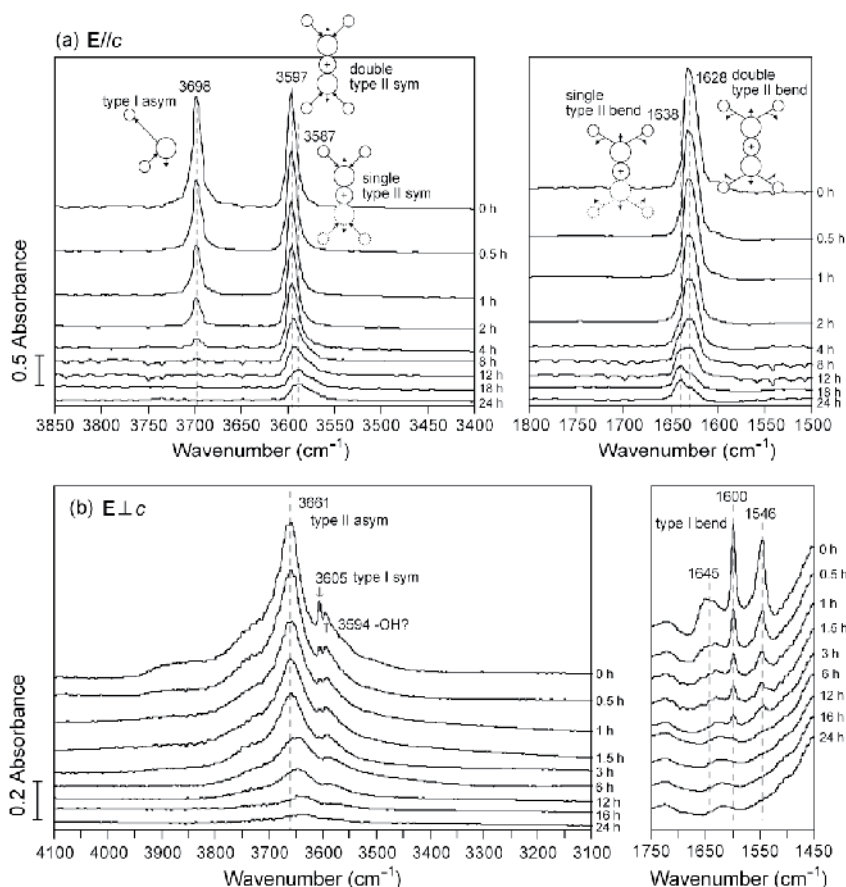


Fig. 8. IR spectra at RT quenched from heating at 850 °C, showing dehydration behaviour (Replotted from Fukuda & Shinoda, 2011). (a) under $E//c$ -axis. (b) under $E\perp c$ -axis. Heating times at 850 °C are shown at the right of each spectrum.

A cation is coordinated by one or two type II H₂O due to a spatial restriction of the channel (Fig. 4). Therefore, the dominant band at 3597 (ν_1 -II) and 1628 cm⁻¹ (ν_2 -II) before heating would be mainly due to doubly-coordinated type II to a cation, mainly Na⁺. Since type II H₂O dehydrates by heating, singly-coordinated type II are created. The wavenumbers of singly- and doubly-coordinated H₂O have been calculated for free H₂O molecules. According to a numerical approach for water vibrations by Bauschlicher et al. (1991), the wavenumbers of H₂O-Na⁺-H₂O is higher in its stretching modes and lower in the bending modes than those of Na⁺-H₂O in approximately 10 cm⁻¹. This is consistent with wavenumber shifts in beryl due to the formation of singly-coordinated type II at 3587 (ν_1 -II) and 1638 cm⁻¹ (ν_2 -II).

Another possibility for the wavenumber shifts of the ν_1 -II and ν_2 -II bands is the presence of Li⁺ in the channels. According to the calculation in Lee et al. (2004) for free H₂O molecules, the wavenumbers of Li⁺-H₂O is higher in its stretching modes and lower in the bending modes than those of Na⁺-H₂O. Also, binding energy of Li⁺ to H₂O is higher than that of Na⁺ to H₂O, which indicates the stable stability of Li⁺-H₂O during dehydration. If Li⁺ is trapped in the beryl channels, it can cause the wavenumber shifts observed in this study.

A sharp and unassigned band is seen at 3594 cm⁻¹ under E_{Lc}-axis. This band is also more stable than that for type I bands. The wavenumber of this band is different from any vibrational modes of type I/II H₂O. Judging from the thermal stability and the wavenumber, this band may be related to Na⁺-OH in beryl, as its presence has been argued in Andersson (2006).

5. IR mapping measurements for deformed rocks

Rocks are deformed at shear zones in the interior of the earth. Rocks, which underwent brittle and plastic deformation at shear zones, are called as cataclasites and mylonites, respectively. Brittle deformation of continental crusts (mainly granitoids) is dominated from the ground to 10-20 km depth. Plastic deformation of rocks is dominated below that with increasing temperature and pressure. Another important factor that significantly contributes to plastic deformation of rocks is water. Water contents in ppm order dramatically promote plastic deformation of minerals, as confirmed by deformation experiments (e.g., Griggs, 1967; Jaoul et al., 1984; Post & Tullis, 1998; Dimanov et al., 1999). Also, water contributes to solution-precipitation which sometimes involves reactions among minerals (especially, feldspar and mica in granitoids) (e.g., summarized in Thompson & Rubie, 1985; Dysthe & Wogelius, 2006). Then, solution-precipitation creep may also contribute to the strength of the crusts (Wintsch & Yi, 2002; Kenis et al., 2005). Thus, water contents and distribution as well as its species are important for rock deformation.

In this section, I use IR spectroscopy to map two-dimensional water distributions as well as to consider its species in deformed granites. I especially focus on water distributions associated with solution-precipitation process of feldspar, and consider possible transport mechanisms of water.

5.1 Samples and analyses

Deformed granites were collected from outcrops in an inner shear zone of the Ryoke Metamorphic Belt in the Kishiwada district, Osaka Prefecture, SW Japan, and believed to be

deformed at ~500 °C (Takagi, 1988; Imon et al., 2002; 2004). Sample thin sections of ~50 µm were at first observed under a polarized optical microscope and a back-scattered electron (BSE) image which reflects compositional differences in a scanning electron microscope (SEM). After IR mapping measurements, thin sections were again polished to suitable thickness (~20 µm) to observe detailed microstructures under the optical microscope.

IR mapping measurements were carried out along ~1000 µm traverses with 30 µm spatial resolution (aperture size) in steps of 30 µm. See Section 2 for the instrument of IR spectroscopy. The integral absorbances of the water stretching bands in the range 3800–2750 cm⁻¹ are displayed as a color-contoured image for a measured sample area. Color-contoured images can be used as a qualitative representation of the distribution of water, since absorption coefficients tend to increase linearly with decreasing wavenumbers (Paterson, 1982; Libowitzky & Rossman, 1997). When the absolute water contents of the minerals are to be determined, Beer-Lambert law is applied, using the absorption coefficients for each mineral. For K-feldspar and plagioclase, I used the absorption coefficients of integral water stretching bands reported by Johnson & Rossman (2003) (15.3 ppm⁻¹ cm⁻²), and for quartz, those reported by Kats (1962). Kats (1962) reported following relation between water content in quartz and integral absorbance of water stretching bands; $C(H/10^6 Si) = 0.812 \times A_{int}/d$, where A_{int} is the integral absorbance and d is the sample thickness in cm. Then, I converted $H/10^6 Si$ value to a ppm H₂O unit (1 ppm = 6.67 H/10⁶ Si), as also adopted in Gleason & DeSisto (2008). To distinguish Si-OH and H₂O contents separately, their combination bands of the stretching and bending modes should be used, as shown in Section 3. However, it is difficult for these samples, since sample thicknesses are thin for texture observations under the optical microscope, and 1 mm thickness is needed to measure the combination bands.

5.2 Typical water distribution in deformed granite

At first, I introduce water distribution in the granite mylonite with typical microtexture (Fig. 9) (See Passchier & Trouw, 2005 for many textures of deformed rocks). As can be seen under the polarized optical microscope (Fig. 9a), quartz is recrystallized by subgrain rotation, and plastically deformed by dislocation creep. Quartz grains are elongated with the aspect ratio of ca. 3:1 and the long axis is ca. 250 µm. Feldspar is a relatively hard mineral in this deformation condition, is not plastically deformed, and behaves as rigid body sometimes with fracturing (i.e., brittle deformation). Such relatively hard minerals are called as porphyroclasts. Under the BSE image, rims of plagioclase are replaced by K-feldspar, which would be due to solution-precipitation with or without reaction called myrmekitization (e.g., Simpson & Wintsch, 1989). Myrmekitization is the following reaction; $K\text{-feldspar} + Na^+ + Ca^{2+} = \text{plagioclase} + \text{quartz} + K^+$, where cations are included in circulating fluid water. Water contents in these replaced K-feldspar are difficult to determine in this region because of the limitation of its distribution, and discussed for other regions later.

The IR spectra for both plagioclase and quartz show broad bands at 3800–2750 cm⁻¹, which is due to the stretching vibration of fluid water (Fig. 9d) (See Section 3). Fluid water must be trapped as fluid inclusions within both minerals, since spatial resolution of 30 µm (aperture size) covers intracrystalline regions, rather than intergranular regions. The IR spectra for the plagioclase porphyroclast also exhibit sharp bands at 3625 and 3700 cm⁻¹, which are due to the stretching vibrations of structural hydroxyl in plagioclase (e.g., Hofmeister & Rossman, 1985; Beran, 1987; Johnson & Rossman, 2003). The band at 1620 cm⁻¹ in plagioclase is due to

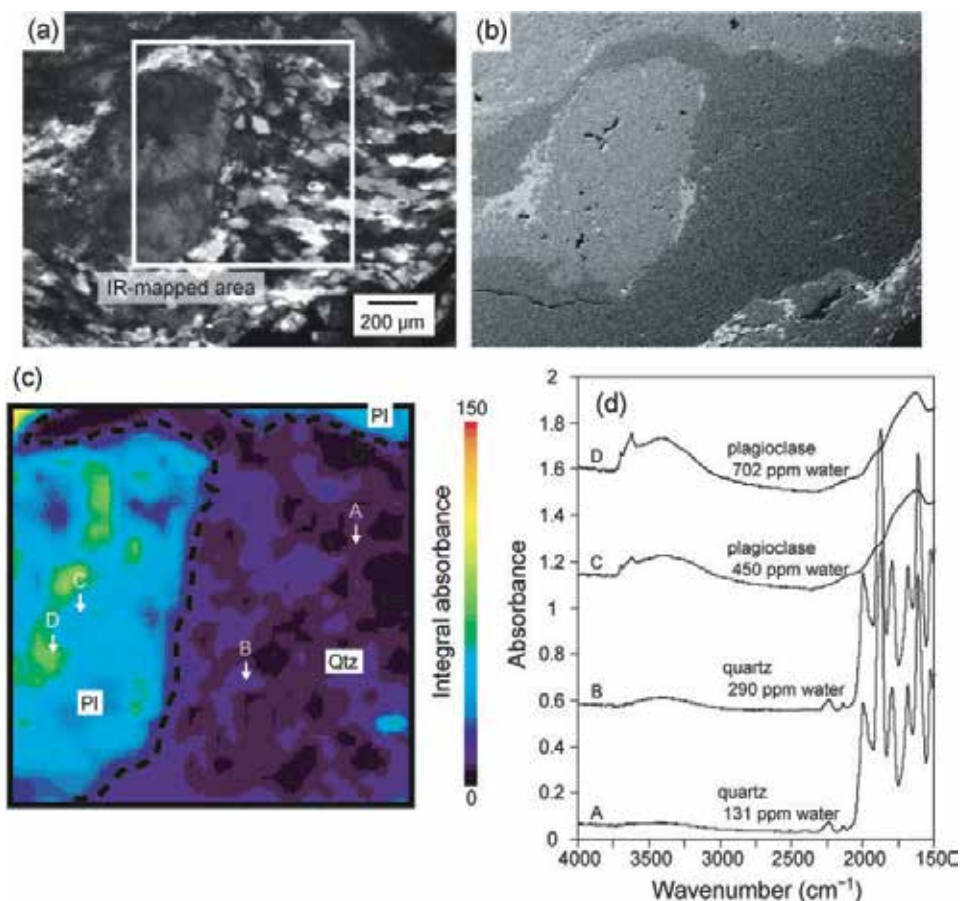


Fig. 9. (a) Optical microscopic image including the IR mapped area (bold square). (b) SEM-BSE image of the IR mapped area shown in (a): light gray; K-feldspar, medium gray; plagioclase, dark gray; quartz. (c) Water distribution mapped by integral absorbance of water stretching bands in the 3800–2750 cm^{-1} range of the IR spectra. The color contours from black to red approximately correspond to water contents from low to high. The boundaries of minerals are shown as dotted lines. Arrows with letters show the locations used to illustrate the various selected IR spectra in (d). Pl; plagioclase, Qtz; quartz.

the bending vibrations of fluid water. Other bands in the range of 2500–1500 cm^{-1} are due to the structural vibrations of plagioclase. Six sharp bands between 2000 and 1500 cm^{-1} for quartz are due to the structural vibrations of quartz, which are same with the spectra for chalcedonic quartz (Fig. 1). Recognition of the bending vibrations of fluid water in quartz is difficult because of these sharp structural bands. Water concentration in this plagioclase porphyroclast ranges from 200 to 700 ppm, with an average of 450 ppm, consistent with values reported in the literature (Hofmeister & Rossman, 1985; Beran, 1987; Johnson & Rossman, 2003). The heterogeneity of water distribution in plagioclase does not directly correspond to textures under the optical microscope and BSE. The amount of water in the quartz is much lower than that in the plagioclase, ranging from 80 to 300 ppm, with an average of 130 ppm.

5.3 Water distribution around feldspar fine grains and possible water transportation

Water distribution was measured for an area where fine-grained K-feldspar develops around K-feldspar and plagioclase porphyroclasts (Fig. 10a). The BSE image shows that fine-grained K-feldspar regions, which are constructed by $\sim 20\ \mu\text{m}$ grains, contain patchy distribution of plagioclase (Fig. 10b). This indicates that solution-precipitation of K-feldspar, which may be accompanied with myrmekitization, occurred for the development of fine grains. The IR-mapped image shows that water contents in these regions are 220 ppm H_2O in average; low and homogeneously distributed, although fluid water must be participated in the solution-precipitation process. The features of water stretching bands of fine-grained K-feldspar and K-feldspar porphyroclasts do not show structural $-\text{OH}$ bands, differently from plagioclase (Fig. 10d); only broad bands can be seen at $3800\text{--}2750\ \text{cm}^{-1}$. Water contents in K-feldspar and plagioclase porphyroclasts are 200–1150 ppm; heterogeneously distributed compared with those in fine-grained K-feldspar regions.

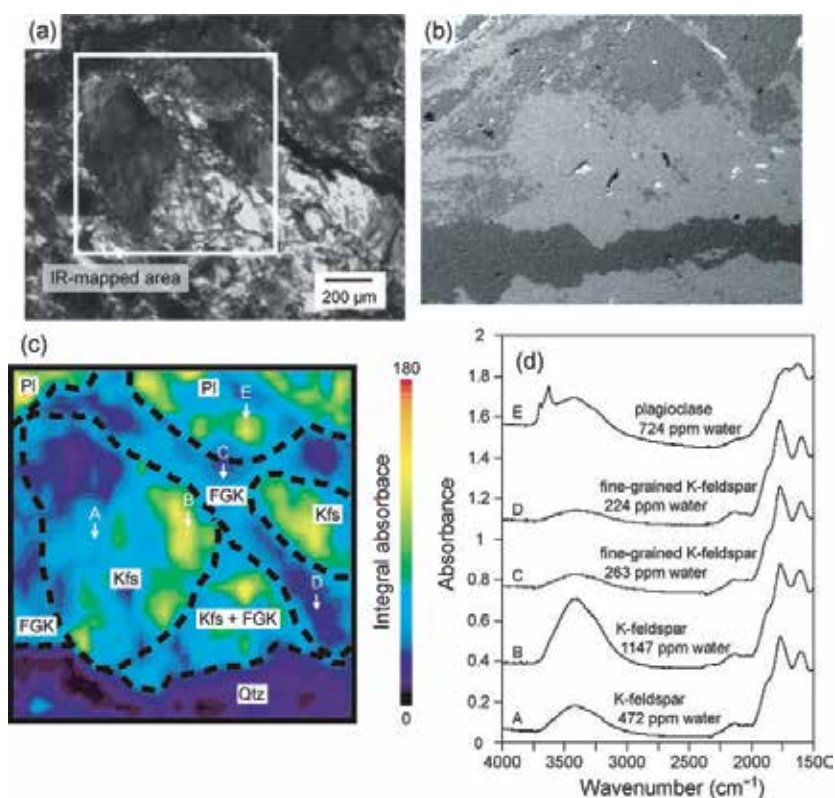


Fig. 10. (a) Optical microscopic image including the IR mapped area (bold square). (b) SEM-BSE image of the mapped area shown in (a): light gray; K-feldspar, dark gray; quartz. Fine-grained K-feldspar regions contain patchy-distributed plagioclase, indicating solution-precipitation occurred for the developments of these regions. (c) Water distribution mapped by integral absorbance of water stretchings of bands in the $3800\text{--}2750\ \text{cm}^{-1}$ range of the IR spectra. The boundaries of minerals are shown as dotted lines. Arrows with letters show the locations used to illustrate the various selected IR spectra in (d). Pl; plagioclase, Kfs; K-feldspar, FGK; fine-grained K-feldspar, Qtz; quartz.

Figure 11 shows water distribution in an area that dominantly includes fine-grained plagioclase. The fine-grained plagioclase develops around plagioclase porphyroclasts, and some of it is closely associated with K-feldspar under the BSE image (Fig. 11b). Quartz in this region can be identified from its characteristic structural vibrations in the IR spectra (Fig. 11d), indicating that myrmekitization ($\text{K-feldspar} + \text{Na}^+ + \text{Ca}^{2+} = \text{plagioclase} + \text{quartz} + \text{K}^+$; see Section 5.2) occurred during rocks deformation. Water contents in the area where fine-grained plagioclase grains are associated with small amounts of K-feldspar and quartz are roughly 2–4 times lower than those within plagioclase porphyroclasts, as inferred from the color contrasts in the IR mapping image (Fig. 11c). However, it is not possible to measure the absolute water contents in this area because of a mixture of plagioclase, K-feldspar, and quartz; consequently, the absorption coefficients are not clear.

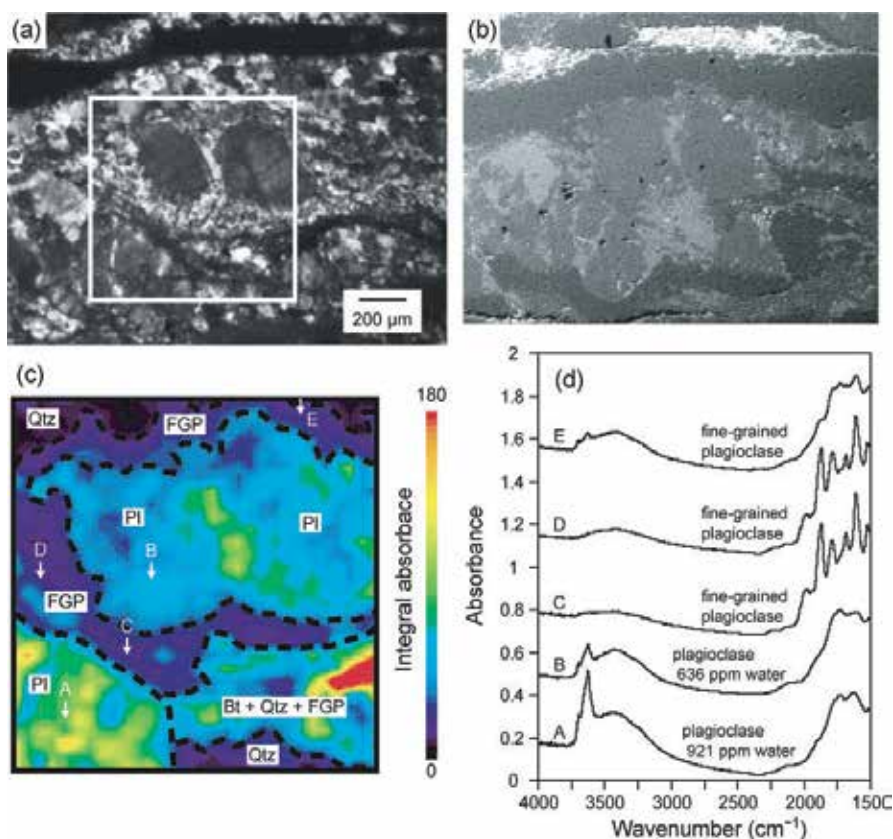


Fig. 11. (a) Optical microscopic image including the IR mapped area (bold square). (b) SEM-BSE image of the mapped area shown in (a): light gray; K-feldspar, medium gray; plagioclase, dark gray; quartz. (c) Water distribution mapped by integral absorbance of water stretching bands in the 3800–2750 cm^{-1} range of the IR spectra. The boundaries of minerals are shown as dotted lines. Arrows with letters show the locations used to illustrate the various selected IR spectra in (d). Pl; plagioclase, FGP; fine-grained plagioclase, Qtz; quartz. IR spectra show quartz vibrational bands in fine-grained plagioclase. Absolute water contents for fine-grained plagioclase are not determined due to the mixtures of quartz and K-feldspar.

In general, fluid water can be trapped at intergranular regions (grain boundaries) up to a few thousand ppm H₂O, as reported for quartz aggregates whose each grain size is a few tens of micrometers to a few hundred micrometers (e.g., Nakashima et al., 1995; Muto et al., 2004; O'kane et al., 2005). In this study, intergranular regions must also be covered in the measurements for fine-grained K-feldspar- and plagioclase-dominant regions. The solution-precipitation process that produces fine-grained K-feldspar and plagioclase are subsequently and/or simultaneously enhanced by the ability of fluid water along intergranular regions to carry ions in solution, especially in situations where intergranular diffusion was promoted by an increase in surface area. (e.g., Simpson & Wintch, 1989; Fitz Gerald & Stünitz, 1993; Tsurumi et al., 2003). However, contrary to the previous knowledge on water contents at intergranular regions, water contents in fine-grained K-feldspar- and plagioclase-dominant regions are low and homogeneous (av. 250 ppm). Therefore, it can be inferred that fluid water may not abundantly be trapped in newly-created grains, and rather released during and/or after the solution-precipitation process. The release of fluid water and dissolved ions, which contributed to the process, was a result of the concentration gradients formed in the context of numerous newly-created intergranular regions within the mix of fine-grained feldspar and quartz. As a consequence, the entire process results in a positive feedback to promote the solution-precipitation process.

6. Conclusions

I investigated high temperature behaviour of water in rocks and minerals. Chalcedonic quartz was used as a representative rock which contains abundant fluid water at intergranular regions and -OH in quartz crystal structures. The average coordination numbers of water molecules were decreased with increasing temperature, which causes shifts of stretching vibrations to higher wavenumbers. Dehydration of fluid water in the chalcedonic quartz was monitored by keeping at high temperatures. Fluid water was rapidly dehydrated through intergranular regions at 500 °C, and new hydroxyl bands appeared with dehydration of fluid water.

States of water molecules, which are not clustered like fluid water, were investigated for beryl, typical cyclosilicate, using high temperature polarized IR spectroscopy. The beryl channels, open cavities in the crystal structures, contain two types of water molecules which freely exist or coordinate to cations from up and/or below them. The former type of water easily loses its specific position, resulting the rapid decreases of its IR band heights without dehydration, and shows rapid dehydration at 850 °C. The latter type of water shows significant changes in its wavenumbers with increasing temperatures. There are slight modifications in the wavenumbers during dehydration due to changes of coordination to cations during dehydration.

Distribution of fluid water was measured for deformed granites. K-feldspar and plagioclase fine grains were formed around porphyroclasts by solution-precipitation process. Water contents in fine-grained K-feldspar- and plagioclase-dominant regions show low and homogeneous distribution of fluid water, while water distributions in host porphyroclasts were heterogeneous. This indicates that fluid water, which was involved in the solution-precipitation process, was released during and/or after the solution-precipitation process.

7. Acknowledgment

I thank K. Shinoda, J. Muto, T. Okudaira, and T. Hirono for their helpful comments on the manuscript. K. Shinoda is especially thanked for the advice on IR measurements and supports on sample preparation of beryl. T. Okudaira is also thanked for the supports for sample collection of the deformed rocks. This work was financially supported by a Grant-in-Aid for Scientific Research (212327) and (233694) by the Japan Society for the Promotion of Science for Young Scientists.

8. References

- Aines, R.D. & Rossman, G.R. (1984). Water in minerals? A peak in infrared. *Journal of Geophysical Research*, Vol. 89, pp. 4059-4071
- Andersson, L.O. (2006). The position of H^+ , Li^+ and Na^+ impurities in beryl. *Physics and Chemistry of Minerals*, Vol. 33, pp. 403-416
- Artioli, G., Rinaldi, R., Ståhl, K. & Zanazzi, P.F. (1993). Structure refinements of beryl by single-crystal neutron and X-ray diffraction. *American Mineralogist*, Vol. 78, pp. 762-768
- Aurisicchio, C., Fioravanti, G., Grubessi, O. & Zanazzi, P.F. (1988). Reappraisal of the crystal chemistry of beryl. *American Mineralogist*, Vol. 73, pp. 826-837
- Bauschlicher, C.W., Langhoff, S.R., Partridge, H., Rice, J.E. & Komornicki, A. (1991). A theoretical study of $Na(H_2O)_n^+$ ($n = 1-4$). *Journal of Chemical Physics*, 95, 5142-5148.
- Beran, A., (1987). OH groups in nominally anhydrous framework structures: an infrared spectroscopic investigation of Danburite and Labradorite. *Physics and Chemistry of Minerals*, Vol. 14, pp. 441-445
- Brubach, J.B., Mermet, A., Filabozzi, A., Gerschel, A. & Roy, A. (2005). Signatures of the hydrogen bonding in the infrared bands of water. *Journal of Chemical Physics*, Vol. 122, Article No. 184509
- Charoy, B., de Donato, P., Barres, O. & Pinto-Coelho, C. (1996). Channel occupancy in an alkali-poor beryl from Serra Branca (Goiás, Brazil): spectroscopic characterization. *American Mineralogist*, Vol. 81, pp. 395-403
- Della Ventura, G., Bellatreccia, F., Cesare, B., Harley, S. & Piccinini, M. (2009). FTIR microspectroscopy and SIMS study of water-poor cordierite from El Hoyazo, Spain: application to mineral and melt devolatilization. *Lithos*, Vol. 113, pp. 498-506
- Dimanov, A., Dresen, G., Xiao, X., & Wirth, R. (1999). Grain boundary diffusion creep of synthetic anorthite aggregates: the effect of water. *Journal of Geophysical Research*, Vol. 104, pp. 10483-10497
- Dysthe, D.K. & Wogelius, R.A. (2006). Confined fluids in the Earth's crust – Properties and processes. *Chemical Geology*, Vol. 230, pp. 175-181
- Eisenberg, D. & Kauzman, W. (1969). *The Structure and Properties of Water*, Oxford University Press, Oxford
- Falk, M. (1984). The frequency of the H–O–H bending fundamental in solids and liquids. *Spectrochimica Acta*, Vol. A40, pp. 43-48
- Fitz Gerald, J.D. & Stünitz (1993). Deformation of granitoids at low metamorphic grade. I: reactions and grain size reduction. *Tectonophysics*, Vol. 221, pp. 269-297
- Frondel, C. (1982). Structural hydroxyl in chalcedony (Type B quartz). *American Mineralogist*, Vol. 67, pp. 1248-1257

- Fukuda, J. & Shinoda, K. (2008). Coordination of water molecules with Na⁺ cations in a beryl channel as determined by polarized IR spectroscopy. *Physics and Chemistry of Minerals*, Vol. 35, pp. 347-357
- Fukuda, J. & Nakashima, S. (2008). Water at high temperatures in a microcrystalline silica (chalcedony) by in-situ infrared spectroscopy: physicochemical states and dehydration behavior. *Journal of Mineralogical and Petrological Sciences*, Vol. 103, pp. 112-115
- Fukuda, J., Peach, C.J., Spiers, C.J. & Nakashima, S. (2009a). Electrical impedance measurement of hydrous microcrystalline quartz. *Journal of Mineralogical and Petrological Sciences*, Vol. 104, pp. 176-181
- Fukuda, J., Shinoda, K., Nakashima, S., Miyoshi, N. & Aikawa, N. (2009b). Polarized infrared spectroscopic study of diffusion of water molecules along structure channels in beryl. *American Mineralogist*, Vol. 94, pp. 981-985
- Fukuda, J., Yokoyama, T. & Kirino, Y. (2009c). Characterization of the states and diffusivity of intergranular water in a chalcedonic quartz by high temperature in-situ infrared spectroscopy. *Mineralogical Magazine*, Vol. 73, pp. 825-835
- Fukuda, J. & Shinoda, K. (2011). Water molecules in beryl and cordierite: high-temperature vibrational behavior, dehydration, and coordination to cations. *Physics and Chemistry of Minerals*, Vol. 38, pp. 469-481
- Gibbs, G.V., Breck, D.W. & Meagher, E.P. (1968). Structural refinement of hydrous and anhydrous synthetic beryl, Al₂(Be₃Si₆)O₁₈ and emerald, Al_{1.9}Cr_{0.1}(Be₃Si₆)O₁₈. *Lithos*, Vol. 1, pp. 275-285
- Gleason, G.C. & DeSisto, S. (2008). A natural example of crystal-plastic deformation enhancing the incorporation of water into quartz. *Tectonophysics*, Vol. 446, pp. 16-30
- Goldman, D.S. & Rossman, G.R. (1977). Channel constituents in cordierite. *American Mineralogist*, Vol. 62, pp. 1144-1157
- Graetsch, H., Flörke, O.W. & Mieke, G. (1985). The nature of water in chalcedony and opal-C from Brazilian agate geodes. *Physics and Chemistry of Minerals*, Vol. 12, pp. 300-306
- Griggs, D.T. (1967). Hydrolytic weakening of quartz and other silicates. *Geophysical Journal of the Royal Astronomical Society*, Vol. 14, pp. 19-32
- Hawthorne, F.C. & Černý, P. (1977). The alkali-metal positions in Cs-Li beryl. *Canadian Mineralogist*, Vol. 15, pp. 414-421
- Hiraga, T., Nishikawa, O., Nagase, T. & Akizuki, M. (2001). Morphology of intergranular pores and wetting angles in pelitic schists studied by transmission electron microscopy. *Contributions to Mineralogy and Petrology*, Vol. 141, pp. 613-622
- Hofmeister, A.M. & Rossman, G.R. (1985). A model for the irradiative coloration of smoky feldspar and the inhibiting influence of water. *Physics and Chemistry of Minerals*, Vol. 12, pp. 324-332
- Imon, R., Okudaira, T. & Fujimoto, A. (2002). Dissolution and precipitation processes in deformed amphibolites: an example from the ductile shear zone of the Ryoke metamorphic belt, SW Japan. *Journal of Metamorphic Geology*, Vol. 20, pp. 297-308
- Imon, R., Okudaira, T. & Kanagawa, K. (2004). Development of shape- and lattice-preferred orientations of amphibole grains during initial cataclastic deformation and subsequent deformation by dissolution-precipitation creep in amphibolites from the Ryoke metamorphic belt, SW Japan. *Journal of Structural Geology*, Vol. 26, pp. 793-805

- Ingrin, J., Hercule, S. & Charton, T. (1995). Diffusion of hydrogen in diopside: results of dehydration experiments. *Journal of Geophysical Research*, Vol. 100, pp. 15489-15499
- Jacobsen, S.D. & Van der Lee, S. (2006). *Earth's Deep Water Cycle*, Geophysical Monograph Series, Vol. 168, American Geophysical Union, Washington, D.C.
- Jaoul, O. (1984). Sodium weakening of Heavittree quartzite: preliminary results. *Journal of Geophysical Research*, Vol. 89, pp. 4271-4280
- Johnson, E. & Rossman, G.R. (2003). The concentration and speciation of hydrogen in feldspars using FTIR and ^1H MAS NMR spectroscopy. *American Mineralogist*, Vol. 88, pp. 901-911
- Kats, A. (1962). Hydrogen in alpha quartz. *Philips Research Report*, Vol. 17, pp. 1-31, 133-195, 201-279
- Kenis, I., Urai, J.L., Van der Zee, W., Hilgers, C. & Sintubin, M. (2005). Rheology of fine-grained siliciclastic rocks in the middle crust—evidence from structural and numerical analysis. *Earth and Planetary Science Letters*, Vol. 233, pp. 351-360
- Keppler, H. & Smyth, J.R. (2006). *Water in Nominally Anhydrous Minerals*, Reviews in Mineralogy and Geochemistry, Vol. 62, The Mineralogical Society of America
- Kihara, K. (2001). Molecular dynamics interpretation of structural changes in quartz, *Physics and Chemistry of Minerals*, Vol. 28, pp. 365-376
- Kronenberg, A.K. & Wolf, G.H. (1990). Fourier transform infrared spectroscopy determinations of intragranular water content in quartz-bearing rocks: implications for hydrolytic weakening in the laboratory and within the earth, *Tectonophysics*, Vol. 172, pp. 255-271
- Lee, H.M., Tarakeshwar, P., Park, J., Kołaski, M.R., Yoon, Y.J., Yi, H.B., Kim, W.Y. & Kim, K.S. (2004). Insights into the structures, energetics, and vibrations of monovalent cation-(water) $_{1-6}$ clusters. *Journal of Physical Chemistry A*, Vol. 108, pp. 2949-2958
- Libowitzky, E. & Rossman, G.R. (1997). An IR absorption calibration for water in minerals. *American Mineralogist*, Vol. 82, pp. 1111-1115
- Łodziński, M., Sitarz, M., Stec, K., Kozanecki, M., Fojud, Z. & Jurga, S. (2005). ICP, IR, Raman, NMR investigations of beryls from pegmatites of the Sudety Mts. *Journal of Molecular Structure*, Vol. 744, pp. 1005-1015
- Muto, J., Nagahama, H., & Hashimoto, T. (2004). Microinfrared reflection spectroscopic mapping: application to the detection of hydrogen-related species in natural quartz. *Journal of Microscopy-Oxford*, Vol. 216, pp. 222-228
- Nakahara, M., Matubayasi, N., Wakai, C. & Tsujino, Y. (2001). Structure and dynamics of water: from ambient to supercritical. *Journal of Molecular Liquids*, Vol. 90, pp. 75-83
- Nakashima, S., Matayoshi, H., Yuko, T., Michibayashi, K., Masuda, T., Kuroki, N., Yamagishi, H., Ito, Y. & Nakamura, A. (1995). Infrared microspectroscopy analysis of water distribution in deformed and metamorphosed rocks. *Tectonophysics*, Vol. 245, pp. 263-276
- O'kane, A., Onasch, C.M. & Farver, J.R. (2007). The role of fluids in low temperature, fault-related deformation of quartz arenite. *Journal of Structural Geology*, Vol. 29, pp. 819-836
- Okumura, S. & Nakashima, S. (2004). Water diffusivity in rhyolitic glasses as determined by in situ IR spectroscopy. *Physics and Chemistry of Minerals*, Vol. 31, pp. 183-189
- Passchier, C.W. & Trouw, R.A.J. (2005). *Microtectonics (2nd Ed)*. Springer-Verlag, Heidelberg

- Paterson, M.S. (1982). The determination of hydroxyl by infrared absorption in quartz, silicate glasses and similar materials. *Bulletin de Minéralogie*, Vol. 105, pp. 20-29
- Post, A. & Tullis, J. (1998). The rate of water penetration in experimentally deformed quartzite: implications for hydrolytic weakening. *Tectonophysics*, Vol. 295, pp. 117-137
- Schwarzer, D. (2005). Energy relaxation versus spectral diffusion of the OH-stretching vibration of HOD in liquid-to-supercritical deuterated water. *Journal of Chemical Physics*, Vol. 123, Article No. 161105
- Simpson, C. & Wintsch, R.P. (1989). Evidence for deformation-induced K-feldspar replacement by myrmekite. *Journal of Metamorphic Geology*, Vol. 7, pp. 261-275
- Takagi, H., Mizutani, T. & Hirooka, K. (1988). Deformation of quartz in an inner shear zone of the Ryoke belt – an example in the Kishiwada area, Osaka Prefecture. *Journal of the Geological Society of Japan*, Vol. 94, pp. 869-886 (in Japanese with English abstract).
- Thompson, A.B. & Rubie, D.C. (1985). *Metamorphic Reactions, Kinetics, Textures and Deformation*, Springer, New York
- Tsurumi, J., Hosonuma, H. & Kanagawa, K. (2003). Strain localization due to a positive feedback of deformation and myrmekite-forming reaction in granite and aplite mylonites along the Hatagawa Shear Zone of NE Japan. *Journal of Structural Geology*, Vol. 25, pp. 557-574
- Wintsch, R.P. & Yi, R. (2002). Dissolution and replacement creep: a significant deformation mechanism in mid-crustal rocks. *Journal of Structural Geology*, Vol. 24, pp. 1179-1193
- Wood, D.L. & Nassau, K. (1967). Infrared spectra of foreign molecules in beryl. *Journal of Chemical Physics*, Vol. 47, pp. 2220-2228
- Yamagishi, H., Nakashima, S. & Ito, Y. (1997). High temperature infrared spectra of hydrous microcrystalline quartz, *Physics and Chemistry of Minerals*, Vol. 24, pp. 66-74

Attenuated Total Reflection – Infrared Spectroscopy Applied to the Study of Mineral – Aqueous Electrolyte Solution Interfaces: A General Overview and a Case Study

Grégory Lefèvre¹, Tajana Preočanin² and Johannes Lützenkirchen³

¹*Chimie ParisTech - LECIME -
CNRS UMR 7575, Paris*

²*Laboratory of Physical Chemistry, Department of Chemistry,
Faculty of Science, University of Zagreb, Zagreb*

³*Karlsruhe Institute of Technology (KIT), Institute for
Nuclear Waste Disposal (INE), Karlsruhe*

¹*France*

²*Croatia*

³*Germany*

1. Introduction

The present chapter gives an overview of the application of Attenuated total reflection – Infrared spectroscopy (ATR-IR) to the environmentally important mineral – aqueous electrolyte interface. At these interfaces the important adsorption processes occur that limit the availability of potentially toxic solutes. These retention processes may retard for example the migration of solutes in aquifer systems or even immobilize them on the aquifer material, which is usually a natural mineral. Selected solutes may also via a preliminary adsorption process, which weakens bonds, enhance both dissolution kinetics and the equilibrium solubility of a given mineral.

In the context of retardation (oxy)(hydr)oxide minerals are of major importance. At the surface of these minerals surface functional groups exist that are able to bind metal ions and organic ligands as well as they may promote the formation of so-called ternary surface complexes involving both metal ions and some ligand. To be able to quantify these retention phenomena in porous media (such as aquifers or soils) a physical model of solvent movement is coupled to a (chemical) adsorption model (usually some variant of the surface complexation approach). The intent in the chemical part of the model is to invoke as much understanding of the adsorption process as possible. Thus it turns out to be important whether an adsorption process results in monodentate or multidentate surface complexes. This can have profound consequences in the use of a surface complexation model under different conditions (Kulik et al., 2010; Kallay et al., 2011). Evaluating a surface complexation

model based on macroscopic adsorption data alone usually is not unambiguous. Consequently, it is required to study the adsorption process at the molecular level. Various spectroscopic approaches have been used to resolve the adsorption mechanism, one being ATR-IR.

We give an introduction to the approach and an overview of its possible applicability (and in this context its use in contributing to the understanding of the acid-base chemistry of (oxy)(hydr)oxide mineral surfaces, the adsorption of anions and cations like the uranyl-ion, and the formation of ternary surface complexes can be mentioned in general). Our contribution focuses on a review on the interaction of small organic molecules with oxidic surfaces and we highlight previous studies and point to some controversial issues in selected studies that continue to exist despite extensive research. Obviously such studies relate to other vibrational spectroscopies like Raman or sum frequency generation vibrational spectroscopies.

Finally we discuss results from an experimental study on the mineral gibbsite ($\text{Al}(\text{OH})_3$) in the presence of 5-sulfosalicylic acid (5-SSA). We show how ideally such a study should be designed, starting from the study of the gibbsite-electrolyte solution system (i.e. in absence of 5-SSA) and that of 5-SSA in aqueous solution (i.e. in the absence of gibbsite). Furthermore, we show that it is necessary to study in aqueous solution the interaction of 5-SSA with dissolved aluminium, since the pH - dependent solubility of gibbsite will ultimately cause the appearance of aluminium ions in solution. The system involving gibbsite and 5-SSA is discussed in more detail. We relate the data to calculations of the species distribution for the solution systems, which indicate the dominant aqueous species thus facilitating the assignment of bands.

2. Review of use of ATR in studies about adsorption of selected small organic molecules

2.1 Principles of ATR

The Attenuated Total Reflection effect is based on the existence of an evanescent wave in a medium of lower index of refraction in contact with an optically denser medium in which the infrared beam is sent. This evanescent field decays exponentially in the less dense medium according to equation (1).

$$E = E_0 \exp \left[-\frac{2\pi}{\lambda_1} (\sin^2 \theta - n_{21}^2)^{1/2} Z \right] \quad (1)$$

where $\lambda_1 = \lambda / n_1$ is the wavelength of the radiation in the denser medium, λ the wavelength in free space, θ the angle of incidence with respect to the normal. The parameter n_{21} is defined as the ratio of the refractive indices, i.e. $n_{21} = n_2 / n_1$, where n_1 and n_2 are respectively, the refractive indices of the optically denser and less dense media, and Z is the distance from the surface (Mirabella, 1993) (see Fig. 1).

From the ATR element, the infrared beam probes only the first few micrometers of the sample medium. From equation (1), different parameters can be defined to characterize the depth of penetration. A first definition was the depth at which the electric field amplitude

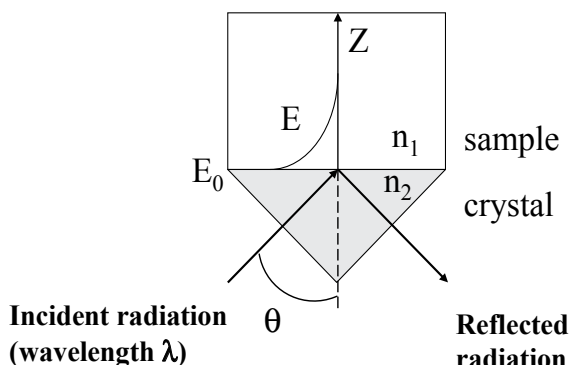


Fig. 1. Schematic diagram of the attenuated total reflection of the infrared beam in a monoreflection ATR accessory.

falls to half its value at the interface ($Z = 0.69 / \gamma$). Another definition of the depth of penetration (d_p) is given by $Z = 1 / \gamma$, i.e. a decay of the electric field of 63 %. Moreover, this value is lower than the actual depth sampled (d_s), which is about three times d_p (decay of the electric field of 95%) (Mirabella, 1993; Tickanan et al., 1991). Equation (1) can be used to obtain the value of d_p in a homogeneous solution, but the determination of the penetration across oxy-hydroxide films is more complex. The depth of penetration, d_p , is expressed as (Coates, 1993):

$$d_p = \frac{\lambda_1}{2\pi} (\sin^2 \theta - n_{21}^2)^{-1/2} \quad (2)$$

or, with ν , the wavenumbers (cm^{-1}):

$$d_p = \frac{10000}{2\pi\nu n_1} (\sin^2 \theta - n_{21}^2)^{-1/2} \quad (3)$$

In studies on the adsorption of ions onto layers of particles deposited on ATR crystals, it is important that the whole layer be probed. Otherwise sorption which takes place in the top of the layer (i.e. further away from the crystal) does not significantly contribute to the observed signal. To take into account the presence of a layer of particles (pores filled with solution) formula (1) can be used with a volume-weighted average of the refractive index of the particle material and the aqueous solution (Hug and Sulzberger, 1994):

$$d_p = F_v \times n_{\text{par}} + (1 - F_v) \times n_{\text{water}} \quad (4)$$

where F_v is the volume fraction of solid and n_{par} the refractive index of the pure solid. A volume fraction between 0.30 and 0.40 was estimated for TiO_2 ($n_{\text{par}} = 2.6$), leading to a maximum d_p of $2.6 \mu\text{m}$ at 1100 cm^{-1} . Thus, the actual depth sampled would be *ca.* $7 \mu\text{m}$ ($d_s = 3 \times d_p$), indicating that the deposited layer should be thinner than this value.

2.2 Experimental

Using an accessory allowing to record infrared spectra in ATR mode is the first requirement to get *in situ* signals of the solid/solution interface. However, the way to prepare this interface and even the choice of the accessory is not straightforward.

2.2.1 Protocols to produce a suitable solid-liquid interface

The first step in ATR-related studies involves the formation of a suitable solid-liquid interface. To obtain a metal oxide / solution interface which can be probed by ATR, several methods have been described in literature.

The first one, described in the pioneering work by Tejedor-Tejedor and collaborators (Tejedor-Tejedor and Anderson, 1986; Tejedor-Tejedor and Anderson, 1990; Tickanen et al., 1991) consisted in a cylindrical internal reflection cell (a rod-shaped crystal of ZnSe) dipped in a suspension of 100 g/L goethite. This method is now less frequently used, to the advantage of horizontal ATR crystals. Using such instrumentation, Hug and Sulzberger (1994) have developed a method which has become standard. The approach consists in coating the ATR crystal by colloidal particles to form a film. As a typical protocol, a mixture of solid and ethanol is spread over the ATR crystal, then dried using a nitrogen flux. After drying, the layer is rinsed with water or with an electrolyte solution. More details are given in articles by Hug (1997) or Peak et al. (1999).

In another method, the equilibrium of the system solid/solution is reached by a classical batch experiment, using diluted suspensions of the solid. Then the suspensions are centrifuged to obtain a higher mass/volume ratio, for example 100-1000 g/L, or even a paste. The sample is then spread on the ATR crystal using a spatula (Villalobos and Leckie, 2001).

A final possibility is to use the surface of the crystal as the sample itself. Either the surface of the crystal is used as received, as ZnSe on which sodium dodecyl sulfate (Gao and Chorover, 2010) or Ge on which heptyl xanthate (Larsson et al., 2004) formed a monolayer, or the surface was chemically modified and is different from the bulk. Thus, Asay and Kim (2005) studied the adsorption of water molecules on the native layer of silica present on a silicium ATR crystal, or Wang et al. (2006) studied the adsorption of hexane and ethylbenzene from the vapor phase on a layer of zeolite grown directly on the surface of a silicium ATR crystal. Frederiksson and Holmgren (2008) have formed a PbS film on a ZnS ATR crystal by a chemical bath deposition process in order to study the adsorption of heptyl xanthate. In these latter studies, the system is very close to a film obtained by drying of a suspension, but the optical properties are expected to be better. Couzis and Gulari (1993) have deposited 600 Å of alumina by sputtering on a ZnSe crystal.

The advantages and drawbacks of the three methods to prepare the solid/solution interface discussed above are listed in table 1. As of today, the most common method is to prepare a dry layer, even though it is simpler to use a paste. However, using a paste has a major drawback since the contact between particles and the ATR crystal is not optimal, the sensitivity is low and depends on the suspension structure (which in general is pH-dependent). On the other hand, using the results obtained with a dry layer to interpret macroscopic data obtained in well-dispersed suspensions can be tricky, since effects due to

Method	Paste	Dried layer	Film growth or crystal only
Ease of preparation	++	+	-
Variety of solids to best studied	++	+	-
Optical quality (sensitivity)	-	+	++
Quantitative evaluation of spectra	-	+	++
Representativity/suspension	++	+	-
Flow cell	-	+	++

Table 1. Summary of characteristics of the three methods of preparation of the solid/solution interface probed by ATR-IR: (++) strong advantage, (+) advantage, (-) drawback.

the confinement of the solutions are ignored. The last advantage of using a film is the possibility to perform experiments with a flow cell. This set-up allows recording spectra, while varying the composition of the solution, e.g. by modifying pH, or the concentration of adsorbing species.

2.2.2 Limitations in the wavenumber range

Once the procedure to prepare the interface has been chosen, the wavenumber range covered by the measurement is another important experimental aspect. Indeed, a number of interferences may occur between bands of adsorbed species and the experimental set-up.

The main limitation may arise from the **ATR element** itself. Each material has a transmission threshold, which may be located at a high wavenumber, such as silicium. Other materials with a low transmission threshold may be too reactive towards solutions. Thus, ZnSe can be attacked by acid or zinc-complexing species. A usual choice made by ATR-elements-dealers is an element made in ZnSe, but covered by a thin layer of diamond to increase its chemical resistance. This possibility exists only for small ATR crystals, allowing only few reflections of the infrared beam. To increase sensitivity, large ATR crystals are used. For example 40 mm × 10 mm crystals with a thickness of around 1 mm allow dozens of reflections. Such crystals usually consist of a pure material.

Besides the above limitations due to the ATR element, two gases present in the ambient **atmosphere** lead to absorption bands in IR spectra: carbon dioxide, and water. The main bands (Fig. 2) consist in a doublet at 2361 and 2339 cm⁻¹ (CO₂), and numerous narrow peaks in the range 2000 – 1300 (H₂O bending) and 4000 – 3400 (H₂O stretching). Generally, the band of CO₂ does not interfere with bands of adsorbates, but H₂O bending can interfere with adsorbed organic molecules. Several methods exist to solve this problem. In fact, the presence of CO₂ and water in the atmosphere of the spectrometer is not the actual problem since it is taken into account in the background spectrum. It is rather the evolution of their concentrations (or partial pressures) during the subsequent spectra collection that leads to the presence of bands, which varies with time. The less concentrated these gases are, the

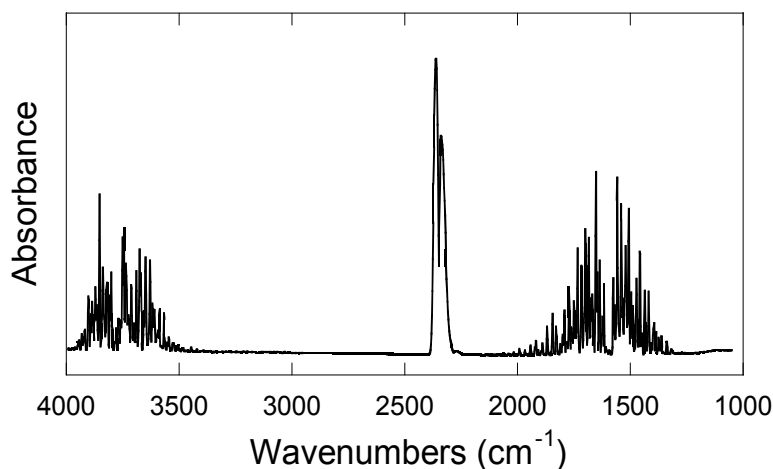


Fig. 2. Spectrum of the atmosphere showing the contributions as discussed in the text.

lower are the bands, since the signal comes from the fluctuation of the partial pressures. Thus, some spectrometers are evacuated to enhance sensitivity and stability. Other spectrometers are purged with inert gas or with compressed dried air. Another possible solution to the problem consists in the use of spectrometers which are sealed and equipped with desiccant powder. In all cases, if bands of atmospheric compounds remain, they can be tentatively removed by subtracting the atmosphere spectra.

Since the studies generally consist in probing the species adsorbed on a **solid deposited** on the ATR crystal, it is important to take into account bands from the solid itself. For metal oxides, the absorption bands are generally located at low wavenumbers, which does not cause interferences with adsorbed species. Exceptions exist with light metals as SiO_2 (around 1060 cm^{-1}). For metal hydroxides, stretching of M-OH can lead to the presence of bands above 800 cm^{-1} as is the case with goethite (900 and 800 cm^{-1}) or gibbsite (around 1000 cm^{-1}).

Ideally, if the layer formed by particles is stable, the signal coming from the solid can be subtracted from the final spectra, and the presence of these bands does not hamper the detection and interpretation of bands from adsorbed species. However, in practice subtraction is often difficult due to the evolution of the signal of the solid with time or solution composition. Phenomena such as re-entrainment of particles by flowing solution, or swelling/shrinkage due to the change in surface potential can explain this problem.

Water is the most common **solvent** in environmental studies and its absorption bands can be a problem too. Stretching of H_2O occurs around $3000\text{--}3600\text{ cm}^{-1}$ and interferes with stretching of surface hydroxyl groups. Bending takes place at 1643 cm^{-1} (Venyaminov and Prendergast, 1997), close to the stretching of C=O groups (see below). This can complicate the accurate measurement of $\nu_{\text{C=O}}$ maxima. Finally, water absorption is very strong below ca. 900 cm^{-1} , and this can prevent the measurement of any bands in the lowest wavenumber range. In fact the actual threshold appears to depend on the number of reflections in the ATR system. For a monoreflexion accessory, a measurement can be made down to 650 cm^{-1} without large absorption of H_2O , while for a 25-reflection crystal, the signal becomes noisy

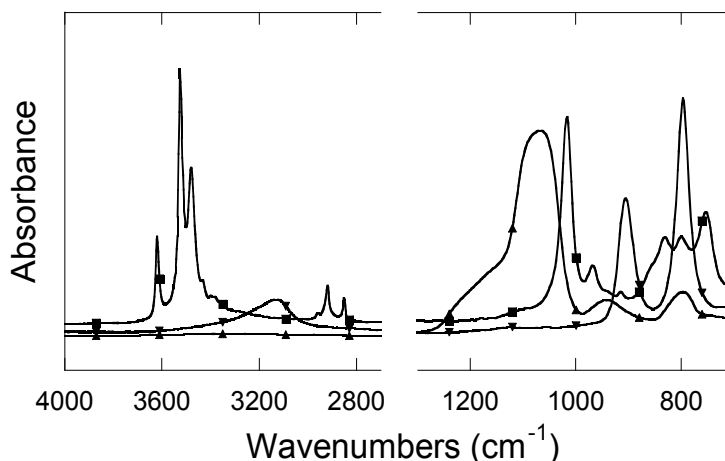


Fig. 3. Spectra of solids as dried layer on an ATR element: silica (▲), gibbsite (■), goethite (▼)

below 890 cm^{-1} (Lefèvre et al., 2006). To be able to record spectra at lower wavenumbers, heavy water (D_2O) can be used because the absorption bands are shifted by a factor of ca. 1.4 to lower wavenumbers. Thus, a good signal can be obtained for bands located between 850 and 950 cm^{-1} (Lefèvre et al., 2008) using the same 25-reflection crystal. It can be useful to avoid interferences with bands around 1650 cm^{-1} since D_2O bending is located at 1209 cm^{-1} (Venyaminov and Prendergast, 1997).

2.3 Review of adsorption of carboxylic acids onto metal (hydr)oxides by ATR-IR

2.3.1 Monoacids: Formic, acetic, benzoic, lauric

A number of monoacids are discussed in the context of this review. Table 2 gives some information on the monoacids both in solution and at the interface. The systems are discussed in detail in the remainder of the section.

Acid	pKa	R	Δ_{COO} (cm^{-1}) in solution	Δ_{COO} (cm^{-1}) adsorbed
Formic	3.75 *	-H	230	192 (TiO_2)
Acetic	4.76 *	$-\text{CH}_3$	137	90 (TiO_2)
Benzoic	4.19 *	$-\text{C}_6\text{H}_5$	154	109 (TiO_2) 117 (Ta_2O_5) 122 (goethite) 141 (ZrO_2)
Lauric	4.90 **	$-\text{CH}_2-(\text{CH}_2)_9-\text{CH}_3$	136	185 (alumina)

from *Lide (1998), ** Dean (1999)

Table 2. Characteristics of carboxylic acid ($\text{R}-\text{C}(\text{O})\text{OH}$). $\Delta_{\text{COO}} = \nu_{\text{as}}(\text{COO}) - \nu_{\text{s}}(\text{COO})$

Several surface complexes can be formed with monoacids, such as monodentate, or bidentates (Fig. 4). Monodentate surface complexes can be distinguished from bidentates based on the occurrence or not of the free C=O group band, with a stretching frequency at about 1700 cm^{-1} .

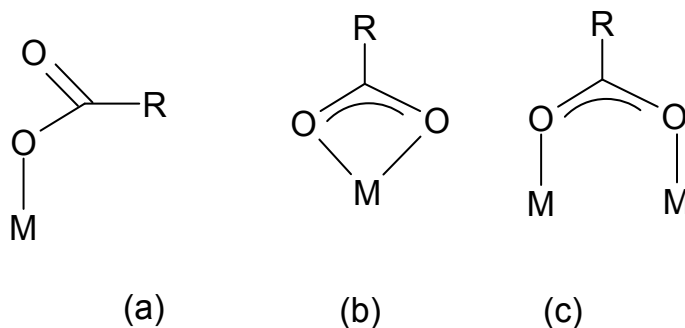


Fig. 4. Surface complexes between a monoacid and a metal oxide: (a) monodentate, (b) mononuclear bidentate and (c) binuclear bidentate

The ATR-FTIR spectrum of 1M of **formate** ion is characterized by bands located at 1350, 1383 and 1580 cm^{-1} , assigned to $\nu_s(\text{COO})$, $\delta(\text{HCO})$ and $\nu_{as}(\text{COO})$, respectively (Rotzinger et al., 2004). Spectra of formate adsorbed on TiO_2 at pH 5.0, up to 30 mM display the presence of bands of formate ions and a new peak at 1540 cm^{-1} , assigned to $\nu_{as}(\text{COO})$ of species interacting with the surface. Spectra in D_2O confirmed this assignment since only a small shift (8 cm^{-1}) of this band was observed, which precludes the vibration of a protonated/deuterated species. A decrease of pH from 9 to 3 leads to the decrease of the peak area. A series of experiments where the adsorption of formic acid as a gas has been studied has shown the presence of bands of formic acid, formate, and a peak at ca. 1540 cm^{-1} . In support of this, molecular calculations have been performed for the three hypothetical surface complexes (Fig. 4), leading to calculated frequencies. Calculations on the stability of the surface complexes were found to support the binuclear bidentate coordination.

Sorption of **acetate** ions has been studied by ATR on rutile (Rotzinger et al., 2004) and several other minerals (Kubicki et al., 1999). In solution, the acetate ion is characterized by bands at 1348-1349, 1415-1422 and 1552-1555 cm^{-1} (Rotzinger et al., 2004; Kubicki et al., 1999) assigned to $\delta(\text{CH}_3)$, $\nu_s(\text{COO})$, and $\nu_{as}(\text{COO})$, respectively. Acetic acid is characterized by bands at 1279-1283, 1370-1371, 1392-1397 (δ_{CH_3}), 1642-1650 and 1711-1717 ($\nu_{\text{C=O}}$) (Rotzinger et al., 2004; Kubicki et al., 1999). Spectra of adsorbed species have been recorded at pH 5.0 (ca. 1:1 mixtures of the acetate ion and acetic acid in solution since pH is close to pK_a), and at total acetate concentrations up to 25 mM on TiO_2 (Rotzinger et al., 2004), and at pH 3 and 6 in the presence of 2 M acetate on quartz, albite, illite, kaolinite and montmorillonite (Kubicki et al., 1999). On TiO_2 , bands of acetate are present with a new band at 1512 cm^{-1} assigned to $\nu_{as}(\text{COO})$ shifted due to the adsorption. The absence of a band at ca. 1700 cm^{-1} indicates that the C=O group is not present in the surface species. On several minerals (Kubicki et al., 1999), spectra recorded at pH 3 and pH 6 are similar to spectra of solution species. With acetic acid adsorbed on quartz, two bands are seen around 1720 cm^{-1} (at 1709 and 1732), suggesting two different bonding environments. For the other minerals, the authors

conclude that chemisorption is below the detection limit of the spectroscopy. This might be due to the low specific surface area of the minerals used in the study.

Adsorption of **benzoic** acid on minerals was studied by several authors on quartz, albite, illite, kaolinite and montmorillonite (Kubicki et al., 1999), goethite (Tejedor-Tejedor et al., 1990), TiO_2 (Tunesi and Anderson, 1992; Dobson and McQuillan, 1999), as well as Al_2O_3 , ZrO_2 and Ta_2O_5 (Dobson and McQuillan, 1999). Aqueous benzoate is characterized by bands at 1542 cm^{-1} ($\nu_{\text{as}}(\text{COO})$), 1388 cm^{-1} ($\nu_{\text{s}}(\text{COO})$) and 1593 cm^{-1} ($\nu_{\text{C}=\text{C}}$). At $\text{pH} < \text{pK}_a$, spectra are characterized by bands at 1705 cm^{-1} ($\nu_{\text{C}=\text{O}}$), 1319 cm^{-1} (ν_{COH}), 1279 cm^{-1} (δ_{COH}), and bands associated with C=C and C-H vibrations (1603 , 1494 , 1452 , 1178 , 1073 and 1026 cm^{-1}). Benzoic acid adsorbed on quartz displays bands of the aqueous species with two new peaks (at 1604 and 1569 cm^{-1}). The lower frequency was found by calculation to correspond to a monodentate complex, and the higher one to an outer-sphere complex. On albite at $\text{pH} 3$, no peaks above 1700 cm^{-1} were observed, indicating that the C=O group is absent from the surface complex even in the pH range where the acid species predominates over the benzoate anion. This result is a direct evidence of the formation of a bidentate complex, stable over a wide range of pH . On goethite at $\text{pD} 3.9$ (Tejedor-Tejedor et al., 1990) and on TiO_2 at $\text{pH} 3.6$ (Tunesi and Anderson, 1992), the $\nu_{\text{C}=\text{O}}$ mode is also absent. Another interesting point is that the asymmetric / symmetric carboxylate group stretching ratio decreases when benzoate interacts with Fe(III), which can be explained by the increase of coplanarity between the benzene ring and the $\nu_{\text{as}}(\text{COO})$. These observations are consistent with the formation of a bidentate complex. c.f. Fig. 5 (Tejedor-Tejedor et al., 1990).

On TiO_2 , the difference between $\nu_{\text{as}}(\text{COO})$ et $\nu_{\text{s}}(\text{COO})$ for the adsorbed species is lower by 45 cm^{-1} compared to the corresponding difference for the solute species. It is believed that a lower value is indicative of a bidentate complex, and that such a large value indicates a chelate structure with a single centre (Fig. 5) (Tunesi and Anderson, 1992). On goethite, the difference was lower by 32 cm^{-1} , consistent with a bridging complex (Tunesi and Anderson, 1992).

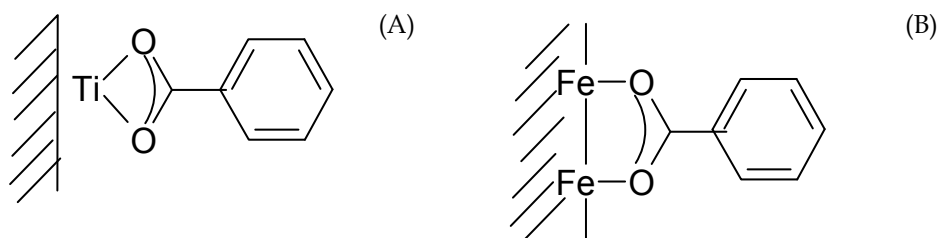


Fig. 5. Proposed surface complexes of benzoate on (A) TiO_2 and (B) goethite.

The bands pertaining to $\nu_{\text{as}}(\text{COO})$ and $\nu_{\text{s}}(\text{COO})$ modes of **laurate** in solution are located at 1547 and 1411 cm^{-1} , respectively. Between 2850 and 3000 cm^{-1} , several bands are reported corresponding to hydrocarbon stretching. Laurate anions were adsorbed onto alumina, which had been deposited on the ATR element by a sputtering technique the thickness of the film being 600 \AA (Couzis and Gulari, 1993). The recorded spectra depended on contact time and pH . At $\text{pH} 8$, up to 20 minutes after initiation of the solid-liquid contact, the observed peaks mainly corresponded to the solute species and the authors inferred the presence of an outer-sphere surface complex, since the surface is positively charged at this

pH. For longer times of exposure, a new band appeared at 1597, along with the increase of the band at 1412 cm^{-1} . This new band was assigned to $\nu_{\text{as}}(\text{COO})$ of the adsorbed species. The difference between $\nu_{\text{as}}(\text{COO})$ and $\nu_{\text{s}}(\text{COO})$ for the surface species was higher than the value obtained for the solute species. This behaviour, contrary to that observed for carboxylic acids with a shorter alkyl chain (Table 3) has been interpreted as a different, i.e. monodentate, surface coordination. From the evolution of the spectra recorded in the hydrocarbon stretching range (2750 – 3000 cm^{-1}), a chain-chain interaction is inferred after adsorption of laurate for short contact times, suggesting the association of the aliphatic chains at low surface coverage. For longer contact times, corresponding to a higher surface coverage, the chain-chain interactions become negligible.

2.3.2 Saturated and unsaturated diacids

This section in a similar way as the previous one summarizes a number of studies on the adsorption saturated and unsaturated diacids to (oxy)(hydr)oxide minerals. The chemical speciation (in terms of the number of species in solution) becomes more complex for these compounds, which concomitantly enhances the possibilities of the diacids to form surface complexes of different stoichiometries in terms of bonding and proton balances. The diacids addressed are summarized in tables 3 (saturated diacids) and 4 (unsaturated diacids). The remainder of the section discusses in some detail published findings from ATR-FTIR spectroscopy.

Acid	$\text{pK}_{\text{a}1}$, $\text{pK}_{\text{a}2}$ Lide (1998)	R
Oxalic	1.23, 4.19	N.A.
Malonic	2.83, 5.69	$-\text{CH}_2-$
Succinic	4.16, 5.61	$-(\text{CH}_2)_2-$
Glutaric	4.31, 5.41	$-(\text{CH}_2)_3-$
Adipic	4.43, 5.51	$-(\text{CH}_2)_4-$

Table 3. Characteristics of dicarboxylic acids ($\text{HO}(\text{O})\text{C}-\text{R}-\text{C}(\text{O})\text{OH}$).

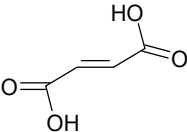
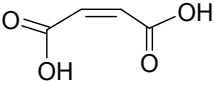
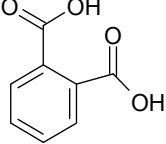
Acid	$\text{pK}_{\text{a}1}$, $\text{pK}_{\text{a}2}$ fom Lide (1998)	Formula
<i>trans</i> -Fumaric	3.03, 4.44	
Maleic	1.83, 6.07	
<i>o</i> -Phtalic	2.89, 5.51	

Table 4. Characteristics of unsaturated dicarboxylic acids.

Oxalic acid is the simplest polyacid molecule $(\text{COOH})_2$ and its adsorption is the most common subject of study by ATR-IR on oxy-hydroxides of aluminum (Axe and Persson, 2001; Johnson et al., 2004; Rosenqvist et al., 2003; Yoon et al., 2004; Dobson and McQuillan, 1999), iron (Borda et al., 2003; Duckworth and Martin, 2001; Persson and Axe, 2001), chromium (Degenhardt and McQuillan, 1999; Garcia Rodenas et al., 1997), titanium (Hug and Sulzberger, 1994; Weisz et al., 2001; Weisz et al., 2002; Dobson and McQuillan, 1999), silicon (Kubicki et al., 1999), tantalum (Dobson and McQuillan, 1999) and zirconium (Dobson and McQuillan, 1999). The spectra of species in solution, i.e. $(\text{COOH})_2$, HOCCOO^- and $(\text{COO}^-)_2$ were reported in several studies. The oxalate ion is characterized by two peaks at 1307 and 1571 cm^{-1} , respectively, which are assigned to $\nu_{\text{as}}(\text{COO})$ and $\nu_{\text{s}}(\text{COO})$ modes. The spectrum of the oxalic acid species in solution is dominated by C=O stretching at 1735 cm^{-1} and C-OH stretching at 1227 cm^{-1} . These features of oxalate and oxalic acid are consistent with theoretical frequency calculations (Axe and Persson, 2001). The spectra of hydrogen oxalate shows three peaks assigned to C=O stretching (1725 cm^{-1}), $\nu_{\text{as}}(\text{COO})$ (1620 cm^{-1}), and C-OH stretching (1240 cm^{-1}) (Degenhardt and McQuillan, 1999).

Sorption of oxalate on boehmite was studied as a function of oxalate concentration and pH (Axe and Persson, 2001). Two different complexes were identified: an outer-sphere complex characterized by a spectrum similar to that of dissolved oxalate (two bands at 1577 and 1308 cm^{-1}), and an inner-sphere complex. The assignment of this latter was based on the comparison of the spectra of the boehmite surface after sorption of oxalate (characterized by strong bands at 1722, 1702, 1413, 1288 cm^{-1}) with the spectra of dissolved $[\text{Al}(\text{Ox})(\text{H}_2\text{O})_4]^+$ (1725, 1706, 1412, 1281 cm^{-1}). The very close resemblance suggests a mononuclear five-membered chelate geometry. The possibility of a symmetric bridging coordination to two equivalent Al(III) ions was ruled out by Raman spectra of the surface species. Indeed, the comparison of Raman spectra of $[\text{Al}(\text{Ox})(\text{H}_2\text{O})_4]^+$ with theoretical frequency calculations have indicated that the intensity of Raman bands can be used to distinguish a ring chelate from a bridging structure.

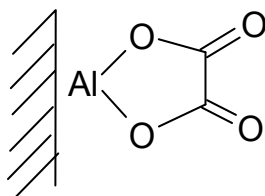


Fig. 6. Ring chelate of oxalate on alumina (Axe and Persson, 2001)

This interpretation has been supported by a study of oxalate sorption on corundum modelled by the CD-MUSIC model involving ATR-IR spectroscopy (Johnson et al., 2004). A mononuclear bidentate complex was found up to 14 $\mu\text{mol}/\text{m}^2$, whereupon oxalate additionally adsorbed as an outer-sphere complex. Sorption of oxalate has also been studied on boehmite and corundum by Yoon et al. (2004) The peaks assigned to the inner-sphere complex in previous works (near 1286, 1418, 1700 and 1720 cm^{-1}) were claimed to arise from the presence of several species. Evidence for this phenomenon comes from the observation that peaks at 1286 and 1418 cm^{-1} are shifted to 1297 and 1408 cm^{-1} as the oxalate surface coverage increases. The authors finally postulated the existence of two species: species "A" at 1286 and 1418 cm^{-1} , and species "B" at 1297 and 1408 cm^{-1} , respectively, which were

assigned to an inner-sphere surface complex on boehmite and to dissolved oxalate coordinated to aqueous Al(III). This assumption is supported by oxalate promoted dissolution of the aluminum oxy-hydroxide arising from the complexation reactions of dissolved Al(III) cations. Quantum calculations of infrared vibrational frequencies of possible surface complexes were carried out on aluminium oxide clusters ($\text{Al}_{18}\text{O}_{12}$ and $\text{Al}_{14}\text{O}_{22}$) including monodentate, bidentates with 4- and 5-membered ring, and bridging bidentates. They showed that the bidentate 5-membered ring most closely matched the experimental observations (within 15 cm^{-1}), while the simulation results for the other models showed deviations between 17 and 102 cm^{-1} .

On hematite (Duckworth and Martin, 2001), the spectra of sorbed oxalate are similar to the above discussed surface complex on an aluminum oxy-hydroxide and consequently a 5-member bidentate complex was proposed. The effect of pH on the sorption of oxalate on goethite has also been studied (Persson and Axe, 2001). An outer-sphere surface complex and a 5-member ring inner-sphere surface complex were inferred from spectra of the goethite/oxalate system and the aqueous Fe(III)-oxalate complex. At low pH, the presence of outer-sphere surface complexes $(\text{COOH})_2$ was ruled out because of the absence of a band corresponding to these species in aqueous solutions (around 1735 and 1233 cm^{-1}).

Oxalate sorption on chromium oxide (Degenhardt and McQuillan, 1999) is characterized by bands at 1708 , 1680 , 1405 and 1269 cm^{-1} , which was interpreted as a side-on surface complex (both carboxylic groups interact with the surface), but without distinguishing between a 5- or a 7-member ring. An additional weakly bound oxalate ion was detected (bands at 1620 - 1580 and around 1306 cm^{-1}). The absence of absorption at 1725 cm^{-1} (corresponding to C=O group) eliminates the singly protonated oxalate species. However, an upward shift of $\nu_{\text{as}}(\text{COO})$ is observed (from 1571 cm^{-1} in Ox^{2-}), suggesting hydrogen bonding with the surface. On chromium oxide (Garcia Rodenas et al., 1997), spectra were recorded after exposure to 0.1 M oxalate solution at pH 3.6 followed by washing with pure water. The resulting spectra were compared to the spectra of $\text{Cr}(\text{Ox})_3^{3-}$ species in solution. As in the work by Degenhardt and McQuillan (1999), an inner-sphere surface complex was inferred from the bands at 1710 , 1680 , 1410 and 1260 cm^{-1} . The remaining shoulder at 1620 cm^{-1} and the peak at 1310 cm^{-1} were attributed to uncoordinated oxalate ions. Since the solid has been washed after contacting with oxalate solution, the solute species are expected to be removed, and these data could be reinterpreted as a species involving hydrogen bonding.

Oxalate sorption onto TiO_2 was amongst the first *in situ* adsorption studies involving ATR-IR spectroscopy at the solid/solution interface (Hug and Sulzberger, 1994). Hug and Sulzberger (1994) have focused their study on the measurement of adsorbed oxalate to plot an isotherm curve. The isotherm at constant pH (3) was fitted by three Langmuir components, correlated with the three possible solute species ($\text{H}_2\text{Ox}/\text{HOx}^-/\text{Ox}^{2-}$). Weisz et al. (2001, 2002) have used the same protocol, and have measured three Langmuir stability constants. Dobson and McQuillan (1999) have recorded the spectra of $\text{Na}_2[\text{TiO}(\text{Ox})_2]_2 \cdot 3\text{H}_2\text{O}_{(\text{s})}$, where the oxalate ion forms a μ_2 -oxo bridged Ti dimeric complex. Its spectrum is close to those obtained with oxalate adsorbed onto TiO_2 and the comparison would lead to the interpretation of the spectroscopic results in terms of a bidentate-bridging surface complex. However, this interpretation disagrees with observations by Scott et al. (1973) who have shown on oxalato-Co(III) complexes that bidentate-chelating and bidentate-bridging oxalato ligands are characterized by nearly identical spectra.

ATR-FTIR studies of the sorption of other saturated diacids $\text{HO(O)C}-(\text{CH}_2)_n-\text{C(O)OH}$ with $n=1$ to 4 have been reported, as malonic (Dobson and McQuillan, 1999; Dolamic and Bürgi, 2006; Duckworth and Martin, 2001; Rosenqvist et al., 2003), succinic (Dobson and McQuillan, 1999; Duckworth and Martin, 2001), glutaric (Duckworth and Martin, 2001) and adipic (Dobson and McQuillan, 1999; Duckworth and Martin, 2001) acids. In solution, the dicarboxylate ions are characterized by $\nu_{\text{as}}(\text{CO}_2)$ around $1560\text{--}1550\text{ cm}^{-1}$ and $\nu_{\text{s}}(\text{CO}_2)$ around $1410\text{--}1350\text{ cm}^{-1}$ (Dobson and McQuillan, 1999). The value of $\nu_{\text{as}}(\text{CO}_2)$ is close for all values of n (and equal to frequency in oxalate), but $\nu_{\text{s}}(\text{CO}_2)$ increases with n , from ca. 1360 cm^{-1} (1310 cm^{-1} in oxalate) to 1400 cm^{-1} . Dicarboxylic acids are characterized by $\nu(\text{C}=\text{O})$ at 1718 cm^{-1} (malonic) and $\nu(\text{C}-\text{O})$ at 1328 cm^{-1} (malonic). The $-\text{CH}_2-$ bending frequencies are located at $1410\text{--}1440\text{ cm}^{-1}$ and $1300\text{--}1250\text{ cm}^{-1}$. Malonate adsorbed on hematite at pH 5 is characterized by peaks at 1260 ($\delta(-\text{CH}_2-)$), 1349 ($\nu_{\text{s}}(\text{CO}_2)$), 1439 ($\delta(-\text{CH}_2-)$) and 1631 ($\nu(\text{C}=\text{O})$) cm^{-1} . $\nu_{\text{s}}(\text{CO}_2)$ remains at 1349 cm^{-1} without shift. In comparison with solution spectra, the intensity of $-\text{CH}_2-$ bending is enhanced, and the CO_2 asymmetric stretching is replaced by $\nu(\text{C}=\text{O})$ (70 cm^{-1} higher). Such an assignment is consistent with a single-bonded surface complex, a structure similar to adsorbed oxalate. The $-\text{CH}_2-$ bending band enhancement indicates a change of the dipole moment, which may be an indication of a strained surface structure with increased bond angles (Dobson and McQuillan, 1999). On other metallic oxides, as TiO_2 (Dobson and McQuillan, 1999; Dolamic and Bürgi, 2006), ZrO_2 (Dobson and McQuillan, 1999), Al_2O_3 (Dobson and McQuillan, 1999; Rosenqvist et al., 2003) and Ta_2O_5 (Dobson and McQuillan, 1999), the spectra of sorbed malonate species are similar: $\delta(-\text{CH}_2-)$ at $1430\text{--}1450$ and $1270\text{--}1280\text{ cm}^{-1}$, $\nu(\text{C}=\text{O})$ at $1580\text{--}1600\text{ cm}^{-1}$, and unshifted $\nu_{\text{s}}(\text{CO}_2)$ at $1360\text{--}1380\text{ cm}^{-1}$. On gibbsite (Rosenqvist et al., 2003), the study of the evolution of the spectra with pH has shown two independent species: an inner-sphere complex (corresponding to a peak at 1438 cm^{-1}) and an outer-sphere complex (corresponding to the unshifted $\nu_{\text{s}}(\text{CO}_2)$). Since the other authors (Dobson and McQuillan, 1999; Dolamic and Bürgi, 2006; Duckworth and Martin, 2001) have not studied the effect of pH, it is not possible to rule out the presence of an outer-sphere complex in their studies, even if they have not mentioned this possibility.

Duckworth and Martin (2001) and Dobson and McQuillan (1999) have studied the effect of longer carbon chains on the adsorption of dicarboxylic acids. Dobson and McQuillan (1999) found surface structures similar to malonate (bridging bidentate via a loop) consistent with greater molecular flexibility. On the contrary, Duckworth and Martin (2001) have found either a bridging bidentate via a loop for malonate and glutarate, or a monodentate complex for succinate and adipate. This interpretation is supported by the behaviour of these ions in the dissolution of hematite: oxalate, malonate and glutarate promote the dissolution whereas succinate and adipate show less of an effect. However, the spectral evidence for this difference in the geometry of complexes is the presence of a peak at $1550\text{--}1540\text{ cm}^{-1}$, *i.e.* at a similar location as ($\nu_{\text{as}}(\text{CO}_2)$) of the solution species, whereas this stretching mode was absent in malonate and glutarate surface species.

Three unsaturated dicarboxylic acids have been studied by ATR: fumaric (Dobson and McQuillan, 1999; Rosenqvist et al., 2003), maleic (Dobson and McQuillan, 1999; Borda et al., 2003; Rosenqvist et al., 2003, Johnson et al., 2004), (respectively *trans*- and *cis*- butendioic acids), and phthalic (Boily et al., 2000; Dobson and McQuillan, 1999; Hwang et al., 2007; Klug and Forsling, 1999; Kubicki et al., 1999; Nordin et al., 1997; Rosenqvist et al., 2003; Tunesi and Anderson, 1992) acid. On gibbsite, the spectra of these three species after sorption are

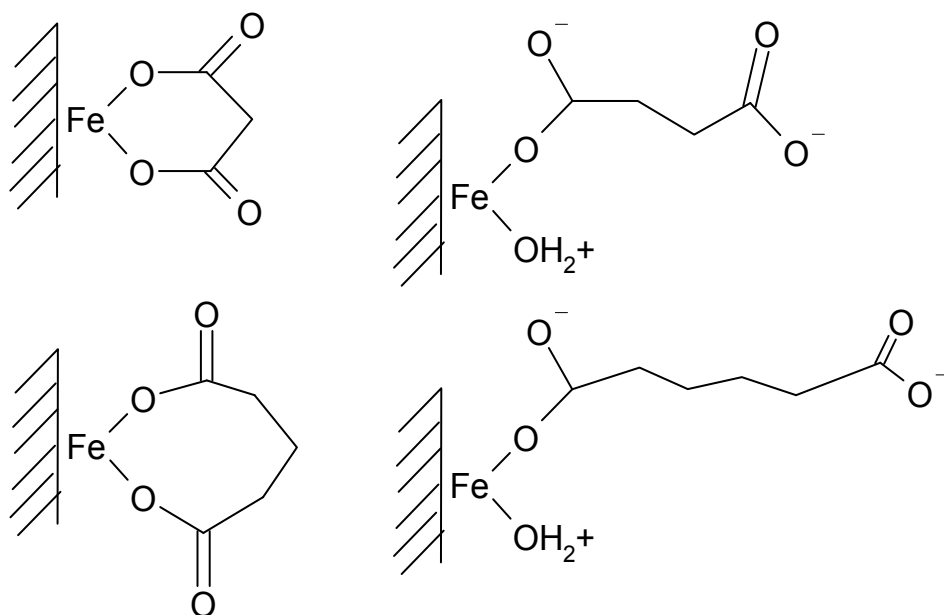


Fig. 7. Proposed structures of diacids adsorbed on hematite (Duckworth and Martin, 2001)

very similar to spectra of the carboxylate ion in solution. Consequently, Rosenqvist et al. (2003) have concluded that an outer-sphere complex was formed. On Al_2O_3 , the same behaviour was shown for maleate and fumarate (Dobson and McQuillan, 1999). On corundum, high resolution spectra of the adsorbed maleate ion were recorded (Johnson et al., 2004), and only small differences between bands of dissolved and adsorbed species have been detected, supporting outer-sphere complexation. For phthalate, inner-sphere and outer-sphere complexes were found on ferric oxy-hydroxides (Boily et al., 2000; Hwang et al., 2007).

3. Adsorption of 5-sulfosalicylic acid onto gibbsite

3.1 Introduction

The system 5-sulfosalicylic acid (5-SSA)/gibbsite is part of a broader study involving Cm adsorption onto gibbsite (Huittinen et al., 2009). Interaction of dissolved Cm with 5-SSA (Panak, 1996) and acid-base equilibria of gibbsite (Adekola et al., 2011) have been studied separately. Gibbsite as used in this study has a platelike morphology. Most of its surface relates to the basal plane. A very complex issue is the interfacial behaviour of the bare gibbsite. While the basal plane from a conventional point of view is considered quite inert, there are a number of indications that rather show that the basal plane can be quite reactive (Rosenqvist et al., 2002; Gan and Franks, 2006). The present view is that a number of effects can be of importance, such as the precise conditions for the preparation of the gibbsite particles. This has been further studied by mimicking the basal plane by individual single crystals of sapphire, which are structurally very similar to the ideal basal plane of gibbsite (Lützenkirchen et al., 2010). Here we present some results on the interaction of 5-SSA with the gibbsite particles used in the Cm adsorption and basic

charging studies mentioned above to lay a foundation to the study of the ternary Cm-SSA-gibbsite system.

Adsorption of 5-SSA to related minerals (i.e. alumina) has been previously studied previously by Jiang et al. (2002) by both a set of electrokinetic data and batch adsorption. Furthermore they reported IR data which they interpreted in terms of 5-SSA forming a bidentate surface complex involving the carboxylate group and the phenol group.

3.2 Experimental

3.2.1 Chemicals

The gibbsite particles were synthesized by the following procedure: 1 mol.dm⁻³ aluminum chloride solution was titrated with 4 mol.dm⁻³ NaOH until pH reached a value of about 4.6. Dialysis was carried out at 70 °C during four months, with initially one change of water per day. Subsequently, water was changed two to three times a week. The gibbsite was stored as a suspension at a concentration of 41.9 g.dm⁻³. The radius of the particles was determined by several methods, including AFM and field flow fractionation yielding an average width of the platelets of about 200 nm and a thickness of about 10 nm.

The suspension and solution were prepared with de-ionized water (conductivity ~ 18.2 MΩ cm). All solutions and suspensions were prepared in plastic containers. The following chemical reagents were used: NaCl (*p.a.*, Merck), HCl (0.1 mol.dm⁻³, titrival, Merck), NaOH (0.1 mol.dm⁻³, titrival, Merck), 5-sulfosalicylic acid (5-Sulfosalicylic acid.2H₂O, Sigma Aldrich), AlCl₃.6H₂O (Merck *p.a.*), standard buffers (pH = 3, 5, 7, 9 and 11).

Speciation of 5-SSA in solution results in four species. The occurrence of these species depends on pH (Fig. 8).

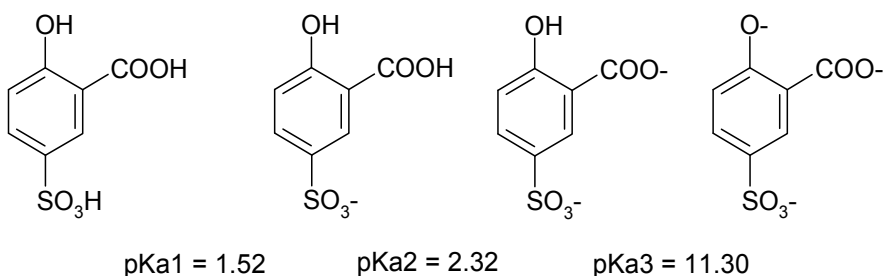


Fig. 8. Equilibrium constants for the deprotonation of 5-SSA (Panak, 1996).

In presence of aluminium ions, a number of Al(5-SSA)_x species (with x=1 to 3) can be formed. The speciation of 5-SSA and Al as a function of pH for 5×10⁻² mol.dm⁻³ of each component is plotted in Fig. 9. The relevant Al-species are shown in the upper part, indicating that Al is preferably bound to 5-SSA up to pH 8. Above pH 8, the tetra-hydroxo species of aluminium dominates the speciation under the given conditions. The lower part of Figure 9 shows the distribution of 5-SSA for the equimolar solution. 5-SSA is predominantly bound in Al-complexes up to pH 11.

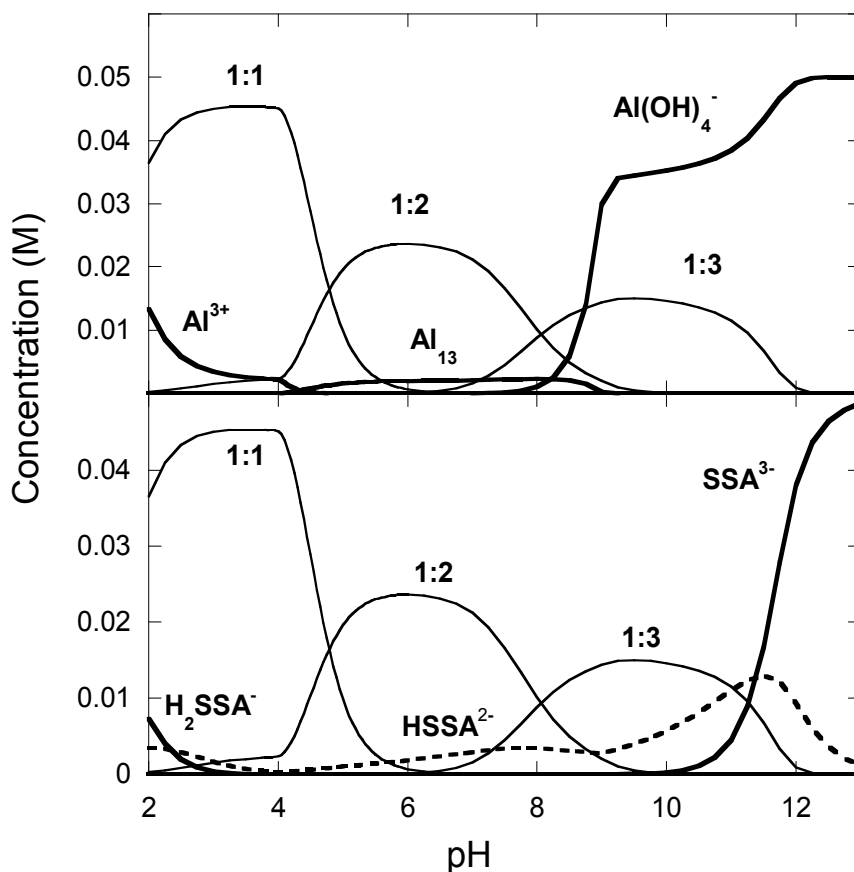


Fig. 9. Calculated speciation for an equimolar solution (5×10^{-2} M) of Al(III) (top) and 5-SSA (bottom). Uncomplexed species are in thin lines, and complex Al:5-SSA are in bold lines. Only species whose concentration are higher than 5% are represented.

3.2.2 Electrokinetics

The electrokinetic (zeta) potential of gibbsite particles was measured after adsorption of 5-SSA on gibbsite surfaces by means of a ZetaPals (Brookhaven Instruments). The mass concentration of gibbsite particles was 0.1 g.dm^{-3} and 5-SSA concentration was $10^{-3} \text{ mol.dm}^{-3}$. The experiments were performed at two different ionic strength values ($I_c = 10^{-1} \text{ mol.dm}^{-3}$ and $10^{-2} \text{ mol.dm}^{-3}$). The results are shown in Figure 10 together with zeta potential of gibbsite particles in the absence of 5-SSA (Adekola et al., 2011).

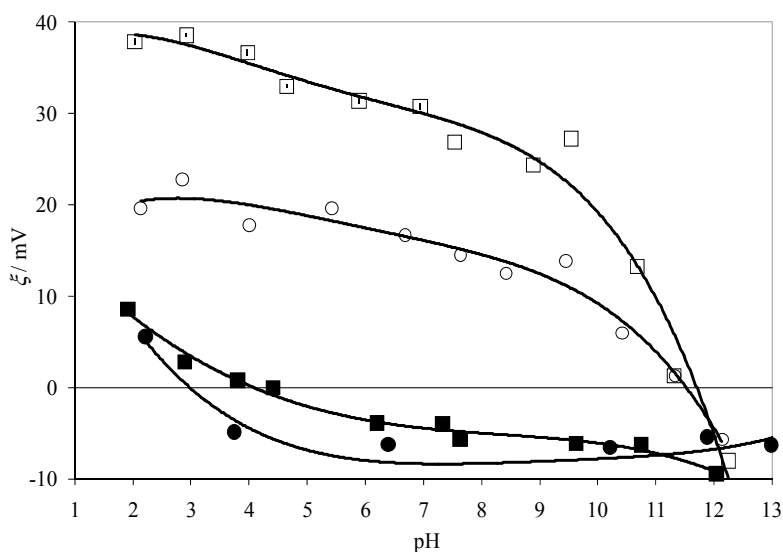


Fig. 10. Zeta-potentials of gibbsite particles in the absence (\square, \circ) and in the presence (\blacksquare, \bullet) of 5-SSA. Ionic strength was controlled by NaCl: 10^{-1} mol. dm^{-3} (circles) and 10^{-2} mol. dm^{-3} (squares). Temperature was 25 °C.

For both ionic strengths studied, the electrokinetic data show (i) a strong shift of the isoelectric point and (ii) negative zeta-potentials over a wide pH range, indicating adsorption of 5-SSA and transfer of negative charges to the gibbsite surface. The speciation diagram (Fig. 9) actually shows that the speciation of 5-SSA is dominated both in the absence and the presence of Al by negatively charged aqueous species.

3.2.3 Spectroscopy

The IR-ATR spectra of gibbsite in absence and presence of 5-SSA, as well as spectra of the aqueous solutions of the 5-SSA and 5-SSA/ Al^{3+} were obtained using a Bruker spectrometer (IFS 55). A ZnSe crystal (multibounce) was used and for each measurement 1024 scans were recorded with a resolution of 4 cm^{-1} . All measurements were made under dry argon atmosphere. The effect of pH, which has an influence on gibbsite surface charge as well on the speciation of 5-SSA in solution was examined. For spectra of the gibbsite layer in contact with solution of 5-SSA, the gibbsite layer was prepared by drying an aliquot of a suspension.

3.3 Results and discussion

3.3.1 Spectral characterization of 5-SSA in solution

Solution spectra of 5-SSA, with and without aluminium ions have been recorded by ATR-IR. For pure 5-SSA solution at pH 2, 5 and 12, the spectra are shown in Fig. 11. At pH 2, the spectrum consists in several bands which have been assigned following previous works by Varghese et al. (2007) and Jiang et al. (2002) as shown in Table 5. From pH 2 to 5, some differences can be seen: bands around 1200 cm^{-1} decrease, bands at 1270 and 1306 cm^{-1}

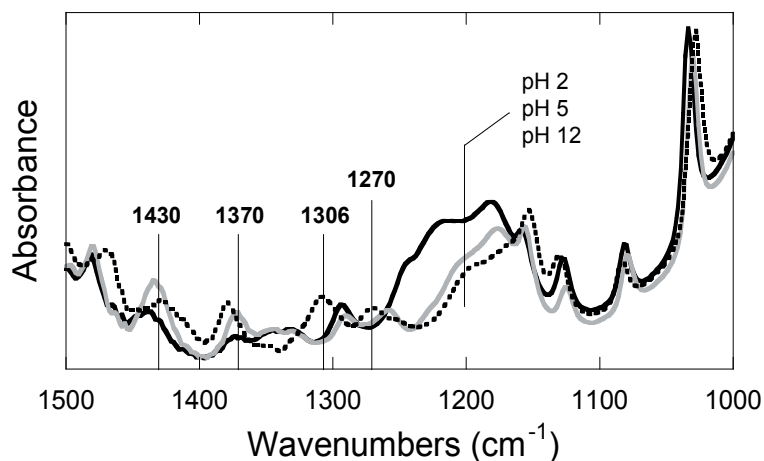


Fig. 11. Spectra of 5-SSA at pH 2 (black line), pH 5 (grey line), pH 12 (dotted line)

Assignments from literature	wavenumbers (cm ⁻¹)		
	pH 2	pH 5	pH 12
vPh *	1480	1479	1468
vPh, δ COH _c *	1439	1431	1425
v _s CO _c **	1371	1373	1379
v _{as} SO ₂ *	1346-1330	1346-1330	1306
vPh-OH **	1292	1294	1269
v _s SO ₂ *	1242sh		
	1218sh	1201sh	1198sh
vC-OH, δ SOH *	1180	1175	
δ CH *	1159	1159	1151
vC-COOH *	1082	1080	1084
vS-OH *	1034	1030	1028

* Varghese et al. (2007),

** Jiang et al. (2002), sh: shoulder, c:carboxyl

Table 5. Assignments of bands in spectra of 5-SSA in solution at different pH values.

appear, while bands at 1370 cm⁻¹, 1430 cm⁻¹ increase. Around 1200 cm⁻¹, bands corresponding to vibration of the sulfate group are expected, so this evolution would be in agreement with the change in the molecule from -SO₃H to -SO₃⁻ at pH 1.5. From pH 5 to 12, the shift of several bands is visible, the most important is 1292 cm⁻¹ to 1306 cm⁻¹. According to Jiang et al. (2002), this band corresponds to stretching of Ph-OH, which is deprotonated at pH > 11.3. Thus, the difference between these spectra would correspond to the change of speciation from pH 5, where only HSSA²⁻ is present to pH 12, dominated by 83% of SSA³⁻.

The main impact would be on the vibration band of hydroxyl group which is deprotonated, but a consequence on vibration of other groups would be possible.

3.3.2 Spectral characterization of 5-SSA in presence of aluminium ions or adsorbed onto gibbsite

Spectra of solutions of 5-SSA in the absence and presence of aluminium ions have been recorded. The results are shown as dotted and grey lines in Figure 12. The main difference is the presence of bands at 1330 and 1270 cm^{-1} at pH 2 and pH 5. At pH 12, the pure 5-SSA presents the same band too, yet a difference between the spectra is rather observed in the shift of bands at 1308, 1428, 1470 cm^{-1} to 1326, 1431, 1480 cm^{-1} respectively. Speciation calculation suggests predominance of Al-SSA at pH 2, a mixture of Al-SSA and Al-SSA₂ at pH 5 and no Al-SSA complex at pH 12.

From the study of the effect of pH on pure SSA, it was concluded that the band visible at 1270 cm^{-1} indicates the presence of Ph-O⁻, while a band at 1294 cm^{-1} which indicates the presence of Ph-OH is absent in spectra at pH 5 in presence of aluminium ion, or less intense at pH 2. At both pH values, the spectra would indicate that the presence of aluminium promotes the deprotonation of the phenol group, which leads to a bond between 5-SSA and the aluminium ion. The band corresponding to carboxyl groups at 1370 cm^{-1} is not shifted in presence of aluminium. However, a hypothetical carboxyl-Al group could perturb also the intramolecular hydrogen bond, as suggested for salicylate-iron interaction, which makes difficult to use this method to evaluate the interaction with carboxyl groups. We may conclude that the affinity of carboxyl groups for aluminium ion is well known, and an interaction is expected, despite any direct experimental evidence. At pH 12, the speciation calculation indicates the favourable formation of Al(OH)₄⁻ and the absence of any Al-SSA complexes. However, the spectra evolves in presence of aluminium ions, mainly by the shift of bands at 1425 and 1468 cm^{-1} towards values close to the spectra of pure SSA at pH 2. This result remains unexplained but suggests an interaction between both species.

As the last step, the spectra of 5-SSA in the presence of gibbsite have been recorded. The results are shown as black lines in Figure 12. In the 1500-1000 cm^{-1} range, no difference between spectra of pure 5-SSA solution and gibbsite-SSA was observed at pH 2 and 12. At pH 2, this behaviour is different from that of aluminium in solution. This might be consistent with an extent of 5-SSA adsorption that is too low to be detectable by the ATR measurements.

A comparison of the spectroscopic results to the zeta-potential measurements shown in Fig. 10 suggests the following picture. The differences in zeta potential of gibbsite particles with and without 5-SSA being present are substantial over the complete pH range investigated, except for pH 12. At pH 12, no adsorption is expected according to the electrokinetic results, but the spectra of 5-SSA in the presence of gibbsite do show a slight shift of 1425 cm^{-1} and 1468 cm^{-1} bands, similar to that observed with aluminium in solution. At pH 5, the spectra in presence of gibbsite are similar to that of 5-SSA in presence of aluminium ions, mainly due to the presence of a peak near 1270 cm^{-1} . The effect of 5-SSA on zeta potential is strong, so it can be concluded that a complex between 5-SSA and aluminium atom occurs at the gibbsite surface at pH 5, similar to what has been observed with aluminium ion. In such a geometry (Fig. 13), the negative charge observed in the electrokinetic data would be consistent with

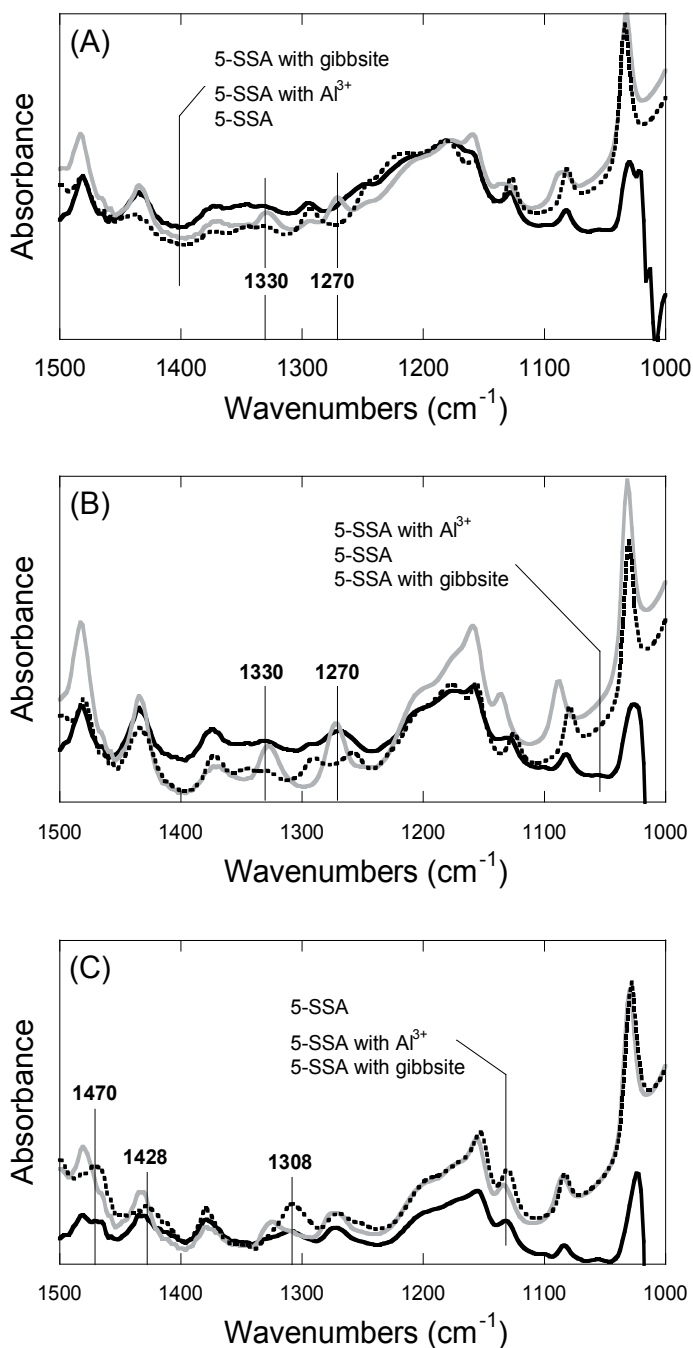


Fig. 12. Spectra of SSA at (A) pH 2, (B) pH 5, (C) pH 12, as a pure solution (dotted line), a solution in presence of aluminium ions (grey line), a solution after the deposition of a gibbsite layer (black line).

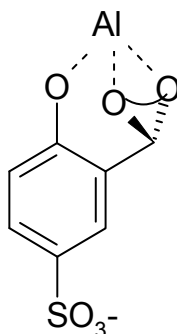


Fig. 13. Structure of the Al-SSA complex. Al is either an ion in solution, or bound to surface in surface complexes.

the free sulfonate group, deprotonated in the whole pH range. At very low pH, the zeta-potential turns positive even in the presence of 5-SSA, which can be explained by the speciation of the organic molecule itself, which would on average be less negative than at higher pH.

At pH 12, there might still be adsorption of 5-SSA, since the spectra of 5-SSA/gibbsite system is close to those of 5-SSA/Al(III). However, it would be difficult to detect by the electrokinetic method, since the gibbsite itself turns negative at $\text{pH} > 11.3$. The fact that the solution spectra of 5-SSA are different with or without Al(III) species indicates the possibility that there is some interaction. Again, the importance of spectroscopic studies in pinpointing interactions which are not detectable by macroscopic methods can be highlighted here.

4. Conclusions

In the first part of this chapter, the principles and experimental protocols of the use of ATR-IR to probe solid/solution interfaces have been described. A review of the literature has shown that ATR-IR can be useful to get information about the surface speciation of adsorbed carboxylic acids.

The second part was devoted to the comprehensive study of the adsorption of 5-SSA onto gibbsite platelets, and it was suggested that this phenomenon occurs via a dominant tridentate surface complex involving the phenolic and carboxylic groups. The ring structure of this surface complex had been previously postulated by Jiang et al. (2002) based on a limited set of spectra. The fact that the sulphate group is not involved in co-ordination to the surface, and therefore oriented towards the solution side of the interface, agrees with the negative charge of the gibbsite in the presence of 5-SSA.

The solution study strongly indicates that the present speciation schemes for the 5-SSA-dissolved aluminium system are incomplete. The spectra show differences between the absence and presence of Al(III) in solution at high pH, where within the current speciation scheme no complexes are expected. At high pH in the 5-SSA-gibbsite-system, the spectroscopic data also suggest interaction, which is undetectable by the electrokinetic method, since the gibbsite surface has an overall negative charge in that pH-range.

A general conclusion of our experimental study would be that comprehensive studies of solid-solution interfaces via ATR-IR may contribute to solving the structure of surface complexes. Furthermore, such studies may help finding previously unidentified species in solution speciation schemes. Overall the interplay of surface complexation and solution complexation in this system indicates that the adsorption process may be very complex and that multi-method approaches are best suited to gain deeper understanding.

5. References

- Adekola, F., Fédoroff, M., Geckeis, H., Kupcik, T., Lefèvre, G., Lützenkirchen, J., Plaschke, M., Preocanin, T., Rabung, T., & Schild, D. (2011). Characterization of acid-base properties of two gibbsite samples in the context of literature results, *J. Colloid Interface Sci.* Vol. 354, 306-317, 0021-9797.
- Asay, D. B. , & Kim, S.H. (2005). Evolution of the Adsorbed Water Layer Structure on Silicon Oxide at Room Temperature, *J. Phys. Chem. B* Vol. 109, 16760-16763, 1089-5647.
- Axe, K., & Persson, P. (2001). Time-dependent surface speciation of oxalate at the water-boehmite (γ -AlOOH) interface: implications for dissolution, *Geochim. Cosmochim. Acta* Vol. 65, 4481-4492, 0016-7037.
- Boily, J.-F., Persson, P., & Sjöberg, S. (2000). Benzenecarboxylate surface complexation at the goethite (α -FeOOH)/water interface: II. Linking IR spectroscopic observations to mechanistic surface complexation models for phthalate, trimellitate, and pyromellitate, *Geochim. Cosmochim. Acta* Vol. 64, No. 20, pp. 3453-3470, 0016-7037.
- Borda, M. J. , Strongin, D. R., & Schoonen, M. A. (2003). A novel vertical attenuated total reflectance photochemical flow-through reaction cell for Fourier transform infrared spectroscopy, *Spectrochim. Acta A* Vol. 59, 1103-1106, 0584-8539.
- Coates, J.P. (1993). The Industrial Applications of Infrared Internal Reflection Spectroscopy, *In: Internal Reflection Spectroscopy*, Dekker, New York, Mirabella, F. M. (Ed.), pp.53-96.
- Couzist, A., & Gulari E. (1993). Adsorption of sodium laurate from its aqueous solution onto an alumina surface. A dynamic study of the surface-surfactant interaction using attenuated total reflection Fourier transform infrared spectroscopy, *Langmuir* Vol. 9, 3414-3421, 0743-7463.
- Dean, J.A. (1999) Lange's Handbook of Chemistry (15th ed.), McGraw-Hill.
- Degenhardt, J., & McQuillan, A.J. (1999) Mechanism of oxalate ion adsorption on chromium oxide-hydroxide from pH dependance and time evolution of ATR-IR spectra, *Chem. Phys. Lett.* Vol. 31, 179-184, 0009-2614.
- Dobson, K. D., & McQuillan, A. J. (1999). In situ infrared spectroscopic analysis of the adsorption of aliphatic carboxylic acids to TiO₂, ZrO₂, Al₂O₃, and Ta₂O₅ from aqueous solutions, *Spectrochim. Acta A* Vol. 55, 1395-1405, 0584-8539.
- Dolamic, I., & Bürgi, T. (2006). Photoassisted decomposition of malonic acid on TiO₂ studied by in situ attenuated total reflection infrared spectroscopy, *J. Phys. Chem. B* Vol. 110, 14898-14904, 1089-5647.

- Duckworth, O.W. , & Martin, S.T. (2001), Surface complexation and dissolution of hematite by C₁-C₆ dicarboxylic acids at pH = 5.0, *Geochim. Cosmochim. Acta* Vol. 65, 4289-4301, 0016-7037.
- Fredriksson, A., & Holmgren, A. (2008). An in situ ATR-FTIR investigation of adsorption and orientation of heptyl xanthate at the lead sulphide/aqueous solution interface. *Miner. Engineer.* Vol. 21, 1000-1004, 0892-6875.
- Gan, Y., & Franks, G.V. (2006). Charging Behavior of the Gibbsite Basal (001) Surface in NaCl Solution Investigated by AFM Colloidal Probe Technique. *Langmuir* Vol. 22, pp. 6087-6092.
- Gao, X., & Chorover, J. (2010). Adsorption of sodium dodecyl sulfate (SDS) at ZnSe and α -Fe₂O₃ surfaces: Combining infrared spectroscopy and batch uptake studies. *J. Colloid Interface Sci.* Vol. 348, pp. 167-176, 0021-9797.
- Garcia Rodenas, L. A., Iglesias, A. M., Weisz, A. D., Morando, P. J., & Blesa, M. A. (1997). Surface complexation description of the dissolution of chromium(III) hydrous oxides by oxalic acid, *Inorg. Chem.* Vol. 36, 6423-6430, 0020-1669.
- Hwang, Y. S., Liu, J, Lenhart, J. J. , & Hadad, C. M. (2007). Surface complexes of phthalic acid at the hematite/water interface, *J. Colloid Interface Sci.* Vol. 307, 124-134, 0021-9797.
- Hug, S.J., & Sulzberger, B. (1994). In situ Fourier transform infrared spectroscopic evidence for the formation of several different surface complexes of oxalate on TiO₂ in the aqueous phase, *Langmuir* Vol. 10, pp. 3587-3597, 0743-7463.
- Hug, S. H. (1997). In situ Fourier transform infrared measurements of sulfate adsorption on hematite in aqueous solutions. *J. Colloid Interface Sci.* Vol. 188, pp. 415-422, 0021-9797.
- Jiang, L. , Gao, L. , & Liu, Y. (2002). Adsorption of salicylic acid, 5-sulfosalicylic acid and Tiron at the alumina-water interface, *Colloids Surf. A.* Vol. 211, 165-172, 0927-7757.
- Johnson, S. B. , Yoon, T. H. , Slowey, A. J. , & Brown, G. E. (2004). Adsorption of organic matter at mineral/water interfaces: 3. Implications of surface dissolution for adsorption of oxalate, *Langmuir* Vol. 20, 11480-11492, 0743-7463.
- Johnson, S. B. , Yoon, Kocar, B.D. , & Brown, G.E. (2004). Adsorption of organic matter at mineral/water interfaces. 2. outer-sphere adsorption of maleate and implications for dissolution processes, *Langmuir* Vol. 20, 4996-5006 , 0743-7463.
- Kallay, N., Preočanin, T., Kovačević, D., Lützenkirchen, J., & Villalobos, M. (2011), Thermodynamics of the Reactions at Solid/Liquid Interfaces, *Croat. Chem. Acta* Vol. 84, 1, pp. 1-10, 0011-1643.
- Klug, O., & Forsling, W. (1999). A spectroscopic study of phthalate adsorption on γ -aluminum oxide, *Langmuir* Vol. 15, 6961-6968, 0743-7463.
- Kubicki, J.D., Schroeter, L.M., Itoh, M.J., Nguyen, B.N., & Aplitz, S.E. (1999). Attenuated total reflectance Fourier-transform infrared spectroscopy of carboxylic acids adsorbed onto mineral surfaces, *Geochim. Cosmochim. Acta* Vol. 63, 2709-2725, 0016-7037.

- Kulik, D. A., Luetzenkirchen, J., & Payne, T. (2010). Consistent treatment of 'denticity' in surface complexation models. *Geochim. Cosmochim Acta* Vol. 74, 12, pp. A544-A544, 0016-7037.
- Larsson, M.L., Fredriksson, A., & Holmgren, A. (2004). Direct observation of a self-assembled monolayer of heptyl xanthate at the germanium/water interface: a polarized FTIR study. *J. Colloid Interface Sci.* Vol.273, 345-349, 0021-9797.
- Lefèvre, G., Noinville, S., & Fédoroff, M. (2006). Study of uranyl sorption onto hematite by in situ attenuated total reflection - infrared spectroscopy, *J. Colloid Interface Sci.* Vol. 296, 608-613, 0021-9797.
- Lefèvre, G., Kneppers, J., & Fédoroff, M. (2008). Sorption of uranyl ions on titanium oxide studied by ATR-IR spectroscopy, *J. Colloid Interface Sci.* 327, 15-20, 0021-9797.
- Lide, D.R. (1998). Handbook of Chemistry and Physics 79th.; Lide, D.R., Ed.; CRC Press: Boca Raton.
- Huittinen, N., Rabung, Th., Lützenkirchen, J., Mitchell, S.C., Bickmore, B.R., Lehto, J., & Geckeis, H. (2009). Sorption of Cm(III) and Gd(III) onto gibbsite, α -Al(OH)₃: A batch and TRLFS study, *J. Colloid Interface Sci.* Vol. 332, 158-164, 0021-9797.
- Lützenkirchen, J., Kupcik, T., Fuss, M., Walther, C., Sarpola, A., & Sundman, O. (2010). Adsorption of Al(13)-Keggin clusters to sapphire c-plane single crystals: Kinetic observations by streaming current measurements, *Appl. Surf. Sci.* Vol. 256, 5406-5411, 0169-4332.
- Mirabella, F.M. (1993). Principles, Theory, and Practice of Internal Reflection Spectroscopy, In: *Internal Reflection Spectroscopy*, Dekker, New York, Mirabella, F. M. (Ed.), pp.17-52.
- Nordin, J., Persson, P., Laiti, E., & Sjöberg, S. (1997). Adsorption of o-phthalate at the water-boehmite (γ -AlOOH) interface: evidence for two coordination modes, *Langmuir* Vol. 13, 4085-4093, 0743-7463.
- Panak, P. (1996). Untersuchung von intramolekularen Energietransferprozessen in Cm(III)- und Tb(III) Komplexen mit organischen Liganden mit Hilfe der zeitaufgelösten Laserfluoreszenzspektroskopie. Ph.D. Thesis, Technische Universität München, 236 p.
- Peak, D., Ford, R.G., & Sparks, D.L. (1999). An in-situ FTIR-ATR investigation of sulfate bonding mechanisms on goethite. *J. Colloid Interface Sci.* Vol. 218, pp. 289-299, 0021-9797.
- Persson, P., & Axe, K. (2005). Adsorption of oxalate and malonate at the water-goethite interface: molecular surface speciation from IR spectroscopy, *Geochim. Cosmochim. Acta* Vol. 69, No. 3, pp. 541-552, 0016-7037.
- Rosenqvist, J., Persson, P., & Sjöberg, S. (2002). Protonation and Charging of Nanosized Gibbsite (α -Al(OH)₃) Particles in Aqueous Suspension. *Langmuir* Vol. 18, pp. 4598-4604.
- Rosenqvist, J., Axe, K., Sjöberg, S., & Persson P. (2003). Adsorption of dicarboxylates on nano-sized gibbsite particles effects of ligand structure on bonding mechanisms, *Colloids Surf. A* Vol. 220, 91-104, 0927-7757.
- Rotzinger, F.P., Kesselman-Truttman, J.M., Hug, S.J., Shklover, V., & Grätzel, M. (2004). Structure and vibrational spectrum of formate and acetate adsorbed from aqueous

- solution onto the TiO₂ rutile (110) surface, *J. Phys. Chem. B* Vol. 108, 5004-5017, 1089-5647.
- Scott, K.L., Wieghardt, K., & Sykes, A.G. (1973). Mu-oxalato-cobalt(III) complexes, *Inorg. Chem.* Vol. 12, 655-663, 0020-1669.
- Tejedor -Tejedor, M.I., & Anderson, M.A. (1986). "In situ" attenuated total reflection Fourier transform infrared studies at the goethite (α-FeOOH)-aqueous solution interface. *Langmuir* Vol. 2, pp. 203-210, 0743-7463.
- Tejedor -Tejedor, M.I., & Anderson, M.A. (1990). Protonation of phosphate on the surface of goethite as studied by CIR-FTIR and electrophoretic mobility. *Langmuir* Vol. 6, pp. 602-611, 0743-7463.
- Tejedor-Tejedor, M.I., Yost, E.C., & Anderson, M.A. (1990), Characterization of benzoic and phenolic complexes at the goethite/aqueous solution interface using cylindrical internal reflection Fourier transform infrared spectroscopy. Part 1. Methodology. *Langmuir* Vol. 6, 979-987, 0743-7463.
- Tickanan, L.D., Tejedor-Tejedor, M.I., & Anderson, M.A. (1991). Quantitative characterization of aqueous suspensions using attenuated total reflection Fourier transform infrared spectroscopy: influence of internal reflection element-particle interactions on spectral absorbance values. *Langmuir* Vol. 7, pp. 451-456, 0743-7463.
- Tunesi, S., & Anderson, M.A. (1992). Surface effects in photochemistry: an in situ cylindrical internal reflection-Fourier transform infrared investigation of the effect of ring substituents on chemisorption onto TiO₂ ceramic membranes, *Langmuir* Vol. 8, 487-495, 0743-7463.
- Varghese, H.T., Panicker, C. Y., & Philip, D. (2007). IR, Raman and SERS spectra of 5-sulphosalicylic acid dihydrate, *J. Raman Spectr.* Vol. 38, 309-315, 1097-4555.
- Venyaminov, S.Y., & Prendergast, F.G. (1997). Water (H₂O and D₂O) molar absorptivity in the 1000–4000 cm⁻¹ range and quantitative infrared spectroscopy of aqueous solutions. *Anal. Biochem.* Vol. 248, 234-245, 0003-2697.
- Villalobos, M., & Leckie, J. O. (2001). Surface complexation modeling and FTIR study of carbonate adsorption to goethite. *J. Colloid Interface Sci.* Vol. 235, pp. 15-32, 0021-9797.
- Wang, Z., Grahn, M., Larsson, M.L., Holmgren, A., Sterte, J., & Hedlund, J. (2006). Zeolite coated ATR crystal probes, *Sensors Actuators B.* Vol. 115, 685-690, 0925-4005.
- Weisz, A.D., Regazzoni, A.E., & Blesa, M.A. (2001). ATR-FTIR study of the stability trends of carboxylate complexes formed on the surface of titanium dioxide particles immersed in water, *Solid State Ionics* Vol. 143, 125-130, 0167-2738.
- Weisz, A.D., Garcia Rodenas, L., Morando, P.J., Regazzoni, A.E., & Blesa, M.A. (2002). FTIR study of the adsorption of single pollutants and mixtures of pollutants onto titanium dioxide in water: oxalic and salicylic acids, *Catal. Today* Vol. 76, 103-112, 0920-5861.
- Yoon, T. H., Johnson, S. B., Musgrave, C. B., & Brown, G. E (2004). Adsorption of organic matter at mineral/water interfaces: I. ATR-FTIR spectroscopic and quantum chemical study of oxalate adsorbed at boehmite/water and corundum/water interfaces, *Geochim. Cosmochim. Acta* Vol. 68, No. 22, pp. 4505-4518, 0016-7037.

Yost, E.C., Tejedor-Tejedor, M.I., & Anderson, M.A. (1990). In situ CIR-FTIR characterization of salicylate complexes at the goethite/aqueous solution interface, *Environ. Sci. Technol.* Vol. 24, pp. 822-828, 0013-936X.

Research of Calcium Phosphates Using Fourier Transform Infrared Spectroscopy

Līga Berzina-Cimdina and Natalija Borodajenko

*Riga Technical University,
Institute of General Chemical Engineering
Latvia*

1. Introduction

In the biomaterial research field, nowadays a great attention is driven onto calcium phosphates synthesis and obtaining of ceramics that can be used in orthopedics and dentistry, in the form of coatings, granules, porous or solid blocks, as well as in the form of various composite materials. The most frequently studied, clinically tested and used synthetic materials based on calcium phosphate (CaP) are hydroxyapatite [HAp - $\text{Ca}_{10}(\text{PO}_4)_6(\text{OH})_2$], β -tricalcium phosphate [β -TCP - $\text{Ca}_3(\text{PO}_4)_2$] and biphasic HAp/ β -TCP mixture. CaP ceramic demonstrates high biocompatibility and bioactivity while it contacts bone cells, builds a direct chemical connection between bone tissues and ceramic implant. As practice shows, purchased materials, most often commercial CaP materials, not always have properties and qualities defined by the manufacturer. Frequently, the manufacturer's information about the offered product is not complete or precise, by it troubling usage of raw CaP material for development of implants. The most common imperfections of CaP materials are - unpredictable properties after the high temperature treatment (composition and clarity of crystal phases, chemical composition, thermal stability, etc.) which become clear only after the high temperature treatment of the ready implant material has occurred. For several years, Riga Biomaterial Innovation and Development Centre (RBIDC) of Riga Technical University perform a wide range of property studies of various commercial CaP raw materials.

Properties of bioceramic implants obtained from various commercial and laboratory synthesized calcium phosphate precursors are different, since behavior of those precursors is different within the thermal treatment processes, which are a significant stage of obtaining ceramics.

CaP synthesis methods and their technological parameters can significantly impact stoichiometry of the synthesis product, its grade of crystallization, particle size, bioceramic phase composition, thermal stability, microstructure and mechanical properties. The important technologic parameters that impact properties of calcium phosphate synthesis product and then also of bioceramic, are temperature of synthesis, pH of synthesis environment, reagent type and concentration, as well as selection of raw materials, their purity and quality. All of the above mentioned also brings a significant impact on the tissue response of these bioceramic implants.

Fourier transform infrared spectroscopy (FTIR) is one of the methods which, systematically monitoring variations of structural characteristic groups and vibrations bonds, can provide an indirect evaluation of the synthesized Ca/P implant materials from TCP up to HAp and bioceramics, obtained from these materials.

FTIR spectroscopy has numerous advantages when used for chemical analysis of CaP products. First of all, an obtained spectrogram provides useful information about location of peaks, their intensity, width and shape in the required wave number range. Secondly, FTIR is also a very sensitive technique for determining phase composition. In the third place, FTIR is a comparatively quick and easy everyday approach.

During recent years, many authors' attention is turned onto synthesis of CaP and research of structure of the synthesized products depending on their technological parameters, with various methods, including an X-ray diffraction (XRD) and FTIR methods. However, the data of the literary sources is often incomplete or sometimes even contradictory. Studying various literary sources and analyzing the taken spectra of laboratory synthesized and commercial CaP products was aimed onto creating summary IR spectrum tables for the characteristic calcium phosphate chemical groups absorption bands. HAp stoichiometry is very important if the material has undergone a high temperature treatment.

A minor misbalance of synthesis product in a stoichiometric ratio (standard molar ratio of Ca/P is 1.67) during high temperature treatment can lead to composition of β -, α -TCP, or other phases. Thermally treating the stoichiometric calcium phosphates, it is possible to obtain stable phases at temperatures up to 1300 °C. One of the main non-stoichiometry reasons is inclusion of impurities, often substitutions of Ca^{2+} or interpenetration of other ions in the crystal lattice. In total, biological calcium phosphates are defined as calcium hydroxyapatites with deficient of calcium, $\text{Ca}_{10-x}(\text{PO}_4)_{6-x}(\text{HPO}_4)_x(\text{OH})_{2-x}$ ($0 < x < 2$), including the substituting atoms or groups, as, for example, Mg^{2+} , Na^+ , K^+ , Sr^{2+} , or Ba^{2+} substitute Ca^{2+} , CO_3^{2-} , H_2PO_4^- , HPO_4^{2-} ; SO_4^{2-} substitute PO_4^{3-} ; F^- , Cl^- , CO_3^{2-} , PO_4^{3-} substitute OH^- .

The main target of our work was to perform a FTIR spectroscopy analysis of the CaP products synthesized in RBIDC laboratory and make summarizing conclusions about chemical groups of calcium phosphates, their variations under impact of synthesis parameters and further thermal treatment, as well as creating summary tables for:

- CaP powders synthesized in the laboratory with a chemical solution precipitation method with different synthesis parameters (temperature, final suspension pH, maturation time) as-synthesized and then thermally treated at various temperatures from 200°C up to 1400°C;
- Commercial CaP products;
- CaO containing materials of various origins (marble, eggshells, land snail shells) and FTIR spectra of obtained products;

2. Calcium phosphates and FTIR absorption bands of their chemical groups

2.1 Calcium phosphates

Calcium phosphates as chemical compounds arise interest of the numerous fields of science, like geology, chemistry, biology and medicine. Many forms of calcium phosphates are

determined by their Ca/P molar ratio. From the point of view of chemistry, they are formed by three main elements: calcium, phosphorus and oxygen. Many calcium phosphates also contain hydrogen in an acidic phosphate anion (for example, HPO_4^{2-}), hydroxyl groups (for example, $\text{Ca}_{10}(\text{PO}_4)_6(\text{OH})_2$) or in a form of bonded water (for example, $\text{CaHPO}_4 \cdot 2\text{H}_2\text{O}$). Majority of compounds of this class are poorly soluble in the water and non-soluble in alkaline solutions, but all of them easily dissolve in acids. Chemically pure calcium orthophosphates are white crystals with an average hardness, while natural materials are always of some other color which depends on the type and amount of impurities. Biologic calcium phosphates are main mineral components in the calcified tissues of the vertebrates (Dorozhkin, 2009a).

Main components of the natural bone tissues are calcium phosphates which, along with the other elements (Na, K, F, and Cl) form ~ 70% of the bone tissue mass. Also, bone tissues contain water (10% of mass) and collagen along with the other organic materials in small amounts. In living system CaP are found in the form of crystalline hydroxyapatite (HAp) and in the amorphous calcium phosphate (ACP) form.

As bone substitution materials, calcium orthophosphates are researched for more than 80 years. The most significant characteristics of calcium phosphates are their bioresorption and bioactivity. They are non-toxic and biocompatible. Bioactivity shows as an ability to create a physical chemical bond between an implant and a bone. This process is called osteointegration (Dorozhkin, 2009b).

Depending on the calcium/phosphorus (Ca/P) molar ratio and solubility of the compound, it is possible to obtain numerous calcium phosphates of different composition. Molar Ca/P ratio and solubility are connected with the pH of the solution. Majority of materials of this class are resorbable and dissolve when inserted in a physical environment. Calcium phosphates that are most frequently used in the biomaterial field are demonstrated in Table 1 (Dorozhkin, 2009c; El Kady, 2009; Shi, 2006).

For biomedical application, the following calcium phosphates are most frequently used: HAp (Ca/P = 1.67) and β -TCP (Ca/P=1.5), as well as biphasic calcium phosphate which mainly consists of HAp and β -TCP mixture in various ratios.

2.2 FTIR absorption bands of the synthesized HAp

Hydroxyapatite $\text{Ca}_{10}(\text{PO}_4)_6(\text{OH})_2$ is dominating and the most significant mineral phase in the solid tissues of the vertebrates. It consists of the same ions that form mineral part of teeth and bones.

A biological HAp usually has a calcium deficient; it is always substituted with a carbonate. Two types of carbonate substitution are possible: (1) direct substitution of OH^- with CO_3^{2-} (A-type substitution ($\text{CO}_3^{2-} \leftrightarrow 2\text{OH}^-$)) and (2) necessity after charge compensation, PO_4^{3-} substituting a tetrahedral group with CO_3^{2-} (B-type substitution). Substitution groups may provoke characteristic changes in the lattice parameters, crystallinity, crystal symmetry, thermal stability, morphology, and solubility, physical, chemical and biological characteristics (Shi, 2006).

The most characteristic chemical groups in the FTIR spectrum of synthesized HAp are PO_4^{3-} , OH^- , CO_3^{2-} , as well as HPO_4^{2-} that characterize non-stoichiometric HAp.

Name	Abbreviation	Chemical formula	Ca/P
Amorphous calcium phosphate	ACP	$\text{Ca}_x\text{H}_y(\text{PO}_4)_z \cdot n\text{H}_2\text{O}$	1.2-2.2
Dicalcium phosphate anhydride	DCPA	CaHPO_4	1.00
Dicalcium phosphate dehydrate	DCPD	$\text{CaHPO}_4 \cdot 2\text{H}_2\text{O}$	1.00
Octacalcium phosphate	OCP	$\text{Ca}_8(\text{HPO}_4)_2(\text{PO}_4)_4 \cdot 5\text{H}_2\text{O}$	1.33
β -tricalcium phosphate	β -TCP	$\text{Ca}_3(\text{PO}_4)_2$	1.50
α -tricalcium phosphate	α -TCP	$\text{Ca}_3(\text{PO}_4)_2$	1.50
Hydroxyapatite with calcium deficient	CDHA	$\text{Ca}_{10-x}(\text{HPO}_4)_x(\text{PO}_4)_{6-x}(\text{OH})_{2-x}$ $0 \leq x \leq 1$	1.5-1.67
Hydroxyapatite	HAp	$\text{Ca}_{10}(\text{PO}_4)_6(\text{OH})_2$	1.67
Tetra calcium phosphate	TTCP (TetCP)	$\text{Ca}_4(\text{PO}_4)_2\text{O}$	2.00
β -Ca pyrophosphate	CPP	$\text{Ca}_2\text{P}_2\text{O}_7$	<1.5
Oxyapatite	OAp	$\text{Ca}_{10}(\text{PO}_4)_6\text{O}$	1.67

Table 1. Calcium phosphates used in the biomaterial field.

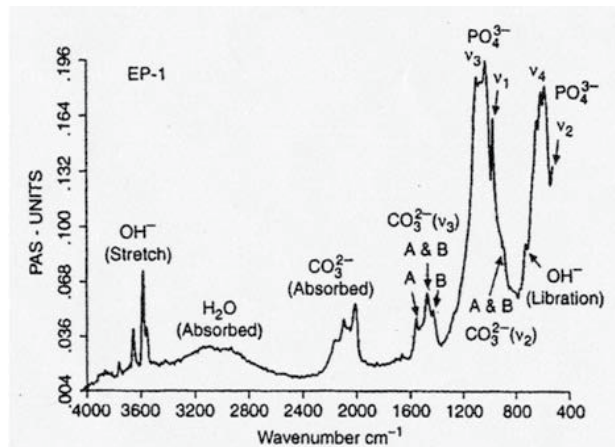


Fig. 1. A typical FTIR spectrum of hydroxyapatite (Ratner, 2004)

PO_4^{3-} group forms intensive IR absorption bands at 560 and 600 cm^{-1} and at 1000 – 1100 cm^{-1} . Adsorbed water band is relatively wide, from 3600 to 2600 cm^{-1} , with an explicit peak at 3570 cm^{-1} , a weaker peak is formed at 630 cm^{-1} . CO_3^{2-} group forms weak peaks between 870 and 880 cm^{-1} and more intensive peaks between 1460 and 1530 cm^{-1} . Absorption bands of chemical bonds of the synthesized HAp spectrum are summarized in Table 2.

Chemical groups	Absorption bands, (cm ⁻¹)	Description
CO ₃ ²⁻	873; 1450; 1640 (Meejoo, et al., 2006) 1650 (Raynaud, et al., 2002); 870 and 880; 1460 and 1530 (Ratner, 2004)	Substitutes phosphate ion, B-type HAp is formed (Meejoo, et al., 2006)
OH ⁻	3500 (Meejoo, et al., 2006) 630 and 3540 (Destainville, et al., 2003), (Raynaud, et al., 2002); 3570 and 3420 (Han J-K., et al., 2006); 1650 (Raynaud, et al., 2002)	OH ⁻ ions prove presence of HAp
Adsorbed water	2600 - 3600 (Meejoo, et al., 2006)	Under influence of thermal treatment, absorption band becomes narrower
HPO ₄ ²⁻	875 (Destainville, et al., 2003), (Raynaud, et al., 2002); 880 (Kwon, et al., 2003)	Characterizes HAp with deficient of calcium. (Raynaud, et al., 2002); Refers to non-stoichiometric HAp (Kwon, et al., 2003);
PO ₄ ³⁻	460 (Destainville, et al., 2003); (Raynaud, et al., 2002);	v2 (Destainville, et al., 2003);
	560 - 600 (Destainville, et al., 2003), (Raynaud, et al., 2002), (Mobasherpour & Heshajin, 2007); 602 un 555 (Han J-K., et al., 2006)	v4 (Destainville, et al., 2003); bending mode (Han J-K., et al., 2006)
	960 (Destainville, et al., 2003), (Raynaud, et al., 2002)	v1 (Destainville, et al., 2003);
	1020 -1120 (Destainville, et al., 2003), (Raynaud, et al., 2002); 1040 (Han J-K., et al., 2006); 1000 - 1100 (Mobasherpour & Heshajin, 2007);	v3 (Destainville, et al., 2003); bending mode (Han J-K., et al., 2006);
NO ₃ ⁻	820 and 1380 (Destainville, et al., 2003); (Raynaud, et al., 2002)	Synthesis residue that disappears during the calcifying process (Destainville, et al., 2003)

Table 2. FTIR absorption bands of synthesized HAp chemical groups.

2.3 FTIR absorption bands of thermally treated calcium phosphates

As a biomaterial, HAp is mainly used in its ceramic form that was obtained by sintering the powder at 1000 - 1350 °C or as a coating on the implant surface. During the process of thermal decomposition of HAp, sintering of ceramic or obtaining the coating, physical, chemical, mechanical and, most important, biomedical properties may be negatively affected. Thus, HAp and other CaP materials should be thoroughly studied while thermally treated.

Temperature, °C	Chemical groups and phases	Absorption bands, (cm ⁻¹)	Description
250	H ₂ O		Molecules of adsorbed water disappear (Mobasherpour & Heshajin, 2007);
600	NO ₃ ⁻	820 and 1380 (Raynaud, et al., 2002)	Synthesis impurities disappear (Raynaud, et al., 2002);
700	CO ₃ ²⁻	1450 (Meejoo, et al., 2006)	Intensity decreases;
	H ₂ O, OH ⁻	3500 (Meejoo, et al., 2006) 630 and 3540 (Destainville, et al., 2003);	Adsorbed water band becomes narrower (Meejoo, et al., 2006); Refers to variations of OH ⁻ (Destainville, et al., 2003);
800	CO ₃ ²⁻	1450 (Meejoo, et al., 2006)	Disappears (Meejoo, et al., 2006)
900	OH ⁻		Disappears (Meejoo, et al., 2006)
	β- TCP	947, 974 and 1120(Meejoo, et al., 2006)	β-TCP shoulders begin to show up (Meejoo, et al., 2006);
	PO ₄ ³⁻	603 and 565; 1094 and 1032 (Meejoo, et al., 2006)	Shifts position at 1200 °C (Meejoo, et al., 2006);
1200	β- TCP		Can see the characteristic peaks better (Ratner, 2004);
	PO ₄ ³⁻	601 and 571; 1090 and 1046 (Meejoo, et al., 2006)	Indicates that under influence of temperature, phosphates decompose and β-TCP shoulders become wider (Meejoo, et al., 2006).
1200 - 1400			β- TCP transforms onto α-TCP (Mobasherpour & Heshajin, 2007);
1400	α-TCP	551; 585; 597; 613; 984; 1025; 1055 (Han J-K., et al., 2006)	

Table 3. FTIR absorption bands of thermally treated CaP chemical bonds.

During the thermal treatment, behavior of CaP is affected by various factors, like, atmosphere of sintering, ratio of Ca/P, method and conditions of powder synthesis, type and amount of impurities, sample size, particle size, etc.

During thermal treating HAp undergoes the following processes:

- dehydration (separation of adsorbed water);
- dehydroxylation (separation of structured water), forming oxy-hydroxyapatite (OHAp) and oxyapatite (OAp);
- HAp decomposition with formation of other phases.

In Tables 3-5, the data obtained from literary sources about the FTIR absorption bands of thermally treated CaP chemical groups, is summarized.

Temperature, °C	Chemical groups and phases	Absorption bands, (cm ⁻¹)	Description
650	TCP;		Synthesis residue is taken away, but the initial TCP remains unchanged (Destainville, et al., 2003);
750	TCP → β-TCP (Destainville, et al., 2003);		Agglutination begins (Destainville, et al., 2003);
950 - 1000			Maximum speed of compaction, comparing with HAp, β-TCP sintering occurs at a lower temperature. (Destainville, et al., 2003);
	OH ⁻	630 (Destainville, et al., 2003);	Disappeared; spectrum is similar β-TCP (Kwon, et al., 2003)
	P ₂ O ₇ ⁴⁻	727 and 1200 (Destainville, et al., 2003)	Lack of P ₂ O ₇ ⁴⁻ proves that there is no CPP phase and spectrum is similar to pure β-TCP (Destainville, et al., 2003);
1200	β-TCP → αTCP		(Destainville, et al., 2003);

Table 4. FTIR absorption bands of thermally treated TCP chemical groups.

Losing the adsorbed water do not impact lattice parameters. The water adsorbed on the surface discharges under temperature of less than 250°C, when the moisture is discharged from pores up to 500°C. With temperature rising, wide water bands at 3540 cm⁻¹ become narrower and gradually disappear, but the sharp narrow peaks at 630 and 3570 cm⁻¹ refer to variations of structural OH⁻ groups, which is characteristic to structure of HAp. Depending on the synthesis condition, a carbonate containing apatite is often obtained. Then, it should be considered that CO₂ is discharged from the sample between 450-950°C.

Thermal stability is characterized by the decomposition temperature of HAp sample. The decomposition occurs when a critical dehydration point is achieved. In the temperatures less than the critical point, crystal structure of HAp remains unchanged in spite of the stage of dehydration. Achieving the critical point, a complete and irreversible dehydroxillation occurs, which results damage of HAp structure, decomposing onto tricalcium phosphate (β-TCP under 1200 °C and α-TCP in higher temperatures) and tetracalcium phosphate (TTCP).

At 900°C, β-TCP shoulders begin to show up at 947, 974 and 1120 cm⁻¹, but during heating at higher temperature as, for example, 1200°C, β-TCP phase becomes more visible and PO₄³⁻ peaks shift from 603 and 565 cm⁻¹ to 601 and 571 cm⁻¹, also from 1094 and 1032 to 1090 and 1046 cm⁻¹.

Temperature, °C	Chemical groups	Absorption bands, (cm ⁻¹)	Description
350	HPO ₄ ²⁻		Begins showing up (Raynaud, et al., 2002);
350-720	HPO ₄ ²⁻	875 (Raynaud, et al., 2002);	As a result of condensation, P ₂ O ₇ is formed (Raynaud, et al., 2002);
400	P ₂ O ₇ ⁴⁻	720 (Raynaud, et al., 2002);	Begins showing up if 1.5 < Ca/P < 1.677 (Raynaud, et al., 2002);
600	NO ₃ ⁻	820 and 1380 (Raynaud, et al., 2002);	Disappears (Raynaud, et al., 2002)
750	OH ⁻	630 and 3540 (Destainville, et al., 2003);	Proves presence of HAp (Destainville, et al., 2003);
800	P ₂ O ₇ ⁴⁻	715 (Meejoo, et al., 2006);	Forming of pyrophosphate groups (Meejoo, et al., 2006);
700-900			HAp with deficient of calcium, by decomposing, forms HAp and β-TCP (Raynaud, et al., 2002);
1000	P ₂ O ₇ ⁴⁻	720 (Raynaud, et al., 2002);	Disappears above 1000 °C, if 1.5 < Ca/P < 1.677 (Raynaud, et al., 2002);

Table 5. Analysis of FTIR absorption bands of thermally treated biphasic calcium phosphate (HAp/β-TCP) chemical groups

For stoichiometric HAp, HPO₄²⁻ group is not detected, even though it can appear from the synthesis impurities (NO₃⁻, NH₄⁺).

Various studies show that in the result of HAp (OAp) decomposition, apart from TCP and TTCP, also other calcium compounds may form, like calcium pyrophosphate (CPP, β-Ca₂P₂O₇) and calcium oxide (CaO).

Apatitic TCP (ap-TCP) Ca₉(HPO₄)(PO₄)₅(OH) is a calcium orthophosphate which, during thermal treatment at temperature higher than 750°C, transforms onto β-tricalcium phosphate Ca₃(PO₄)₂.

During the synthesis of TCP, the most important controllable parameters are temperature and pH. According to the literary sources, pH is almost neutral or slightly acidic, and is synthesized at lower temperatures.

A pure stoichiometric β-TCP with a molar ratio Ca/P=1.500, is formed in the result of temperature treatment. If Ca/P > 1.500, HAp is formed as the second phase. When Ca/P ratio is changed for 1%, HAp is formed for 10 wt%. If Ca/P < 1.500, then DCPA is formed, this is proven by presence of calcium pyrophosphate Ca₂P₂O₇.

In order to control speed of biodegradation, a biphasic calcium phosphate (BCP) bioceramic is developed, containing both HAp and TCP. By variation HAp/TCP ratio, it is possible to control bioactivity and biodegradation of implant. Since β -TCP is more soluble and HAp allows a biological precipitation of apatites, solubility of BCP depends on the ratio of HAp/TCP. Osteoconductivity among BCP, HAp and TCP does not significantly differ.

BCP is formed, if $1.500 < \text{Ca/P} < 1.667$, which refers to a hydroxyapatite with calcium deficient, its chemical formula is $\text{Ca}_{10-x}(\text{PO}_4)_{6-x}(\text{HPO}_4)_x(\text{OH})_{2-x}$ ($0 < x < 2$). Ca/P ratio of synthesis sedimentary is not directly connected with the initial Ca/P ratio. At the constant pH, molar ratio of calcium phosphates may be varied by changing the temperature during the synthesis process.

3. Materials and methods

3.1 Synthesis of calcium phosphates

In order to achieve higher assay of the obtained material, its thermal stability and predictability of other properties, the calcium phosphates were synthesized in a laboratory using a wet chemical precipitation method from CaO (or calcium hydroxide $\text{Ca}(\text{OH})_2$) of various origins (commercial, marble, eggshells, land snails shells) as precursors and orthophosphoric acid H_3PO_4 .

Main advantages of this method are a simple synthesis process, a relatively quick obtaining of end product, possibility to obtain large quantities of end product, relatively cheap raw materials and the only by-product it gives is water. It is also important that calcium phosphates with nanometric crystal size can be obtained at a low process temperature (from room to water boiling temperature).

During synthesis, technological parameters like final pH of calcium phosphate suspension and synthesis temperature ($T, ^\circ\text{C}$) were changed. Final suspension pH was stabilized in the range of 5-11, using solution of acid. Synthesis temperature was changed in the range from room temperature (21°C) up to 70°C , the following parameters were controlled: acid solution adding speed (ml/min), stirring speed (rpm), synthesis temperature ($T, ^\circ\text{C}$), final suspension pH, stabilization time (h), maturity time (τ , h), drying temperature and time ($T, ^\circ\text{C}$; h), calcifying temperature and time ($T, ^\circ\text{C}$; h).

For further obtaining HAp or biphasic bioceramic synthesized under impact of various parameters (final pH and synthesis temperature), powder is thermally treated. Samples are heated in different environments (air, vacuum and water vapor), varying thermal treatment temperature in range $200\text{-}1400^\circ\text{C}$ and processing time.

3.2 Analysis methods and sample preparation

In order to determine raw materials, structure of synthesized and heated powder, phase composition and functional groups, two important methods are used, complementing each other: Fourier transform infrared spectroscopy (FTIR) and X-ray diffractometry (XRD). XRD method is widely used for apatite characterization, for it provides data about the crystal structure of material and its phase composition, however, it is not convenient to determine

amount of [OH] or [CO₃] groups in hydroxyapatite. FTIR method, in many cases is more sensitive than XRD when determining presence of new phases. Using FTIR, CaP can be characterized, considering three spectrum parameters:

- Location of absorption maximum indicates material composition, even slight variations of the composition influence energy of material bondings and, as follows, frequency of variations;
- Peak width shows degree of the atoms' order in the apatite elementary cell.
- Considering the absorption maximum of [OH] vibrations, presence of HAp and its thermal stability can be determined, as well as hydroxyl group concentration in the sample.

During the research process, *X'Pert PRO* X-ray diffractometer has been used (*PANalitical*, the Netherlands). Samples were measured in a spinning mode, in the 2θ angle range from 20-90°, with a scanning step 0,0334°, with a CuK α radiation. Ratio of HAp/TCP is determined using a XRD semi-quantitative method after calibration line.

Calcium phosphate spectra are measured and analyzed with a FTIR spectrometer „*Varian 800*” of Scimitar Series, with a wave length range from 400 - 4000 cm⁻¹, with precision of 4 cm⁻¹ and RESOLUTION software.

Samples are prepared by mixing powder with KBr and pressing the pellet. This method of sample preparation has some complications and requires a certain experience, in order to obtain a good quality spectrum in everyday work routine. Special factors should be considered in order to perform invariable sample analysis by using a KBr method, and these include pellet thickness, particle dispersion, ensuring vacuum state during the pressing, pressure influence, ion exchange, etc.

In a prepared KBr pellet, there should be material concentration of 2-10% from the total weight. For preparing a 300g KBr pellet, from 1 to 5mg of the sample is required, and the pellet size will be 13 mm.

Powder grain size should be ~150 μ m. The analyzed sample is crashed in a powder and thoroughly mixed with the KBr powder. A powder mixer „*Pulverisette 23*” was used for crashing and mixing of the powder. Prepared powder was located in a specific SPECAC (d = 13 mm) mould, and the required pressure was achieved by applying a uniaxial press (required pressure is ~5·10³ kg/cm², pressing time 1 min).

KBr attracts water molecules from the environment and they create wide water bands in the spectrum, so they are hard to or even impossible to analyze. KBr powder should be of the highest assay, Riedel-de-Haen KBr (Lot 51520) brand was used with an assay in the range of 99.5-100.5%. Usually, absorption bands of the main impurities in the KBr are: OH⁻ groups and H₂O molecules (3500 cm⁻¹ and 1630 cm⁻¹), NO₂ (1390 cm⁻¹), SO₄²⁻ (1160-1140 cm⁻¹). Spectrum of the KBr used in our research is demonstrated on the Fig. 2. Considering that the powder is hygroscopic, KBr powder is dried at 105°C and kept in special hermetic containers. Prepared pellets with the analyzed material are dried once again for 24 h. The obtained pellets should be transparent and equally colored. Weak bands connected with water can also be compensated by using a KBr pellet of the same thickness, but not containing the analyzed material, for background spectrum measuring.

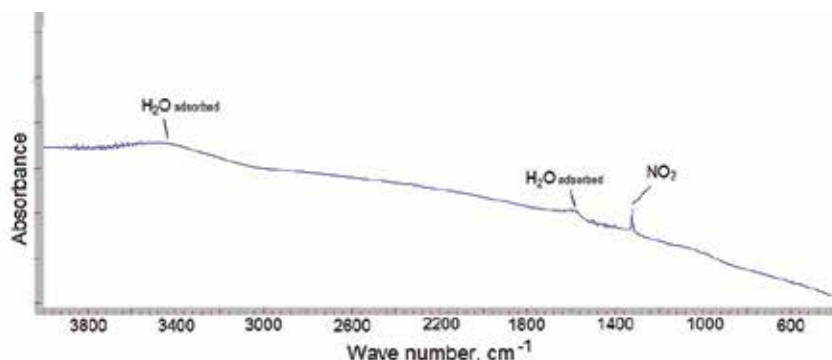


Fig. 2. FTIR spectrum of the KBr pellet

4. Results and discussion

4.1 Commercial HAp products description

While preparing bioceramic samples from various commercial materials available on the market, we have come across hardly predictable properties of the end product, like crystallinity degree, phase composition and, following, bioactivity and mechanical characteristics. One of the disadvantages while purchasing commercial calcium phosphate powders or commercial calcium phosphate ceramic materials is insufficient information about synthesis conditions of these calcium phosphates, raw materials and in which proportions these materials are taken.

It is significant to know if the purchased powder is thermally treated, and in which temperature range this thermal treatment was performed. Exactly temperature, at which the sample was obtained and processed, is one of the conditions that influences outcome of ceramic and phase composition.

For example, in spectra of several overviewed commercial hydroxyapatites, OH⁻ and PO₄³⁻ groups are observed, but band shape, width and intensity are different. Differences in spectra are also observed at CO₃²⁻ and HPO₄²⁻ groups location and intensity. On Fig. 3, there are three spectra from different commercial HAp compared: „Fluka” (F), „Riedel-de Haën®”

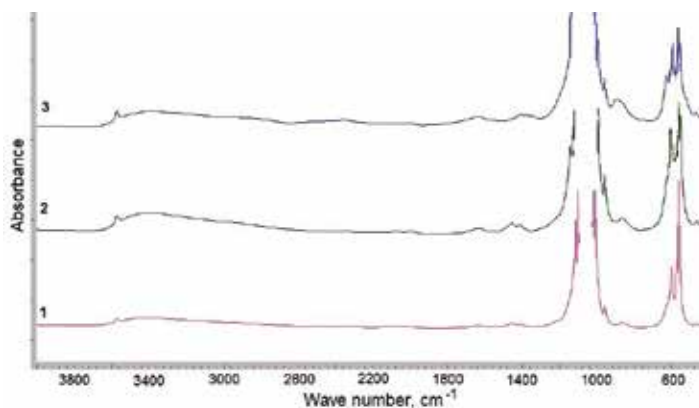


Fig. 3. FTIR spectra of commercial HAp products (1 - S-A; 2 - R-dH; 3 - Fluka)

(R-dH) and „Sigma Aldrich” (S-A). IR spectrum of commercial S-A product has a lower CO_3^{2-} and HPO_4^{2-} intensity that could mean a higher assay degree than the other materials have. These spectra also demonstrate that the products have a low crystallinity degree and they were not thermally treated.

Characteristic chemical groups of the commercial synthesized products are summarized in table 6.

Commercial HAp	Fluka	R-dH	S-A
Chemical groups	Absorption bands, cm^{-1}		
CO_3^{2-}	1386; 1411; 1635; 1997; (2359 $\text{C}\equiv\text{C}$)	1382; 1413; 1457; 1634; 1997	1382; 1417; 2457; 1639; 1990; 2359
H_2O adsorbed	3100 - 3600	3000 -3600	3200 - 3600
OH^-	635; 3568	3568	630; 3569;
HPO_4^{2-} ; CO_3^{2-}	891; 875	870	874
PO_4^{3-}	470; 553 - 600; 964; 1000 - 1156	470; 553 - 610; 964; 1000 - 1150	471; 561; 601; 605; 964; 1013 - 1120

Table 6. Characteristic chemical groups of commercial HAp FTIR absorption bands

In the FTIR spectra of commercial β -TCP products, PO_4^{3-} groups are observed, which is characteristic to β -TCP (Fig. 4). In HAp IR spectrum, OH^- group peaks are observed (at 630 and 3570 cm^{-1}), but there are no such in the IR spectrum of commercial β -TCP, which means that there is no HAp phase in this β -TCP product. In addition, at 725 cm^{-1} , presence of $\text{P}_2\text{O}_7^{4-}$ group can be observed, which is characteristic to calcium pyrophosphate phase.

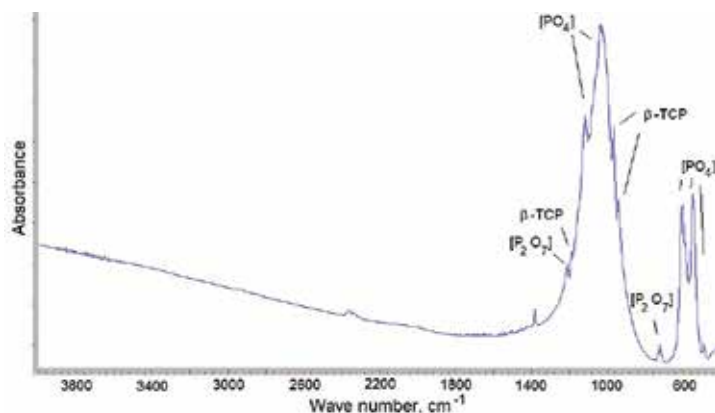


Fig. 4. FTIR spectra of commercial product (Fluka β -TCP)

4.2 Phase composition control during synthesis reaction

As above mentioned, CaP material synthesis was performed in our laboratory, varying synthesis and further sample heating parameters, searching for their optimal combination depending on the required properties of the obtained material.

In order to control reaction process and possible appearance of by-products, control samples were taken every 5 minutes and analyzed by measuring their spectra. After taking a sample from reactor with a plastic dropper, it was inserted in a glass bottle, hermetically sealed and frozen by putting it in the mixture of dry ice and acetone. After full freezing, the temperature is supported by storing the bottle in the dry ice. Before inserting in the cryogenic drying device, bottles are covered with a perforated plastic film. From the spectra of samples prepared this way (Fig.5), synthesis with a final pH=9,3 and synthesis temperature 45°C, it can be seen that the synthesized material is formed with an apatitic HAp structure with a slight Ca deficient, which is proven by presence of the CO_3^{2-} group, amount of which is constantly reducing along with reaction approaching its end. No by-products were detected, during the reaction, CaO has reacted fully which is proven by an OH- peak disappearing at 3642 cm^{-1} and forming OH- peaks at 3571 cm^{-1} and 631 cm^{-1} which is characteristic for HAp phase.

Such control is very important for scaling the synthesis, relatively increasing amount of synthesis and amount of obtained CaP.

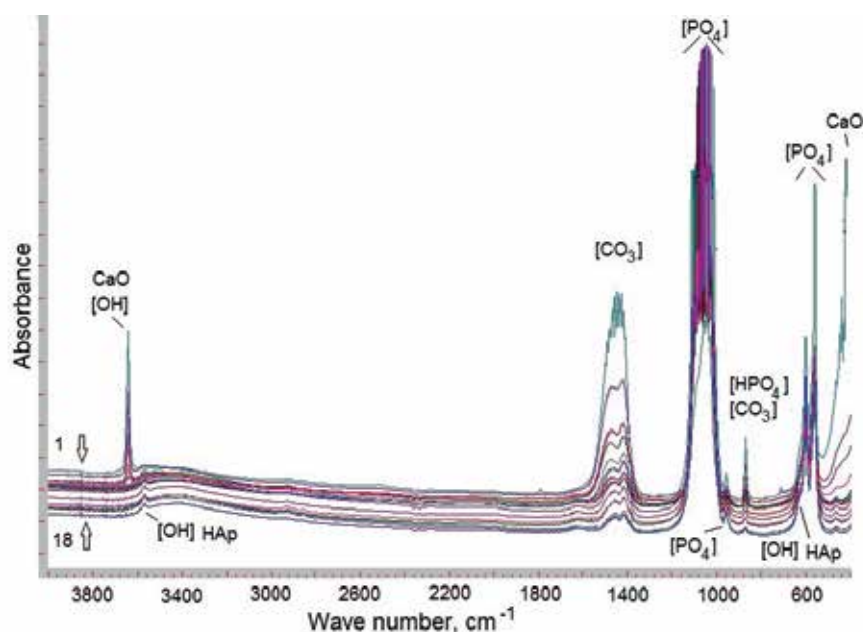


Fig. 5. FTIR spectra of the samples from the synthesis series with final pH=9,3 at temperature 45°C, depending on the reaction occurrence time (from 1 to 18).

4.3 Selection of CaO containing materials of various origins (marble, eggshells, snail shells) and its influence on the CaP product properties

Scientific literature contains very few information about research of how raw materials' (for example, CaO, $\text{Ca}(\text{OH})_2$) quality (chemical and physical properties) impacts properties of the obtained bioceramics.

Before starting synthesis of CaP products, selection of CaO containing raw material and complex research were performed. For „Ca” precursors, two commercial available synthetic

CaO powders from „Riedel-de Haën®” (CaO_R) and „Fluka” (CaO_F) and two materials of biogenic origin, widespread in the nature – egg shells and land snail (*Arianta arbustorum*) shells, were chosen. These materials were selected as raw materials for obtaining CaO and further usage in the synthesis process of CaP.

In composition of commercial CaO, presence of Ca(OH)_2 phase, small amount of MgO phase, as well as small amount of polymorphous CaCO_3 modification – calcite phase (Fig. 6), is detected. Presence of CaCO_3 is undesirable in CaO, for during the process of suspension obtaining, Ca(OH)_2 creates an error in preparation of precise amount of the reagent and, as follows, product reproduction, also preventing obtaining a homogenous Ca(OH)_2 suspension which is required for further synthesis of CaP. After heating biogenic and commercial CaO at 1000°C , X-ray diagrams of all the synthesis materials demonstrated a CaO crystal phase with a small amount of MgO phase, along with Ca(OH)_2 that formed in the result of CaO contact with air moisture; considering that CaO is hygroscopic (Siva Rama Krishna, et al., 2007).

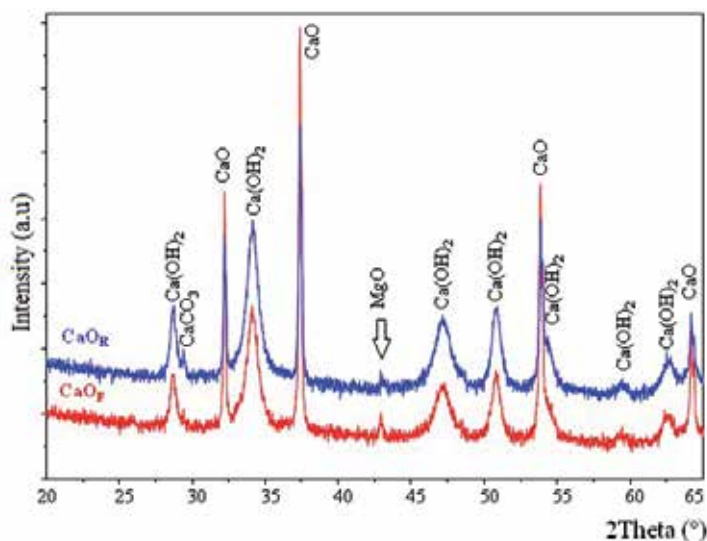


Fig. 6. Commercial CaO X-ray diffractograms before calcifying

FTIR spectra were also taken for the thermally treated CaO samples, and their compositions were similar (Fig. 7.). In all the IR spectra, an explicit absorption peak is visible at 3642 cm^{-1} , that indicates stretching variations of Ca(OH)_2 (Ji, et al., 2009) and [OH] groups (Siva Rama Krishna, et al., 2007). Presence of CaO is also proven by a wide intensive absorption band of [Ca-O] group, which is centered at $\sim 400\text{ cm}^{-1}$ (Ji, et al., 2009). Absorption peaks at 874 cm^{-1} , 1080 cm^{-1} [113], as well as at 1420 cm^{-1} prove presence of the $[\text{CO}_3]$ groups in the samples which, therefore, shows a slight carboxylation of Ca(OH)_2 from CO_2 of the atmosphere. Absorption band from $3430\text{--}3550\text{ cm}^{-1}$ proves presence of adsorbed water molecules in the samples.

FTIR spectra of the synthesized powders demonstrate absorption bands of the chemical functional groups, characteristic to HAp phase (Fig. 8.). Number of $[\text{CO}_3]$ groups in those is different, but after thermal treatment at 1100°C for 1 h, the spectra become very similar (Fig. 9).

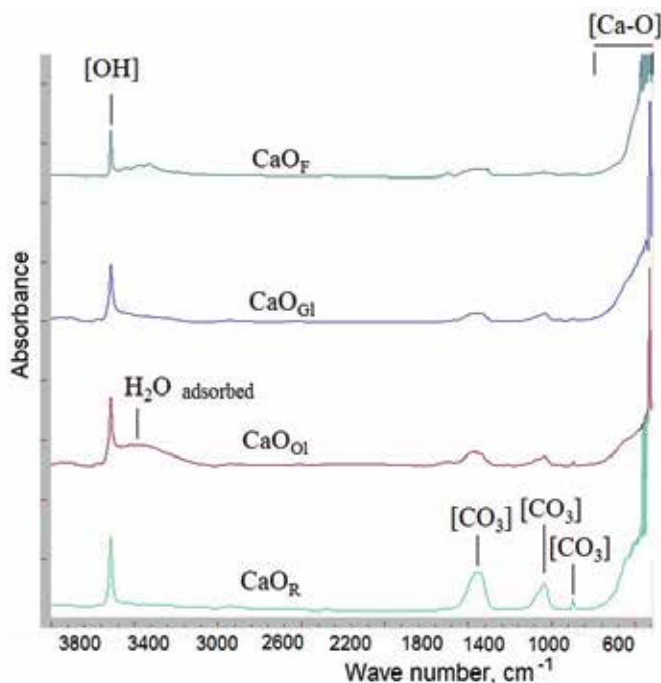


Fig. 7. FTIR spectra of biogenic and commercial CaO after heating at 1000°C for 1 h (F - „Fluka”, Gl - land snail shells, OI - egg shells and R - „Riedel-de Haën®”).

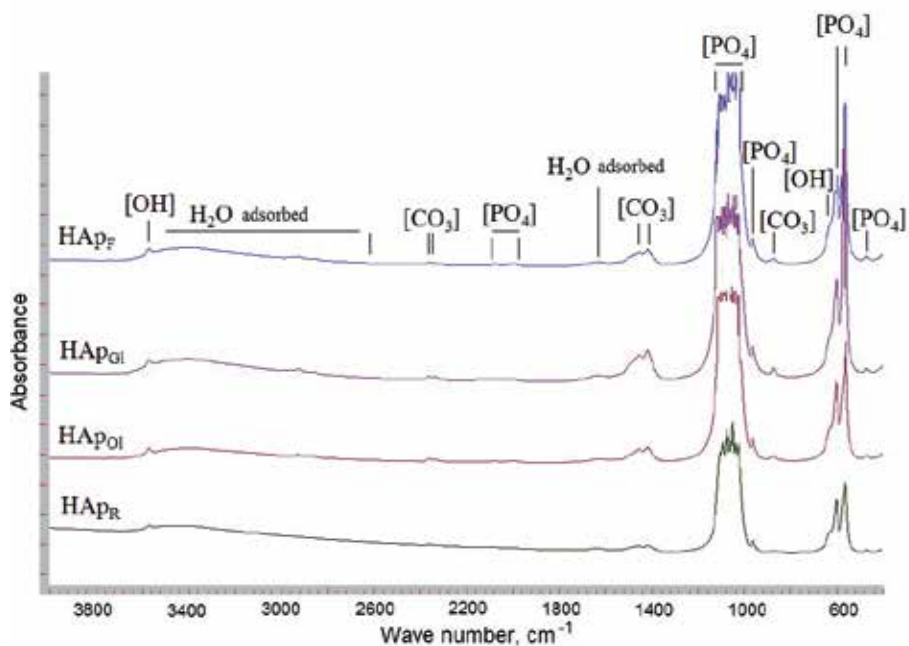


Fig. 8. FTIR spectra of HAp products as-synthesized after drying at 105°C for ~ 20 h from various CaO (F - „Fluka”, Gl - land snail shells, OI - egg shells and R - „Riedel-de Haën®”).

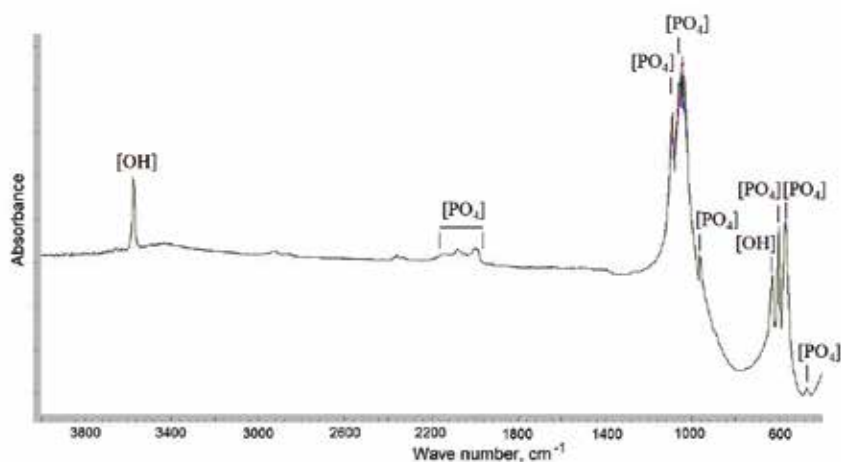


Fig. 9. FTIR spectra of HAp bioceramics obtained from various CaO after thermal treatment at 1100°C for 1 h.

Using CaO containing materials of various origins, including the commercial CaO available on the market that seemingly correspond with the assay specification, it is still impossible to obtain a completely reproducible HAp bioceramic materials. XRD and FTIR of the HAp products synthesized and heated at 1100°C, produce similar pictures, and post-synthesis morphology, phase composition and molecular structure of these bioceramics are identical. However, analyzing it with FE-SEM micrographs, it can be observed that obtained HAp products demonstrate different microstructures.

A homogenous, fine-grained microstructure with a small grain size – about 150-200 nm, is observed at the HAp bioceramic from commercial reagents, and non-homogenic grainy structure with irregular grain size in the range from 200 nm up to 1 μm is observed at the ceramic which was synthesized using Ca of natural origin.

Therefore, the samples from commercial reagents demonstrated color changing, from white in the synthesized and just dried powder to average aquamarine, at ceramic samples heated at 1000 °C, up to light blue color at 1300 °C. It can be explained by oxidizing of the manganese impurities from Mn^{2+} up to Mn^{5+} and substitution of hydroxyapatite (PO_4^{3-}) group with (MnO_4^{3-}) (Ślósarczyk, et al., 2010). Color change can be also explained by other microelements or defects in the crystal lattice, but, in this case, FTIR and XRD analysis cannot give a precise answer to this.

4.4 Thermal behavior of calcium phosphates depending on synthesis parameters

Sample structure, phase composition and thermal stability after heating depend on synthesis parameters, especially from final pH and synthesis temperature. Also, connection between pH value and temperature (with temperature increasing, pH decreases); so, by combining and analyzing those parameters, both pure HAp and TCP materials with a good thermal stability are obtained and biphasic materials with various Ca/P ratios and various percentages of phase composition.

Thermal behavior data of laboratory synthesized calcium phosphates with various synthesis parameters were summarized. Final reaction pH was varied in the range from 5.0 up to 10.7 and synthesis temperature was chosen as room (22°C), 45°C and 70°C (Table 7).

Nr. of synthesis	Final pH of synthesis	Synthesis temperature, °C	Phase composition by XRD after thermal treatment at 1100°C (1h)
1	5,0	room	TCP+CaHPO ₄
2	5,1	70	HAp/TCP (60/40)
3	5,3	45	HAp/TCP (35/65)
4	5,9	room	TCP
5	7	45	HAp/TCP (80/20)
6	9,3	45	HAp
7	10,7	45	HAp/CaO

Table 7. Variable parameters of some calcium phosphate synthesis and calcium phosphate products phase composition after thermal treatment at 1100°C for 1 h

It can be ascertained that, in spite of variable parameters of synthesis, all the spectra and XRD diffraction diagrams, are similar, all the functional groups correspond with non-stoichiometric apatitic HAp structure with a low crystallinity degree (Fig. 10). The only slight differences that can be observed between spectra, are intensities of CO₃²⁻ group bands, however, no significant differences in the number of OH⁻ groups, depending on the synthesis parameters at the non-calcified samples, are detected (Table 8).

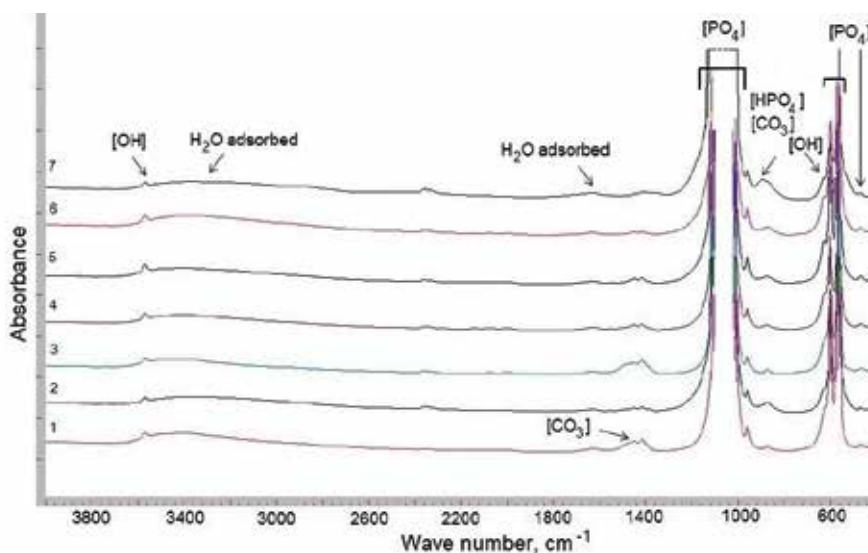


Fig. 10. FTIR spectrum of as-synthesized and drying at 105°C (20 h) CaP products of 1-7 synthesis

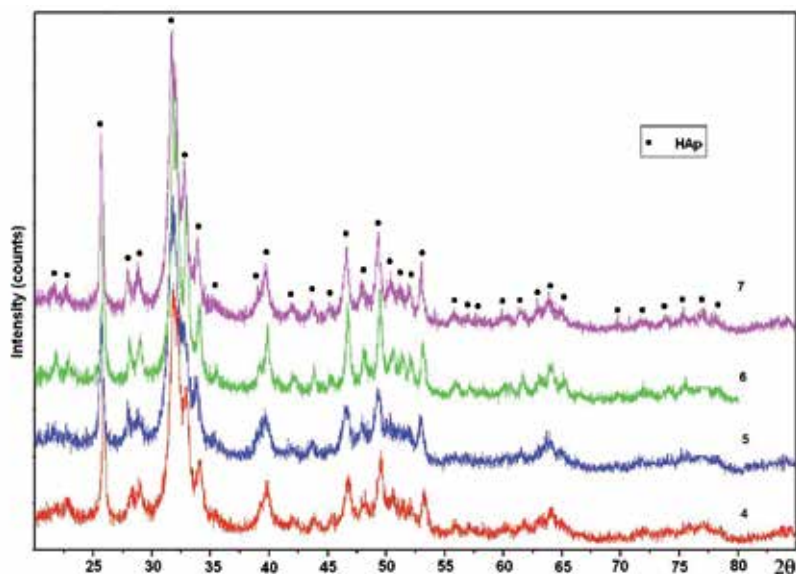


Fig. 11. XRD patterns of as-synthesized CaP products from 4, 5, 6, 7 synthesis.

Chemical groups	Absorption bands, cm^{-1}
PO_4^{3-}	472; 570; 602; 963; 1000 - 1140;
H_2O adsorbed	3100 - 3600;
OH^-	631; 3570;
HPO_4^{2-}	875 (identifies HAp with deficient of calcium and non-stoichiometric structure)
CO_3^{2-}	875; 1418; 1458; 1632 and 1650; 1994

Table 8. Absorption bands of as-synthesized and drying at 105°C (20 h) CaP products

Absorption bands of chemical functional groups characteristic to HAp phase can be defined as follows:

- Absorption bands at 3570 cm^{-1} and 631 cm^{-1} are referable to structural $[\text{OH}]$ groups (O-H) stretching and libration modes at the HAp crystallite surface or at the crystallites.
- Presence of $[\text{PO}_4]$ groups, characteristic to tetrahedral apatite structure, is proven by absorption bands at 472 cm^{-1} , which is characteristic to $[\text{PO}_4]_{\text{v}_2}$ group (v_2 O-P-O) bending variations; double band at 570 cm^{-1} and 602 cm^{-1} with a high resolution is referable to asymmetric and symmetric deformation modes of $[\text{PO}_4]_{\text{v}_4}$ group (v_4 O-P-O); absorption band at 963 cm^{-1} corresponds to a symmetric stretching mode; intensive absorption band in the range of $1040\text{-}1090\text{ cm}^{-1}$ corresponds to a band characteristic to $[\text{PO}_4]_{\text{v}_3}$ groups (v_3 P-O) at 1040 cm^{-1} and 1090 cm^{-1} asymmetrical stretching mode, which, as explicit maximums, can be observed after thermal treatment of the samples;
- An absorption band of weak intensity within the range between $1950\text{-}2100\text{ cm}^{-1}$ is connected with combinations of $[\text{PO}_4]_{\text{v}_3}$, v_1 modes.

These locations of absorption bands of the functional groups explicitly indicate forming of a typical HAp structure in the synthesized samples (Nilen & Richter, 2008; Siva Rama Krishna, et al., 2007; Kothapalli, et al., 2004; Landi, et al., 2000; Lioua, et al., 2004).

Weak absorption bands at 2365 cm^{-1} and 2344 cm^{-1} appeared due to attraction of CO_2 from the atmosphere.

Presence of $[\text{CO}_3]$ bands can be identified with explicitly visible absorption bands within the range between $1600\text{--}1400\text{ cm}^{-1}$ and at 875 cm^{-1} , which are observed in the spectra of synthesized samples. Absorption bands of weak intensity, centered at 1418 cm^{-1} and 1458 cm^{-1} correspond to symmetrical and asymmetrical stretching modes of the $[\text{CO}_3]_{\text{v}_3}$ groups (C-O). Absorption band at $\sim 875\text{ cm}^{-1}$ can prove presence of $[\text{CO}_3]_{\text{v}_2}$ stretching mode (at $\sim 872\text{ cm}^{-1}$), intensity of which is approximately 1/5 share of $[\text{CO}_3]_{\text{v}_3}$, or presence of $[\text{HPO}_4]$ group absorption maximum (Siva Rama Krishna, et al., 2007; Landi, et al., 2000). Considering that the $[\text{HPO}_4]$ group band partially covers $[\text{CO}_3]_{\text{v}_2}$, it is complicated to detect, of which group is this band. Presence of this absorption band ascertains solution of atmosphere CO_2 in the suspension, if synthesis occurs in the alkaline environment.

Combination of absorption bands – absorption bands of $[\text{CO}_3]_{\text{v}_3}$ groups at 1418 cm^{-1} and 1458 cm^{-1} , as well as at 875 cm^{-1} , proves substitution of „B-type“ $[\text{PO}_4]$ groups with $[\text{CO}_3]$ groups in the HAp crystal lattice (Barinov, et al., 2006; Siva Rama Krishna, et al., 2007).

Absorption maximum of $[\text{CO}_3]$ group at 875 cm^{-1} can also prove that „AB-type“ ($[\text{PO}_4]$ and $[\text{OH}]$ groups) substitution in the structure of HAp, as well as a weak absorption band at 3571 cm^{-1} in the synthesized HAp samples can mean the „AB-type“ substitution (Barinov, et al., 2006).

A wide absorption band within the range from $\sim 3600\text{ cm}^{-1}$ up to 3100 cm^{-1} points on v_3 and v_1 with H_2O molecules bonded with hydrogen for stretching modes and an absorption band at 1629 cm^{-1} is referable onto deformation mode v_2 of H_2O molecules (Siva Rama Krishna, et al., 2007), that proves presence of physically adsorbed water in the synthesized samples.

Processing the samples in the temperature range between $200\text{ }^\circ\text{C}$ to $1400\text{ }^\circ\text{C}$ in the air atmosphere, a similar sample behavior, even up to characteristic bioceramic sintering temperatures, is observed in all the syntheses. Dehydration of the samples occurs up to 500°C , and at 600°C , the spectra demonstrate that adsorbed water band disappears from the spectrum, adsorbed and capillary water is eliminated from CaP. Within the temperature range between 500°C and 800°C , amount of CO_3^{2-} groups in the samples also reduces, and bands of CO_3^{2-} group fully disappear at $900\text{ }^\circ\text{C}$. FTIR spectra (Fig. 12) and XRD diffractograms (Fig. 13) of the thermally treated at 1100°C samples considerably differ, comparing with the samples that just have been synthesized. A restructurization of functional $[\text{PO}_4]$ groups have occurred, and sample phase composition is considerably different from the combination of the initial synthesis parameters. It can be concluded that phases with a high crystallinity degree were formed.

A pure, stoichiometric and stable HAp in a wide temperature range is obtained using the following synthesis parameters: final $\text{pH}=9,3$ and synthesis temperature $T_s=45^\circ\text{C}$ (synthesis 6). Sample thermal treatment is performed in the air atmosphere, in the temperature range $200^\circ\text{C} - 1400^\circ\text{C}$ for 1 h. HAp spectra at various heating temperatures are demonstrated on the Fig. 14 and 15.

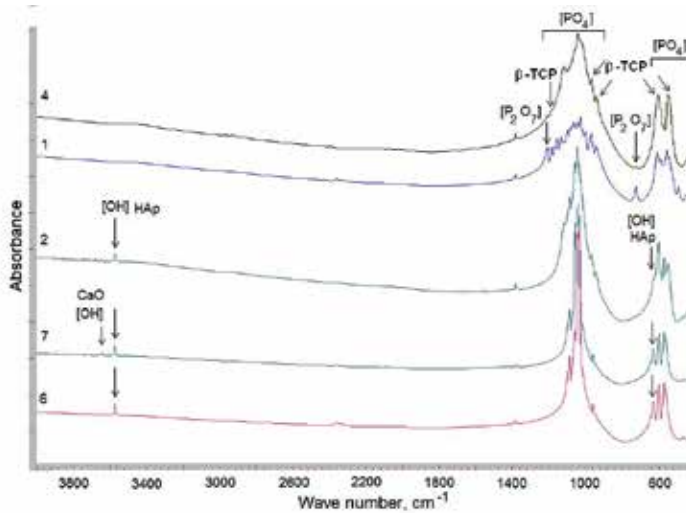


Fig. 12. FTIR spectra of calcium phosphates thermally treated at 1100°C for 1 h, depending on synthesis parameters (1, 2, 4, 6 and 7 synthesis)

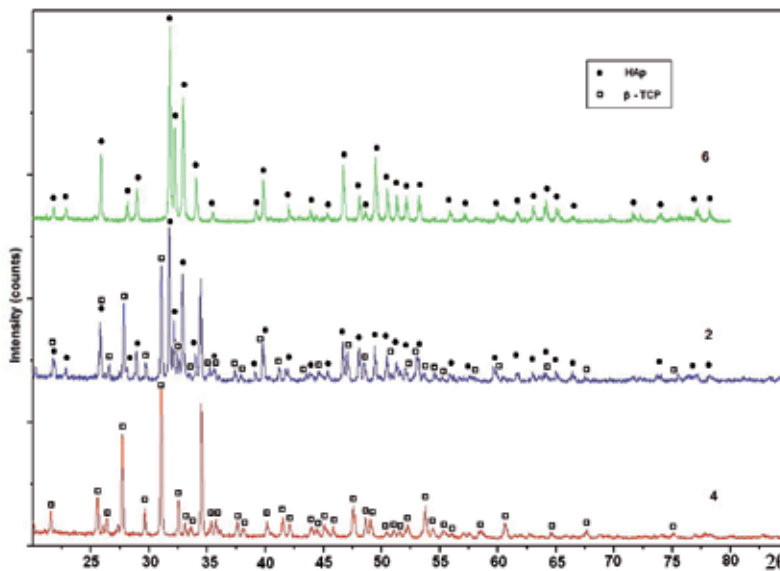


Fig. 13. X-ray diffraction patterns of different calcium phosphate of calcium phosphates thermally treated at 1100°C for 1 h with different phase compositions for synthesis 6 – pure HAp, 4 – pure β -TCP and 2 – biphasic mixture of HAp/ β -TCP

As can be seen after FTIR analysis which is often more sensitive than XRD, HAp begins to decompose when a sample is heated for 1 h at more than 1200°C, forming TCP shoulders at 948 cm^{-1} , 975 cm^{-1} and poorly intensive band at 432 cm^{-1} , which proves dehydroxilation of HAp and forming of α -TCP or OHAp phases. Therefore, XRD analysis shows that the decomposition occurs only at 1400°C, and is resulted with mixture of α -tricalcium phosphate (α -TCP, $\text{Ca}_3(\text{PO}_4)_2$), tetracalcium phosphate (TTCP, $\text{Ca}_4(\text{PO}_4)_2\text{O}$) and HAp. By

heating and then cooling a HAp sample in the air atmosphere, a complete HAp decomposition cannot be achieved, for during cooling [OH] groups get back in the structure from the air and therefore a partial reversible α -TCP and TTCP transform into HAp.

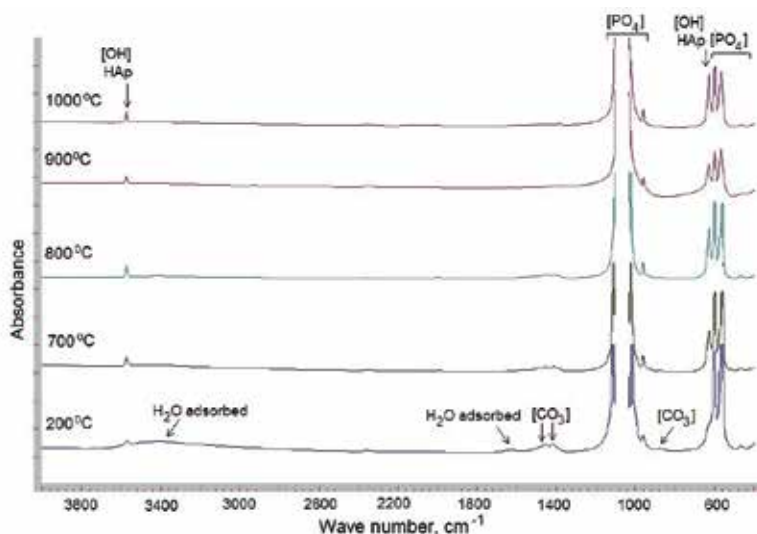


Fig. 14. FTIR spectra of HAp (synthesis 6) depending of thermal treatment temperature in range 200 – 1000°C for 1 h

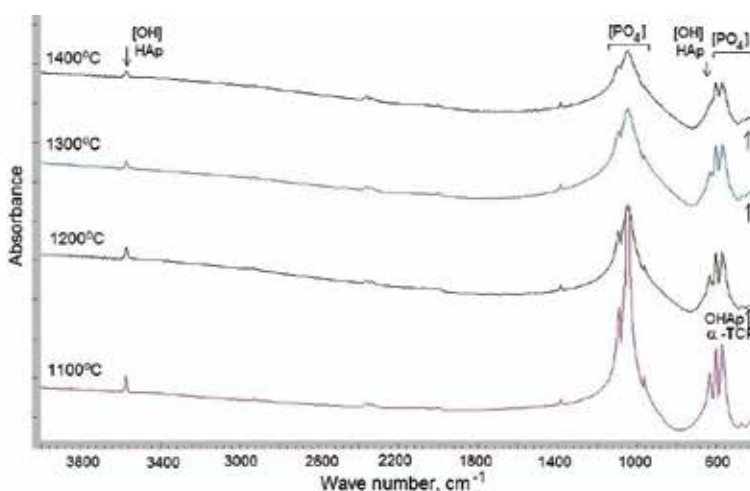


Fig. 15. FTIR spectra of HAp (synthesis 6) depending of thermal treatment temperature in range 1100 – 1400°C

A pure β -tricalcium phosphate phase $\text{Ca}_3(\text{PO}_4)_2$, obtained using the following synthesis parameters: final pH=5,8 and $T=22^\circ\text{C}$ (synthesis 4), it is synthesized at low temperatures and pH is acidic.

OH- group bands completely disappear at 700°C with a wave length 3569 cm⁻¹ and 631 cm⁻¹, which is characteristic for HAp. It can also be observed that at 900°C, bands that

correspond to a CO_3^{2-} functional group, disappear. At 700°C , a β -TCP phase begins to form, which is shown by characteristic shoulders which become more sharply explicit with increasing temperature. Until 1100°C , also poorly intensive pyrophosphate (CPP) group bands at 727 and 1212 cm^{-1} , that disappear at higher temperatures.

Since the sample does not contain CPP and HAp any longer, a pure TCP is obtained in the result, and it is stable up to 1400°C (Fig. 16 and 17). A β -TCP phase can be identified in the spectrum by appearance of characteristic bands at 947 cm^{-1} and 975 cm^{-1} .

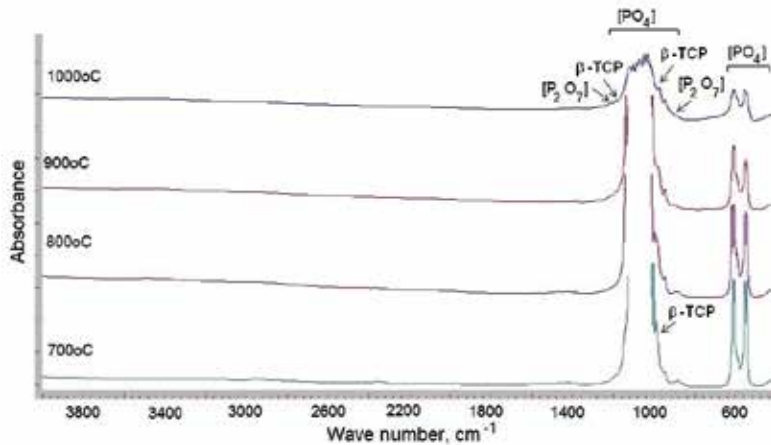


Fig. 16. FTIR spectra of β -TCP (synthesis 4) depending of thermal treatment temperature in range $700 - 1000^\circ\text{C}$ for 1 h

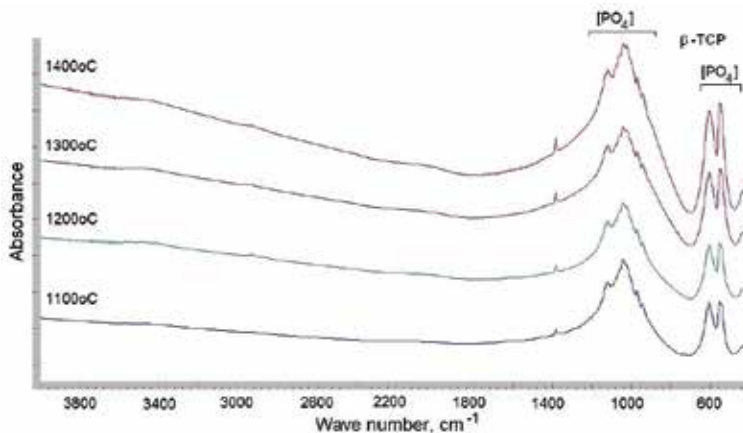


Fig. 17. FTIR spectra of β -TCP (synthesis 4) depending of thermal treatment temperature in range $1100 - 1400^\circ\text{C}$ for 1 h

In the CaP syntheses with final $\text{pH}=7$, $T=45^\circ\text{C}$ (synthesis 5), final $\text{pH}=5,1$ and $T=70^\circ\text{C}$ (synthesis 2), final $\text{pH}=5,3$ and $T=45^\circ\text{C}$ (synthesis 3), spectra demonstrate that a biphasic mixture with various HAp/TCP proportions, respectively $80/20$, $60/40$ and $35/65$, measured at 1100°C with an XRD semi-quantitative method, is formed in the synthesized samples.

In the synthesis with final pH=5,00 and T=22 °C (synthesis 1), a complicated phase composition is formed from β -TCP, CaHPO_4 and TTCP phases, and it remains stable up to 1200 °C. CaHPO_4 phase can be recognized after a HPO_4^{2-} group band at 897 cm^{-1} , which is visible in the spectra already at 200 °C.

In the synthesis with a final pH=10,74 and T=45°C (synthesis 7), a HAp structure is formed but at 1000°C, and additional OH- peak appears at 3644 cm^{-1} , which means that there is a unreacted CaO left. The reaction did not occur completely and this synthesis, as well as the above mentioned synthesis 1, cannot be used in practice.

Chemical groups and phases \ T, °C	800	900	1000	1100	1200	1300	1400
CO_3^{2-}	875; 1418; 1456; 1466; 1636	875; 1384; 1418; 1457; 1636	875; 1385; 1419; 1457	-	-	-	-
HPO_4^{2-}	875	875	875	-	-	-	-
H_2O adsorbed	3100 - 3600	3250-3600	3330 - 3595	-	-	-	-
OH-	3572; 634	3572; 634	3572; 633	3572; 632	3570	3570	3570
PO_4^{3-} β -TCP (OAp)	-	-	-	435;	436;	434	434
PO_4^{3-}	1000 -1120	1006 - 1120	1046; 1091	1046; 1091	1046; 1091	1045; 1094;	1037; 1045; 1090
PO_4^{3-} HAp	473; 550 - 640; 963	471; 556-604; 963	473; 554-601; 963	472; 570; 602; 963	472; 569; 602; 962	472; 568; 602; 961	472; 568 601; 961
PO_4^{3-} β -TCP	946; 975	946; 975	946; 975; 1127	944; 971 1127	944; 970; 1121	944; 970; 1121	943; 970; 1120
$\text{P}_2\text{O}_7^{4-}$	725; 1211	725; 1212	725;1210	-	-	-	-

Table 9. FTIR absorption bands (cm^{-1}) of thermally treated laboratory synthesized HAp and β -TCP (synthesis 6 and 4) chemical groups.

4.5 Thermal stability of HAp in various environments

Dehydroxilation of HAp under temperature influence is proven by reduction of [OH] absorption maximums intensity. Absorption band of [OH] bonding at 632 cm^{-1} is very

sensitive to temperature changes and at higher heating temperatures (over 1300°C) is only shown as shoulder of $[\text{PO}_4]$ absorption band at 601 cm^{-1} , when $[\text{OH}]$ bonding at 3572 cm^{-1} is more stable in the higher temperatures (Fig. 18).

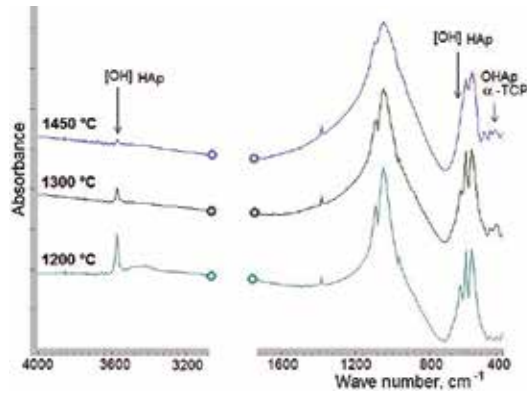


Fig. 18. FTIR spectra of HAp heated in the air at 1200, 1300, 1450°C (1h)

Temperature, °C	Heating time, h	Phase composition	
		After XRD	after FTIR
1000	8	HAp	HAp
1100	1	HAp	HAp
1200	1	HAp	HAp + TCP
1300	1	HAp	HAp + TCP
	12	HAp	HAp + TCP
1400	1	HAp + α -TCP + TTCP	HAp + TCP
	3	HAp + α -TCP + TTCP	HAp + TCP + TTCP
1450	1	HAp + α -TCP + TTCP	HAp + TCP + TTCP
	3	HAp + α -TCP + TTCP	HAp + TCP + TTCP
	6	HAp + α -TCP + TTCP	HAp + TCP + TTCP
1500	1	HAp + α -TCP + TTCP	HAp + TCP + TTCP

Table 10. Phase composition after HAp thermal treatment in the air

Stability of hydroxyapatite phase depends on the partial pressure of the water in the atmosphere, so, in an environment with no presence of water, by addition of sufficient amount of energy, HAp will turn into more stable calcium phosphates in the waterless environment. After thermally treating the sample in vacuum, there is an absorption band detected at 948 cm^{-1} in the FTIR spectrum already at $600\text{ }^\circ\text{C}$. It appears in the result of $[\text{PO}_4]$ group fluctuations and usually points onto TCP phase, however the literary sources mention that the absorption band at this wave length could also be characteristic to oxyapatite phase. In the result of thermal treatment, in vacuum at $1300\text{ }^\circ\text{C}$, HAp phase has completely decomposed and absorption bands, characteristic to TCP and TTCP phases, are visible in the FTIR spectrum (overlapping

of numerous $[\text{PO}_4]$ groups vibrations occurs, so it is not possible to distinguish, which absorption bands belong to TCP, and which to TTCP phase).

Temperature, °C	Processing time, h	Phase composition	
		after XRD	after FTIR
600	1	HAp	HAp + OAp/TCP
800	1	HAp	HAp + OAp/TCP
900	1	HAp	HAp + OAp/TCP
1000	1	HAp + α -TCP	HAp + OAp/TCP/TTCP
1100	1	HAp + α -TCP + TTCP	HAp + TCP + TTCP
1200	1	HAp + α -TCP + TTCP	TCP + TTCP
1300	1	α -TCP + TTCP	TCP + TTCP

Table 11. Phase composition after thermal treatment of HAp in the vacuum oven.

According to XRD data, supplying water vapor during heating of hydroxyapatite does not change phase composition, however slight changes in the sample structure are detected with FTIR analysis. After thermal treatment in the water vapor, absorption intensity of $[\text{OH}]$ group increases in ratio to $[\text{PO}_4]$, comparing with a sample heated in the air, which could improve HAp properties and make this phase more stable.

5. Conclusions

This summarizing work can help to evaluate both synthesized CaP and structure, phase composition and properties of the CaP bioceramic products. FTIR spectrometry along with XRD is one of the most important, quickest and most available methods for studying CaP materials and in many cases more sensitive than XRD in order to detect forming of new phases. Using these methods, it was possible to detect synthesis parameters in order to obtain a pure and thermally stable HAp and β -TCP, as well as biphasic mixtures with controllable ratio. From the results of above mentioned studies it can be concluded that a thorough selection of environment is required for processing HAp powder and it is also required to monitor behavior of the material during the heating, in order to obtain the desirable product. By varying conditions of thermal treatment, it is possible to improve structure of the synthesized HAp, for example, eliminate carbonate groups included in the structure during synthesis, increase number of $[\text{OH}]$ groups, as well as slow (by thermal treatment with water vapor presence) or quicken (by thermal treatment in vacuum) HAp decomposition.

6. References

- Barinov S.M., Rau J.V., Cesaro S.N. (2006). Carbonate release from carbonated hydroxyapatite in the wide temperature range// *J. Mater. Sci. Mater. Med.*, Vol.17., pp. 597.-604

- Destainville A., Champion E., Bernache-Assollante D., et al. (2003). Synthesis, characterization and thermal behaviour of apatite tricalcium phosphate // *Materials Chemistry and Physics*, No. 80, pp. 269 – 277
- Dorozhkin S.V. (2009). Calcium Orthophosphates in Nature, Biology and Medicine. *Materials*, 2: pp. 399-498
- Dorozhkin S.V. (2009). Calcium orthophosphate-based biocomposites and hybrid biomaterials. *J. Mater. Sci.*, 44(9): pp. 2343-2387
- Dorozhkin S.V. (2009). Calcium Orthophosphate Cements and Concretes. *Materials*, 2: pp. 221-291
- El Kady A.M., K.R.M., El Bassyouni G.T. (2009). Fabrication, characterization and bioactivity evaluation of calcium pyrophosphate/polymeric biocomposites. *Ceram. Int.*
- Ji G., Zhu H., Jiang X., et. al. (2009). Mechanical Strenght of Epoxy Resin Composites Reinforced by Calcined Pearl Shell Powders. *J. Appl. Polym. Sci.*, Vol.114, pp. 3168.-3176
- Han J-K., Song H-Y., et al. (2006). Synthesis of height purity nano-sized hydroxyapatite powder by microwave-hydrothermal method. *Materials Chemistry and Physics*, No. 99, pp 235 – 239
- Kothapalli C., Wei M., Vasiliev A., et. al. (2004). Influence of temperature and concentration on the sintering behavior and mechanical properties of hydroxyapatite// *Acta Mater*, Vol.52, pp. 5655-5663
- Kwon S-H., Jun Y-K., Hong S-H., el al. (2003). Synthesis and dissolution behaviour of β - TCP and HA/ β -TCP composite powders. *Journal of European Ceramic Society*, No. 23, pp. 1039-1045
- Landi E., Tampieri A., Celotti G., et. al. (2000). Densification behaviour and mechanisms of synthetic hydroxyapatites. *J. Eur. Ceram. Soc.*, Vol. 20, pp. 2377-2387
- Lioua S.-C., Chena S.-Y., Lee H.-Y., et. al. (2004). Structural characterization of nano-sized calcium deficient apatite powders. *Biomaterials*, Vol. 25, pp. 189-196.
- Meejoo S., Maneeprakorn W., Winotai P. (2006). Phase and thermal stability of nanocrystalline hydroxyapatite prepared via microwave heating. *Thermochimica Acta*, No. 447, pp. 115-120
- Mobasherpour I., Heshajin M. (2007). Synthesis of nanocrystalline hydroxyapatite by using precipitation method. *Journal of Alloys and Compounds*, N 430, pp. 330 – 333
- Nilen R.W.N., Richter P.W. (2008). The thermal stability of hydroxyapatite in biphasic calcium phosphate ceramics. *J. Mater. Sci. Mater. Med.*, Vol. 19(4), pp. 1693-1702
- Ratner B., Hoffman A., Schoen F. et. al. (2004). *Biomaterials Scienc. An Introduction to Materials in Medicine*, Second Edition // Academic Press, pp. 851
- Raynaud S., Champion E., Bernache-Assollant D. Et al. (2002). Calcium phosphate apatite with variable Ca/P atomic ratio I. Synthesis, characterisation and thermal stability of powders. *Biomaterials* No 23, pp. 1065-1072
- Shi D., (2006). *Introduction to biomaterials*. World Scientific Publishing, p. 253.
- Siva Rama Krishna D., Siddharthan A., Seshadri S. K., et. al. (2007). A novel route for synthesis of nanocrystalline hydroxyapatite from eggshell waste. *J. Mater. Sci. - Mater. Med.*, Vol.18., pp. 1735-1743
- Ślósarczyk A., Paszkiewicz Z., Zima A. (2010). The effect of phosphate source on the sintering of carbonate substituted hydroxyapatite. *Ceram Int.*, Vol. 36, pp. 577-582

FTIR Spectroscopy of Adsorbed Probe Molecules for Analyzing the Surface Properties of Supported Pt (Pd) Catalysts

Olga B. Belskaya^{1,2}, Irina G. Danilova³,
Maxim O. Kazakov¹, Roman M. Mironenko¹,
Alexander V. Lavrenov¹ and Vladimir A. Likholobov^{1,2}

¹*Institute of Hydrocarbons Processing SB RAS*

²*Omsk State Technical University*

³*Boreskov Institute of Catalysis SB RAS
Russia*

1. Introduction

Supported metal catalysts are important for many fields of applied chemistry, including chemical synthesis, petrochemistry, environmental technology, and energy generation/storage. For prediction of catalyst performance in a chosen reaction and optimization of its functions, it is necessary to know the composition of the surface active sites and have methods for estimating their amount and strength. One of the most available and well-developed methods for studying the composition and structure of the surface functional groups of supported metal catalysts is vibrational spectroscopy, in particular with the use of adsorbed probe molecules.

Although Fourier transform infrared (FTIR) spectroscopy is widely employed for characterization of the catalyst surface (Paukshtis, 1992; Ryczkowski, 2001), it is still unclear whether the regularities obtained under conditions of spectral pretreatments and measurements (evacuation, temperature) can be used for interpreting and predicting the surface properties during adsorption of a precursor or in a catalytic reaction. Thus, aim of the present work is not only to demonstrate the possibilities of FTIR spectroscopy of adsorbed molecules for investigation of the surface functional groups in the chosen catalytic systems, but also to compare FTIR spectroscopy data with the data obtained for supported metal catalysts by other physicochemical methods and with the catalyst properties in model and commercially important reactions. Main emphasis will be made on quantitative determination of various surface groups and elucidation of the effect of their ratio on the acid-base, adsorption and catalytic properties of the surface.

The study was performed with model and commercially important supports and catalysts: gamma alumina, which is among the most popular supports in the synthesis of supported metal catalysts for oil refining, petrochemistry, and gas emissions neutralization; supported platinum and palladium catalysts containing sulfated zirconia (Pt/SZ, Pd/SZ) or alumina-

promoted SZ (Pt/SZA), which are suitable for low-temperature isomerization of n-alkanes and hydroisomerization of benzene-containing fractions of gasoline.

2. Vibrational spectroscopy of adsorbed probe molecules for investigation of supported catalysts – Estimation of the strength and concentration of various surface sites

2.1 FTIR spectra of adsorbed probe molecules

FTIR spectroscopy of adsorbed probe molecules is one of the most available and well-developed methods for studying the composition and structure of the surface functional groups of supported metal catalysts. As the vibrational spectrum reflects both the properties of the molecule as a whole and the characteristic features of separate chemical bonds, FTIR spectroscopy offers the fullest possible information on the perturbation experienced by a molecule on contact with the solid surface, and often determines the structure of adsorption complexes and of surface compounds. Examination of supported metal catalysts deals with two types of surfaces strongly differing in their properties: surface of a support and surface of a metal-containing particle. Various species can reside on the support surface: hydroxyl groups of different nature; Lewis acid sites (coordinatively unsaturated surface cations); base sites (bridging oxygen atoms or oxygen atoms of OH groups); structures formed by impurity anions that remain after the synthesis (sulfate, nitrate and ammonia groups) or form upon contacting with air (carbonate-carboxylate structures).

Various spectroscopic probe molecules are widely used for characterization of Lewis and Brønsted acid sites on the surfaces of oxide catalysts. Among such probes are strong bases: amines, ammonia and pyridine, and weak bases: carbon oxide, carbon dioxide and hydrogen (Knözinger, 1976a; Kubelková et al., 1989; Kustov, 1997; Morterra & Magnacca, 1996; Paukshtis, 1992). Being a weaker base than ammonia, pyridine interacts with the sites widely varying in acidity. However, within each type of Lewis acid site, which is determined with pyridine as a probe molecule, there are distinctions in acidity that cannot be revealed with the use of strong bases. In this connection, very advantageous is the adsorption of weak bases like CO. The application of such probe molecules as CO or pyridine makes it possible to estimate both the concentration and the acid strength of OH groups and Lewis acid sites in zeolites, oxide and other systems (Knözinger, 1976b; Paukshtis, 1992). Concentration of the surface groups accessible for identification by FTIR spectroscopy is above 0.1 $\mu\text{mol/g}$.

In the case of base surface sites, the concentration and strength can be characterized with deuteriochloroform (Paukshtis, 1992). Surface of a metal-containing particle may consist of metal atoms with various oxidation states or different charge states caused by the metal-support interaction. Metal cations and atoms on the surface can be detected only from changes in the spectra of adsorbed molecules, since vibrations of the metal-oxygen bonds on the surface belong to the same spectral region as lattice vibrations and thus are not observed in the measurable spectra, whereas vibrational frequencies of the metal-metal bonds are beyond the measuring range of conventional FTIR spectrometers. Surface atoms and nanoparticles of metals and metal ions are usually identified by the method of spectroscopic probe molecules such as CO (Little, 1966; Sheppard & Nguyen, 1978). Examination of the nature of the binding in Men^+CO complexes suggests that the frequency of adsorbed CO (ν_{CO}) should depend on the

valence and coordination states of the cations, that is, on their abilities to accept σ -donation (increasing ν_{CO}) and to donate π -orbitals of the CO (decreasing ν_{CO} , as for carbonyl complexes) (Davydov, 2003; Hadjiivanov & Vayssilov, 2002; Little, 1966). Carbonyls involving π -donation can have different structures – linear or bridged – and the number of metal atoms bonded to the CO molecules can also be different. Complexes involving cations only be linear (terminal) because in an M-O-M situation the distance between cations is too great to form a bond between a CO molecule and two cation sites simultaneously.

2.2 Experimental

The FTIR spectra were measured on a Shimadzu FTIR-8300 spectrometer over a range of 700-6000 cm^{-1} with a resolution of 4 cm^{-1} and 100 scans for signal accumulation. Before spectra recording, powder samples were pressed into thin self-supporting wafers (8-30 mg/cm^2) and activated in a special IR cell under chosen conditions and further in vacuum ($p < 10^{-3}$ mbar). FTIR spectra are presented in the optical density units referred to a catalyst sample weight (g) in 1 cm^2 cross-section of the light flux.

Quantitative measurements in FTIR spectroscopy are based on the empirical Beer-Lambert-Bouguer law interrelating the intensity of light absorption and the concentration of a substance being analyzed. For FTIR spectroscopy of adsorbed molecules, this law is applied in the integral form:

$$A \approx \int \log(T_0/T)_v dv, \quad (1)$$

where A is the integral absorbance (cm^{-1}), T_0 and T are the transmittance along the base line, and the band contour, respectively.

The concentration of active sites on the catalyst surface was estimated by the formula

$$N[\mu\text{mol} / \text{g}] = \frac{A \cdot S}{p \cdot A_0}, \quad (2)$$

where A_0 is the integral absorption coefficient (integral intensity of absorption band (a.b.) for 1 μmol of the adsorbate per 1 cm^2 cross-section of the light flux), p is the weight of a sample wafer (g), and S is the surface area of a sample wafer (cm^2).

The concentration of surface OH groups in $\gamma\text{-Al}_2\text{O}_3$ was determined from the integral intensities of absorption bands ν_{OH} in the region of 3650-3800 cm^{-1} using the integral absorption coefficient $A_0 = 5.3 \text{ cm}/\mu\text{mol}$ (Baumgarten et al., 1989).

In the present study, acidic properties of the samples were examined by FTIR spectroscopy using CO adsorption at -196°C and CO pressure 0.1-10 mbar. An increase in the ν_{CO} band frequency of adsorbed CO relative to the value of free CO molecules (2143 cm^{-1}) is caused by the formation of complexes with Lewis or Brønsted acid sites. Complexes with Lewis acid sites are characterized by the bands with a frequency above 2175 cm^{-1} , whereas the frequency range from 2150 through 2175 cm^{-1} is typical of CO complexes with OH groups.

The concentration of Lewis acid sites was measured by the integral intensity of CO band in the range of 2170-2245 cm^{-1} . For alumina and compositions with prevailing fraction of

alumina (Al_2O_3 and $\text{SO}_4^{2-}\text{-ZrO}_2\text{-Al}_2\text{O}_3$), the following A_0 values ($\text{cm}/\mu\text{mol}$) were used: 1.25 (2245-2220 cm^{-1}), 1.0 (2200 cm^{-1}), 0.9 (2190 and 2178-2180 cm^{-1}); for zirconia and sulfated zirconia, A_0 was equal to 0.8 $\text{cm}/\mu\text{mol}$ (Paukshtis, 1992). A value of the upward ν_{CO} frequency shift determines the strength of Lewis acid sites, as it is related to the heat of complex formation by the following formula (Paukshtis, 1992):

$$Q_{\text{CO}} = 10.5 + 0.5 \cdot (\nu_{\text{CO}} - 2143) \quad (3)$$

The concentration of Brønsted acid sites in the modified aluminum oxides was measured by the integral intensity of CO band in the range of 2170-2175 cm^{-1} , $A_0 = 2.6 \text{ cm}/\mu\text{mol}$. The concentration of Brønsted acid sites in sulfated samples was determined from the integral intensity of absorption band due to the pyridinium ion with a maximum at 1544 cm^{-1} ($A_0 = 3.5 \text{ cm}/\mu\text{mol}$) (Paukshtis, 1992). Adsorption of carbon monoxide on Brønsted acid sites at -196 °C results in the shift of OH bands to the lower frequency region due to perturbation of OH stretch by hydrogen bonding with CO molecule. The higher the shift of OH stretching vibration, the stronger the acidity of this OH group (Maache et al., 1993; Paze et al., 1997).

Basic properties of the samples were studied by FTIR spectroscopy using CDCl_3 adsorption at 20 °C. At the formation of H bonds, deuteriochloroform behaves as a typical acid. A decrease in the frequency of ν_{CD} band of CDCl_3 adsorbed relative to the value of physisorbed molecules (2265 cm^{-1}) is caused by the formation of complexes with base sites. The strength of base site was determined by the band shift of the CD stretching vibrations that occurred under CDCl_3 adsorption. The strength can be recalculated into the proton affinity (PA) scale using the formula (Paukshtis, 1992):

$$\log(\Delta\nu_{\text{CD}}) = 0.0066\text{PA} - 4.36 \quad (4)$$

The concentration of base sites was measured by the integral intensity of CD band in the range of 2190-2255 cm^{-1} . The integral absorption coefficient was calculated from the correlation equations (Paukshtis, 1992):

$$A_0 = 0.375 + 0.0158\Delta\nu_{\text{CD}} \text{ for } \Delta\nu_{\text{CD}} > 13 \text{ cm}^{-1} \quad (5)$$

$$A_0 = 0.125 + 0.0034\Delta\nu_{\text{CD}} \text{ for } \Delta\nu_{\text{CD}} < 13 \text{ cm}^{-1} \quad (6)$$

3. Investigation of supports and catalysts by FTIR spectroscopy

3.1 Gamma alumina. The role of studying the surface functional groups for understanding the processes of adsorption and catalysis

Owing to its unique acid-base and structural properties, aluminum oxide, first of all $\gamma\text{-Al}_2\text{O}_3$, remains the most popular catalyst and catalyst support. The analysis of catalytic reactions usually deals with Lewis acid and base sites of Al_2O_3 . However, in the catalyst synthesis, adsorption properties of the surface during its interaction with aqueous solutions strongly determine the composition of surface hydroxyl cover of alumina. It should be noted that modern concepts of the surface structure of aluminum oxides, which were developed in recent 50 years, are based mainly on the vibrational spectroscopy data. Various structural models of the aluminum oxide surface were suggested to explain the experimental data

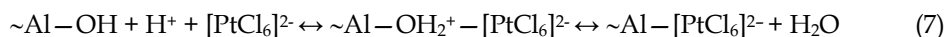
(Egorov, 1961; Peri, 1965; Tsyganenko & Filimonov, 1973; Zamora & Córdoba, 1978; Knözinger & Ratnasamy, 1978). These models are based on the spinel structure of transitional alumina modifications. Recent attempts to develop advanced models of the surface structure or refine the existing models were made by Tsyganenko and Mardilovich (Tsyganenko & Mardilovich, 1996) as well as Liu and Truitt (Liu & Truitt, 1997). Such advanced models admit the existence of fragments on the alumina surface, which comprise pentacoordinated aluminum atom.

At present, 7 absorption bands characterizing the isolated OH groups are commonly distinguished in FTIR spectrum of γ -Al₂O₃. Low-frequency bands are assigned to the bridging OH groups located between aluminum atoms with different coordination: 3665-3675 (Al^{IV}(OH)Al^{IV}), 3685-3690 cm⁻¹ (Al^{VI}(OH)Al^{IV}), 3700-3710 cm⁻¹ (Al^{VI}(OH)Al^V), and 3730-3740 (Al^{VI}(OH)Al^{VI})¹. High-frequency bands correspond to the terminal OH groups bound to one aluminum atom with different coordination: 3745-3758 (Al^VOH), 3765-3776 (Al^{IV}OH), and 3785-3792 (Al^{IV}OH) cm⁻¹. In addition, there is a broad a.b. at 3600 cm⁻¹ attributed to hydrogen-bonded OH groups (Paukshtis, 1992).

The surface Lewis acidity is formed by electron-acceptor sites represented by coordinatively unsaturated aluminum cations on the Al₂O₃ surface. The use of CO as a probe molecule makes it possible to estimate both the strength and the amount of Lewis acid sites, which is essential when alumina is employed as a catalyst or catalyst support. CO is adsorbed on the γ -Al₂O₃ surface to form three types of surface complexes (Della Gatta et al., 1976; Zaki & Knözinger, 1987; Zecchina et al., 1987). FTIR spectra of adsorbed CO show the following a.b. corresponding to stretching vibrations of CO molecule: 2180-2205 cm⁻¹ (weak Lewis acid sites), 2205-2220 cm⁻¹ (medium strength Lewis acid sites), and 2220-2245 cm⁻¹ (strong Lewis acid sites). The high-frequency bands are related with two types of Lewis acid sites including Al^{IV} ions located in configurations with crystallographic defects. The low-frequency bands correspond to Al^{VI} ions in the regular defects of low-index faces of crystallites.

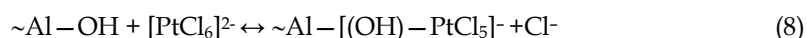
3.1.1 FTIR spectroscopy for determining the sites of precursor anchoring during synthesis of Pt/Al₂O₃ catalysts

In the synthesis of supported platinum catalysts, chloride complexes of platinum (IV) are commonly used as precursors. Their sorption on the alumina surface occurs from aqueous solutions and implies the involvement of OH groups of the support surface. Therewith, two main mechanisms of the interaction between metal complex and support are considered, implementation of each mechanism depending both on the chemical composition of a complex (degree of hydrolysis) and the ratio of various OH groups (Belskaya et al., 2008, 2011; Bourikas, 2006; Lycourghiotis, 2009). The first mechanism consists in the formation of outer sphere complexes; it implies electrostatic interaction between chloroplatinate and alumina surface, which is protonated and positively charged at low pH of the solution:



¹Al^{IV}, Al^V and Al^{VI} are aluminum atoms in tetrahedral, pentahedral and octahedral coordination, respectively

The formation of inner sphere complexes is accompanied by a deeper interaction of a complex with the oxide surface via ligand exchange with the surface OH groups:



FTIR spectroscopy is widely used to investigate state of the surface at different stages of catalyst synthesis. When studying the precursor-support interaction, this method allows identification of OH groups involved in chemisorption of the metal complex. Analysis of

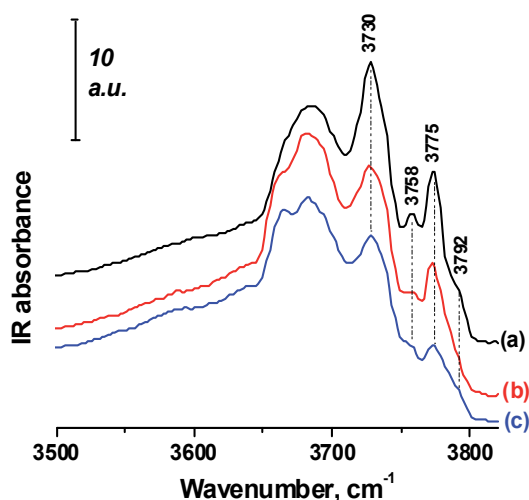


Fig. 1. FTIR spectra of surface hydroxyl groups of $\gamma\text{-Al}_2\text{O}_3$ (a), 0.5% Pt/ $\gamma\text{-Al}_2\text{O}_3$ (b) and 1% Pt/ $\gamma\text{-Al}_2\text{O}_3$ (c). The samples were calcined and outgassed at 500 °C

Sample		$\gamma\text{-Al}_2\text{O}_3$	0.5%Pt/ $\gamma\text{-Al}_2\text{O}_3$	1%Pt/ $\gamma\text{-Al}_2\text{O}_3$	$\gamma\text{-Al}_2\text{O}_3$ Hydrothermal treatment 180 °C, 3 h
		Type of OH group			
Concentration, $\mu\text{mol/g}$	$\text{Al}^{\text{IV}}\text{OH}$ (3790-3795 cm^{-1})	12	9	8	6
	$\text{Al}^{\text{V}}\text{OH}$ (3775 cm^{-1})	35	29	16	33
	$\text{Al}^{\text{VI}}\text{OH}$ (3758 cm^{-1})	34	27	20	28
	$\text{Al}^{\text{VI}}(\text{OH})\text{Al}^{\text{VI}}$ (3730-3740 cm^{-1})	107	96	78	89
	$\text{Al}^{\text{V}}(\text{OH})\text{Al}^{\text{VI}}$ (3705-3710 cm^{-1})	50	54	52	52
	$\text{Al}^{\text{VI}}(\text{OH})\text{Al}^{\text{IV}}$ (3690 cm^{-1})	62	75	67	62
	$\text{Al}^{\text{V}}(\text{OH})\text{Al}^{\text{IV}}$ (3665-3670 cm^{-1})	36	35	34	43
	Σ OH	336	325	275	313

Table 1. Types and concentrations of hydroxyl groups in calcined alumina and Pt/alumina samples as determined by FTIR spectroscopy data

experimental data presented in Fig. 1 and Table 1 shows that adsorption of platinum complexes followed by anchoring of oxide platinum species forming on the γ -Al₂O₃ surface decreases the intensity only of high-frequency bands. As the amount of supported platinum species increases (platinum content of 0.5 and 1.0 wt%), the concentration of all types of terminal groups (Al^{VOH}, Al^{VI}OH, Al^{IV}OH) decreases; so does the concentration of bridging OH groups Al^{VI}(OH)Al^{VI} bonded to octahedral aluminum. Exactly these types of OH groups seem to be involved in anchoring the anionic complexes of platinum (IV). Having more strong base properties, they are capable of interacting with chloroplatinate by mechanism (8), acting as the attacking ligand. However, the bridging groups with a.b. 3665-3710 cm⁻¹ (Al^{VI}(OH)Al^{IV}, Al^{IV}(OH)Al^{IV}, Al^{VI}(OH)Al^{IV}) are virtually not involved in platinum anchoring (Table 1).

According to analysis of the spectra of adsorbed CO, in the region of CO stretching vibrations all the samples have a.b. at 2245 and 2238 cm⁻¹ characterizing CO complexes with strong Lewis acid sites, absorption bands at 2220 and 2205 cm⁻¹ characterizing CO complexes with medium strength Lewis acid sites, and absorption bands at 2189-2191 cm⁻¹ characterizing CO complex with weak Lewis acid sites. Deposition of platinum raises the concentration of nearly all types of Lewis acid sites, which is related with introduction of Cl⁻ ion of the complex. Along with this, a substantial decrease in the concentration of weak Lewis acid sites is observed (Table 2). These electron-deficient sites may also take part in the anchoring of anionic platinum complexes via electrostatic interaction (Kwak et al., 2009; Mei et al., 2010).

Type of Lewis acid site	Super strong	Strong	Medium I	Medium II	Weak
ν_{CO} , cm ⁻¹	2245	2238	2220	2205	2189-2191
Q _{CO} , kJ/mol	61.5	58	48.5	41.5	34
Samples	Concentration, $\mu\text{mol/g}$				
γ -Al ₂ O ₃	0.9	2.5	5	9	460
1% Pt/ γ -Al ₂ O ₃	1.2	2.9	6	27	380
γ -Al ₂ O ₃ Hydrothermal treatment 180 °C, 3 h	1.1	4.2	5	24	470

Table 2. Types and concentrations of Lewis acid sites according to FTIR spectroscopy of adsorbed CO

Thus, the analysis of FTIR spectra of alumina provides data on the nature and amount of various surface sites; moreover, it allows identification of the sites where active component precursor is anchored during catalyst synthesis, and makes it possible to hypothesize about mechanism and strength of the metal complex-support interaction.

3.1.2 Novel approaches to varying the composition of surface functional groups of alumina

Variation of the acid-base properties of alumina surface is commonly performed by chemical modifying via the introduction of additional anions (halogens, sulfates, phosphates) or cations (alkaline or alkaline earth metals) (Bocanegra et al., 2006; Ghosh & Kydd, 1985; Lisboa et al., 2005; López Cordero et al., 1989; Marceau et al., 1996; Requies et

al., 2006; Rombi et al., 2003; Scokart et al., 1979; Wang et al., 1994). These methods complicate the process of catalyst synthesis and can lead to non-reproducible results.

This Section presents some unconventional approaches to alumina modifying for controlling the state of its surface functional cover. One of approaches consists in altering the relative content of hydroxyl groups and Lewis acid sites on the γ - Al_2O_3 surface without changes in the chemical composition of support (Mironenko et al., 2009, 2011). For this purpose, two techniques are employed: chemisorption of aluminum oxalate complexes followed by their thermal decomposition, and hydrothermal treatment of γ - Al_2O_3 . Besides, there is an approach leading to considerable enhancement of acidic properties of the surface. Such effect is provided by γ - Al_2O_3 promotion with silica. The formation of SiO_2 takes place in the pore space of alumina during thermal decomposition of preliminarily introduced silicon-containing precursor.

3.1.2.1 Modifying the functional cover of the γ - Al_2O_3 surface using aluminum oxalate complexes

The proposed method of modifying implies the chemisorption (in distinction to conventional methods of incipient wetness impregnation) of anionic aluminum oxalate complexes $[\text{Al}(\text{C}_2\text{O}_4)_2(\text{H}_2\text{O})_2]^-$ and $[\text{Al}(\text{C}_2\text{O}_4)_3]^{3-}$ on the γ - Al_2O_3 surface. It is essential that this approach excludes both the formation of a bulk alumina phase in the porous space after decomposition of supported complexes, and considerable changes in the texture parameters. Analysis of FTIR spectra of the modified alumina surface hydroxyl cover revealed (Fig. 2) that chemisorption of the oxalate complexes and subsequent formation of aluminum oxide compounds supported on γ - Al_2O_3 (calcination at 550 °C) decreased mainly the intensity of two a.b. at 3670 and 3775 cm^{-1} . These bands characterize the bridging and terminal OH groups bound to pentacoordinated aluminum atom. Probably these are exactly the groups that are involved in anchoring of aluminum oxalate complexes.

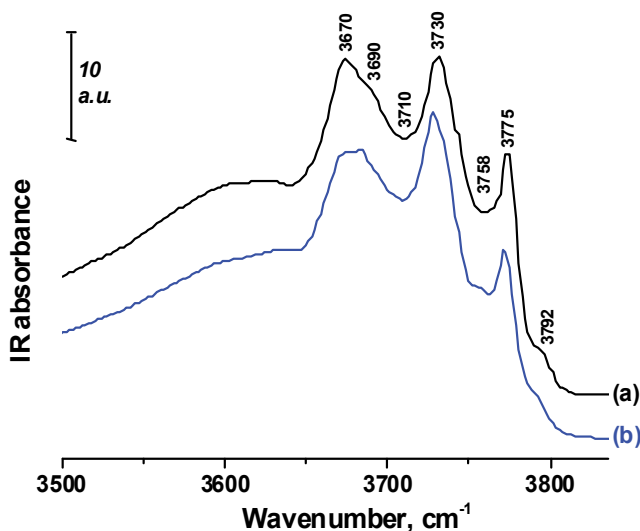


Fig. 2. FTIR spectra of surface hydroxyl groups of γ - Al_2O_3 (a) and 3% $\text{Al}_2\text{O}_3/\gamma$ - Al_2O_3 (b). The samples were calcined and outgassed at 500 °C

However, the formation of aluminum oxide compounds having their own surface OH groups ($\text{Al}_2\text{O}_3/\gamma\text{-Al}_2\text{O}_3$) resulted in substantial changes in the adsorption and acidic properties of the $\gamma\text{-Al}_2\text{O}_3$ surface. Thus, investigation of the sorption of chloride complexes of platinum (IV) on the modified $\gamma\text{-Al}_2\text{O}_3$ showed a 1.5-fold increase in the sorption capacity and an increased strength of the metal complex-support interaction (Mironenko et al., 2009).

According to FTIR spectroscopy of adsorbed CO (Fig. 3, Table 3), the anchoring of aluminum oxide compounds on the surface of initial $\gamma\text{-Al}_2\text{O}_3$ support decreased the concentration of weak Lewis acid sites with a.b. $\nu_{\text{CO}} = 2191 \text{ cm}^{-1}$ (regular defects of the alumina surface including the octahedral aluminum ion) without changes in the concentration of other types of Lewis acid sites.

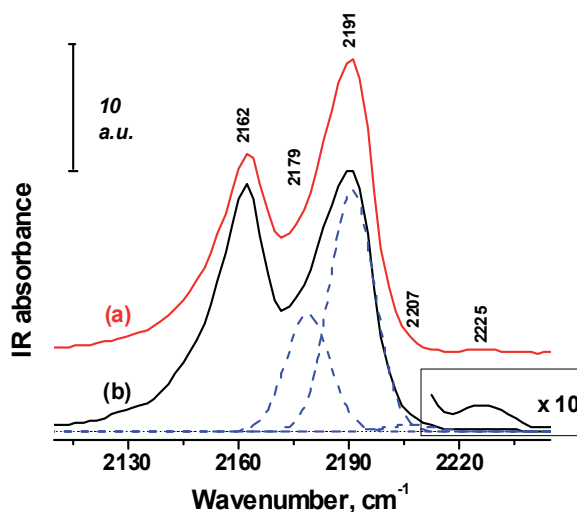


Fig. 3. FTIR spectra of CO adsorbed at $-196 \text{ }^\circ\text{C}$ and a CO pressure of 4 mbar: (a) $\gamma\text{-Al}_2\text{O}_3$, (b) $3\%\text{Al}_2\text{O}_3/\gamma\text{-Al}_2\text{O}_3$. The dashed line shows the deconvolution of spectrum (b) into its components. Inset: portion of spectrum (b) magnified 10 times

Sample	Lewis acid site concentration, $\mu\text{mol/g}$				
	2179 cm^{-1}	2191 cm^{-1}	2207 cm^{-1}	2225 cm^{-1}	Σ
$\gamma\text{-Al}_2\text{O}_3$	155	360	8	3	526
$3\%\text{Al}_2\text{O}_3/\gamma\text{-Al}_2\text{O}_3$	155	330	7	2	494

Table 3. Concentrations of Lewis acid sites characterized by different absorption bands in the FTIR spectrum of adsorbed CO

A decrease in the surface acidity revealed by FTIR spectroscopy of adsorbed CO is in good agreement with the results of catalytic testing (Fig. 4). Alumina samples before and after modifying were compared in a model reaction of 1-hexene double-bond isomerization, which is sensitive to amount and strength of Lewis acid sites. Although the reaction conditions radically differ from conditions of spectral measurements, the observed decrease in 1-hexene conversion can be predicted and interpreted using FTIR spectroscopy data.

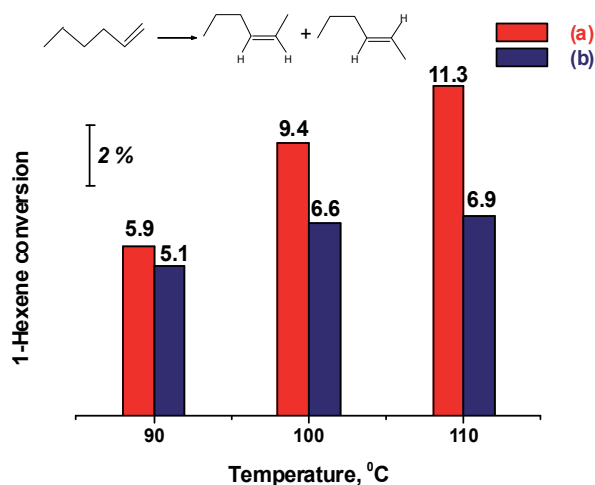


Fig. 4. Temperature dependence of the 1-hexene conversion: (a) γ - Al_2O_3 , (b) 3% $\text{Al}_2\text{O}_3/\gamma$ - Al_2O_3 . Reaction conditions: atmospheric pressure, $T = 90$ - 110 °C, He : C_6H_{12} molar ratio 3.3

3.1.2.2 Modifying the functional cover of the γ - Al_2O_3 surface at hydrothermal treatment

Hydrothermal treatment of γ - Al_2O_3 is commonly used for alteration of the porous structure parameters (Chertov et al., 1982). Our study demonstrated that this technique is efficient for controlling the state of the oxide surface. Hydrothermal treatment of γ - Al_2O_3 was carried out in a temperature range of 50-200 °C with the treatment time varying from 0.5 to 12 h. This produced a hydroxide phase of boehmite $\text{AlO}(\text{OH})$ on the γ - Al_2O_3 surface, which amount can be readily controlled by the treatment conditions. After hydrothermal treatment, the samples were calcined at 550 °C to reduce the oxide phase.

The FTIR spectroscopic examination revealed the hydrothermal treatment effect on the concentration and ratio of functional groups on the γ - Al_2O_3 surface. Figure 5 shows FTIR spectra of the surface hydroxyl cover of initial γ - Al_2O_3 and γ - Al_2O_3 subjected to hydrothermal treatment at various temperatures with subsequent calcination at 550 °C. The quantitative analysis of FTIR spectroscopy data (Fig. 5 and Table 1) showed changes in the relative content of different surface OH groups of γ - Al_2O_3 with elevation of hydrothermal treatment temperature. This modifying technique was found to increase the fraction of low-frequency bridging hydroxyl groups ($\nu_{\text{OH}} = 3710$ - 3670 cm^{-1}) from 50 to 70% of all OH groups and decrease the content of terminal hydroxyl groups ($\nu_{\text{OH}} = 3790$ - 3760 cm^{-1}) and especially the bridging group $\text{Al}^{\text{VI}}(\text{OH})\text{Al}^{\text{VI}}$ ($\nu_{\text{OH}} = 3730$ cm^{-1}). A decrease in the content of basic OH groups necessary for the anchoring of chloride platinum complexes decreased the adsorptivity of support with respect to $[\text{PtCl}_6]^{2-}$. The adsorption isotherms of $\text{H}_2[\text{PtCl}_6]$ on the support pretreated at different temperatures (Fig. 6) demonstrate that the difference in adsorptivity can be quite high (more than a twofold), and calcination restoring the oxide phase cannot restore the relative content of functional groups of the surface and its adsorption properties in aqueous solutions. The presented experimental data illustrate that conclusions on the state of the surface obtained by FTIR spectroscopy can reflect and explain the processes occurring at the solid-liquid interface, i.e. under real conditions of the catalyst synthesis.

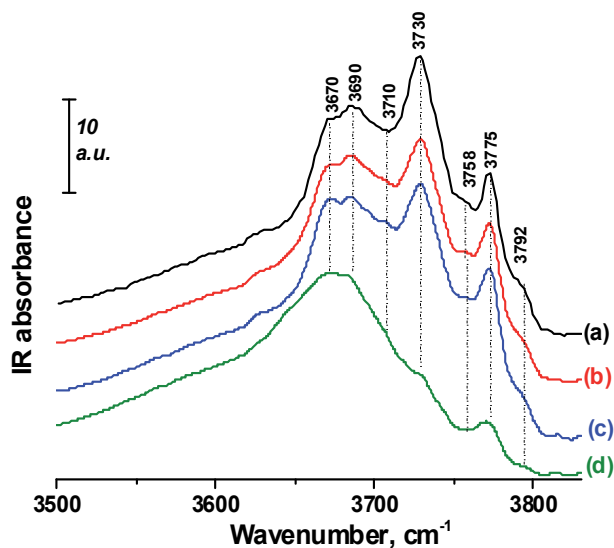


Fig. 5. FTIR spectra of hydroxyl cover of γ -Al₂O₃ (a) and γ -Al₂O₃ after hydrothermal treatment for 3 h at 150 (b), 180 (c) and 200 °C (d). The samples were calcined and outgassed at 500 °C

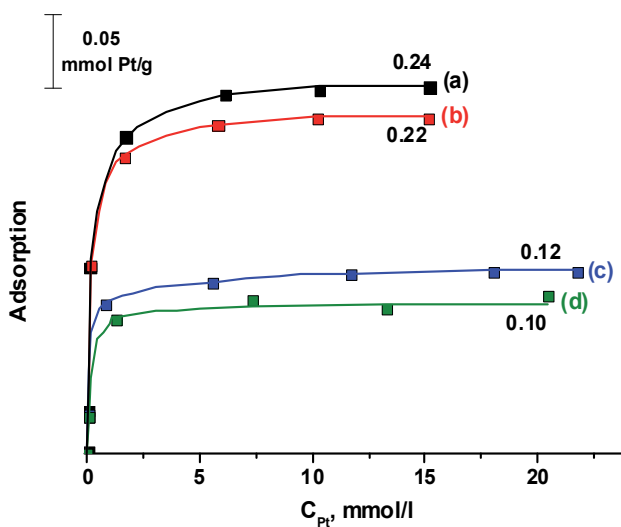


Fig. 6. Isotherms of H₂[PtCl₆] adsorption from aqueous solutions on γ -Al₂O₃ (a) and γ -Al₂O₃ after hydrothermal treatment for 3 h at 150 (b), 180 (c) and 200 °C (d) followed by heat treatment at 550 °C

Analysis of the FTIR spectra of adsorbed CO shows (Table 2) that introduction of the hydrothermal treatment step increases the concentration of all Lewis acid site types: weak (2180 and 2190 cm⁻¹), medium strength (2205 cm⁻¹), and strong (2225 cm⁻¹). The obtained result is important for application of this modifying method in the synthesis of catalytic compositions for the reactions requiring the presence of acid sites.

Thus, the FTIR spectroscopy study demonstrated that the main effect of the proposed method for modifying of the alumina surface consists in changing the ratio of different type sites capable of anchoring the active component precursor, in particular, in diminishing the fraction of more basic OH groups capable of coordination binding of the complexes (the formation of inner sphere complexes). The conclusions based on FTIR spectroscopy data and concerning changes in the surface state able to affect the mechanisms of precursor-support interaction and strength of such interaction were supported by independent ^{195}Pt NMR study. ^{195}Pt MAS NMR can be used to acquire data on the composition of adsorbed complexes and their interaction with the surface (Shelimov et al., 1999, 2000). Among advantages of this method for investigation of platinum complexes is a wide overall range of chemical shift (ca. 15000 ppm). This allows a relatively simple identification of Pt (IV) complexes with different structure from their ^{195}Pt chemical shift, which is very sensitive to the ligand environment. Thus, substitution of a Cl^- ligand in $[\text{PtCl}_6]^{2-}$ by H_2O or OH^- produces chemical shifts by 500 and 660 ppm, respectively.

However, in the study of complexes adsorbed on the support surface, the ^{195}Pt NMR signals are observed only if octahedral symmetry of the complexes is retained or slightly distorted during the adsorption. Coordination anchoring of a complex on alumina, when one or several chloride ligands of $[\text{PtCl}_6]^{2-}$ are substituted by hydroxyl groups of the support (see equation (8)), is accompanied by a substantial decrease in intensity and broadening of the peaks; sometimes NMR signals are not detected. Such situation is observed at the adsorption of complexes on the unmodified $\gamma\text{-Al}_2\text{O}_3$. At a maximum possible concentration of a metal complex for the chemisorption (platinum content of 4.5 wt%), the spectrum has only a broad peak with low intensity in the region characterizing $[\text{PtCl}_6]^{2-}$ (Fig. 7(a)).

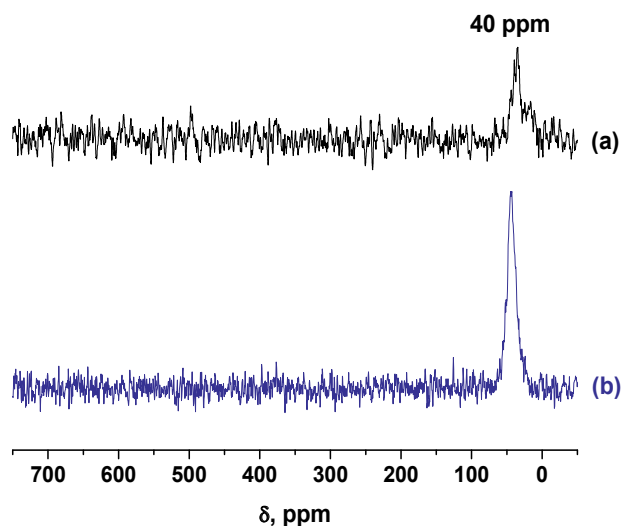


Fig. 7. ^{195}Pt MAS NMR spectra of 4.5%Pt/ $\gamma\text{-Al}_2\text{O}_3$ (unmodified support) (a) and 2.0%Pt/ Al_2O_3 with modified support (hydrothermal treatment at 180 °C, 3 h) (b)

This fact agrees with the diffuse reflectance electron spectroscopy and EXAFS examination of adsorbed complexes (Belskaya et al., 2008, 2011) showing that platinum on the $\gamma\text{-Al}_2\text{O}_3$ surface is mainly a component of the hydrolyzed coordinatively anchored complexes.

Meanwhile, in the case of modified support (Fig. 7(b)), there is an intense peak in the spectrum even at a two times lower platinum content corresponding to chloride complex $[\text{PtCl}_6]^{2-}$. Hence, anchoring of the complex does not produce noticeable changes in its chemical composition; moreover, there is a considerable decrease in the contribution of coordination binding with the surface involving OH groups of the support. Electrostatic interaction of a metal complex with the modified support with respect to equation (7) seems to prevail here. In addition, temperature-programmed reduction followed by chemisorption of H_2 and CO probe molecules was used to confirm that a decrease in the bond strength between precursor and support decreases the reduction temperature of adsorbed platinum species and diminishes the dispersion of supported particles by a factor of more than 3.

3.1.2.3 The effect of $\gamma\text{-Al}_2\text{O}_3$ modifying with silica on acid-base properties of the surface

Due to its high thermal stability, alumina modified with silica is a promising support for exhaust neutralization catalysts. Acid-base properties of the developed composition can be optimized by means of FTIR spectroscopy of adsorbed probe molecules. Composition of the support was varied by changing the silica concentration from 1.5 to 10 wt%. The modifying SiO_2 compound was formed in the pore space of $\gamma\text{-Al}_2\text{O}_3$ support during thermal decomposition of preliminarily introduced tetraethoxysilane $\text{Si}(\text{OC}_2\text{H}_5)_4$.

Figure 8 shows FTIR spectra in the region of OH group stretching vibrations of the aluminum oxide samples modified with silica in comparison with the spectrum of initial $\gamma\text{-Al}_2\text{O}_3$. The spectra of all modified oxides show a decrease in intensity of absorption bands corresponding to OH groups of the bridging and terminal types as compared to initial $\gamma\text{-Al}_2\text{O}_3$. The additional absorption bands appear at $3740\text{-}3745\text{ cm}^{-1}$, their intensity growing with silicon content of the sample. The band at 3745 cm^{-1} can be assigned to the terminal $\text{Si}(\text{OH})$ groups.

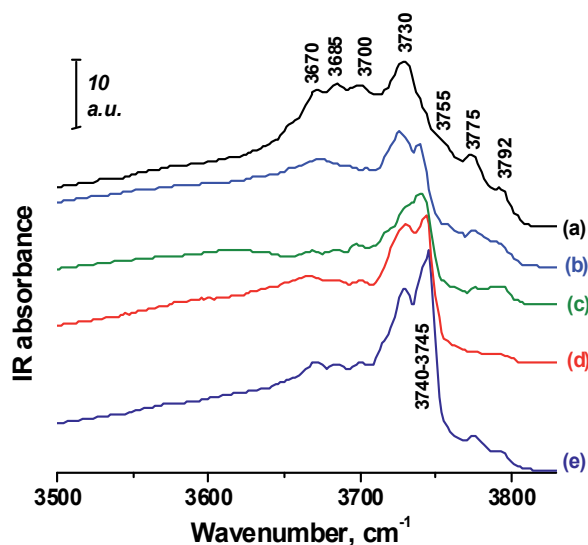


Fig. 8. FTIR spectra of hydroxyl groups for $\gamma\text{-Al}_2\text{O}_3$ calcined at $550\text{ }^\circ\text{C}$ (a) and of 1.5% $\text{SiO}_2/\gamma\text{-Al}_2\text{O}_3$ (b), 5% $\text{SiO}_2/\gamma\text{-Al}_2\text{O}_3$ (c), 7% $\text{SiO}_2/\gamma\text{-Al}_2\text{O}_3$ (d), 10% $\text{SiO}_2/\gamma\text{-Al}_2\text{O}_3$ (e) calcined at $450\text{ }^\circ\text{C}$. The samples were outgassed at $450\text{ }^\circ\text{C}$

Adsorption of CO on γ -Al₂O₃ at -196 °C results in the shift of OH bands with ν_{OH} 3700 and 3775 cm⁻¹ to the lower frequency region due to perturbation of OH stretch by hydrogen bonding. Aluminum oxides have no Brønsted acidity according to the minor shift of OH stretching vibration ($\Delta\nu_{\text{OH/CO}}$) by 120-130 cm⁻¹ (Maache et al., 1993; Paze et al., 1997). A large shift of OH stretching vibrations for the silicon-containing samples with $\Delta\nu_{\text{OH/CO}}$ equal to 240-290 cm⁻¹ indicates the formation of strong Brønsted acid sites on the sample surface. As demonstrated by Crépeau et al. (Crépeau et al., 2006), high acidity for amorphous silica-alumina can be shown by free silanol groups located nearby an Al atom. Acidity of OH groups at 3740 cm⁻¹ of the 10% SiO₂/Al₂O₃ sample approaches the acidity of bridged Si(OH)Al groups in zeolites with the band at 3610 cm⁻¹ according to the value of the low frequency shift of OH vibrations with adsorbed CO ($\Delta\nu_{\text{OH/CO}} = 300$ cm⁻¹).

For all tested systems, the spectrum of adsorbed CO has a.b. with $\nu_{\text{CO}} = 2158$ -2163 cm⁻¹ attributed to CO hydrogen-bonded with hydroxyl groups, and a.b. with $\nu_{\text{CO}} = 2130$ -2135 cm⁻¹ related with absorption of physisorbed CO. Besides, for all silicon-containing systems, there is a.b. with $\nu_{\text{CO}} \approx 2170$ cm⁻¹, which was assigned to CO hydrogen-bonded with Brønsted acid sites. Concentrations of these sites estimated from the intensity of a.b. with $\nu_{\text{CO}} \approx 2170$ cm⁻¹ are listed in Table 4. One may see that concentration of Brønsted sites increases with the silica content in the sample.

Sample	Specific surface area, m ² /g	$\Delta\nu_{\text{OH}}$, cm ⁻¹	Concentration of Brønsted acid sites, $\mu\text{mol/g}$
γ -Al ₂ O ₃	162	120-130	-
1.5% SiO ₂ /Al ₂ O ₃	120	240	14
5% SiO ₂ /Al ₂ O ₃	131	240	28
7% SiO ₂ /Al ₂ O ₃	179	240	30
10% SiO ₂ /Al ₂ O ₃	191	290	33

Table 4. Surface concentrations of Brønsted acid sites and specific surface area of silica promoted aluminum oxides

By using low-temperature CO adsorption, the concentration and strength of coordinatively unsaturated surface sites of the synthesized oxide systems were also estimated. The absorption bands and their intensities observed in the spectrum of γ -Al₂O₃ calcined at 550 °C (Table 5) are close to those reported in the previous Sections. Minor distinctions are related with the preparation procedures and texture characteristics of γ -Al₂O₃. The types of Lewis acid sites identified by CO adsorption on the surface of silicon-containing systems are close to the types of Lewis acid sites for γ -Al₂O₃. The concentration of super strong Lewis acid sites ($Q_{\text{CO}} = 59.5$ kJ/mol) decreases, whereas the concentration of strong Lewis acid sites ($Q_{\text{CO}} = 54$ kJ/mol) and medium strength Lewis acid sites ($Q_{\text{CO}} = 42.5$ kJ/mol) increases. The type of Lewis acid sites with $\nu_{\text{CO}} \approx 2230$ cm⁻¹ is typical of aluminosilicate structures and can be assigned to aluminum in a defect octahedral coordination, which is bonded to silicon atom in the second coordination sphere (Paukshtis, 1992).

Four types of base sites were identified on the alumina surface using deuteriochloroform as a probe molecule. The spectra are shown in Fig. 9; site strengths and concentrations are listed

Type of Lewis acid site	Super strong	Strong	Medium I	Medium II	Weak
$\nu_{\text{CO}}, \text{cm}^{-1}$	2240	2230	2220	2205	2190
$Q_{\text{CO}}, \text{kJ/mol}$	59.5	54	48.5	42.5	33
Samples	Concentration, $\mu\text{mol/g}$				
$\gamma\text{-Al}_2\text{O}_3$	0.4	1	8	6	300
1.5% $\text{SiO}_2/\text{Al}_2\text{O}_3$	0.3	5	4	22	330
5% $\text{SiO}_2/\text{Al}_2\text{O}_3$	-	6	4	15	290
7% $\text{SiO}_2/\text{Al}_2\text{O}_3$	-	7	4	18	300
10% $\text{SiO}_2/\text{Al}_2\text{O}_3$	-	12	4	17	320

Table 5. Types and concentrations of Lewis acid sites according to FTIR spectroscopy of adsorbed CO

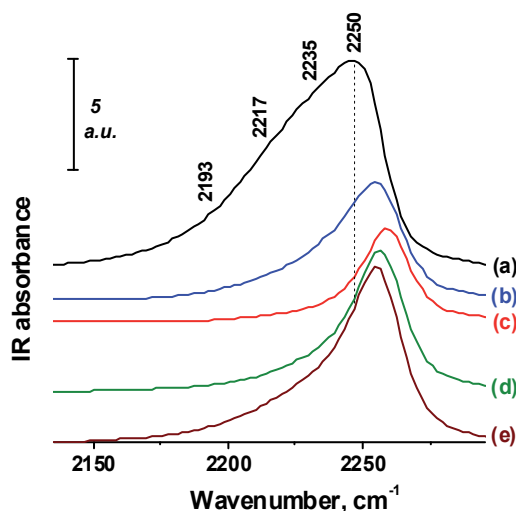


Fig. 9. FTIR spectra of adsorbed deuteriochloroform on $\gamma\text{-Al}_2\text{O}_3$ (a) and aluminum oxides modified with 1.5% (b), 5% (c), 7% (d), and 10% (e) of SiO_2

in Table 6. Strong base sites of alumina are characterized by a.b. with ν_{CD} 2193 and 2217 cm^{-1} , which correspond to the calculated PA values of 942 and 915 kJ/mol . The band at 2235 cm^{-1} corresponds to medium-strength base sites, whereas the band at 2250 cm^{-1} is attributed to weak base sites. Paukshtis (Paukshtis, 1992) hypothesized that the strong and medium-strength base sites are bridging oxygen atoms (Al–O–Al), whereas the weak sites are oxygen atoms of OH groups (Al–OH). The introduction of 1.5–5% SiO_2 results in disappearance of super strong base sites and an abrupt decrease in the concentration of other types of base sites, which can be related with sequential blocking of the surface by silica. The introduction of 7–10% SiO_2 increases the concentration of strong and medium strength base sites, which evidences the formation of a new surface phase, probably aluminosilicate one. This phase blocks only partially the surface of initial alumina. All the samples modified with silica have high-frequency a.b. of adsorbed deuteriochloroform at 2255–2258 cm^{-1} characterizing the sites which basicity is close to that of silica gel OH groups.

Type of base site	Super strong	Strong	Medium	Weak I	Weak II
$\Delta\nu_{CD}$, cm^{-1}	72	48-43	30-23	15	10-7
PA, kJ/mol	942	915-908	885-857	839	
Samples	Concentration, $\mu\text{mol/g}$				
$\gamma\text{-Al}_2\text{O}_3$	48	130	163	210	
1.5% $\text{SiO}_2/\text{Al}_2\text{O}_3$	-	38	74	-	570*
5% $\text{SiO}_2/\text{Al}_2\text{O}_3$	-	-	21	-	560*
7% $\text{SiO}_2/\text{Al}_2\text{O}_3$	-	26	56	-	730*
10% $\text{SiO}_2/\text{Al}_2\text{O}_3$	-	80	124	-	700*

Table 6. Types and concentrations of base sites according to FTIR spectroscopy of adsorbed CDCl_3 . * The concentration may be overrated due to close proximity of the band of adsorbed and physisorbed deuteriochloroform

Thus, Section 3.1 demonstrated the conventional approaches employed in FTIR spectroscopy for investigation of functional groups on the alumina surface. Original methods for modifying of this most popular support were reported. Applicability of FTIR spectroscopy for estimating the effect of modifying on the surface acid-base properties and optimizing the composition of surface sites was shown. Thus, FTIR spectroscopy in combination with other methods can explain changes in adsorption and catalytic characteristics and predict the behavior of oxide surface under real conditions of catalyst synthesis and testing.

3.2 State of palladium in Pd/SZ catalysts

Sulfated zirconia (SZ) promoted with noble metals is a very effective catalyst for isomerization of alkanes due to its high activity at low temperatures and high selectivity of isomers formation (Song & Sayari, 1996). Information on the state of metal in isomerization catalyst is quite topical. For example, metallic platinum or palladium improve the dehydrogenating capacity of the catalyst, which affects the formation of isoalkanes and enhance the production of atomic hydrogen which is necessary for the removal of coke precursors (Vera et al., 2002, 2003). It should be noted that state of the metal is determined to a great extent by the conditions of oxidative and reductive treatment of catalysts before the reaction. Thus, the challenge is to find the optimal pretreatment temperatures allowing the formation of acid sites and retaining the metallic function.

A convenient method for solving this problem is FTIR spectroscopy of adsorbed CO molecules. In our earlier work (Belskaya et al., 2010), this method was used for studying the state of supported palladium particles in Pd/SZ under different conditions of catalyst pretreatment. In the experiment, the catalyst treatment in various gas media (air, hydrogen) and at different temperatures (100-400 °C) was performed directly in a spectrometer cell. CO adsorption was carried out over a pressure range of 0.1 to 10 mbar at room temperature.

IR spectra of CO adsorbed on the surface of Pd/SZ pretreated under different conditions are shown in Fig. 10. The spectrum of CO adsorbed on the sample that was activated in air shows several a.b. located at 1935, 2030, 2090, 2125, 2150, 2170 and 2198 cm^{-1} (Fig. 10(a)). The

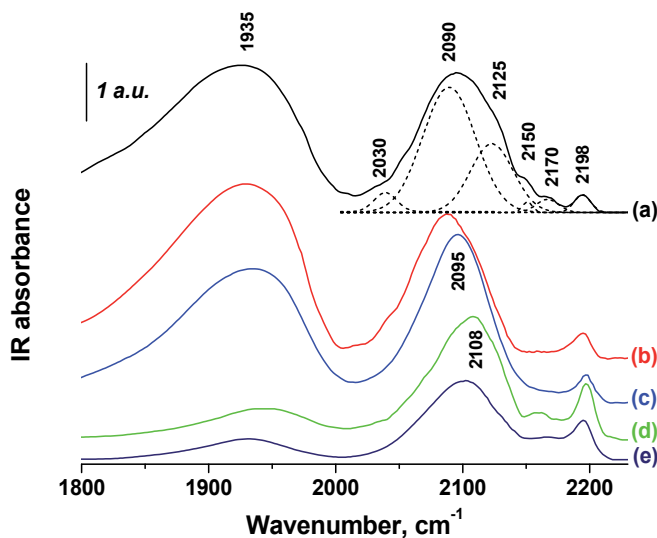


Fig. 10. FTIR spectra of CO adsorbed on Pd/SZ (25 °C; 10 mbar) after oxidation in air at 400 °C (a), after reduction in hydrogen at 150 °C (b), 200 °C (c), 300 °C (d) and 350 °C (e). All spectra are background subtracted. Spectra were offset for clarity

sharp band at 2090 cm^{-1} and the broad band around 1935 cm^{-1} are ascribed to terminal and bridge-coordinated CO on Pd^0 , respectively (Sheppard & Nguyen, 1978). The bands at 2030, 2125 and 2150 cm^{-1} can be attributed, respectively, to bridged CO complex with Pd^+ and linear CO complexes with Pd^+ and Pd^{2+} isolated ions; the band at 2170 cm^{-1} can be assigned to CO linearly adsorbed on Pd^{2+} in PdO species (Hadjiivanov & Vayssilov, 2002). Besides, the band at 2196–2198 cm^{-1} is present in all spectra and may be assigned to CO adsorption on Zr^{4+} ions (Morterra et al., 1993). The highest intensity of this a.b. is observed for the sample reduced in H_2 at 300 °C. This fact confirms studies concerning the necessity of high-temperature reduction of SZ to obtain the greatest Lewis acidity of the catalyst after metal incorporation.

According to FTIR spectroscopy data, in oxidized Pd/SZ sample a part of palladium is presented as Pd^0 (high intensities of a.b. at 1935 and 2090 cm^{-1}). Supposedly, the formation of metallic palladium can be caused by evacuation at high temperatures during the pretreatment in IR cell. This assumption was confirmed in a special experiment by means of UV-vis spectroscopy (Belskaya et al., 2010). Pd/SZ catalyst after the oxidation is characterized by a.b. at 20500, 34000, 39500 and 46000 cm^{-1} . The a.b. at 20500 and 39500 cm^{-1} can be attributed, respectively, to d–d transition and ligand-to-metal charge transfer of Pd^{2+} ions in D_{4h} oxygen environment (Rakai et al., 1992). Evacuation at 300 °C decreases the concentration of Pd^{2+} ions in PdO (a decrease in the intensity of a.b. at 20500 cm^{-1} was observed). This experiment clearly demonstrates that a possible effect of pretreatment conditions on the state of catalyst surface in IR spectroscopy study (in this case, the effect of evacuation at elevated temperatures) should be taken into account.

In the FTIR spectra of CO adsorbed on Pd/SZ samples that were reduced at 150–200 °C (Fig. 10(b), (c)), the a.b. at 1930 and 2090–2095 cm^{-1} attributed to metallic palladium dominate. Bands at 2125–2170 cm^{-1} , assigned to CO adsorbed on oxidized Pd ions, almost

vanish. The differences between spectra of adsorbed CO on Pd/SZ samples reduced at 200 and 300–350 °C are dramatic (Fig. 10(c)–(e)). An increase in the reduction temperature suppresses the bridge coordinated CO IR bands, decreases the intensity and slightly shifts the stretching frequency of linearly adsorbed CO to higher wavenumbers. Such shift occurs when CO is chemisorbed on the sulfur-saturated Pd surface (Guerra, 1969; Jorgensen & Madix, 1985). So, appearance of the band at 2105–2108 cm^{-1} can be attributed to linear CO complexes with palladium in an electron-deficient state with high S-coverage. According to (Jorgensen & Madix, 1985; Ivanov & Kustov, 1998) a possible reason for the decrease in concentration of bridging CO is the partial covering of Pd surface by sulfur species. Thus, we suppose that low CO chemisorption capacity of Pd⁰ atoms in Pd/SZ samples reduced at high temperatures is due to partial sulfur coating of the metal surface. Therewith, new a.b. at 2135 and 2160 cm^{-1} are observed in the spectra of CO adsorbed on Pd/SZ samples that were reduced at 300–350 °C. These bands appear on admission of 0.1 mbar CO and grow in intensity with increasing CO pressure (Belskaya et al., 2010); they are attributed to CO complexes with oxidized Pd⁺ and Pd²⁺ species, probably in Pdⁿ⁺-S²⁻ sites (Vazquez-Zavala et al., 1994).

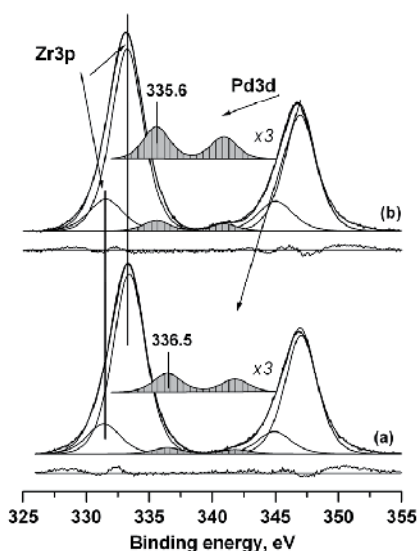


Fig. 11. Zr3p and Pd3d core-level spectra of the samples after oxidation in air at 400 °C (a) and after reduction in hydrogen at 300 °C (b). For clear identification, Pd3d spectra are multiplied by 3

IR spectroscopic data on the state of supported palladium in Pd/SZ after oxidation and reduction were compared with X-ray photoelectron spectroscopy (XPS) data for the same samples. Figure 11 shows the X-ray photoelectron spectra in the spectral region of Zr3p and Pd3d core-level lines. The difference curves between experimental spectrum and the envelope of the fit are presented under each spectrum. After calcination in air at 400 °C (Fig. 11(a)), palladium spectrum can be described by one doublet line with binding energy (E_b) of Pd3d_{5/2} 336.5 eV. Such value of E_b is close to that for the oxidized palladium species in palladium oxide PdO (Brun et al., 1999; Pillo et al., 1997). After the action of H₂ (Fig. 11(b)), Pd3d spectrum gives a peak with E_b (Pd3d_{5/2}) 335.6 eV, which is assigned to

small metal particles. Bulk metal palladium is known to have E_b of $Pd3d_{5/2}$ at 335.2 eV (Brun et al., 1999; Otto et al., 1992). In our case, a small increase of E_b is likely to originate from the size effect (Mason, 1983). The formation of bulk palladium sulfide was not observed because the corresponding value of E_b of $Pd3d_{5/2}$, which is about 337.2 eV (Chaplin et al., 2007), was not detected. Thus, changes of the metal surface after high temperature reduction in the H_2 atmosphere, which are demonstrated by the FTIR spectra, have no significant effect on the electronic state of metal particles: according to XPS data, Pd remains in the metallic state. H_2S resulting from sulfate reduction blocks the active metal surface, most likely without formation of PdS in large amounts. However, it cannot be unambiguously concluded from Pd3d and S2p core-level spectra whether the sulfide film forms on the palladium surface after reduction or not.

For assessment of the state of palladium, we also used a model reaction which is commonly employed to test the metallic function of catalysts – low-temperature (50-90 °C) hydrogenation of benzene. There was a clear effect of pretreatment conditions on the conversion of benzene to cyclohexane. Pd/SZ catalyst reduced at the temperature corresponding to metal formation (according to TPR data) demonstrated the highest conversion. In the case of reduction temperature above 120 °C, before the catalytic test H_2S was detected in the exhaust gases, and poisoning of the metal function was observed. Thus, in Pd/SZ catalysts, after the reduction treatment at 300 °C, hydrogenation activity of palladium is strongly inhibited. However, the constant activation energy and complete recovery of hydrogenation activity under mild regeneration conditions (Belskaya et al., 2010) indicate that the metal surface is only blocked by sulfate decomposition products without their chemical interaction with palladium.

Thus, FTIR spectroscopy of adsorbed CO used to examine the state of supported palladium in Pd/SZ catalysts provided data that agree well with the data obtained by independent methods – XPS and a model reaction for testing the metal function. Analysis of changes in the state of surface revealed by FTIR spectroscopy can be useful for explaining the adsorption and catalytic properties as well as for optimizing the conditions of thermal stages during catalyst synthesis.

3.3 Alumina promoted Pt/SO_4^{2-} - ZrO_2

The approaches for controlling the SO_4^{2-} - ZrO_2 acidity are of great practical importance, as they can change the catalyst activity and selectivity in various acid-catalyzed reactions (Hua et al., 2000; Lavrenov et al., 2007; Zalewski et al., 1999). In our works (Kazakov et al., 2010, 2011, 2012), we optimized the acidic and hydrogenation properties of bifunctional Pt/SO_4^{2-} - ZrO_2 catalyst for the one-step hydroisomerization of benzene-containing fractions, which is intended for elimination of benzene in gasoline while minimizing the octane loss. The introduction of alumina into the catalyst was suggested as the main modifying procedure. IR spectroscopy allowed us to elucidate the effect of catalyst composition on the properties of surface functional groups, to reveal the role of alumina in the formation of metal and acid sites, and provided a detailed characterization of the surface properties of optimal hydroisomerization catalyst. The work was performed with catalysts Pt/SO_4^{2-} - ZrO_2 (4.5 wt% SO_4^{2-}), Pt/SO_4^{2-} - ZrO_2 - Al_2O_3 , (3.1 wt% SO_4^{2-} and 67.8 wt% Al_2O_3) and Pt/Al_2O_3 . Samples were denoted as Pt/SZ, Pt/SZA and Pt/A, respectively. Platinum concentration was 0.3 wt%. We studied also the supports used for the catalyst synthesis (SZ, SZA and A,

respectively). The preparation procedure for supports and catalysts is reported in (Kazakov et al., 2010, 2011).

3.3.1 The effect of alumina introduction on the state of supported platinum

The formation of platinum sites and the state of metal in a finished catalyst strongly depend on the interaction of precursor with the surface groups of support. As it was shown earlier, the composition and amount of hydroxyl groups on the support surface play a significant role in the platinum compounds anchoring from a solution of $H_2[PtCl_6]$. Infrared spectra of the OH stretching region for SZ, SZA and A supports are shown in Fig. 12. The spectrum of sample SZ is represented by a.b. at 3651 cm^{-1} , which corresponds to bridging OH groups with acidic properties (Kustov et al., 1994; Manoilova et al., 2007). The FTIR spectrum of SZA sample has a.b. at 3772 and 3789 cm^{-1} assigned to terminal OH groups, and a.b. 3677 and 3728 cm^{-1} corresponding to bridging OH groups (Knözinger & Ratnasamy, 1978). The presence of these types of OH groups is typical for the $\gamma\text{-Al}_2\text{O}_3$ surface (sample A in Fig. 12).

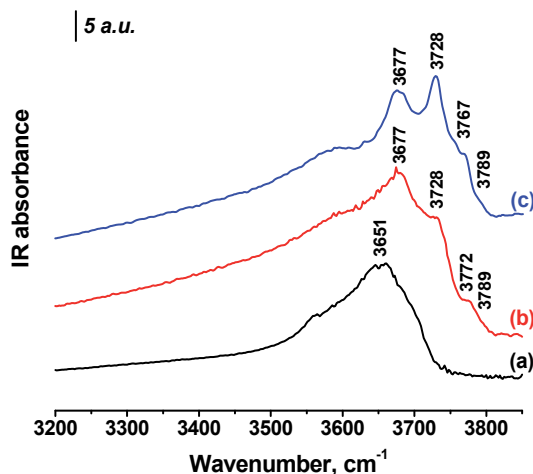


Fig. 12. FTIR spectra of the catalyst supports in the OH stretching region: SZ (a), SZA (b), A (c). Spectra were offset for clarity. Prior to recording, the samples were evacuated at $400\text{ }^\circ\text{C}$

Significant distinctions in the hydroxyl cover suggest different mechanisms of the interaction between metal complex and support. Indeed, the presence of only the hydroxyl groups with acidic properties on the SZ surface explains the absence of chemisorption anchoring of the anionic $[PtCl_6]^{2-}$ complex. After the introduction of 67.8 wt% alumina into sulfated zirconia sites for chloroplatinate ions sorption appear on the surface of mixed $SO_4^{2-}\text{-ZrO}_2\text{-Al}_2\text{O}_3$ support. However, the concentration of bridging $Al^{VI}(\text{OH})Al^{VI}$ groups (3728 cm^{-1}) that are most active in chloroplatinate anchoring, and terminal groups (3772 and 3789 cm^{-1}) on SZA support is lower than their concentration on the alumina surface, which causes a smaller fraction of complexes anchored by chemisorption (81% for SZA and 100% for A).

The reduction temperature of platinum species anchored on SZA support, which characterizes the strength of precursor – support interaction, also has a medium value.

According to TPR data, platinum reduction on SZ surface (sample Pt/SZ) in the absence of chemisorption interaction starts from 90 °C. However, in the samples with alumina this process shifts toward higher temperatures, and a maximum rate of hydrogen consumption is observed at 210 and 225 °C for Pt/SZA and Pt/A.

The state of supported platinum in finished catalysts after reduction in hydrogen was investigated by FTIR spectroscopy of adsorbed CO (Fig. 13). The band with ν_{CO} 2200-2208 cm^{-1} , which is present in all the spectra, corresponds to CO complexes with Lewis acid sites of the catalysts (Morterra et al., 1993). The spectrum of Pt/A sample shows a.b. with ν_{CO} 2065 cm^{-1} corresponding to stretching vibrations of CO linearly adsorbed on Pt^0 , and a broad band at 1830 cm^{-1} characterizing the bridging CO species on Pt^0 (Apesteguia et al., 1984; Kooh et al., 1991). After CO adsorption on Pt/SZ, there appear bands at 2100 and 2150 cm^{-1} , which have close intensities and correspond to linear CO complexes with Pt^0 and $\text{Pt}^{\delta+}$, respectively (Grau et al., 2004; Morterra et al., 1997). In the case of Pt/SZA, the frequencies of CO (a.b. 2085 cm^{-1}) adsorbed on metal platinum particles are intermediate in comparison with frequencies for samples Pt/A and Pt/SZ.

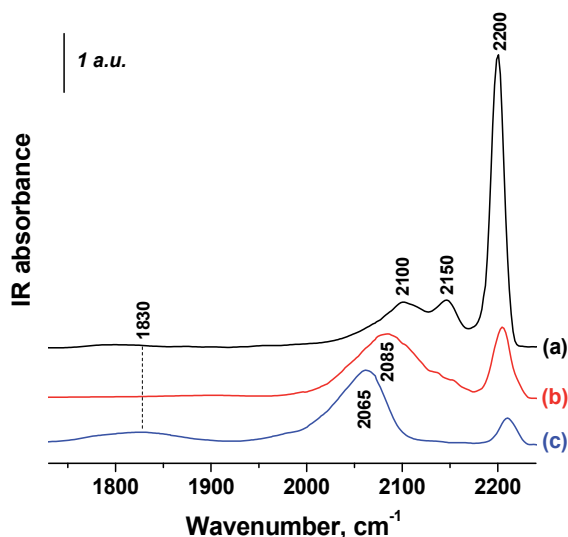


Fig. 13. FTIR spectra of CO (25 °C; 10 mbar) adsorbed on the catalysts: Pt/SZ (a), Pt/SZA (b), Pt/A (c). Prior to recording, the samples were reduced in hydrogen flow at 300 °C and then evacuated at 500 °C

In comparison with Pt/SZ, the band corresponding to CO - Pt^0 complexes for samples Pt/SZA and Pt/SZ is shifted toward higher frequencies by 20 and 35 cm^{-1} , respectively. Such upward shift of ν_{CO} was also observed for Pd/SZ samples (Section 3.2) and can be related to the presence of sulfur species on the metal surface (Apesteguia et al., 1984, 1987; J.R. Chang & S.L. Chang, 1998). These sulfur species are formed both at the stage of oxidative treatment and during the reduction; they can poison the metal partially or completely (Dicko et al., 1994; Iglesia et al., 1993). As a result, Pt/SZ demonstrates very poor hydrogenation activity and does not chemisorb hydrogen (Table 7). Pt/SZA sample has an enhanced hydrogenation activity in comparison with Pt/SZ; nevertheless, it is lower than that observed for Pt/A.

Catalyst	H/Pt	Benzene conversion, %
Pt/SZ	0.00	1.8
Pt/SZA	0.44	40.7
Pt/A	0.85	97.1

Table 7. Hydrogen chemisorption and benzene hydrogenation over Pt/SZ, Pt/SZA and Pt/A catalysts. Benzene hydrogenation conditions: 200 °C, 0.1 MPa, weight hourly space velocity 4.0 h⁻¹, H₂ : C₆H₆ molar ratio 8

The increasing accessibility of platinum sites for adsorption and catalytic reaction in a series Pt/SZ < Pt/SZA < Pt/A can be attributed both to a decrease in the content of sulfur compounds in the catalyst upon dilution of sulfated zirconia with alumina, and to a higher resistance to poisoning of more disperse supported platinum crystallites produced by chemisorption anchoring of a precursor (J.R. Chang et al., 1997).

3.3.2 The effect of alumina introduction on the acidic properties of Pt/SO₄²⁻-ZrO₂

The strength and concentration of acid sites of catalysts Pt/SZ, Pt/SZA and Pt/A reduced at 300 °C were estimated from FTIR spectra of adsorbed CO and pyridine molecules. After CO adsorption, spectra of all the samples had the a.b. 2180-2208 cm⁻¹ corresponding to CO complexes with Lewis acid sites of different strength, a.b. 2168-2171 cm⁻¹ assigned to CO complexes with Brønsted acid sites, a.b. 2160-2162 cm⁻¹ characterizing CO complexes with hydroxyl groups having weak acidic properties, and a.b. 2133-2148 cm⁻¹ corresponding to the adsorption of physisorbed CO molecules. In all cases, only the medium strength (a.b. with ν_{CO} 2204-2208 cm⁻¹ for Pt/SZ, 2202-2208 cm⁻¹ for Pt/SZA, and 2204 cm⁻¹ for Pt/A) and weak Lewis acid sites (a.b. with ν_{CO} 2194, 2188, 2180 cm⁻¹ for Pt/SZ, and 2192 cm⁻¹ for Pt/SZA and Pt/A) were detected. After the pyridine adsorption, we observed a.b. corresponding to complexes of pyridine molecules with Brønsted acid sites (1544 cm⁻¹) and Lewis acid sites (1445 cm⁻¹).

Data on the concentration of Lewis acid sites (calculated from the integral intensities of adsorbed CO a.b.) and Brønsted acid sites (calculated from the integral intensities of adsorbed pyridine a.b.) for the tested catalysts are listed in Table 8. The Pt/SZ catalyst has the highest content both of Lewis and Brønsted acid sites. For sample Pt/A, Brønsted acid sites able to protonate pyridine were not observed. Pt/SZA has intermediate position with respect to its acidic properties. The Brønsted acid sites content in this sample is 3.5 times lower as compared to Pt/SZ, which virtually corresponds to a decrease of ZrO₂ amount in its composition (29.1 against 95.5 wt%, respectively). The total amount of Lewis acid sites in comparison with Pt/SZ decreases twofold. However, the ratio of medium strength and weak Lewis acid sites for Pt/SZA sample corresponds to the ratio revealed for Pt/SZ. Thus, the introduction of alumina into Pt/SZ system decreases the amount of Lewis and Brønsted acid sites, which is related to the effect of its dilution with a component having a lower intrinsic acidity. The observed nonadditive change in the concentration of acid sites, in particular Lewis acid sites, may be caused by interaction of the system components, which was noted earlier (Kazakov et al., 2010).

Catalyst	ν_{CO} , cm ⁻¹	Lewis acid sites, $\mu\text{mol/g}$	Lewis acid sites, $\mu\text{mol/g}$		Total Lewis acid sites, $\mu\text{mol/g}$	Total Brønsted acid sites, $\mu\text{mol/g}$
			medium	weak		
Pt/SZ	2208	25	115	530	645	32
	2204	90				
	2194	260				
	2188	240				
	2180	30				
Pt/SZA	2208	15	60	250	310	9
	2202	45				
	2192	250				
Pt/A	2204	29	29	350	379	0
	2192	350				

Table 8. Acidic properties of Pt/SZ, Pt/SZA and Pt/A catalysts according to FTIR spectroscopy of adsorbed CO and pyridine. Prior to recording, samples were reduced in hydrogen flow at 300 °C and then evacuated at 500 °C

Results of FTIR spectroscopic study are in good agreement with the model acid-catalyzed reactions of n-heptane and cyclohexane isomerization. The introduction of alumina into Pt/SZ decreases the total catalyst activity in n-C₇H₁₆ isomerization, which shows up as increase of the temperature of 50% n-heptane conversion from 112 to 266 °C (Table 9). For isomerization of cyclohexane to methylcyclopentane, higher operating temperatures are thermodynamically more favorable (Tsai et al., 2011). As a result, Pt/SZA catalyst is more efficient for cyclohexane isomerization due to higher selectivity at higher temperatures (Table 10).

Catalyst	X n-C ₇ , %	t, °C	Iso-C ₇ yield, %	Selectivity to iso-C ₇ , %
Pt/SZ	50.0	112	43.3	86.5
Pt/SZA	50.0	266	47.1	94.2
Pt/A	12.9	300	6.3	47.0

Table 9. Isomerization of n-heptane over Pt/SZ, Pt/SZA and Pt/A catalysts. Reaction conditions: 1.5 MPa, weight hourly space velocity 4.0 h⁻¹, H₂ : n-C₇H₁₆ molar ratio 5. X - conversion

Catalyst	200 °C			275 °C		
	X CH, %	MCP yield, %	Selectivity to MCP, %	X CH, %	MCP yield, %	Selectivity to MCP, %
Pt/SZ	70.0	57.1	81.7	91.8	26.2	29.6
Pt/SZA	4.4	4.4	99.3	74.4	69.6	93.7
Pt/A	-	-	-	0.2	0.0	-

Table 10. Isomerization of cyclohexane over Pt/SZ, Pt/SZA and Pt/A catalysts. Reaction conditions: 1.5 MPa, weight hourly space velocity 4.0 h⁻¹, H₂ : C₆H₁₂ molar ratio 5. X - conversion; CH - cyclohexane; MCP - methylcyclopentane

Thus, FTIR spectroscopy applied to investigation of Pt/SZA system proved to be a highly informative method, which allowed us to elucidate the role of alumina both in the formation of platinum sites and in the catalyst behavior in the acid-catalyzed reactions. Although state of the surface under conditions of FTIR spectroscopic examination strongly differ from its state upon contacting with aqueous solutions of metal complexes or in catalytic reactions, FTIR spectroscopy data on the state of supported platinum as well as on the nature and strength of acid sites can be used to optimize the composition of bifunctional catalyst Pt/SZA designed for hydroisomerization of benzene-containing fractions.

4. Conclusion

The possibilities of FTIR spectroscopy, in particular with the use of adsorbed CO, pyridine or deuteriochloroform probe molecules, for investigation of some model and industrially important supports and catalysts were demonstrated. The effect of chemical composition of a support (Al_2O_3 , $\text{Al}_2\text{O}_3\text{-SiO}_2$, $\text{SO}_4^{2-}\text{-ZrO}_2$, $\text{SO}_4^{2-}\text{-ZrO}_2\text{-Al}_2\text{O}_3$) and modification technique on the concentration and ratio of different types of OH groups and coordinatively unsaturated surface sites was shown.

Concentrations of the surface sites on supports before and after anchoring of the active metal component were compared to demonstrate a relation between composition of the functional surface groups, adsorption capacity of the support and strength of the interaction between metal complex precursor and support, and to identify the sites involved in anchoring of the active component. The impact of support nature and composition, conditions of oxidation and reduction treatments on the metal-support interaction and ratio of oxidized and reduced forms of supported metal (platinum or palladium) was revealed.

FTIR spectroscopy data for the examined catalytic systems were compared with the data of XPS, diffuse reflectance electron spectroscopy, H_2 and CO chemisorption for determination of supported metal dispersion, and temperature-programmed reduction as well as with the results of testing in the following catalytic reactions: double-bond isomerization of 1-hexene, hydrogenation of benzene and isomerization of n-heptane and cyclohexane.

5. Acknowledgment

This study was supported by the Russian Foundation for Basic Research, grant no. 09-03-01013.

6. References

- Apestequia, C.R., Brema, C.E., Garetto, T.F., Borgna, A., & Parera, J.M. (1984). Sulfurization of Pt/ $\text{Al}_2\text{O}_3\text{-Cl}$ Catalysts: VI. Sulfur-Platinum Interaction Studied by Infrared Spectroscopy. *Journal of Catalysis*, Vol.89, No.1, (September 1984), pp. 52-59, ISSN 0021-9517
- Apestequia, C.R., Garetto, T.F., & Borgna, A. (1987). On the Sulfur-Aided Metal-Support Interaction in Pt/ $\text{Al}_2\text{O}_3\text{-Cl}$ Catalysts. *Journal of Catalysis*, Vol.106, No.1, (July 1987), pp. 73-84, ISSN 0021-9517

- Baumgarten, E., Wagner, R., & Lentjes-Wagner, C. (1989). Quantitative Determination of Hydroxyl Groups on Alumina by IR Spectroscopy. *Fresenius Zeitschrift für Analytische Chemie*, Vol.334, No.3, (January 1989), pp. 246-251, ISSN 0016-1152
- Bel'skaya, O.B., Karymova, R.Kh., Kochubey, D.I., & Duplyakin, V.K. (2008). Genesis of the Active-Component Precursor in the Synthesis of Pt/Al₂O₃ Catalysts: I. Transformation of the [PtCl₆]²⁻ Complex in the Interaction between Chloroplatinic Acid and the γ -Al₂O₃ Surface. *Kinetics and Catalysis*, Vol.49, No.5, (September 2008), pp. 720-728, ISSN 0023-1584
- Belskaya, O.B., Danilova, I.G., Kazakov, M.O., Gulyaeva, T.I., Kibis, L.S., Boronin, A.I., Lavrenov, A.V., & Likholobov, V.A. (2010). Investigation of Active Metal Species Formation in Pd-Promoted Sulfated Zirconia Isomerization Catalyst. *Applied Catalysis A: General*, Vol.387, No.1-2, (October 2010), pp. 5-12, ISSN 0926-860X
- Belskaya, O.B., Duplyakin, V.K., & Likholobov, V.A. (2011). Molecular Design of Precursor in the Synthesis of Catalytic Nanocomposite System Pt-Al₂O₃. *Smart Nanocomposites*, Vol.1, No.2, pp. 99-133, ISSN 1949-4823
- Bocanegra, S.A., Castro, A.A., Guerrero-Ruíz, A., Scelza, O.A., & de Miguel, S.R. (2006). Characteristics of the Metallic Phase of Pt/Al₂O₃ and Na-Doped Pt/Al₂O₃ Catalysts for Light Paraffins Dehydrogenation. *Chemical Engineering Journal*, Vol.118, No.3, (May 2006), pp. 161-166, ISSN 1385-8947
- Bourikas, K., Kordulis, C., & Lycourghiotis, A. (2006). The Role of the Liquid-Solid Interface in the Preparation of Supported Catalysts. *Catalysis Reviews - Science and Engineering*, Vol.48, No.4, (December 2006), pp.363-444, ISSN 0161-4940
- Brun, M., Berthet, A., & Bertolini, J.C. (1999). XPS, AES and Auger Parameter of Pd and PdO. *Journal of Electron Spectroscopy and Related Phenomena*, Vol.104, No.1-3, (July 1999), pp. 55-60, ISSN 0368-2048
- Chang, J.R., Chang, S.L., & Lin, T.B. (1997). γ -Alumina-Supported Pt Catalysts for Aromatics Reduction: A Structural Investigation of Sulfur Poisoning Catalyst Deactivation. *Journal of Catalysis*, Vol.169, No.1, (July 1997), pp. 338-346, ISSN 0021-9517
- Chang, J.R., & Chang, S.L. (1998). Catalytic Properties of γ -Alumina-Supported Pt Catalysts for Tetralin Hydrogenation: Effects of Sulfur-Poisoning and Hydrogen Reactivation. *Journal of Catalysis*, Vol.176, No.1, (May 1998), pp. 42-51, ISSN 0021-9517
- Chaplin, B.P., Shapley, J.R., & Werth, C.J. (2007). Regeneration of Sulfur-Fouled Bimetallic Pd-Based Catalysts. *Environmental Science & Technology*, Vol.41, No.15, (June 2007), pp. 5491-5497, ISSN 0013-936X
- Chertov, V.M., Zelentsov, V.I., & Lyashkevich, B.N. (1982). Production of Finely Divided Boehmite Powder. *Journal of Applied Chemistry of the USSR*, Vol.55, pp. 2120-2122, ISSN 0021-888X
- Crépeau, G., Montouillout, V., Vimont, A., Mariey, L., Cseri, T., & Maugé F. (2006). Nature, Structure and Strength of the Acidic Sites of Amorphous Silica Alumina: An IR and NMR Study. *Journal of Physical Chemistry B*, Vol.110, No.31, (August 2006), pp. 15172-15185, ISSN 1520-6106
- Davydov, A. (2003). *Molecular Spectroscopy of Oxide Catalyst Surfaces*, John Wiley & Sons Ltd, ISBN 0-471-98731-X, Chichester, England

- Della Gatta, G., Fubini, B., Ghiotti, G., & Morterra, C. (1976). The Chemisorption of Carbon Monoxide on Various Transition Aluminas. *Journal of Catalysis*, Vol.43, Nos.1-3, (June 1976), pp. 90-98, ISSN 0021-9517
- Dicko, A., Song, X.M., Adnot, A., & Sayari, A. (1994). Characterization of Platinum on Sulfated Zirconia Catalysts by Temperature Programmed Reduction. *Journal of Catalysis*, Vol.150, No.2, (December 1994), pp. 254-261, ISSN 0021-9517
- Egorov, M.M. (1961). The Nature of the Surface of Catalytically Active Aluminum Oxide. *Proceedings of the Academy of Sciences of the USSR, Physical Chemistry Section*, Vol.140, Nos.1-6, (September-October 1961), pp. 697-700, ISSN 0271-5007
- Ghosh, A.K., & Kydd, R.A. (1985). Fluorine-Promoted Catalysts. *Catalysis Reviews – Science and Engineering*, Vol.27, No.4, (December 1985), pp. 539-589, ISSN 0161-4940
- Grau, J.M., Yori, J.C., Vera, C.R., Lovey, F.C., Condo, A.M., & Parera, J.M. (2004). Crystal Phase Dependent Metal-Support Interactions in Pt/SO₄²⁻-ZrO₂ Catalysts for Hydroconversion of n-Alkanes. *Applied Catalysis A: General*, Vol.265, No.2, (July 2004), pp. 141-152, ISSN 0926-860X
- Guerra, C.R. (1969). Infrared Spectroscopic Studies of CO Adsorption by Metals. The Effect of Other Gases in Adsorption. *Journal of Colloid and Interface Science*, Vol.29, No.2, (February 1969), pp. 229-234, ISSN 0021-9797
- Hadjiivanov, K.I., & Vayssilov, G.N. (2002). Characterization of Oxide Surfaces and Zeolites by Carbon Monoxide as an IR Probe Molecule, In: *Advances in Catalysis*, B.C. Gates, H. Knözinger, (Ed.), pp. 307-511, Academic Press, Inc, ISBN 0-12-007847-3, New York, The United States of America
- Hua, W., Xia, Y., Yue, Y., & Gao, Z. (2000). Promoting Effect of Al on SO₄²⁻/M_xO_y (M=Zr, Ti, Fe) Catalysts. *Journal of Catalysis*, Vol.196, No.1, (November 2000), pp. 104-114, ISSN 0021-9517
- Iglesia, E., Soled, S.L., & Kramer, G.M. (1993). Isomerization of Alkanes on Sulfated Zirconia: Promotion by Pt and by Adamantyl Hydride Transfer Species. *Journal of Catalysis*, Vol.144, No.1, (November 1993), pp. 238-253, ISSN 0021-9517
- Ivanov, A.V., & Kustov, L.M. (1998). Investigation of the State of Palladium in the Pd/SO₄/ZrO₂ System by Diffuse-Reflectance IR Spectroscopy. *Russian Chemical Bulletin*, Vol.47, No.1, (January 1998), pp. 55-59, ISSN 1066-5285
- Jorgensen, S.W., & Madix, R.J. (1985). Steric and Electronic Effects of Sulfur on CO Adsorbed on Pd(100). *Surface Science*, Vol.163, No.1, (November 1985), pp. 19-38, ISSN 0039-6028
- Kazakov, M.O., Lavrenov, A.V., Mikhailova, M.S., Allert, N.A., Gulyaeva, T.I., Muromtsev, I.V., Drozdov, V.A., & Duplyakin, V.K. (2010). Hydroisomerization of Benzene-Containing Gasoline Fractions on a Pt/SO₄²⁻-ZrO₂-Al₂O₃ Catalyst: I. Effect of Chemical Composition on the Phase State and Texture Characteristics of SO₄²⁻-ZrO₂-Al₂O₃ Supports. *Kinetics and Catalysis*, Vol.51, No.3, (June 2010), pp. 438-443, ISSN 0023-1584
- Kazakov, M.O., Lavrenov, A.V., Danilova, I.G., Belskaya, O.B., & Duplyakin, V.K. (2011). Hydroisomerization of Benzene-Containing Gasoline Fractions on a Pt/SO₄²⁻-ZrO₂-Al₂O₃ Catalyst: II. Effect of Chemical Composition on Acidic and Hydrogenating and the Occurrence of Model Isomerization Reactions. *Kinetics and Catalysis*, Vol.52, No.4, (July 2011), pp. 573-578, ISSN 0023-1584

- Kazakov, M.O., Lavrenov, A.V., Belskaya, O.B., Danilova, I.G., Arbuzov, A.B., Gulyaeva, T.I., Drozdov, V.A., Duplyakin, V.K. (2012). Hydroisomerization of Benzene-Containing Gasoline Fractions on a Pt/SO₄²⁻-ZrO₂-Al₂O₃ Catalyst: III. Hydrogenating Properties of the Catalyst. *Kinetics and Catalysis*, Vol.53, No.1, (January-February 2012), Accepted, In Press, ISSN 0023-1584
- Knözinger, H. (1976a). Hydrogen Bonds in Systems of Adsorbed Molecules, In: *The Hydrogen Bond: Resent Developments in Theory and Experiments*, P. Schuster, G. Zundel, & C. Sandorfy, (Ed.), pp. 1263-1364, North-Holland Pub. Co., ISBN 0720403154, Amsterdam, The Netherlands
- Knözinger, H. (1976b). Specific Poisoning and Characterization of Catalytically Active Oxide Surfaces, In: *Advances in Catalysis*, D.D. Eley, H. Pines, & P.B. Weisz, (Ed.), pp. 184-271, Academic Press, Inc, ISBN 0-12-007825-2, New York, The United States of America
- Knözinger, H. & Ratnasamy, P. (1978). Catalytic Aluminas: Surface Models and Characterization of Surface Sites. *Catalysis Reviews - Science and Engineering*, Vol.17, No.1, (January 1978), pp. 31-70, ISSN 0161-4940
- Kooh, A.B., Han, W.-J., Lee, R.G., & Hicks, R.F. (1991). Effect of Catalyst Structure and Carbon Deposition on Heptane Oxidation over Supported Platinum and Palladium. *Journal of Catalysis*, Vol.130, No.2, (August 1991), pp. 374-391, ISSN 0021-9517
- Kubelková, L., Beran, S., & Lercher, J.A. (1989). Determination of Proton Affinity of Zeolites and Zeolite-Like Solids by Low-Temperature Adsorption of Carbon Monoxide. *Zeolites*, Vol.9, No.6, (November 1989), pp. 539-543, ISSN 0144-2449
- Kustov, L.M., Kazansky, V.B., Figueras, F., & Tichit, D. (1994). Investigation of the Acidic Properties of ZrO₂ Modified by SO₄²⁻ Anions. *Journal of Catalysis*, Vol.150, No.1, (November 1994), pp. 143-149, ISSN 0021-9517
- Kustov, L.M. (1997). New Trends in IR-Spectroscopic Characterization of Acid and Basic Sites in Zeolites and Oxide Catalysts. *Topics in Catalysis*, Vol.4, Nos.1-2, (November 1997), pp. 131-144, ISSN 1022-5528
- Kwak, J.H., Hu, J., Mei, D., Yi, C.-W., Kim, D.H., Peden, C.H.F., Allard, L.F., & Szanyi, J. (2009). Coordinatively Unsaturated Al³⁺ Centers as Binding Sites for Active Catalyst Phases of Platinum on γ -Al₂O₃. *Science*, Vol.325, No.5948 (September 2009), pp. 1670-1673, ISSN 0036-8075
- Lavrenov, A.V., Basova, I.A., Kazakov, M.O., Finevich, V.P., Belskaya, O.B., Buluchevskii, E.A., & Duplyakin, V.K. (2007). Catalysts on the Basis of Anion-Modified Metal Oxides for Production of Ecologically Pure Components of Motor Fuels. *Russian Journal of General Chemistry*, Vol.77, No.12, (December 2007), pp. 2272-2283, ISSN 1070-3632
- Lisboa, J. da S., Santos, D.C.R.M., Passos, F.B., & Noronha, F.B. (2005). Influence of the Addition of Promoters to Steam Reforming Catalysts. *Catalysis Today*, Vol.101, No.1, (March 2005), pp. 15-21, ISSN 0920-5861
- Little, L.H. (1966). *Infrared Spectra of Adsorbed Species*, Academic Press, Inc, ISBN 0124521509, London, England
- Liu, X., & Truitt, R.E. (1997). DRFT-IR Studies of the Surface of γ -Alumina. *Journal of the American Chemical Society*, Vol.119, No.41, (October 1997), pp. 9856-9860, ISSN 0002-7863

- López Cordero, R., Gil Llambías, F.J., Palacios, J.M., Fierro, J.L.G., & López Agudo, A. (1989). Surface Changes of Alumina Induced by Phosphoric Acid Impregnation. *Applied Catalysis*, Vol.56, No.2, (August 1989), pp. 197-206, ISSN 0166-9834
- Lycourghiotis, A. (2009). Interfacial Chemistry, In: *Synthesis of Solid Catalysts*, K.P. de Jong, (Ed.), pp. 13-31, WILEY-VCH Verlag GmbH & Co. KGaA, ISBN 978-3-527-32040-0, Weinheim, Germany
- Maache, M., Janin, A., Lavalley, J.C., Joly, J.F., & Benazzi E. (1993). Acidity of Zeolites Beta Dealuminated by Acid Leaching: An FTi.r. Study Using Different Probe Molecules (Pyridine, Carbon Monoxide). *Zeolites*, Vol.13, No.6, (July-August 1993), pp. 419-426, ISSN 0144-2449
- Manoilova, O.V., Olindo, R., Otero Areán, C., & Lercher, J.A. (2007). Variable Temperature FTIR Study on the Surface Acidity of Variously Treated Sulfated Zirconias. *Catalysis Communications*, Vol.8, No.6, (June 2007), pp. 865-870, ISSN 1566-7367
- Marceau, E., Che, M., Saint-Just, J., & Tatibouët, J.M. (1996). Influence of Chlorine Ions in Pt/Al₂O₃ Catalysts for Methane Total Oxidation. *Catalysis Today*, Vol.29, Nos.1-4, (May 1996), pp. 415-419, ISSN 0920-5861
- Mason, M.G. (1983). Electronic Structure of Supported Small Metal Clusters. *Physical Review B*, Vol.27, No.2, (January 1983), pp. 748-762, ISSN 0163-1829
- Mei, D., Kwak, J.H., Hu, J., Cho, S.J., Szanyi, J., Allard, L.F., & Peden, C.H.F. (2010). Unique Role of Anchoring Penta-Coordinated Al³⁺ Sites in the Sintering of γ -Al₂O₃-Supported Pt Catalysts. *Journal of Physical Chemistry Letters*, Vol.1, No.18, (September 2010), pp. 2688-2691, ISSN 1948-7185
- Mironenko, R.M., Belskaya, O.B., & Likholobov, V.A. (2009). Investigation of the Interaction of Chloride Complexes of Platinum (IV) with Aluminum Oxide in a Structural Modification of the Surface (in Russian), *Proceedings of 24th International Chugaev Conference on Coordination Chemistry*, pp. 116-117, ISBN 5-85263-026-8, Saint Petersburg, Russia, June 15-19, 2009
- Mironenko, R.M., Belskaya, O.B., Danilova, I.G., Talsi, V.P., & Likholobov, V.A. (2011). Modifying the Functional Cover of the γ -Al₂O₃ Surface Using Organic Salts of Aluminum. *Kinetics and Catalysis*, Vol.52, No.4, (August 2011), pp. 629-636, ISSN 0023-1584
- Morterra, C., Cerrato, G., Emanuel, C., & Bolis, V. (1993). On the Surface Acidity of Some Sulfate-Doped ZrO₂ Catalysts. *Journal of Catalysis*, Vol.142, No.2, (August 1993), pp. 349-367, ISSN 0021-9517
- Morterra, C., & Magnacca, G. (1996). A Case Study: Surface Chemistry and Surface Structure of Catalytic Aluminas, as Studied by Vibrational Spectroscopy of Adsorbed Species. *Catalysis Today*, Vol.27, Nos.3-4, (February 1996), pp. 497-532, ISSN 0920-5861
- Morterra, C., Cerrato, G., Di Ciero, S., Signoretto, M., Pinna, F., & Strukul, G. (1997). Platinum-Promoted and Unpromoted Sulfated Zirconia Catalysts Prepared by a One-Step Aerogel Procedure: 1. Physico-Chemical and Morphological Characterization. *Journal of Catalysis*, Vol.165, No.2, (January 1997), pp. 172-183, ISSN 0021-9517
- Otto, K., Haack, L.P., & de Vries, J.E. (1992). Identification of Two Types of Oxidized Palladium on γ -Alumina by X-ray Photoelectron Spectroscopy. *Applied Catalysis B: Environmental*, Vol.1, No.1, (February 1992), pp. 1-12, ISSN 0926-3373

- Paukshtis, E.A., & Yurchenko, E.N. (1983). Study of the Acid-Base Properties of Heterogeneous Catalysts by Infrared Spectroscopy. *Russian Chemical Reviews*, Vol.52, No.3, (March 1983), pp. 242-258, ISSN 0036-021X
- Paukshtis, E.A. (1992). *Infrared Spectroscopy of Heterogeneous Acid-Base Catalysis* (in Russian), Nauka, ISBN 5-02-029281-8, Novosibirsk
- Paze, C., Bordiga, S., Lamberti, C., Salvalaggio, M., Zecchina, A., & Bellussi, G. (1997). Acidic Properties of H- β Zeolite as Probed by Bases with Proton Affinity in the 118-204 kcal mol⁻¹ Range: A FTIR Investigation. *Journal of Physical Chemistry B*, Vol.101, No.24, (June 1997), pp. 4740-4751, ISSN 1520-6106
- Peri, J.B. (1965). A Model for the Surface of γ -Alumina. *Journal of Physical Chemistry*, Vol.69, No.1, (January 1965), pp. 220-230, ISSN 0022-3654
- Pillo, T., Zimmermann, R., Steiner, P., & Hufner, S. (1997). The Electronic Structure of PdO Found by Photoemission (UPS and XPS) and Inverse Photoemission (BIS). *Journal of Physics: Condensed Matter*, Vol.9, No.19, (May 1997), pp. 3987-3999, ISSN 0953-8984
- Rakai, A., Tessier, D., & Bozon-Verduraz, F. (1992). Palladium-Alumina Catalysts - a Diffuse Reflectance Study. *New Journal of Chemistry*, Vol.16, No.8-9, (August-September 1992), pp. 869-875, ISSN 1144-0546
- Requies, J., Cabrero, M.A., Barrio, V.L., Cambra, J.F., Güemez, M.B., Arias, P.L., La Parola, V., Peña, M.A., & Fierro, J.L.G. (2006). Nickel/ Alumina Catalysts Modified by Basic Oxides for the Production of Synthesis Gas by Methane Partial Oxidation. *Catalysis Today*, Vol.116, No.3, (August 2006), pp. 304-312, ISSN 0920-5861
- Rombi, E., Cutrufello, M.G., Solinas, V., De Rossi, S., Ferraris, G., & Pistone, A. (2003). Effects of Potassium Addition on the Acidity and Reducibility of Chromia/Alumina Dehydrogenation Catalysts. *Applied Catalysis A: General*, Vol.251, No.2, (September 2003), pp. 255-266, ISSN 0926-860X
- Ryczkowski, J. (2001). IR Spectroscopy in Catalysis. *Catalysis Today*, Vol.68, No.4, (July 2001), pp. 263-381, ISSN 0920-5861
- Scokart, P.O., Selim, S.A., Damon, J.P., & Rouxhet, P.G. (1979). The Chemistry and Surface Chemistry of Fluorinated Alumina. *Journal of Colloid and Interface Science*, Vol.70, No.2, (June 1979), pp. 209-222, ISSN 0021-9797
- Shelimov, B.N., Lambert, J.-F., Che, M., & Didillon, B. (1999). Initial Steps of the Alumina-Supported Platinum Catalyst Preparation: a Molecular Study by ¹⁹⁵Pt NMR, UV-Visible, EXAFS and Raman Spectroscopy. *Journal of Catalysis*, Vol.185, No.2, (July 1999), pp. 462-478, ISSN 0021-9517
- Shelimov, B.N., Lambert, J.-F., Che, M., & Didillon, B. (2000). Molecular-Level Studies of Transition Metal - Support Interactions During the First Steps of Catalysts Preparation: Platinum Speciation in the Hexachloroplatinate/Alumina System. *Journal of Molecular Catalysis A: Chemical*, Vol.158, No.1, (September 2000), pp. 91-99, ISSN 1381-1169
- Sheppard, N., & Nguyen, T.T. (1978). The Vibrational Spectra of Carbon Monoxide Chemisorbed on the Surface of Metal Catalysts - a Suggested Scheme of Interpretation, In: *Advances in Infrared and Raman Spectroscopy*, R.J.H. Clark, R.E. Hester, (Ed.), pp. 67-147, Heyden & Son Inc, ISBN 0-85501-185-8, Philadelphia, The United States of America

- Song, X., & Sayari, A. (1996). Sulfated Zirconia-Based Strong Solid-Acid Catalysts: Recent Progress. *Catalysis Reviews - Science and Engineering*, Vol.38, No.3, (August 1996), pp. 329-412, ISSN 0161-4940
- Tsai, K.-Y., Wang, I., & Tsai, T.-C. (2011). Zeolite Supported Platinum Catalysts for Benzene Hydrogenation and Naphthene Isomerization. *Catalysis Today*, Vol.166, No.1, (May 2011), pp. 73-78, ISSN 0920-5861
- Tsyganenko, A.A., & Filimonov, V.N. (1973). Infrared Spectra of Surface Hydroxyl Groups and Crystalline Structure of Oxides. *Journal of Molecular Structure*, Vol.19, (December 1973), pp. 579-589, ISSN 0022-2860
- Tsyganenko, A.A., & Mardilovich, P.P. (1996). Structure of Alumina Surfaces. *Journal of the Chemical Society, Faraday Transactions*, Vol.92, No.23, (December 1996), pp. 4843-4852, ISSN 0956-5000
- Vazquez-Zavala, A., Fuentes, S., & Pedraza, F. (1994). The Influence of Sulfidation on the Crystalline Structure of Palladium, Rhodium and Ruthenium Catalysts Supported on Silica. *Applied Surface Science*, Vol.78, No.2, (June 1994), pp. 211-218, ISSN 0169-4332
- Vera, C.R., Pieck, C.L., Shimizu, K., Yori, J.C., & Parera, J.M. (2002). Pt/SO₄²⁻-ZrO₂ Catalysts Prepared from Pt Organometallic Compounds. *Applied Catalysis A: General*, Vol.232, No.1-2, (June 2002), pp. 169-180, ISSN 0926-860X
- Vera, C.R., Yori, J.C., Pieck, C.L., Irusta, S., & Parera, J.M. (2003). Opposite Activation Conditions of Acid and Metal Functions of Pt/SO₄²⁻-ZrO₂ Catalysts. *Applied Catalysis A: General*, Vol.240, No.1-2, (February 2003), pp. 161-176, ISSN 0926-860X
- Wang, H., Tan, S., & Zhi, F. (1994). IR Characterization of Base Heterogeneity of Solid Catalysts, In: *Acid-Base Catalysis II*, H. Hattori, M. Misono, & Y. Ono, (Ed.), pp. 213-216, Elsevier, Inc, ISBN 978-0-444-98655-9, Amsterdam, The Netherlands
- Zaki, M.I., & Knözinger, H. (1987). Carbon Monoxide – a Low Temperature Infrared Probe for the Characterization of Hydroxyl Group Properties on Metal Oxide Surfaces. *Materials Chemistry and Physics*, Vol.17, Nos.1-2, (April-May 1987), pp. 201-215, ISSN 0254-0584
- Zalewski, D.J., Alerasool, S., & Doolin, P.K. (1999). Characterization of Catalytically Active Sulfated Zirconia. *Catalysis Today*, Vol.53, No.3, (November 1999), pp. 419-432, ISSN 0920-5861
- Zamora, M., & Córdoba, A. (1978). A Study of Surface Hydroxyl Groups on γ -Alumina. *Journal of Physical Chemistry*, Vol.82, No.5, (March 1978), pp. 584-588, ISSN 0022-3654
- Zecchina, A., Escalona Platero, E., & Otero Areán, C. (1987). Low Temperature CO Adsorption on Alum-Derived Active Alumina: An Infrared Investigation. *Journal of Catalysis*, Vol.107, No.1, (September 1987), pp. 244-247, ISSN 0021-9517

Hydrothermal Treatment of Hokkaido Peat – An Application of FTIR and ¹³C NMR Spectroscopy on Examining of Artificial Coalification Process and Development

Anggoro Tri Mursito¹ and Tsuyoshi Hirajima²

*¹Research Centre for Geotechnology,
Indonesian Institute of Sciences (LIPI),
Jl. Sangkuriang Komplek LIPI, Bandung*

*²Department of Earth Resources Engineering,
Faculty of Engineering, Kyushu University,
Motooka, Nishiku, Fukuoka*

¹Indonesia

²Japan

1. Introduction

There have been great changes in attitude toward the use of peat as an energy source since World War II (WEC, 2001). In Japan, peatland covers over 2500 km² and accounts for a total energy resource of approximately 1.99 GJ.10¹⁰ (Spedding, 1988). Peatland in Japan is widely distributed throughout Hokkaido, which is the northernmost area of the country's four main islands. Although peatland also exists in other regions, its distribution is extremely localized. Peatland is distributed over an area of approximately 2000 km² in Hokkaido (Noto, 1991), which is equivalent to approximately 6% of the flat area on this island. Peatland is also widespread in the northeastern part of Sapporo, which is the largest city in Hokkaido. Peatland in Japan is often lacustrine peat, which is formed when lakes and marshes become filled with dead plants from their surrounding areas and are then transformed into land. This type of peat is characterized by the spongy formation of plant fiber. In the peatland of Hokkaido, peat usually accumulates to a thickness of three to five meters on the ground surface, while the soft clay layer underlying the peat is often over 20 meters thick. In some areas, a sand layer exists between the peat and the clay layers.

One approach to study artificial coalification process is dewatering and conversion by hydrothermal treatment. Hydrothermal treatment of peat has been studied recently by the authors (Mursito et al., 2010; Mursito et al., 2010). In this method, raw peat is directly transformed without pretreatment or drying, which leads to greatly reduced costs. However, few studies have been conducted to evaluate the hydrothermal treatment of raw peat by means of all coalification process. Despite this lack of study, experiments imitating coalification by subjecting materials to heating with high pressure water were reported first by Bergius in 1913, who termed the method hydrothermal carbonization.

The conversion of cold climate peat into liquid fuel has been studied and conducted in Germany, Canada, Sweden, Finland, Iceland and Israel (Björnbom et al., 1986). Although there has been much less interest in peat liquefaction than coal liquefaction, a large number of batch autoclave studies have evaluated the use of cold climate peat as the raw material for the formation of liquid fuel. The conversion of peat to liquid fuel in Sweden produced an organic product similar to very heavy oil after raw peat was treated with CO under high pressures and temperatures (Björnbom et al., 1981). In Canada, the conversion of peat to gas and liquid employed CO and/or H₂ and water (Cavalier & Chornet, 1977).

Hydrothermal treatment of Hokkaido cold climate peat has also been investigated. However, it is still necessary to evaluate the liquid and gas products formed during the process to facilitate its energy and chemical utilization. The aim of this chapter is to characterize and determine the effectiveness of hydrothermal treatment for upgrading and dewatering processes on the solid products of Hokkaido cold climate peat as well as to determine its artificial coalification process by applying of FTIR and ¹³C NMR spectroscopy. A fundamental study of the effects of processed temperature on the products of hydrothermal treatment of cold climate peat is also described in this Chapter.

2. Experimental

2.1 Materials

Raw cold climate peat samples were obtained from peatland areas owned by the Takahashi Peat Moss Company, Hokkaido, Japan. The site is located in a peat mining area that consists of about 40 ha that already contained an open and systematic drainage system. The peat mining method used at the site is the cut and block and dry method, and the peat moss products are primarily used for agriculture and gardening. The peat in the study area is approximately 5–10 m thick and the water level is about 50 cm. Prior to World War II, about 1200 ha of peatland in this area were owned by the Japan Oil-Petroleum Company, which converted the harvested peat into oil. The typical properties of the peat from this mining site are shown in Table 1.

2.2 Apparatus and experimental procedure

All experiments were conducted in a 0.5 L batch-type reactor (Taiatsu Techno MA22) that was equipped with an automatic temperature controller and had a maximum pressure of 30 MPa and a maximum temperature of 400°C (Fig. 1) (Mursito et al., 2010). The raw peat samples were introduced to the reactor without any pretreatment except for milling. The amount of the raw peat added to the reactor was 300 g, which corresponded to 40 g of moisture-free peat. The reactor was pressurized with N₂ to 2.0 MPa at ambient temperature, after which the raw peat was agitated at 200 rpm while the reaction temperature was automatically adjusted from 150°C to 380°C at an average heating rate of 6.6°C/min. Under supercritical conditions (380°C), the charge was 230 g and the initial pressure was 0.1 MPa. After the desired reaction time of 30 min, the reactor was cooled immediately.

After cooling, the gas products were released through a gasometer (Shinagawa DC-1) and their volume was determined by collection into a gas micro syringe (ITO MS-GANX00). The evolved gas composition was then determined by gas chromatography (GC) using a GC equipped with a thermal conductivity detector (Shimadzu GC-4C) using Molecular Sieve 5A

Properties	Raw	Treated temperatures (°C)							
		150°C	200°C	250°C	270°C	300°C	330°C	350°C	380°C
Proximate analysis (wt%)									
Moisture (a.r)	86.9	-	-	-	-	-	-	-	-
Equilibrium									
Moisture (X) (a.r)	13.3	12.3	12.8	5.6	5.3	4.8	3.2	3.0	2.4
Volatile Matter (d.a.f)	68.1	67.5	65.0	56.4	52.8	48.4	45.4	44.0	37.2
Fixed Carbon (d.a.f)	31.9	32.5	35.0	43.6	47.2	51.6	54.6	56.0	62.8
Ash (d.b)	4.4	12.8	9.1	8.3	7.1	6.0	7.4	7.5	8.2
Ultimate analysis (wt%) (d.a.f)									
C	54.7	57.6	59.6	67.0	68.0	72.2	74.3	75.2	79.1
H	5.7	5.8	5.7	5.5	5.4	5.5	5.5	5.4	5.4
N	1.1	2.2	1.7	1.7	1.6	1.6	1.7	1.7	1.7
O (diff.)	38.0	33.8	32.3	25.1	24.3	20.0	17.9	17.2	13.3
S	0.5	0.7	0.6	0.6	0.6	0.6	0.5	0.5	0.5
Yield of solid products (Y) (wt%) (d.b)									
	-	77.7	77.6	65.3	65.2	61.2	53.9	50.4	48.3
Calorific value (CV) (kJ.kg ⁻¹) (d.b)									
	21,527	20508	22427	25008	25836	27985	28299	29296	30047
Effective calorific value (ECV) (kJ.kg ⁻¹)									
	17307	16727	18263	22436	23268	25457	26242	27264	28233

d.b = dry basis; *a.r* = as received basis; *d.a.f* = dry ash free basis; *diff.* = differences

Table 1. Proximate and ultimate analysis, yield of solid products and calorific value of Takahashi peat moss and hydrothermally upgraded peat.

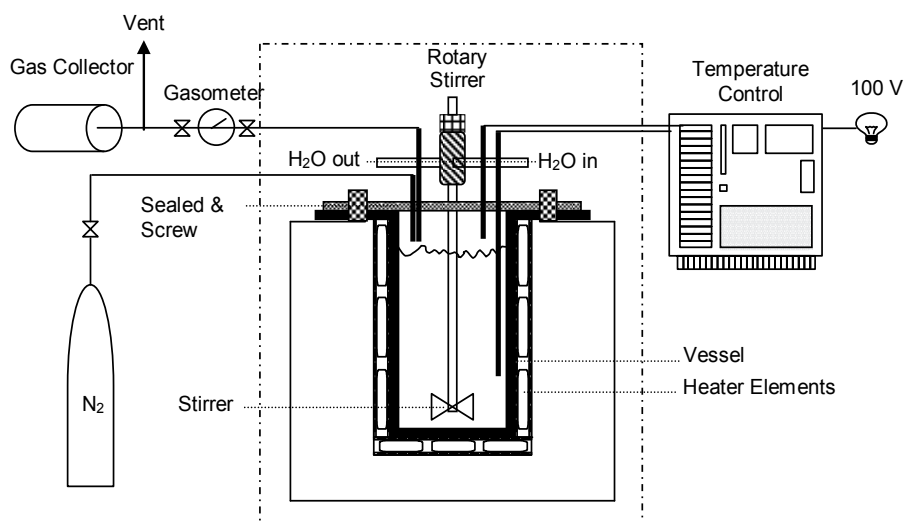


Fig. 1. Schematic figures of hydrothermal batch type reactors.

and Porapak Q columns. The column temperature was set at 60° C and argon was applied as the carrier gas at a rate of 30 mL/min. The results were recorded using a Shimadzu C-R8A Chromatopac data processor. The results of GC analysis are discussed elsewhere. The solid

and liquid phases were then collected from the reactor and separated by filtration (ADVANTEC 5C) using a water aspirator. The total moisture content of the filtered solid products was then determined using a moisture content analyzer (Sartorius MA 150).

2.3 Analysis

The liquid product was filtered through a sheet of Advantec 0.45 μm pore size membrane filter prior to analysis. After dilution by a factor of 1000 using ultra-pure water, the total organic carbon (TOC) content and total inorganic carbon (TIC) content of the liquid product was determined using a Shimadzu TOC-5000A VCSH TOC analyzer. The organic compounds in the liquid product were identified and quantified by GC-MS (Agilent 6890N and JEOL Jms-Q1000GC (A)) using a J&W Scientific methyl silicon capillary column measuring 0.32 mm \times 60 m. The split ratio was 99 and the column temperature was maintained at 40° C for 3 minutes, followed by an increase of 15 °C/min. to 250° C, which was maintained for 10 minutes. The composition of the sugar compounds in the liquid products was determined by high-performance liquid chromatography (HPLC) using a JASCO RI-2031 refractive index detector and Shodex KS-811, with 2 mM HClO₄ applied at 0.7 mL/min. as the eluent. The results of liquid products content analysis are discussed elsewhere.

The elemental composition of the raw peat and solid product was determined using an elemental analyzer (Yanaco CHN Corder MT-5 and MT-6). Additionally, proximate analysis (based on JIS M 8812) total sulfur analysis (based on JIS M 8819) and calorific analysis (based on JIS M 8814) were conducted separately. The gross calorific value (CV) was measured using the bomb calorimetric method and the effective calorific value (ECV) of the sample at a constant pressure was determined based on JIS M 8814, which is followed by ISO 1928. The equilibrium moisture content of the dried solid product was further analyzed while maintaining their moisture contents according to JIS M 8811. Briefly, an aliquot of the sample was placed inside a desiccator containing saturated salt solution and then measured rapidly using a moisture content analyzer (Sartorius MA 150).

The primary components and the chemical structure of the raw peat and the solid product were further analyzed by Fourier transform infrared spectroscopy (FTIR) (JASCO 670 Plus) using the Diffuse Reflectance Infrared Fourier Transform Spectroscopy (DRIFTS) technique and the JASCO IR Mentor Pro 6.5 software for spectral analysis. The cross polarization/magic angle spinning (CP/MAS) ¹³C NMR spectrum of raw peat and the solid product was measured using a solid state spectrometer (JEOL CMX-300). The measurement conditions were as follows: spinning speed in excess of 12 kHz, contact time of 2 ms, pulse repetition time of 7 s and scan number of 10,000. Chemical shifts are in ppm referenced to hexamethylbenzene. The curve fitting analysis of the spectrum was conducted using the Grams/AI 32 Ver. 8.0 software (Galactic Industries Corp., USA).

2.4 Sequential extraction of peat bitumen, plant constituents and humic substances

After drying at room temperature, the raw peat was milled and sieved through an 80-mesh screen, after which the plant constituents (hemicelluloses, cellulose and lignin), peat bitumen, humic substances (humic acid (HA), fulvic acid (FA) and humin (Hm)) and other insoluble contents were fractionated using methods that have been previously described. Briefly, the peat bitumen (benzene/ethanol-soluble) was extracted in a Soxhlet apparatus for

8 hours with a mixture of benzene and ethanol (4:1 vol./vol.). The bitumen-free peat was then extracted in ultra-pure water at 100° C for 5 hours to obtain the water-soluble materials. Next, the samples were dried at room temperature, after which the residual peat was sequentially extracted with 2% HCl at 100 °C for 5 hours to obtain the hemicelluloses. The samples were then incubated in 72% H₂SO₄ at room temperature for 4 hours, after which the concentration of H₂SO₄ was adjusted to 4% by the addition of ultra-pure water and the samples were heated at 100 °C for 3 hours to obtain the cellulose.

The residual peat was then correlated with the humic substances, lignin and other insoluble compounds. To accomplish this, the humic substances were removed by acid and alkali extraction. Briefly, the air-dried peat was washed twice with 0.01 M HCl and then treated with NaOH at pH 13.5 for 48 hours, which gave a supernatant fraction (humic and fulvic acids), and a fraction that contained the humin and other insolubles. All fractions were separated by filtration and centrifugation.

3. Results and discussion

3.1 Sequential extraction of raw peat and solid products

The liquid content of the raw peat was 86.9 wt.%, which corresponded to the moisture content, and the products increased from 87.3 wt.% to 89.4 wt.% as the temperature increased. As the temperature increased, the gas products content increased from 1.6 wt.% to 4.8 wt.%. The increase in the liquid and gas products in response to increasing temperature suggest that dewatering and decomposition occurred during the process. Takahashi peat that contained most of the organic constituents of the original plant materials were least decomposed and peatification occurred shortly. The amounts and concentration of plant constituents, peat bitumen (benzene/ethanol soluble) and humic substances in Takahashi moss peat are described in Table 2.

Humic substances, insoluble fractions and lignin	(wt.%) <i>dry-base</i>
<i>Humic and fulvic acids (HA and FA)</i>	0.9
<i>Humin (Hm), insoluble fractions and lignin</i>	4.2
Carbohydrates	
<i>Hemicelluloses</i>	30.7
<i>Cellulose</i>	40.7
Extracted peat bitumen (benzene/ethanol soluble)	9.0
Water soluble compounds	14.5

Table 2. Humic substances, plant constituents and bitumen of Takahashi moss peat.

Extracted peat bitumen can be formed during natural decomposition and accounted for 9.0 wt.% of the raw peat, suggesting that the extracted materials correspond to the wax like hydrophobic formations. The hemicellulose and cellulose content was 30.7 wt.% and 40.7 wt.%, respectively. The high levels of carbohydrate indicate that the plant constituents still remained and were decomposed during peatification. The materials from which Takahashi moss peat is formed consist of cattails and reed grass (in Japanese, gama and ashi, which differ greatly from the raw materials that lead to the formation of tropical peat. This difference may explain why Takahashi peat differs from Pontianak peat. The water soluble

content of the raw peat was 14.5 wt.%. The total humic substances, lignin and other insoluble fractions comprised 5.1 wt.% of the raw peat, of which HA and FA comprised 0.9 wt.%.

Figure 2 shows the effect of the processing temperature on the contents of peat bitumen, water soluble compounds and carbohydrates in the solid products. All other compounds consisted of char and other insoluble materials. The peat bitumen content in the solid products ranged from 4.7 to 26.0 wt.%, which suggests that peat bitumen formed in solid products formed in response to hydrothermal treatment. The peat bitumen decreased at low temperatures (150°C to 250°C), then increased slightly at 250°C and continued to increase with increasing temperature. Under supercritical conditions, the peat bitumen decreased slightly when compared to the peat bitumen content at 350°C, which may have been due to the intensive decomposition of organics in raw peat during the formation of gaseous and liquid products as a result of the supercritical reaction. The water soluble content accounted for 14.5 wt.% of the raw peat and 6.2 wt.% of the product formed at 380°C, indicating that this fraction decreased with increasing temperature. Both carbohydrates (hemicellulose and cellulose) decreased with increasing temperature and were no longer present in products formed at 300°C and above. Hydrothermal dewatering was highly affected by the decomposition of carbohydrates at 150°C to 270°C, suggesting that organics containing polysaccharides will be obtained in the liquid products.

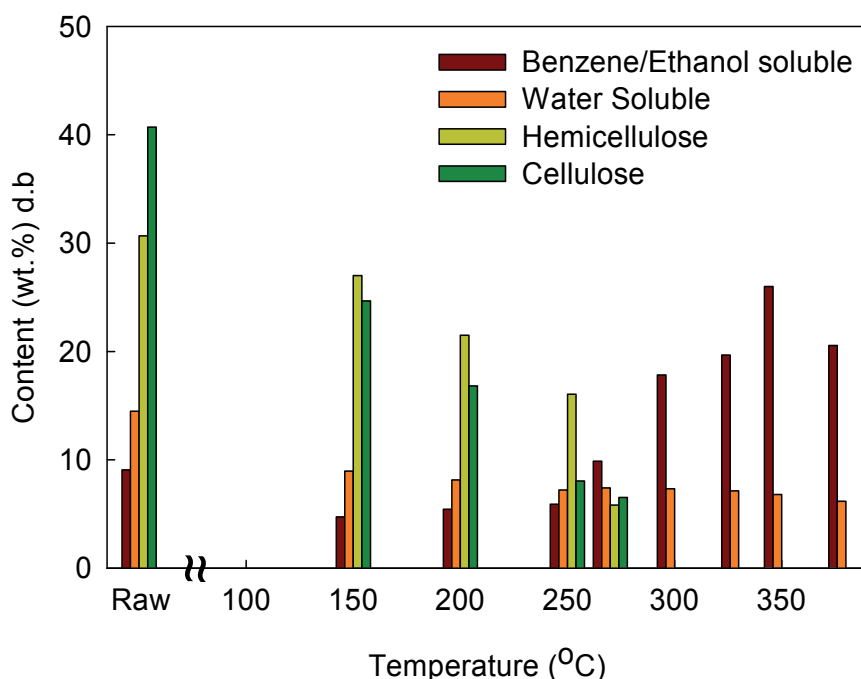


Fig. 2. The effect of temperature on the concentration of peat bitumen (benzene/ethanol soluble), water soluble compounds and carbohydrates in solid products

3.2 Properties of solid products

Table 1 show the effects of temperature on the yield and moisture contents of solid products, respectively. The yield decreased as the temperature increased. Specifically, the maximum

solid product yield was 77.7 wt.% at the lower temperature of 150°C, while the minimum yield was 48.3 wt.% at the supercritical temperature (380°C). The decrease in the yield of the solid product was due to the extensive thermal decomposition of the raw material into liquid and gaseous products. Dewatering also occurred during the decomposition reaction. Indeed, the minimum moisture content of the filtered solid products was 20.9 wt.% when the reaction was conducted at 380°C, while the maximum moisture content of 47.9 wt.% was obtained at 150°C. Moreover, the equilibrium moisture content of the solid products obtained at 380°C was 2.4 wt.%, while it was 13.3 wt.% at 150°C. As the temperature increased, the equilibrium moisture content of the solid products decreased when the products were maintained at a constant humidity (77–79%), indicating that the product may be hydrophobic when subjected to high temperatures. In general, the use of higher temperatures for the hydrothermal treatment of raw peat improves the dewaterability of the solid product; therefore, solid products produced at higher temperatures have better resistance against moisture adsorption when they are maintained at high humidity.

Lower equilibrium moisture contents resulted in the solid products having higher calorific values. In addition, the effective calorific value of peat fuel decreased as the level of moisture increased. The gross calorific value (CV) determined by the bomb calorimetric method and the effective calorific value (ECV) of the samples are shown in Table 1. The ECV was calculated using the equation as described on (JIS M 8814) :

$$ECV = [CV - 212.2 \times H - 0.8 \times (O + N)] \times (1 - 0.01 X) - 24.43 X \quad (1)$$

where ECV is the effective calorific value, which is the net calorific value at a constant pressure of the equilibrium moisture content sample in kJ/kg, CV is the gross calorific value at a constant volume of the dry sample in kJ/kg, H, O and N are the hydrogen, oxygen and nitrogen contents of the dry sample in mass percentage, respectively, X is the moisture content in mass percentage for which the ECV is desired.

In the present study, CV increased from 20,508 kJ/kg in the 150°C product to 30,047 kJ/kg in the 380°C product, while the ECV of the 150°C product was 16,727 kJ/kg and that of the 380°C product was 28,233 kJ/kg. However, the yield decreased as the temperature increased.

In addition, the fixed carbon content increased from 31.9 wt.% to 62.8 wt.%, and the volatile matter decreased from 68.1 wt.% to 37.2 wt.% as the temperature increased. The ash content of the raw peat and solid products also increased from 4.4 wt.% and 8.2 wt.%. All of the solid products had lower levels of volatile material than the raw peat. Moreover, the chemical variations in the C, H, N and O contents of the solid products following the hydrothermal reaction of peat at different temperatures were also very interesting. Hydrothermal treatment decomposed the raw peat, which resulted in the oxygen content decreasing from 38.0 wt.% to 13.3 wt.% as the temperature increased. These findings suggest that oxygen loss corresponds to dewatering and the decreased yield of solid product. There was also a significant correlation between oxygen loss and the calorific value. The extensive removal of oxygen-rich compounds from the raw peat resulted in a solid product with a low oxygen content and a high calorific value. Additionally, the carbon content of the solid products increased from 54.7 wt.% to 79.1 wt.%. Moreover, the hydrogen content decreased slightly while the nitrogen content increased slightly in response to increased temperature. The sulfur content was relatively stable (0.5 wt.% to 0.7 wt.%), regardless of treatment.

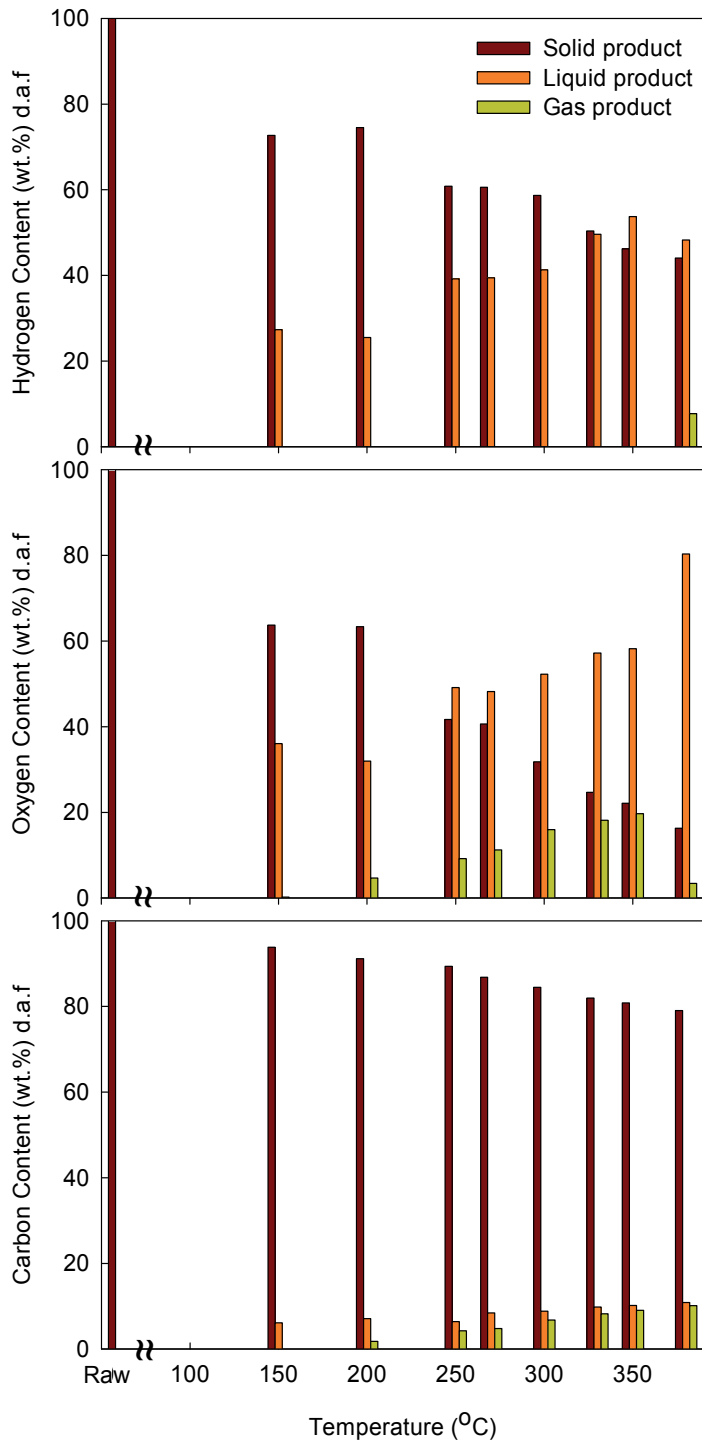


Fig. 3. The effect of temperature on the conversion of C, H and O of raw peat into solid, liquid and gas products.

The carbon, hydrogen and oxygen contents of solid, liquid and gas products calculated based on analysis of the product are shown in Fig. 3. Conversion of the carbon in raw peat into solid, liquid and gas products was relatively slower than conversion of the hydrogen and oxygen. The oxygen and hydrogen content in the liquid product increased rapidly because the decomposition of peat increased suddenly, as shown in the yield of the solid products.

3.3 Coalification properties of solid products

Figure 4 shows a plot of the coalification band of the cold climate peat and hydrothermally upgraded and coalified solid products. As the temperature of the hydrothermal treatment increased, the atomic H/C and O/C ratio of the solid products decreased. These results indicate that hydrothermally upgraded solid products produced at 250°C and 380°C had similar atomic H/C and O/C ratios following coalification between lignite and sub-bituminous coals. Heat and pressure causes a disruption of the colloidal nature of peat during hydrothermal treatment (Cavalier & Chornet, 1977; Lau et al., 1987), which results in the solid products having a low equilibrium moisture content. Extensive losses of oxygen also led to decreases in the equilibrium moisture content of the solid products. Moreover, oxygen from the peat could be removed by reduction (loss of oxygen) and dehydration reactions. Dehydration followed decarboxylation, while reduction followed by dehydrogenation (Kalkreuth & Chornet, 1982; Van Krevelen, 1950) of the solid products began at the same temperature (150°C). Hydrothermal dewatering causes dehydration, reduction and decarboxylation of the product to liquid and gas; therefore, decarboxylation

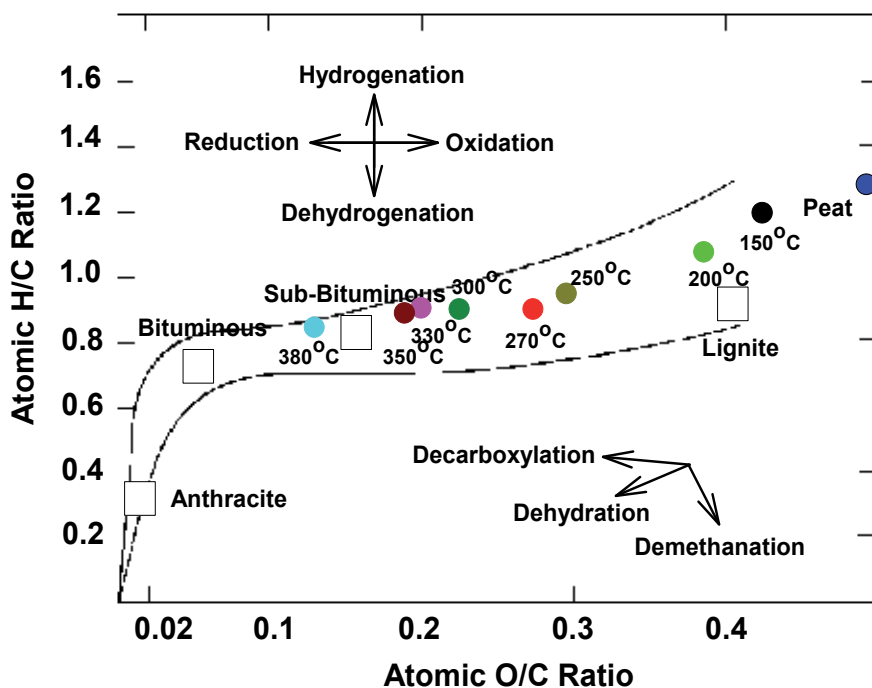


Fig. 4. Coalification band representing raw moss peat and hydrothermally coalified solid products.

by hydrothermal treatment of raw tropical peat can produce organic soluble materials that contain carboxylic groups in the wastewater as well as gaseous products. Moreover, disruption of colloidal forms of peat by hydrothermal treatment can lead to extensive dehydration and possibly increase the number of organic soluble materials in wastewater.

3.4 FTIR results of solid products

Figure 5 shows the FTIR spectra of the raw peat and solid products. Assignments of the peaks in each spectrum of the main functional groups were conducted using the JASCO IR

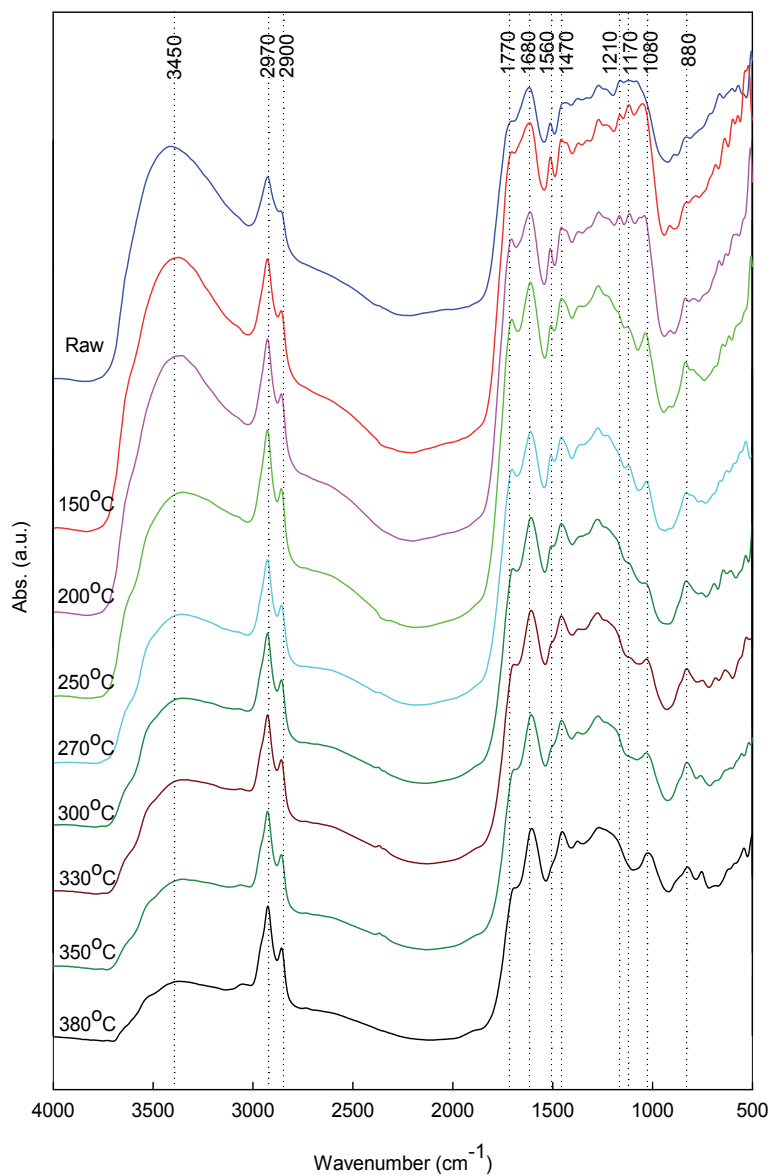
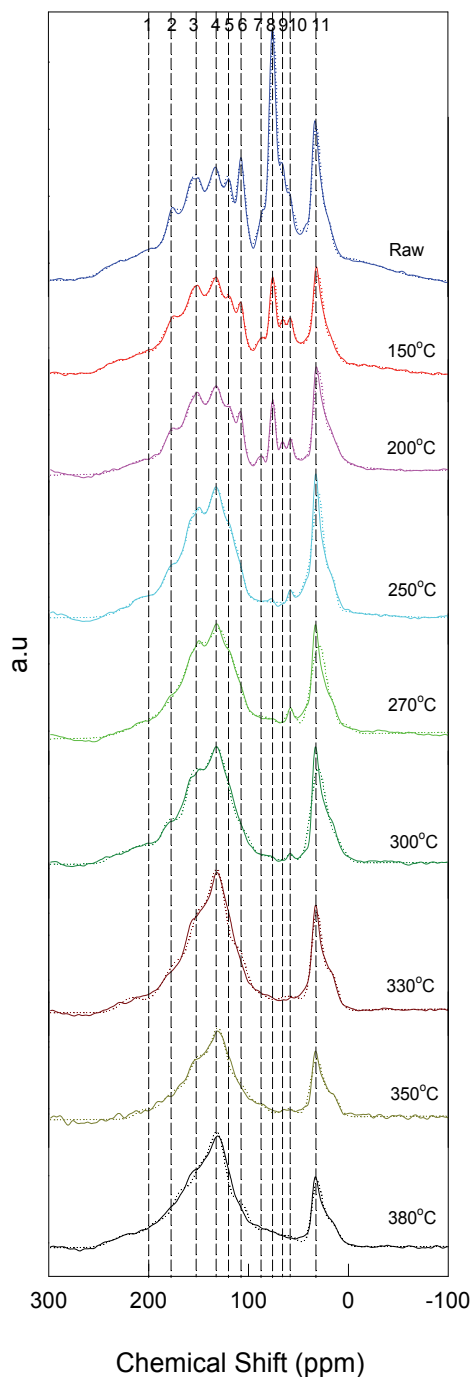


Fig. 5. FTIR spectra of raw peat and solid products produced at all processing temperatures.

Mentor Pro 6.5 software and several publications (Kalkreuth & Chornet, 1982; Van Krevelen, 1950; Orem et al., 1996; Painter et al., 1981; Ibarra & Juan, 1985; Ibarra et al., 1996; Xuguang, 2005). Examination in a range of 3500–3300 cm⁻¹ zone revealed a progressive lowering in relative peak intensity in –OH stretching mode of the solid products at 380°C. This peak is somewhat diminished in relative intensity, probably due to the dewatering of raw peat during hydrothermal treatment and the loss of hydroxyl-functionalized carbohydrates (Kalkreuth & Chornet, 1982). The spectrum in a range of 3000–2800 cm⁻¹ showed existence of –CH_x stretching mode in an aliphatic carbon. In addition, significant changes can also be observed in a range of 1800–1100 cm⁻¹. The carbonyl C=O stretching vibration mode of carboxylic acid at 1770 cm⁻¹ was observed initially but the signal was almost completely disappeared with treatment at 350–380°C. The relative intensity of the ketone carbonyl band C=O groups was clearly observed at 1680 cm⁻¹ and shifted slightly at higher temperatures. A peak at 1470–1511 cm⁻¹ assigned to the stretching vibration mode of C=C in aromatic ring carbons (Kalkreuth & Chornet, 1982), was gradually sharpened in relative intensity with increase in temperature. Peak assigned to the bending vibration mode of C–O–R in ethers were observed at 1080 cm⁻¹, and with increasing temperature, were no longer present at 270°C. Peak assigned to the bending vibration mode of –C–H in aromatics was also observed at 900–700 cm⁻¹ during the hydrothermal process at all temperatures. Peak assigned to aromatic nuclei CH at 880 cm⁻¹ tended to sharpen in its relative intensity with temperature. Dehydration and decarboxylation were also affected, with lowering in relative intensity of OH stretch bonding and carboxyl groups being observed in response to treatment. The relative peak intensity of the aromatic ring carbons was sharply observed due to the thermal decomposition that occurred during treatment, and this greatly affected the other carbon functional groups.

3.5 ¹³C NMR results of solid products

The ¹³C NMR spectra of the carbon-functional groups of raw peat and hydrothermally treated solid products produced at different treated temperature are shown in Fig. 6. Determination and assignment of the peak area distribution of carbon-functional groups was based on several publications (Orem et al., 1996; Hammond et al., 1985; Freitas et al., 1999; Yoshida et al., 1987; Yoshida et al., 2002). The strongest peak in the ¹³C NMR spectrum was at 74–76 ppm, which corresponds to methoxyl carbons (OCH₃) may have been related to the presence of carbohydrate carbons (i.e., hemicelluloses, cellulose). These were confirmed on Section 3.1 that the major components of Hokkaido peat are hemicelluloses and cellulose for about 71.4 wt.%. Secondly, the peaks at 30–32 ppm in raw peat containing aliphatic carbons (CH_x (CH₂ and CH₃)), which was likely due to the occurrence of humic acids and related substances (i.e., humic substances). Peat contains the most important organic fraction in nature, humic substances, which are composed of humic acid (HA), fulvic acid (FA) and humin (Hm) (Cavalier & Chornet, 1977). Lignin, cellulose and hemicellulose decreased as the humification of peat increased. In addition, the peak areas of the aliphatic carbons (CH_x) decreased progressively as the temperature increased. The spectrum of raw peat contained a peak area at 56–59 ppm and 64–65 ppm, which may have been due to ether carbons in lignin and cellulose in the ¹³C NMR spectrum. These results suggest that most organic constituents in the original plant material were least biodegraded, decomposed during peatification. These peaks decreased with increasing temperature and the ether carbon peak was nearly completely gone at 330°C. The area at 74–76 ppm, which



1: C=O; 2: COOH; 3: Ar-O; 4: Ar-C; 5: Ar-H; 6, 7, 8, 9 and 10: methoxyl carbons OCH₃; 11: aliphatic carbons CH_x (CH₂ and CH₃)

Fig. 6. ^{13}C NMR spectra of raw peat and solid products produced at all processing temperatures.

corresponds to methoxyl carbons (OCH₃) may have been related to the presence of carbohydrate carbons. This peak area decreased with increasing temperature, eventually decreasing to almost undetectable limits. These findings indicate that carbohydrate carbons were decomposed easily by hydrothermal treatment. The peak representative of aromatic carbons bound to the hydrogen (Ar-H), aromatic non-oxygenated carbon (Ar-C) and aromatic oxygenated carbon (Ar-O) were observed at the area of 100–106 ppm, 127–130 ppm and 151–155 ppm respectively. Furthermore, increasing the temperature of the hydrothermal treatment resulted in an increase in relative area intensity of the aromatic carbons. Finally, the peak area of carboxyl carbons (COOH) in the region of 171–180 ppm and carbonyl carbon (C=O) peaks at 195–200 ppm were observed in the spectrum of raw peat.

4. Conclusion

In this Chapter, the effectiveness of hydrothermal upgrading and dewatering of Hokkaido cold climate peat was evaluated at temperatures ranging from 150°C to 380°C, a maximum final pressure of 25.1 MPa and a residence time of 30 minutes. The hydrothermally dewatered peat fuel product had a significantly higher ECV than raw peat, with the raw peat having an ECV of 17,307 kJ/kg and the products having ECV values ranging from 16,727 kJ/kg to 28,233 kJ/kg. Hydrothermal dewatering may also have impacted the extensive dehydration process by causing a significant loss in the oxygen content. Additionally, the carbon content of the solid products increased from 54.7 wt.% to 79.1 wt.% as the temperature increased. The hydrothermally upgraded peat fuel also had an equilibrium moisture content that ranged from 2.4 wt.% to 13.3 wt.%. A significant loss of oxygen could result in the formation of solid products with low equilibrium moisture.

An application of FTIR and ¹³C NMR spectroscopy on hydrothermal coalification could determine the decomposition of organic compounds in peat at different treated temperature. Increasing the temperature of the hydrothermal treatment resulted in an increase in relative area intensity of the aromatic carbons bound to the hydrogen (Ar-H), aromatic non-oxygenated carbon (Ar-C) and aromatic oxygenated carbon (Ar-O). These mean and also correspond to the increasing of aromaticity as well as coalification degree.

5. Acknowledgment

Financial support was provided by a Grant-in-Aid for Science Research (No. 18206092 and No. 21246135) from the Japan Society for the Promotion of Science (JSPS), the Global-Centre of Excellence in Novel Carbon Resource Sciences, Kyushu University and the New Energy and Industrial Technology Development Organization (NEDO).

6. References

- Björnbom, E.; Olsson, B. & Karlsson, O. (1986). Thermochemical refining of raw peat prior to liquefaction. *Fuel*, Vol.65, pp. 1051–1056.
- Björnbom, P.; Granath, L.; Kannel, A.; Karlsson, G.; Lindstrijm, L. & Björnbom, EP. (1981). Liquefaction of Swedish peats. *Fuel*, Vol.60, pp. 7–13.
- Cavalier, JC. & Chornet, E. (1977). Conversion of peat with carbon monoxide and water. *Fuel*, Vol.56, pp. 57–64.

- Freitas, JCC.; Bonagamba, TJ. & Emmerich, FG. (1999). ^{13}C High-resolution solid-state NMR study of peat carbonization. *Energ Fuel*, Vol.13, pp. 53–59.
- Hammond, TE.; Cory, DG.; Ritchey, M. & Morita, H. High resolution solid state ^{13}C n.m.r. of Canadian peats. *Fuel* 1985;64:1687–1695.
- Ibarra, JV. & Juan, R. (1985). Structural changes in humic acids during the coalification process. *Fuel*, Vol.64, pp. 650–656.
- Ibarra, JV.; Muñoz, E. & Moliner, R. (1996). FTIR study of the evolution of coal structure during the coalification process. *Org Geochem*, Vol.24, pp. 725–735.
- Japanese Industrial Standards Committee. JIS M 8814. (2003). *Coal and coke*. Determination of gross calorific value by the bomb calorimetric method, and calculation of net calorific value. Japanese Standards Association. Tokyo
- Kalkreuth, W. & Chornet, E. (1982). Peat hydrogenolysis using H_2/CO mixtures: Micropetrological and chemical studies of original material and reaction residues. *Fuel Process Technol*, Vol.6, pp. 93–122.
- Lau, FS.; Roberts, MJ.; Rue, DM.; Punwani, DV; Wen, WW. & Johnson, PB. (1987). Peat beneficiation by wet carbonization. *Int J Coal Geol*, Vol.8, pp. 111–121.
- Mursito, AT.; Hirajima, T. & Sasaki, K. (2010). Upgrading and dewatering of raw tropical peat by hydrothermal treatment. *Fuel*, Vol.89, pp. 635–41.
- Mursito, AT.; Hirajima, T.; Sasaki, K. & Kumagai S. (2010). The effect of hydrothermal dewatering of Pontianak tropical peat on organics in wastewater and gaseous products. *Fuel*, Vol.89, pp. 3934–3942.
- Noto, S. (1991). *Peat engineering handbook*. Civil Engineering Research Institute of Hokkaido Development Bureau
- Orem, WH.; Neuzil, SG.; Lerch, EL. & Cecil, CB. (1996). Experimental early-stage coalification of a peat sample and a peatified wood sample from Indonesia. *Org Geochem*, Vol.24, pp. 111–125.
- Painter, PC.; Snyder, RW.; Starsinic, M.; Coleman, MM.; Kuehn, DW. & Davis, A. (1981). Concerning the application of FT-IR to the study of coal: a critical assessment of band assignments and the application of spectral analysis programs. *Appl Spectrosc*, Vol.35, pp. 475–485.
- Spedding, PJ. (1988). Peat. *Fuel*, Vol.67, pp. 883–900.
- Van Krevelen, DW. (1950). Graphical-statistical method for the study of structure and reaction processes of coal. *Fuel*, Vol.29, pp. 269–284.
- World Energy Council (WEC). (2001). Survey of Energy Resources. *Peat*.
- Xuguang, S. (2005). The investigation of chemical structure of coal macerals via transmitted-light FT-IR microspectroscopy. *Spectrochim Acta*, Vol.62, pp. 557–564.
- Yoshida, T. & Maekawa, Y. (1987). Characterization of coal structure by CP/MAS carbon-13 NMR spectrometry. *Fuel Process Technol*, Vol.15, pp. 385–395.
- Yoshida, T.; Sasaki, M.; Ikeda, K.; Mochizuki, M.; Nogami, Y. & Inokuchi, K. (2002) Prediction of coal liquefaction reactivity by solid state ^{13}C NMR spectral data. *Fuel*, Vol.81, pp. 1533–1539.

Section 2

Polymers and Biopolymers

FTIR – An Essential Characterization Technique for Polymeric Materials

Vladimir A. Escobar Barrios,
José R. Rangel Méndez, Nancy V. Pérez Aguilar,
Guillermo Andrade Espinosa and José L. Dávila Rodríguez
*Instituto Potosino de Investigación Científica y Tecnológica,
A.C. (IPICYT), División de Ciencias Ambientales
Mexico*

1. Introduction

Infrared spectroscopy is an essential and crucial characterization technique to elucidate the structure of matter at the molecular scale. The chemical composition and the bonding arrangement of constituents in a homopolymer, copolymer, polymer composite and polymeric materials in general can be obtained using Infrared (IR) spectroscopy (Bhargava et al. 2003)

The FTIR spectrometers obtain the IR spectrum by Fourier transformation of the signal from an interferometer with a moving mirror to produce an optical transform of the infrared signal. Numerical Fourier analysis gives the relation of intensity and frequency, that is, the IR spectrum. The FTIR technique can be used to analyze gases, liquids, and solids with minimal preparation. (Lee, 1977).

The spectrometer may operate in transmission or reflection, but also in attenuated total reflection (ATR) mode, which have been widely used during the last two decades. The transmission mode is very suitable for quantitative analysis, since the main parameters to apply on the Beer-Lambert law are known or easily estimated. The reflection mode is used when polymer is not well dissolved at room temperature, and a film or pellets of the sample is characterized. Such is the case of polyolefins and some engineering polymers like PET.

The ATR objective has a polished face of diamond, germanium or zinc selenide (ZnSe) that is pressed into contact with the sample (Sawyer et al. 2008). Infrared reflection is attenuated by absorption within a surface layer a few micrometers deep. In this case, a good contact is required, but that is easy for most polymers, and the advantage is that no sample preparation is required. Therefore, powders, films, gels and even polymer solutions can be characterized.

The absorption versus frequency characteristics of light transmitted through a specimen irradiated with a beam of infrared radiation provides a fingerprint of molecular structure. Infrared radiation is absorbed when a dipole vibrates naturally at the same frequency in the absorber. The pattern of vibrations is unique for a given molecule, and the intensity of absorption is related to the quantity of absorber. In the IR region, each group has several

and different patterns of vibration such as: stretching, bending, rocking, etc. The absorbance of these bands is proportional to their content based on the Lambert-Beer law. Because of the complexities of the structures (for example, polybutadiene unit has 1,4-cis, 1,4-trans and 1,2-vinyl microstructure while polyisoprene unit has other additional 3,4-microstructure), the general methods for quantitative analysis require external standards, which are usually characterized by primary technique like Nuclear Magnetic Resonance (Zhang et al, 2007). Nevertheless, it is possible to characterize polymers, quantitatively, using FTIR as it will be discussed later.

Thus, infrared spectroscopy permits the determination of components or groups of atoms that absorb in the infrared at specific frequencies, permitting identification of the molecular structure (Bower, 1989; Koenig, 2001). These techniques are not limited to chemical analysis. In addition, the tacticity, crystallinity, and molecular strain can also be measured. Copolymer compositions can be determined as block copolymers absorb additively, and alternating copolymers deviate from this additivity due to interaction of neighboring groups.

The aim of this chapter is to present some examples in the context of different areas, in order to remark the importance of FTIR to determine different aspects as identification of functional groups, to elucidate mechanisms of reaction or even to determine the time of reaction.

The track of a reaction in real time when xerogels are synthesized, interaction of different materials like chitin with polyurethane during synthesis of biocomposite, identification of functional groups attached to nanotubes during their modification and establishment of microstructure of polybutadiene during its hydrogenation are the main examples of the use of FTIR, even being semi-quantitative, quantitative or qualitative analysis, that will be presented and analyzed.

The synthesis of xerogels involves basically two steps, hydrolysis and condensation. The follow of such steps is important to establish the time needed to change process conditions and optimize the xerogel. Even when FTIR analysis is a qualitative technique, this analysis could be used as a semi-quantitative indirect measure of the variation of functional groups, during hydrolysis or condensation reactions.

Biocomposites are very fascinating materials since they offer characteristics of two or more different materials, in order to have very specific features that would be practically impossible to obtain by every single material of biocomposite. Chitin is an abundant biopolymer obtained from shrimp, insects and some vegetal species. This material is capable to remove some contaminants like fluoride from water. Nevertheless, in order to improve the mechanical characteristics of chitin, in order to be applied in water treatment in real conditions, it must be supported. Polyurethane is a very versatile polymer due to its chemical structure. During its synthesis, interactions between functional groups take place in order to create the urethane group. The synthesis of biocomposite must bear in mind that interaction between compounds is essential to create a mechanical and chemical resistant material. FTIR with ATR analysis was carried out to characterize a biocomposite based on chitin and polyurethane, demonstrating that interaction between them occurs.

The characterization of carbon nanotubes usually is carried out using Raman spectroscopy. Nonetheless, the use of FTIR allows the determination of functional groups when carbon

nanotubes are chemically treated in order to improve its interaction with other entities like polymeric matrix, for example. In this sense, oxidized nitrogen-doped nanotubes were analyzed by FTIR, corroborating that functional groups are present in these carbon nanotubes.

2. Xerogels

The xerogels are materials that have precise microstructure and they are synthesized by sol-gel synthesis. Two steps are implied in the sol-gel process, hydrolysis and condensation, which are very sensitive to reaction conditions, being faster or slower and giving xerogels with different characteristics, in terms of structure, surface area, and porosity (Fidalgo and Ilharco, 2005).

In this sense, the trace of each reaction with time, hydrolysis and condensation, is important in order to establish the end and beginning of each of these reactions. FTIR is a very useful characterization technique to follow reactions during sol-gel synthesis, since there are specific functional groups that participate in the sol-gel process.

In the case of hydrolysis, silanol is produced from reaction between silane and water molecules. The silanol exhibits a strong absorbance around 945 cm^{-1} , which can be followed during the reaction.

The condensation reaction, where the silanol groups react between them, creating siloxane groups, gives an intense absorbance band at 1080 cm^{-1} . Therefore, it is also possible to see variation of such band with time (Andrade et al., 2010).

2.1 Kinetics by FTIR

The main functional group that is produced during hydrolysis of silanes is silanol, which has a characteristic absorbance band at 945 cm^{-1} . The hydrolysis reaction, usually, is carried out in presence of some alcohol, depending of the silane. For example, if the hydrolysis is carried out with tetra methoxy silane, then the chosen alcohol is methanol, or with tetra ethoxy silane, the preferred alcohol is ethanol. This is because the by-product of hydrolysis reaction is an alcohol. Therefore, the intense signals in the infrared bands located at 945 and 880 cm^{-1} , corresponding to silanol and ethanol (for example) can be followed during hydrolysis reaction.

In the Figure 1 it is shown the spectra for hydrolysis of tetra ethoxy silane (TEOS) in presence of ethanol at different reaction time. The absorbance band at 945 cm^{-1} can be assigned to the vibration of the Si-O from the silanol residual groups $[\text{Si}(\text{OH})_4]$, whereas the band at 880 cm^{-1} can be assigned to OH groups from ethanol. The time at which no more increment of the absorbance band of silanol and OH groups occurs was established as the time at which the hydrolysis reaction was completed.

From Figure 1, it can be seen that the absorbance bands corresponding to silanol and OH, from ethanol, increased up to 30 min. After this time, there was no increase of these bands (spectra not shown), which can indicate that the hydrolysis reaction has been completed.

Determination of the time needed to carry out the hydrolysis reaction is critical since the knowledge of the complete conversion to silanol groups is required to promote a more efficient condensation reaction.

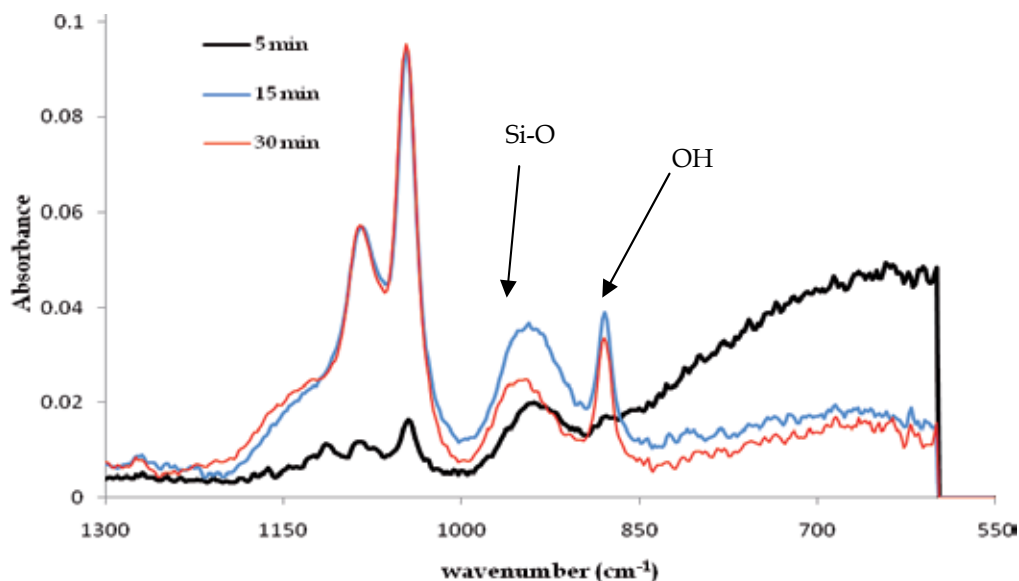


Fig. 1. Spectra of hydrolysis of TEOS at different times.

In the case of the condensation reaction, the silanols are reacting, between them, to produce siloxane groups. The siloxane group has a characteristic absorbance band, corresponding to the vibration mode (Si-O-Si) at 1080 cm⁻¹, that can be followed with time. In fact, from Figure 1, it is noted that after 15 minutes of reaction, there is an important increment of the band at 1080 cm⁻¹ compared to the spectrum at 5 minutes of reaction. It is important to have in mind that hydrolysis and condensation can take place at same time, but condensation is catalyzed with alkaline chemicals, as amines. The fact that the band at 1080 cm⁻¹ had not an increment, from 15 to 30 minutes, could be attributed to the absence of alkaline catalyst in the media reaction. It was shown (Andrade et al., 2010) that the absorbance was increased when an alkaline catalyst was added to the media reaction, and the band corresponding to silanol (945 cm⁻¹) was reduced with time.

3. Biocomposites

Biocomposites i.e. composite materials comprising one or more phase(s) derived from a biological origin (Fowler et al., 2006), are very interesting materials since they offer characteristics of two or more different materials, in order to have very specific features that would be practically impossible to obtain by every single material of biocomposite. Many types of biocomposites have been proposed, depending of the application objective of each material. Water treatment researchers have recently proposed the use of biocomposites as adsorbent materials, in order to remove many different contaminants from water. Synthesis of biocomposites to use them as adsorbents has been necessary, for example, because biosorbents (adsorbents from a biological origin) usually have poor physical/chemical resistance. The roll of the matrix in biocomposite is to reinforce the biosorbent, by establishing physical and/or chemical links between both phases.

One of the most studied biosorbent is chitin, which is an abundant biopolymer found in crustaceans, insects and fungus. This biopolymer is commercially purified by alkaline deproteinization, acid demineralization and decoloration by organic solvents of crustaceans wastes (Pastor, 2004). An additional stronger alkaline treatment of chitin produces deacetylated chitin. If the acetylation degree (DA) decreases at 39% or less, the biopolymer is named chitosan. Hence, the DA of chitin is variable and depends on the process conditions (alkali concentration, contact time, temperature, etc.), which produces DA values from 100 to 0%. Because of this, chitin is known as the biopolymer which has a DA from 100 to 40%; likewise, when the chitinous biopolymer has DA lower than 40%, the biopolymer is named chitosan. Chitosan is, therefore, a biopolymer with structure very similar to that of chitin (see Figure 2); however, chitosan solubility is much greater, especially in acid mediums.

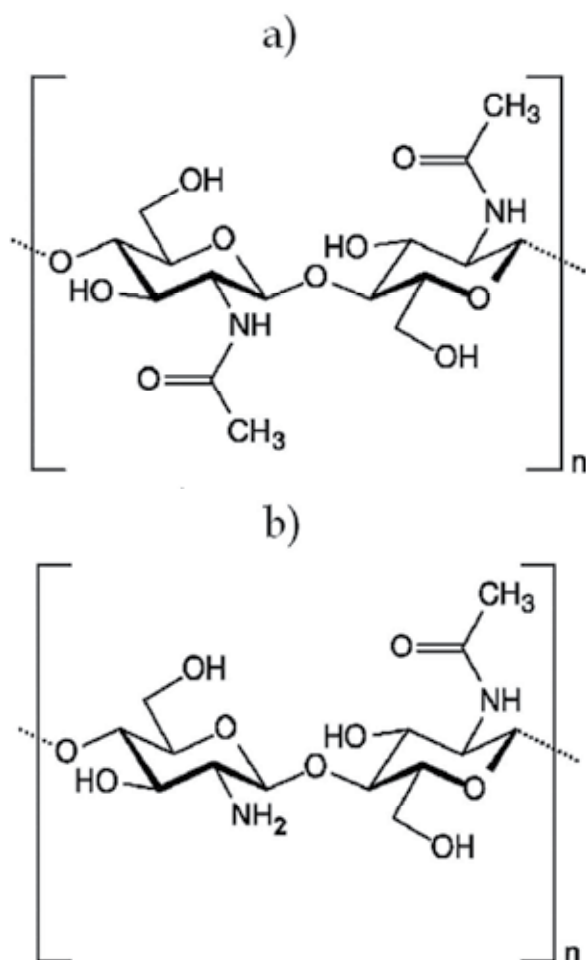


Fig. 2. Chemical structures of a) chitin and b) chitosan (Elnashar, 2010).

Chitin is capable to remove many contaminants from water. A wide variety of studies have demonstrated the ability of chitin to uptake substances as metals, anions and organics.

Nevertheless, in order to improve the mechanical characteristics of chitin to be applied for water treatment in real conditions, it must be supported. The use of polymers as supporting matrix of biosorbents has given encouraging results. In this sense, polyurethane has been one of the most used polymers.

Polyurethane includes a group of polymers derived from the isocyanates, organic compounds which have the isocyanate group ($-N=C=O$) in their structures and, owing to this, are very reactive. Polyurethane shows advantages as easy handling and the possibility to obtain malleable and resistant biocomposites. The Figure 3 shows a general polyurethane prepolymer structure and how isocyanate group reaction gives rise to different type of chemical linkages.

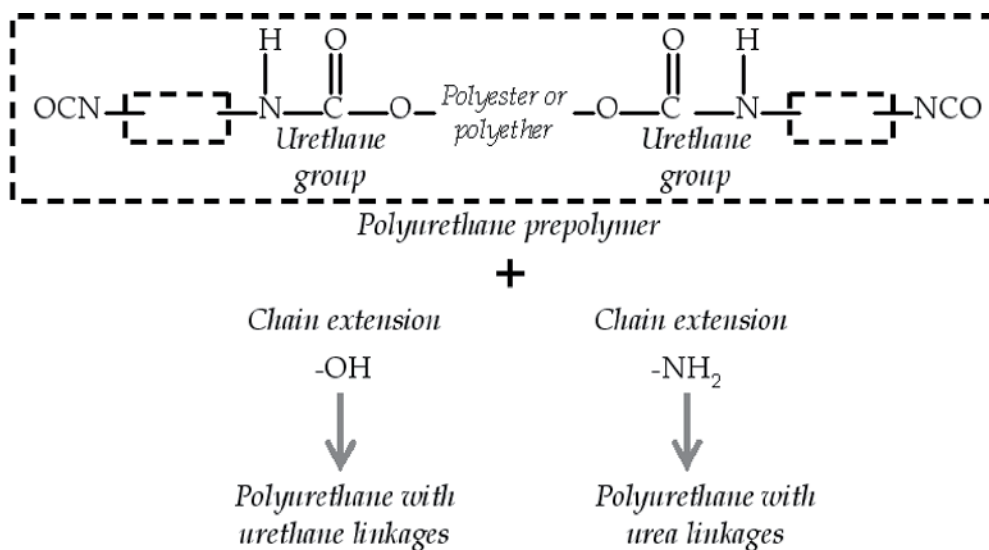


Fig. 3. General chemical structure of polyurethane prepolymer (modified from Hepburn, 1982).

Chemical reaction between the isocyanate and a primary amine group produces the urea group, whereas the reaction between isocyanate and hydroxyl group forms the urethane group. Both urea and urethane are very stable chemical groups, which make the polyurethane a polymer very useful in applications that must resist extreme conditions of temperature, friction and UV radiation (Hepburn, 1982). Due to the high reactivity of the isocyanate with the primary amine and hydroxyl groups, it is valid to assume that the polyurethane establish strong unions with biosorbents to form biocomposites. Hence, such unions make polyurethane a good support matrix for biosorbents. In fact, more and more studies have been recently published about the use of polyurethane as support of biosorbents as seaweed (Alhakawati & Banks, 2004; Zhang & Banks, 2006), moss, sunflower waste and maize plant (Zhang & Banks, 2006), bacteria (Vullo et al., 2008; Mao et al., 2010), fungi (Sudha & Abraham, 2003; Li et al., 2008) and chitin (Davila-Rodriguez et al., 2009). Most of these studies have focused on the biocomposite biosorption capacity; however, the interaction polyurethane-biosorbent has been practically not studied. Infrared spectroscopy is a good methodology to characterize such interaction.

3.1 Methods

One research has recently reported characterization of the polyurethane-chitin interaction in a novel fluoride biosorbent biocomposite, using attenuated total reflection Fourier transform infrared spectroscopy (FTIR-ATR) (Davila-Rodriguez et al., 2009). Such a biocomposite was produced by mixing chitin flakes with polyurethane (60:40 w/w) during the polymerization reaction, which was carried out under intense stirring. The biocomposite consisted, therefore, of chitin flakes covered by a thin film of polyurethane of approximately 1 μm thickness, according to different observations performed by scanning electron microscopy. The novel composite material showed greater chemical resistance compared to pure chitin, measured as a decrease of around ten times in the loss of mass when the material was submerged in an acid aqueous medium at pH 5 (from 19.6 to 1.5%). These results demonstrated the strong interaction between chitin and polyurethane on their contact surface. Nevertheless, FTIR-ATR methodology was used in order to get a better understanding of the biopolymer-matrix links formed during the biocomposite synthesis. For the FTIR-ATR analysis, a sample of the chitin-polyurethane biocomposite was used as produced. The FTIR-ATR instrument used was a Nicolet 6700 (Thermo Scientific) operating in the wavenumber range of 650 to 4000 cm^{-1} , with ZnSe crystal, 32 scans and 4 cm^{-1} resolution.

3.2 Results and discussion

Analysis of FTIR-ATR spectra showed that the biocomposite spectrum was very similar to that of polyurethane. In addition, it is important to point out that main bands of chitin spectrum were at the same wavenumber intervals that those of polyurethane (see Figure 4).

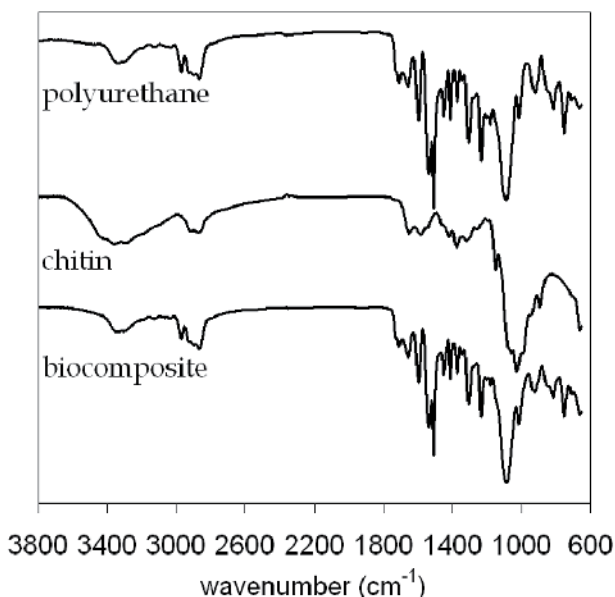


Fig. 4. FTIR-ATR spectra of chitin, polyurethane and chitin-polyurethane biocomposite (modified from Davila-Rodriguez et al., 2009).

Such an aspect contributed to produce the similarity between biocomposite and polyurethane spectra. This fact was predictable because chitin and polyurethane have similar chemical groups on their structures, including amine, amide and carbonyl. Nevertheless, some of the bands observed in the biocomposite spectrum were different in intensity compared to those of polyurethane and chitin. Bands located at 660, 1590 and 3300 cm^{-1} , corresponding to amine/amide groups, and the band located at 3350 cm^{-1} , corresponding to hydroxyl group, experimented appreciable changes in intensity. This phenomenon could be due to the chitin-polyurethane chemical interaction. As previously mentioned, primary amine and hydroxyl groups (both present in chitin structure) are able to react chemically with the polymer functional groups i.e. isocyanate, to form urea and urethane groups, respectively.

On the other hand, it is important to say that chitin-polyurethane interaction has an important physical component, since attraction forces as Van der Waals interactions and hydrogen bonds are present at the interface chitin-polyurethane. This aspect could have caused that chitin-polyurethane chemical interaction was not strong enough to be more clearly observed by means of the FTIR-ATR analysis. In addition, chitin was added to the biocomposite in solid form, which limits the achievability of amine and hydroxyl groups of chitin surface due to a steric impediment. Other important aspect to point out is that polyurethane film thickness over the interface chitin-polyurethane could be irregular, which could difficult to reach the chitin-polyurethane interface by infrared light.

FTIR-ATR characterization of interface chitin-polyurethane could be improved by controlling the uniformity of polyurethane film thickness. This would be achieved by polymerizing the polyurethane in the necessary quantity to cover a high-sized chitin flake (e.g. 1 cm diameter), trying to produce a very thin film. As reported in literature, infrared light penetration depth can range from some hundred nanometers to several micrometers (Kane et al., 2009). Therefore, 1 μm thickness for polyurethane film is sufficient to infrared light reaches the chitin-polyurethane interface; this is part of future work in this research.

4. Carbon nanotubes: Synthesis, properties and modification

Carbon nanotubes (CNT) are key elements in nanotechnology. The structure of carbon nanotubes is depicted as a rolled segment of a graphene sheet, formed by linking each carbon atom to three equivalent neighbors by covalent bonds resulting in a hexagonal network. Carbon nanotubes can be structured by only one graphene sheet (single-wall carbon nanotubes, SWCNT) or by several coaxial graphene sheets (multiwall carbon nanotubes, MWCNT) (Dresselhaus et al., 2001). Synthesis of carbon nanotubes can be carried out by catalytic chemical vapor deposition (CVD) from carbon-containing gaseous compounds which decompose catalytically on transition-metal particles at temperatures lower than 1000 $^{\circ}\text{C}$. CVD processes are becoming the major way for synthesizing carbon nanotubes in a controlled way (Loiseau et al., 2006). It is possible to modify and control the physicochemical properties of carbon nanotubes by doping processes, introducing either non-carbon atoms or molecules at small concentrations in the plane of the graphene lattice.

Doping carbon nanotubes with nitrogen atoms at lower concentrations than 6.5 wt% induce crystalline disorder in the graphene sheets, as well as an excess of electron donors on the nitrogen-rich areas may result in a more reactive structure compared to pure carbon nanotubes. For nitrogen-doped carbon nanotubes (N-MWCNT) two types of C-N bonds

could occur: the first is a three-coordinated N atom within the sp^2 - hybridized network, with the presence of additional electrons. The second type is the pyridine type (two-coordinated N) which can be incorporated in the nanotube lattice; an additional carbon atom is removed from the framework. N-MWCNTs have stacked-cone morphology (bamboo-type) and the degree of tubular perfection decreases as a result of the N incorporation into the hexagonal carbon lattice (Terrones et al., 2002). Moreover, properties of CNTs can also be modified by oxidation with thermal treatment or with acidic solutions (HNO_3 , $KMnO_4^+$, H_2SO_4 , $K_2Cr_2O_7$, H_2O_2). Under acidic oxidation bonds of carbon nanotubes could follow several reactions, for example the formation of quinones which further evolve to different oxygen acidic groups, such as phenolic, lactonic and carboxylic groups. The attached oxygenated groups change the surface chemistry of carbon nanotubes, in particular their wetting behavior and also can be used to attach different chemical groups or to improve their chemical interaction with other substances (Hirsch, 2002; Niyogi et al., 2002). Studies reported previously about oxidation of CNTs in liquid phase suggest that defects at the tips and sidewalls are the most reactive sites to attach oxygen functional groups to the nanotubes structure. These bonded atoms pull the reactive C atom out of the base plane, reducing the curvature strain of nanotubes and creating holes and pores. Long periods of oxidation lead to the shortening and destruction of the nanotubes (Ago et al., 1999; Ovejero et al., 2006; Zhang et al., 2003).

Raman spectroscopy is widely used to evidence the enhancement in defects density along the walls of the carbon nanotubes when oxidation is applied. The main bands of carbon materials are the graphite band (G-band) and the disorder-induced phonon mode (D-band). The relative intensity between the D-band and G-band (ID/IG ratio) indicate a continuously covalent bonding of oxygenated groups along the walls of nanotubes, disrupting the aromatic system of π -electrons (Liu et al., 2004). Complementary information can be obtained with FTIR spectroscopy; it allows determination of functional groups attached to surface of CNTs. This tool was used in some studies carried out by our research group with N-MWCNT, MWCNT and SWCNT, which were oxidized with nitric acid solution (70%) at 80 ± 3 °C for 5 h, as detailed by Perez-Aguilar et al., (2010). Oxidized carbon nanotubes were identified as ox-N-MWCNT, ox-MWCNT and ox-SWCNT, and their morphology was observed by electronic microscopy (Figure 5). As the oxidation of carbon nanotubes was carried out in liquid phase, oxygen containing functional groups were attached along their entire length. Reactions between carbon materials and nitric acid involve strong electrophilic species in solution, which form nitrogen oxides that eventually are reduced to N_2 through oxidation of carbon. Introduction of a small content of nitrogen has been reported, mainly due to the introduction of nitro ($-NO_2$) groups (Chen and Wu, 2004; Zawadski, 1980).

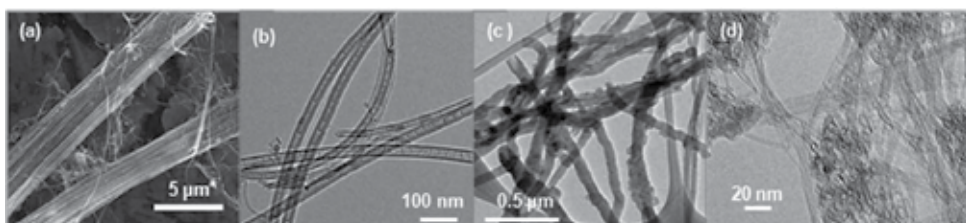


Fig. 5. Micrographs of carbon nanotubes observed by (a) SEM and (b) HRTEM for oxidized N-MWCNTs; HRTEM for (c) oxidized MWCNTs and (d) oxidized SWCNTs. Oxidation with nitric acid at 80 ± 3 °C by 5 h

After the oxidation Van der Waals forces that kept CNTs aggregated were overcome by repulsion forces, as a result of reducing the π -conjugation of nanotubes and enhancing the surface dipoles by oxygen-containing functional groups. This effect was monitored by determining the elemental composition of pristine nanotubes and partially oxidized CNTs.

An important increment in oxygen content was registered as the carbon content was reduced, caused by the destruction of graphene lattice by electrophilic reaction. The hydrogen content also increased in oxidized nanotubes, maybe as a result of the introduction of carboxylic groups. However, for N-MWCNTs the nitrogen content remained almost constant, probably these atoms might change from pyridinic-type or quaternary-type to an aliphatic form. Equilibrium could be established between the consumption of nitrogen atoms of the lattice and the attachment of nitrogen atoms in some sites of the lattice as nitro groups, as occurs when oxidizing some organic molecules or activated carbons with nitric acid (Zawadski, 1980; Chen and Wu, 2004).

4.1 FTIR characterization of oxidized carbon nanotubes

Functional groups attached to oxidized carbon nanotubes were identified by Fourier-transformed infrared spectroscopy by attenuated total reflectance, ATR-FTIR in a Nicolet 6700 FT-IR spectrophotometer at 1068 scans, in the frequency interval of 4000 cm^{-1} to 650 cm^{-1} with resolution of 8 cm^{-1} .

The main functional group attached to oxidized carbon nanotubes was carboxylic. Comparison between spectra of pristine nanotubes and oxidized N-MWCNTs showed that the bands at 1444 cm^{-1} , 1373 cm^{-1} and 1251 cm^{-1} , attributed to vibration of MWCNTs and C-N bonding in N-MWCNTs, were overcome by several vibrations in carbonyl and carboxylic functionalities in the range of 1720 to 1250 cm^{-1} (Choi et al., 2004; Misra et al., 2007). A strong band appeared from 3600 cm^{-1} to 3300 cm^{-1} by the stretching of the bonding -OH of carboxylic group in oxidized nanotubes (Zawadski, 1980; Chen and Wu, 2004).

The nitro group ($-\text{NO}_2$) is isoelectronic with the carboxylate ion group and their spectra are very similar, but a weak feature related to nitro group was observed at 1535 cm^{-1} for oxidized nanotubes (Zawadski, 1980). By other side, spectra obtained for three types of oxidized CNTs (Figure 6) showed broad features from 3400 cm^{-1} to 3000 cm^{-1} by the stretching of the bonding -OH in carboxylic and hydroxyl groups. Signals near 1710 cm^{-1} and 1685 cm^{-1} were of carbonyl vibrations in carboxyl bonding, a weak band about 1640 cm^{-1} of quinones, and the broad band from 1200 to 1000 cm^{-1} was attributed to single-bonded oxygen atoms such as phenols and lactones.

Two weak signals related to the nitro group were observed at 1538 and 1340 cm^{-1} for ox-N-MWCNTs. Similar spectra have been reported for oxidized multiwall carbon nanotubes; characteristic peaks were assigned to carboxylic, carbonyl, and hydroxyl groups (Wang et al., 2007). These results have probe that spectra carefully acquired by FTIR-ATR are a useful tool for identification of chemical groups attached to surface of carbon nanotubes chemically modified.

5. Microstructure of styrene-butadiene copolymers and its hydrogenation

Elastomers like polybutadiene or thermoplastic elastomers like styrene-butadiene-styrene copolymers are widely used in diverse industries. However, the presence of double bonds

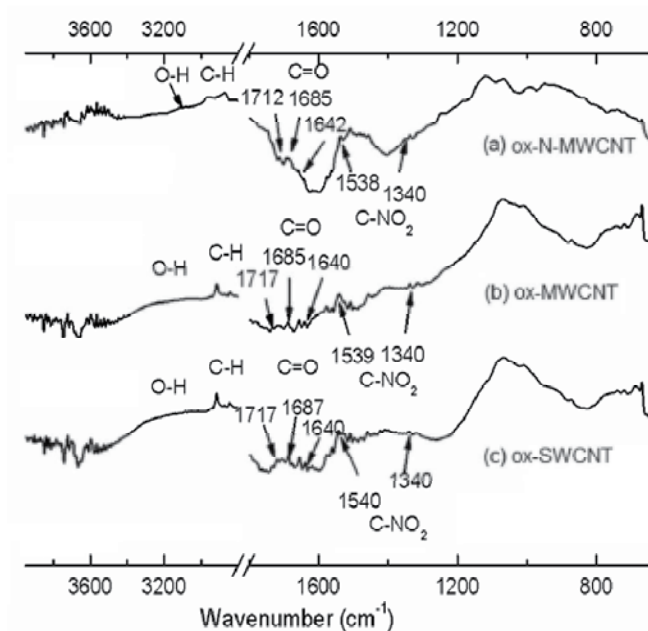


Fig. 6. FTIR spectra of (a) oxidized nitrogen-doped carbon nanotubes, ox-N-MWCNT; (b) oxidized multiwall carbon nanotubes, ox-MWCNT; (c) oxidized single-wall carbon nanotubes, ox-SWCNT, obtained by attenuated total reflectance (ATR)

into their structures promotes degradation by heat or light, making them materials with low outdoor resistance. The hydrogenation of these materials is an effective method to improve their performance for outdoor or high temperatures applications (De Sarkar et al., 1997). In this context, the determination of microstructure (relative quantities of isomers), before and after the hydrogenation, is important since chemical and mechanical resistances are related to it.

In the case of butadiene-containing polymers, the microstructure of the polybutadiene segment (i.e. the relative amount of 1,2 vinyl, 1,4-trans and 1,4-cis bonds) plays an important role in determining their thermal and mechanical properties, as well as their interaction with other materials in the production of composites, such as high-impact polystyrene, modified asphalt, pressure sensitive adhesives, etc. It is also known that anionic polymerization gives copolymers with well-controlled monomer distribution and microstructure, a narrow molecular weight distribution, and the possibility to have end group functionality (Escobar et al., 2000). Hydrogenation of styrene-diene copolymers has received special interest (Bhattacharjee et al., 1993) since the double bond present in the diene segment of the elastomer is susceptible to thermal and oxidative degradation. Hydrogenation of styrene-diene block copolymers allows the production of thermo-oxidative resistant thermoplastics, and selective saturation of diene units (over the rigid units of styrene) permits to control mechanical and thermal properties. Thus, FTIR is essential to determine quantitatively the microstructure, using a liquid cell. Microstructure can be evaluated with time of hydrogenation by FTIR, allowing the establishment of the mechanism of hydrogenation for styrene-butadiene copolymers.

Most of styrene-butadiene copolymers hydrogenation studies have focused on global saturation of polybutadiene double bonds (i.e. 1,4-trans, 1,4-cis and 1,2-vinyl) and on obtaining high saturation percentages (>90%), however, only a few of them have made a distinction on the saturation of the different types of double bonds present in polybutadiene (Escobar et al., 2000).

The evaluation of microstructure and composition (relative quantity of polystyrene in the copolymer) in styrene-butadiene copolymers by FTIR has been conventionally carried out considering just two of three isomers, and the third isomer percentage has been obtained by difference. The previous characterization by RMN is essential in order to contrast the results. However, if it is considered that evaluation of microstructure and composition, of such butadiene-based copolymers, by FTIR takes in account the Beer-Lambert law, expressed as:

$$A = K C L \quad (1)$$

where:

A represents the absorbance at certain wave number,
K is the extinction coefficient at certain wave number,
C is the solution concentration,
L is the path length for the laser light

Therefore, it is possible to express the Beer-Lambert law (Huang, 1995) for each component as follows:

$$A_i = K_{ij} C_j L \quad (2)$$

where:

A_i represents the absorbance at wave number i ,
 K_{ij} represents the extinction coefficient for j unit at wave number i ,
 C_j is the solution concentration of j unit,
L is the path length for the laser light

In the case of liquid cell the path length, L, is the spacer thickness between the KBr windows.

5.1 Experimental

The samples of commercial products were weighted (0.25 g) and dissolved in carbon bisulfide (10 ml). A liquid cell with KBr window was used with a spacer thickness of 0.2 mm. The FTIR equipment was a Magna 560 from Nicolet, with 32 scans, in the mid-red: 4000 a 400 cm^{-1} . These samples also were characterized by ^1H NMR.

5.2 Results and discussion

The results for microstructure and composition determination of polybutadiene portion in styrene-butadiene copolymers are presented in the following section. Such characterization was carried out using the indicated spectrometer and contrasted with the results obtained by ^1H NMR.

The structures corresponding to the polybutadiene isomers, which can be evaluated as it is detailed in the next section, are shown in Figure 7.

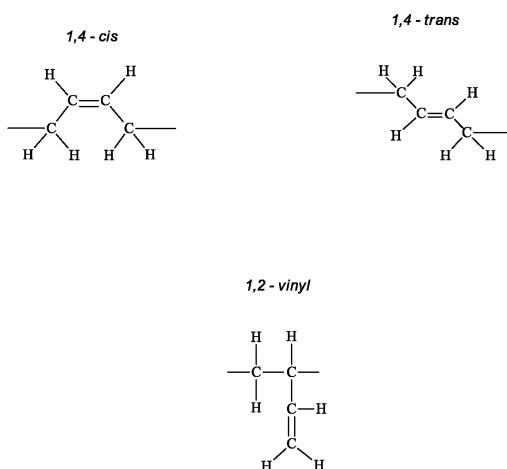


Fig. 7. Isomer structure for the polybutadiene

It is important to mention that the studied styrene-butadiene copolymers and the polybutadiene homopolymer were synthesized by anionic polymerization. Therefore, just three isomers are possible to obtain, the 1,4-cis; 1,4-trans and the 1,2-vinyl.

These isomers are present at different relative quantities, depending on the polymerization conditions. One key factor to modify the microstructure is the presence of chemical named microstructure modifier, which has an interaction with the counterion of the initiator, modifying the bond length and promotes the ion pair formation.

5.2.1 Microstructure and composition

Considering the Beer-Lambert law, and knowing the extinction coefficients for each isomer at specific wave numbers: 698, 728, 910 and 966 cm^{-1} , for the case of styrene-butadiene copolymers, it is possible to evaluate microstructure. The Beer-Lambert law can be expressed as:

$$A_i = \sum K_{ij} C_j L \quad (3)$$

Thus, the equation system can be expressed as a matrix, which can be solved since L and K_{ij} are constants. The reported (Huang, 1995) values for the extinction coefficient are shown in Table 1.

Entity	Extinction coefficient (K)			
	A_{698}	A_{728}	A_{910}	A_{966}
1,4-cis	0.385	0.551	0.037	0.058
1,4-trans	0.005	0.007	0.055	2.542
1,2-vinyl	0.153	0.05	3.193	0.098
styrene	2.703	0.038	0.064	0.05

Table 1. Extinction coefficients for styrene and isomers of styrene-butadiene copolymers

The path length was constant (0.02 cm). Therefore, the matrix is:

$$A_{698} = 7.7 \times 10^{-3} C_{\text{cis}} + 3.06 \times 10^{-3} C_{\text{vinyl}} + 1 \times 10^{-4} C_{\text{trans}} + 5.406 \times 10^{-2} C_{\text{St}}$$

$$A_{728} = 1.102 \times 10^{-2} C_{\text{cis}} + 1 \times 10^{-3} C_{\text{vinyl}} + 1.4 \times 10^{-4} C_{\text{trans}} + 7.6 \times 10^{-4} C_{\text{St}}$$

$$A_{910} = 7.4 \times 10^{-4} C_{\text{cis}} + 6.386 \times 10^{-2} C_{\text{vinyl}} + 1.1 \times 10^{-4} C_{\text{trans}} + 1.28 \times 10^{-3} C_{\text{St}}$$

$$A_{966} = 1.16 \times 10^{-3} C_{\text{cis}} + 1.96 \times 10^{-3} C_{\text{vinyl}} + 5.084 \times 10^{-2} C_{\text{trans}} + 1 \times 10^{-3} C_{\text{St}}$$

Once it was established the equations, they were solved. Thus, several commercial samples were evaluated according with matrix. The obtained values are shown in Table 2.

As it can be seen from Table 2, there is a good agreement in the microstructure calculated by FTIR and ^1H NMR. Bearing in mind that microstructure and composition calculated by ^1H NMR are the real values, the higher deviation, for cis and trans values, was achieved when the styrene content was above 39 % w/w. The last is probably due for overtones for vinyl and trans isomers, which appear with such styrene content.

Sample	% St (^1H NMR)	% Vinyl (^1H NMR)	% Cis (^1H NMR)	% Trans (^1H NMR)	% St	% Vinyl	% Cis	% Trans
S-200	0	9.12	40.21	50.67	0	9.51	42.39	48.1
S-1110	16.15	9.12	38.95	51.93	15.43	9.43	40.11	50.44
S-1205	24.39	9.39	40.63	49.98	24.05	9.74	38.5	51.76
S-1322	30.43	8.59	40.18	51.22	29.72	8.87	42.68	48.44
S-1430	39.94	8.82	39.07	52.12	39.14	8.74	43.21	48.05
S-314	69.69	16.89	27.12	55.98	67.35	14.79	33.78	51.43
S-411	30.37	14.56	35.54	49.89	29.7	15.07	35.71	49.23
S-416	29.96	12.69	36.51	50.79	29.37	13.71	36.89	49.39
S-4318	33.17	13.44	36.12	50.44	32.04	14.05	37.29	49.39

Table 2. Microstructure and composition of several commercial samples.

Nevertheless, there was a good correlation between the obtained results by both methods, corroborating that FTIR can be used with confidence, in order to evaluate composition and microstructure of styrene-butadiene copolymers. Nevertheless, it is important to mention that the use of the liquid cell is not infallible, since the path length can be modified when the cell is cleaned.

5.2.2 Hydrogenation

Once the method for microstructure by FTIR was established, the hydrogenation of butadiene-based copolymers can be traced. Disappearance of each isomer of butadiene can be recorded with time. Thus, it is possible to see if hydrogenation is selective toward certain isomer or not, and also it is possible to see if polystyrene portion is saturated or affected by hydrogenation.

The hydrogenation of elastomeric portion (polybutadiene) in the styrene-butadiene copolymers can be visualized as it is shown the Figure 8.

The spectra of styrene-butadiene copolymer and the hydrogenated counterpart are shown in the Figure 9.

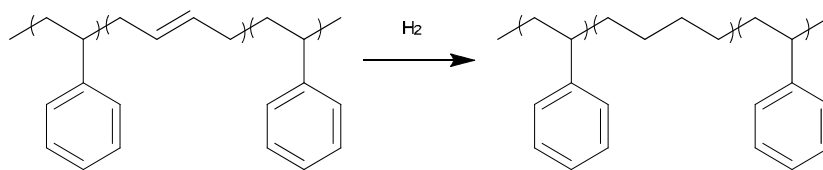


Fig. 8. Hydrogenation of styrene-butadiene copolymer

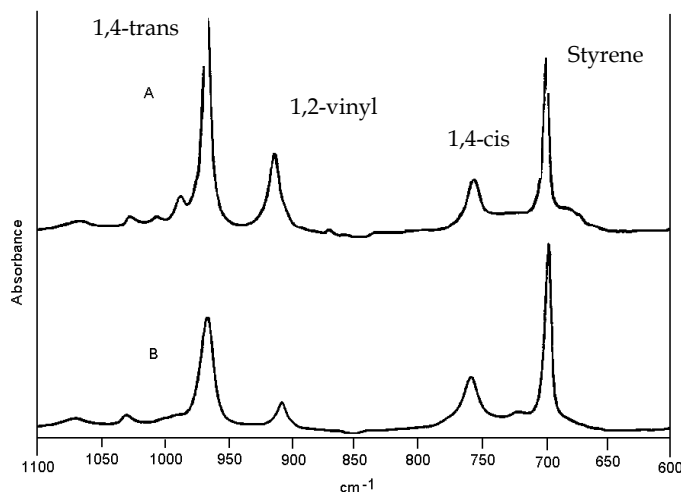


Fig. 9. Spectra of styrene-butadiene copolymer (A) and its hydrogenated product (B)

The spectra shown in Figure 9 indicate that there was a noticeable reduction of the absorbance of 1,2-vinyl, then 1,4-trans followed by 1,4-cis and the absorbance corresponding to styrene remains constant. In previous work (Escobar et al, 2000) it was shown that kinetics of hydrogenation is higher for 1,2-vinyl bonds than for 1,4-trans and 1,4-cis bonds.

The 1,2-vinyl bonds are pendant from the backbone and, therefore, they are more accessible to hydrogen. The FTIR is a useful characterization technique in this case, since it was possible to establish the hydrogenation selectivity toward the 1,2-vinyl bonds and showed that polystyrene remained unsaturated during hydrogenation.

6. Conclusions

FTIR is a powerful and useful characterization method for polymers, and materials in general. This is an economic, short time characterization that allows to establish the chemical composition, microstructure, chemical interactions and even to follow variation of specific functional groups with time, during reactions.

All this features, makes the FTIR an essential characterization technique for polymers. From homopolymers, copolymers to nanocomposites and biocomposites, can be characterized, qualitative and quantitatively, giving the possibility to understand specific interactions and to establish mechanism of reaction, between materials. Thus, the FTIR has contributed to the development of new materials in the polymer science.

In the examples presented herein, the FTIR has permitted to follow specific functional groups with time, to establish the end and/or beginning of a particular reaction.

In addition, FTIR was useful to elucidate about interactions between polymeric matrix (polyurethane) and biopolymer (chitin). However, it is necessary to obtain thinner samples in order to see specific interaction in the interface of materials.

Regarding the nanotubes, it was possible to establish carbon functional group present in the surface of them once these were chemically modified. This is important since this allows figuring out what kind of interactions with other materials could be taken place, and understanding the mechanism of such interactions.

In the case of the establishment of microstructure of styrene-butadiene copolymers, it was demonstrated the capacity of FTIR to be used with confidence as an alternative technique to primary technique like $^1\text{H-NMR}$. The FTIR gives very close values of the relative quantities of the different isomers to those obtained by NMR, besides the composition. Once the methodology was established, it was possible to follow the hydrogenation reaction, in order to see its selectivity toward the isomers.

7. Acknowledgments

The authors are grateful to the Instituto Potosino de Investigacion Cientifica y Tecnologica, A.C. (IPICYT) and to Consejo Nacional de Ciencia y Tecnologia (CONACYT) through Fondos Mixtos CONACYT-State of Puebla (PUE-2004-C02-5), Fondos Mixtos CONACYT-State of San Luis Potosi (FMSLP-2009-C02-106795) and Fondos SEP-CONACYT (SEP-2004-C01-45764 and SEP-CB-2008-01-105920) for the economical support to carry out this work.

In addition, the authors appreciate the technical support of M.C. Dulce Partida-Gutierrez, M.C. Guillermo Vidriales Escobar and Ing. Daniel Ramirez-Gonzalez, the National Laboratory of Nanosciences and Nanotechnology (LINAN) and the National Laboratory of Agricola Biotechnology, Medical and Environmental (LANBAMA) of IPICYT.

8. References

- Ago, H., Kugler, T., Cacialli, S., Salaneck, W., Shaffer, M., Windle, A., & Friend, R. (1999). Work functions and surface functional groups of multiwall carbon nanotubes, *Journal of Physical Chemistry B*, Vol.103, No.38, (September 1999) pp. 8116-8121, ISSN 1520-6106
- Alhakawati, M. S. & Banks, C. J. (2004). Removal of copper from aqueous solution by *Ascophyllum nodosum* immobilised in hydrophilic polyurethane foam. *Journal of Environmental Management*, Vol.72, No.4, (September 2004), pp.195-204, ISSN 0301-4797
- Andrade-Espinosa, G, Escobar-Barrios, V.A. & Rangel-Mendez, J.R. (2010). Synthesis and characterization of silica xerogels obtained via fast sol-gel process, *Colloid and Polymer Science*, Vol. 288, pp. 1697-1704, ISSN 1435-1536
- Bhattacharjee, S., Bhowmick, A. K., & Avasthi, B.N. (1993). Selective hydrogenation of olefinic bonds in styrene-isoprene-styrene triblock copolymer by palladium acetate catalyst. *Polymer*, Vol. 49, No. 11, pp. 1971-1977
- Bhargava, R., Wang, S., & Koenig, J. L. (2003). FTIR Microspectroscopy of polymeric systems, *Advances in Polymer Science*, Vol.163, pp. 137-191, Springer, Verlag Berlin Heidelberg, Germany
- Bower, D.I., Maddams, W.F. (1989) *The Vibrational Spectroscopy of Polymer*, Cambridge University Press, ISBN 0-521-24633-4, Cambridge, UK
- Chen, J., Wu, S. (2004). Acid/base-treated activated carbons: characterization of functional groups and metal adsorptive properties, *Langmuir*, Vol.20, No.6, (March 2004) pp. 2233-2242, ISSN 0743-7463

- Choi, H., Bae, S., Park, J., Seo, K., Kim, C., Kim, B., Song, H., & Shin, H. (2004). Experimental and theoretical studies on the structure of N-doped carbon nanotubes: Possibility of intercalated molecular N₂, *Applied Physics Letters*, Vol.85, No.23, (November 2004) pp. 5742-5744, ISSN 0003-6951
- Davila-Rodriguez, J. L., Escobar-Barrios, V. A., Shirai, K. & Rangel-Mendez, J. R. (2009). Synthesis of a chitin-based biocomposite for water treatment: Optimization for fluoride removal. *Journal of Fluorine Chemistry*, Vol.130, (August 2009), No.8, pp.718-726, ISSN 0022-1139
- De Sarkar, M., De, P.P., & Bhowmick A.K., (1997). Thermoplastic elastomeric hydrogenated styrene-butadiene elastomers: Optimization of reaction conditions, thermodynamics and kinetics. *Journal of Applied Polymer Science*, Vol.66, No. 6, pp. 1151-1162
- Dresselhaus, M., Dresselhaus, G., & Avouris, Ph. (2001). *Carbon Nanotubes. Synthesis, structure, properties and applications*, Springer, ISBN 3-540-41086-4, Verlag Berlin Heidelberg, Germany
- Escobar-Barrios, V. A., Herrera-Najera, R., Petit, A. & Pla, F. (2000) Selective Hydrogenation of butadiene-styrene copolymers using a Ziegler-Natta type catalyst. Part 1. Kinetic study. *European Polymer Journal*, Vol. 36, pp. 1817-1834
- Elnashar, M. M., (Ed.). (2010). *Biopolymers*, Sciyo, ISBN 978-953-307-109-1, Rijeka, Croatia
- Fidalgo, A., Ilharco L.M. (2005). The influence of the wet gels processing on the structure and properties of silica xerogels. *Microporous and Mesoporous Materials* Vol. 84, pp. 229-235, ISSN 1387-1811
- Fowler, P. A., Hughes, J. M. & Elias, R. M. (2006). Biocomposites: technology, environmental credentials and market forces. *Journal of the Science of Food and Agriculture*, Vol.86, (September 2006), No.12, pp.1781-1789, ISSN 1097-0010
- Hepburn, C. (1982). *Polyurethane Elastomers*, Applied Science Publishers, London and New York
- Hirsch A (2002) Functionalization of single-walled carbon nanotubes, *Angewandte Chemie International Edition*, Vol.41, No.11, (June 2002) pp. 1853-1859, ISSN 1521-3773
- Huang, D., Lin, Y. Y., & Tsiang, Ch. (1995). Synthesis of SBS thermoplastic block copolymers in cyclohexane in the presence of diethylether used as a structure modifier. *Journal of Polymer Research*, Vol. 2, No. 2, pp. 91-98 ISSN 1022-9760
- Kane, S. R., Ashby, P. D. & Pruitt, L. A. (2009). ATR-FTIR as a thickness measurement technique for hydrated polymer-on-polymer coatings. *Journal of Biomedical Materials Research Part B: Applied Biomaterials*, Vol.91B, No.2, (November 2009), pp.613-620, ISSN 1552-4981
- Koenig, J.L. (2001). *Infrared and Raman Spectroscopy of Polymers*, Rapra Technology, ISBN-10: 1859572847, Shropshire. UK
- Lee, L.H., Ed. (1977). *Characterization of Metal and Polymer Surfaces: Polymer Surfaces* Academic Press, ISBN-10: 0124421016, New York, USA
- Li, H., Liu, T., Li, Z. & Deng, L. (2008). Low-cost supports used to immobilize fungi and reliable technique for removal hexavalent chromium in wastewater. *Bioresource Technology*, Vol.99, (May 2008), No.7, pp.2234-2241, ISSN 0960-8524
- Liu, Y., Pan, C., & Wang, J. (2004) Raman spectra of carbon nanotubes and nanofibers prepared by ethanol flames, *Journal of Materials Science*, Vol.39, No.3, (February 2004) pp. 1091-1094, ISSN 0022-2461
- Loiseau, A., Blasé, X., Charlier, J., Gadelle, P., Journet, C., Laurent, Ch., & Peigney, A. (2006). Synthesis methods and growth mechanisms, In: *Understanding carbon nanotubes. From basics to applications*, A. Loiseau, P. Launois, P. Petit, S. Roche, J.P. Salvetat (Eds.), 49-130, Springer, ISBN 103-540-26922-3, Berlin Heidelberg, Germany

- Mao, J., Won, S. W., Vijayaraghavan, K. & Yun, Y.-S. (2010). Immobilized citric acid-treated bacterial biosorbents for the removal of cationic pollutants. *Chemical Engineering Journal*, Vol.162, No.2, (August 2010), pp.662-668, ISSN 1385-8947
- Misra, A., Tyagi, P., Rai, P., & Misra, D. (2007). FTIR spectroscopy of multiwalled carbon nanotubes: A simple approach to study the nitrogen doping, *Journal of Nanoscience and Nanotechnology*, Vol.7, No.12, (December 2007) pp. 1820-1823, ISSN 1533-4880
- Niyogi, S., Hamon, M., Hu, H., Zhao, B., Bhowmik, P., Sen, R., Itkis, M., & Haddon, R. (2002). Chemistry of single-wall carbon nanotubes, *Accounts of Chemical Research*, Vol.35, No.12, (October 2002) pp. 1105-1113, ISSN 0001-4842
- Ovejero, G., Sotelo, J., Romero, M., Rodríguez, A., Ocana, M., Rodríguez, G., & Garcia, J. (2006). Multiwalled carbon nanotubes for liquid-phase oxidation. Functionalization, characterization and catalytic activity. *Industrial Engineering Chemistry Research*, Vol.45, No.7, (March 2003) pp. 2206-2212, ISSN 0888-5885
- Pastor, A., (Ed.). (2004). *Quitina y Quitosano: obtención, caracterización y aplicaciones*, Programa CYTED, CIAD, A.C., Fondo Editorial de la Pontificia Universidad Católica del Perú, ISBN 9972-42-659-9, Lima, Perú
- Perez-Aguilar NV, Muñoz-Sandoval E, Diaz-Flores PE, & Rangel-Mendez JR (2010) Adsorption of cadmium and lead onto oxidized nitrogen-doped multiwall carbon nanotubes in aqueous solution. *Journal of Nanoparticle Research*, Vol.12, No.2, (February 2010) pp. 467-480, ISSN 1388-0764
- Sawyer, L.C., Grubb, D.T., & Meyers, G.F. (2008). *Polymer Microscopy* (3rd. edition), Springer, ISBN 978-0-387-72627-4, Verlag Berlin Heidelberg, Germany
- Sudha Bai, R., Abraham, T. E. (2003). Studies on chromium(VI) adsorption-desorption using immobilized fungal biomass. *Bioresource Technology*, Vol.87, No.1, (March 2003), pp.17-26, ISSN 0960-8524
- Terrones, M., Ajayan, P.M., Banhart, F., Blasé, X., Carroll, D.L., Charlier, J.C., Czerw, R., Foley, B., Grobert, N., Kamalakaran, R., Kohler-Redlich, P., Ruhle, M., Seeger, T., & Terrones, H. (2002). N-doping and coalescence of carbon nanotubes: synthesis and electronic properties, *Applied Physics A Materials Science & Processing*, Vol.74, No.3, (December 2001), pp. 355-361, ISSN 0947-8396
- Vullo, D. L., Ceretti, H. M., Daniel, M. A., Ramirez, S. A. M. & Zalts, A. (2008). Cadmium, zinc and copper biosorption mediated by *Pseudomonas veronii* 2E. *Bioresource Technology*, Vol.99, No.13, (September 2008), pp.5574-5581, ISSN 0960-8524
- Wang, H., Zhou, A., Peng, F., Yu, H., & Yang, J. (2007). Mechanism study on adsorption of acidified multiwalled carbon nanotubes to Pb(II), *Journal of Colloid and Interface Science*, Vol.316, No.2, (December 2007) pp. 277-283, ISSN 0021-9797
- Zawadzki, J. (1980). IR Spectroscopic investigations of the mechanism of oxidation of carbonaceous films with HNO₃ solution, *Carbon*, Vol.18, No.4, (April 2003) pp. 281-285, ISSN 0008-6223
- Zhang, J., Zou, H., Qing, Q., Yang, Y., Li, Q., Liu, Z., Guo, X., & Du, Z. (2003). Effect of chemical oxidation on the structure of single-walled carbon nanotubes, *Journal of Physical Chemistry B*, Vol.107, No.16, (March 2003) pp. 3712-3718, ISSN 1520-6106
- Zhang, P. He, J., & Zhou, X. (2008). An FTIR standard addition method for quantification of bound styrene in its copolymers, *Polymer Testing*, vol. 27, pp. 153-157 ISSN 0142-9418
- Zhang, Y., Banks, C. (2006). A comparison of the properties of polyurethane immobilised Sphagnum moss, seaweed, sunflower waste and maize for the biosorption of Cu, Pb, Zn and Ni in continuous flow packed columns. *Water Research*, Vol.40, No.4, (February 2006), pp.788-798, ISSN 0043-1354

Preparation and Characterization of PVDF/PMMA/Graphene Polymer Blend Nanocomposites by Using ATR-FTIR Technique

Somayeh Mohamadi
*Polymer group,
School of Chemistry,
University College of Science,
University of Tehran, Tehran
Iran*

1. Introduction

With improvement in the human life, the requisite of the new materials with special properties for many different applications ranging from food packaging and consumer products to use as medical devices and in aerospace technologies can be sensed, strongly. Polymeric materials offer this opportunity to scientists and engineers for designing these new materials. In this regard, precise understanding of Structure and Properties Relationship (SPR) should be very crucial.

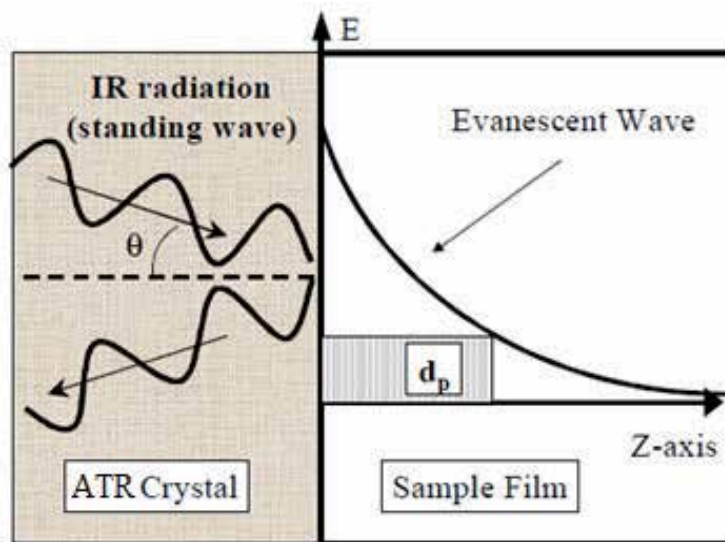
Recently, polymeric nanocomposites have opened a new research area and attracted strong attentions. The synthesis of polymer nanocomposites by inserting the nanometric inorganic compounds is an integral aspect of polymer nanotechnology (A. Lagashetty, 2005). These materials, depending upon the inorganic materials present, have particular and improved properties respect to pure polymers that invest their applications.

Fourier transform infrared (FTIR) spectroscopy is a powerful and reliable technique that for many years has been an important tool for investigating chemical processes and structures. In the polymer fields, FTIR data is used in order to study characterization of chemical bonds, polymer microstructure, chain conformation, polymer morphology, crystallinity and etc, consequently is useful in SPR studies.

The combination of infrared spectroscopy with the theories of reflection has made advances in surface analysis possible. Attenuated Total Reflectance (ATR) spectroscopy is an innovative technique for proving chemical information of a sample surface and the ability to quantify newly formed species, based upon Fick's second law. The fundamentals of attenuated total reflection (ATR) spectroscopy date back to the initial work of Jacques Fahrenfort and N.J. Harrick, both of whom independently devised the theories of ATR spectroscopy and suggested a wide range of applications. The schematic showing ATR-FTIR configuration is illustrated in Fig. 1 (KS. Kwan, 1998). The penetration depth, d , can be estimated as:

$$d = \frac{1}{2\pi n_c \sigma (\sin^2 \theta - n_x^2)^{1/2}} \quad (1)$$

where n_c is the refractive index of the ATR crystal and n_x is the ratio between the refractive indexes of the sample and the ATR crystal (which both of them are assumed to be constant in the considered frequency range). σ is the wave number and θ is the incident angle. The penetration depth for PVDF as an example by the assumption of $n_c = 2.4$, $n_x = 1.5$ and $\theta = 45^\circ$ from 500 to 4000 cm^{-1} is approximately 0.5-4 μm (Y. Jung Park, 2005).



Scheme 1. Schematic illustration of ATR-FTIR configuration (KS. Kwan, 1998)

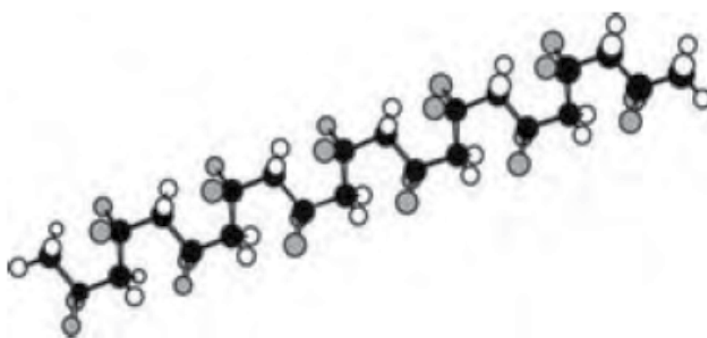
Graphene and graphite have recently attracted strong attention as versatile, environmentally friendly and available carbon materials which can be used as inexpensive filler in the composite materials (S. Stankovich, 2006, 2007 & L. Al-Mashat, 2010). Crystalline graphites are used in polymeric systems in order to improve polymer properties such as thermal and electrical conductivity, IR absorption, flame retardancy, barrier resistance, electromagnetic shielding, lubrication and abrasion resistance. When the crystalline graphite is exfoliated to individual graphene sheets, the specific surface would be as large as 2600 $\text{m}^2 \cdot \text{g}^{-1}$ and novel electronic and mechanical properties appeared (Steurer, 2009). Actually graphene sheets are one-atom two-dimensional layers of sp^2 - network carbon that their fracture strength should be comparable to that of carbon nanotubes with similar types of defects (S. Stankovich, 2007). How to exfoliate the flakes of natural graphite was first described in a US patent in 1891 (Inagaki, 2004). An exfoliation phenomenon was studied mostly and occurs when the graphene layers are forced apart by the sudden vaporization or decomposition of intercalated species (E. H. L. Falcao, 2007).

However, the mentioned properties of graphene-polymer nanocomposites are strongly dependent on the uniformly dispersion in polymeric matrices which is affected by functional groups present on the graphene surface.

The modification of graphene sheets via organic oligomeric and polymeric chains is a favorable way to promote the compatibility of these nanoparticles with polymeric media. So understanding of the functional groups present on the graphene surface should be very vital for designing of modification procedure.

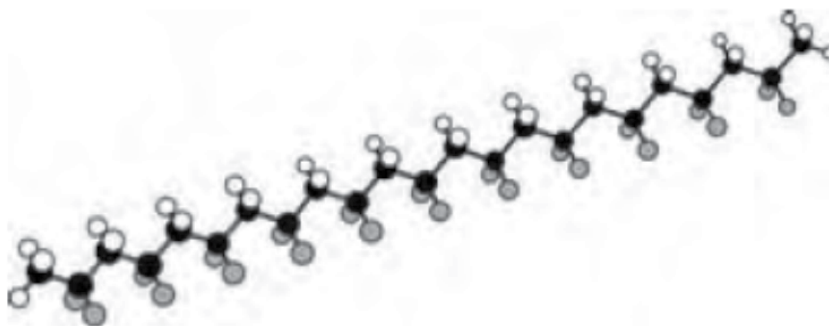
Poly(vinylidene fluoride) (PVDF) is a semicrystalline engineering polymer with very good resistance to chemicals, oxidation, and UV radiation (J. H. Yen, 2006). PVDF is known for its polymorphism crystalline structure and complicated microstructure. It is one of the most widely studied polymers due to its non-linearity, piezo- and pyro-electricity (L. T. Vo, 2007 & K. Pramoda, 2005). PVDF can crystallize in at least five well-known crystalline phases (E. Giannetti, 2001, A. Lovinger, 1982 & N. S. Nalwa, 1995):

α and δ with conformation of the alternating trans-gauche (TG^+TG^-) which the α is the most common form and is the most thermodynamically stable.



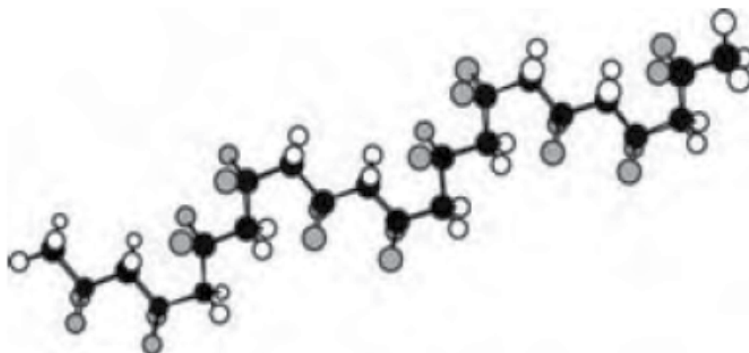
Scheme 2. α and δ form with alternating trans-gauche conformation (J. H. Yen, 2006)

β with all trans (TTT) planer zigzag conformation is polar form and has been extensively studied for its potential applications. This form develops under mechanical deformation (K. Matsushige, 1980) (S. Ramasundaram, 2008) , growth from solution (J. Wang, 2003 & R. L. Miller, 1976), addition of metal salts (X. He, 2006 & W. A. Yee, 2007) , melt crystallization at high pressures (D. Yang, 1987), application of a strong electric field (J. I. Scheinbeim, 1986), blending with carbonyl-containing polymers (C. Lbonard, 1988 & K. J. Kim, 1995), and recently, addition of nanoparticles (S. Ramasundaram, 2008, T. Ogoshi, 2005 & L. He, 2010). This structure provides some unique properties for PVDF piezo- and pyro-electric activity:



Scheme 3. β form all trans planer zigzag conformation (J. H. Yen, 2006)

γ and ϵ with $T_3G^+T_3G^-$ conformation is also polar but less than β form.



Scheme 4. γ and ϵ crystalline form with $T_3G^+T_3G^-$ conformation (J. H. Yen, 2006)

Subsequently due to specific chain conformation in crystal unit cell and providing the highest remnant polarization, β phase has attracted more attention than the others in pyro- and piezoelectric applications (J.Jungnickel, 1996).

Poly methylmethacrylate (PMMA) can interact with graphene sheets by the interaction of delocalized π -bonds of graphene with π -bonds of PMMA. On the other hand, as reported in articles, PVDF/PMMA blend is a miscible system. Consequently, in attempt to achieve a homogenous dispersion of nanographene layers in PVDF matrix, the use of PMMA chains as a compatibilizer can be useful.

In addition, presence of PMMA chains in the close touch with PVDF molecules causes the formation of polar crystalline form in PVDF (J. Wang, 2003). Furthermore, previous studies on the CNTs indicated TTT molecular chain prefers to be absorbed on the CNT surface compared with TGTG' molecular chain, and the configuration in which H atoms and CNT surface are face-to-face are more stable than that where F atoms and CNT surface are face-to-face. Since in the PVDF, the negative charge transfer from H to C atom and the negative charge is accumulated around the F atoms, the interaction between the H atoms with positive charge in PVDF and C atoms with π orbital in CNT should be stronger (S. Yu, 2009)

FT-IR is a powerful and reliable technique for description of chemical characterization of graphene and also study of the structure and properties relationships in PVDF/PMMA/graphene polymer blend nanocomposite. The interactions between these three components including: PVDF, PMMA and graphene sheets can be revealed and described by using this technique. As well, exploration of PVDF chains conformations (crystalline structures) are affected by presence of graphene sheets and PMMA chains can be done which is very important in order to design the new material with special properties.

2. Experimental

2.1 Materials

The graphite used in this study was natural graphite powders with the size of $>150 \mu\text{m}$, and bulk density of 1.65 gr/cm^3 supplied by Iran Petrochemical Co. The PVDF pelletlet (Kynar®

1000HD) was provided by Atofina Co. The methyl methacrylate (MMA) and Methacrylic anhydride were supplied by Aldrich Co. and MMA used after purification and distillation in order to remove inhibitors. Concentrated sulfuric acid and nitric acid with concentration of 63% were used as chemical oxidizer to prepare expanded graphite. The initiator, Benzoyl peroxide (BPO), dichloromethane (CH_2Cl_2), dimethylformamide (DMF), triethylamine (TEA) were bought from Merck Co. and used as received.

2.2 Preparation of exfoliated graphite

The method which was used in this study is as same as general procedure employed in industry for producing exfoliated graphite. Natural graphite powders as starting material were treated with a mixture of 4:1 sulfuric and nitric acid at 80°C for 24h to produce Graphite Intercalated Compounds (GIC)s. Graphite can accept many species into the gallery between graphite layer planes to form GICs.

Sulfuric acid is the most conventional intercalate for achieving a high degree of exfoliation of natural graphite and so it is used most commonly in the industry. Nitric acid was also added as an oxidant to generate some functional groups such as hydroxyl, carboxyl, epoxid groups on the surface and edge of graphene sheets.

The suspension of acid-treated graphite was added to excess distilled water, and this was followed by centrifugation with 5000 rpm and washing with water until the pH of the centrifuge drainage extraction was natural.

These particles dried at oven at 100°C for 12h and vacuumed oven at 80°C for 8h. The oxidized graphite was heat-treated at 1050°C for 45s to obtain expanded graphite. Actually, In Chung's review, exfoliation phenomena were classified into reversible and irreversible ones. When the oxidized graphite was heated to around 300°C , it expanded to a fractional expansion of about 30 and upon cooling collapsed, again. This expansion-collapse phenomenon was reversible, and was thus called reversible exfoliation.

But if it is heated to a higher temperature (e.g., 1000°C), the intercalating compound and some of functional groups decompose completely and at the same time the host graphite flakes exfoliate up to about $300\times$ in volume, particularly by rapid heating. This exfoliated graphite never returns to the original thickness upon cooling to room temperature, that is, we have irreversible exfoliation. The expanded graphite was immersed in absolute ethanol and sonicated for 30 min in order to exfoliate and break down to individual layers. The dispersion was filtered and dried at oven at 80°C for 8h and vacuumed oven at 80°C for 4h to remove residual moisture in the graphite particles (S. Mohamadi N. S.-S., 2011).

2.3 Modification with methacrylic anhydride

The above Functionalized Graphite, which is called FG, was reacted with methacrylic anhydride to provide some organic groups and vinyl moieties on the surface of graphene. Actually, the functional groups which were introduced in the previous process could further react with methacrylic anhydride through hydroxyl groups. A 250-mL flask was charged with 100 mL of DMF, 10 mL TEA and 100 mg FG and after sonication for 30 min, a solution of containing 5 mL methacrylic anhydride and 90 mL DMF was added in to the mixture.

This mixture was allowed to react at 90°C for 24h under magnetic stirring. After that the Modified Graphite, for simplicity it is called MG, were collected by filtration and followed by thorough washing with distilled water to remove any residual TEA and then washed with CH₂Cl₂, in order to remove any unreacted methacrylic anhydride. The washed particles were dried in oven and vacuum oven at 80°C for 8h, separately.

2.4 Preparation of PMMA/ graphene masterbatch

The PMMA-graphene masterbatch (PMMA-G master) was prepared via polymerization of MMA with BPO as an initiator. 300 mg of MG was dispersed in 15 mL MMA via ultrasonication for 30 min. The polymerization was initiated by (1.1% wt) of BPO respect to monomer in flask at 90°C, until the polymerization was solidified, completely. Later then, the prepared masterbatch was kept in vacuum oven at 120°C to remove any remaining MMA. The content amount of graphite was kept in 2.5 wt%.

2.5 Preparation of PVDF/PMMA/graphene nanocomposite

PVDF and PMMA-G master solutions were prepared separately by dissolving in DMF at 50°C with stirring for 1 day. Both of the resulting solutions were blended, so that the final concentration of mixture adjusted in 12% wt. on the weight of PVDF/PMMA-G master respect to solvent. The mixture was sonicated for about 30 min, stirred 2 days and spread on a well-cleaned glass slide of petridish. The prepared sample was carefully evaporated at 60°C in an oven for 20 h and then divided into three parts and annealed at three different temperatures of 50, 90 and 120°C in vacuum oven for 24 h. three samples with varying PVDF/PMMA-G master ratios of 80:20, 70:30 and 60:40 were prepared and analyzed. For convenience the samples were named as 80:20, 70:30, 60:40 and 70:30 No G, respectively (S. Mohamadi, 2011).

2.6 Characterization

The Fourier transform infrared (FT-IR) analysis was performed on a Bruker Equinox55 Analyzer, equipped with a DTGS detector and a golden gate micro ATR from 600 –3500 cm⁻¹. Scanning electron microscopic (SEM) and TEM images were obtained on a Zeiss CEM 902A (Oberkochen, Germany) and Philips-CM-120, Netherlands at an accelerating voltage of 120 KV, respectively. The thermal behavior was measured with a DSC Q100 from the TA instruments with the heating and cooling ramp of 10 °C min⁻¹ from room temperature to 250 °C under argon flow. The X-ray diffraction (XRD) patterns of the samples were recorded by Philips, Netherlands advanced diffractometer using Cu(K α) radiation (wavelength: 1.5405Å) at room temperature in the range of 2 θ from 4 to 70° with a scanning rate of 0.04° . S⁻¹.

3. Results and discussion

As reported by others in several literatures, presence of the relatively broad peak at 3427 cm⁻¹ and also the peak at 1402 cm⁻¹ in the FTIR spectra of graphite oxide indicate existence of hydroxyl groups. In addition, the peaks at 1720, 1640, 1580 and 1060 cm⁻¹ can be assigned to the stretching vibration of carboxyl, carbonyl moiety of quinone, aromatic C=C bonds and epoxide groups, respectively (scheme 1) (C. Hontoria-Lucas, 1995) . To determine which

functional groups existed in the graphene sheets after heat treated of graphene oxide (FG) and functionalization with methacrylic anhydride, the related FTIR spectra has been illustrated in Fig. 1.

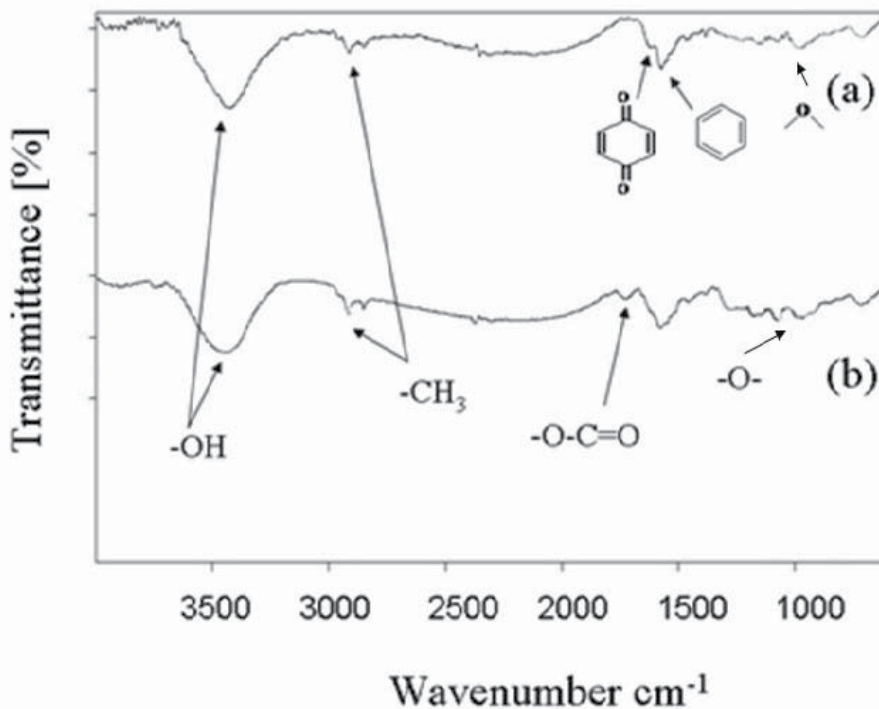
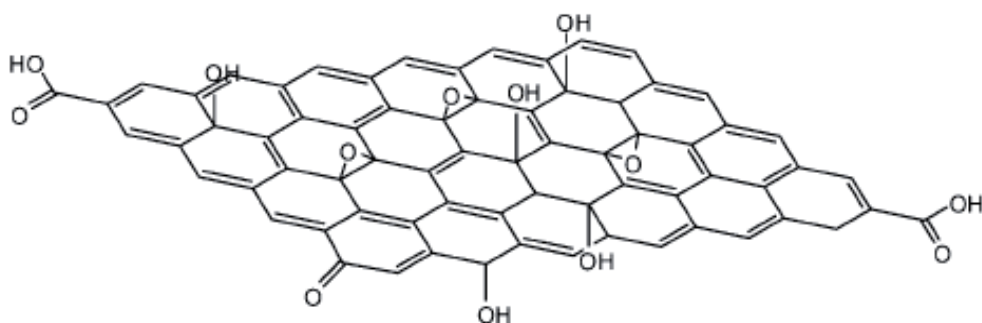


Fig. 1. FTIR spectrums of FG (a) and MG (b).

As can be seen in Fig. 1 (a) most of carboxyl groups in the graphene oxide has decomposed during heat-treatment of graphite oxide so that the peak at 1720 cm^{-1} disappeared. In fact, during the acid treatment various oxygen-functional groups were produced on the graphene surface. While, in the heat-treatment step, the oxygen containing of graphene was reduced but some introduced functional groups remained and still the particles can contain significant amount of oxygen (Steurer, 2009).

In addition, the peaks at 2960 and 2930 cm^{-1} are related to the asymmetric and symmetric stretching vibration of pendant methyl groups. Symmetric vibrations are generally weaker than asymmetric vibrations since the former lead to less of a change in dipole moment. Actually, during sonication it may graphene flakes are broken and this pendant methyl groups came into sight.

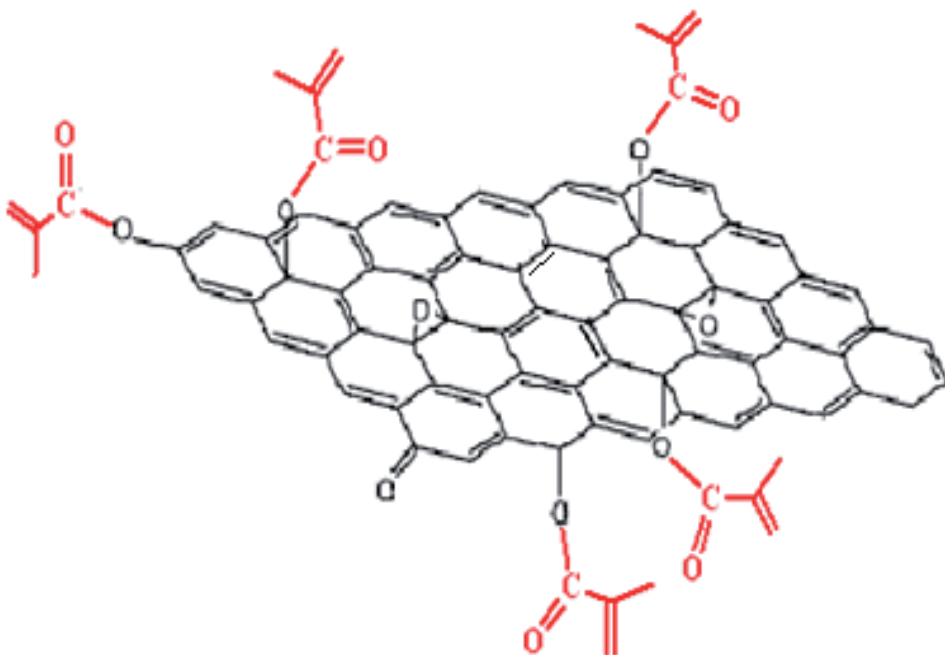
In the case of MG, (Fig. 1 (b)) appearance of a new peak at 1740 cm^{-1} which has been assigned to vibration of ester carbonyl group is due to the formation of esteric linkages between hydroxyl groups of FG and methacrylic anhydride (Scheme 6). Modification of FG by methacrylic anhydride (MG), causes appearance of the new methyl groups which show the peaks at 2960 and 2930 cm^{-1} . Furthermore, C=C band at 1580 cm^{-1} has become



Scheme 5. Graphite oxide (P. Steurer, 2009)

more broader in MG rather than FG may due to presence of aromatic and aliphatic double bonds.

ATR-FTIR spectrum of pure PVDF film which was annealed at 50°C, from 550-3500 cm^{-1} is also shown in Fig.2. The observed pattern originates from oscillations of large parts of the skeleton and/or the skeleton and attached functional groups. Below 1500 cm^{-1} , most single bonds absorb at similar frequencies, and the vibrations couple.



Scheme 6. Modified graphene with methacrylic anhydride (S. Mohamadi, 2011)

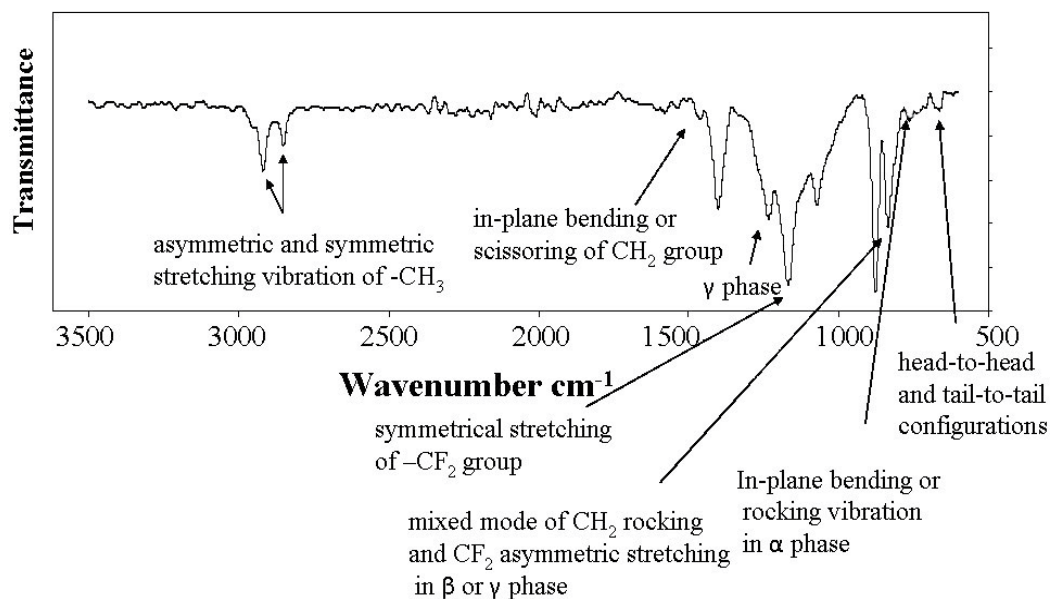


Fig. 2. ATR-FTIR spectrum of pure PVDF film which was annealed at 50°C

It should be pointed that since the β- and γ-phase are similar to each other in short segmental conformations the identification of crystal phase between β and γ in FTIR spectrum is still in dispute. On the basis of the data from literature the absorption band at 763 cm⁻¹ is related to In-plane bending or rocking vibration in α phase (N. Betz, 1994 & S. Lanceros-Mendez, 2001), the band at 840 cm⁻¹ stretching in β or γ phase (G. Chi Chen, 1994 , V. Bharti, 1997, B. Mattsson, 1999 & M. Benz, 2002), the band at 1173 cm⁻¹ is associated to the symmetrical stretching of -CF₂ group (M. Rajendran, 2010). The band at 1234 cm⁻¹ is related to the γ phase and 1453 cm⁻¹ is assigned to in-plane bending or scissoring of CH₂ group (M. Rajendran, 2010 & Garton, 1992).

In addition, some irregularities of head-to-tail addition, leading to defect structures, can occur during polymerization for several reasons in polymers of the vinylidene class, sequence isomerism may occur. The transmission band at 677 cm⁻¹ points to the presence of head-to-head and tail-to-tail configurations (B. Hilczer, 1998). Such defects are produced during the polymerization process and reduce the dipole moment of the all-trans conformation.

Fig. 3 shows ATR-FTIR spectra for pure PVDF film (a), G-PMMA master (b), 80:20 (c), 70:30 (d), 70:30 NoG (e), 60:40 (f) which were annealed at 50°C from 550-2000 cm⁻¹. When MG was incorporated in PMMA matrix (G-PMMA master), the absorption originating from MG particles alone were hardly visible. G-PMMA master spectrum clearly shows several characteristic peaks at 1723, 1449 and 1142 cm⁻¹ which are related to the presence of PMMA chains, assigned to ester carbonyl (C=O), O-CH₃ and C-O (ester bond) stretching.

Polymer- polymer interactions may also affect PVDF chain conformations. Specific interactions are very sensitive to the distance between the interacting groups and to their

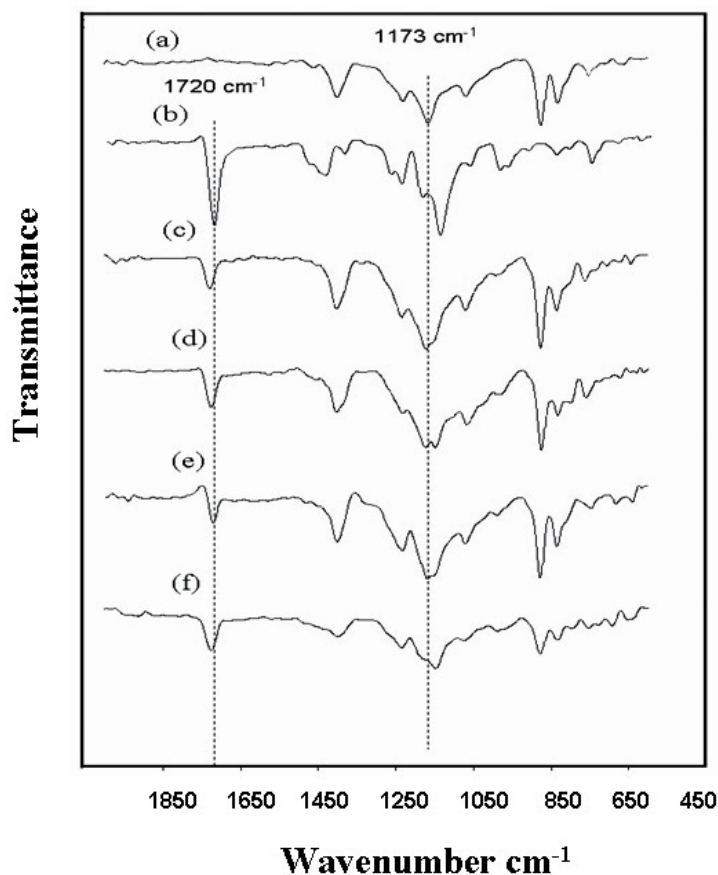


Fig. 3. ATR-FTIR spectra of pure PVDF (a), G-PMMA master (b), 80:20 (c), 70:30 (d), 70:30 NoG (e), 60:40 (f) which were annealed at 50°C.

relative orientation: hydrogen bonding strength falls off rapidly when the atomic distance increases or when the bond is bent instead of linear. This infers that the efficiency of the contact between two unlike chains depends on their respective conformation (eventually tacticity) and flexibility. The chains are expected to adopt an optimum conformation for interacting (C. Lbonard, 1988).

To identify the nature of the interactions in the polymer blend nanocomposite, we choose the band at 1720 cm^{-1} which is due to the stretching vibration of the C=O group in PMMA as a characteristic peak of PMMA. This band shows a little shift to the higher frequencies and has become broader in both of the polymer blend with no graphene and nanocomposites. These changes can be ascribed by the interaction between PMMA and PVDF chains (I. S. Elashmawi, 2008 & M. M. Coleman, 1995).

The strong absorption peak which appeared at 1173 cm^{-1} is assigned to the symmetrical stretching of $-\text{CF}_2$ groups, was chosen as characteristic peak of PVDF in polymer blend nanocomposites. The precise consideration reveals shifting of this band to the higher frequencies in the synthesised samples comparing to pure PVDF. Since this shifting is

slighter for 70:30 NO G than polymer blend nanocomposites, it can be imagined this change is related to the specific interactions between PVDF and graphene surface in the nanocomposites. Also, it can be concluded GNPs increase the compatibility of PVDF and PMMA.

On the other hand as mentioned above, presence of polymer-polymer interactions can also affect the polymer conformations. PVDF exhibits short bond sequences tt and tg; the probability of a gg bond is negligible because of steric hindrance. Energy calculations emphasize that PMMA conformation remains close to all trans conformation of PVDF. In our study, presence of graphene particles along with PMMA chains makes it complex due to PVDF-PMMA, PVDF-graphene and PMMA-graphene interactions.

The surface morphology of the casted films was studied using SEM analysis. In each sample, the surface which is exposed to the air is examined. The distinguishable spherulitic structure on the top surface of pure PVDF film could be seen which had extended from 9 μm to about 15 μm with increasing the annealing temperature from 50 to 120°C. But in 70:30 some new elongated ribbon like crystals on the spherulitic structures can be observed which became more visible with increasing annealing temperature to 120°C (Fig. 4). Y. J. Park et al reported the oriented align crystalline PVDF lamella which has bamboo-like structure can be achieved when PVDF film casted from polar solvent such as DMF and DMSO and crystallize in the confined spaces of the specific mold at high temperature. In their view, these structures are due to the formation of γ crystals (Y. J. Park, 2005).

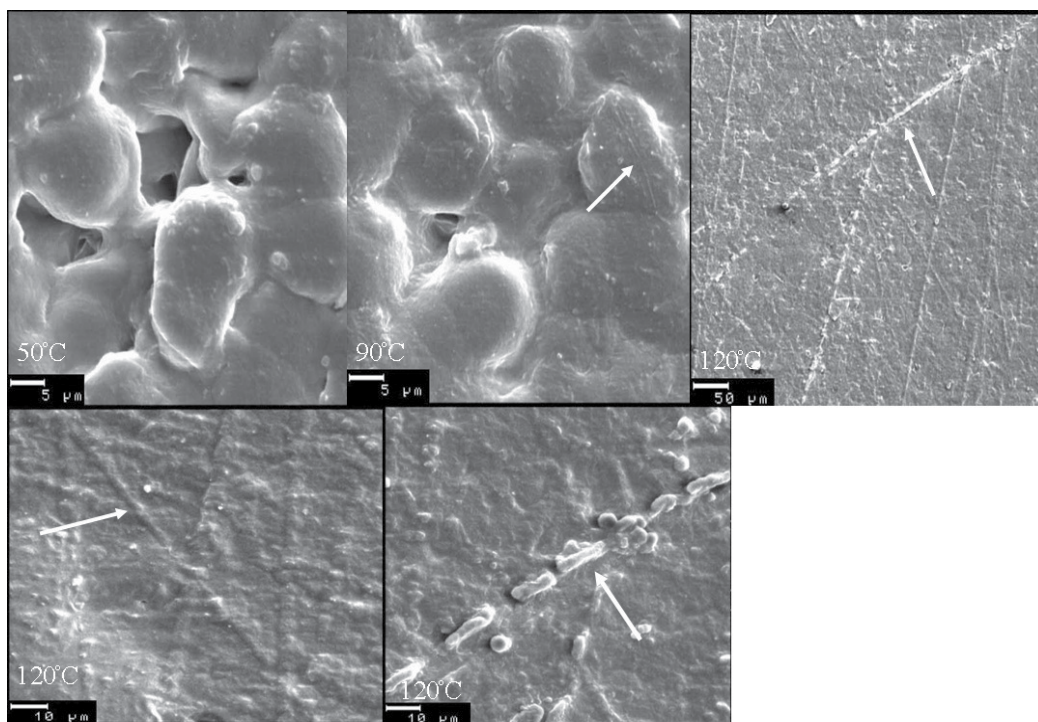


Fig. 4. The surface morphology of the casted 70:30 film were annealed at 50, 90 and 120°C.

We analyzed ATR-FTIR spectrum of 70:30 sample which were annealed at 50, 90 and 120° C (Fig. 5). From the previous reports on the spectral features of each crystal phase in PVDF, two IR absorptions band at 762 cm^{-1} and 1234 cm^{-1} as the representative of α - and γ -phase were selected to compare the peak intensities in each annealed samples.

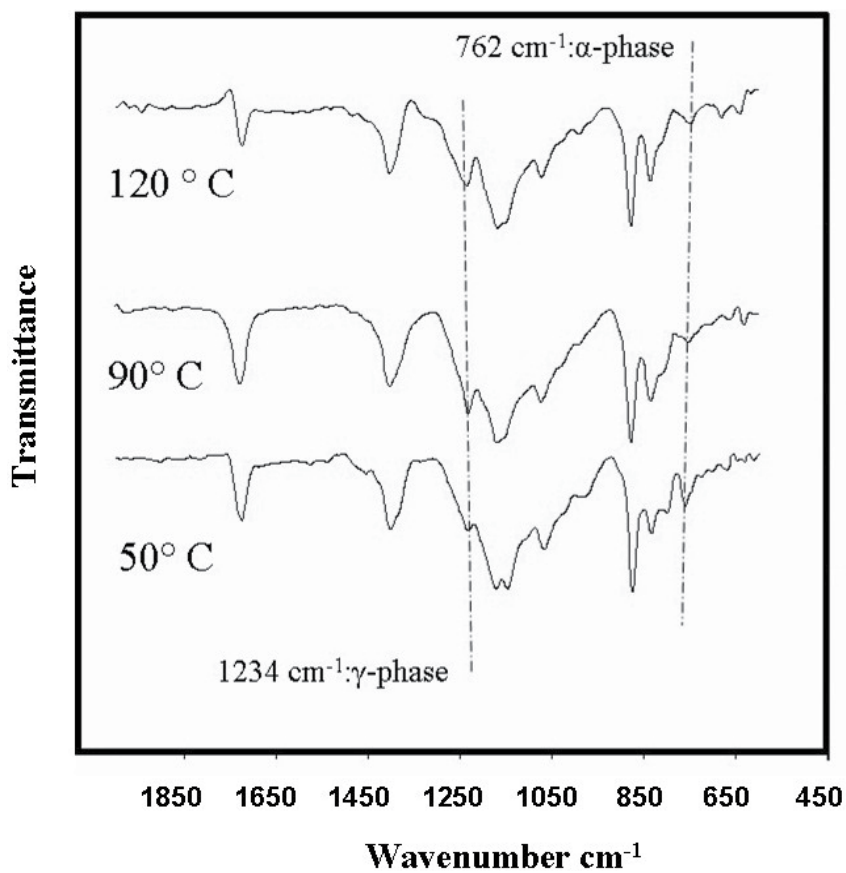


Fig. 5. ATR-FTIR spectra of 70:30 were annealed at 50, 90 and 120° C.

It indicated with increasing annealing temperature the percentage of γ -phase on the surface increased while α -crystal decreased at 90° C and then didn't change significantly, at 120°C. In this regards, this new droplet like structure identities on the top of the films can be related to γ -phase. Of course, this result is in agreement with X-ray Diffraction (XRD) and Differential Scanning Calorimetry (DSC) results (Fig. 6).

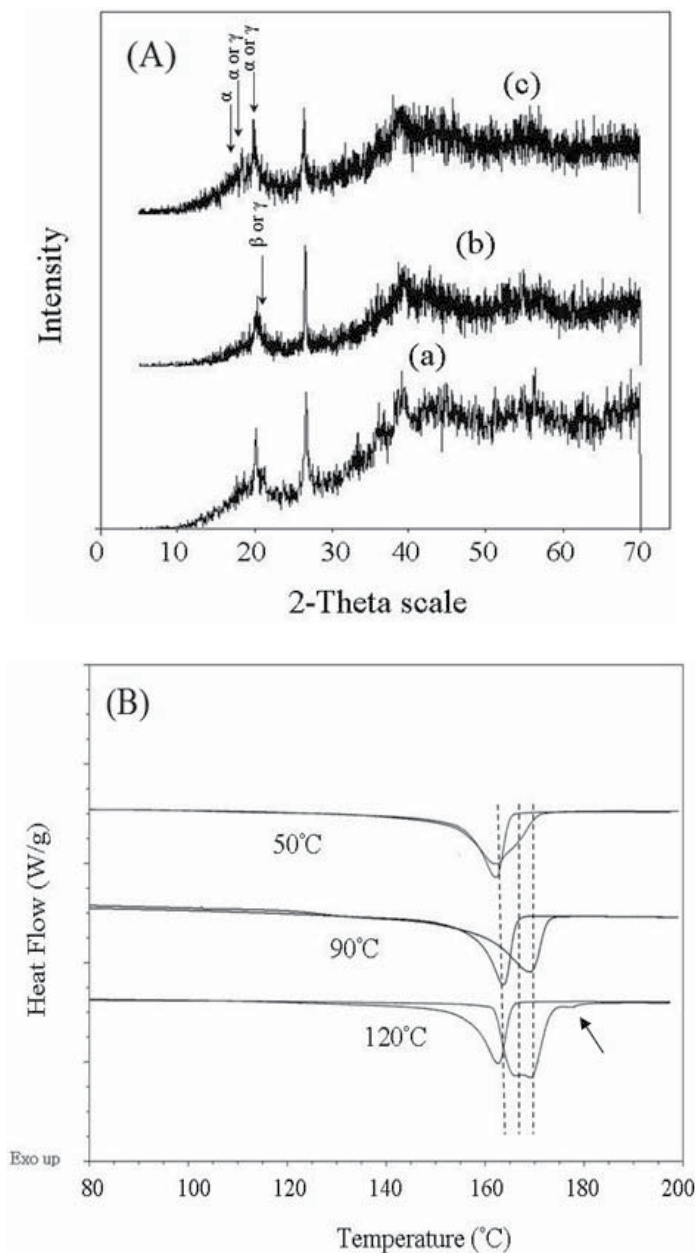


Fig. 6. X-ray diffraction pattern (A) and DSC thermograms of first and second heating (B) of 70:30 films annealed at 50, 90 and 120°C for 24h (S. Mohamadi, 2011)

On the basis of the reported data in literatures, WAXD data of neat PVDF contain 100, 020, 110, 021 reflections at $2\theta = 17.9^\circ$, 18.4° , 20.1° , and 26.7° for α - and only 200/110 reflection at $2\theta = 20.8^\circ$ for β -crystalline form (A. Kaito, 2007, L.Yu, 2009 & G. Guerra, 1986). γ -crystal planes are known to have overlapping reflections with (020), (110) and (021) α -crystal planes and also 200/110 reflection of β -phase. The (100) peak of α - phase at $2\theta = 17.9^\circ$ is the only peak that doesn't have any overlapping with γ -phase. Also the sharp diffraction peak at 26.38° in 70:30 is related to the crystallographic plane of graphite with d-spacing of 3.37\AA , indicating that the graphite retained its crystalline structure in nanocomposite but there is a different degree of stacking order and disordered microstructure (K. P. Pramoda, 2010 & T. Ramanathan, 2007). Furthermore, the film which was annealed at 50°C shows the 100, 020, 110 reflections of α -phase and 200/110 reflection of β -crystal. In XRD pattern of the films were annealed at 90°C , 200/100 reflection of β -crystal has become stronger, while the 100 peak of α has not changed considerably. It means with increasing temperature to 90°C , the growth of β -crystals is more favorable than α -crystals. Increasing the annealed temperature to the 120°C caused the substantial variation in the intensity of reflections. The decrease in the intensity of 200/100 reflection of β -crystal and increase in 020, 110 reflections of α - or γ -phase without any significant change in 100 reflection of α -crystal implies some of β -crystals convert to γ -crystals at 120°C . The DSC results also matched well with those of X-ray diffractions and indicated the existence of the different types of crystal structures. The new appeared endotherm in the film which was annealed at 177°C can be attributed to the melting of the new formed ribbon-like structures on the surface.

Actually, in our work, it can be imagined PVDF chains which are trapped between graphene sheets and are in close contact with PMMA chains, crystallize in the confined spaces that are provided by graphene sheets and PMMA chains. It is demonstrated that exfoliated graphene-based materials are often compliant, and when dispersed in a polymer matrix are typically not observed as rigid disks, but rather as bent or crumpled platelets (J. R. Potts, 2011). Consequently, as can be seen in TEM image of 70:30 sample (Fig. 7), the wrinkled surface of

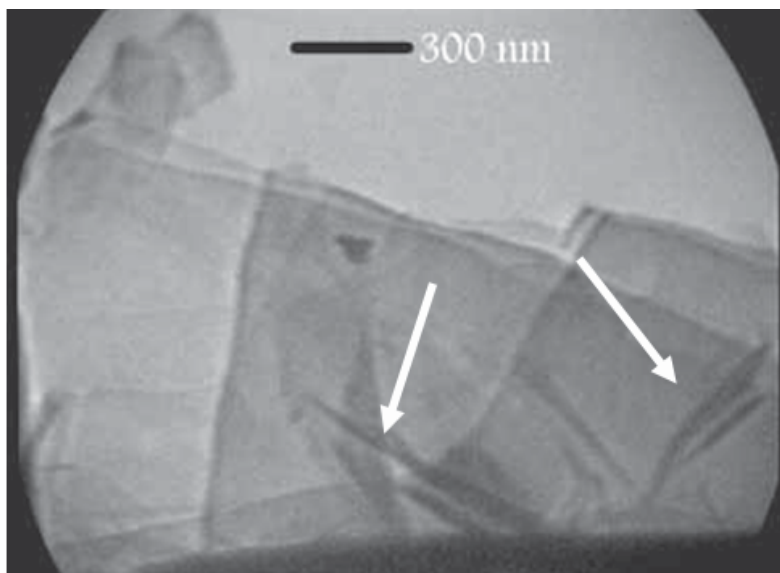
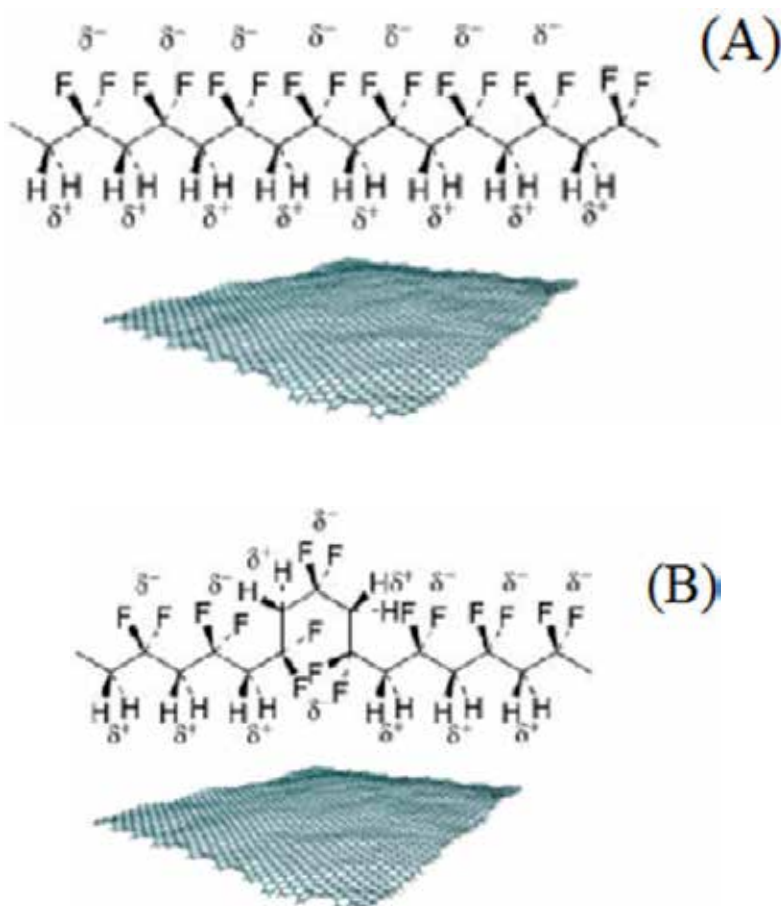


Fig. 7. TEM image and Wrinkled surface of graphene sheets in 70:30 polymer blend nanocomposite (S. Mohamadi, 2011)

the graphene sheets can act as micropattern molds for crystallization of PVDF. In other words, a well-defined feature of micropattern can be provided by the wrinkles on the surface of graphene sheets.

Crystallization results basically in the succession of two events: the primary nucleation of a new phase and then the three-dimensional growth of lamellae; these steps can be followed by lamellar thickening, fold surface smoothing, or reorganization into more perfect crystals. As reported by others, with increasing the annealing temperature in PVDF/PMMA blend film, the amount of α phase increases due to easier local internal chain rotation at higher temperature and most of β and γ form convert to α form.

While in our study with increasing the annealing temperature the amount of α phase decreased and γ form increased. It can be said graphene sheets can stabilize the β - and γ -phase at elevated temperature due to restricting effect of graphene sheets on TT conformation chains as is illustrated in scheme:



Scheme 7. Schematic illustration of the restricting effect of graphene sheets on TT (A) and TTTG+TTTG- (B) conformation chains

4. Conclusion

In this study, modification of graphite was carried out via introduction of hydroxyl groups and then vinyl groups on the surface of graphite by oxidation and estrification reaction respectively. The modified graphene (MG) was used to prepare the PMMA-graphene as a master batch by in-situ polymerization and followed by solution blending with PVDF in different ratios. The series of prepared polymer blend nanocomposite films were annealed at three different temperatures of 50, 90 and 120°C, and characterized.

FTIR results for FG and MG confirmed presence of different oxygen containing function groups on the surface of FG and vinyl organic moieties on the MG sheets.

ATR-FTIR spectra revealed the specific interaction between PVDF and PMMA chains in polymer blend nanocomposites. The surface morphology of 70:30 film which was annealed at 120°C, some new elongated ribbon like crystals formed. From ATR-FTIR data of this sample the identity of these new structures on the film surface can be related to the formation of γ crystals.

5. Acknowledgment

We are thankful to the Research Council of the University of Tehran. We gratefully acknowledge the kind assistance from Ms. Fotouhi from the thermal analysis laboratory of the University College of Science at University of Tehran for DSC analyses. The authors would also like to thank Dr. Saeed Sepehrisesht from Tehran Heart Center for TEM analyses and helpful recommendations.

6. References

- Al-Mashat, L., Shin, K., Kalantar-zadeh, K., D. Plessis, J., H. Han, S., W. Kojima, R., B. Kaner, R., Li, D., Gou, X., I J. Ippolito, S. & Wlodarski, W., (2010) Graphene/Polyaniline Nanocomposite for Hydrogen Sensing, *Journal of Physical chemistry C*, Vol. 114, pp. 16168–16173, 1932-7447.
- Benz, M., Euler, W. B., & Gerory, O. J., (2002) The Role of Solution Phase Water on the Deposition of Thin Films of Poly (vinylidene fluoride), *Mocromolecules*, Vol. 35, No. 7, pp. 2682-2688, ISSN 0024-9297.
- Betz, N., Le Moel, A., Balanzat, E., Ramillon, J.M., Lamotte, J., & Gallas, J. P., (1994) FTIR Study of PVDF Irradiated by Means of Swift Heavy Ions, *Polymer Science Part B: Polymer Physics*, Vol. 32, pp.1493–1502, ISSN 1099-0518.
- Bharti, V., Kaura, & T., Nath, R., (1997) Ferroelectric Hysteresis in Simultaneously Stretched and Corona-Poled PVDF Films, *IEEE Transactions on Dielectrics and Electrical Insulation*, Vol 4, No. 6, (December 1997) pp. 738–741, ISSN 1070-9878.
- Chi Chen, G., Su, J., Fina, L. J., (1994) FTIR-ATR Studies of Drawing and Poling in Polymer Bilaminate Films, *J. Polymer Science: Part B, Polymer Physics*, Vol.32, pp.2065-2075, ISSN 1099-0518
- Coleman, M. M., Painter. P.C., (1995) Hydrogen bonded polymer blends, *Progress in Polymer Science*, Vol. 20, No. 1, pp.1- 59, ISSN 0079-6700.

- Elashmawi, I. E., Hakeem, N.A., (2008), Effect of PMMA Addition on Characterization and Morphology of PVDF, *Polymer Engineering Science*, Vol. 48, pp. 895-901, ISSN 1548-2634.
- Falcao, E. H. L., Blair, R. G., Mack, J. J., Viculis, L. M., Kwon, C., Bendikov, M., Kaner, R. B., Dunn, B. S., & Wudl, F., (2007). Microwave exfoliation of a graphite intercalation compound, *Carbon*, Vol. 45, No. 6, pp. 1364-1369, ISSN 0008-6223.
- Garton, A., (1992) *Infrared Spectroscopy of Polymer Blends, Composites and Surfaces*, Hanser Publisher, Munich, Germany, ISBN 1-56990-034-5
- Giannetti. E., (2001), Semi-crystalline fluorinated polymers, *Polymer International*, Vol: 50, No. 1, (February 2000), pp. 10-26, ISSN 1097-0126.
- Grafting of PMMA Chains Through in-situ Polymerization. *Macromolecular Science Part A: Pure & Applied Chemistry*, Vol. 48, pp. 577-582, ISSN 1060-1325.
- Guerra, G., Karasz, F. E. , Macknight. W. J., (1986), On blends of poly(vinylidene fluoride) and poly(vinyl fluoride), *Macromolecules*, Vol. 19, No.7, (March, 1986) pp. 1935-1938, ISSN 0024-9297
- He, L., Xu, Q., Hua, C., Song. R., (2010) Effect of multi-walled carbon nanotubes on crystallization, thermal, and mechanical properties of poly(vinylidene fluoride), *Polymer Composite*, Vol. 31, No. 5, (April 2009), pp. 921-927, ISSN 0272-8397.
- He, X. & Yao, K., (2006), Crystallization mechanism and piezoelectric properties of solution-derived ferroelectric poly(vinylidene fluoride) thin films, *Applied Physics letter*. Vol. 89, No. 11, pp. 112909-1 – 112902-3, ISSN 0003-6951.
- Hilczler, B., & Kulek. J., (1998) The Effect of Dielectric Heterogeneity on Pyroelectric Response of PVDF, *IEEE Transactions on Dielectrics and Electrical Insulation*, Vol. 5, No. 1, pp. 45-50, ISSN 1070-9878.
- Hontoria-Lucas, C., Lopez-Peinado, A. J., DE D. Lopez-Gonzalez, J., Rojas-Cervantes, M. L., & Martin-Aranda, R. M., (1995). Study of oxygen-containing groups in a series of graphite oxides: physical and chemical characterization , *Carbon*, Vol. 33, No. 11, pp. 1585-1592 ISSN, 0008-6223.
- Inagaki, M., Kang, F., & Toyoda, M. (2004) Exfoliation of Graphite via Intercalation Compounds in: *Chemistry and Physics of Carbon A Series of Advances* , Radovic, L. R., pp. (1-65) Marcel Dekker, NewYork, ISBN 0-8247-4088-2.
- J.Jungnickel, B. (1996). *Polymeric Materials Handbook*, J. C., Salamone, New York : CRC press Inc, . pp. 7115-7122.
- Kaito, A., Iwakura, Y., Hatakeyama, K., & Li, Y., (2007) Organization of Oriented Lamellar Structures in a Miscible Crystalline/Crystalline Polymer Blend under Uniaxial Compression Flow near the Melting Temperature, *Macromolecules*, Vol. 40, (February, 2007), pp. 2751-2759, ISSN 0024-9297
- Kim, K. J. , Cho, Y. J. , & Kim. Y. H. , (1995) Factors determining the formation of the β crystalline phase of poly(vinylidene fluoride) in poly(vinylidene fluoride)-poly(methyl methacrylate) blends, *Vibrational Spectroscopy*, Vol. 9, No. 2. (September 1994), pp. 147-159, ISSN 0924-2031.
- Kwan, KS. (1998) The Role of Penetrant Structure in the Transport and Mechanical Properties of a Thermoset Adhesive, Ph.D. Thesis, Faculty of the Virginia Polytechnic Institute, Blacksburg, 285f.

- Lagashetty, A., & Venkataraman, A., (2005) Polymer Nanocomposites, *RESONANCE*, Vol. 10, Num. 7, (July 2005) pp. 49-57.
- Lanceros-Mendez, S., Mano, J. F., Costa. A. M. (2001) FTIR AND DSC STUDIES OF MECHANICALLY DEFORMED B-PVDF FILMS, *Macromolecular Science: Physics*, Vol. B40, No. 3&4, pp. 517-527, ISSN 0022-2348.
- Lbonard, C., Halary, J. L., & Monnerie, L., (1988), Crystallization of poly(vinylidene fluoride)-poly(methyl methacrylate) blends: analysis of the molecular parameters controlling the nature of poly(vinylidene fluoride) crystalline phase, *Macromolecules*, Vol: 21, No. 10, (October 1998) pp. 2988-2994, ISSN 0024-9297.
- Lovinger, A., (1982) Annealing of poly(vinylidene fluoride) and formation of a fifth phase, *Macromolecules*, Vol. 15, No. 1, pp. 40-44, ISSN 0024-9297.
- Matsushige, K., Nagata, K., Imada, S., & Takemura. T., (1980) The II-I crystal transformation of poly(vinylidene fluoride) under tensile and compressional stresses, *Polymer*, Vol. 21, No. 12, (October 1979), PP. 1391-1397, ISSN 0032-3861.
- Mattsson, B., Ericson, H., Torell, L. M., Sundholm. F., (1999) Micro-Raman Investigations of PVDF-Based Proton-Conducting Membranes. *Polymer Science Part A: Polymer Chemistry*, Vol. 37, pp.3317-3327, ISSN 1099-0518.
- Miller, R. L., Raison, J. J., (1976) Single crystals of poly(vinylidene fluoride), *Polymer science polymer physics*, Vol. 14, No. 12 (March 2003), pp. 2325-2326, ISSN 1099-0518.
- Mohamadi, S., Sharifi-Sanjani, N. & Mahdavi. H., (2011) Functionalization of Graphene Sheets via Chemically
- Mohamadi. S., & Sharifi-Sanjani, N., (2011) Investigation of the crystalline structure of PVDF in PVDF/PMMA/Graphene polymer blend nanocomposites, *Polymer Composites*, Vol. 32, pp. 1451-1460, ISSN 0272-8397.
- Nalwa. N. S., (1995) *Ferroelectric Polymers*, Marcel Dekker, NewYork , INC, ISBN 0-8247-9468-0.
- Ogoshi, T., & Chujo, Y., (2005) Synthesis of poly(vinylidene fluoride) (PVdF)/silica hybrids having interpenetrating polymer network structure by using crystallization between PVdF chains, *Polymer Science: Part A, Polymer Chemistry*, Vol. 43, No. 16, pp. 3543-3550, ISSN 1099-0518.
- Park, Y. J., Kang , Y. S., Park. C. (2005) Micropatterning of semicrystalline poly(vinylidene fluoride) (PVDF) solutions, *European Polymer Journal*, Vol. 41, pp. 1002-1012, ISSN 0014-3057.
- Potts, J. R., Dreyer, D. R., Bielawski, C. W., Ruoff. R. S., (2011), Graphene-based polymer nanocomposites, *Polymer*, Vol. 53, No. 1, (November 2010), pp. 5-25, ISSN 0032-3861.
- Pramoda, K. P., Linh, N.T.T. , Tang , P.S. , Tjiu, W.C. , Goh, S. H., He. C.B. , (2010) Thermo-mechanical properties of poly(vinylidene fluoride) modified graphite/poly(methyl methacrylate) nano composites, *Composite Science and Technology*, Vol. 70, No. 4,(December 2009) pp. 578-583, ISSN 0266-3538.
- Pramoda, K., Mohamed, A., Phang, I. Y., & Liu. T., (2005) Crystal transformation and thermomechanical properties of poly(vinylidene fluoride)/clay nanocomposites, *Polymer International*, Vol. 54, No. 1, (April 2004)pp. 226-232, ISSN 1097-0126.

- Ramanathan, T., Stankovich, S., Dikin, D. A., Liu, H., Shen, H., Nguyen, S. T., & Brinson. L. C., (2007), Graphitic nanofillers in PMMA nanocomposites – An investigation of particle size and dispersion and their influence on nanocomposite properties, *Polymer Science : Part B: Polymer Physics*, Vol. 45, No. 15, pp. 2097-2112, ISSN 1099-0488.
- Ramasundaram, S., Yoon, S., Kim, K. J. , Park. C., (2008). Preferential Formation of Electroactive Crystalline Phases in Poly(vinylidene fluoride)/Organically Modified Silicate Nanocomposites, *Polymer science: Part B: Polymer Physics*, Vol. 46, 2173–2187, ISSN 1099-0518.
- Scheinbeim, J. I., Newman, B. A., Sen. A., (1986), Field-induced crystallization in highly plasticized poly(vinylidene fluoride) films, *Macromolecules*, Vol. 19 (November, 1985), PP. 1454-1458. ISSN 0024-9297.
- Stankovich, S., Dikin, D. A., Dommett, G. H. B., Kohlhaas, K. M., Zimney, E. J., Stach, E. A., & Piner, R. D. (2006) Graphene-based composite materials, *Nature*, Vol, 442, pp. 282-286, ISSN 0028-0836.
- Stankovich, S., Dikin, D. A., Piner, R. D., Kohlhaas, K. A., Kleinhammes, A., Jia, Y., Wu, Y., Nguyen, S. T., & Ruoff, R. S. (2007) Synthesis of graphene-based nanosheets via chemical reduction of exfoliated graphite oxide , *Carbon*, Vol. 45, pp. 1558-1565, ISSN 0008-6223.
- Steurer, P., Wissert, R., Thomann, R., & Mülhaupt. R. (2009) Functionalized Graphenes and Thermoplastic Nanocomposites Based upon Expanded Graphite Oxide, *Macromolecular Rapid Communication*, Vol. 30, No. 4-5. pp. 316-327, ISSN 1521-3927.
- Steurer. P., Wissert, R., Thomann, R., Mülhaupt. R., (2009), Functionalized Graphenes and Thermoplastic Nanocomposites Based upon Expanded Graphite Oxide, *Macromolecular Rapid Communication*. Vol. 30, pp. 316–327, ISSN 1521-3927.
- Ulaganathan, M., & Rajendran, S. (2010) Preparation and characterizations of PVAc/P(VdF-HFP)-based polymer blend electrolytes, *Ionics*, Vol. 16, (December 2009) pp. 515-521, ISSN 0947-7047.
- Vo, L. T., & Giannelis. E. P., (2007) Compatibilizing Poly(vinylidene fluoride)/Nylon-6 Blends with Nanoclay. *J. Macromolecules*, Vol. 41, No. 23(August , 2007) pp. 8271-8226, ISSN 0024-9297.
- Wang, J., Li, H., Liu, J., Duan, Y., Jiang, S., Yan. S., (2003), On the $\alpha \rightarrow \beta$ Transition of Carbon-Coated Highly Oriented PVDF Ultrathin Film Induced by Melt Recrystallization, *Journal of American chemical society*, Vol. 125, No. 6, (November, 2002) pp. 1496-1497, ISSN 0002-7863.
- Yang, D., & Chen. Y., (1987), β -phase formation of poly(vinylidene fluoride) from the melt induced by quenching, *Journal of material science letter*, Vol. 6, No. 5, pp. 599-603, ISSN 0261-8028.
- Yee, W. A., Kotaki, M., Liu, Y., Lu. X., (2007) Stress-induced structural changes in electrospun polyvinylidene difluoride nanofibers collected using a modified rotating disk, *Polymer*, Vol. 49, No. 19, pp. 4196-4203, ISSN 0032-3861.
- Yen, J. H., Amin-Sanayei, R., (2006). Polyvinylidene Fluoride, in: *Encyclopedia of Chemical Processing, Vol.1*, Lee. S, pp. (2379-2381), Taylor & Francis, ISBN 9780824755003, New York.

- Yu, L., & Cebe. P., (2009) Effect of nanoclay on relaxation of poly(vinylidene fluoride) nanocomposites, *Journal of Polymer Science: Part B: Polymer Physics*, Vol. 47, No. 24, (August 2009) pp. 2520–2532, ISSN 1099-0518.
- Yu, S., Zheng, W., Yu, W., Zhang, Y., Jiang, Q., & Zhao. Z., (2009) Formation Mechanism of β -Phase in PVDF/CNT Composite Prepared by the Sonication Method, *Macromolecules*, Vol. 42, No. 22, pp. 8870, ISSN 0024-9297.

Reflectance IR Spectroscopy

Zahra Monsef Khoshhesab
Payame Noor University
Department of Chemistry
Iran

1. Introduction

Infrared spectroscopy is study of the interaction of radiation with molecular vibrations which can be used for a wide range of sample types either in bulk or in microscopic amounts over a wide range of temperatures and physical states. As was discussed in the previous chapters, an infrared spectrum is commonly obtained by passing infrared radiation through a sample and determining what fraction of the incident radiation is absorbed at a particular energy (the energy at which any peak in an absorption spectrum appears corresponds to the frequency of a vibration of a part of a sample molecule).

Aside from the conventional IR spectroscopy of measuring light transmitted from the sample, the reflection IR spectroscopy was developed using combination of IR spectroscopy with reflection theories. In the reflection spectroscopy techniques, the absorption properties of a sample can be extracted from the reflected light.

Reflectance techniques may be used for samples that are difficult to analyze by the conventional transmittance method. In all, reflectance techniques can be divided into two categories: *internal reflection* and *external reflection*. In internal reflection method, interaction of the electromagnetic radiation on the interface between the sample and a medium with a higher refraction index is studied, while external reflectance techniques arise from the radiation reflected from the sample surface. External reflection covers two different types of reflection: *specular* (regular) reflection and *diffuse* reflection. The former usually associated with reflection from smooth, polished surfaces like mirror, and the latter associated with the reflection from rough surfaces.

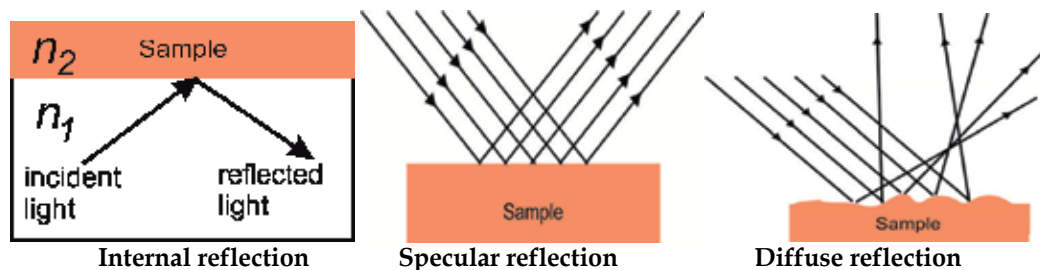


Fig. 1. Illustration of different reflection phenomenon.

2. Reflectance methods

Upon interaction of electromagnetic radiation with a sample surface, depending on the characteristic of the surface and its environment, the light may undergo three types of reflection, *internal reflection*, *specular reflection* and *diffuse reflection*. In practice, all three types of reflections can occur at the same time, although with different contributions. Specular reflection is defined as light reflected from a smooth surface such as a mirror (any irregularities in the surface are small compared to λ) at a definite angle whereas diffuse reflection produced by rough surfaces that tend to reflect light in all directions.

2.1 Internal reflectance spectroscopy (IRS)

Internal reflectance Spectroscopy (IRS) date back to the initial work of Jacques fahrenheit and N.J.Harrick [1, 2] that independently devised the theories of IRS spectroscopy and suggested a wide range of applications. Internal reflection Spectroscopy is often termed as attenuated total reflection (ATR) spectroscopy. ATR became a popular spectroscopic technique in the early 1960s.

Attenuated total reflection spectroscopy utilizes total internal reflection phenomenon[3]. An internal reflection occurs when a beam of radiation enters from a more dense medium (with a higher refractive index, n_1) into a less-dense medium (with a lower refractive index, n_2), the fraction of the incident beam reflected increases as the angle of incidence rises. When the angle of incidence is greater than the critical angle θ_c (where is a function of refractive index of two media), all incident radiations are completely reflected at the interface, results in *total internal reflection* (Figure 2). In ATR spectroscopy a crystal with a high refractive index and excellent IR transmitting properties is used as internal reflection element (IRE, ATR crystal) and is placed in close contact with the sample (Figure 3). The beam of radiation propagating in IRE undergoes total internal reflection at the interface IRE- sample, provided the angle of incidence at the interface exceeds the critical angle θ_c . Total internal reflection of the light at the interface between two media of different refractive index creates an "*evanescent wave*" that penetrates into the medium of lower refractive index [3].

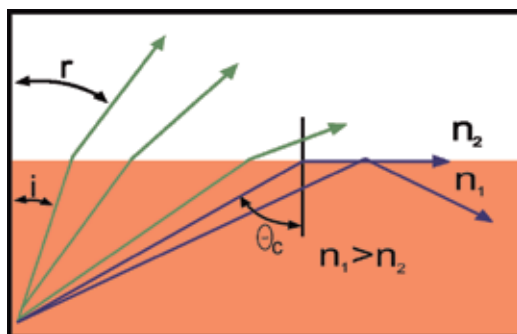


Fig. 2. Illustration of total internal reflection.

The evanescent field is a non-transverse wave along the optical surface, whose intensity decreases with increasing distance into the medium, normal to its surface, therefore, the field exists only the vicinity of the surface. The exponential decay evanescent wave can be expressed by Eq. (1):

$$I_{ev} = I_0 \exp (-Z/P) \quad (1)$$

Where z is the distance normal to the optical interface, dp is the penetration depth (path length), and I_0 is the intensity at $z = 0$.

The depth of penetration, dp , is defined as the distance from the IRE- sample boundary where the intensity of the evanescent wave decays to $1/e$ (37%) of its original value), is given by Eq. (2):

$$dp = \lambda / \{ 2\pi n_1 [\sin^2 \theta - (n_2/n_1)^2]^{1/2} \} \quad (2)$$

Where λ is the wavelength of the radiation, n_1 is the refractive index of the IRE (ATR crystal), and n_2 refractive index of the sample, and θ is the angle of incidence. Figure 3 illustrates the evanescent wave formed at the internal reflection element- sample interface.

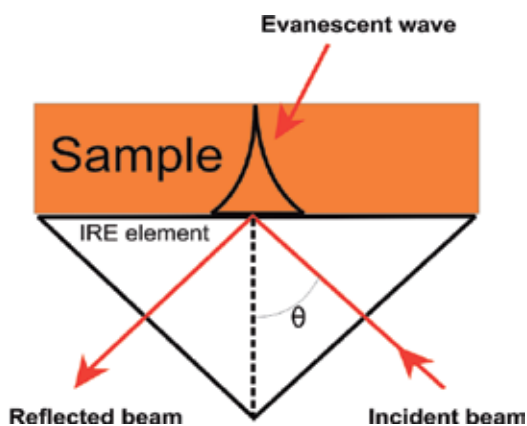


Fig. 3. Penetration of evanescent wave into the sample.

An ATR spectrum can be obtained by measuring the interaction of the evanescent wave with the sample. If an absorbing material is placed in contact with ATR crystal, the evanescent wave will be absorbed by the sample and its intensity is reduced (attenuated) in regions of the IR spectrum where the sample absorbs, thus, less intensity can be reflected (attenuated total reflection). The resultant attenuated radiation as a function of wavelength produces an ATR spectrum which is similar to the conventional absorption spectrum except for the band intensities at longer wavelengths (Figure 4). This difference is due to the dependency of the penetration depth (dp) on wavelength: at longer wavelength, the evanescent wave penetrates deeper into the sample, thus, the absorption bands at longer wavelengths are relatively more intense than those shorter wavelengths. This results in greater absorption on the longer wavelength side of an absorption band, contributing to band distortion and band broadening.

Additionally, compared to the transmission spectrum, small differences may be seen in an ATR spectrum which arises from dispersion effects (variation of refractive index of a material with change of wavelength). An anomalous dispersion causes the refractive index and the penetration depth changes through an absorption band. For instance the effect of dispersion on penetration depth for cocaine is demonstrated in Figure 5. As can be seen, penetration depth changes strongly at wavelength in which the dispersion is the highest.

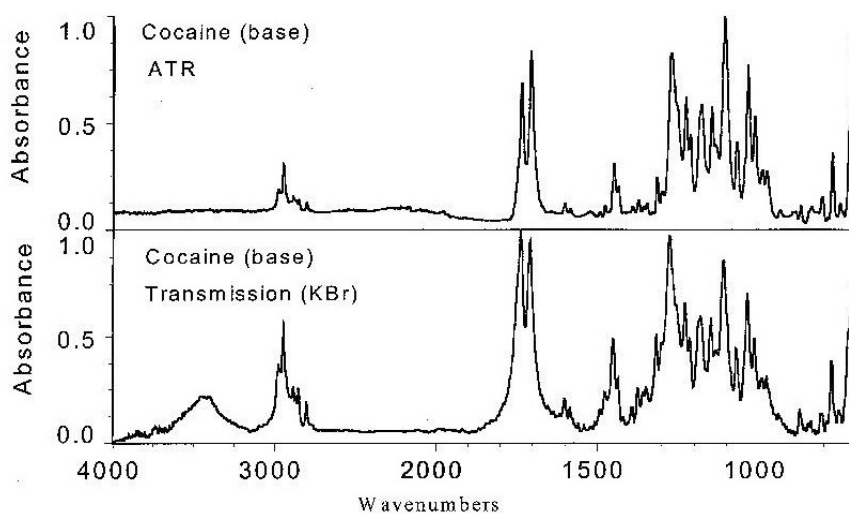


Fig. 4. Representation of ATR and Transmittance IR spectrum of Cocaine [4].

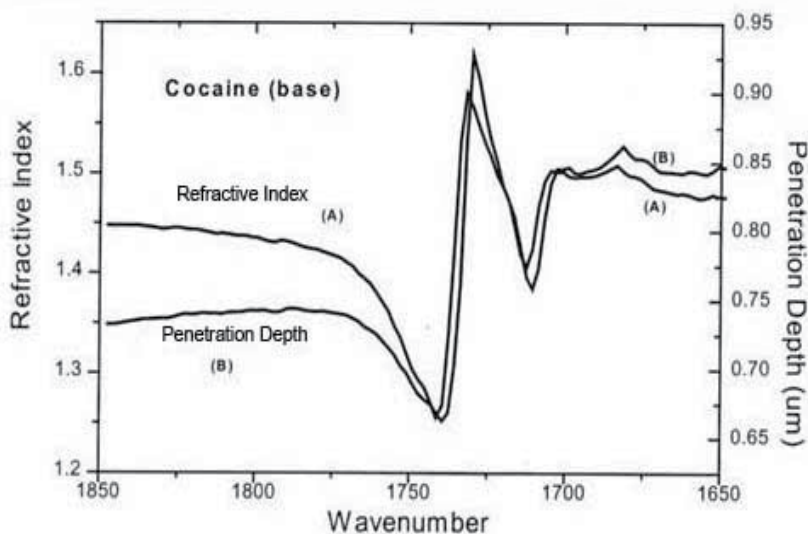


Fig. 5. Penetration depth and refractive index for cocaine at carbonyl absorbance band [4].

Sometimes an empirical so-called ATR correction is applied to compensate across the spectrum for linear wavelength increase, which is termed as Eq.(3):

$$R_{\text{corr}} \sim R / \lambda \quad (3)$$

Other differences may occur due to the surface effects between the sample and internal reflection element (IRE crystal). For instance, the degree of physical contact between IRE and the sample influences the sensitivity of an ATR spectrum. Since the evanescent wave only propagates 2-15 μm beyond the surface of the crystal, thus, an intimate contact of the IRE with the sample is essential.

Two configurations of ATR accessory are available. In a single bounce-ATR, a single internal reflection occurs using a prism whereas Multi-Bounce ATR, undergoes multiple internal reflections (up to 25) using special prisms, as shown in Figure 6. In a multiple internal reflection cell, the effective path length of the sampling surface is the product of the number of reflections at measurement surface and penetration depth. In practice, multiple internal reflections (in Multi-Bounce ATR technique) produce more intensive spectra by multiple reflections and, hence it is useful for weak absorbers, while the single bounce-ATR is suitable for strong absorbers.

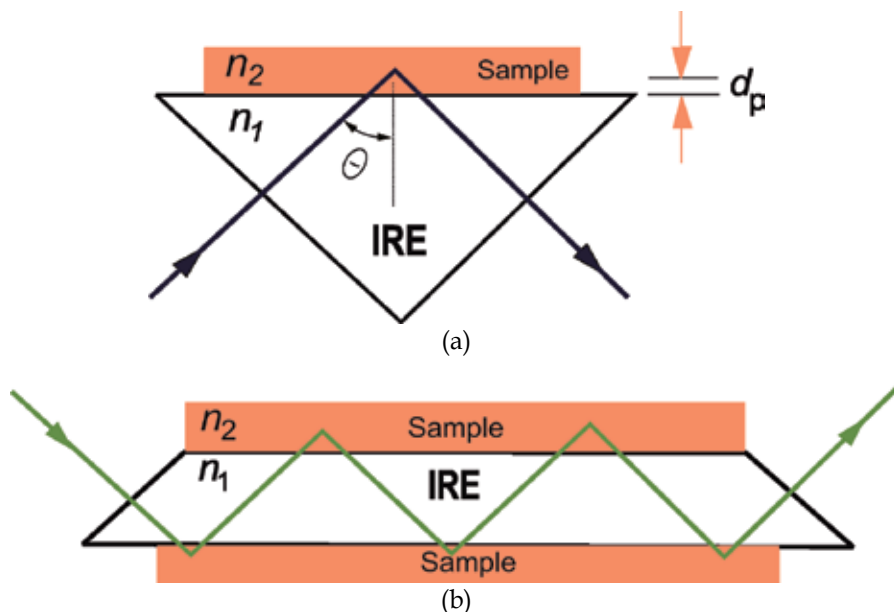


Fig. 6. Schematic representation of total internal reflection with (a) Single reflection, and (b) Multiple reflections.

There are different designs of ATR cell including traditional ATR, horizontal ATR and cylindrical ATR for solids and liquids samples. In the traditional ATR, a thin sample is clamped against the vertical face of the crystal. This design has been replaced by more modern designs, horizontal and cylindrical designs. In horizontal ATR (HATR), the crystal is a parallel-side plate (typically 5 cm by 1 cm) with the upper surface exposed (Figure 6 (b)). The number of reflections at each surface of the crystal depends on length and thickness crystal as well as the angle of incidence (usually between five and ten).

The traditional design is used for continuous surface such as sheets and horizontal ATR (HATR) cells are suitable for liquids and pastes as well as soft powder and sheets films. Application of cylindrical ATR (Figure 7) cell is limited to mobile fluids.

2.1.1 ATR crystals

The ATR crystals are made from materials that have a very high refractive index and low solubility in water. Table 1 summarizes some of the commonly materials used in ATR crystals. Amongst these materials, diamond, zinc selenide (ZnSe) and germanium (Ge) are

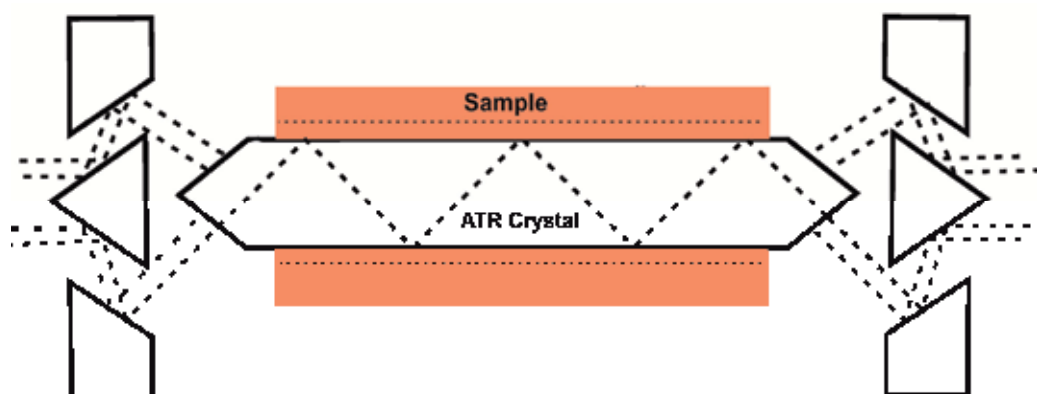


Fig. 7. Schematic representation cylindrical ATR cell.

Material	Wave range (cm ⁻¹)	Refractive index (at 1000 cm ⁻¹)
Zinc Sulfide (ZnS)	17,000 - 950	2.2
Zinc Selenide (ZnSe)	20,000- 650	2.41
Diamond	45000-2500; 1800 -< 200	2.4
Germanium (Ge)	5,5 00 -870	4.0
Cd telluride (CdTe)	10,000-450	2.65
Sapphire (Al ₂ O ₃)	25,000-1800	1.74
Cubic Zirconia (ZrO ₂)	25,000-1800	2.15
KRS-5 (TlI ₂ /TlBr ₂)	20,000-350	2.37
AMTIR (As/Ge/Se glass)	11,000-750	2.5

Table 1. Materials used as ATR crystals

the most common materials used ATR crystals. Diamond can be used for a wide range of samples, because it is resistant to scratching and abrasion and can tolerate a wide pH range as well as strong oxidants and reductants. Also, due to its ideal properties, it often used as a protective film for ATR crystals such as zinc sulfide (ZnS). However, high cost of diamond causes that its application is limited. Ge with a higher refractive index is suitable for analyzing of samples with high refractive index. However, ZnSe preferred for all routine applications, but because of its low resistivity towards surface etching, reactivity with complexing agents such as ammonia, and damaging with strong acids and alkalis, its application is limited. AMTIR with similar refractive is a good alternative for ZnSe crystal, when involve strong acids.

2.1.2 Application of ATR spectroscopy

ATR technique is used commonly in the near -infrared for obtaining absorption spectra of thin films and opaque materials. However, ATR spectra can be obtained using dispersive IR instruments, but the higher-quality spectra are obtained using FTIR spectrometers.

ATR is one of the most versatile sampling techniques that requires little or no sample preparation for most samples. It only requires that the sample is placed in intimate contact with the IRE crystal, which achieved by pressing the solid onto the crystal with a high pressure

clamp. Powders and soft pliable films can be used without any additional preparation and highly crystalline solids should be ground before application. It is an ideal method for liquids and oils, because the contact between the crystal and a liquid is inherently close and hence without requiring the high pressure clamp, liquids are applied directly onto the crystal.

As a conclusion, ATR is a non-destructive technique for a variety of materials including soft solid materials, liquids, powders, gels, pastes, surface layers, polymer films, samples solutions after evaporation of the solvent. It is an ideal technique for thick and dark colored materials which often absorb too much energy to be measured by IR transmission. Despite of these advantages, lack of a good contact between the sample and IRE can lead to non-accurate results. Also, there are a few IRE crystals to be compatible with the samples properties, especially from pH point of view.

2.2 Specular reflectance spectroscopy

The incident radiation focused onto the sample may be directly reflected by the sample surface, giving rise to specular reflection, and it may also undergo multiple reflections at the sample, resulting in diffuse reflection. In external reflectance techniques, the radiation reflected from a surface is evaluated (Figure 8).

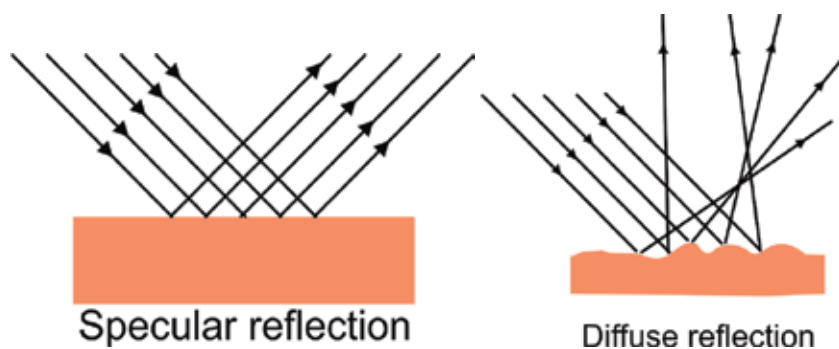


Fig. 8. Illustration of external reflection.

Specular reflectance techniques basically involve a mirror-like reflection from the sample surface that occurs when the reflection angle equals the angle of incident radiation. It is used for samples that are reflective (smooth surface) or attached to a reflective backing. Thus, specular techniques provide a reflectance measurement for reflective materials, and a *reflection-absorption (transflectance)* measurement for the surface films deposited on, or pressed against reflective surfaces (Figure 9).

The reflectance spectra differ from those recorded in transmission, they appear as "derivative-like" bands. These spectra can be converted into absorption one by using of Kramers-Kronig transformation (K-K transformation) that is available in most spectrometer software package. Figure 10 depicts specular reflectance spectrum of oil on surface of machined steel cylinder.

In absorption-reflection measurement, one fraction of the radiation is reflected on the upper interface and contributes towards the spectrum via specular reflection. Another part of the radiation penetrates the surface film and is reflected by the reflective surface, thus, the light

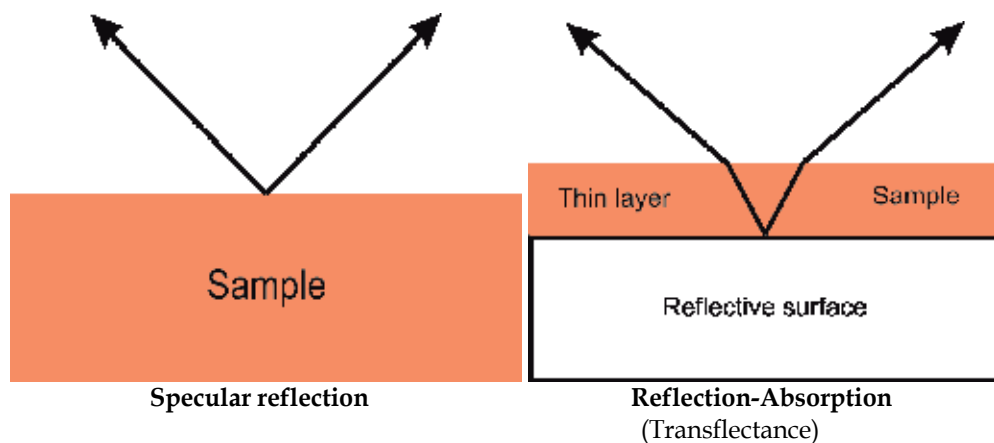


Fig. 9. Illustration of specular reflectance.

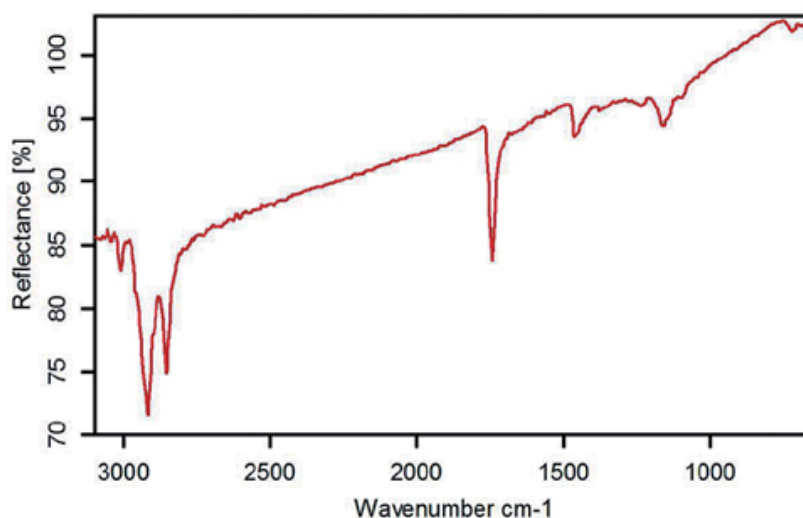


Fig. 10. Specular reflectance spectrum of oil on surface of machined steel cylinder.

passes through the surface layer twice-to and from the reflective surface, leading to increase the intensity of the reflectance spectrum as compared to the normal transmission. The effective path length depends on the angle of incidence, therefore, for thin films, a grazing angle of incidence as high as 80°- 85° from normal incidence should be used, and for thick films an angle close to normal incidence is applied.

The most common applications of this technique are evaluation of surfaces such as: coating, thin films, contaminated metal surface.

2.3 Diffuse Reflectance Spectroscopy (DRS)

In diffuse reflectance spectroscopy, the electromagnetic radiation reflected by roughened surfaces is collected and analyzed. When this technique is applied in (FT) IR region, it is termed as diffuse reflectance infrared Fourier transform spectroscopy (DRIFTS). It is also

known "Kubelka-Munk" reflection, because they developed a theory on the radiation transport in scattering media [5].

Light incident onto a solid sample may be partly reflected regularly (specular reflection) by the sample surface, partly scattered diffusely, and partly penetrates into the sample. The latter part may be absorbed within the particles or be diffracted at grain boundaries, giving rise to diffusely scattered light in all directions. Diffuse reflectance spectroscopy associated with the reflected lights which are produced by diffuse scattering (Figure 11). Since regular reflection distorts the DRS spectra, thus, the regular reflection component should be eliminated in diffuse reflectance measurement. The DRIFTS accessory is designed to eliminate the specularly reflected radiation.

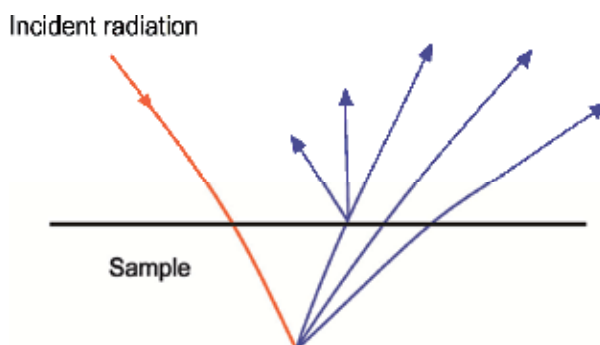


Fig. 11. Representation of diffuse reflectance.

In diffuse reflectance spectroscopy, there is no linear relation between the reflected light intensity (band intensity) and concentration, in contrast to traditional transmission spectroscopy in which the band intensity is directly proportional to concentration. Therefore, quantitative analyzes by DRIFTS are rather complicated. The empirical Kubelka - Munk equation relates the intensity of the reflected radiation to the concentration that can be used for quantitative evaluation. The Kubelka-Munk equation is defined as:

$$f(R_{\infty}) = (1 - R_{\infty})^2 / 2R_{\infty} = c/k = K/s \quad (4)$$

where $f(R_{\infty})$ is Kubelka-Munk function, R_{∞} is the absolute reflectance of layer (the ratio of the sample diffuse reflectance spectrum and a non-absorbing reference (normally KBr or KCl)), both measured at indefinite depth. K is the absorption coefficient, s is the diffusion (scattering) coefficient which is proportional to the fraction of diffused light, k is molar absorption coefficient (proportional to the fractional of transmitted light) and c is sample concentration. The reflectance, R_{∞} , indicates the sample is thick enough that no radiation reaches the back surface (indefinite thickness). Applying Kubelka-Munk function on the reflectance spectrum produces a spectrum (corrected spectrum) that resembling the transmission spectrum (Figure 12). Also the corrected spectrum demonstrates a linear relationship between band intensity and the sample concentration.

In the case of $R_{\infty} < 0.01$, the simpler function $\log 1/R_{\infty}$ is often used for measuring the diffuse reflectance. Since such small R_{∞} value is usually found in the near-IR region, therefore, an alternative relationship between concentration and reflected intensity in near-IR is defined as:

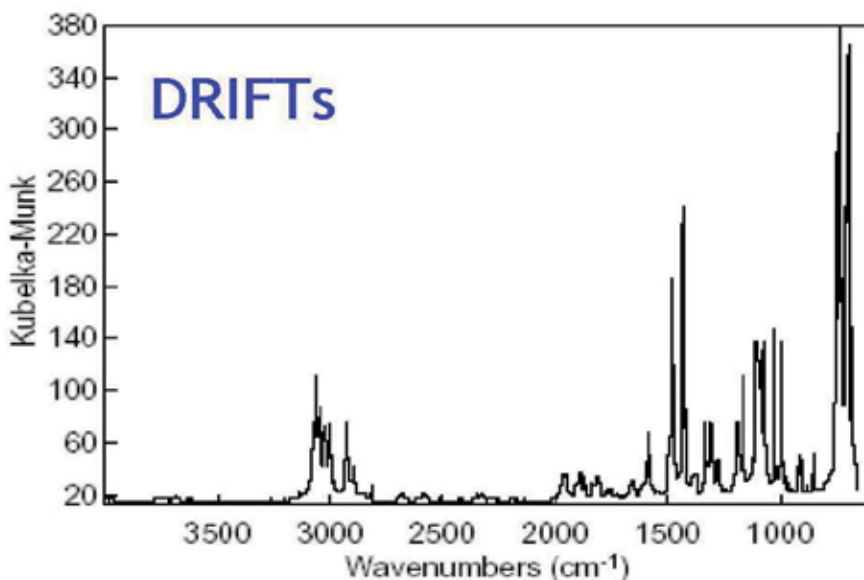


Fig. 12. DRIFT spectrum of 1,2-bis (diphenyl phosphino) ethane, pure powder [6].

$$\log (1/R_{\infty}) = k'c \quad (5)$$

where k' is a constant.

In Kubelka-Munk equation it is assumed that s is independent of wavelength and the sample is weakly absorbing. The former condition is achieved by proper sample preparation and the latter by dilution of strong absorbing samples with non-absorbing substrate powder (such as KBr or KCl). Therefore, to obtain reproducible results, particle size, sample packing and dilution should be carefully controlled, especially for quantitative analysis.

2.3.1 Application of diffuse reflectance spectroscopy

Diffuse reflectance technique is used for powders and solid samples having rough surface such as paper, cloth. In diffuse reflectance technique, particles size, homogeneity, and packing density of powdered samples play important role on the quality of spectrum. A sample with smaller particle size having narrow size distribution is preferred. Thus, in order to obtain a qualified spectrum, the sample should be ground into smaller size.

In this method, the sample can be analyzed either directly in bulk form or as dispersions in IR transparent matrices such as KBr and KCl. Sometimes, a thin film of KBr powder placed on the sample surface to improve the quality of the spectrum. Dilution of analyte in a non-absorbing matrix increases the proportion of diffuse reflectance in the reflected light. Typically, the solid sample is diluted homogeneously to 5 to 10% by weight in KBr. The spectra of diluted samples are similar to those obtained from pellets when plotted in units such as $\log 1/R$ (R is the reflectance) or Kubelka- Munk units.

Diffuse reflectance measurement in near-IR is more common than in mid-IR. Because non-absorbing scattering substrates are rare in mid-IR, and also more efficient scattering occurs at shorter wavelengths (near-IR). Additionally, due to lower efficiency of the scattering in

mid-IR, diffuse reflectance is very weak in this region, as a consequent, in mid-IR, diffuse reflectance could only be measured by FT-IR spectrometer (DRIFTS).

In diffuse reflectance spectroscopy, diffusely scattered light can be directly, collected from material in a sampling cup or, alternatively, collected by using an abrasive sampling pad. In mid-IR, the diffusely reflected light from sample is generally collected by large ellipsoidal mirrors, which cover as much area above the sample as possible. In near-IR, diffuse reflectance spectra are usually measured by an integrating sphere, described by Ulbrich, (Figure 14). The inner surface of "Ulbrich sphere" is coated by strongly scattering, non-absorbing powder. After repeated reflection, all radiations reach the detector. Thus, with Ulbrich sphere the entire radiation reflected by the sample is integrated.

In mid-IR region, the inner surface of diffuse scattering sphere is treated with gold vapor to guarantee a high degree of reflection, while in near- IR region, Ulbrich sphere consists of spectralon (a thermostatic resin) which is applied as white standard due to its high degree of reflection.

DRIFTS is a versatile technique for analyzing nontransparent samples, powders, roughened surfaces and coating. It offers the advantages of easy sample preparation and applicability to analyze samples at elevated temperature and pressure [6]. Consideration spectrum obtained for an organic material by transmission IR using KBr pellet and DRIFTS reveals the capacity of DRIFTS compared to transmission (Figure 12,13). Both spectra show similar spectrum that corresponds to absorption bands of the sample, but in the spectrum recorded in transmission mode an intensive band appeared at 3500 cm^{-1} which is related to the water present in the KBr pellet. This example, demonstrates DRIFTS combines the advantages of easy sample preparation with the absence of water band in the spectrum.

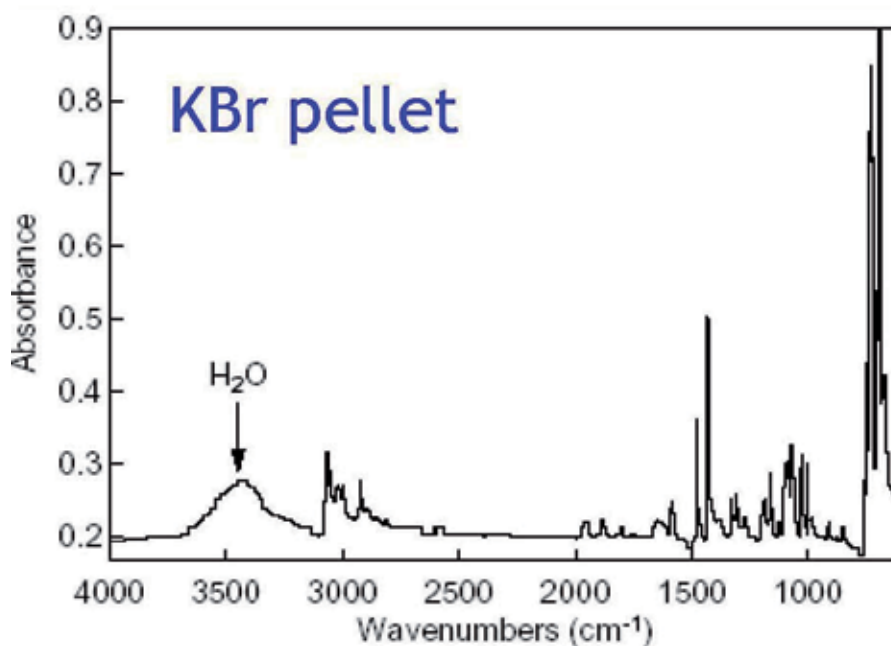


Fig. 13. Transmission spectrum of 1,2-bis (diphenyl phosphino) ethane, KBr pellet [6].

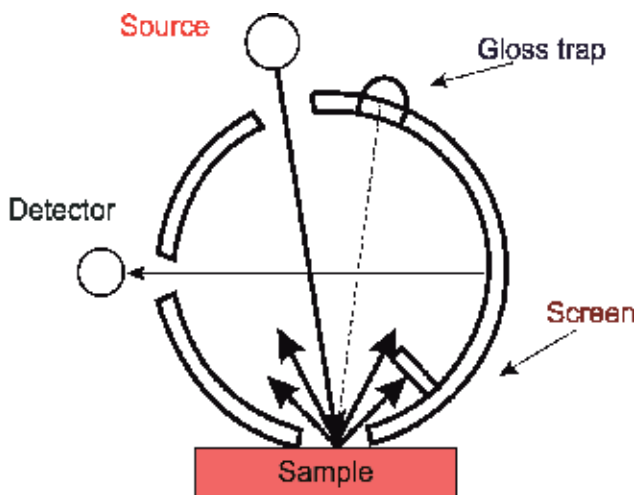


Fig. 14. Integrating Sphere.

The most disadvantage of this technique is difficulty of quantitative analyses. Since the diffusion coefficient strongly depends on sample preparation, thus the reflectance intensity is influenced by the sample preparation. A same sample may produce different spectra in different experiments.

3. References

- [1] J. Fahrenfort, Attenuated total reflection- A new principles for the production of useful infrared reflection spectra of organic compounds. *Molecular Spectroscopy* (Proceeding IV Int. Meeting, Bologna, 1959), 2, Mangini A, editor, London: Pergamon, 1962, 437.
- [2] N.J. Harrick, *Internal Reflection Spectroscopy*. New York, John Wiley & Sons, Int.,1967.
- [3] F.M. Maribeli, "Principles, Theory, and Practice of Internal Reflection Spectroscopy," *Internal Reflection Spectroscopy-Theory and Applications*, ed. F.M. Mirabella, Jr., Marcel Dekker, Inc. New York 1993.
- [4] C.V. Koulis, J.A. Reffner, B.A. John, A.M. Bibby, Comparison of transmission and internal reflection infrared spectra of cocaine. *J. Forensic Science*,46(4),(2001) 822.
- [5] P.Kubleka and F. Munk, *Z.Physik*, 12(1931) 593.
- [6] T. Armaroli, T.becue and S. Gautier, *Oil, Gas Science and technology - Rev.IFP*, 59 (2004) 2, 215.

Evaluation of Graft Copolymerization of Acrylic Monomers Onto Natural Polymers by Means Infrared Spectroscopy

José Luis Rivera-Armenta¹, Cynthia Graciela Flores-Hernández¹,
Ruth Zurisadai Del Angel-Aldana¹, Ana María Mendoza-Martínez¹,
Carlos Velasco-Santos² and Ana Laura Martínez-Hernández²

¹*Instituto Tecnológico de Ciudad Madero,
División de Estudios de Posgrado e Investigación*

²*Instituto Tecnológico de Querétaro,
Departamento de Metal-Mecánica
México*

1. Introduction

Infrared spectroscopy (IR spectroscopy) is a technique based on the vibrations of atoms of a molecule. An IR spectrum is commonly obtained by passing IR radiation through a sample and determining what fraction of the incident radiation is absorbed at a particular energy. The energy at which any peak in an absorption spectrum appears corresponds to the frequency of a vibration of a part of a sample molecule (Bickford, 2008).

For a molecule to show IR absorptions, it must possess specific feature: electric dipole moment of molecule must change during the movement that means changes in molecular dipoles which are associated with vibrations and rotations. The atoms in molecules can move relative to one another. This is a description of stretching and bending movements that are collectively referred to as vibrations. Vibrations can involve either change in bond length (stretching) or bond angle (bending). Some bonds can stretch in-phase (symmetrical stretching) or out-of-plane (asymmetric stretching) (Bickford, 2008).

The IR is divided into three regions; the near-, mid- and far- IR. The mid-IR is the most common region to identification and study of organic compounds based on fundamental vibrations and associated rotational-vibrational structure.

IR spectroscopy is a popular method for characterizing polymers. This spectroscopy may used to identify the composition of polymers, to monitor polymerization processes, to characterize polymer structure, to examine polymer surface, and to investigate polymer degradation processes. There are several reports of use of IR spectroscopy to evaluate grafting of acrylic monomers onto natural materials as carboxymethyl cellulose (CMC) and chicken feathers (CF) (Martínez et al, 2003, 2005, Vasile et al, 2004 , Zohuriann-Mehr et al, 2005, Joshi and Sinha, 2006).

Now a days have been an increasing interest in obtation and use of polymeric materials using naturals sources from a diversity of systems, getting atention such biopolymers in research areas as medicine, electronics, textil, corrosion and nanotechnology among others. This rising interest is due variety of properties that offers on depending of chemical structure and source (Martínez et al, 2008).

Use of natural fibers is an research area that allows obtain materials for cotidiane applications, using more resistance materials and with outstanding properties and specially materials that are environmental friendly. Keratin is a natural protein which can be found in wool, hair, claws, horns or nails, and is the main component in birds' feathers, represents from 5% to 7% of the body weight of chickens. Keratin is durable and resistant to organic solvents and chemically unreactive, which give benefits when is exposure to environmental conditions, thinking in industrial applications.

Chicken feathers (CF) are more abundant material of keratin in nature. Birds' feathers characterize by a complex branched structure formed by keratinic filaments that grow in a unique mechanism in cylindric feather follicles. This branched structure is a distinctive characteristic in feathers morphology and its origin is biologic evolution (Xu et al., 2001, 2003).

CF are considered residues of a byproduct of poultry, corresponding to more than 5 million tons around the world (Barone et al 2005). Aminoacids content of CF on depend of breed, feeding and environment of study animals. The aminoacids present in CF are mainly aspartic acid, glutamic acid, arginine, proline, glycine, phenylalanine, alanine, cystine, isoleucine, among others (Schmidt 1998) (see table 1).

Functional group	Aminoacid	Content (as % mole)
Negatively charged	Aspartic acid	5
	Glutamic acid	7
Positively charged	Arginine	5
Conformationally special	Proline	12
	Glycine	11
Hydrophobic	Phenylalanine	4
	Alanine	4
	Cystine	7
	Valine	9
	Isoleucine	5
	Leucine	6
	Tyrosine	1
Hydrophilic	Threonine	4
	Serine	16

Table 1. Aminoacid content in keratin fiber from chicken feather (Martínez et al 2005).

Carboxymethyl cellulose (CMC) is a very important cellulose derivative and it is known by its superabsorbent properties. It is an anionic polymer water soluble. It is produced by reaction of alkali cellulose and monochloroacetic sodium salt under strict reaction conditions (Klemm et al, 1998). Byproducts as sodium chloride and sodium glycolate are obtained in reaction whose are removed obtaining CMC sodium salt highly purified. Higher swelling capacity of CMC can be reached and controlled by addition of crosslinking agent, thermal treatment or ionic state conversion. The conversion of some hydroxyl groups from cellulose in hydrophobic substituents diminishes hydrogen bonding decreasing crystallinity and increasing water solubility. Multiple applications of Na-CMC in several areas of food industry made it and almost indispensable material. Other applications are: laundry detergent for instance, mainly as a viscosity modifier or thickener, as a soil suspension to deposit onto cotton and other cellulosic fabrics (Klemm et al, 1998). Other use of CMC is as a lubricant in non-volatile eye drops. These properties on depend of preparation method, degree of polymerization and degree of substitution (DS), that means how much of hydroxylic groups are displaced for carboxymethyl groups in anhydroglucose (AGU) structure. The more useful DS value is from 0.7 to 1.5. Due these CMC is an interesting material and properties can be modify by means graft reactions.

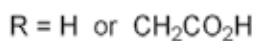
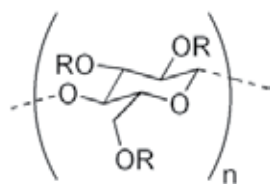


Fig. 1. Carboxymethyl cellulose structure.

Modification of natural protein through grafting have become in a widely used path and some works have carry out studies with acrylic monomers as ethylacrylate, acrylic acid, methacrylic acid and methyl methacrylate (Mostafa, 1995; Athawale and Rathi, 1997; Jia and Yong, 2006; Zampano, et al 2009), which carried out graft of natural fibers and proteins. However, just few of works report grafting of hydroxyethyl methacrylate onto naturals fibers (Joshi and Sinha, 2006) (Martínez et al., 2003, 2005).

Graft copolymerization of acrylic monomers onto natural polymers is one of the most useful paths to modify physicochemical properties on order to add new properties to final copolymer with minimal. Acrylic monomers are the most grafted monomers in this kind of research works; being acrylonitrile, acrylic acid, methyl methacrylate more studied species. Redox initiation is an efficient method frequently used to obtain graft copolymers. Polymers with OH groups can react with ceric ion or an oxidant agent to form polymer radical capable to initiate copolymerization. In a redox initiation frequently there is a minimum degree of homopolymerization, due only polymer radicals can be formed. However, limitation of this method is only useful with polymers with functional groups; there are reports of polymers with amides, urethane and nitrile groups by means redox initiation.

Several natural polymers as chitin, cellulose, functionalized cellulose and natural fibers are some of most studied natural polymers in graft copolymerization using redox system as initiator, being cerium ion one with more reports.

Infrared spectroscopy is a useful tool to identify functional groups through vibrational frequencies in polymers to evaluate changes in structure. This research was focused in graft copolymerization of Hydroxyethyl methacrylate (HEMA) onto chicken feathers fibers (CFF) and carboxymethyl cellulose (CMC), evaluating effect of reaction conditions (time reaction, monomer concentration, initiator concentrations) on grafting yield and probe presence of HEMA in copolymers by means Infrared Spectroscopy (IR).

2. Methodology

2.1 Raw materials

Chicken Feathers (CF) were obtained from a local slaughterhouse. A clean up procedure was carried out before use them for reaction, CF were washed several times with ethanol and dried at room temperature to have them clean white, sanitized and odor-free. Manual procedure by cutting to separate fibers from barbs and barbules was carried out. Chicken feather fiber (CFF) was used in graft copolymerization reaction.

CMC supplied by Sigma-Aldrich with 0.7 degree of substitution was used to graft reactions, without further purification process, same as all other reactivities: Hydroxyethyl methacrylate (HEMA) (98%) and malic acid, potassium permanganate (KMnO_4), hydrochloric acid (HCl), methanol, ethanol, sulfuric acid (H_2SO_4), Cerium ammonium nitrate were from Sigma-Aldrich. Distilled water was used as reaction medium and finally to wash the homopolymer residues.

2.2 CFF graft copolymers

To carry out the grafting reaction procedure proposed by Martínez-Hernández et al. (2003) was used. In this process the following reagents were used: 0.5 g CFF, distilled water, malic acid (0.005M), sulfuric acid (0.01M), KMnO_4 (0.003M) and HEMA monomer in 3 different levels (0.025, 0.05 and 0.075 M).

The substances were mixed at a temperature of 60 °C, under constant magnetic stirring. The reactions were carried out at three different times: 2, 3 and 4 h. Once the reaction time passed, proceeded to filter and wash the reaction product with hot water and methanol in order to remove residual monomer and homopolymer. Grafting yield was evaluated after a hydrolysis to reaction product, to determinate HEMA amount grafted in CFF. Hydrolysis procedure was: 1g of CFF grafted was swamped in a 6M HCl solution at 130°C for 24 hours in a soxhlet extractor. Once the time was over, hydrolysis residue was dried and weight was determinate, this weight correspond to grafted HEMA, due CFF decompose in hydrolysis process.

Grafted polymer percentage was determinate according with next formulae (Martínez-Hernández et al, 2003; Gupta and Sahoo, 2001):

$$\% \text{Grafted PHEMA} = (X_4 / X_1) * 100 \quad (1)$$

Where:

X_1 = CFF without modification

X_2 = container

X_3 = container + hydrolyzed sample

X_4 = residual polymer after hydrolysis ($X_3 - X_2$)

2.3 CMC graft copolymers

2.3.1 Initiator preparation

It was necessary preparation of Ce (IV) initiator solution. The required amount of cerium ammonium nitrate salt (0.1, 0.25 and 0.5 M), was dissolved in 100 mL of 1M HNO₃ solution. This solution was stored under refrigeration in an amber bottle.

2.3.2 Grafting reaction

For graft reaction 5 g of CMC were placed in the reactor with distilled water and HEMA was added in selected amount (3 levels: 0.2, 0.3 or 0.4 M), under constant stirring at 70 ° C, the initiator was added and reaction was carried out for 3 hours. Once the reaction ends, it was necessary to neutralize the mixture with a NaOH 10% w/w solution, copolymer was precipitated with acetone, and then the material was milled and washed with 90% methanol solution, then dried. After, the material was subjected to a Soxhlet extraction with methanol, in order to extracting the material that has not been in the copolymer. Grafting yield was determined by weight differences according with next formulae:

$$\text{Grafting yield} = ((W_1 - W_0)/W_0) * 100 \quad (2)$$

Where:

W_0 = CMC weight

W_1 = graft copolymer weight

2.4 IR Spectroscopy characterization of graft copolymers

IR analysis was carried out to evaluate structural changes of CMC and CFF and its grafted copolymers, by means main functional groups signals. IR spectra were recorded with a Perkin-Elmer Spectrum One Fourier Transform IR spectrophotometer, using an Attenuated Total Reflectance (ATR) accessory, with ZnSe plate, using 12 scans and resolution of 4 cm⁻¹, ranging from 4000 to 600 cm⁻¹.

3. Results and discussion

Results will be presented in sections following next order. First, the effect of HEMA concentration and time reaction over grafting yield onto CFF and HEMA and CAN concentration over grafting yield onto CMC. Next, IR spectra are presented for ungrafted and grafted CFF, as well as a comparison of IR spectra for different grafting yield of CFF. Also for CMC grafted and ungrafted are presented the IR spectra and comparison to different grafting yield of HEMA onto CMC.

3.1 CFF-g-HEMA copolymer

Effect of reaction conditions over graft yield were studied. Table 2 shows effect of time reaction and HEMA concentration on grafting yield of CFF, initiators concentration was constant. It can observe that an HEMA concentration increase causes an increase of grafting yield value at 3 reaction times studied. That increase is due the amount of free radicals formed in reaction system, and CFF main component is keratin which posses several pendant functional groups, for like $-NH_2$, $-COOH$, $-SH$ and $-OH$, which can form active sites where HEMA can be grafted. This behavior was also reported by Martínez et al (2003) that observed a maximum graft yield value. A higher HEMA concentration value was studied (1 M), but a fiber saturation was observed and also homopolymerization predominated over graft reaction which is not convenient for this study. Scanning Electron Microscopy shows the HEMA cover the CFF structure growing poly HEMA chains (figure 2) on fiber surface of CFF, but CFF reached a saturation of active sites and then homopolymerization happens.

Time/hr	HEMA conc./ M	Grafting yield
2	0.075	85%
2	0.05	70%
2	0.025	26%
3	0.075	92%
3	0.05	83%
3	0.025	57%
4	0.075	76%
4	0.05	38%
4	0.025	35%

Table 2. Effect of time reaction and HEMA concentration on grafting yield over CFF

The increase on graft yield can be also attributed that keratin forms a charge transfer complex with HEMA molecules, so it is possible increase monomer activity at higher concentrations of HEMA which leads homopolymerization.

Other reports (Joshi and Sinha, 2006) indicate an increase of monomer concentration increases graft yield, until a maximum and then decreases the obtained percentage. The difference is attributed to graft yield diminish due the saturation of available active sites in CFF. Also on depend of initiator system.

In the other hand, it can observe that when reaction time increase the graft yield has a maximum value at 3 h and then decrease at 4 h. this behavior is attributed that at higher reaction time the keratin pendant groups open and diffusion of HEMA molecules into the structure occurs, allowing the grafting on keratin structure not only on surface of CFF. However, when reaction time is high, a denaturalization of keratin can occurs, due the acidic medium where reaction is carried out, leading to HEMA homopolymerization. Other reason of this decrease in grafting yield is a reduction in number of free radicals available for grafting as the reaction proceeds, creating a saturation of active sites.

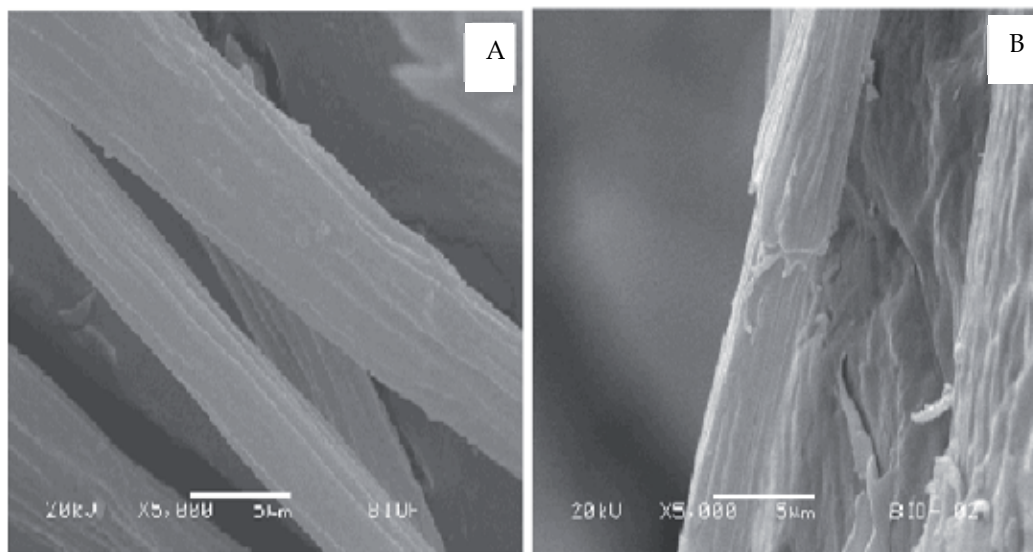


Fig. 2. SEM micrograph of CFF unmodified and CFF-g-HEMA

3.2 CMC-g-HEMA copolymer

The graft copolymerization of HEMA onto CMC had differences compared with HEMA-g-CFF: Redox initiator system used was CAN and was conducted at 3 different concentrations; HEMA concentrations values were higher 0.05, 0.1 and 0.15M and reaction time was constant in 3 hours. Table 3 resumes the effect of HEMA and CAN concentrations over grafting yields values of CMC.

CAN [M]	HEMA [M]	Grafting yield
0.1	0.05	69 %
0.1	0.1	207 %
0.1	0.15	249 %
0.25	0.05	88 %
0.25	0.1	214 %
0.25	0.15	275 %
0.5	0.05	82 %
0.5	0.1	179 %
0.5	0.15	397 %

Table 3. Effect of CAN and HEMA concentration on grafting yield over CMC

Graft copolymerization of HEMA onto CMC present a similar behavior as grating of HEMA onto CFF, grafting yield increased continuously with increase in concentration of HEMA when CAN concentration was constant, and reaches a maximum value with 0.15M at 3 CAN concentrations. This behavior could be explained by the fact of that an increase of HEMA

concentration lead to the accumulation of monomer molecules in close proximity to CMC backbone. There are reports of modified polysaccharides grafted with HEMA that found with CAN concentration of 0.2 M around 200% attributed the primary radicals attack the monomer instead of reacting with backbone polymer (Joshi and Sinha 2006). In this research higher CAN concentration studied was 0.5 M and higher grafting yield was reached with this concentration (397%). Also lower CAN concentrations (0.05 M) were tried in this research work, but not good results in grafting yield was obtained

In the other hand, about effect of CAN concentration over grafting yield, results show the initial increase in grafting yield with increase in initiator concentration levels off and decrease with further increase in CAN concentration. It would seem that termination of graft copolymerization would proceed by the reaction of the growing graft polymer chain with ceric ions, the reaction point is OH groups of anhydroglucose, which form a complex with ceric ion. This complex may dissociate, and giving rise to free radical sites onto the polysaccharides backbone and these radicals initiate the graft copolymerization (Zohuriaan-Mehr et al 2005).

Figure 3 shows SEM micrographs of CMC unmodified and CMC-g-HEMA. It is clearly seen that CMC morphology was totally modified by grafting of HEMA. CMC shows a porous surface which is covered by grafting of HEMA resulting in a homogeneous surface, which suggests that HEMA chains formed are long.

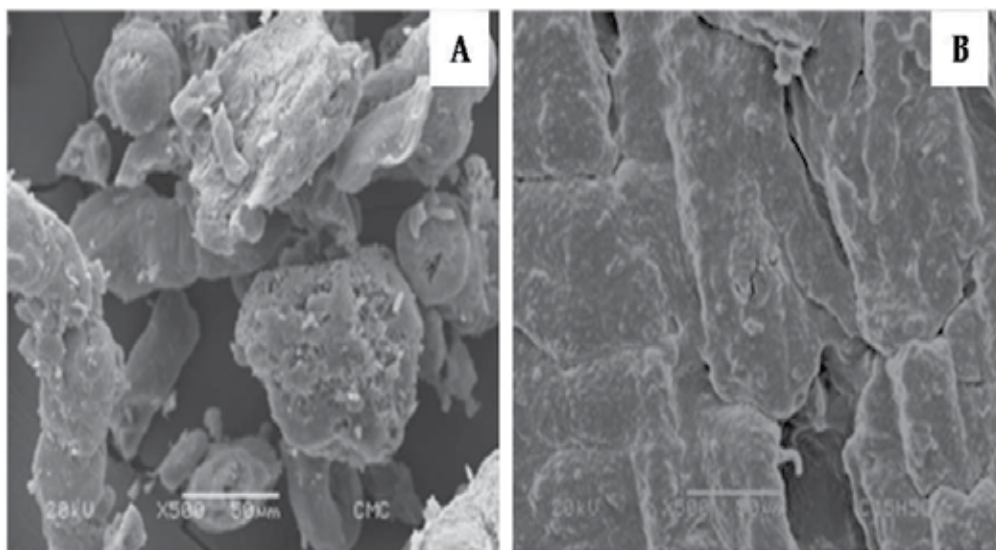


Fig. 3. SEM micrograph of CMC unmodified (A) and CMC-g-HEMA (B).

3.3 IR of CFF-g-HEMA copolymer

IR spectroscopy is a useful technique to evaluate if a graft reaction is carried out and also to evaluate grafting yields on graft copolymers. Several research works used IR with this purpose for keratin (Martínez et al 2003; Martínez et al 2008; Kavitha et al 2005), starch (Meshram et al 2009), modified starch (Cao et al 2002), chitosan (Mun et al 2008), carboxymethyl chitosan (Joshi and Sinha, 2006), cellulose (Zampano et al 2009),

carboxymethyl cellulose (Okieimen and Ogbeifun, 1996; Vasile et al , 2004), ethyl cellulose (Kang et al 2006), which make it a powerfull tool in graft reactions.

Figure 4 shows IR spectrum of CFF, which main component is keratin, a mixture of aminoacids as serine, proline, glycine, valine, cysteine, and others. The main vibrations attributed to CFF structure were identified according to wavenumber. The region around 3300 cm^{-1} corresponds to range of amide bands, figure shows a peak in 3297 cm^{-1} associated with ordered regions of NH group of amide A α -helix conformation, peak in 2945 cm^{-1} is assigned to the assimetric vibration of CH group od metyl, the strong band at 1715 cm^{-1} is matched with vibration of amide I of β -sheet conformation, band at 1650 cm^{-1} assigned to C=O group of amide I α -helix conformation, peaks at 1520, 1449 and 1243 cm^{-1} attributed to in plane bending of NH group corresponding to β -sheet conformation, bending of CH_3 group and CN group of amide III respectively; vibrations on 1136, 1074 and 1023 cm^{-1} corresponds to assigned to vibrations of C-C group; and finally a peak around 700 cm^{-1} attributed to vibration of C-S group.

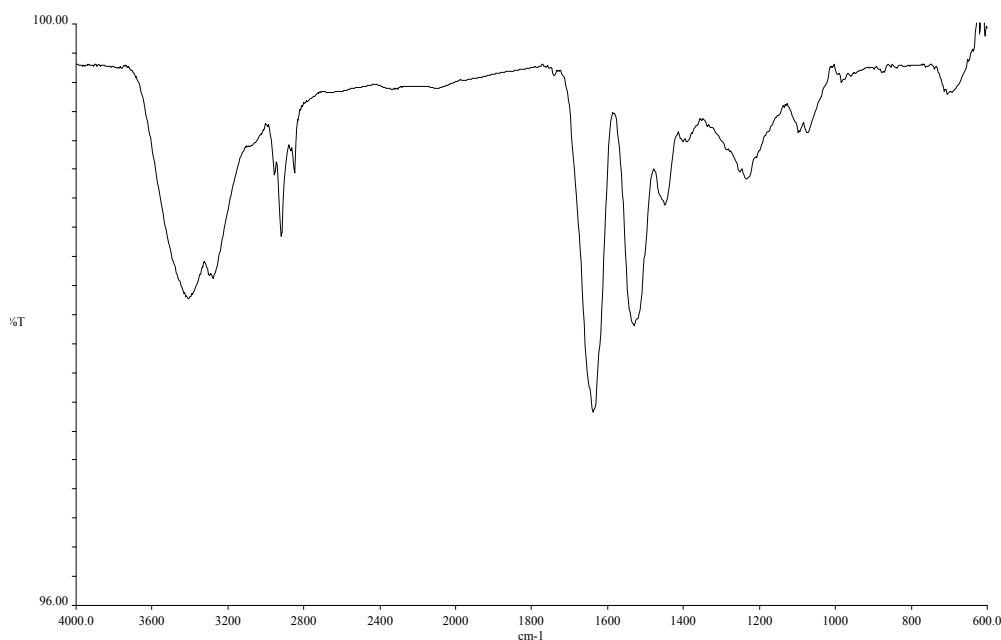


Fig. 4. IR spectrum of CFF ungrafted.

In figure 5 presents IR spectrum of PHEMA which presents signals at 3394 cm^{-1} attributed to vibration of OH group, 2956 cm^{-1} from antisymmetric vibration of CH_2 and CH_3 , 2925 cm^{-1} symmetric vibration of CH_2 , CH_3 , 2855 cm^{-1} symmetric vibration of CH_2 , 1720 of stretching C=O, a small shoulder around 1652 from stretching C=C, 1369 cm^{-1} deformation of CH_2 , CH_3 , a shoulder at 1260 cm^{-1} from C=O stretching, 1164 vibration of C-O-C, 1048 stretching of CO(H), and 771 CH_2 coupled with skeletal stretching. This is according for reports of IR spectrum of PHEMA (Prachayawarakorn and Boonsawat, 2007).

Figure 6 shows IR spectra of CFF and CFF grafted. It can observe that main differences are IR spectrum of CFF grafted show peaks at 1720, 1160 and a shoulder around 1260 cm^{-1} ,

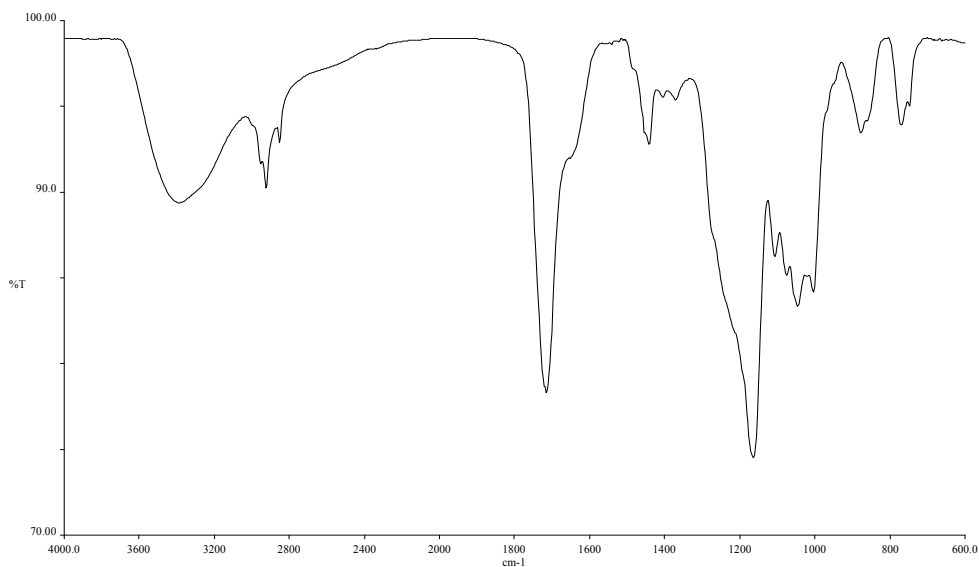


Fig. 5. IR spectrum of PHEMA

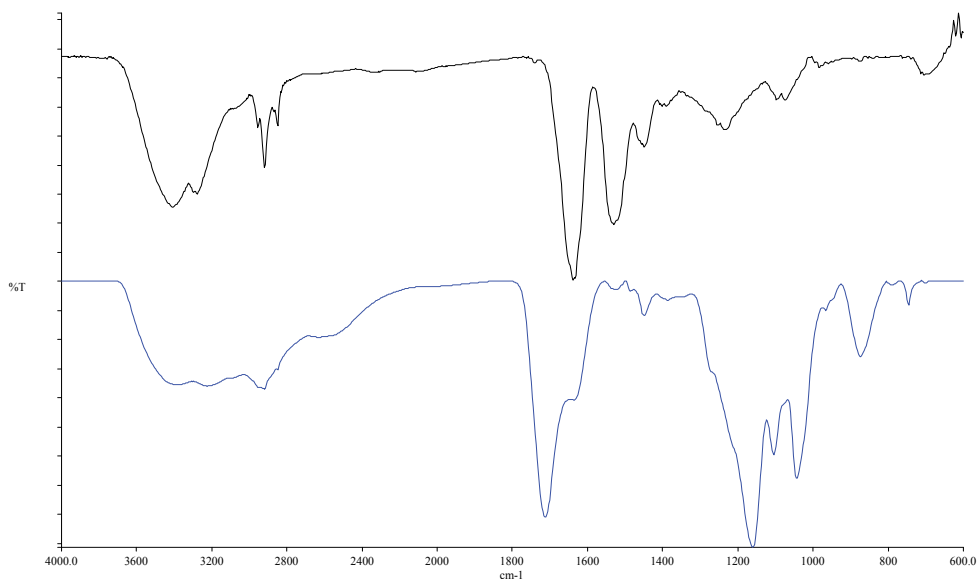


Fig. 6. IR spectra of ungrafted CFF (black) and CFF grafted (blue).

attributed to groups C=O and OH respectively, from HEMA structure, and which does not appear in CFF spectrum, which can indicate the graft reaction is carried out. CFF possesses functional groups as $-NH_2$, $-SH$ and $-OH$ where graft reaction can carry out, signals from NH (3290 , 3080 and 1525 cm^{-1}) changed which make it suppose that graft reaction is taking place between NH groups and free radical of HEMA.

A comparison of main assignments from functional groups of ungrafted CFF and PHEMA are summarized in table 4.

PHEMA		CFF (Martínez 2005)	
Approximate assignments, cm^{-1}	Functional groups	Approximate assignments, cm^{-1}	Functional groups
3390	ν (OH)	3290	ν (NH) Amide A, α -helix
2950	ν_a (CH ₃ , CH ₂)	3080	ν_a (NH) Amide B
2920	ν_s (CH ₃ , CH ₂)	2930	ν_a (CH ₃)
2850	ν (CH ₂)	1700	ν (C=O) Amide I β -sheet
1720	ν (C=O) ester group	1650	ν (C=O) Amide I α -helix
1650	(C=C) stretching	1525	δ (N-H) Amide II β -sheet
1370	δ (CH ₃ , CH ₂)	1450	δ_α (C-H ₃)
1260	C=O stretching	1230	ν (CN) Amide III
1160	ν (C-O-C)	1170	ν (C-C)
1050	(CO-H) stretching	1075	ν (C-C)
770	(CH ₂) stretching	685	ν (C-S)

Table 4. IR assignments of main functional groups of ungrafted CFF and PHEMA.

In figure 7 present IR spectra of CFF grafted with 26 and 92% grafting yield, to evaluate effect of grafting on main assignments. It is evident when graft yield increase assignments attributed to PHEMA are more evident in spectrum (3390 and 1720, 2850 and 1150 cm^{-1}), and signals attributed to NH and OH groups disappear because there are sites where graft reaction is carrying out. There are several reports about use of IR spectroscopy for evaluate graft reactions on keratin from chicken feathers (Martínez et al 2003, Martínez et al 2008 and Kavitha et al 2005). They use IR spectra for identify main functional groups of keratin and of acrylic monomers in ungrafted and grafted copolymers, in addition to evaluate changes in peaks according with grafting yield.

3.4 IR of CMC-g-HEMA copolymer

IR spectra of the CMC is presented in figure 8. We can notice the characteristic broad band attributed to OH stretching vibration at 3360 cm^{-1} due the CMC has a degree of substitution of 0.7, in average 2.3 OH groups of anhydroglucose ring are present in structure, peak at 2920 cm^{-1} due stretching of C-H, peak at 1620 cm^{-1} a strong absorption band that confirm the presence of carboxy group (COO⁻), 1420 and 1320 cm^{-1} are assigned to -CH₂ scissoring and hydroxyl group bending vibration respectively, signal at 1060 cm^{-1} is due to >CH-O-CH₂ stretching vibration and vibrations of the ether groups at 1060, 1110 cm^{-1} . It is worth to remark that CMC used in this work was as sodium salt. The assignments are according with reports of IR spectroscopy studies of CMC (Bono et al 2009, Heydarzadeh et al 2009, Vasile et al 2004).

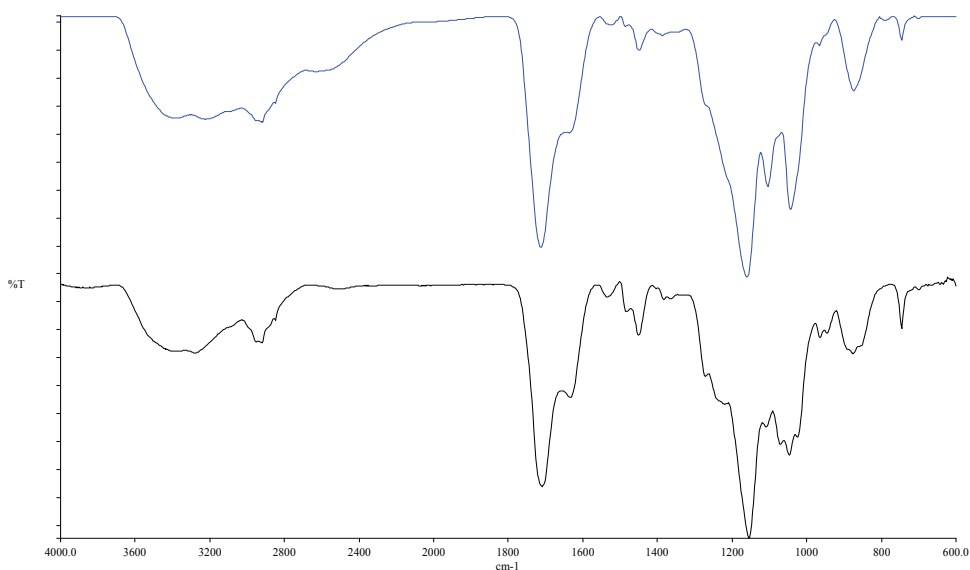


Fig. 7. IR spectra of CFF-g-HEMA with 26 (blue) and 92% (black) graft yield

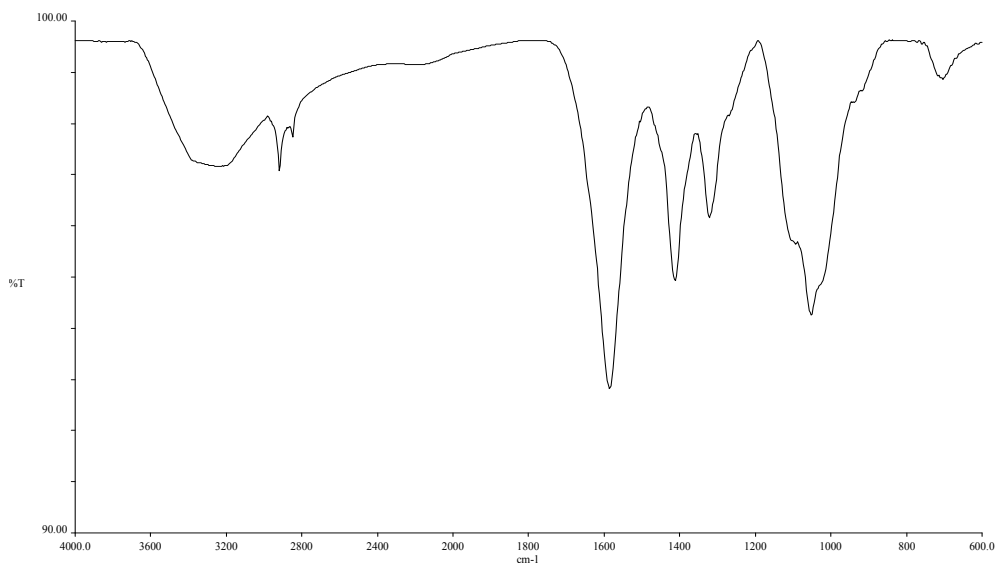


Fig. 8. IR spectrum of CMC

Figure 9 presents a comparative of IR spectra of CMC ungrafted and grafted with HEMA. Before, the main assignments for PHEMA were discussed. The CMC grafted present appearance of peak at 2930 cm^{-1} due antisymmetric stretching CH_3 , 1715 cm^{-1} from stretching vibration of $\text{C}=\text{O}$ and peaks at 1410 , 1250 , 1150 and 902 cm^{-1} assigned to bending vibration of CH_3 , CH_2 , stretching of $\text{C}=\text{O}$, stretching of CO-H and $=\text{CH}_2$ groups respectively, all those signals are from PHEMA structure, and also peaks attributed to CMC structure as 3340 , 1650 and broad peak at 1050 cm^{-1} , which are from OH , COO- and C-O-C from CMC, which is indicative the graft reaction was carried out.

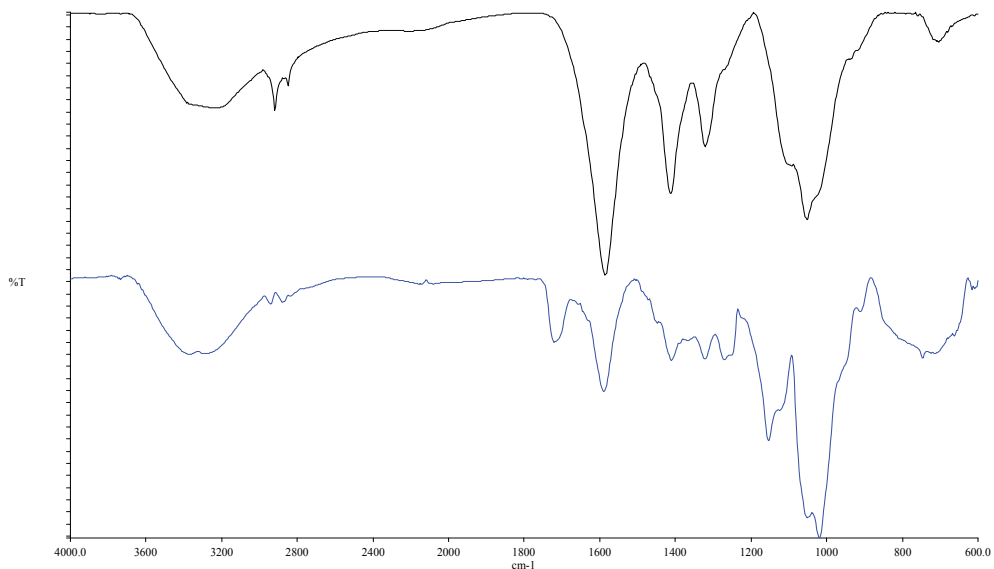


Fig. 9. IR spectra of CMC ungrafted (black) and with 69% grafting yield (blue)

Effect of grafting yield on IR assignments was evaluated in figure 10. It can observe that main peaks attributed to PHEMA (2940, 1720, 1270 and 1060 cm^{-1}) increase according with graft yield, which makes sense due the PHEMA is an higher proportion compared with CMC.

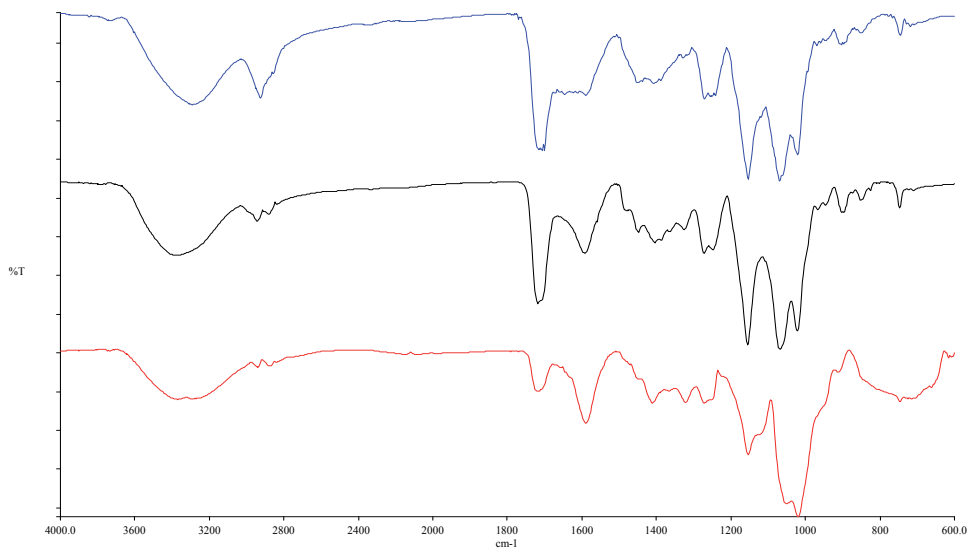


Fig. 10. IR spectra of CMC grafted with 69% (red), 249 % (black) and 397% (blue) grafting yield.

4. Concluding remarks

From results presented in this research work it can be concluded that it is possible to graft HEMA onto CFF and CMC using different initiator systems, and that grafting yield obtained depends on the kind of initiator system, being higher with the CAN initiator system than with KMnO₄ malic acid. SEM micrographs give evidence that the grafting reaction takes place on CFF and CMC surface until a saturation of active sites, and then homopolymerization happens.

One of the most common applications of IR spectroscopy is to the identification of organic compounds. In polymers, it may be used to identify the composition, to monitor the polymerization process, to characterize polymer structure. In present research, IR spectroscopy showed to be a useful tool to evaluate if the graft reaction takes place. It was possible to identify the main functional groups of CFF and CMC ungrafted, and PHEMA. The IR spectra of grafted copolymers presented assignments due to ungrafted materials and PHEMA giving evidence that the graft reaction carried out. Furthermore, it was possible to evaluate the changes in peaks of the grafted materials according to grafting yield, increasing signals attributed to PHEMA.

5. Acknowledgment

The financial support from Dirección General de Educación Superior Tecnológica (DGEST) from Public Education Secretary (SEP) through projects 3616.10-P and 2203-09-P for development of this research work is gratefully acknowledged. The authors would like to thank to Pollos Villafranca for providing chicken feathers, and the micrography department of CFATA of Universidad Nacional Autónoma de México campus Juriquilla, especially to Alicia Del Real López for technical assistance.

6. References

- Athawale, V.D., Rath, S.C., (1997), Effect of chain length of the alkyl group of alkyl methacrylates on graft polymerization onto starch using ceric ammonium nitrate as initiator. *European Polymer Journal*, vol. 33, No. 7, (July 1997), pp 1067-1071, ISSN 0014-3057.
- Barone, J.R., Schmidt, W.F., Liebner, C.F., (2005). Thermally processed keratin films. *Journal of Applied Polymer Science*, Vol. 97, No. 4, (August 2005), pp 1644-1651, ISSN 1097-4628.
- Bickford, M., (2008). *Characterization and Analysis of Polymers*. John Wiley and Sons. ISBN 978-0-470-23300-9, Hoboken, New Jersey, United States.
- Bono, A., Ying, P.H., Yan, F.Y., Muei, C.L., Sarbatly, R., Krishnaiah, (2009), Synthesis and Characterization of Carboxymethyl Cellulose from Palm Kernel Cake. *Advances in Natural and Applied Sciences*, Vol. 3, No. 2, (January 2009), pp 5-11, ISSN 1995-0772.
- Cao, Y., Qing, X., Sun, J., Zhou, F., Lin, S., (2002), Graft copolymerization of acrylamide onto carboxymethyl starch. *European Polymer Journal*, vol. 38, No. 9, (September 2002), pp 1921-1924, ISSN 0014-3057.
- Elizalde Peña, E., Flores Ramírez, N., Luna Barcenás, G., Vásquez García, S. R., Arámbula Villa, G., García Gaitan, B., Rutiaga-Quiñones, J.G., González-Hernández, J. (2007). Synthesis and characterization of chitosan-g-glycidyl methacrylate with methyl

- methacrylate. *European Polymer Journal*, Vol. 43, No. 9, (September 2007) pp 3963-3969, ISSN 0014-3057.
- Gupta, K.C., Sahoo, S., (2001) Graft copolymerization of 4-vinylpyridine onto cellulose using Co (III) acetylacetonate complex in aqueous medium. *Cellulose*, Vol. 8, No. 3, (September 2001), pp 233-242, ISSN 0969-0239.
- Heydarzadeh, H.D., Najafpour, G.D., Nazari-Moghaddam, A.A., (2009), Catalyst-free conversion of alkali cellulose to fine carboxymethyl cellulose at mild conditions. *World Applied Science Journal*, Vol. 6, No. 4, (2009), pp 564-569, ISSN 1818-4952.
- Jia, Z., Yong, Y., (2006); Surface Modification of Poly Acrylic Fibers (PAC) via Grafting of Soybean Protein Isolates (SPI). *Iranian Polymer Journal*, Vol. 15, No. 10, (October 2006), pp 789-798, ISSN 1026-1265.
- Joshi, J.M., Sinha, V.K., (2006), Graft copolymerization of 2-hydroxyethylmethacrylate onto carboxymethyl chitosan using CAN as an initiator. *Polymer*, Vol. 47, No. 6, (March 2006), pp 2198-2204, ISSN 0032-3861.
- Kang, H., Liu, W., He, B., Shen, D., Ma, L., Huang, Y., (2006), Synthesis of amphiphilic ethyl cellulose grafting poly (acrylic acid) copolymers and their self-assembly morphologies in water. *Polymer*, Vol. 47, No. 23, (October 2006), pp 7927-7934, ISSN 0032-3861.
- Klemm, D., Philipp, B., Heinze, T., Heinze, U., Wagenknecht, W., (1998). *Comprehensive cellulose chemistry volume 2*, Wiley-VCH, ISBN 3-527-29489-9, Weinheim, Federal Republic of Germany.
- Kavitha, A., Boopalan, K., Radhakrishnan, G., Sankaran, S., Das, B., Sastry, T., (2005), Preparation of Feather Keratin Hydrolyzate-Gelatin Composites and Their Graft Copolymers. *Journal of Macromolecular Science Part A: Pure and Applied Chemistry*, Vol. 42, No. 12, (December 2005), pp 1703-1713, ISSN 1060-1325.
- Martínez-Hernández, A.L., Santiago-Valtierra A. L., Alvarez-Ponce M. J., (2008), Chemical modification of keratin biofibres by graft polymerisation of methyl methacrylate using redox initiation. *Materials Research Innovations*, Vol. 12, No. 4, (December 2008), pp 184-191, ISSN 1432-8917.
- Martínez-Hernández, A.L., Velasco-Santos, C., de Icaza, M., Castaño, V.M., (2005), Microstructural characterization of keratin fibers from chicken feathers. *International Journal Environmental and Pollution*, Vol. 23, No. 2, (MES 2005), pp 162-178 ISSN 0957-4352.
- Martínez-Hernández, A.L., Velasco-Santos, C., de Icaza, M., Castaño, V.M., (2003), Grafting of Methyl methacrylate onto natural keratin. *e-polymers*, No. 016, (April 2003), pp 1-11, ISSN 1618-7229.
- Meshram, M.W., Patil, V.V., Mhaske, S.T., Thorat, B.N., (2009) Graft copolymers of starch and its application in textiles. *Carbohydrate Polymers*, 75, 1, (January 2009), pp 71-78, ISSN 0008-6215.
- Mostafa, M., Graft polymerization of methacrylic acid on starch and hydrolyzed starches. *Polymer Degradation and Stability*, (1995), Vol. 50, No. 2, (March 1995), pp 189-194, ISSN 0141-3910.
- Mun, G.A., Zauresh, S., Nurkeeva, S.A., Dergunov, I.K., Nam, T.P., Maimakov, E.M., Shaikhutdinov, Lee, S.Ch., Park, K., (2008), Studies on graft copolymerization of 2-hydroxyethyl acrylate onto chitosan. *Reactive and Functional Polymers*, Vol. 68, No. 1, (January 2008), pp 389-395, ISSN 1381-5148.

- Okieimen, F.E., Ogbeifun, D.E., (1996), Graft copolymerization of modified cellulose: grafting of methyl acrylate, ethyl acrylate and ethyl methacrylate on carboxymethyl cellulose. *European Polymer Journal*, Vol. 32, No. 3, (March 1996), pp 311-315, ISSN 0014-3057.
- Prachayawarakorn, J., Boonsawat, K., (2007), Physical, chemical and dyeing properties of bomboymori silks grafted by 2-hydroxyethyl methacrylate. *Journal of Applied Polymer Science*, Vol. 106, No. 3., (November 2007), pp 1526-1534, ISSN 1097-4628.
- Radhakumary, C., Nair, P. D., Mathew, S., Nair, C.P., (2006), HEMA-Grafted Chitosan for Dialysis Membrane Applications. *Journal of Applied Polymer Science*, Vol. 101, No 5, (September 2006), pp 2960-2966, ISSN 1097-4628.
- Schmidt, W.F., (1998), Innovative feather utilization strategies. *Proceedings of National Poultry Waste Management conference*, pp 276-282, Springdale, Ar., October 19-22, 1998.
- Vasile, C., Bumbu, G.G., Dumitriu, R.P., Staikos, G., (2004), Comparative study of the behavior of carboxymethyl cellulose-g-poly(N-isopropylacrylamide) copolymers and their equivalent physical blends. *European polymer Journal*, Vol. 40, No. 6, (June 2004) pp 1209-1215, ISSN 0014-3057.
- Xu, X. Zhou, Z., Prum, R.O., (2001), Branched integumental structures in Sinornithosaurus and the origin of feathers. *Nature*, Vol. 410, No. 6825, pp 200-204, (March 2001), ISSN 0028-0836.
- Xu, X., Zhou, Z., Wong, X., Kuang, X. Zhang, F., Du, X., (2003), Four-winged dinosaurs from China. *Nature*, Vol. 421, No. 6921, pp 335-340, (January 2003), ISSN 0028-0836.
- Zampano, G., Bertoldo, M., Bronco, S., (2009) Poly(ethyl acrylate) surface-initiated ATRP grafting from Wood pulp cellulose fibers. *Carbohydrate Polymers*, Vol. 75, No. 1, (January 2009), pp 22-31, ISSN 0008-6215.
- Zohuriaan-Mehr, J.M., Pourjavadi, A., Sadeghi, M., (2005), Modified CMC: Part1-Optimized Synthesis of Carboxymethyl cellulose-g-Polyacrylonitrile. *Iranian Polymer Journal*, Vol. 14, No. 2, (February 2005), pp 131-138, ISSN 1026-1265.

Applications of FTIR on Epoxy Resins – Identification, Monitoring the Curing Process, Phase Separation and Water Uptake

María González González, Juan Carlos Cabanelas and Juan Baselga
*University Carlos III of Madrid
Spain*

1. Introduction

Epoxy resins are a family of thermosetting materials widely used as adhesives, coatings and matrices in polymer composites because of the low viscosity of the formulations, good insulating properties of the final material even at high temperatures and good chemical and thermal resistance (May, 1988). Epoxy thermosets can be described as 3D polymer networks formed by the chemical reaction between monomers (*“curing”*). This 3D covalent network structure determines the properties of thermosetting polymers: unlike thermoplastics, this kind of polymers does not melt, and once the network has been formed the material cannot be reprocessed. Maybe one of the main advantages of epoxy thermosets is that the starting monomers have low viscosity so that complex geometries can be easily shaped and fixed after curing the monomers. Thus the formation of the network via chemical reaction is a key aspect in this kind of materials.

Epoxy formulations usually include more than one component, although there are different crosslinking mechanisms involving either chemical reaction between one single type of monomer (homopolymerization) or two kinds of monomers with different functional groups. In both cases, a common constituent is always found: the epoxy monomer. The main feature of the epoxy monomer is the oxirane functional group, which is a three member ring formed between two carbon atoms and an oxygen, as shown in Figure 1. This atomic arrangement shows enhanced reactivity when compared with common ethers because of its high strain. Due to the different electronegativity of carbon and oxygen, the carbon atoms of the ring are electrophilic. Thus epoxies can undergo ring opening reactions towards nucleophiles. The polarity of the oxirane ring makes possible detection by IR spectroscopy.

There are mainly two families of epoxies: the glycidyl epoxies and non-glycidyl epoxies (also called aliphatic or cycloaliphatic epoxy resins). The absence of aromatic rings in aliphatic epoxies makes them UV resistant and suitable for outdoor applications and also reduces viscosity. The most common epoxy monomers of each family are diglycidylether of bisphenol A (known as DGEBA) and 3,4-Epoxy cyclohexyl-3'4'-epoxycyclohexane carboxylate (ECC) respectively and their structures are given in Figure 2 (a, b). Cycloaliphatic resins are usually found in the form of pure chemicals with a definite

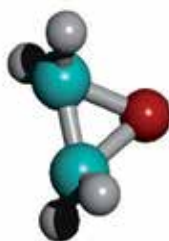


Fig. 1. Oxirane ring

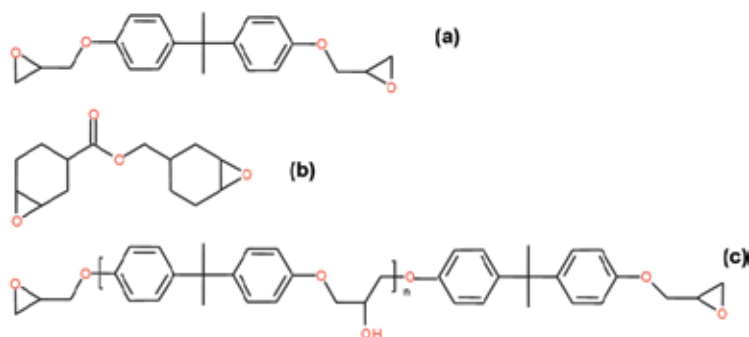


Fig. 2. Chemical structures of common epoxy resins: a) 2,2-Bis[4-(glycidyoxy)phenyl]propane (DGEBA); b) 3,4-Epoxy cyclohexylmethyl-3,4-epoxy cyclohexane carboxylate (ECC); c) DGEBA oligomer, $n = 0.2$ typically.

molecular mass. But DGEBA-based resins are synthesized via the addition of epichlorohydrine and bisphenol A so oligomers with a relatively narrow distribution of polymerization degrees are obtained instead; their chemical structure is presented in Figure 2 (c) where n is typically 0.2. DGEBA oligomers typically contain a certain amount of hydroxyl groups, that play an important catalytic role in the kinetics of the curing process, providing a higher viscosity which is dependent on n . In addition, all of them have at least two oxirane functional groups, so they can finally lead to the 3D network. The nature and functionality of the epoxy monomer will determine its reactivity as well as the properties and performance of the final material.

Despite of having the same main functional group, the reactivity of both families of epoxies is completely different as a consequence of the structure of the molecules. It is worthy to note that the linkage between the aromatic ring and the oxygen (ether) in DGEBA has a strong electron-withdrawing effect that makes the oxirane group highly reactive towards nucleophilic compounds (like amines), unlike the cyclohexyl group in aliphatic epoxies which is reactive towards Lewis acids like anhydrides (Mark, 2004). Additionally, a protecting effect of axial and equatorial protons of the cyclohexyl ring against nucleophilic attack has been proposed as an explanation of the characteristic low reactivity of the oxirane ring in these aliphatic epoxies (Soucek et al., 1998). This way, the best performance and the highest crosslinking degree for DGEBA-based resins is achieved when cured via an addition mechanism with diamines (either aliphatic or aromatic), whilst cycloaliphatic epoxies are commonly cured with anhydrides (Barabanova et al., 2008; Chen et al., 2002; Tao et al., 2007;

Wang et al., 2003) or homopolymerized via a cationic mechanism induced by UV radiation (Crivello, 1995; Crivello & Fan, 1991; Crivello & Liu, 2000; Hartwig et al., 2003; Wang & Neckers, 2001; Yagci & Reetz, 1998).

The chemical reactivity of the epoxies enables using a wide variety of molecules as curing agents depending on the process and required properties. The commonly used curing agents for epoxies include amines, polyamines, polyamides, phenolic resins, anhydrides, isocyanates and polymercaptans. The choice of both the resin and the hardener depends on the application, the process selected, and the properties desired. It is worthy to note that the reaction mechanism, the curing kinetics and the glass transition temperature (T_g) of the final material are also dependent on the molecular structure of the hardener. As it has been previously mentioned, amines are the best performance curing agents for diglycidylether-type epoxies. Aliphatic diamines like *m*-xylylenediamine or 1,2-trans-cyclohexyldiamine can be used for curing from room to moderate temperatures (Paz-Abuin, 1997a, 1997b, 1998), although the glass transition temperature of the material is also moderate. For high T_g materials aromatic amines, like 4,4'-methylene-bis(3-chloro-2,6-diethylaniline) or 4,4'-diaminodiphenyl sulphone (Blanco et al., 2004; Girard-Reydet et al., 1999; Marieta et al., 2003; Siddhamalli, 2000a) are used, although high curing temperatures are needed.

1.1 Curing process. Gelation and vitrification. Conversion degree

The curing process is the set of chemical reactions that leads to the formation of a highly crosslinked 3D network. For epoxy/amine the chemical process that leads to network formation can be described according to the scheme:

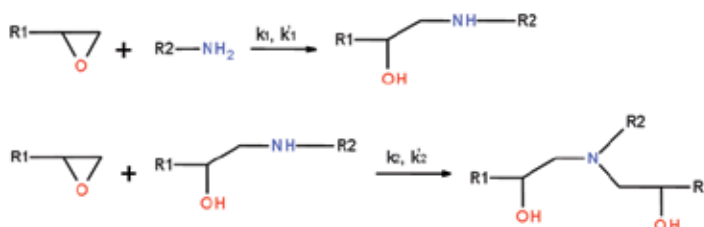


Fig. 3. Epoxy-amine reaction scheme. k_1 and k_2 correspond to the non catalyzed kinetic constants for the addition of primary and secondary amines respectively. k'_1 and k'_2 correspond to the catalyzed processes.

The reaction between monomers leads to the formation of the network and there are two important points during this process: gelation and vitrification. During the first stage the primary amino groups transform sequentially in secondary and tertiary amino groups. If R1 and R2 blocks contain a second reactive group (oxirane and amino, respectively), addition of more molecules proceeds at the ends of the branched molecule as well as with fresh monomers. Therefore, during the chemical reaction, both molecular weight and polydispersity increase until one single macromolecule is formed. At this point, if temperature is high enough, the behavior of the system changes irreversibly from liquid-like to rubber-like: the reactive system becomes a gel. According to the Flory-Stockmayer's theory of gelation (Flory, 1953) the extent of reaction at this point can be determined using the expression:

$$\alpha_{gel} \cdot \beta_{gel} = \frac{1}{(f_e - 1)(f_a - 1)}$$

Where α_{gel} and β_{gel} are epoxy and amine conversions at the gel point and f_e and f_a are the functionality of the epoxy and amine components respectively ($f_e = 2$ and $f_a = 4$ typically, so under stoichiometric conditions, gel point appears at $\alpha_{gel} = \beta_{gel} = 0.57$). Gelation usually has no effect on the curing kinetics.

Common diamines with relatively small molecular volume act as crosslinking points of the 3D network (since each diamine has four active hydrogen atoms, they can be visualized as points in space from which four chains emerge, each of them connecting other points of the network). As the reaction proceeds, along with molecular weight, the crosslinking degree of the system increases, and so the viscosity and the glass transition temperature (Tg). In those processes in which curing temperature is not very high, Tg of the reacting mixture may reach the curing temperature value; then, molecular mobility becomes severely restricted so diffusion of reactants controls the kinetics and the reaction rate decreases dramatically. At this point, the reaction becomes almost stopped and the properties of the material (at room temperature) depend on the extent of the reaction achieved. Unlike gelation, vitrification is a reversible process, so when heating above Tg the reaction is reactivated and higher conversions are attained. Postcuring processes, which are designed to allow volume and internal stresses relaxation, make use also of this chemical reactivation and have deep effects on the mechanical performance of these systems.

The extent of reaction is very commonly determined by differential scanning calorimetry (DSC) as the ratio between the heat released by the reaction at each moment and the total heat released. Although this procedure is useful, accuracy at high conversions is low and problems arise when monitoring fast reactions. Additionally, DSC only provides an overall conversion degree being impossible to independently determine epoxy and amine conversions. On the contrary, infrared spectroscopy allows a very accurate determination of both conversions by band integration of the corresponding IR signals (epoxy and amino) being low the integration error and allowing more accurate values at high conversions. Considering the reaction mechanism, we can define the extent of reaction in terms of epoxy groups (α) and in terms of N-H bonds (β) from the areas of the oxirane ring and the N-H absorptions respectively:

$$\alpha_e = \frac{A_e(0) - A_e(t)}{A_e(0)} \quad \beta_{N-H} = \frac{A_{N-H}(0) - A_{N-H}(t)}{A_{N-H}(0)} \quad (1)$$

In equation (1) subscript "e" indicates epoxy, "N-H" amine, "0" initial and "t" indicates a certain reaction time. Although epoxy and amino groups have absorptions in the mid-range, more accurate results are obtained working in the near range

1.2 Epoxy blends. Reaction induced phase separation

The main drawback of epoxy thermosets is its brittleness. To solve this problem, they are commonly modified with reinforcements of different nature (elastomers, thermoplastics, inorganic particles), geometry (particles, fibers, platelets) and size (micro and nano) which provide additional mechanical energy absorption mechanisms. The dispersion of a second phase can be obtained using mainly two strategies (Pascault et al., 2002):

- Directly mixing preformed particles in the starting monomers. The initial system is therefore heterogeneous.
- Reaction induced phase separation (RIPS) from a homogeneous initial mixture. A third component which is initially soluble in the epoxy precursors but segregates during the chemical reaction (usually a thermoplastic or an elastomer) is incorporated in the system. Segregation generates the final two-phase morphology.

Morphology development in modified thermosets takes place essentially between the “cloud point” conversion (beginning of the phase separation) and the gel point conversion (Bucknall & Partridge, 1986; Inoue, 1995; Mezzenga et al., 2000a), although it keeps evolving up to the vitrification of the system. Thermodynamics is the driving force for RIPS, but diffusion kinetics between phases is the controlling factor from the gel point on (Kiefer et al., 1996; Rajagopalan et al., 2000).

As a consequence of phase separation particles or domains of very small size and different refraction index appear. When they are big enough they become light scatterers and the mixture becomes cloudy in the visible range. But the size of domains plays with the wavelength, so IR radiation can also be used to determine the onset of phase separation and characterize the growth of the nascent structures.

2. Epoxy resins and FTIR

For in-situ monitoring processes such as curing, phase separation or even ageing, the interpretation of the spectra and the assignment of the bands are critical.

Mid infrared spectroscopy has been widely used for characterization of organic compounds and plenty of reliable information and spectra libraries can easily be found. Both qualitative and quantitative information can be obtained by this technique, although its use in epoxy systems is quite restricted because of the location and intensity of the oxirane ring absorptions. Two characteristic absorptions of the oxirane ring are observed in the range between 4000 cm^{-1} and 400 cm^{-1} . The first one, at 915 cm^{-1} , is attributed to the C-O deformation of the oxirane group, although some works done by Dannenberg (Dannenberg & Harp, 1956) showed that this band does not correspond exclusively to this deformation but also to some other unknown process. The second band is located at 3050 cm^{-1} approximately and is attributed to the C-H tension of the methylene group of the epoxy ring. This band is not very useful since its intensity is low and it is also very close to the strong O-H absorptions; but in low polymerization degree epoxy monomers it can be used as a qualitative indicative of the presence of epoxy groups.

Near IR is far more useful for epoxies. nIR spectrum covers the overtones of the strong vibrations in mIR and combination bands. In this range, fewer and less overlapped bands are observed so it has been used by several authors (Mijovic & Andjelic, 1995; Poisson et al., 1996; Xu & Schlup, 1998) for monitoring the curing reaction. The intensity of the bands in this region is much lower than in the mid range, allowing the use of thicker and undiluted samples to get good quality data. There are two absorptions related with the oxirane group in this region:

- a. 4530 cm^{-1} : It corresponds to a combination band of the second overtone of the epoxy ring stretching with the fundamental C-H stretching at 2725 cm^{-1} (Chicke et al., 1993).

Anyway, this band is sufficiently separated from others and is suitable for quantitative analysis (Mijovic et al., 1995; Paz-Abuín et al., 1997a; Poisson et al., 1996; Xu & Schlup, 1998).

- b. 6070 cm^{-1} : First overtone of terminal CH_2 stretching mode (Musto et al., 2000). This band interferes with the aromatic C-H stretching overtone at 5969 cm^{-1} (Xu et al., 1996), so in case there are aromatic rings in the structure (i.e. DGEBA) is not suitable for quantification.

2.1 Characterizing epoxy resins by IR

Characterization of epoxies involves much more than the location of the oxirane ring bands. There are many epoxy resins with different structures, different polymerization degrees...etc. IR spectroscopy can be used to characterize the nature of the epoxy. Figure 4 shows the mIR and nIR spectra of two similar epoxy resins: Diglycidylether of bisphenol A (DGEBA) and its hydrogenated derivative (HDGEBA).

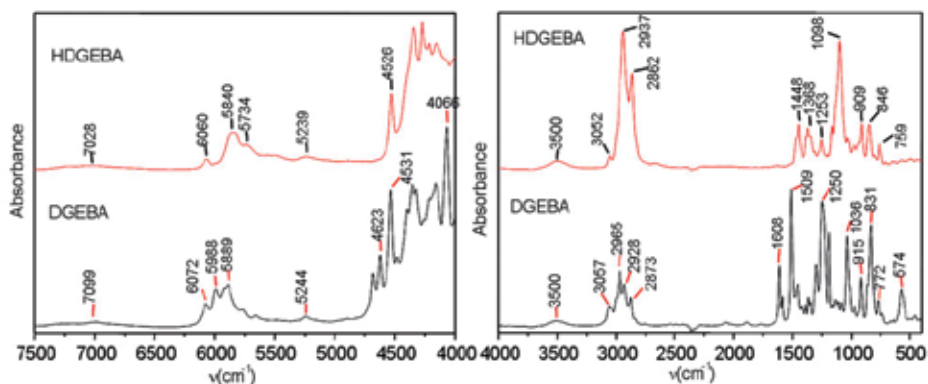


Fig. 4. FTIR spectra of DGEBA and HDGEBA in the medium and near ranges

The difference between both resins is the absence of aromatic rings in HDGEBA, which conditions both the properties (T_g , viscosity...etc) and reaction rate towards amines. Table 1 shows the assignation of bands for both resins in the mid range. The C-O deformation band is centered at 915 cm^{-1} in DGEBA and at 909 cm^{-1} in HDGEBA. C-H stretching of terminal oxirane group is observed in both cases at 3050 cm^{-1} . The broad band at 3500 cm^{-1} is assigned to O-H stretching of hydroxyl groups, revealing the presence of dimers or high molecular weight species. There are also bands corresponding to the ether linkage located at 1000-1100 cm^{-1} in both cases. In HDGEBA no signals corresponding to neither aromatic rings nor double bonds are observed, so these two epoxies can be easily distinguished through these bands.

Spectra in the near range are shown in Figure 4 also and assignments in Table 2. The combination band of the second overtone of the epoxy ring stretching with the fundamental C-H stretching is centered at 4531 cm^{-1} in DGEBA and at 4526 cm^{-1} in HDGEBA. The region from 4000 to 4500 cm^{-1} contains the overtones from the fingerprint of the molecule.

The hydroxyl bands are sometimes useful for characterization although its quantitative use is very limited. Their presence is associated to the use of oligomers of low polymerization

Resin	Band (cm ⁻¹)	Assignment
DGEBA	≈ 3500	O-H stretching
	3057	Stretching of C-H of the oxirane ring
	2965- 2873	Stretching C-H of CH ₂ and CH aromatic and aliphatic
	1608	Stretching C=C of aromatic rings
	1509	Stretching C-C of aromatic
	1036	Stretching C-O-C of ethers
	915	Stretching C-O of oxirane group
	831	Stretching C-O-C of oxirane group
	772	Rocking CH ₂
HDGEBA	≈ 3500	O-H stretching
	3052	Stretching of C-H of the oxirane ring
	2937- 2862	Stretching C-H of CH ₂ and CH
	1448	Deformation C-H of CH ₂ and CH ₃
	1368	Deformation CH ₃ of C-(CH ₃) ₂
	1098	Stretching C-O-C of ethers
	909	Stretching C-O of oxirane group
	846	Stretching C-O-C of oxirane group
	759	Rocking CH ₂

Table 1. Characteristic bands of DGEBA and HDGEBA in the mid IR.

Resin	Band (cm ⁻¹)	Assignment
DGEBA	7099	O-H overtone
	6072	First overtone of terminal CH ₂ stretching mode
	5988- 5889	Overtone of -CH and -CH ₂ stretching
	5244	Combination asymmetric stretching and bending of O-H
	4623	Overtone of C-H stretching of the aromatic ring
	4531	Combination band of the second overtone of the epoxy ring stretching with the fundamental C-H stretching
	4066	Stretching C-H of aromatic ring
HDGEBA	7028	O-H overtone
	6060	First overtone of terminal CH ₂ stretching mode
	5840- 5734	Overtone of -CH and -CH ₂ stretching
	5239	Combination asymmetric stretching and bending of O-H
	4526	Combination band of the second overtone of the epoxy ring stretching with the fundamental C-H stretching

Table 2. Characteristic bands of DGEBA and HDGEBA in the near IR. (George et al., 1991; Mijovic et al., 1995).

degree, as shown in Figure 2. In the mid range, quantification of OH is quite difficult because of the shape and overlapping of the band at around 3500 cm^{-1} . In the near range, the absorption of the first O-H overtone is located at around 7000 cm^{-1} , and although it has been used for quantification, no good results were obtained because of its weakness.

3,4-Epoxy cyclohexyl-3'4'-epoxycyclohexane carboxylate (ECC) is probably the most common cycloaliphatic epoxy. The oxirane ring is in this case located in a six-member aliphatic cycle (Figure 2), shifting its absorptions in the mid range towards lower wave numbers, so the main absorption band is located at 790 cm^{-1} (Figure 5). This band has been used for quantitative analysis of photochemical reactions (Hartwig et al., 2002; Kim et al., 2003). Apart from the oxirane absorptions this resin shows the bands corresponding to the stretching C-O-C of ethers (1100 cm^{-1}) and the C=O stretching (1730 cm^{-1}) of esters, which can be useful for identification.

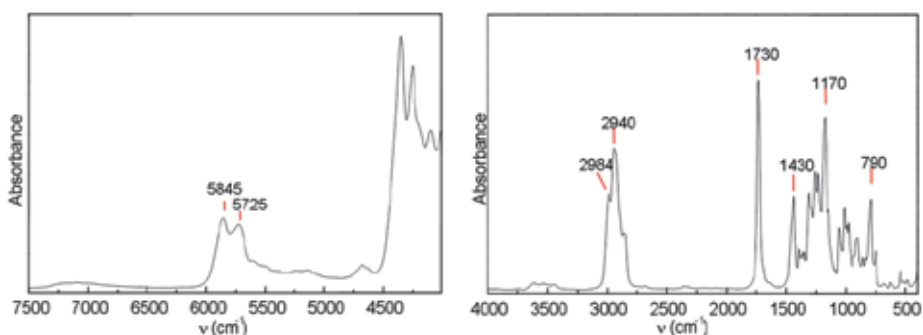


Fig. 5. FTIR spectra of ECC in the mid and near ranges

In the near range (Figure 5), it is worthy to note that the oxirane combination band (bending+ stretching) usually located at around 4530 cm^{-1} for common epoxies cannot be observed in the nIR spectrum of ECC probably because it may be overlapped with C-H combination bands. Neither the C=O second overtone (usually located at around $5100\text{--}5200\text{ cm}^{-1}$) is clearly observed. The main features observed in the spectrum are only the overtones of C-H and CH_2 stretching bands. Although near infrared spectroscopy does not provide much useful information for this resin, it can still be used for monitoring the curing process through the evolution of the bands assigned to the curing agent (M. Gonzalez et al., 2011).

2.2 Characterizing diamine hardeners by IR

Among all the curing agents used to obtain epoxy thermosets, this chapter will be focused on one specific type: diamines. Their high reactivity is attributed to the high nucleophilicity of the nitrogen atom of the amino group although it is conditioned by its chemical structure. For instance, aliphatic diamines such as ethylene diamine, show a very high reactivity, while substituted aromatic amines like 4,4'-methylene-bis(3-chloro-2,6-diethylaniline) show lower reactivity because of the electronic effects of the aromatic ring and the substituents.

The amino group shows well defined absorptions both in the mid and in the near infrared ranges. The main absorptions in the mid range are stretching and deformation of N-H bonds. These bands also reflect some differences between primary and secondary amines:

- Although the N-H stretching is located between 3500 and 3300 cm^{-1} , primary amines show a doublet (reflecting the symmetric and antisymmetric stretching modes) while the secondary amines show one single band.
- The N-H deformation is located at 1650- 1500 cm^{-1} in primary amines, while in secondary amines it is shifted towards lower wavenumbers (1580- 1490 cm^{-1}) and is usually weak.

The quantitative use of these bands is limited because of its position in the spectra: the N-H stretching is very close to the strong O-H absorption band (minimal amount of water perturbs its area), while the deformation band is located in the region where many signals corresponding to organic bonds appear.

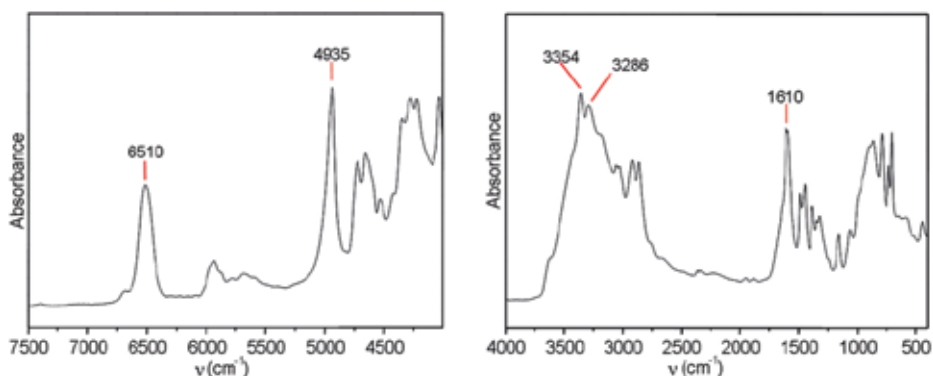


Fig. 6. mIR and nIR spectra of metaxylylenediamine

In the near range, the bands of amines are well defined and intense. There are also differences between the absorptions of primary and secondary amines. Primary amines N-H stretching first overtone is composed of two bands (symmetric and antisymmetric) located between 6897 cm^{-1} and 6452 cm^{-1} , being the symmetric more intense. For secondary amines there is a single band. When both species coexist, this band cannot be used because the two bands overlap. Combination of N-H stretching and bending is observed at around 4900-5000 cm^{-1} , and it can be used for quantitative purposes. (Weyer & Lo, 2002). Example spectra of diamines in both ranges are shown in Figure 6.

3. Curing process

3.1 Monitoring the curing process

As shown in Figure 3, curing of epoxy resins with diamines can be described as a two step reaction: Firstly an epoxy group reacts with a primary amine yielding a secondary amine, which in the second step reacts with another epoxy group yielding a tertiary amine

Considering these chemical reactions, the process can be monitored through the evolution of concentration of epoxy groups, primary amines or in some extent, secondary amines. The concentration of species is quantitatively related to the area of the absorption band only in the linear region, where Lambert Beer's law is satisfied. Taking this into account, changes in concentration of epoxy groups may be determined by mIR measuring the area of the absorption bands at $\approx 3050 \text{ cm}^{-1}$ or at 900 cm^{-1} .

Nevertheless, following curing by IR is not always easy, because the epoxy band at higher wavenumbers shows low sensitivity to changes in concentration as a consequence of its intrinsic low intensity and the 900 cm^{-1} band may be affected by the uncleanliness of the region where it is located. This may induce some uncertainty at the final stages of reaction when the concentration of epoxy groups is small. On the other hand, the quantification of primary and secondary amines in epoxy/amine reactive systems is not possible since the band corresponding to primary amines overlaps both with the band corresponding to secondary amines and the one corresponding to hydroxyl groups, which are species appearing as a consequence of the advance of the chemical reaction. Despite all these facts, mIR has been successfully used for monitoring the epoxy amine chemical reaction in several cases (Nikolic et al., 2010).

Fortunately nIR can be safely used for quantitatively monitor the chemical reaction (Paz-Abuin et al., 1997a, 1997b; Mijovic & Andjelic 1995a; Mijovic et al. 1995). In this region we can find well defined bands free of overlapping related with the epoxy and primary amine: the combination band of the second overtone of the epoxy ring stretching with the fundamental C-H stretching ($\approx 4530\text{ cm}^{-1}$) and the combination band of NH stretching and bending ($\approx 4900\text{--}5000\text{ cm}^{-1}$). In Figure 7, a typical spectral evolution on cure can be observed.

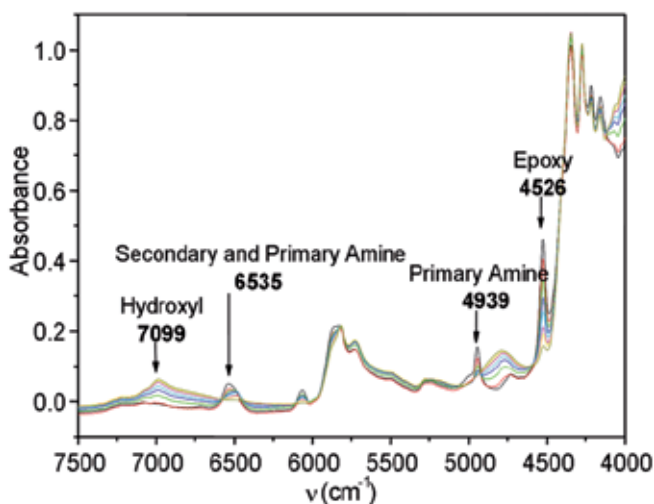


Fig. 7. Time evolution of FTnIR spectra during the isothermal curing at $70\text{ }^{\circ}\text{C}$ of the stoichiometric HDGEBA/poly(3-aminopropylmethyl)siloxane system.

The reaction mechanism indicates that the epoxy concentration decreases, and this is observed in the spectra as the decrease of the band centered at $\approx 4530\text{ cm}^{-1}$ and also of the weak overtone of terminal CH_2 at $\approx 6060\text{ cm}^{-1}$. The primary amine combination band decreases too ($\approx 4900\text{ cm}^{-1}$), and once it is exhausted it can be observed that there are still epoxy groups in the reaction media, which will react with the previously formed secondary amines up to vitrification or until the reaction is completed. The band corresponding to O-H overtones ($\approx 7000\text{ cm}^{-1}$) also increases during curing as a consequence of the oxirane ring-opening, although this band is not suitable for quantification because of the low signal/noise ratio. The behavior of the band located at $\approx 6500\text{ cm}^{-1}$ is more complex: in this

region the overtones of both primary and secondary amines overlap, so an initial decrease is observed, followed by an increase and a shift towards lower wavenumbers (because of the generation of secondary amines) and a final decrease consequence of the transformation of secondary amines into tertiary amines.

For quantitative analysis, changes in concentration of epoxy and primary amines can be directly determined from the integration of the bands at $\approx 4530\text{ cm}^{-1}$ and at $\approx 4900\text{ cm}^{-1}$ respectively, and the epoxy (α) and primary amine (β) conversion degrees can be calculated as shown in eq (1). This fact opens the possibility of using complex models in which the concentration of all species (primary, secondary, tertiary amine and epoxy) can be considered during the curing process and kinetic parameters for the different steps of the reaction can be obtained. In Figure 8 typical conversion-time profiles for both α and β at different temperatures are shown. After an initial fast increase in conversion a “plateau” region is reached, corresponding to the diffusion controlled stage (vitrification). As it is shown, the “plateau” for the primary amine conversion is often achieved at conversions very close to 1, indicating that during curing the primary amine is fully consumed.

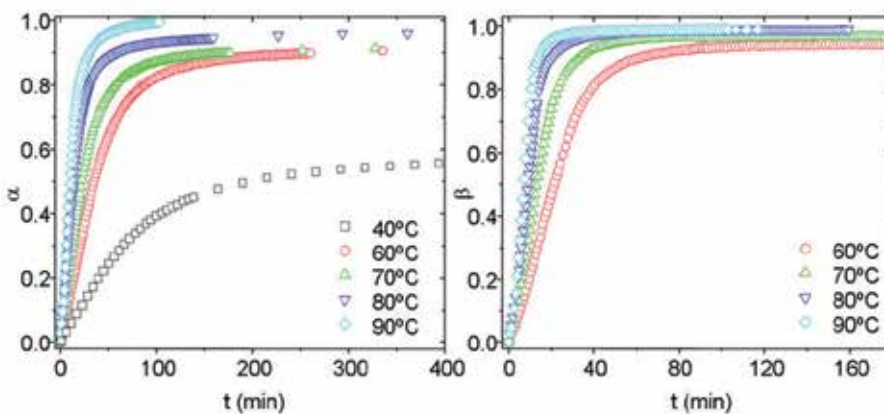


Fig. 8. Epoxy (α) and primary amine (β) conversions at different temperatures for HDGEBA/poly(3-aminopropylmethyl)siloxane.

Shrinkage during curing or initial sample thermostating can lead to major errors in epoxy and primary amino bands integration. To avoid this difficulty, it is useful to normalize the integrated areas to a characteristic band not changing during curing. For this purpose, usually bands corresponding to overtones of the resin skeleton are used.

Curing cycloaliphatic epoxies with amines is not common because of the low reactivity of the system even at high temperatures. Anyway, its thermal curing with some complex amines (like poly (3-aminopropylmethyl)siloxane)) has been reported. Determining conversion in these systems by IR is not an easy task, since the combination bands of the epoxy group in the near range overlap with other bands. Nevertheless, it is possible a semiquantitative approach considering the primary amine combination band at $\approx 4900\text{ cm}^{-1}$ and at longer reaction times (when primary amine is exhausted) progress of the reaction can be qualitatively followed from the primary and secondary amine combination band at 6530 cm^{-1} (Kradjel & Lee, 2008; Mijovic and Andjelic, 1995; M. Gonzalez et al., 2011).

3.2 Modeling kinetics

Curing kinetics is a key aspect in epoxy systems, since it determines the time span available for shaping, storing... As in most chemically reactive systems, reaction rate is temperature dependent.

Several models have been developed for epoxy/amine kinetics through the study of model compounds (Schechter et al., 1956). An acceleration of reaction in the presence of OH groups was observed and explained considering a third order reaction mechanism (Smith, 1961). Horie and coworkers proposed a model in 1970 (Horie et al., 1970) considering the catalysis of both initial OH (due to DGEBA oligomers and impurities) and OH generated during chemical reaction (autocatalysis) which has been used and validated in many epoxy/amine systems at different temperatures (Simon et al., 2000; Vyazovkin & Sbirrazouli, 1996; Cole et al., 1991; Riccardi et al., 1984). Later on, modifications to the model have been introduced, for example considering the different reactivity of hydrogens belonging to primary and secondary amines and the possible homopolymerization reactions between epoxy groups under certain conditions (Cole et al., 1991; Riccardi & Williams, 1986). Thus, following the evolution of concentration of the different species during curing is useful for modeling epoxy/amine systems.

The commonly accepted kinetic scheme for epoxy-amine reactions considers two reaction paths: a non-catalyzed and an autocatalyzed path. The autocatalysis is attributed to the formation of complex between generated or initially present hydroxyl groups, amino groups and epoxy groups. A simple reaction mechanism is presented in Figure 3 although it can be improved considering some equilibrium reactions for the complexes formation (Ehlers et al., 2007). With appropriate mass balances it is possible to set out rate equations that can be fitted to experimental data to extract the relevant kinetic parameters

3.2.1 Determining concentrations during curing

Considering the reaction scheme, the concentration of epoxy groups, primary, secondary and tertiary amine, as well as hydroxyl groups can be determined through the following mass balances:

$$[A_1] = [A_1]_0 - [A_2] - [A_3] \quad ; \quad [E] = [E]_0 - [A_2] - 2[A_3] \quad ; \quad [OH] = [OH]_0 + [E]_0 - [E]$$

If initial concentrations of epoxy and primary amine are known, the concentration of all species at each instant can be determined from the conversion data obtained by nIR:

$$[E] = [E]_0(1 - \alpha) \quad ; \quad [A_1] = [A_1]_0(1 - \beta) \quad ; \quad [A_2] = [E]_0(\beta B - \alpha) \quad ; \quad [A_3] = [E]_0 \left(\alpha - \beta \frac{B}{2} \right)$$

Where $B = 2[A_1]_0/[E]_0$ is the ratio between the initial concentration of primary amine and epoxy. A typical variation of all these species with time is presented in Figure 9.

Assuming that the reactivity ratio between primary and secondary amines (R) is independent of the reaction path, the kinetic equations for the epoxy and primary amine conversion are:

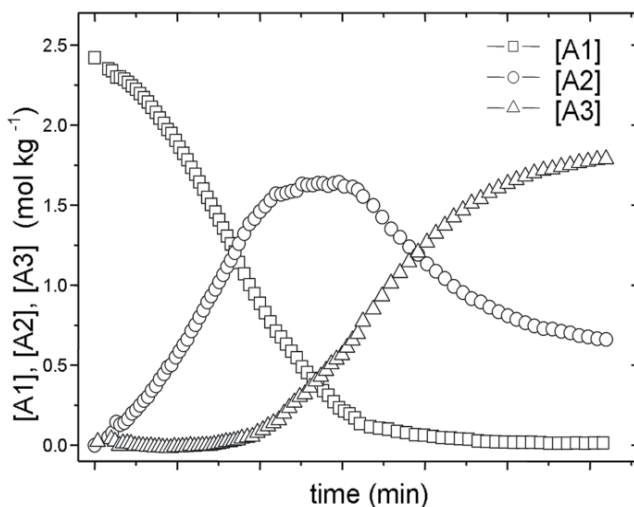


Fig. 9. Typical evolution of concentration of primary (A1), secondary (A2) and tertiary amine (A3) groups during curing. Reactive system: DGEBA/m-Xylylenediamine at 80°C. (Used with permission from (González, M.; Kindelán, M.; Cabanelas, J.C.; Baselga, J. *Macromolecular Symposia*, Vol.200. Copyright (2003)).

$$\frac{d\alpha}{dt} = \frac{B}{2} \frac{d\beta}{dt} + R(B\beta - \alpha)(1 - \alpha) \left(K_1 + K'_1 \left(\frac{[OH]_0}{[E]_0} + \alpha \right) \right) \quad (2)$$

$$\frac{d\beta}{dt} = (1 - \beta)(1 - \alpha) \left(K_1 + K'_1 \left(\frac{[OH]_0}{[E]_0} + \alpha \right) \right) \quad (3)$$

where:

$$K_1 = k_1[E]_0 \quad R = \frac{k_2}{k_1} = \frac{k'_2}{k'_1}$$

$$K'_1 = k'_1[E]_0^2$$

3.2.2 Reactivity ratio between primary and secondary amines

Some kinetic models assume that the reactivity of primary and secondary amines is the same. Considering that primary amines have two reactive hydrogen atoms, equal reactivity yields $R = 0.5$. Nevertheless, in most of epoxy amine systems higher reactivity of primary amines ($R < 0.5$) has been experimentally observed (Matejka, 2000; Paz-Abuin et al., 1997a, 1997b, 1998; Liu et al., 2004; Varley et al., 2006). This behavior is not surprising since the addition of the epoxy molecule to a primary amine causes a steric hindrance. On the other hand, the chemical nature of the new substituent usually decreases the nucleophilic character (and thus the reactivity) of the nitrogen atom in the amine group due to a negative inductive effect.

Paz-Abuín et al. developed a method for quantifying the reactivity ratio from the concentration-time plots of amines (Paz-Abuin et al., 1997a). Considering the classical reaction mechanism, applying the condition for maximum to $[A_2]$, it is obtained that

$R=[A_1]/[A_2]$. Thus, R value can be determined from the concentration curves as the ratio of the concentration of primary amine and secondary amine at the maximum of secondary amine concentration. Usually the R value is below 0.5, i.e. it shows the higher reactivity of primary amines. If R is not very low, the uncertainty in the determination of the maximum is small and the R value can be precisely determined.

3.2.3 Solving kinetic equations

Rate constants can be obtained solving the rate equations (2) and (3) mentioned above. Since both equations are interdependent, two approaches for solving them may be used:

- **Linearization method:** A new variable (λ) is defined as:

$$\lambda = \frac{[A_2]}{[E]_0}$$

Thus a single equation in terms of the derivative of epoxy conversion is obtained, so that the global kinetic constants can be obtained as the intercept and slope of the linear fit at low conversions (far from the diffusion controlled region) of the expression:

$$\frac{\frac{d\alpha}{dt}}{(1-\alpha)(\lambda + R(B - 2\lambda - \alpha))} = K_1 + K'_1 \left(\frac{[OH]_0}{[E]_0} + \alpha \right)$$

A typical example of the linearization method is presented in Figure 10.

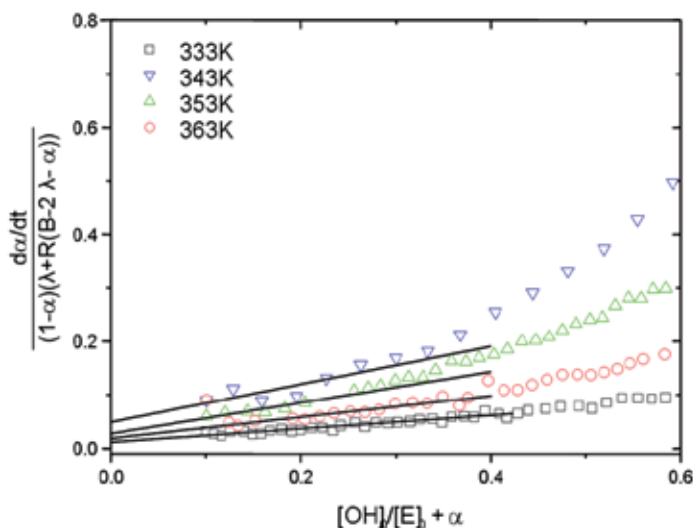


Fig. 10. Determination of K_1 and K'_1 .

- **Non-linear method:** Rate equations (2) and (3) may be solved numerically using a computer program. This approach has been used for several epoxy/aliphatic diamine and good fits of epoxy and primary amine conversions were obtained (Figure 11) (M. Gonzalez et al., 2003).

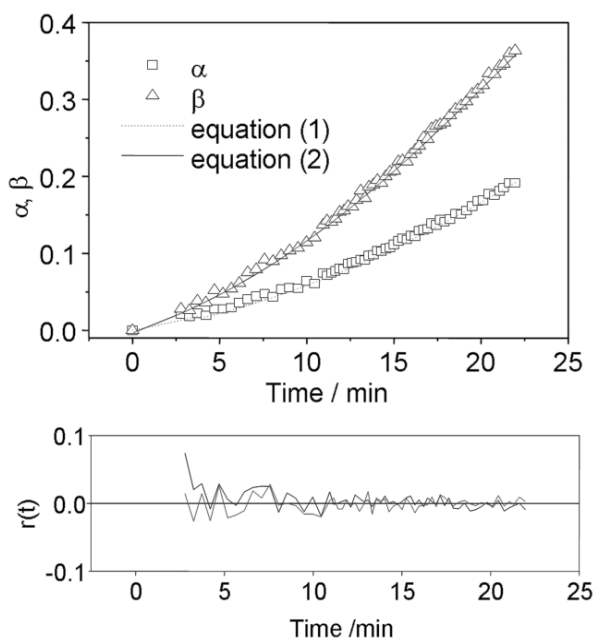


Fig. 11. α and β as a function of curing time for DGEBA / m-XDA at 60 °C. Lines: fitting to eqs (1) and (2). Below: weighted residuals calculated as:

$$r(t_i) = \frac{O(t_i) - C(t_i)}{\sqrt{O(t_i)}}$$

were $O(t_i)$ and $C(t_i)$ are the observed and calculated values of α (or β) respectively. (Used with permission from (González, M.; Kindelán, M.; Cabanelas, J.C.; Baselga, J. *Macromolecular Symposia*, Vol.200. Copyright (2003)).

4. Phase separation influence on IR spectra

Phase separation in blends involves the development of a second phase which usually has a different refractive index, and can be detected by the appearance of turbidity. Most studies analyze the so-called "cloud point" (instant when the sample is no longer transparent) measuring visible transmittance. Particles scatter light when its size is similar to the wavelength of the incident radiation; since infrared radiation ranges from 780 nm to 15 μm (from 780 nm to 1.1 μm for the near range and from 1.1 μm to 15 μm for the mid range), the onset of phase separation can be detected using nIR or mIR although with less accuracy (Bhargava et al, 1999) than using visible light. Therefore, IR measurements give delayed values of the cloud point. This fact is clear, and even more sophisticated techniques like SAXS may give information of the incipient phase separation process, but there is an advantage for IR: it provides additional chemical information during phase separation. Because of its longer wavelength, mIR is rarely used for characterizing phase separation phenomena, although it is used for characterizing other systems containing particles of bigger size or to avoid interferences due to the color of the systems.

Turbidity is observed in IR spectra as an increase of baseline. This parameter can be used to follow the phase separation process in a region where no bands exist, i.e. 6300 cm^{-1} . Alternatively, this method has also been used to follow compatibilization of initially immiscible systems. As an example Cabanelas et al. (Cabanelas et al., 2005) studied the compatibilization process and phase separation of a third component in reactive blends based on DGEBA and poly(3-aminopropylmethylsiloxane) modified with PMMA. As shown in Figure 12, the initial decrease of the baseline was related with the compatibilization between DGEBA and the silicone hardener and the subsequent increase was related with the onset of phase separation of the thermoplastic modifier. IR can also provide information about the interactions between the modifier and the thermosetting matrix. Typical cured epoxy thermosets present a variety of $\text{OH}\cdots\text{N}$, $\text{OH}\cdots\text{NH}$ and $\text{OH}\cdots\text{OH}$ hydrogen bonds. In the presence of PMMA intramolecular interactions become redistributed since the carbonyl groups of PMMA interact with the initially present and newly formed OH groups as it is shown by the presence of a carbonyl-OH hydrogen bonding band centered at 3500 cm^{-1} (Blanco et al., 2009). These changes in IR spectra may be related with the miscibility in complex systems.

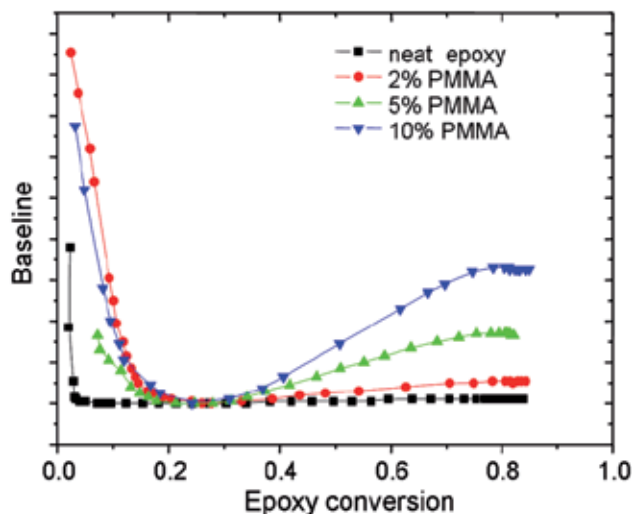


Fig. 12. Baseline from FTIR spectra at 6300 cm^{-1} as a function of epoxy conversion of DGEBA/PAMS for different weight concentrations of PMMA as modifier (Adapted with permission from (Cabanelas, J.C.; Serrano, B.; Baselga, J. *Macromolecules*, Vol.38, No.3, (2005)). Copyright (2005) American Chemical Society).

5. Water uptake

One of the main drawbacks of epoxy resins is its high water uptake. Water deteriorates thermomechanical properties (T_g , modulus, yield strength, toughness...), and adhesion, it induces chemical degradation of the network and also generates stresses because of swelling (Nogueira et al., 2001; Cotugno et al., 2001; Blanco et al., 2006; Ji et al., 2006; Xiao & Shanahan, 2008). Significant efforts have been done to elucidate the interactions of water with epoxy/amine networks and the diffusion mechanisms operating during water uptake,

and many different techniques have been used: from the fast and easy gravimetry to more complex techniques such as NMR spectroscopy (Zhou & Lucas 1999) or fluorescence (Mikes et al., 2003). Also infrared spectroscopy has been widely used. IR shows an advantage when compared with gravimetry: it is not only an accurate technique for determining water concentration, but also provides information at the molecular level about the interactions between water molecules and the thermoset structure and can be used to provide information on dimensional changes of the specimens.

Water has three active vibration modes in infrared corresponding to the stretching of O-H bond ($\approx 3800\text{-}3600\text{ cm}^{-1}$ in liquid state) and bending ($\approx 1650\text{-}1590\text{ cm}^{-1}$ in liquid state). The position of the bands of this molecule is particularly sensitive towards interactions like hydrogen bonding, which originates displacements towards lower wavenumbers ($< 3600\text{ cm}^{-1}$), enabling the distinction between free water, hydrogen bonded and intramolecular hydrogen bonding (Socrates, 1994). When absorbed in epoxy resins, two types of water are found: highly mobile free water molecules ($\approx 3600\text{ cm}^{-1}$) and water bounded to specific sites through hydrogen bonding ($\approx 3300\text{ cm}^{-1}$) (Blanco et al., 2006; Cotugno et al., 2005; Grave et al, 1998). Signals can also be observed in the near infrared range: at 5215 cm^{-1} resulting from the combination of asymmetric stretching and bending and in the range $7800\text{ - }6000\text{ cm}^{-1}$ hydroxyl vibrations are also found. The latter band can be deconvoluted into three peaks centered at 7075 , 6820 and 3535 cm^{-1} attributed to free water, self-associated and hydrogen bonded respectively (Musto et al., 2002).

Infrared spectroscopy in both ranges has been used to monitor water uptake and diffusion coefficients have been determined using Fick's law. The band located at 5215 cm^{-1} can be used to quantify water, although it must be normalized for sample thickness. The band at higher wavenumbers is used to determine the kind of interactions between water and network (Mijovic & Zhang, 2003; Cabanelas et al., 2003), but not with quantitative purposes since it is superimposed on the O-H overtone of the resin (Musto et al., 2000). To overcome the thickness variation it is possible to normalize water signal with a reference band invariant against the presence of water (for example, the band at 4623 cm^{-1} , corresponding to aromatic rings of DGEBA). This peak, in principle should not change by the water ingress, only by the volume change due to swelling. In this way, the fractional absorbed water can be calculated as:

$$\frac{\Delta W_t}{W_0} = \frac{\left(\frac{A_{t,5215}}{A_{t,4623}}\right) - \left(\frac{A_{0,5215}}{A_{0,4623}}\right)}{\left(\frac{A_{0,5215}}{A_{0,4623}}\right)}$$

Ingress of water swells the specimens changing its dimensions. The volume changes related with swelling have been characterized measuring a reference band and using the following expression that can be easily derived from Lambert-Beer law (Cabanelas et al. 2003).

$$\frac{\Delta V(t)}{V_0} = \left(\frac{A_0}{A_t}\right)^{\frac{3}{2}} - 1$$

The small volume changes due to swelling are prone to large errors if determined by usual means (for example, with a caliper). Figure 13 shows good correlations between the fractional volume change during water uptake in an epoxy resin as measured gravimetrically, by FTIR or measuring the change on dimensions of the specimens.

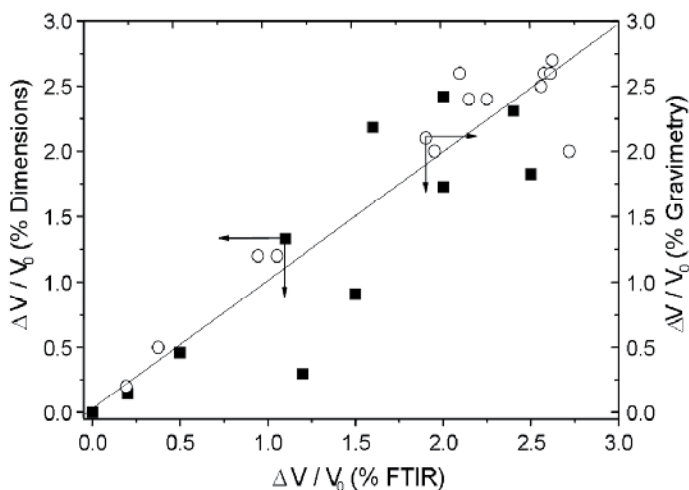


Fig. 13. Comparison of volume change determined by n-FTIR, $(\Delta V/V_0)_{IR}$, and measured with a micrometer, (left) or by gravimetry (right), for fully cured DGEBA/Poly(aminopropylsiloxane) with 0.381 mm thickness.

6. Conclusion

The curing and ageing of epoxy resins are complex phenomena of the prime importance in industry. FTIR appears to be a valuable tool for both qualitative analysis and quantification of these processes. It has been shown how to extract relevant information from spectra to identify typical components of resins and hardeners. Following time variations of specific bands allows extracting relevant kinetic parameters to get more insight about the specific reaction mechanism of curing process. Inspection of subtle changes in baseline can be correlated with both, miscibilization or phase separation processes. Detailed analysis of OH bands allows extracting information about intermolecular interactions within the components of the resin. And, finally, water uptake can be easily quantified and both diffusion coefficients and dimensional changes can be measured with less error than other common methods.

7. Acknowledgment

Authors wish to thank Ministerio de Ciencia e Innovación (Spain) for partial funding under project MAT2010-17091.

8. References

Bhargava, R.; Wang, S.Q.; Koenig, J.L. (1999). Studying polymer-dispersed liquid-crystal formation by FTIR spectroscopy. 2. Phase separation and ordering. *Macromolecules*, Vol.32, No.26, (December 1999), pp.8989-8995, ISSN 0024-9297.

- Barabanova, A.I.; Shevnin, P.L.; Pryakhina, T.A.; Bychko, K.A.; Kazantseva, V.V.; Zavin, B.G.; Vygodskii, Y.S.; Askadskii, A.A.; Philippova, O.E.; Khokhlov, A.R. (2008). Nanocomposites Based on Epoxy Resin and Silicon Dioxide Particles. *Nanocomposites Based on Epoxy Resin and Silicon Dioxide Particles*, Vol. 50, No. 7, (November 2007), pp. 808-819, ISSN 0965-545X.
- Blanco, I.; Cicala, G.; Motta, O.; Recca, A. (2004). Influence of a selected hardener on the phase separation in epoxy/thermoplastic polymer blends. *Journal of Applied Polymer Science*, Vol.94, No. 1, (September 2004), pp. 361-371, ISSN 1097-4628.
- Blanco, I.; Cicala, G.; Costa, M.; Recca, A. (2006). Development of an epoxy system characterized by low water absorption and high thermomechanical performances. *Journal of Applied Polymer Science*, Vol.100, No.6, (June 2006), pp. 4880–4887, ISSN 0021-8995.
- Blanco, M.; Lopez, M.; Fernandez, R.; Martin, L.; Riccardi, C.C.; Mondragon, I. (2009). Thermoplastic-modified epoxy resins cured with different functionalities amine mixtures. Kinetics and miscibility study. *Journal of Thermal Analysis and Calorimetry*, Vol.97, No.3, (June 2009), pp. 969-978, ISSN 1388-6150.
- Bucknall, C.B.; Partridge, I.K. (1986). Phase separation in crosslinked resins containing polymeric modifiers. *Polymer Engineering Science*, Vol.26, No.1, (January 1986), pp. 54-62, ISSN 0032-3888.
- Cabanelas, J.C.; Prolongo, S.G.; Serrano, B.; Bravo, J.; Baselga, J. (2003). Water absorption in polyaminosiloxane-epoxy thermosetting polymers. *Journal of Materials Processing Technology*, Vol.143, No.S1, (2003), pp. 311-315, ISSN 0924-0136.
- Cabanelas, J.C.; Serrano, B.; Baselga, J. (2005). Development of cocontinuous morphologies in initially heterogeneous thermosets blended with poly(methyl methacrylate). *Macromolecules*, Vol.38, No.3, (February 2005), pp. 961-970, ISSN 0024-9297.
- Chen, J.S.; Ober, C.K.; Poliks, M.D. (2002). Characterization of Thermally Reworkable Thermosets: Materials for Environmentally Friendly Processing and Reuse. *Polymer*, Vol.43, No.1, (January 2002), pp. 131-139, ISSN 0032-3861.
- Chike, K.E.; Myrick M.L.; Lyon, R.E.; Angel S.M. (1993). Raman and near infrared studies of an epoxy resin. *Applied Spectroscopy*, Vol.47, No.10, (October 1993), pp. 1631-1635, ISSN 0003-7028.
- Cole, K.C. ; Hecher, J.J.; Noel, D. (1991). A new approach to modeling the cure kinetics of epoxy amine thermosetting resins 2. Application to a typical system based on bis[4-(diglycidylamino)phenyl]methane and bis(2-aminophenyl) sulphone. *Macromolecules*, Vol.24, No.11, (May 1991), pp. 3098-3110, ISSN 0024-9297.
- Cotugno, S.; Mensitieri, G.; Musto, P.; Sanguigno, L. (2005). Molecular interactions in and transport properties of densely cross-linked networks: A time-resolved FT-IR spectroscopy investigation of the epoxy/H₂O system. *Macromolecules*, Vol.38, No.3, (February 2003), pp. 801-811, ISSN 0024-9297.
- Cotugno, S.; Larobina, D.; Mensitieri, G.; Musto, J.; Ragosta, G. (2001). A novel spectroscopic approach to investigate transport processes in polymers: the case of water-epoxy system. *Polymer*, Vol.42, No.15, (July 2001), pp. 6431-6438, ISSN 0032-3861.

- Crivello, J.V.; Fan, M. (1991). Novel platinum-containing initiators for ring-opening polymerizations. *Journal of Polymer Science A: Polyme Chemistry*, Vol.29, No.13, (December 1991), pp. 1853-1863, ISSN 0887-624X.
- Crivello, J.V.; Liu, S. (2000). Photoinitiated cationic polymerization of epoxy alcohol monomers. *Journal of Polymer Science A: Polymer Chemistry*, Vol.38, No.3, (February 2000), pp. 389-401, ISSN 0887-624X.
- Crivello, J.V. (1993). In: *Ring-Opening Polymerization*, DJ Brunelle, pp. 157-159, Ed., Hanser, ISBN 3446162933, Munich.
- Ehlers J.E.; Rondan, N.G.; Huynh, L.K.; Pham, H.; Marks, M.; Truong, T.N. (2007). Theoretical study on mechanisms of the epoxy-amine curing reaction. *Macromolecules*, Vol.40, No.12, (2007), pp.4370-4377, ISSN 0024-9297.
- Dannenberg, H.; Harp, W.R. (1956). Determination of cure and analysis of cured epoxy resins. *Analytical Chemistry*, Vol.28, No.1, (1956), pp.81-90, ISSN 0003-2700.
- Flory, P.J. (1953). *Principles of Polymer Chemistry*, Cornell University Press, ISBN 0801401348, Ithaca.
- George, G.A.; Clarke, P.C.; Jhon, N.S.; Friend, G. (1991). Real time monitoring of the cure reaction of a TGDDM/DDS epoxy resin using fiber optic FT-IR. *Journal of Applied Polymer Science*, Vol.42, No.3, (February 1991), pp. 643-657, ISSN 0021-8995.
- Girard-Reydet, E.; Sautereau, H.; Pascault, J.P. (1999). Use of block copolymers to control the morphologies and properties of thermoplastic/thermoset blends. *Polymer*, Vol.40, No.7, (March 1999), pp.1677-1687, ISSN 0032-3861.
- Gonzalez-Benito, J.; Bravo, J.; Mikes, J.; Baselga, J. (2003). Fluorescence labels to monitor water absorption in epoxy resins. *Polymer*, Vol.44, No.3, (February 2003), pp. 653-659, ISSN 0032-3861.
- Grave, C.; McEwan, I.; Pethrick, R.A. (1998). Influence of stoichiometric ratio on water absorption in epoxy resins. *Journal of Applied Polymer Science*, Vol.69, No.12, (September 1998), pp. 2369-2376, ISSN 0021-8995.
- Hartwig, A.; Schenider, B.; Lühring, A. (2002). Influence of moisture on the photochemically induced polymerisation of epoxy groups in different chemical environment. *Polymer*, Vol.43, No.15, (July 2003), pp. 4243-4250, ISSN 0032-3861 .
- Hartwig, A.; Koschek, K.; Luhring, A.; Schorsch, O. (2003). Cationic polymerization of a cycloaliphatic diepoxide with latent initiators in the presence of structurally different diols. *Polymer*, Vol.44, No.10, (May 2003), pp. 2853-2858, ISSN 0032-3861.
- Horie, K.; Hiura, H.; Sawada, M.; Mitta, I.; Kambe, H. (1970). Calorimetic investigation of polymerization reactions 3: Curing reaction of epoxides with amines. *Journal of Polymer Science Part A-1- Polymer Chemistry*, Vol.8, No.6, (1970), pp. 1357-&, ISSN 0449-296X.
- Inoue, T. (1995). Reaction-induced phase decomposition in polymer blends. *Progress in Polymer Science*, Vol.20, No.1, (1995), pp.119-153, ISSN 0079-6700.
- Ji, W.; Hu, J.; Zhang, J.; Cao, C. (2006). Reducing the water absorption in epoxy coatings by silane monomer incorporation. *Corrosion Science*, Vol.48, No.11, (November 2006), pp. 3731-3739, ISSN 0010-938X.

- Kiefer, J.; Hilborn, J.G.; Hedrick, J.L. (1996). Chemically induced phase separation: A new technique for the synthesis of macroporous epoxy networks. *Polymer*, Vol.37, No.25, (1996), pp. 5715-5725, ISSN 0032-3861.
- Kim, Y.M.; Kostanski, L.K.; Mac Gregor, J.F. (2003). Photopolymerization of 3,4-epoxycyclohexylmethyl-3',4'-epoxycyclohexane carboxylate and tri (ethylene glycol) methyl vinyl ether. *Polymer*, Vol. 44, No.18, (August 2003), pp.5103-5109, ISSN 0032-3861.
- Kradjel, C.; Lee, K.A. (2008). *NIR analysis of polymers, in Handbook of near infrared analysis*, CRC Press, ISBN, Boca Ratón.
- Liu, H.; Uhlherr, A.; Varley, R.J.; Bannister, M.K. (2004). Influence of substituents on the kinetics of epoxy/aromatic diamine resin systems. *Journal of Polymer Science Part A: Polymer Chemistry*, Vol.42, No.13, (July 2004), pp. 3143-3156, ISSN 1099-0518.
- González, M.; Kindelán, M.; Cabanelas, J.C.; Baselga, J. (2003). Modelling auto-acceleration in DGEBA/diamine systems. *Macromolecular Symposia*, Vol.200, (September 2003), pp. 111-119, ISSN 1022-1360.
- Gonzalez, M.; Cabanelas, J.C.; Pozuelo, J.; Baselga, J.(2011). Preparation of cycloaliphatic epoxy hybrids with non-conventional amine-curing agents. *Journal of Thermal Analysis and Calorimetry*, Vol.103, No.2, (February 2011), pp. 717-723, ISSN 1388-6150.
- Marieta, C.; Remiro, G.; Garmendia, G.; Harismendy, I.; Mondragón, I. (2003). AFM approach toward understanding morphologies in toughened thermosetting matrices. *European Polymer Journal*, Vol.39, No.10, (October 2003), pp. 1965-1973, ISSN 0014-3057.
- Mark, H.F. (2004). *Encyclopaedia of polymer science and technology*, Vol. 9, Wiley and Sons, ISBN, New Jersey.
- Matejka, L. (2000). Amine cured epoxide networks: Formation, structure, and properties. *Macromolecules*, Vol.33, No. 10, (May 2000), pp. 3611-3619, ISSN 0024-9297.
- May, C.A. (1988). *Epoxi resins, Chemistry and Technology* (2nd), Marcel Dekker, ISBN 0824776909, New York.
- Mezzenga, R.; Boogh, L.; Manson, J.A.E. (2000). A thermodynamic model for thermoset polymer blends with reactive modifiers. *Journal of Polymer Science Part B: Polymer Physics*, Vol.38, No.14, (July 2000), pp.1893-1902, ISSN 1099-0488.
- Mijovic, J.; Zhang, H. (2003). Local dynamics and molecular origin of polymer network-water interactions as studied by broadband dielectric relaxation spectroscopy, FTIR, and molecular simulations. *Macromolecules*, Vol.36, No.4, (February 2003), pp. 1279-1288, ISSN 0024-9297.
- Mijovic, J.; Andjelic, S. (1995). A study of reaction kinetics by near infrared spectroscopy 1. Comprehensive analysis of a model epoxy/amine. *Macromolecules*, Vol.28, No.8, (April 1995), pp.2787-2796, ISSN 0024-9297.
- Mijovic, J.; Andjelic, S.; Yee, C.F.W.; Bellucci, F.; Nicolais, L. (1995). A study of reaction kinetics by near infrared spectroscopy 2. Comparison with dielectric spectroscopy of model and multifunctional epoxy/amine. *Macromolecules*, Vol.28, No.8, (April 1995), pp. 2797-2806, ISSN 0024-9297.

- Mikes, F.; Baselga, J.; Paz-Abuin, S. (2002). Fluorescence probe-label methodology for in situ monitoring network forming reactions. *European Polymer Journal*, Vol.38, No.12, (December 2002), pp. 2393–2404, ISSN 0014-3057.
- Musto, P.; Mascia, L.; Ragosta, G.; Scarinzi, G.; Villano, P. (2000). The transport of water in a tetrafunctional epoxy resin by near-infrared Fourier transform spectroscopy. *Polymer*, Vol. 41, No.2, (January 2000), pp.565-574, ISSN 0032-3057.
- Musto, P.; Ragosta, G.; Mensitier, G. (2002). Time-resolved FTIR/FTNIR spectroscopy: powerful tools to investigate diffusion processes in polymeric films and membranes. *E-Polymers*, Article N° 017 (April 2002), ISSN 1618-7229.
- Nikolic, G.; Zlatkovic, S.; Cakic, M.; Cakic, S.; Lacnjevac, C; Rajic, Z. (2010). Fast Fourier Transform IR Characterization of Epoxy GY Systems Crosslinked with Aliphatic and Cycloaliphatic EH Polyamine Adducts. *Sensors*, Vol.10, No.1, (January 2010), pp. 684-696, ISSN 1424-8220.
- Nogueira, P.; Ramirez, C.; Torres, A.; Abad, M.J.; Cano, J.; Lopez-bueno, I.; Barral,L. (2001). Effect of water sorption on the structure and mechanical properties of an epoxy resin system. *Journal of Applied Polymer Science*, Vol.80, No.1, (April 2001), pp. 71-80, ISSN 0021-8995.
- Pascault, J.P., Sautereau, H.; Verdu, J.; Williams, R.J.J. (2002). *Thermosetting Polymer*, Marcel Dekker Inc, ISBN 0824706706, New York.
- Paz-Abuin, S.; Lopez-Quintela, A.; Varela, M.; Pellin, M.P.; Prendes, P. (1997). Method for determination of the ratio of rate constants, secondary to primary amine, in epoxy-amine systems. *Polymer*, Vol.38, No.12, (June 1997), pp. 3117-3120, ISSN 0032-3861.
- Paz-Abuin, S.; Pellin, M.P.; Paz-Pazos, M.; Lopez-Quintela, A. (1997). Influence of the reactivity of amine hydrogens and the evaporation of monomers on the cure kinetics of epoxy-amine: kinetic questions. *Polymer*, Vol.38, No.15, (July 1997), pp. 3795-3804, ISSN 0032-3861.
- Paz-Abuín, S.; Lopez-Quintela, A.; Varela, M.; Pellín, M.P.; Prendes, P. (1998). Autoacceleration and inhibition: Free volume. Epoxy-amine kinetics. *Journal of Polymer Science A: Polymer Chemistry*, Vol.36, No.6, (April 1998), pp. 1001-1016, ISSN 0887-624X.
- Poisson, N.; Lachenal, G.; Sautereau, H. (1996). Near- and mid-infrared spectroscopy studies of an epoxy reactive system. *Vibrational Spectroscopy*, Vol.12, No.2, (October 1996), pp.237-247, ISSN 0924-2031.
- Rajagopalan, G.; Gillespie, J.W.; McKnight, S.H. (2000). Diffusion of reacting epoxy and amine monomers in polysulfone: a diffusivity model. *Polymer*, Vol.41, No.21, (October 2000), pp. 7723-7733, ISSN 0032-3861.
- Riccardi, C.C.; Williams, R.J.J. (1986). A kinetic scheme for an amine-epoxy reaction with simultaneous. *Journal of Applied Polymer Science*, Vol.32, No.2, (August 1986), pp. 3445-3456, ISSN 0024-9297.
- Riccardi, C.C.; Addabo, H.E.; Williams, R.J.J. (1984). Curing reaction of epoxy resins with diamines. *Journal of Applied Polymer Science*, Vol.32, No.8, (1984), pp. 2841-2492, ISSN 0021-8995.

- Schechter, L.; Wynstra, J.; Kurkijy, R. (1956). Glycidyl Ether Reactions with Alcohols, Phenols, Carboxylic Acids, and Acid Anhydrides. *Journal of Industrial and Engineering Chemistry*, Vol.48, No.1, (January 1956), pp. 86-93, ISSN 1226-086X.
- Siddhamalli, S.K. (2000). Toughening of epoxy/polycaprolactone composites via reaction induced phase separation. *Polymer Composites*, Vol.21, No.5, (October 2000), pp.846-855, ISSN 0272-8397.
- Simon, S.L.; McKenna, G.B.; Sindt, O. (2000). Modelling the evolution of the dynamic mechanical properties of a commercial epoxy during cure after gelation. *Journal of Applied Polymer Science*, Vol.76, No.4, (April 200), pp. 495-508, ISSN 0021-8995.
- Smith, I.T. (1961). The mechanism of the crosslinking of epoxide resins by amines. *Polymer*, Vol.2, No.1, (1961), pp. 95-108, ISSN 0032-3861.
- Socrates, G. (1994). *Infrared Characteristic Group Frequencies*, Wiley & Sons, ISBN 0471942308, Chischester, England
- Soucek, M.D.; Abu-Shanab, O.L.; Anderson, C.D.; Wu, S. (1998). Kinetic Modeling of the Crosslinking Reaction of Cycloaliphatic Epoxides with Carboxyl Functionalized Acrylic Resins: Hammett Treatment of Cycloaliphatic Epoxides. *Macromolecular Chemistry and Physics*, Vol.199, No.6, (December 1998), pp. 1035-1042, ISSN 1022-1352.
- Tao Z, Yang S, Chen J, Fan L. (2007). Synthesis and characterization of imide ring and siloxane-containing cycloaliphatic epoxy resins. *European Polymer Journal*, Vol.43, No.4, (January 2007), pp. 1470-1479, ISSN 0014-3057.
- Varley, R.J.; Liu, W.; Simon, G.P. (2006). Investigation of the reaction mechanism of different epoxy resins using a phosphorus-based hardener. *Journal of Applied Polymer Science*, Vol.99, No.6 (March 2006), pp. 3288-3299, ISSN 0021-8995.
- Vyazovkin, S.; Sbirrazuoli, N. (1996). Mechanism and kinetics of epoxy-amine cure studied by differential scanning calorimetry. *Macromolecules*, Vol.29, No.6, (March 1996), pp. 1867-1873, ISSN 0024-9297.
- Wang, F.; Neckers, D.C. (2001). Photopolymerization of Epoxides with Platinum(II) Bis(acetylacetonato)/Silane Catalysts. *Macromolecules*, Vol.34, No.18, (August 2001), pp. 6202-6205, ISSN 0024-9297.
- Wang, Z.; Xie, M.; Zhao, Y.; Yu, Y.; Fang, S. (2003). Synthesis and properties of novel liquid ester-free reworkable cycloaliphatic diepoxides for electronic packaging application. *Polymer*, Vol.44, No.4, (January 2003), pp.923-929, ISSN 0032-3861.
- Weyer, L. and Lo, S.-C. (2002). *Spectra-Structure Correlations in the Near-infrared*, In *Handbook of Vibrational Spectroscopy*, Vol. 3, Wiley and Sons, ISBN 0471988472, UK, pp. 1817-1837.
- Xiao, G.Z.; Shanahan, M.E.R. (1998). Swelling of DGEBA/DDA epoxy resin during hygrothermal ageing. *Polymer*, Vol.39, No.14, (June 1998), pp. 3253-3260, ISSN 0032-3861.
- Xu, L.S.; Schlup, J.R. (1998). Etherification versus amine addition during epoxy resin amine cure: An in situ study using near-infrared spectroscopy. *Journal of Applied Polymer Science*, Vol.67, No.5, (January 1998), pp. 895-90, ISSN 0021-8995.
- Xu, L.; Fu, J.H.; Schlup, J.R. (1996). In situ near-infrared spectroscopic investigation of the kinetics and mechanisms of reactions between phenyl glycidyl ether (PGE) and

- multifunctional aromatic amines. *Industrial and Engineering Chemistry Research*, Vol.35, No. 3, (March 1996), pp. 963-972, ISSN 0888-5885.
- Yagci, Y.; Reetz, I. (1998). Externally stimulated initiator systems for cationic polymerization. *Progress in Polymer Science*, Vol.23, No.8, (December 1998), pp. 1485-1538, ISSN 0079-6700.
- Zhou, J.; Lucas, J.P. (1999). Hygrothermal effects of epoxy resin. Part I: the nature of water in epoxy. *Polymer*, Vol.40, No.20, (June 1999), pp. 5505-5512, ISSN 0032-3861.

Use of FTIR Analysis to Control the Self-Healing Functionality of Epoxy Resins

Liberata Guadagno^{1,2,*} and Marialuigia Raimondo¹

¹*Dipartimento di Ingegneria Industriale,
Università di Salerno, Fisciano (SA)*

²*Nano-Mates – Research Centre for NANOMaterials and nanoTEchnology,
Università di Salerno, Fisciano (SA)
Italy*

1. Introduction

In recent years polymer composites are increasingly used to replace the traditional metal alloys in structural applications, ranging from civil infrastructure to high performance vehicles such as racing cars and military aircraft. This popularity is due to their lower weight, as well as to a continuous improvement of their performance aided in recent years by nanotechnology. However, limited storage stability and reliability are critical for polymer composites designed for structural applications [1-4]. In fact, in service, they are subject to damage due to microcracks that are produced in the structure under the action of various kinds of stresses, for example: a) mechanical vibrations or various types of mechanical stresses, b) sudden temperature changes, c) irradiation by electromagnetic radiation causing direct or indirect rupture of chemical bonds (UV light, γ rays, etc.), d) intentional or inadvertent contact with chemical substances that adversely affect the structure, e) various factors which in combination can contribute to compromising the integrity of the structure. Internal damage is difficult to detect and, once developed, even more difficult to repair. This critical point is a real problem in the field of aeronautic vehicles. In fact, for large components, such as parts of primary structures, several non-destructive damage detection techniques have been developed including ultrasonic, infrared thermography, x-ray tomography, and computerized vibro-thermography. This technology has helped to detect damage but repair of this damage has been limited to reinforced patch bonding and/or bolting. Actually, durability and reliability are still problematic in the field of these structural materials; in fact, in order to achieve the mechanical strength required for many structural applications, highly cross-linked polymeric materials are necessary. The trade off for this gain in mechanical strength is that the resulting materials tend to be brittle and are therefore more prone to developing cracks through normal usage, ultimately failing.

In addition to conventional methods for damage detection, and common repair methods, there has recently been the development of self-healing composites which are expected to significantly extend the life of polymeric components by autonomically healing micro-cracks

* Corresponding Author

whenever and wherever they develop [5-15]. For structural applications, self-healing systems are of great interest because they would allow to overcome not only some difficulties connected to damage diagnosis, but also the following appropriate interventions to restore the material functionality. Airlines for example see polymeric composites' potential to cut fuel costs and save on maintenance very attractive, therefore, are willing to entertain the idea to put into action self-healing composites in the development of different materials for aeronautical applications. The challenge facing materials scientists is to assure these systems must be able to stem fatigue damage and preserve their integrity, increase their life span, reduce maintenance costs and provide safety during use. A lot of strategies were formulated up to now in the development of self-healing materials [5,16-27].

One of the strategies to manufacture a thermosetting self-repair material seems to be the storage of healing agents inside composites that restore the strength of the materials after damage.

The first demonstration of self-healing in an engineered material, an epoxy matrix, occurred in 2001 [5] by a team from the University of Illinois (USA). This self-healing system for thermosetting materials is very interesting also in terms of design. The concept was based on the introduction of a microencapsulated healing agent and suspended catalyst phase in a polymer matrix. Since that time, advancement has been made in the field following this conceptual approach, while at the same time alternative concepts have emerged in the scientific literature. Microencapsulation and thermally reversible networks [28] are the two main strategies used for the development of self-healing thermosetting materials. Microencapsulation is the first and most studied self-healing concept. The initial self-healing epoxy system developed by White et al. involves the incorporation of a microencapsulated healing agent, dicyclopentadiene (DCPD) and a dispersed solid catalyst, bis(tricyclohexylphosphine) benzyldiene ruthenium (IV) dichloride (called Grubbs' catalyst) in an epoxy-amine network. In these systems, an approaching crack ruptures embedded microcapsules releasing a polymerizer agent into the crack plane through capillary action. Polymerization of the healing agent is triggered by contact with the embedded catalyst, bonding the crack faces. In these systems the efficiency of self-repair function, in terms of trigger, speed and yield, is related to ring-opening metathesis polymerization of the healing agent by appropriate catalysts. The healing agent is a microencapsulated liquid monomer that must include a long shelf life, prompt deliverability, high reactivity, and low volume shrinkage upon polymerization [29]. The monomer most often used as the healing agent for the manufacture of these first ingenious systems is dicyclopentadiene (DCPD) [5,29]. Very recently, however, blends of DCPD/5-ethylidene-2-norbornene (DCPD/ENB) or DCPD/ 5-norbornene-2-carboxylic acid have also been proposed [30]. Thermosetting auto-repair polymers, which have been proposed so far, include Grubbs' first-generation catalyst (G1); [5,17,29-30] and currently, the possibility of applying other ruthenium catalysts for ring-opening metathesis polymerization-based self-healing applications is being evaluated. This system is a challenge for epoxy structural composites: however, some drawbacks have to be re-evaluated in order to be fully applied to advanced applications. These mainly regard the thermal stability of the Grubbs' catalyst inside the epoxy resin during the curing cycle and the impossibility to utilize primary amines as hardeners, since they can poison the catalyst.

This last drawback forces the use of compounds which have not been fully explored in literature as hardener agents, especially with regard to the cure behavior and mechanical

properties of the manufactured materials. Since 2003, a large number of parameters were investigated by the team from the University of Illinois and other research groups. In a recent paper, the dissolution properties, initial polymerization kinetics, chemical stabilities, and thermal stabilities were analyzed for three catalysts: Grubbs' first (G1) and second generation (G2) catalysts and Hoveyda-Grubbs' second generation catalyst (HG2) [30]. Ruthenium-based catalysts are reported as exhibiting great functional group tolerance, as well as greatly enhanced air and water stability [30,31]. However, thermolytic decomposition can limit the usefulness of these ruthenium systems in self-healing composites based on epoxy resins [32-33]. This is a crucial aspect for self-healing systems in aeronautic applications because, even if linked to the cost reduction from a process aspect, resins have been developed with low temperature manufacturing (under 100 °C), yet the problem of the material treatment at high temperature is not resolved.

In fact, we generally need a glass transition temperature after wet aging of 110 °C minimum, and a curing temperature equal to or less than 100 °C is not enough. To achieve this goal it is necessary to make a post cure with a temperature that could be as high as 180 °C. For this reason, we have carried out our investigation in the temperature range of 150-180 °C. It is worth noting that there are critical issues in the use of epoxy precursors in conjunction with Grubbs metathesis catalysts, because in self healing composites based on epoxy resins, ruthenium systems give rise to a reaction with the oxirane rings of the epoxy precursors, and, therefore, the metathesis catalyst was not subsequently able to promote the polymerization of the reactive monomer, thus losing the self-healing ability. Such phenomena could strongly limit the use in the practice, in self-healing composite materials, of Grubbs' catalysts. In particular, in this chapter, we show that selecting the appropriate curing cycle as well as the specific chemical formulation, the catalyst remains intact in the formed epoxy matrix during the curing process, and is thus capable of subsequently performing its catalytic activity of the polymerization of the reactive monomer consisting in the cyclic olefin (5-ethylidene-2-norbornene -ENB-), when the latter comes out of a microcapsule affected by a crack. Studies on the choice of an appropriate curing cycle for a different self-healing formulation have already been reported in previous papers [32-35]. Another drawback to overcome in the employment of the ROMP catalysts is related to the local availability of the catalyst particles. In particular, the catalyst for the metathesis reaction is embedded in the precursors of the epoxy matrix in the form of solid particles, i.e. powders with different morphology and crystallographic modifications [30]. In practice, the effective concentration of the catalyst depends on the availability of the aforesaid particles at the level of the fracture and on the rate of dissolution of the catalyst in the reactive monomer (healing agent) within the polymer matrix. Even with high concentrations of catalyst particles exposed at the level of the fracture, the effective concentration of the catalyst could be relatively low because of limited rates of dissolution of the catalyst. The rate of dissolution of the catalyst depends not only on the chemical nature of the various components, but also on morphological and structural characteristics of the catalyst particles. It has been found in practice that the presence of the catalyst in the form of crystalline powders has some critical aspects relating to the uniform availability of the catalyst in all the zones in which a micro-crack can potentially develop, compromising the effectiveness of the self-healing process [35].

Figure 1 illustrates as, independently from the catalyst amount, large crystals of catalyst particles can cause loss of catalytic activity in many zones. In addition, a very effective self-

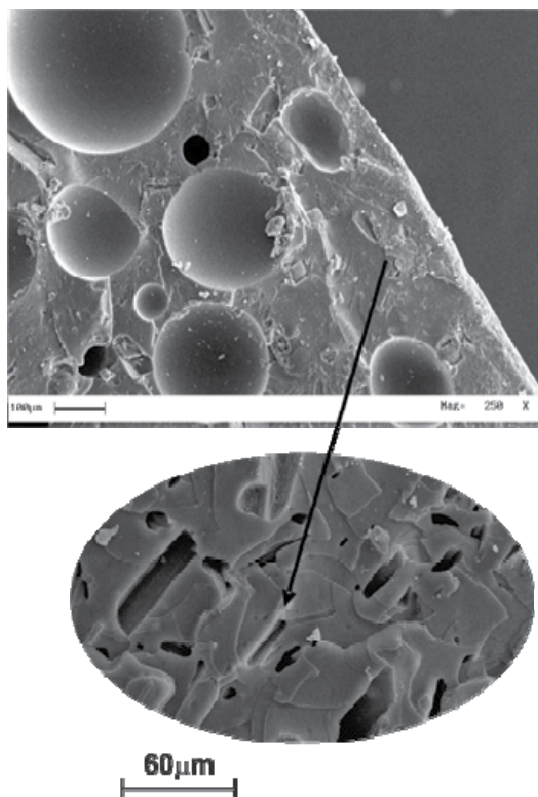


Fig. 1. SEM micrograph of the section surface of the self-healing epoxy specimen in which we can observe the empty geometrical places left by the catalyst in the epoxy matrix (see arrow)

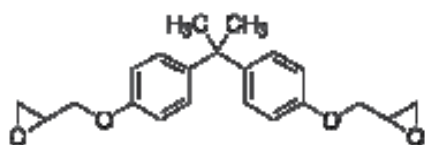
healing system also needs the study and control of the capsule dimensions that act as reserve of healing agent.

Another aim of this chapter is therefore to study a process for the development of a self-healing composite, which does not have the drawbacks mentioned above with respect to the catalyst morphology. This purpose is achieved by a process for the manufacture of a self-healing composite material comprising a preliminary step of dispersing at molecular level the catalyst in an epoxy mixture containing healing agent in nanometric vessels. This solution allows to obtain the catalyst dispersed at molecular level and also able to react with nano-encapsulated healing agent.

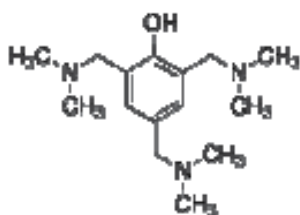
2. Materials

The epoxy matrix composite was prepared by mixing an epoxy (Bisphenol A diglycidyl ether - Acronym BADGE) with a reactive diluent (1,4-Butanediol-diglycidyl ether- Acronym BDDGE) which was used in small percentage to reduce the viscosity of the material, to improve handling and ease of processing and to optimize consequently performance properties. These resins, both containing an epoxy, were obtained by Sigma-Aldrich. The curing agent investigated for this study is an anionic initiator Phenol, 2,4,6-

tris[(dimethylamino) methyl] (Trade name Ancamine K54). This hardener agent was already used for self-healing formulations [5]. The catalyst, Hoveyda-Grubbs' first generation (Dichloro(o-isopropoxyphenyl)methylene)(tricyclo-hexylphosphine)ruthenium(II) (catalyst HG1) also obtained from Aldrich was used to manufacture the epoxy matrix. It was dispersed at molecular level into the epoxy matrix. The healing agents used in this work were dicyclopentadiene (DCPD), which was obtained from Acros Organics, and 5-ethylidene-2-norbornene (ENB), which was obtained from Sigma-Aldrich. Figure 2 shows the chemical structures of compounds used in this work.



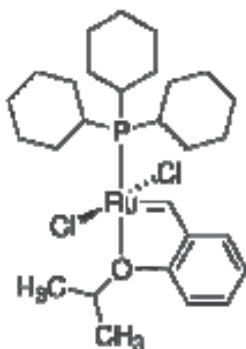
BADGE



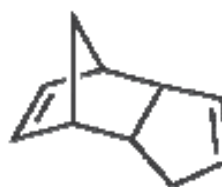
ANKAMINE K 54



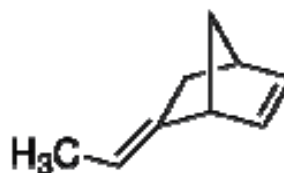
BDDGE



HG1 CATALYST



DCPD



ENB

Fig. 2. Chemical structures of compounds used for the self-healing system.

2.1 Epoxy specimen manufacture

2.1.1 Epoxy matrix

Sample EBA was obtained by mixing BADGE with BDDGE diluent at a concentration of 90%: 10% (by wt) epoxide to diluent. Ancamine K54 was added at a concentration of 10:100 (by wt) hardener to mixture (BADGE and BDDGE).

2.1.2 Self-healing epoxy system

Self-healing epoxy system was obtained by dispersing ENB/DCPD(5%)-filled nanocapsules at a concentration of 20 wt% into the epoxy matrix.

Healing efficiency was also measured by carefully controlled fracture experiments for both the virgin and the healed materials using a well established protocol [5].

2.1.3 Microcapsule manufacture

The microcapsules, with the outer shell composed of poly(urea-formaldehyde) and the inner shell of ethylene maleic anhydride copolymer (EMA) were prepared by *in situ* polymerization in an oil-in-water emulsion in accord with a procedure already described in previous papers [5, 33]. The only change, with respect to the aforementioned synthesis procedure, consisted of using as healing agent a blend of 5ethylidene-2norbornene (95 wt%) and DCPD (5 wt%). According to such a procedure, a desired dimension range can be selected by a suitable variation of the process parameters during the synthesis stage, and/or with the use of molecular sieves. The capsules used to manufacture the self-healing system are shown in Fig. 3. The analysis of the capsule size distribution (obtained from a series of 20

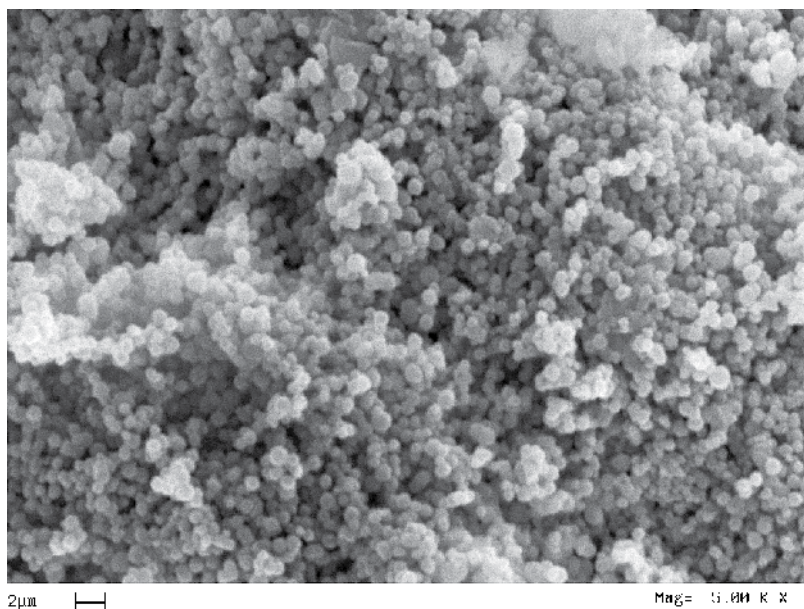


Fig. 3. Scanning electron microscope image of micro and nanocapsules at magnification 5.00 K x

samples) show that the largest part are characterized by a spherical form with average diameter of about 500-600 nm.

The efficiency of the microencapsulation process for the above described formulation was not evaluated because for this new formulation other experiments on the self-healing efficiency were carried out. This analysis does not require a hard-working procedure if we use the infrared spectroscopy; by way of example, hereafter, in the section "Methodologies" we report a procedure to analyze the efficiency of the microencapsulation process for microcapsules only filled with DCPD.

3. Methodologies

3.1 Efficiency of the microencapsulation process

FTIR analysis can be performed to control the success of the microencapsulation process. For this investigation, all the microcapsule fractions were powdered in a mortar; a first small fraction was dried under vacuum and analyzed by FT/IR spectroscopy (red spectrum) (see Figure 4), while another fraction was directly treated with Grubbs' catalyst powder and again analyzed by FT/IR (brown spectrum). Mixing and powdered the fraction of

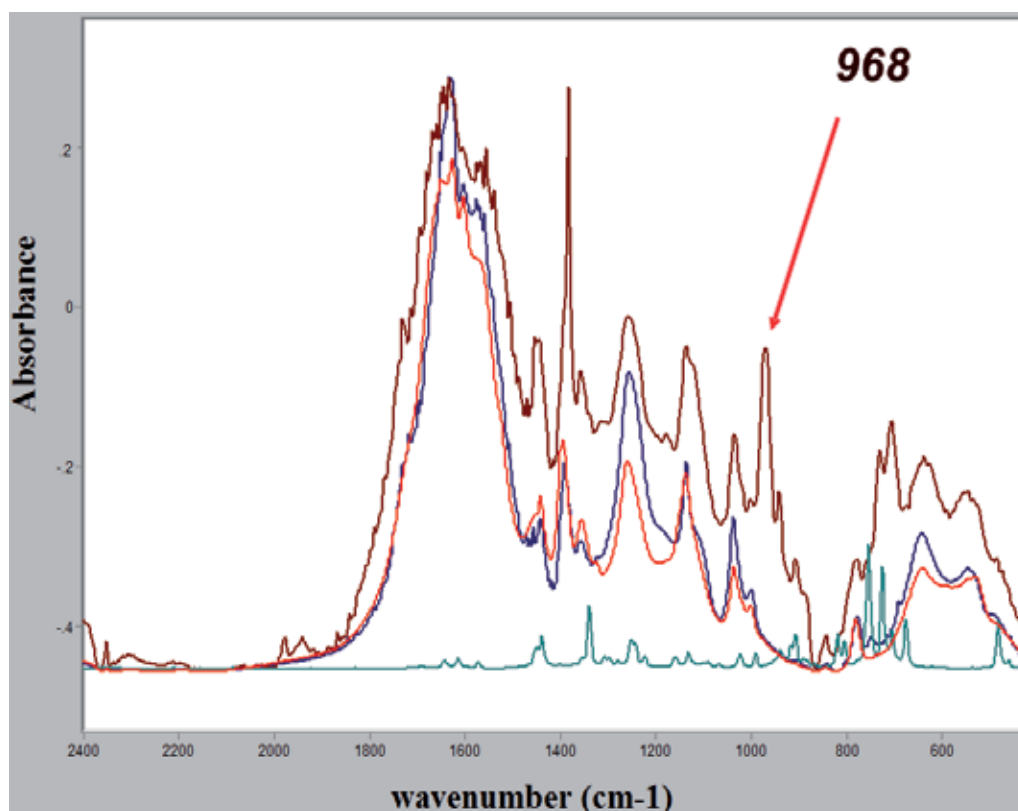


Fig. 4. FTIR spectra of microcapsules (blue spectrum), DCPD (green spectrum), of the microcapsules fraction dried under vacuum (red spectrum) and microcapsules fraction treated with Grubbs' catalyst powder (brown spectrum).

microcapsules (containing DCPD) with the Grubbs catalyst instantaneously initiates ROMP at room temperature. ROMP polymers can display a very rich microstructure. Depending on the monomer, different characteristics can be observed, among these cis/trans isomerism, tacticity, etc.. Cis/trans isomerism is present in all ROMP polymers and relatively easy to quantify using spectroscopic techniques. In fact, in the brown spectrum we can observe the strong and sharp signal at 968 cm^{-1} due to the carbon hydrogen bending vibration of a trans carbon double bond. This signal was already assigned to the absorption of trans poly(DCPD) fractions^{5,36}. Using this procedure ROMP of DCPD primarily produces trans double bonds as observed for the ROMP of DCPD by Grubbs first generation catalyst. In figure 4 FT/IR spectra of DCPD and microcapsules, as obtained from the synthesis, were also reported for comparison. In particular, in the analyzed spectral range, a comparison between red and brown spectra shows many common signals due to poly(urea-formaldehyde) of the microcapsule wall. We can observe, in fact, some of the vibrational mode for the CH_2 group ($\delta_s\text{CH}_2$ at 1465 cm^{-1} - in-plane bending or scissoring; ωCH_2 and τCH_2 between $1350\text{-}1150\text{ cm}^{-1}$ - out-of-plane bending or wagging and/or twisting; ρCH_2 at 720 cm^{-1} - in-plane bending or rocking) and the carbonyl frequency ($\text{C}=\text{O}$) of the wall tertiary amides. This absorption occurs in the spectral range of $1680\text{ - }1630\text{ cm}^{-1}$ as expected (the $\text{C}=\text{O}$ absorption of amides occurs at lower frequencies than “normal” carbonyl absorption due to the resonance effect. The resonance effect increases the $\text{C}=\text{O}$ bond length and reduces the frequency of absorption³⁷).

The highlighted peak at 968 cm^{-1} characteristic of ring-opened poly(DCPD) is present only in the brown spectrum. It clearly evidences that the embedded DCPD is active in the metathesis reaction. As shown by the FT/IR analysis reported in figure 4, the amount of DCPD encapsulated is a sufficient quantity to activate the ROMP reaction [32 – see Supp. Inf.].

3.2 Evaluation of the catalytic activity

In the development of our self-healing epoxy resins, the evaluation of the catalytic activity was investigated for the epoxy matrix (formulation without nanocapsules).

The procedure adopted for preparing this mixture is as follows. The epoxy precursor (BADGE) was mixed mechanically with the reactive diluent (BDDGE) at a temperature of 90°C , maintained with an oil bath, and then the catalyst HG1 in the form of crystalline powder was added. The catalyst was dispersed at molecular level by mechanical agitation of the mixture maintained at 90°C for 90 minutes. To verify complete dispersion and dissolution of the catalyst, and that its catalytic activity remained unchanged, spectroscopic investigation was carried out. For this purpose, four drops of the mixture were deposited on a slide for light microscopy. Complete transparency, which is achieved when the catalyst is completely dissolved, can be verified by light microscopy with observation in transmission. Two drops of ENB were added to the aforesaid drops of mixtures. A thin solid film of metathesis product, whose FT/IR spectrum is shown in Fig. 5, formed immediately.

This spectrum shows a peak at 966 cm^{-1} , which is an indication of the formation of the metathesis product and hence of the fact that the activity of the catalyst has not been compromised by the chemical nature of the oligomers, by the temperature and by the treatments of mechanical mixing.

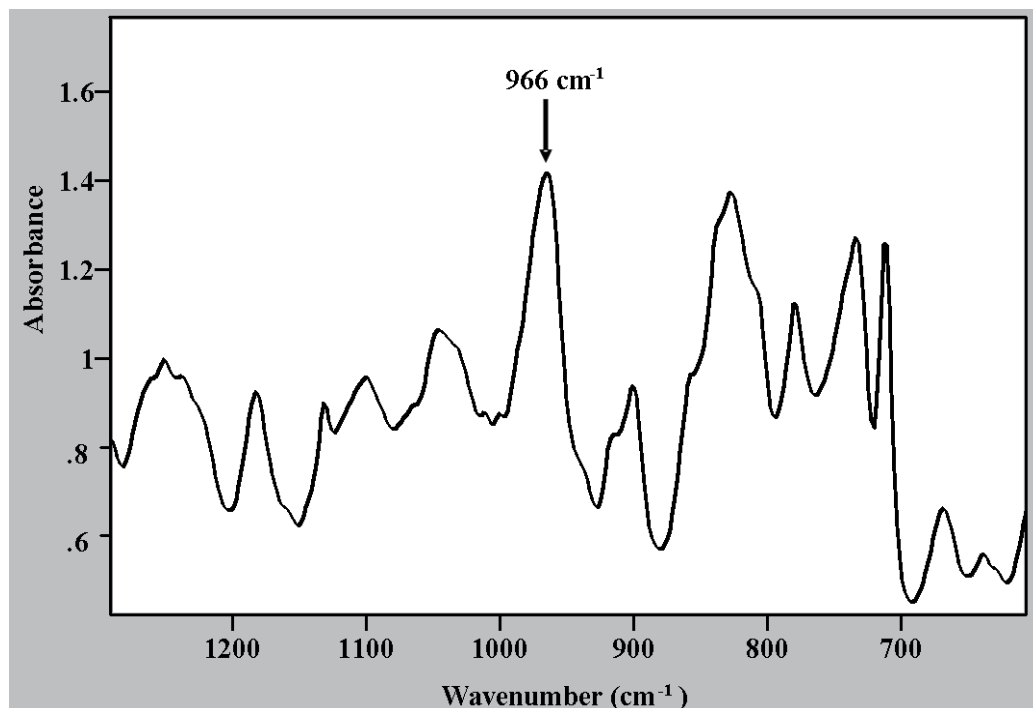


Fig. 5. FT/IR spectrum of the solid film (metathesis product)

The transparent mixture containing the completely dissolved catalyst was then taken out of the oil bath and left to cool 50°C, and then the curing agent was added to it. The mixture thus obtained was cured in a two-stage process. The first stage was carried out at a temperature of 80°C for 3 hours, while the second stage was carried out according to three variants, i.e. at the three different temperatures of 125, 150 and 170°C.

Figs. 6a, 6b, 6c and 6d show FT/IR spectra of the cured material respectively after the intermediate stages, and the second stage carried out with the three variants stated above, to which ENB was then added in the same way as was done after the preliminary step of dissolution of the catalyst.

We can observe that, in conjunction with different signals of the epoxy precursors (among which the C-O-C stretch at 1247 cm⁻¹ and the symmetric stretch at 1039 cm⁻¹) all the spectra show the band at 966 cm⁻¹.

The presence in all cases of the peak at 966 cm⁻¹, indicating formation of the metathesis product, proves that the catalytic activity of the HG1 catalyst within the epoxy matrix remained unchanged after the described treatments. It can be seen, in particular, from the FT/IR spectra that, after the treatment at 110°C, the mixture can be cured up to 170°C for 2 hours without compromising the catalytic activity. This high temperature increases the cross-linking degree, as we can deduce observing the signal at 916 cm⁻¹ in the spectra of figs. 6a-6d. The very small intensity of the signal at 916 cm⁻¹ in the spectrum of fig. 6a and the further progressive decrease up to the disappearance in the spectrum of fig. 6d indicates that almost the epoxy rings have reacted for a treatment up to 110 °C (the signals at 916 cm⁻¹

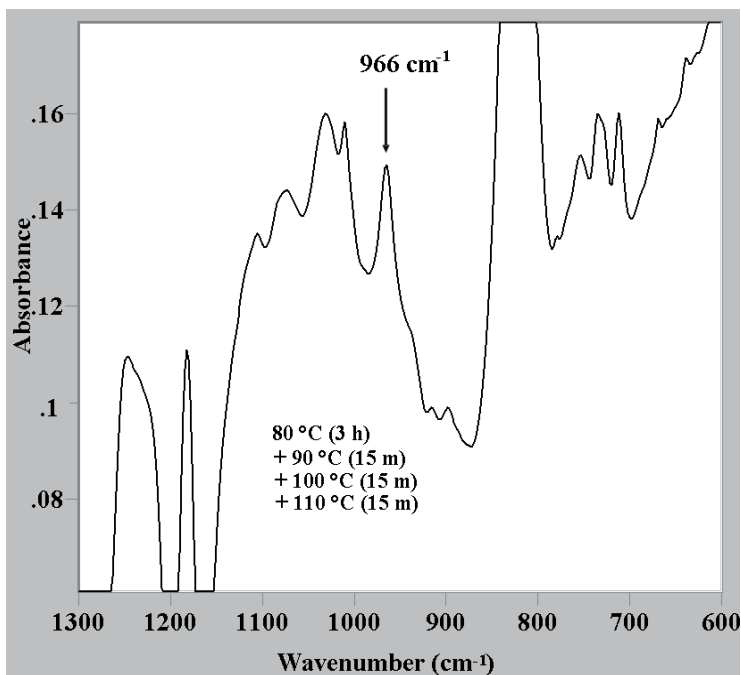


Fig. 6a. FT/IR spectrum of the solid film (metathesis product) in the material cured up to 110 °C.

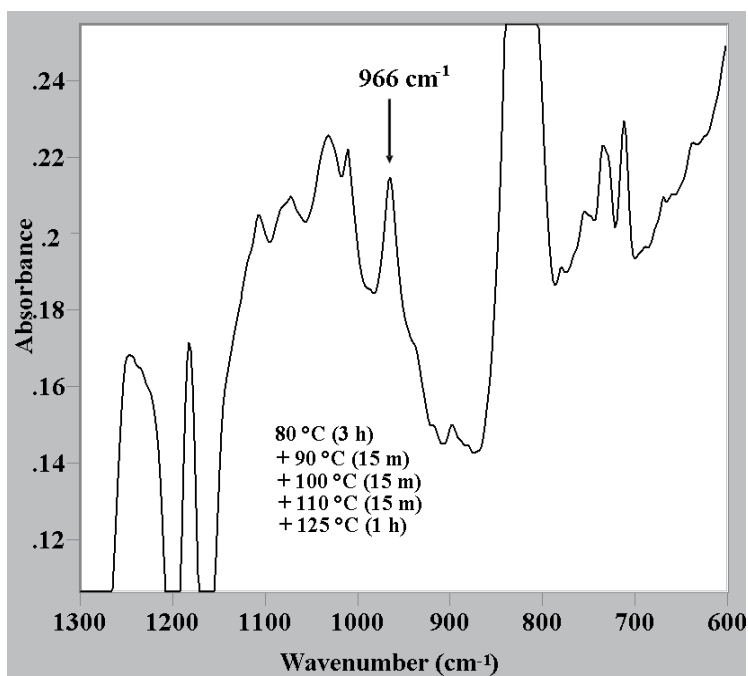


Fig. 6b. FT/IR spectrum of the solid film (metathesis product) in the material cured up to 125 °C

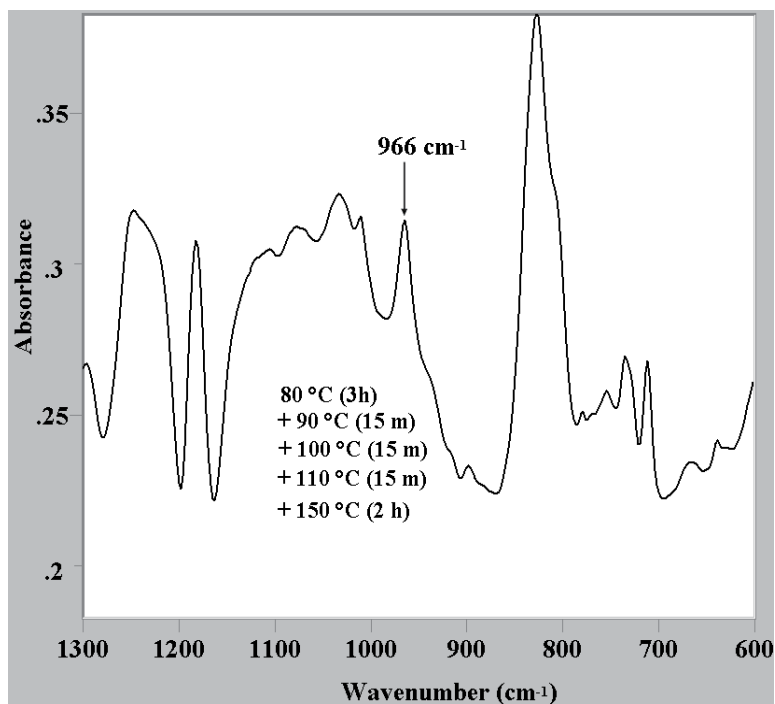


Fig. 6c. FT/IR spectrum of the solid film (metathesis product) in the material cured up to 150 °C

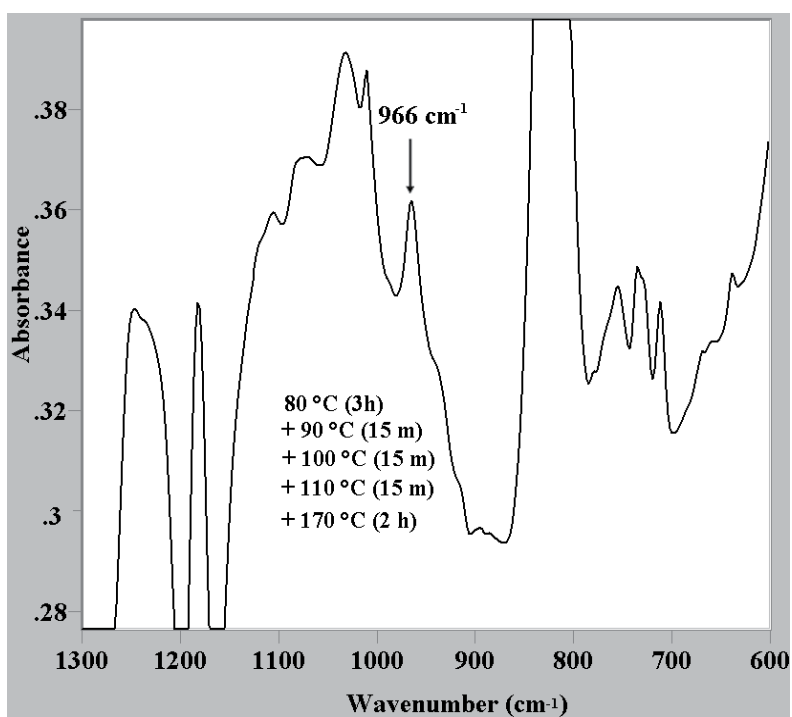


Fig. 6d. FT/IR spectrum of the solid film (metathesis product) in the material cured up to 170 °C

is characteristic of the epoxy groups and assigned to asymmetrical ring stretching in which the C-C bond is stretching during contraction of the C-O bond ³⁷).

Self-healing epoxy system was obtained by dispersing ENB/DCPD(5% wt%)-filled nanocapsules at a concentration of 20 wt% into the epoxy matrix using for the curing process the same procedure above described for the epoxy matrix. Use of a mixture of ENB with low concentrations of DCPD as healing agent was used because It can greatly increase the degree of crosslinking of the metathesis product especially at extremely low temperatures. For example, by carrying out the ring opening metathesis reaction of an ENB/DCPD mixture (at 5% of DCPD) in the molar ratio 1:1000 (Hoveyda-Grubbs 1 catalyst/monomer) at a temperature of -53°C, the degree of crosslinking is found to be 57% (with a degree of conversion of 84%) after a reaction time of 7 hours. In similar conditions, the degree of crosslinking of ENB on its own is 10% with a degree of conversion of 100% [35].

A simplified scheme of the self-healing formulation is shown in Figure 7.

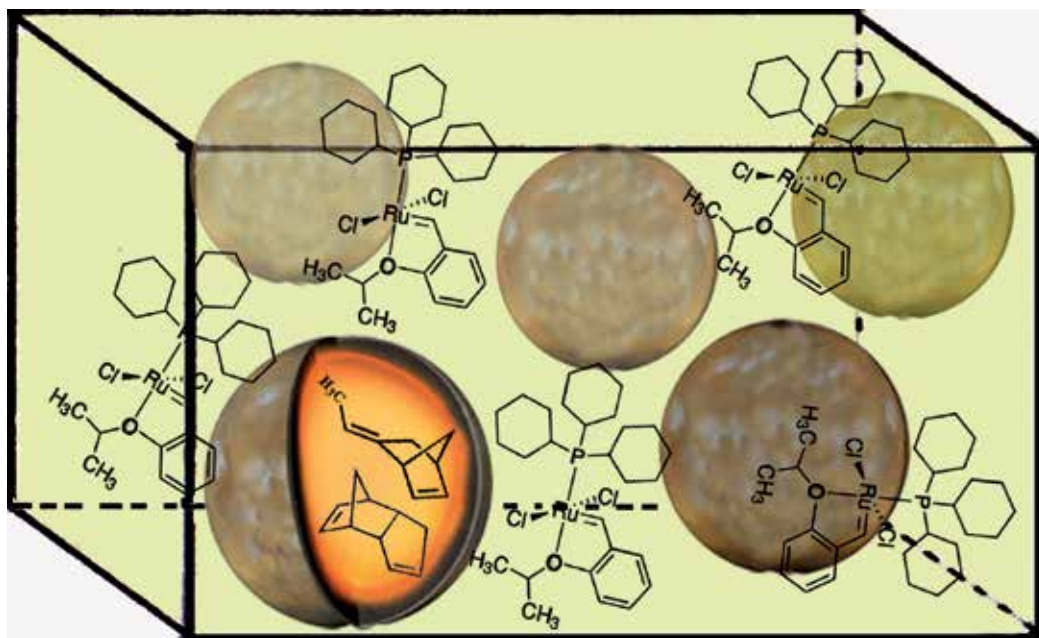


Fig. 7. Scheme of self-healing formulation which includes: a) capsules containing a polymerizer agent (DCPD and ENB); b) a catalyst for the polymerizer (HG1).

3.3 Healing efficiency of the self-healing sample

Crack healing efficiency, η , (defined as the ability to recover fracture toughness) was evaluated for the sample cured up to 170 °C using a tapered double-cantilever beam (TDCB) [23,38] geometry. The healing efficiency η , calculated as the ratio of critical fracture loads for the healed and virgin samples, is obtained from data shown in Figure 8 where we report the Load-Displacement curves for a sample with 5% of Hoveyda-Grubbs I Catalyst and 20% of microcapsules (ENB+DCPD) filled, cured up to 170 °C. The healing efficiency is 72 %.

Fig. 9 shows the sample geometry for getting quantitative results on the self-healing functionality. The figure also reports the morphology of an healed sample after a controlled damage.

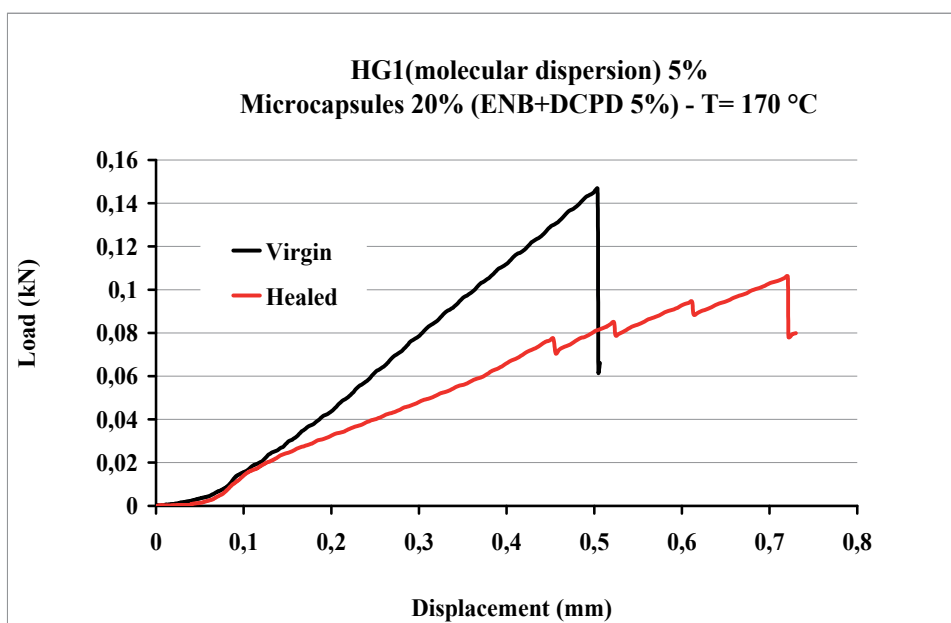


Fig. 8. Load-Displacement curves for Virgin (black curve) and Healed (red curve) sample.

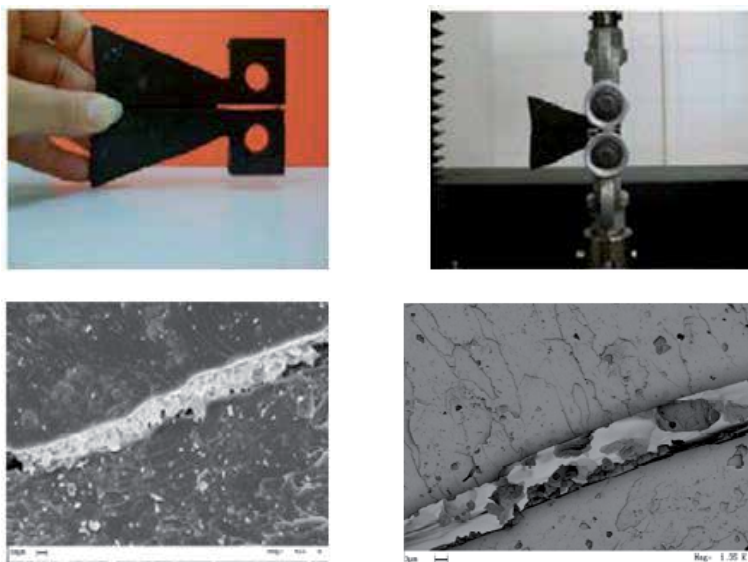


Fig. 9. Samples for getting quantitative results on the self-healing functionality (the first two images on the top); SEM images of healed crack faces closed by means of the metathesis product inside a crack after a (TDCB) test (images on the bottom).

4. Conclusions

We have formulated, prepared and characterized a multifunctional autonomically healing composite with a self-healing efficiency higher than 70 %. Carrying out the curing process in several stages at increasing temperature makes it possible to avoid deactivation of the catalyst. In fact, choosing a relatively low temperature in the first stage means that only the curing agent, and not the catalyst, reacts with the oxirane rings of the epoxy precursor. Therefore, the catalyst remains intact in the epoxy matrix that has formed and is thus able subsequently to perform its catalytic action of polymerization of the reactive monomer, when the latter is released from the vessel and interacts with the epoxy matrix containing the catalyst. Infrared Spectroscopy proves to be a useful way to identify metathesis product directly inside the epoxy resin during the curing reactions of epoxy formulations containing catalyst powder dispersed at molecular level.

5. References

- [1] Riefsnider, K. L.; Schulte, K.; Duke, J. C.; Long term failure behavior of composite materials. ASTM Special Technical Publications. 1983; 813, 136-159.
- [2] Osswald, T.; Menges, G. Mater. Sci. Polym. Eng. Munich: Hanser Publishers, 2003; 447-519.
- [3] Chamis, C.C.; Sullivan, T. L. In situ ply strength: an initial assessment. Cleveland, OH, NASA Lewis Research Center. 1987, 19.
- [4] Wilson, D. J. K.; Wells, J. N.; Hay, D.; Owens, G. A.; Johnson, F. 18th International SAMPE Technical Conference, Washington, USA, 1986; 18, 242-253.

- [5] White, S. R.; Sottos, N. R.; Geubelle, P. H.; Moore, J. S., Kessler, M. R., Sriram, S. R.; Brown, E. N.; Viswanathan, S. *Nature* 2001, 409, 794-797.
- [6] Wu, D. Y.; Meure, S.; Solomon, D. *Prog Polym Sci* 2008, 33, 479-522.
- [7] Jud, K.; Kausch, H. H.; Williams, J. G. *J Mater Sci* 1981, 16, 204-210.
- [8] Dry, C.; Mcmillan, W. *Smart Mater Struct* 1997, 6, 35-39.
- [9] Kessler, M. R.; White, S. R.; *Composites Part A*, 2001, 32, 683-699.
- [10] Kessler, M. R.; Sottos, N. R., White, S. R., *Composites Part A*, 2003, 34, 743-753.
- [11] Cho, S. H., Andersson, H.M.; White, S. R., Sottos, N. R., Braun, P. V. *Adv Mater* 2006, 18, 997-1000.
- [12] Pang, J. W. C.; Bond, I. P. *Composites Part A*, 2004, 36, 183-188.
- [13] Pang, J. W. C.; Jody, W. C.; Bond, I. P. *Comp Sci Tech* 2005, 65, 1791-1799.
- [14] Keller, M. W.; White, S. R.; Sottos, N. R. *Adv Funct Mater* 2007, 17, 2399-2404.
- [15] Toohey, K. S.; Hansen, C. J.; Lewis, J. A.; White, S. R.; Sottos, N. R. *Adv Funct Mater* 2009, 19, 1399-1405.
- [16] Dry, C.; Corsaw, M.; Bayer, E. A comparison of internal self-repair with resin injection in repair of concrete. *J Adh Sci Tech* 2003;17(1):79-89.
- [17] Van der Zwaag, S. editor. *Self Healing Materials: An Alternative Approach to 20 Centuries of Materials Science (Springer Series in Materials)* 2007.
- [18] Dry, C. *Int Patent WO/2007/005657* 2007.
- [19] Dry, C. *Comp Struct* 1996;35(3):263-269.
- [20] Dry, C.; Sottos, N. NASA ADS: Passive smart self-repair in polymer matrix composite materials. In: *Proc. SPIE Vol. 1916, p. 438-444, Smart Structures and Materials 1993: Smart Materials*, Vijay K. Varadan; Ed.
- [21] Dry, C.; Mcmillan, W. *Smart Mater Struct* 1997;6(1):35.
- [22] Motuku, M.; Vaidya, U.K.; Janowski, G.M. *Smart Mater Struct* 1999; 8(5):623.
- [23] Brown, E.N.; Sottos, N.R.; White, S.R. *Exp Mech* 2002;42(4):372-379.
- [24] Brown, E.N.; Kessler, M.R.; Sottos, N.R.; White, S.R. *J. Microencapsulation* 2003;20(6):719-730.
- [25] Brown, E.N.; White, S.R.; Sottos, N.R. *J Mater Sci* 2004;39(5):1703-1710.
- [26] Jones, A.S.; Rule, J.D.; Moore, J.S.; White, S.R.; Sottos, N.R. *Chem Mater* 2006;18:1312-1317.
- [27] Syret, J.A.; Becer, C.R.; Haddleton, D.M. *Polym. Chem.*, 2010,1, 978-987.
- [28] Zhang, Y.; Broekhuis, A. A.; Picchioni, F. *Macromolecules* 42, 1906-1912 (2009).
- [29] Toohey, K.S.; Sottos, N.R.; Lewis, J.A.; Moore, J.S.; White, S.R. Self-healing materials with microvascular networks. *Nature Mater* 2007;6:581-5.
- [30] Wilson, G.O.; Caruso, M.M.; Reimer, N.T.; White, S.R.; Sottos, N.R.; Moore, J.S. Evaluation of ruthenium catalysts for ring-opening metathesis polymerization-based selfhealing applications. *Chem Mater* 2008;20(10):3288-97 [supporting information].
- [31] Grubbs, R.H. editor. *Handbook of metathesis*. Weinheim (Germany): Wiley- VCH; 2003.
- [32] Guadagno, L.; Longo, P.; Raimondo, M.; Naddeo, C.; Mariconda, A.; Vittoria, V.; Iannuzzo, G.; Russo, S.; *Composites Part: B* 42, 296-301(2011).
- [33] Guadagno, L.; Longo, P.; Raimondo, M.; Naddeo, C.; Mariconda, A.; Sorrentino, A.; Vittoria, V.; Iannuzzo, G.; Russo, S. *Journal of Polymer Science Part B: Polymer Physics*, 48, 2413-2423 (2010).

- [34] Guadagno, L.; Longo, P.; Raimondo, M.; Mariconda, A.; Naddeo, C.; Sorrentino, A.; Vittoria, V.; Iannuzzo, G.; Russo, S.; Calvi, E. Publication number: US 2010168280 (A1) Publication date: Jul. 1, 2010.
- [35] Guadagno, L.; Raimondo, M.; Naddeo, C.; Mariconda, A.; Corvino, R.; Longo, P.; Vittoria, V.; Russo, S.; Iannuzzo, G. Publication number: US 2011118385 (A1) Publication date: May. 19, 2011.
- [36] Dall'Asta, G.; Motroni, R.; Manetti, R.; Tosi, C.; *Makromol Chem* 1969, 130, 153-165.
- [37] *Spectrometric Identification Of Organic Compounds*, 6th Ed by Robert M. Silverstein, Francis X. Webster, John Wiley & Sons, Inc.
- [38] Mostovoy, S.; Croseley, P.B.; Ripling, E.J. *J. Mater.* 2, 661-681 (1967).

Infrared Analysis of Electrostatic Layer-By-Layer Polymer Membranes Having Characteristics of Heavy Metal Ion Desalination

Weimin Zhou, Huitan Fu and Takaomi Kobayashi*
*Department of Materials Science and Technology,
Nagaoka University of Technology, Kamitomioka, Nagaoka
Japan*

1. Introduction

Layer-by-layer (LbL) self-assembly is a spontaneous and reversible organization process of interacting organic and polymeric components by their aggregation into ordered structures on substrate. LbL self-assembly process which occurs due to sequential adsorption of materials with complementary functional groups. Producing robust films and allow a precise control over the film thickness and its properties. This technique has been widely applied for the fabrication of multilayer films of organic and polymeric compounds, organic-inorganic hybrid structures, larger objects such as latex particles, and even purely inorganic thin films. By combining various functional materials for the formation of self-assembly multilayer, the LbL technique has led to a wide range of novel materials for various applications.^[1,2]

It has been noticed that the LbL fabrication is usually guided by a driving force of hydrophobic interaction,^[3] hydrogen-bond,^[4] covalent bonding^[5] and electrostatic interaction^[6] between assembled compounds. Among those driving forces, electrostatic interaction between oppositely charged molecules becomes a very fascinating and attractive approach because of its simplicity and efficiency. The technique of alternate layer-by-layer assembly of cationic and anionic polyelectrolytes, generally referred to electrostatic self-assembly (ESA) as a firstly reported by Decher et al in 1991.^[7] They took advantage of the charge-charge interaction between oppositely charged layers to create electrolyte multilayer. The polyelectrolyte conformation and layer interpenetration were due to an idealization of the surface charge reversal with each adsorption step which was based on the electrostatically driven multilayer build-up depicted.

ESA technique provided effective surface modification for thin film and separation membrane.^[8, 9] Because the substrate surface contained negatively or positively charged due to the alternate deposition of polycation or polyanion, the transmission of charged particles like ions through self-assembly polyelectrolyte multilayer membrane might be affected by the charged surface. It was also showed that the presence of fixed charges at the surface of the multilayer resulted in Donnan exclusion of multivalent ions as well as the preferential transport of small

* Corresponding Author

monovalent ions.^[8] Selective ion transport behaviour through ESA composite multilayer films was studied by Take^[8] and Schelenoff.^[9] The results suggested that highly specific ion separation was achieved and was affected by the charge and size of ion that pass through the composite multilayer. These researches made the polyelectrolytes multilayers interesting for the application of water desalination like heavy metal ion removal.

Generally, in LbL systems, infrared analysis method is more important method in studying chemical structures ^[10, 11] of the membranes, because the membranes were usually formed with the hydrogen bond, ion interactions and others which were difficultly investigated using other fundamental analysis methods such as ¹H NMR, XRD (X-ray diffraction) and XPS (X-ray photoelectron spectroscopy). In such infrared (IR) analysis, for example, Arrondo et al. used the infrared (IR) spectroscopy to the study of membrane proteins because the assignment of IR protein bands in H₂O and in D₂O, one of the more difficult points in protein IR spectroscopy.^[12] Similarly, reflection-infrared spectroscopy is a powerful technique for characterizing protein and peptide-membrane interactions.^[13] Mauntele et. al., used the IR to analyze lipid-protein interaction. In his case, lipid protein interactions play a key role in the stability and function of various membrane proteins. The FT-IR technique was used for a label free analysis of the global secondary structural changes and local changes in the tyrosine microenvironment.^[14]

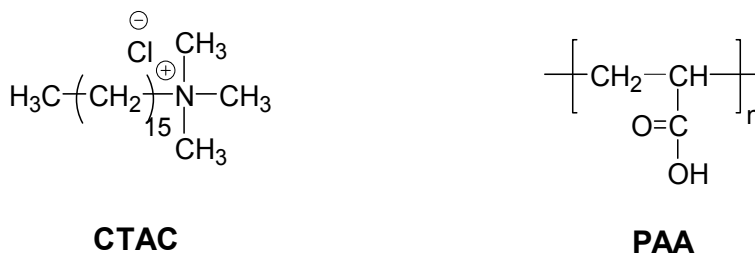
Furthermore, the FT-IR analytical technique was applied in analysis of surface of membranes interacted with other materials. For instance, Luo et. al., fabricated the SPES/Nano-TiO₂ composite ultrafiltration membrane. In their studies, the TiO₂ nanoparticle self-assembly on the SPES membrane surface was confirmed by X-ray photoelectron spectroscopy (XPS) and FT-IR spectrometer. When the nano-TiO₂ was self-assembled on the SPES membrane the absorption peak at 1243 cm⁻¹ attributes to the stretching vibration of the ether C-O-C bond in the SPES polymer shifted to 1239 cm⁻¹. The result of FT-IR spectrometer effectively verified the self-assembly process of nano-TiO₂ on the SPES membrane.^[15]

In study of ionic exchange membrane, FT-IR method was usually used to analyze the chemical structures of formed membrane. Fang et. al., prepared novel anion exchange membranes based on the copolymer of methyl methacrylate, vinylbenzyl chloride and ethyl acrylate. The structure of membrane was mainly verified by measurement of FT-IR. This study remarkably showed the importance of FT-IR method in analysis of chemical structure of membranes.^[16]

Ding et al., confirmed the thermal treatment of precursor composite poly(amic acid) tertiary amine salts (PAAS) membrane using FT-IR/ATR analysis at 150 °C, and obtained composite polyimide hollow fiber membranes. In their studies, the FT-IR spectroscopy effectively evaluated the imidization of the coating layer.^[17]

These reports indicated that importance of IR spectroscopy in analysis of chemical structures of membranes and interactions of membranes with other materials. Accordingly, IR analysis could provide to verify the chemical structure of ESA membranes.

In this chapter, we introduce the ESA modified membranes by forming electrostatic alternate layers of cetyl trimethyl ammonium chloride (CTAC) and poly(acrylic acid) (PAA) onto charged copolyacrylonitrile membranes (Scheme 1). Along with surface characterization of the ESA multilayer, infrared analysis was carried out. Finally, we evaluated the adsorptive properties of ESA multilayer for Fe³⁺ and Fe²⁺, and ESA membranes with chitosan microspheres / PAA for removing of Cu²⁺.



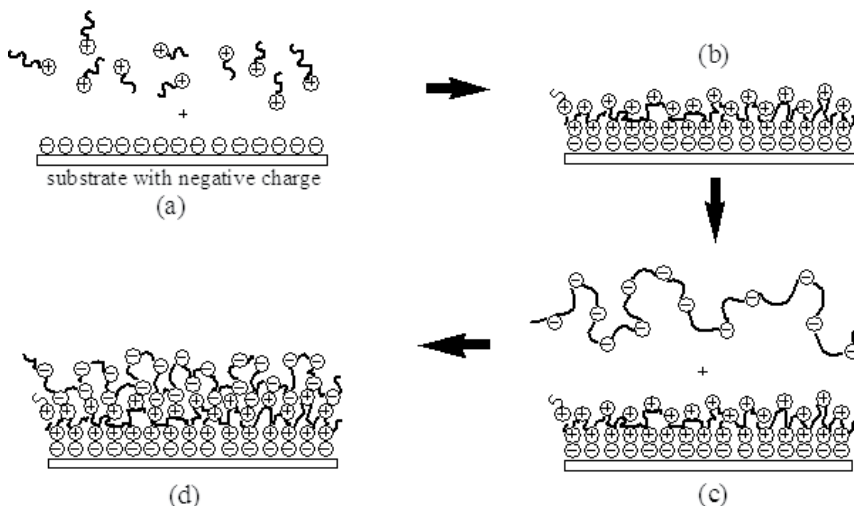
Scheme 1. Chemical structures of CTAC and PAA.

2. Multilayer composite surfaces prepared by an electrostatic self-assembly of quaternary ammonium salt or tetramethyl ammonium chloride and polyacrylic acid onto poly (acrylonitrile-co-acrylic acid) membrane

Preparation of composite multilayer on base membrane surface

Aqueous solutions with 1g / L concentration of CTAC, tetramethyl ammonium chloride (TMAC) and PAA were prepared respectively and used as dipping solutions for the surface modification of base P(AN-co-AA) membrane. As shown in Scheme 2-1, the preparation procedure consisted of the following four steps:

- a. Immersing the base membrane into the CTAC or TMAC solution.
- b. Washing away the loosely adsorbed cations by pure water.
- c. Immersing into the PAA solution.
- d. Washing out the excessive PAA anion adsorbed on membrane surface by pure water.



Scheme 2-1. Preparation procedure of ESA multi-layer on polymer membrane having negative charge.

By alternately immersing the base P(AN-co-AA) membrane into anion and cation solution as indicated by the four steps, ESA multiple layers of CTAC or TMAC and PAA could be formed on the negatively charged base membrane surface.

Confirmation of composite multilayer

The surface nature of resultant membranes modified with CTAC/PAA and TMAC/PAA ESA multiple layers would change alternately due to the alternate deposition of CTAC or TMAC and PAA layer on the surface. In order to estimate the formation of CTAC (or TMAC) and PAA layers on P(AN-co-AA) base membrane, the increment of membrane weight due to the repeated construction of composite layer on membrane surface was measured. Herein, we listed the weight value for each deposited layer of CTAC, TMAC and PAA. Here, the value of [DL] (Deposited Layer)(mmol / g) was calculated from $[DL] = \Delta m / Fw$, where Δm was the corresponding weight increment of membrane induced by each deposition step and Fw were 319.5 g / mol, 109.5 g / mol and 72 g / mol for CTAC, TMAC and PAA, respectively. The obtained average value of [DL] was about 1.4 mmol / g for P(AN-co-AA)/CTAC/PAA system and 1.6 mmol / g for P(AN-co-AA)/TMAC/PAA system.

FT-IR spectroscopy was applied to investigate the chemical component of resultant membranes as to confirm the formation of alternate layers of anion and cation. Figure 2-1 shows IR spectra of base P(AN-co-AA) and P(AN-co-AA) membranes for LbL of the CTAC/PAA composite multilayer on the surface. Spectrum (0) was for P(AN-co-AA), (1) for P(AN-co-AA) with CTAC monolayer, (2) for P(AN-co-AA)/CTAC/PAA, (3) for P(AN-co-AA)/CTAC/PAA/CTAC and (4) for P(AN-co-AA)/CTAC/PAA/CTAC/PAA. In the spectrum (0), there was a wide and strong absorption peak appeared near 3500-2800 cm^{-1} , which was assigned to the dimmer formed by hydrogen bonds of carboxylic acids of the AA segments in the P(AN-co-AA). Also, the characteristic absorption peak assigned to

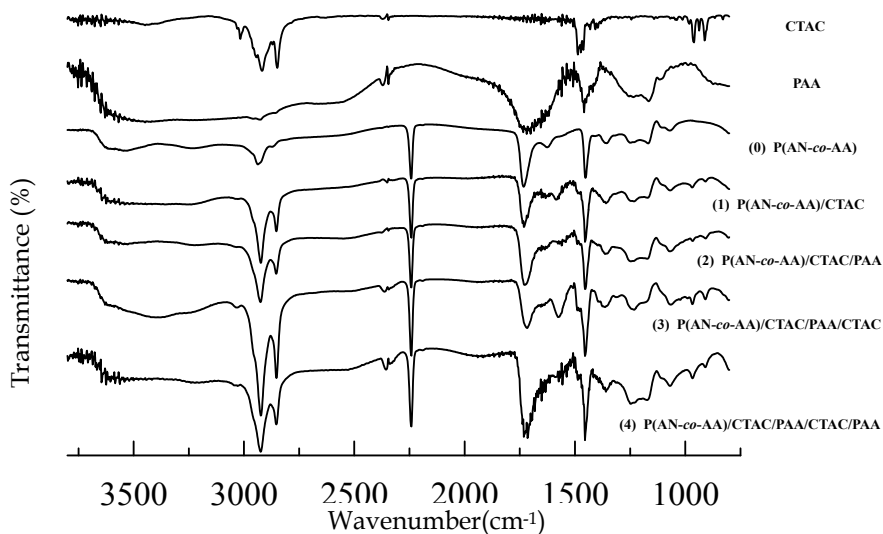


Fig. 2-1. Comparison of FT-IR spectra of the base P(AN-co-AA) and multi-layer composites of CTAC/PAA on the base P(AN-co-AA). The layer number of each spectrum was represented as 0, 1, 2, 3 and 4 for P(AN-co-AA), P(AN-co-AA)/CTAC, P(AN-co-AA)/CTAC/PAA, P(AN-co-AA)/CTAC/PAA/CTAC and P(AN-co-AA)/CTAC/PAA/CTAC/PAA, respectively.

dissociated carboxylic group at about 1645 cm^{-1} and 1720 cm^{-1} existed in the spectrum. In the spectrum (1), it was noticed that the absorption peak around $3500\text{--}2800\text{ cm}^{-1}$ became weaker, indicating that the dimmer band formed by hydrogen bonds was reduced due to the deposition of CTAC over membrane surface. Opposite to the increase of the C-H absorption strength at about 1454 cm^{-1} , the C=O absorption strength at about 1737 cm^{-1} was somewhat lower than that of $\text{C}\equiv\text{N}$ band strength at 2300 cm^{-1} . From the obvious change of the membrane spectra after the deposition of CTAC layer, it was reasonable to say that the change of the chemical structure of LbL suggested the presence of part of carboxylic groups dissociated to react with CTAC by electrostatic attraction.

Compared to the amphiphilic CTAC, TMAC behaved similar cationic property except for long alkyl chain on the quaternary ammonium site. The FT-IR spectra of the base P(AN-co-AA), P(AN-co-AA) with TMAC monolayer and with TMAC/PAA composite multilayer are shown in Figure 2-2. Apparently, the dimmer band in the range from $3500\text{--}2800\text{ cm}^{-1}$ changed alternately after the formation of TMAC layer on the P(AN-co-AA) base membrane surface and then the PAA layer over the P(AN-co-AA)/TMAC. Also, the ratio of $\text{C}=\text{O}$ group at about 1720 cm^{-1} to that of the dissociated carboxylic group at about 1645 cm^{-1}

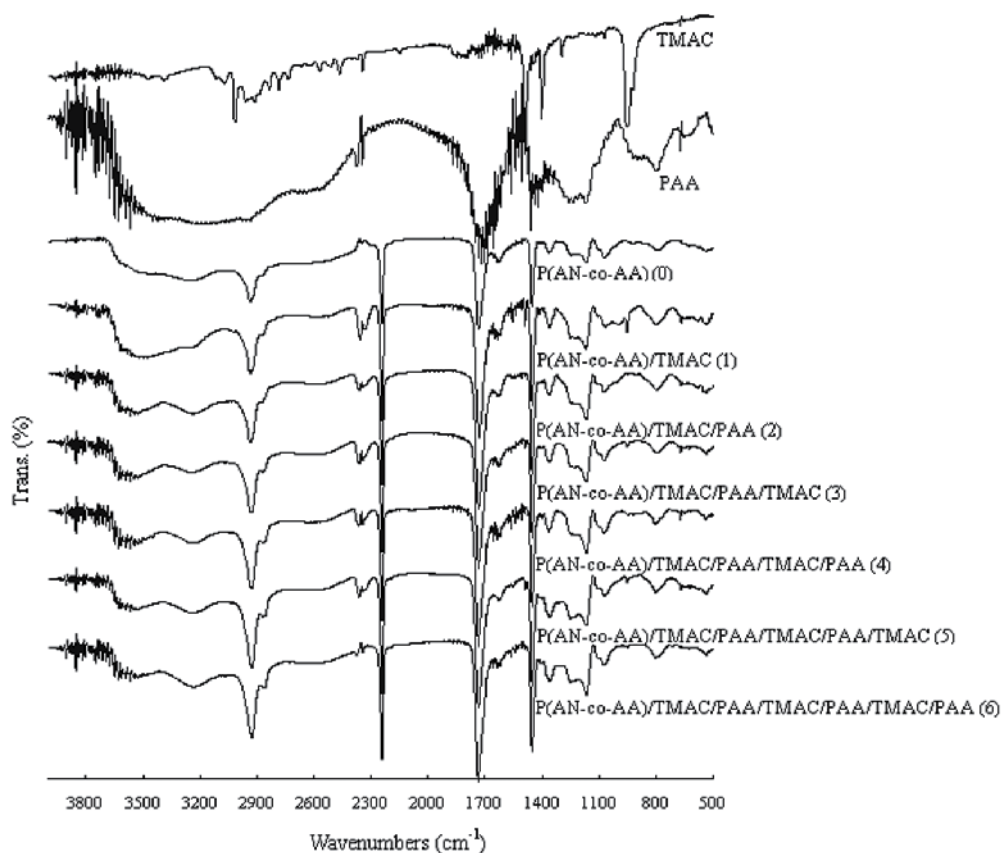


Fig. 2-2. Comparison of FT-IR spectra of the base P(AN-co-AA), P(AN-co-AA)/TMAC/PAA multi-layer composites, the layer numbers.

increased as the TMAC and PAA were deposited. The reason for this phenomena was same with the P(AN-co-AA)/CTAC/PAA system as induced by the fact that the deposition of TMAC layer over PAA layer enhanced the dissociation of carboxylic group which neutralized with TMAC molecules. FT-IR data also showed that the C-H absorption peak around 2920 cm^{-1} increased slightly as the number of TMAC layer increased. Moreover, characteristic absorption peak from TMAC at around 950 cm^{-1} appeared in the spectra of the resultant P(AN-co-AA) membrane with TMAC/PAA composites multilayer on the surface. Moreover, it was noticed that the strength of C-H absorption peak at 1454 cm^{-1} increased with the increase of composite layers on membrane surface, even through the changes were smaller as compared with P(AN-co-AA)/CTAC/PAA. All these changes confirmed the alternate construction of TMAC and PAA layers on base membrane surface which was induced by the electrostatic interaction between two neighboring layers.

Due to the electrostatic interaction between CTAC (or TMAC) and AA segments in the P(AN-co-AA) base membrane as well as between neighboring CTAC (or TMAC) and PAA layers, the composite multilayer of CTAC/PAA and TMAC/PAA successfully self-assembled. To reveal the alternate formation of self-assembly CTAC/PAA and TMAC/PAA multilayer qualitatively, the strength ratio of $>\text{C}=\text{O}$ band at about 1737 cm^{-1} to 1654 cm^{-1} as shown in Figure 2-3 was calculated from FT-IR spectra. It was observed that the bond intensity of $>\text{C}=\text{O}$ group decreased after the deposition of CTAC (or TMAC) layer as part of carboxylic groups of AA segment electrostatically associated with CTAC (or TMAC) the CTAC (or TMAC) layer, and then increased as the PAA layer was formed to be the top layer for the composite multilayer. This alternate change tendency revealed the dissociation extent change of carboxylic acid groups in base membrane or in each PAA layer and strongly confirmed the sequent adsorption of CTAC (or TMAC) and PAA layer on the negatively charged P(AN-co-AA) base membrane surface.

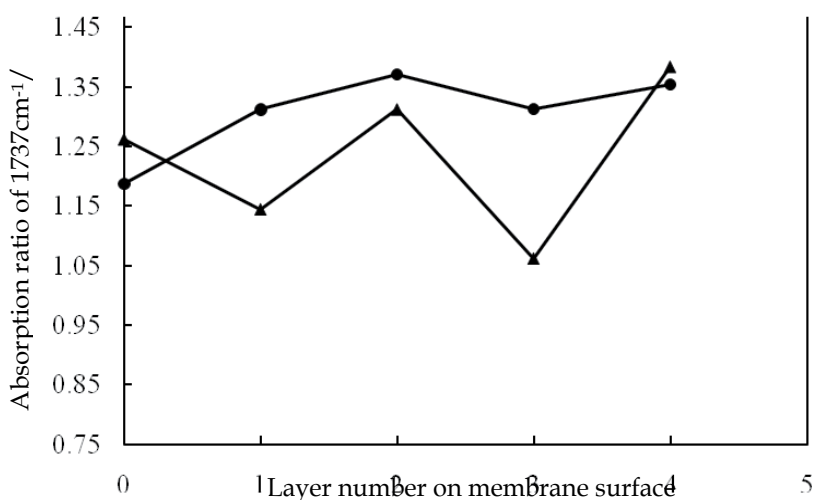


Fig. 2-3. Absorption ratio of observed IR bands for 1737 cm^{-1} , 1645 cm^{-1} C=O assigned to carboxylic acid and to the dissociated carboxylic acid in IR spectra obtained in P(AN-co-AA)/CTAC/PAA (▲) and P(AN-co-AA)/TMAC/PAA (●) multilayer composites. The layer numbers were the same with those described in Figure 2-2.

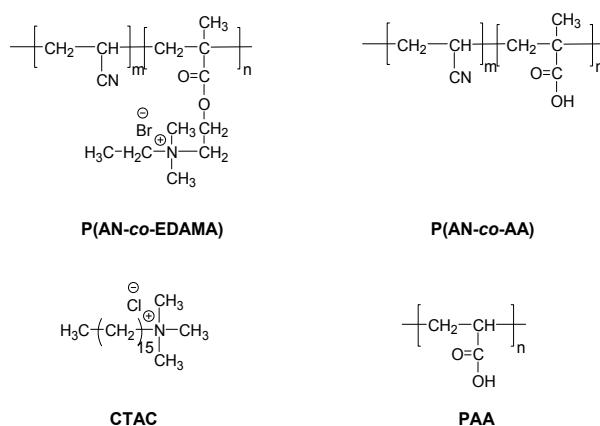
3. Preparation of multilayer composite surfaces prepared by electrostatic self-assembled technique for desalination of Fe³⁺, and Fe²⁺

Multilayer desalination membranes

As presented in scheme 3-1, quaternized *N,N*-dimethylethyl ammonium bromide (EDAMA) was polymerized with AN for preparation of cationic base membrane. After that, AA and the quaternized EDAMA were used for their functional groups in order to provide charged sites for polyacrylonitrile base membranes. Also, Poly(acrylonitrile-*co*-acrylic acid) [P(AN-*co*-AA)] membrane was used as a negatively charged base, while Poly(acrylonitrile-*co*-*N,N*-dimethylethyl ammonium bromide P(AN-*co*-EDAMA) was used as a positively charged substrate.^[18, 19]

Their base membranes of P(AN-*co*-AA) and P(AN-*co*-EDAMA) were prepared by phase-inversion of their respective dimethyl sulfoxide solutions in water.^[20] The base membranes of P(AN-*co*-AA) or P(AN-*co*-EDAMA) were orderly dipped in positive CTAC and negative PAA aqueous solutions. After each deposition step, the resulting membranes were rinsed thoroughly with water. Such deposition process was repeated to obtain desired number of self-assembled layers. In this research, P(AN-*co*-AA) or P(AN-*co*-EDAMA) membranes with ESA layers are referred to as P(AN-*co*-AA)/CTAC/PAA system or as P(AN-*co*-EDAMA)/PAA/CTAC system, respectively.

Before measuring the properties of membranes with ESA multilayer, sample membranes were dehydrated using freeze-drying method in order to preserve the sample structure for the following characterization of the membrane properties.



Scheme 3-1. Chemical structures of membrane materials P(AN-*co*-AA) and P(AA-*co*-EDAMA) and electrolytes of CTAC and PAA.

The metal-ion permselective properties were examined as follows: metal ion solutions containing Fe(NO₃)₃ and FeCl₂ with 2 ppm concentration were prepared, respectively. Before and after the formation of ESA layers, filtration measurement of the metal ion solution through sample membranes was carried out by using an ultrafiltration cell (Amicon 8010, 50 ml volume). The metal-ion rejection (R) was defined by the following equation:

$$R = (1 - c_t / c_0) \times 100\% \tag{3-1}$$

were C_o is the ionic concentration in the feed solution and C_i is the ionic concentration in the permeate solution after a time t .

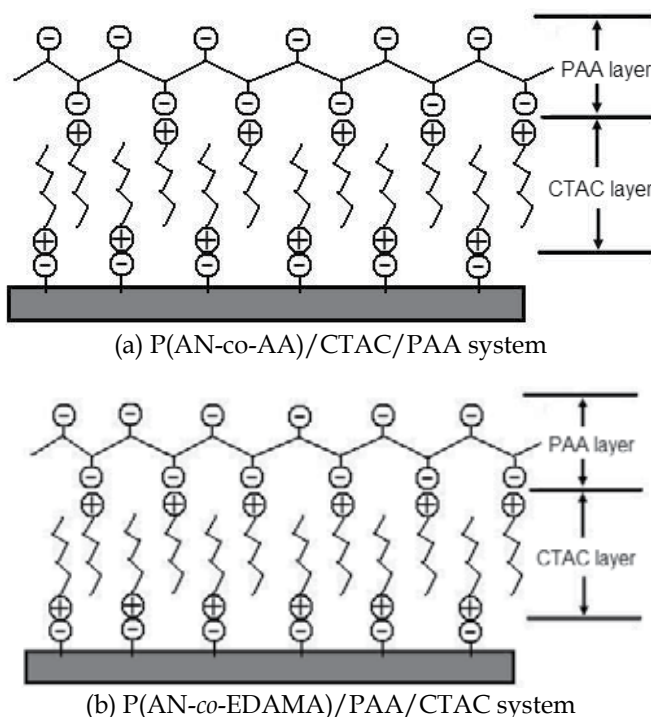
In order to evaluate the selective rejection property of the resultant membranes, the removal selectivity coefficient (S_R) for Fe^{3+} and Fe^{2+} ions was calculated from the following equation:

$$S_R = R_{Fe^{3+}} / R_{Fe^{2+}} \quad (3-2)$$

$R_{Fe^{3+}}$ and $R_{Fe^{2+}}$ were the rejection values of the resultant membranes for Fe^{3+} and Fe^{2+} , respectively.

IR measurement of membranes with ESA multilayer

As presented in Scheme 3-2, the base membrane surface was modified alternately by layer-by-layer formation of CTAC and PAA via ESA treatment. The structure of membrane formed in P(AN-co-AA)/CTAC/PAA system is shown in Figure 2-1. In this section, we mainly introduced the analysis of structure of membrane formed in P(AN-co-EDAMA)/PAA/CTAC system. In Figure 3-1, the FT-IR spectrum indicated that for the positively charged substrate of P(AN-co-EDAMA), the ESA treatment was performed in the deposition cycle order of PAA/CTAC/PAA/CTAC. As a result of the first deposition of the PAA layer, the band strength of the carboxylic group at about 1720 cm^{-1} became stronger, which confirmed the assembly of the PAA layer onto the positively charged base membrane. However, after the deposition of CTAC layer, the carboxylic groups bound on the CTAC



Scheme 3-2. Illustration images of layer-by-layer assembling of CTAC and PAA on negatively charged P(AN-co-AA) membrane surface (a) and on positively charged P(AN-co-EDAMA) membrane surface (b).

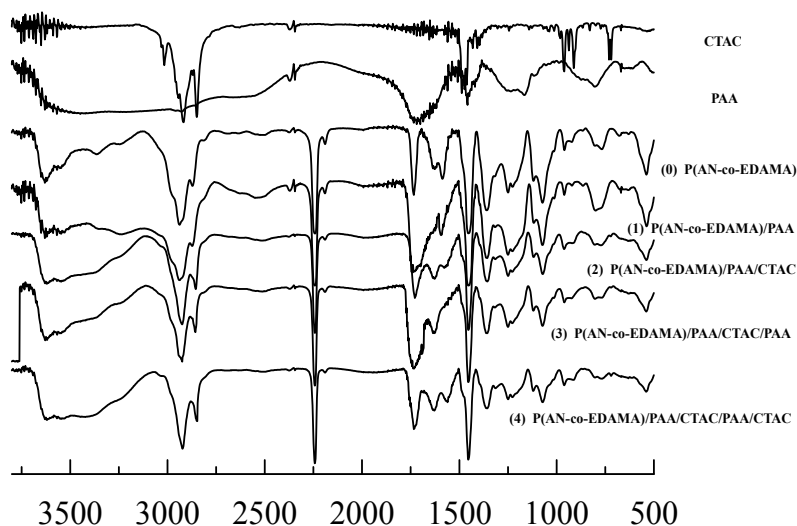


Fig. 3-1. FT-IR spectra of base membrane and membrane with self-assembled layers.

layer resulted that the carboxylic acid absorption peak became weaker relative to that of P(AN-co-EDAMA)/PAA. A similar tendency repeated itself in accordance with the self-assembly of the first cycle of PAA layer and CTAC layer. Hereby, the alternate self-assembly of CTAC and PAA onto the charged base membranes of P(AN-co-AA) and P(AN-co-EDAMA) was confirmed by the FT-IR measurement.

Since the alternate ESA layers on the membrane surface contained charged groups, it was expected that the permeate behaviour of metal ions through the modified membrane could be affected by the ESA layers formed on the membrane surface.^[21, 22] Thus, the desalination of the ESA modified membranes was evaluated by testing the permeability for metal ion solution. Rejection values for metal ions of Fe³⁺ and Fe²⁺ of resultant membranes of the P(AN-co-AA)/CTAC/PAA system and P(AN-co-EDAMA)/PAA/CTAC system are shown in Figure 3-2 and Figure 3-3, respectively, with solid lines for Fe³⁺ and dotted lines for Fe²⁺. It could be seen that the membrane modified with ESA layers showed considerable high rejection for metal ion of Fe³⁺ and the rejection for Fe³⁺ was higher than for Fe²⁺. This may be induced by the smaller hydrated ion radius of Fe²⁺ than that of Fe³⁺ resulting from the fact that Fe²⁺ has a bigger ion radius of about 0.78 nm than the 0.64 nm of Fe³⁺. As revealed by both of the two systems, the metal-ion rejection was strongly related to the charge property of the outer layer on the modified membrane surface. It was noted interestingly that the metal ion rejection changed alternately and was higher in deposition cycle of 1, 3 and 5 for the P(AN-co-AA)/CTAC/PAA system, while higher in deposition cycle of 2, 4 and 6 for the P(AN-co-EDAMA)/PAA/CTAC system. It seemed that the deposition of CTAC layers having positively charged groups enhanced the rejection of membranes for metal ions, might be due to the electrostatic repulsion between metal ion and the CTAC layer on membrane surface. Therefore, it was considered that membrane having the LbL surface terminated by positively charged species, due to the self-assembly of CTAC layers might be effective for the metal ion removal application.

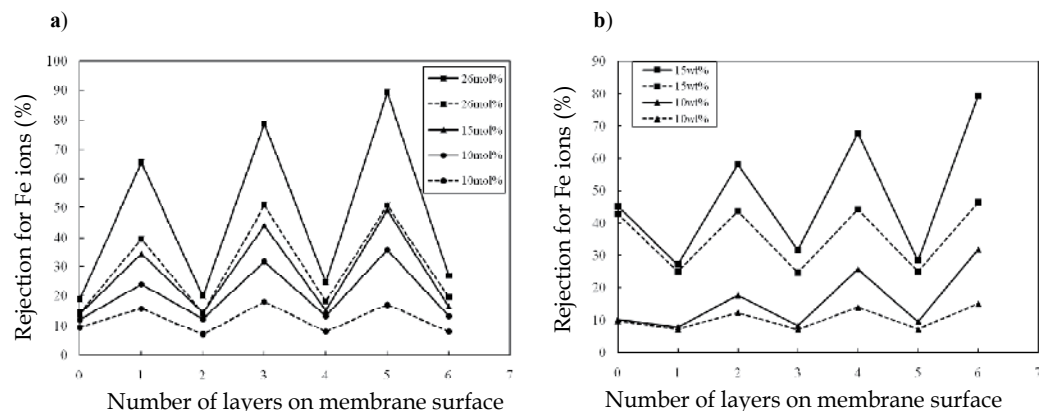


Fig. 3-2. **a)** The effect of AA fraction contained in base membrane on the rejection of Fe³⁺ (—) and Fe²⁺ (---) for P(AN-co-AA)/CTAC/PAA system (cast solution concentration for base membrane: 15wt%; pH of metal ions solution: 7). **b)** The effect of P(AN-co-EDAMA) base membrane on the rejection of Fe³⁺ (—) and Fe²⁺ (---) for P(AN-co-EDAMA)/PAA/CTAC system. (EDAMA contained in base membrane: 2 mol%; pH of metal ions solution: 7).

Additionally, the change tendency of the rejection curves of the two systems for both metal ions behaved oppositely to each other as revealed by Figure 3-2. These indicated that P(AN-co-AA) base membrane having COO⁻ on the surface was negatively charged, while P(AN-co-EDAMA) base membrane having quaternary ammonium groups on the surface was positively charged. Their different charge properties of base membrane surface resulted in different cycle order of self-assembled multilayer deposited on the base membrane surface, as performed in cycle of CTAC/PAA/CTAC/PAA for the former and PAA/CTAC/PAA/CTAC for the latter. The opposite change tendency of the permeability of resultant membranes further confirmed the influence of the ESA terminal layer on its permeability.

Furthermore, we examined the effect of base membrane structure on the rejection behavior of resultant membrane. For P(AN-co-AA)/CTAC/PAA system, the charged sites on P(AN-co-AA) base membrane were different for membranes having different amounts of AA segments.

Three kinds of P(AN-co-AA) copolymers prepared with a AA fraction of 10 mol%, 15 mol% and 26 mol%,^[23] were used as base membranes for ESA treatment. Then, the surfaces were modified with ESA layers of CTAC and PAA to study the effect of AA fractions contained in the base membrane on the removal properties of modified membranes. It was found that, when the base membrane used for self-assembly treatment contained higher AA mol%, the corresponding resultant membranes showed higher removal properties for both Fe³⁺ and Fe²⁺. This meant that base membrane which contained higher AA mol% had more ionized carboxyl charged sites on the surface. Then, there would be more CTAC and PAA adsorbed onto membrane surface during the alternate dipping process, leading to resultant membrane surface having higher charge density and then affecting the permeability for metal ions. For the P(AN-co-EDAMA)/PAA/CTAC system, by increasing the concentration of the cast solution, the effect of the base membrane structure on the permeability of ESA layer modified membranes was studied. As shown in Figure 3-2(b), when the P(AN-co-EDAMA)

base membrane was prepared by cast solution with a higher concentration of 15%, the rejection for Fe³⁺ and Fe²⁺ rose significantly as compared with that of membranes prepared with a concentration of 10%. This result was also induced by the higher charge density of base membrane prepared with higher concentration which consequently affected the formation of ESA layers onto charged base membrane surface.

To study the charge density of PAA layer on membrane surface, we calculated the ratio of dissociated COO⁻ group and COOH group by referring to the characteristic peaks at 1446 cm⁻¹ and 1710 cm⁻¹, respectively, revealed by FT-IR data in Figure 2-1 and Figure 3-1. For the P(AN-co-AA)/CTAC/PAA system, the value of [COO⁻]/[COOH] was 72% for base membrane of P(AN-co-AA), after the surface was converted with CTAC layer, the value became to be 78% and then decreased to 47 % due to the assembly of PAA layer onto membrane surface. Then, the value changed to be 83% and 49% consequently as the second circle of CTAC/PAA layers was formed onto membrane surface.

As the rejection of the resultant membranes for Fe³⁺ and Fe²⁺ was obviously different, it was considered that the resultant membranes were showed permselectivity for Fe³⁺ and Fe²⁺. Herein, the removal selectivity coefficient for Fe³⁺ and Fe²⁺ was calculated according to equation 3-2. The results are shown in Table 3 for the P(AN-co-AA)/CTAC/PAA system and the P(AN-co-EDAMA)/CTAC/PAA system. The results indicated that membrane modified with ESA layers of CTAC and PAA was capable of selectively removing Fe³⁺ and Fe²⁺ along with relatively high selective permeability. For the P(AN-co-AA)/CTAC/PAA system, as shown in Table 3-(a) and 3-(b), base membrane containing 10 mol% AA segment (denoted by a) resulted in ESA modified membrane having relative higher removal selectivity coefficients (S_R) for metal ion pair of Fe³⁺ and Fe²⁺ as compared with base membrane containing 26 mol% AA segment. The results revealed that lower fraction of AA segments in the base membrane led to resultant membrane with lower selective

Number of ESA layers	1	2	3	4	5	6
S _R for Fe ³⁺ /Fe ²⁺ of P(AN-co-AA) ^{a)}	1.54±0.02	1.68±0.04	1.75±0.07	1.61±0.03	2.10±0.06	1.62±0.03
S _R for Fe ³⁺ /Fe ²⁺ of P(AN-co-AA) ^{b)}	1.64±0.03	1.42±0.01	1.53±0.04	1.36±0.05	1.75±0.06	1.37±0.06
S _R for Fe ³⁺ /Fe ²⁺ of P(AN-co-EDAMA) ^{c)}	1.07±0.04	1.32±0.05	1.28±0.05	1.52±0.02	1.13±0.06	1.69±0.03
S _R for Fe ³⁺ /Fe ²⁺ of P(AN-co-EDAMA) ^{d)}	1.07±0.03	1.42±0.02	1.15±0.05	1.82±0.06	1.33±0.04	2.10±0.04

(a) 10 mol% and (b) 26 mol% of AA in the P(AN-co-AA)s were used.
 (c) 10 mol% and (d) 15 mol% of EDAMA were used in the P(AN-co-EDAMA).

Table 3. Selective removal coefficient (S_R) for Fe³⁺ / Fe²⁺ of the P(AN-co-AA)/CTAC/PAA system and Fe³⁺/Fe²⁺ of the P(AN-co-EDAMA)/PAA/CTAC system.

permeability for Fe^{3+} and Fe^{2+} . This may be because that much of the electrolytes self-assembled onto membrane surface, which was enhanced by the higher charge density resulting from the higher fraction of AA segments in the base membrane. So the permeability of membrane for metal ion solution was weakened and then led to lower permselectivity.

Also, the base membrane used for ESA treatment contained 10 mol% AA segment, S_{RS} for metal ion pair of Fe^{3+} and Fe^{2+} of the modified membranes terminated with CTAC, CTAC/PAA/CTAC and CTAC/PAA/CTAC/PAA/CTAC ESA layers were 1.54 ± 0.02 , 1.75 ± 0.07 and 2.10 ± 0.06 , respectively.

While the S_{RS} of membranes deposited with CTAC/PAA, CTAC/PAA/CTAC/PAA, CTAC/PAA/CTAC/PAA/CTAC/PAA ESA layers were 1.68 ± 0.04 , 1.61 ± 0.03 and 1.62 ± 0.03 , respectively. It was reasonable to conclude that the resultant membrane was endowed with higher selective removal property for Fe^{3+} and Fe^{2+} when the surface was self-assembly terminated with positive CTAC layer.

For P(AN-co-EDAMA)/PAA/CTAC system, the S_{RS} for Fe^{3+} and Fe^{2+} ions are shown in Table 3-(c) and (d). It can obviously seen that base membrane prepared by 15 mol% cast solution of P(AN-co-EDAMA)(denoted by c) resulted in ESA modified membranes with higher S_R as compared with base membrane prepared with 10 mol% cast solution (denoted by d). When the base membrane used for ESA treatment was prepared by 15wt% cast solution of P(AN-co-EDMA), S_{RS} of the corresponding resultant membranes modified with PAA/CTAC, PAA/CTAC/PAA/CTAC and PAA/CTAC/PAA/CTAC and PAA/CTAC/PAA/CTAC/PAA/CTAC multilayer were 1.42 ± 0.02 , 1.82 ± 0.06 and 2.10 ± 0.04 , respectively, while the S_{RS} of membranes having CTAC/PAA, CTAC/PAA/CTAC/PAA, CTAC/PAA/CTAC/PAA/CTAC/PAA layers on the surface became 1.07 ± 0.03 , 1.15 ± 0.05 and 1.33 ± 0.04 , respectively. These indicated that positively charged surface induced by the formation of self-assembly CTAC layers was capable of selectively removing Fe^{3+} and Fe^{2+} ions. From these results, it was found out that for the P(AN-co-AA)/CTAC/PAA system, showed higher selectivity but lower rejection for Fe^{3+} and Fe^{2+} . While for the P(AN-co-EDAMA)/PAA/CTAC system, showed considerable high rejection for Fe^{3+} about 90% as well as a relative high permselectivity for Fe^{3+} and Fe^{2+} . It was proposed that the membranes prepared in this experimental could be used for the selective desalination of solution containing Fe^{3+} and Fe^{2+} .

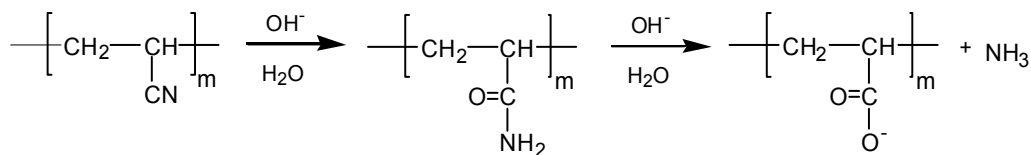
4. Self-assembly functionalized membranes with chitosan microsphere / Polyacrylic acid layers and their application for metal ion removal of Cu^{2+}

Modification of PAN to anionic charged base membrane for adsorption of Cu (II)

PAN membrane, which was used as the base membrane for ESA treatment, was prepared and then treated with 2M KOH solution for negatively charged PAN base membrane (Scheme 4-1)^[19].

Adsorption of Cu(II)

The adsorption experiment for Cu(II) was performed using the static method and was carried out as follows. Immersing the sample membranes was carried out into CuSO_4 solution with a concentration of 2 ppm for 40 min at room temperature and then, the



Scheme 4-1. Chemical reaction of PAN treated by alkali solution.

original and residual ion concentrations remained in the ion solution were measured by Atomic absorption spectrophotometer (AA-6300, Shimadzu Ins). The metal ion adsorption capacity (10^{-6} g / g-membrane) was defined as the amount of Cu^{2+} (g) adsorbed by unit weight of membrane (g), and was calculated by following equation.

$$\text{Cu(II)}(\text{adsorption capacity}) = v(c_0 - c_e) / M \tag{4-1}$$

where c_0 is the initial concentration of Cu(II) (ppm/ml), c_e is the concentration at equilibrium, V is the volume (40 ml) of solution and M is the wet mass of resultant membrane being used.

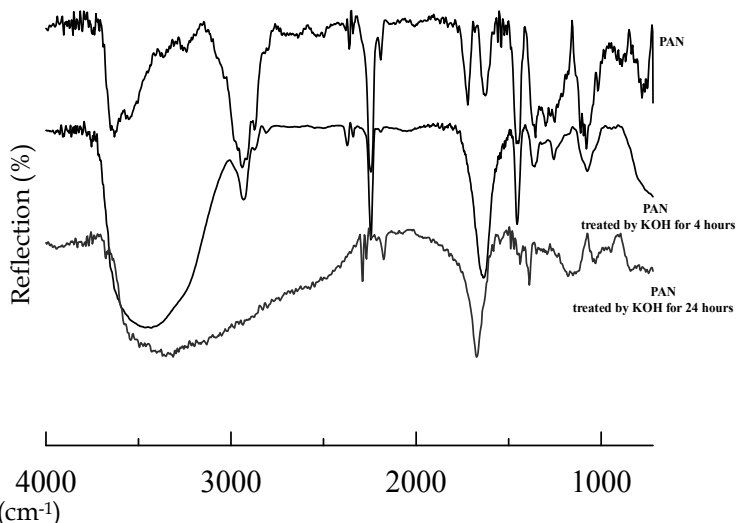
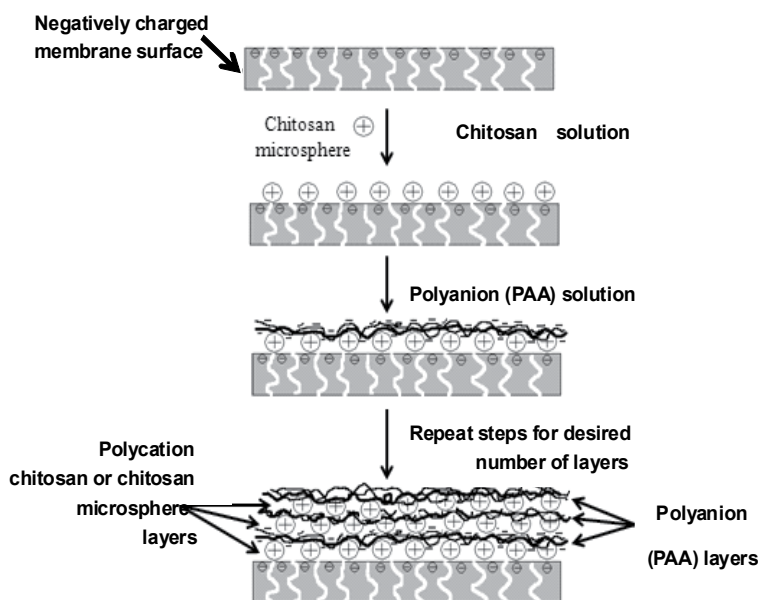


Fig. 4-1. FT-IR spectra of original PAN membrane and membrane treated with KOH solution.

In order to convert the CN groups to negatively charged COO^- group on the PAN membrane surface, the chemical reaction (Scheme 4-1) was performed by using KOH solution. The FT-IR measurement was carried out to study the chemical composition of the PAN membrane surface before and after the KOH treatment. In the spectrum of the PAN membrane treated by KOH for 24 hours, the characteristic absorption peak for the CN group at about 2300 cm^{-1} became weaker while the characteristic peak assigned to carboxyl group in the range from 2800 cm^{-1} to 3700 cm^{-1} appeared stronger. Especially, the band at 1700 cm^{-1} assigned to the carbonyl group from COO^- existed in the FT-IR spectrum. So, it was concluded that the PAN membrane surface was negatively charged due to the formation of carboxyl groups resulting from the KOH treatment.

Formation of the ESA multilayer of chitosan / PAA and chitosan microspheres / PAA

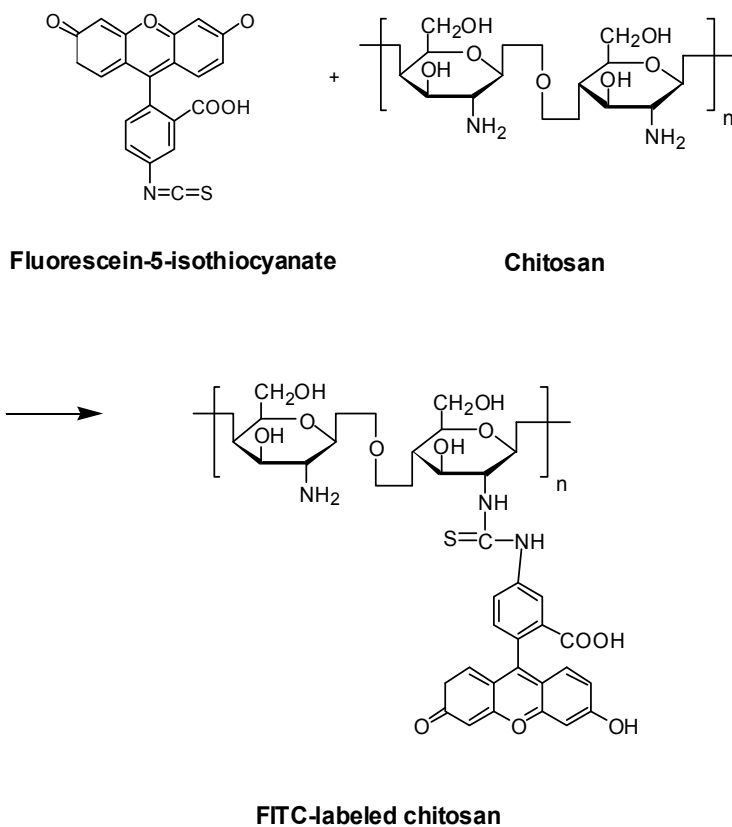
As the surface of treated PAN membrane was negatively charged due to the KOH treatment, positively charged chitosan and negatively charged PAA were alternatively coated to form self-assembly layers onto the charged PAN membrane (Scheme 4-2). Also, chitosan polycation microspheres cross-linked by sulfate groups were used instead of chitosan to form electrostatical self-assembled layers onto the negatively charged base membrane. The deposition process of the alternate formation of chitosan or chitosan microspheres and PAA layers was repeated 4 times. In Scheme 4-2, for the first step, the cationic chitosan or chitosan microspheres electrostatically interacted with the negatively charged groups on the base membrane surface. The membrane surface was then positively charged due to the deposition of chitosan or chitosan microspheres. Then, for the second step, PAA was deposited over the first layer of chitosan or chitosan microspheres due to the electrostatic interaction between amino groups of the chitosan and carboxyl groups of the PAA. These steps were repeated to form multiple ESA layers on the base membrane surface.



Scheme 4-2. Illustration images of layer-by-layer assembling of chitosan/PAA and chitosan microsphere/PAA layers onto charged base membrane.

In order to confirm the fabrication of the multilayer of chitosan or chitosan microsphere and PAA layers. Here, the FTIC labeled-chitosan and PAA layers were alternatively deposited onto charged glass slide for UV-vis measurement (Scheme 4-3).

The FTIC-labeled-chitosan (FTIC-labeled chitosan microsphere)/PAA layers on flat glass after each deposited cycle was detected by UV absorption at 476 nm. The UV absorption results of the samples were represented in Figure 4-2 and Figure 4-3, the odd layers were chitosan (chitosan microsphere) outmost. As we can see from Figure 4-2 that for both of PAN/chitosan/PAA system and PAN/chitosan microsphere/PAA system, the value of UV-absorption increased almost linearly with the increasing cycle of deposition process



Scheme 4-3. Schematic illustration of the chemical synthesis of fluorescein isothiocyanate labelled (FITC) chitosan of free FITC fluorescence signal in the washing medium.

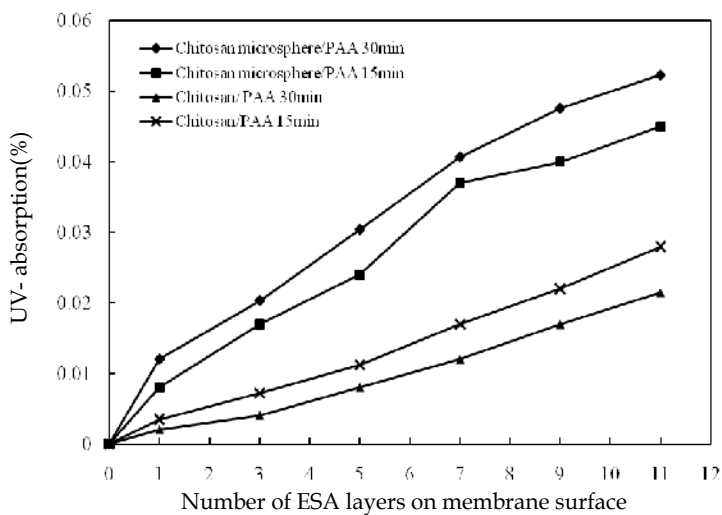


Fig. 4-2. UV-absorption after each deposition of chitosan layer.

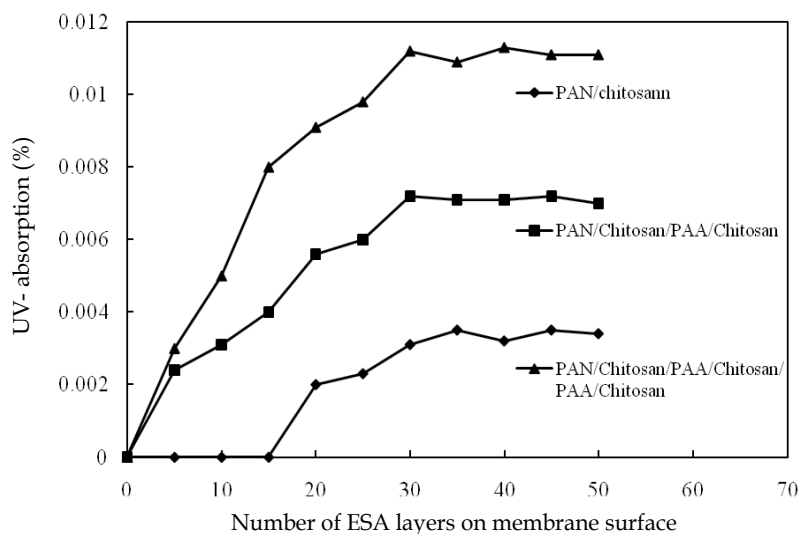


Fig. 4-3. The effect of immersing time on UV-absorption.

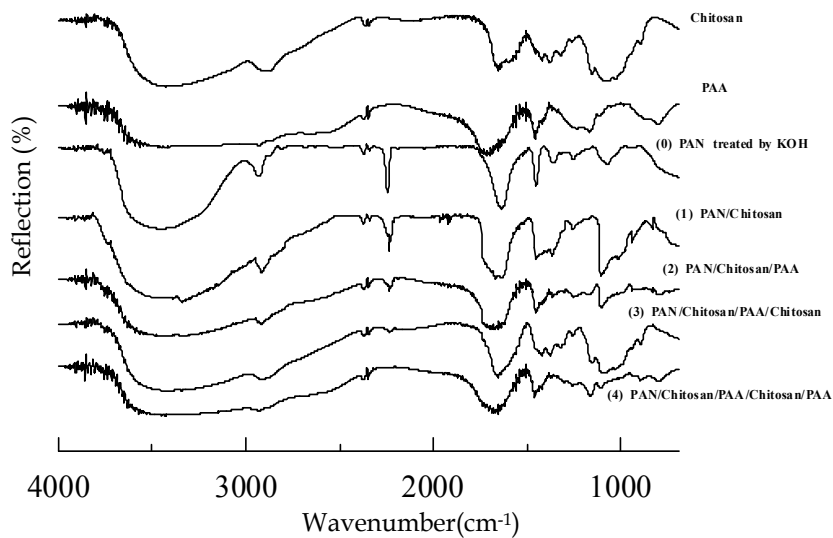
which verified the alternate self-assembly of chitosan (chitosan microsphere) layers and PAA layers onto charged substrate. When the substrate was immersed into chitosan microsphere, there was a remarkable increase in UV-absorption proving that a certain amount of chitosan had deposited onto substrate surface. Also, the samples immersed into the solutions of chitosan (chitosan microsphere) and PAA for 30 mins showed higher UV-absorption, which indicated the increase of the deposited amount of chitosan (chitosan microsphere).

Then, we examined the effect of immersing time on the self-assembly of chitosan for PAN/chitosan/PAA system.

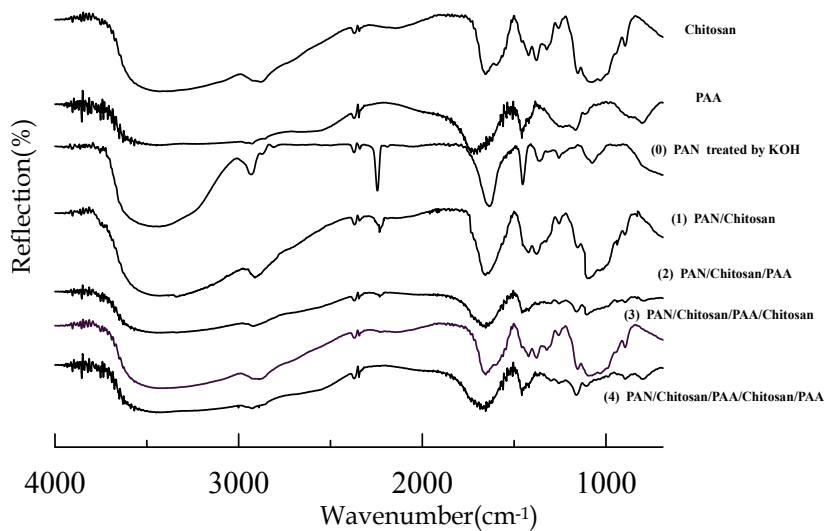
It was thought from data that the self-assembly deposition of chitosan layer onto substrate surface reached saturated state after 30 mins. So, each deposited step lasted for 40 mins as to effectively reversed the charge on the membrane surface.

Characterization of ESA multilayer membranes by FT-IR

The surface of membranes having alternate ESA multilayer was investigated by using reflection FT-IR spectroscopy. Results are shown in Figure 4-4(a) and Figure 4-4(b) for PAN/chitosan/PAA system and PAN/chitosan microspheres/PAA system, respectively. It was found that the characteristic band of CN group from the charged PAN base membrane at about 2300 cm^{-1} became weaker due to the deposition of ESA layers of chitosan or chitosan microgel and PAA. In addition, the characteristic band at about 1170 cm^{-1} corresponding to the primary alcoholic group of chitosan. The peak at about 1400 cm^{-1} was assigned to the stretching vibration of amide band from chitosan appeared in the spectra, especially for cycled 1 and 3, for which the surface was terminated with chitosan layer or chitosan microspheres layer. In the cases of cycle 2 and 4 for surfaces terminated with PAA layer, similar spectra with PAA were observed and it was believed to be resulted by the



(a) PAN/Chitosan/PAA system



(b) PAN/Chitosan microsphere/PAA system

Fig. 4-4. FT-IR spectra of membranes with self-assembled layers.

coverage of PAA on membrane surface. It was also noted that the characteristic peak from chitosan became weaker, while the peak in the range of about 2500 cm^{-1} to 3750 cm^{-1} from the PAA layer became stronger, proving that the PAA layer converted the chitosan or chitosan microspheres layers on the surface. The upper change was repeated alternately along with the alternative deposition of chitosan (chitosan microspheres) layers and PAA layers onto charged PAN membrane as revealed by IR spectrum. These spectral changes proved the successful formation of alternate chitosan or chitosan microspheres layers and PAA layers onto charged PAN membrane surface. Furthermore, the obvious difference between the IR spectrum of PAN/Chitosan/PAA system and PAN/Chitosan microspheres/PAA system was observed in comparison of (a) and (b). For the PAN/Chitosan microspheres/PAA system, the disappearance of the peak of the CN group from the charged PAN base membrane was drastic due to the coverage of the ESA layers.

Surface roughness of the chitosan microspheres/PAA membranes were represented in Figure 4-5. As shown in Figure 4-5, the surface roughness of -1 and 0 which referred to membranes before and after NaOH treatment, indicated that the membrane surface became rougher due to the existence of hydrophilic carboxyl groups resulting from NaOH treatment. It was also apparent that the surface morphology was dramatically altered by the formation of the chitosan microspheres/PAA ESA multilayer. While the corresponding surface roughness values were 8.0 nm, 23.1 nm, 15.0 nm, 39.9 nm and 36.4 nm for the chitosan microspheres/PAA membranes with cycle layers of 0, 1, 2, 3 and 4, respectively.

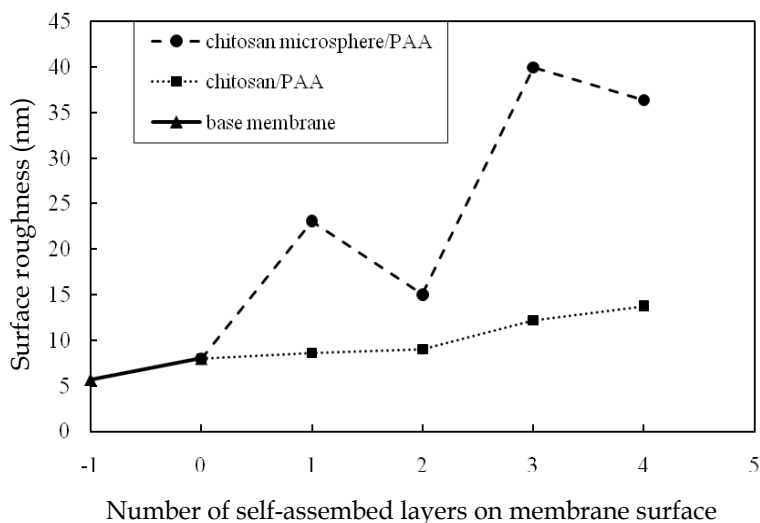


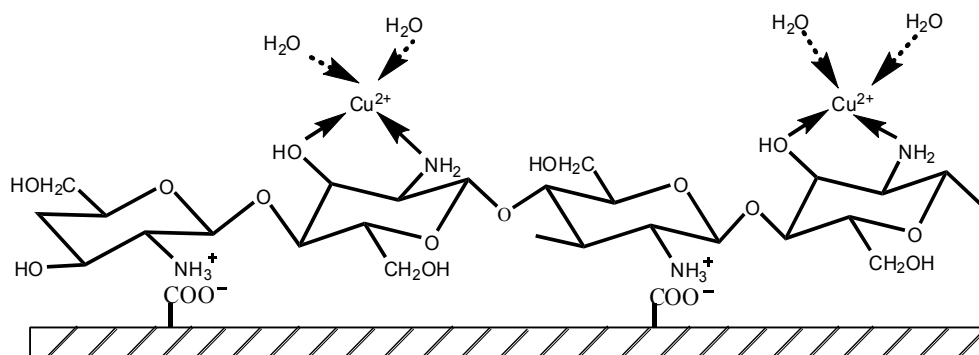
Fig. 4-5. Influence of numbers of self-assembled layers onto the membrane surface on the surface

However, much less change in the surface roughness was observed for the membrane with chitosan/PAA ESA layers. The values of the surface roughness were 8.0 nm, 8.6 nm, 9.0 nm, 12.2 nm, and 13.7 nm for the cycled layers of 0, 1, 2, 3 and 4, respectively. Therefore, the introduction of the chitosan microspheres for the ESA multilayer could be effectively for roughing the base of membrane surfaces. Therefore, this approach could be attractive in the uses of adsorption of such metal ions.

Adsorption capability for copper ion

It was known that chitosan could be applied for adsorption of metal ions since the amino group is capable of binding metal ions as served as coordination sites. For example, Juang et al.,^[25] reported high selectivity for Cu^{2+} ion was observed by chitosan adsorbents. Chang et al.^[26] found that the chitosan-modified microsphere showed the largest equilibrium adsorption capacity at pH 5.5. Therefore, in the present work, we studied the binding capability for Cu^{2+} ion of the resultant membrane at various pHs.

Here, the pH of the Cu^{2+} ion solution was adjusted using buffer solution of 0.2 mol / L CH_3COOH and 0.2 mol / L CH_3COONa . The assembled behaviour of chitosan onto negatively charged base membrane and binding behaviour of chitosan for copper ions is simply illustrated by Scheme 4-4. Figure 4-6 shows the effect of the pH of Cu^{2+} ion solution on the Cu^{2+} adsorption of resultant membranes with Chitosan microspheres/PAA multiple-layers. The adsorption amounts of the Cu^{2+} ion were plotted at the cycle number for the ESA multilayer formation. The odd layers were for the chitosan or chitosan microspheres layers exposed on the membrane surface outmost and evens were for PAA layers on the outmost. It could be seen that when the adsorption was carried out at pH 3, membranes terminated with PAA layers showed higher adsorption capacity rather than those with terminal chitosan or chitosan microspheres layers. But, when pH increased, the change regulation could not be seen at pH 7 in both (a) and (b) systems. In the case of the chitosan microspheres/PAA system, the values of the adsorption capacity were significantly decreased to be in the range of about 50 ppm / g-membrane. However, at pH 5 and 6, the values of the adsorption capacity increased with the increasing of the cycled number of the



Scheme 4-4. Illustration images of the chelation for Cu^{2+} by the assembled chitosan on negatively charged membrane surface.

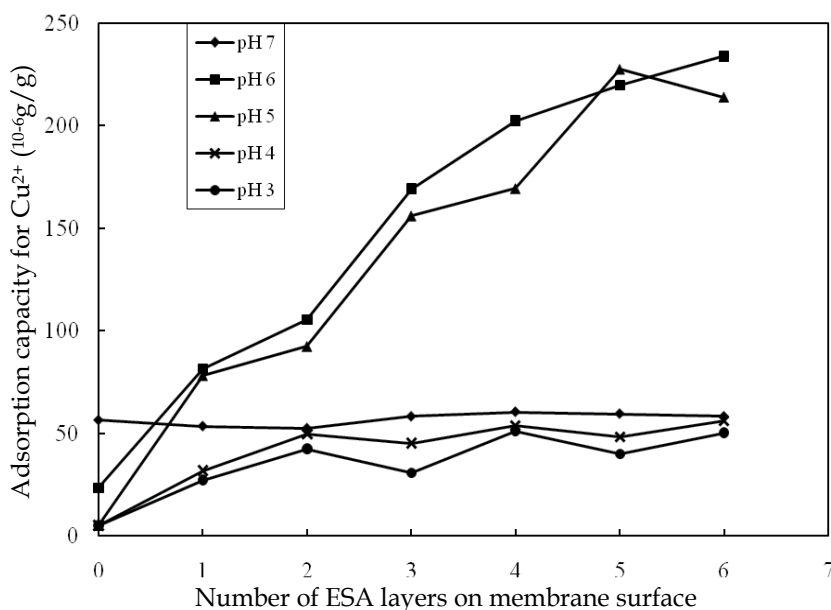


Fig. 4-6. Effect of the copper solution pH on the adsorption capacity of the resultant membranes of PAN/chitosan microsphere/PAA system.

ESA operation and then ranged in about 200-240 ppm / g-membrane. It was thought that the adsorption capacity of resultant membrane depended on the isoelectric point of chitosan, which was at about 6.3. At below the pH, the protonation of amine groups of chitosan could occur, while at higher pH the group behaved as non-protonated group. However, the binding ability of chitosan for copper ions was mainly due to the amine groups which were served as coordination sites for the sequestration of copper ion.^[27] At lower pH, most of the amine groups in the chitosan segments was protonated and not available for copper uptaking by chelation. Thus, the values of the adsorption capacity decreased with decreasing pH. However, as the protonated chitosan at low pH was able to bind anions by electrostatic attraction.^[28] So, the resultant membranes showed a tendency with low adsorption capacity for Cu²⁺ ion at low pH region. But, at pH 7, the adsorption capacity became dramatically lower relative to roughness for the two systems. those at pH 5 and 6 for the chitosan microspheres/PAA system. It was considered that, at higher pH, the destruction of the self-assembled layers might have occurred, since the chitosan layers on membrane surface behaved as non-charged forms.

Especially the chitosan microspheres/PAA system demonstrated low adsorption at pH 7. This meant that the increase of the solution pH restrained the coordination of Cu²⁺ ions, which was induced by the destruction of the ESA multilayer at pH 7. However, at pH 5 and 6, partial amino group remained on the protonation form which was favorable for the stability of chitosan or chitosan microspheres layers on resultant membranes. Also, Figure 4-7 was plotted for comparing the adsorption capacity of resultant membranes with chitosan/PAA ESA layers and chitosan microspheres/PAA ESA layers. It was seen that

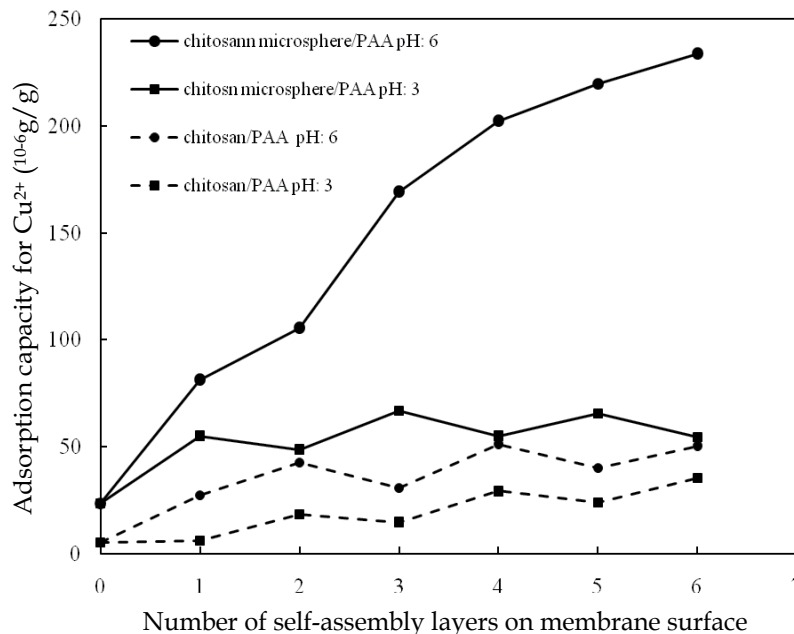


Fig. 4-7. Comparison of the adsorption capacity for Cu^{2+} of the two kinds of resultant membranes.

adsorption capacity of membranes functionalized with chitosan microspheres/PAA ESA layers at pH 6 was several times higher than that of membranes modified with chitosan/PAA ESA layers. The reason for this might be due to the fact that even though the cross-linking of chitosan in the chitosan microsphere significantly reduced the chelating sites. There were still large amounts of residual amino and hydroxyl groups retained in the microsphere which were active for chelation. So, it was suggested that the ESA multilayer of chitosan microspheres/PAA onto charged substrate prepared in the present paper showed great potential in functioning membranes with high removal capability of heavy metal ions.

5. Conclusion

In the present chapter layer-by-layer electrostatic self-assembly technique was used for the preparation of functional polymeric membranes with metal ion removal capability. The fabrication process and properties of the resultant membranes were mentioned by using data of FT-IR spectra in detail.

A negatively charged P (AN-co-AA) membrane and positively charged P (AN-co-EDAMA) were used as the substrates for the ESA treatment. The desalination behaviour of the ESA multilayer modified resultant membranes was studied by evaluating the metal-ion removal properties for Fe^{3+} and Fe^{2+} . It was found that the resultant membrane showed higher rejection for trivalent ion than divalent metal ion. Evidences indicated that the alternate layer-by-layer formation of the ESA multilayer on the base membrane surface effectively influenced the metal-ion removal of the resultant membranes, indicating that ESA technique was useful for introducing the functionality.

Membranes with chelation capability were prepared by the alternate self-assembled of chitosan layer and PAA layer on PAN membrane surface. Taking advantage of the adequate surface area and a large amount of loading sites for metal ions, chitosan microspheres were synthesized and used as cationic species for the construction of ESA multilayer. The result of adsorption experimental for Cu(II) showed that the layer-by-layer deposition of chitosan/PAA or chitosan microspheres/PAA on charged base membrane surface was functionally equipped it with chelating ability for Cu²⁺. Especially, because of the large internal porosities of the chitosan microspheres, resultant membranes with chitosan microspheres multilayer on the surface showed higher adsorption capacity for Cu²⁺ as compared with membranes modified by chitosan multilayer. This confirmed that fabrication of chitosan microsphere ESA multiplayer effectively improved the metal-ion uptake capability of membrane. It suggested that such membranes are expected to be applicable as a novel prospect for wastewater treatment.

6. Acknowledgment

We thank the supporting of Program for Project supported by forming a Hub for Human Resources Development and New Industry Creation Building a Sustainable Society Through Highly Interactive, Cooperative Educational Research with Pacific Rim Countries.

7. References

- [1] Zapotoczny, S.; Golonka, M. & Nowakowska, M. (2005). Novel Photoactive Polymeric Multilayer Films. *Macromol. Rapid Commun*, Vol. 26, pp. 1049-1054.
- [2] Kweon, D. K.; Song, S. B. & Park, Y. Y. (2003). Preparation of water-soluble chitosan/heparin complex and its application as wound healing accelerator. *Biomaterials*, Vol.24, pp. 1595-1601.
- [3] Lojou, E. & Bianco, P. (2004). Buildup of Polyelectrolyte-Protein Multilayer Assemblies on Gold Electrodes. Role of the Hydrophobic Effect. *Langmuir*. Vol.20, pp. 748-755.
- [4] Kozlovskaya, V.; Ok, S.; Sousa, S.; Libera, M. & Sukhishvili, S. A. (2003). Hydrogen-Bonded Polymer Capsules Formed by Layer-by-Layer Self-Assembly. *Macromolecules* Vol.36, pp. 8590-8592.
- [5] Kim, Y. S.; Koo, J. Y. & Kim, H. (2008). Interplay of Hydrogen-Bond and Coordinate Covalent-Bond Interactions in Self-Assembly of NH₃ Molecules on the Si(001) Surface. *Phys. Rev. Lett*, Vol.100, pp. 256105-1-256105-4.
- [6] Jiang, S. P.; Liu, Z. & Tian, Z. Q. (2006). Layer-by-Layer Self-Assembly of Composite Polyelectrolyte – Nafion Membranes for Direct Methanol Fuel Cells. *Adv. Mater*. Vol.18, pp. 1068-1072.
- [7] Decher, G. (1997). Fuzzy Nanoassemblies: Toward Layered Polymeric Multicomposites. *Science*. Vol.277, pp. 1232-1237.
- [8] Krasemann, L. & Tieke, B. Selective Ion Transport across Self-Assembled Alternating Multilayers of Cationic and Anionic Polyelectrolytes. *Langmuir*. Vol.16, pp. 287-290.
- [9] Farhat, T. R. & Schlenoff, J. B.; (2003). Doping-Controlled Ion Diffusion in Polyelectrolyte Multilayers: Mass Transport in Reluctant Exchangers. *J. Am. Chem. Soc*. Vol.125, pp. 4627-4636.
- [10] Li, J. Y.; Ichizuri, S.; Asanato, S.; Mutou, F.; Ikeda, S.; Iida, M.; Miura, T.; Oshima, A.; Tabata, Y. & Washio, M. (2006). Preparation of Ion Exchange Membranes by

- Preirradiation Induced Grafting of Styrene/Divinylbenzene into Crosslinked PTFE Films and Successive Sulfonation. *J. Appl. Polym. Sci.* Vol.101, pp. 3587-3599.
- [11] Cakmak, G.; Zorlu, F.; Severcan, M. & Severcan, F. (2011). Screening of Protective Effect of Amifostine on Radiation-Induced Structural and Functional Variations in Rat Liver Microsomal Membranes by FT-IR Spectroscopy. *Anal. Chem.* Vol.83, pp. 2438-2444.
- [12] Arrondo, J. L. R.; & Goni, F. M. (1999). Structure and dynamics of membrane proteins as studied by infrared spectroscopy. *Progress in Biophysics & Molecular Biology.* Vol.72, pp. 367-405.
- [13] Li, J.; Wong, M. W.; Lin, L.; Bianchi, V.; Edwards, M. & Yip, C. M. (2011) IR Spectroscopy of Protein and Peptide-Membrane Interactions. *Biophys. J.* Vol.100, pp. 495a.
- [14] Sukumaran, S.; Hauser, K.; Rauscher, A. & Mantele, W. (2005) Thermal stability of outer membrane protein porin from *Paracoccus denitrificans*: FT-IR as a spectroscopic tool to study lipid-protein interaction. *FEBS Letters.* Vol.579, pp. 2546-2550.
- [15] Luo, M. L.; Wen, Q. Z.; Liu, J. L.; Liu, H. J. & Jia, Z. (2011) Fabrication of SPES/Nano-TiO₂ Composite Ultrafiltration Membrane and Its Anti-fouling Mechanism. *Chin. J. Chem. Eng.* Vol.19, pp 45-51.
- [16] Xua, H. K.; Fanga, J.; Guo, M.; Lua, X. H.; Wei, X. L. & Tu, S. (2010) Novel anion exchange membrane based on copolymer of methyl methacrylate, vinylbenzyl chloride and ethyl acrylate for alkaline fuel cells. *Journal of Membrane Science.* Vol.354, pp 206-211.
- [17] Tang, B. B.; Wu, P. Y. & Siesler, H. W. (2008). In Situ Study of Diffusion and Interaction of Water and Mono- or Divalent Anions in a Positively Charged Membrane Using Two-Dimensional Correlation FT-IR/Attenuated Total Reflection Spectroscopy. *J. Phys. Chem. B.* Vol.112, pp. 2880-2887.
- [18] Ding, Y.; Bikson, B. & Nelson, J. K. (2002). Polyimide Membranes Derived from Poly(amic acid) Salt Precursor Polymers. 2. Composite Membrane Preparation. *Macromolecules* Vol.35, pp. 912-916.
- [19] Kobayashi, T.; Fu, H. T.; Cui, Q. & Wang, H. Y. (2008). Multilayer Composite Surfaces Prepared by an Electrostatic Self-Assembly Technique with Quaternary Ammonium Salt and Poly(acrylic acid) on Poly(acrylonitrile-co-acrylic acid) Membranes. *J. Appl. Polym. Sci.* Vol.110, pp. 3234-3241.
- [20] Kobayashi, T.; Kumagai, K.; Nosaka, Y.; Miyama, H.; Fujii, N. & Tanzawa, H. (1991). Permeation behavior of dextrans by charged ultrafiltration membranes of polyacrylonitrile photografted with ionic monomers. *J. Appl. Polym. Sci.* Vol.43, pp. 1037-1043.
- [21] Arica, M. Y.; Yilmaz, M. & Bayramoglu, G. (2007). Chitosan-grafted poly(hydroxyethyl methacrylate-co-glycidyl methacrylate) membranes for reversible enzyme immobilization. *J. Appl. Polym. Sci.* Vol.103, pp. 3084-3093.
- [22] Wang, D. X.; Su, M.; Yu, Z. Y.; Wang, X. L.; Ando, M. & Shintani, T. (2005). Separation performance of a nanofiltration membrane influenced by species and concentration of ions. *Desalination.* Vol.175, pp. 219-225.
- [23] Wang, X. L.; Tsuru, T.; Nakao, S. & Kimura, S. (1997). The electrostatic and steric-hindrance model for the transport of charged solutes through nanofiltration membranes. *J. Membr. Sci.* Vol.135, pp. 19-32.

- [24] Kobayashi, T.; Wang, H. Y. & Fujii, N. (1998). Molecular imprint membranes of polyacrylonitrile copolymers with different acrylic acid segments. *Anal. Chim. Acta.* Vol.365, pp. 81-88.
- [25] Jang, R. S. & Shao, H. J. (2002). Effect of pH on Competitive Adsorption of Cu(II), Ni(II), and Zn(II) from Water onto Chitosan Beads. *Adsorption.* Vol.8, pp. 71-78.
- [26] Chang, Y. C.; Chang, S. W. & Chen, D. H. (2006). Magnetic chitosan nanoparticles: Studies on chitosan binding and adsorption of Co(II) ions. *Reac. Func. Polym.* Vol.66, pp. 335-341.
- [27] Dambies, L.; Guimon, C.; Yiacoumi, S. & Guibai, E. (2000). Characterization of metal ion interactions with chitosan by X-ray photoelectron spectroscopy. *Colloids Surf. A.* Vol.77, pp. 203-214.
- [28] Guibal, E. (2004). Interactions of metal ions with chitosan-based sorbents: a review. *Separation and Purification Technology.* Vol.38, pp. 43-74.

Infrared Spectroscopy as a Tool to Monitor Radiation Curing

Marco Sangermano¹, Patrick Meier² and Spiros Tzavalas^{2,*}

¹*Politecnico di Torino*

²*ABB Corporate Research*

¹*Italy*

²*Switzerland*

1. Introduction

Photoinitiated polymerization of multifunctional monomers and oligomers is one of the most efficient methods to produce quasi-instantly highly cross-linked polymer networks. It has found a large number of commercial applications, mainly in the coating and printing industry. Among the advantages of this technology the high cure speed, the reduced energy consumption, and the absence of VOC emissions are the most remarkable. It is well known that the UV curing can be performed either by a radical or a cationic mechanism. The cationic photoinduced process presents some advantages compared to the radical one; in particular lack of inhibition by oxygen, lower shrinkage, good mechanical properties of the UV cured materials, and good adhesion properties to various substrates [Fouassier & Rabek, 1993]. The properties of a UV-cured material depend not only on the photocurable composition but also on its photopolymerization kinetics, it is very important to have access to an analytical technique that will facilitate this purpose.

One of the common features of all UV-curable systems is the rapidity at which the polymerization takes place under intense illumination, usually less than one second. Therefore it is difficult to accurately follow the kinetics of such ultrafast reactions, which is a prerequisite for a better understanding and control of the curing process. Moreover, evaluation of the kinetic parameters (rate of polymerization, kinetic chain length, propagation and termination rate constant) is essential in order to compare the reactivity of different photosensitive resins and assess the performance of novel photoinitiators and monomers.

Two types of analytical methods are currently used to study the kinetics of radiation curing:

1. Those based on discrete measurements of the physical or chemical modifications induced after a short exposure to UV light.
2. Those based on the continuous monitoring in real time of some physical or chemical modifications induced by light.

* Corresponding Author

The first method, which provides quantitative and reliable information on the extent of cure, is a time-consuming technique. In addition, there is certain error included in the measurement owing to the post-polymerization reaction, which occurs during the lapse of time between the end of exposure and the measurements

Among the real-time (RT) techniques RT-FTIR spectroscopy is one of the most powerful analytical methods for monitoring UV-initiated curing processes, which proceed rather rapidly. RT-FTIR has several advantages over other real-time methods such as photo-DSC. The most important limitation of photo-DSC is its long response time, which makes it inadequate for the monitoring of fast polymerization reactions. In addition, using photo-DSC requires the knowledge on the theoretical enthalpy of reaction for the conversion of functional groups to be calculated using the heat release measured. Finally, the sample thickness is much higher than that in most practical applications (coatings, printing, etc), moreover, the thickness of the layer in the sample pan is poorly controlled.

In contrast, RT-FTIR spectroscopy allows a rapid and quantitative measurement of the conversion of specific reactive functional groups under variable conditions as light intensity, photoinitiator concentration, coating thickness, etc., which are closer matched to those in technical coating and printing processes. In the past, RT-FTIR spectroscopy has been successfully used to study the kinetics of photopolymerization reactions in dependence on the irradiation conditions and other experimental parameters, the reactivity of monomers and oligomers and the efficiency of newly developed photoinitiator systems.

One of the unique advantages of the IR technique is to permit an instant and precise evaluation of the amount of un-reacted groups (residual bonds or monomer groups), which remain trapped in the glassy polymer network. Its value is highly dependent on the monomer functionality as well as on the glass transition temperature, T_g , of the network. It should be emphasized that RT-FTIR spectroscopy has been proven to be very valuable for the precise determination both of the rate of polymerization and the amount of residual un-reacted groups where the knowledge of the initial group content is not required.

2. Real time FTIR spectroscopy

Real Time (RT-) FTIR spectroscopy permits not only to follow quantitatively the polymerization by monitoring the disappearance of the IR absorption characteristic of the polymerizable reactive groups (acrylates, methacrylates, epoxy rings, vinyl ether double bonds, thiol groups etc.) but also to determine at any moment the actual degree of conversion and hence the residual unreacted groups content. This analytical method has proved extremely valuable for measuring the polymerization rates and quantum yields of reactions that develop in the millisecond time scale.

The polymerization rate, R_p , being the rate of monomer conversion, can be determined by measuring the decrease of the infrared absorption of the reactive group:

$$R_p = \frac{-d[M]}{dt} = \left(\frac{A_1 - A_2}{A_0} \right) \cdot \left(\frac{[M_0]}{t_1 - t_2} \right) \quad (1)$$

where A_1 and A_2 are IR absorption values of the reactant A after exposure to UV-light during time t_1 and t_2 , respectively; A_0 and $[M_0]$ are the absorption and the molar initial concentration values of the monomer, A, before irradiation.

In the RT-FTIR technique, the sample is simultaneously exposed to the polymerizing UV-irradiation beam and to the analyzing IR beam (Fig. 1), which monitors the resulting drop of absorbance. In all the reported data the UV light was a medium pressure mercury lamp, with a broad UV spectra emission.

As an example the RT-FTIR spectra for a methacrylic resin at different irradiation time are shown in Figure 2 [Amerio et al. 2008]. It is evident that the band at 1630 cm^{-1} (C=C), attributed to the methacrylic functional group, decreases during irradiation of the sample with the UV beam. The decrease in intensity of the band at 1630 cm^{-1} is accompanied by an increase and shift to higher wavenumbers of the C=O oscillation mode related to the change in mobility of the C=O bonds with the gradual opening of the C=C bonds.



Fig. 1. Set up for RT-FTIR monitoring of UV irradiation curing

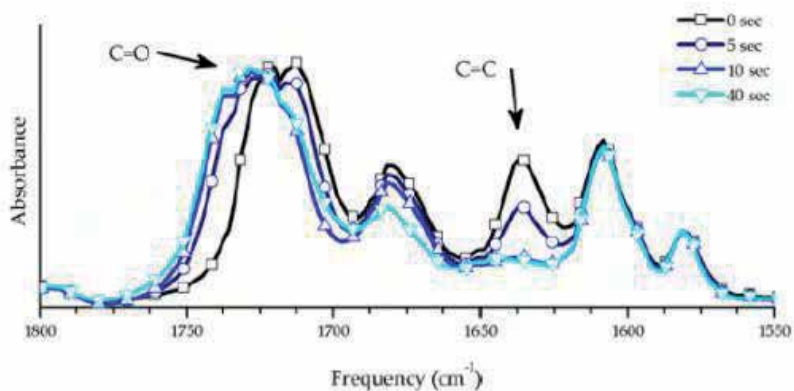


Fig. 2. RT-FTIR spectroscopy during UV curing of a methacrylated system [Amerio et al. 2008]

The reactivity and the kinetics of a UV curable system is affected by numerous parameters i.e. nature and amount of photoinitiator and functionalized monomers and oligomers, thickness, light intensity, concentration of O_2 , the presence of fillers or additives etc. RT-FTIR has been extensively used for the rapid and quantitative assessment of the effect of such parameters on the UV curing kinetics. Further down characteristic examples of the use of this powerful analytical technique are listed.

2.1 Irradiation time

The reaction kinetics curve follows a characteristic sigmoid, S-shaped profile (Fig. 3) due to two major factors: (i) the initial induction period is resulting from the well-known inhibition effect of O_2 on the radical-induced polymerization, which disappears completely for experiments carried out in vacuum or in N_2 ; (ii) the progressive slowing down observed at degrees of conversion above 30-40% is the direct consequence of the network formation and the subsequent gelification, which reduces the segmental mobility of the growing polymer chains and of the un-reacted double bonds [Fouassier & Rabek, 1993].

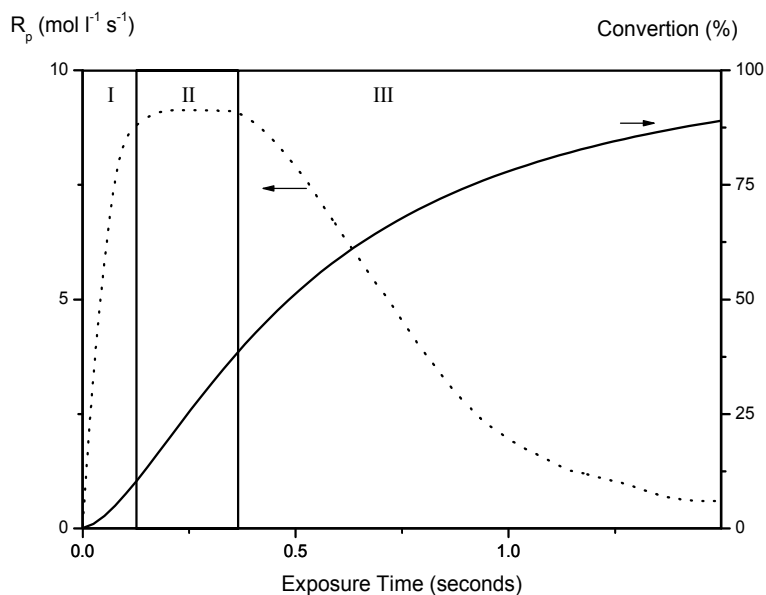


Fig. 3. Conversion curve and R_p curve as a function of irradiation time for a radical induced polymerization [Fouassier & Rabek, 1993].

2.2 Presence of O_2

The free radicals formed by the photolysis of the initiator are rapidly scavenged by O_2 molecules to yield peroxy radicals. These species are not reactive towards the acrylate double bonds and can therefore not initiate or participate in any polymerization reaction. An additional amount of photoinitiator (and of UV energy) is therefore needed to consume/compensate the oxygen dissolved in the resin, as well as the atmospheric O_2 diffusing into the sample during the UV exposure, in order to obtain coatings with the desired mechanical properties and tack-free surfaces.

Overcoming this unwanted reaction has turned into a major challenge. Different methods have been considered: A clear, illustrative example is reported in Figure 4 in which the effect of air and inert atmosphere (CO_2 and N_2) was investigated [Studer et al., 2003]. In the presence of air, the polymerization starts after an induction period of 0.2 s, at a speed four times lower than that in an inert atmosphere (Fig. 4). After 0.35 s, once 15% of the acrylate double bonds have polymerized, the reaction begins already to slow down because of the continuous diffusion of air into the sample. To prevent the diffusion of oxygen into the sample, a UV-transparent polypropylene (PP) film was placed on top of the liquid coating (laminated sample). The induction period is then slightly shorter than in air (oxygen is still dissolved in the film) and the polymerization proceeds three times faster than in air to reach an 85% conversion by the end of the UV-irradiation (35 s).

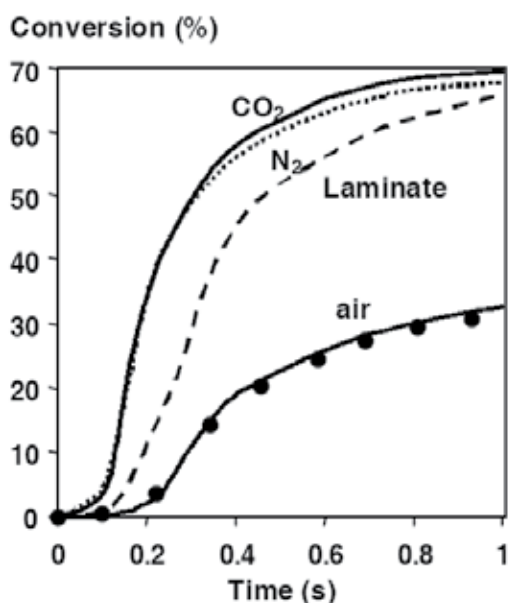


Fig. 4. Conversion curves as a function of irradiation time. Profiles recorded by RT-FTIR spectroscopy for a PUA (Polyurethane) resin exposed to UV light under different atmospheres and with a PP-film as oxygen barrier ("laminated"). [Studer et al., 2003]

2.3 Photoinitiator

The efficiency of the radical photo-initiator can be described by two quantum yields: The *quantum yields of initiation*, which represents the number of starting polymer chains per photons absorbed, and the *quantum yields of polymerization*, which is the number of monomer units polymerized per photons absorbed. Therefore, it is clear that if the monomers are absorbing in the same UV range as the photoinitiator the competition will limit the photons absorbed by the latter. This can lead to a decrease of quantum yields and therefore to a lower degree of conversion as well as polymerization rate. In such cases special care needs to be taken when selecting the proper photoinitiator. This issue becomes particularly important when dealing with formulations containing fillers which absorb light in the same spectral range as the photoinitiator.

In Figure 5 the UV-Vis spectra of a radical photoinitiator and the BaTiO₃ (BT) filler that was used in an acrylic formulation are presented. It is evident that there is a competitive absorption between the photo-initiator and the ceramic powder in the UV region between 200 and 400 nm. That leads to a linear decrease of acrylic double bond during UV irradiation by increasing the filler content in the photocurable formulation [Lombardi et al., 2011].

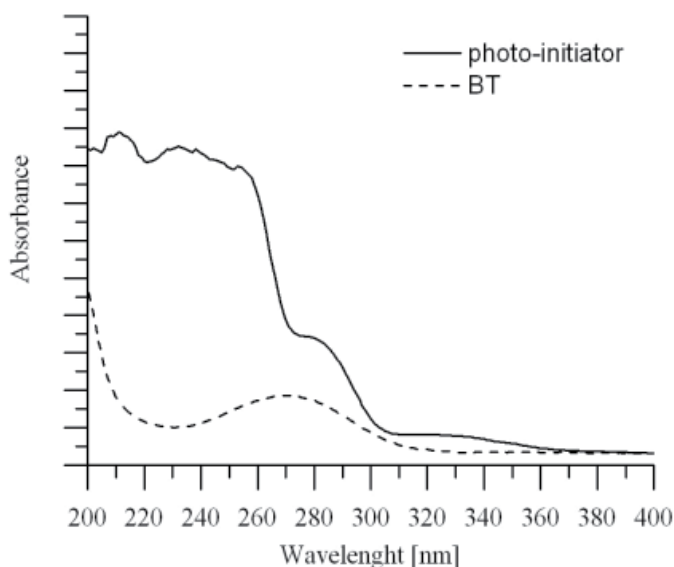


Fig. 5. UV-VIS spectra of the 2-hydroxy-2-methyl-1-phenyl-propan-1-one (DAROCUR® 1173, Ciba®) photo-initiator and the BaTiO₃ (BT) filler. [Lombardi et al., 2011]

2.4 Monomers

From the slope of the RT-FTIR kinetic curves it is easy to evaluate the rate of polymerization (R_p) which can be calculated at any moment of the reaction. It is therefore possible to plot the R_p values as a function of the conversion rate. The overall polymerization quantum yield, ϕ_p , can be calculated from the ratio of polymerization, R_p , over the absorbed light intensity.

In a pioneer study from Christian Decker the photopolymerization of polyurethane-diacrylates was investigated by using the RT-FTIR technique [Decker & Moussa, 1988]. The RT-FTIR conversion curves as a function of irradiation time were examined for different systems (Fig. 6).

The polymerization rate, R_p , values as a function of the percentage of conversion are presented in figure 7. R_p reaches its maximum value ($= 8 \text{ mole l}^{-1}\text{s}^{-1}$ for the most reactive system) at a degree of conversion of 25% for the 3 systems investigated. This peak corresponds to the phase at which the O₂ inhibition has been overcome and gelification has not yet slowed down the polymerization rate. Higher R_p values up to $10^3 \text{ mole l}^{-1} \text{ s}^{-1}$, were obtained with such multiacrylic monomers by merely increasing the intensity of the UV source [Decker & Bendaika, 1984].

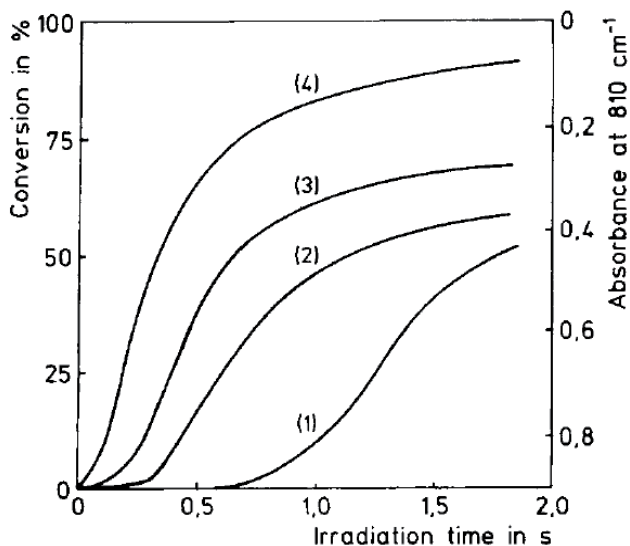


Fig. 6. Photopolymerization profiles (left) and variation of the rate of photopolymerization, R_p , (right) recorded by RT-FTIR spectroscopy for: (1) ethyldiethylenglycol monoacrylate, (EDGA) (2) EDGA + TPGDA, (3) tripropylenglycol diacrylate (TPGDA), (4) Oxazolidone monoacrylate. [Decker & Moussa, 1988]

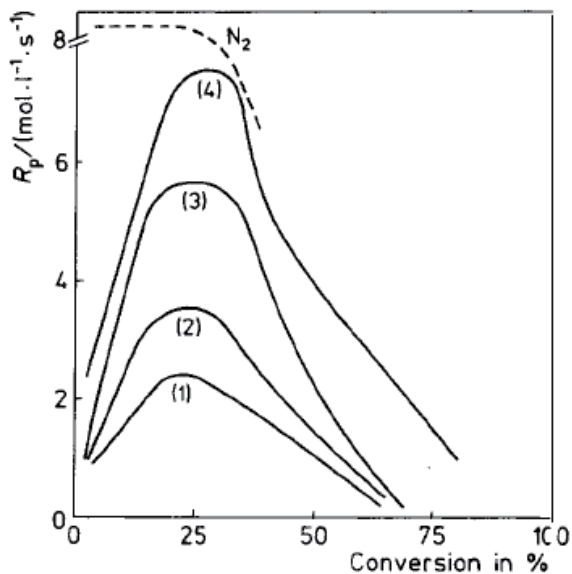


Fig. 7. Variation of the rate of photopolymerization, R_p , recorded by RT-FTIR spectroscopy for: (1) ethyldiethylenglycol monoacrylate, (EDGA) (2) EDGA + TPGDA, (3) tripropylenglycol diacrylate (TPGDA), (4) Oxazolidone monoacrylate. [Decker & Moussa, 1988]

2.5 Additives: Photosensitizers

In a recent paper [Beyazit et al., 2011] long wavelength free radical photopolymerization of (meth)acrylic monomers (TMPTA) is described. The polymerization was carried out using a conjugated thiophene derivative (3,2-diphenyldithieno[3,2-b-2,3-d]thiophene, DDT) as photosensitizer and a diphenyliodonium hexafluorophosphate ($\text{Ph}_2\text{I}^+\text{PF}_6^-$) as photoinitiator. The progress of conversion versus time as well as the final conversion level (Fig. 8) shows that the presence of DDT affects significantly the polymerisation of TMPTA. In general the extension of spectral sensitivity by adding a photosensitizer consists of an energy transfer processes as schematized in the following:



The photosensitizer is excited by light and it is able to transfer the energy, through orbital overlap, to the photoinitiator that is indirectly activated. In the cited work, the photosensitizer DDT that is photoexcited by a UV source in the range of 350–450 nm is rapidly quenched by the onium salt, which is transparent in that range.

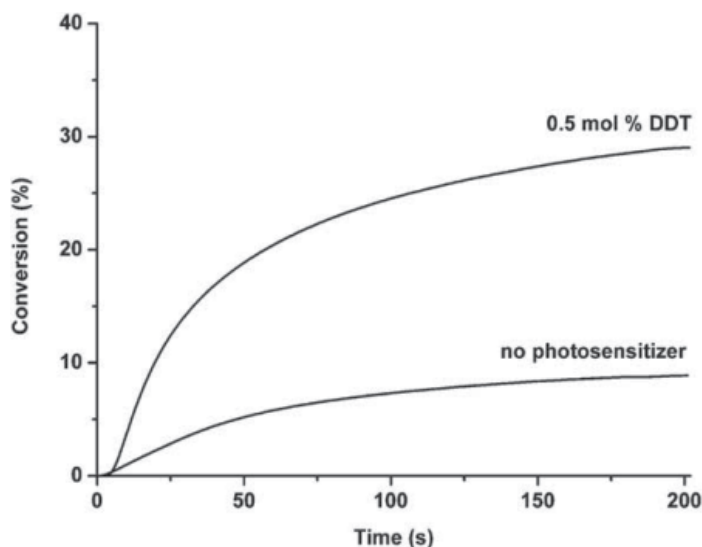


Fig. 8. Real-time FT-IR conversion curves as a function of irradiation time for TMPTA w/wo a photosensitizer, DDT. [Beyazit et al., 2011]

2.6 Fillers

Recently [Sangermano et al., 2008] reported for the first time the preparation of antistatic epoxy coatings via cationic UV curing of an epoxy resin in the presence of a very low content of carbon nanotubes (CNT). After dispersing the CNT into the epoxy resin, in the range between 0.025–0.1 wt.-%, the formulations were cured by means of UV light in the presence of a sulfonium salt as cationic photoinitiator.

The effect of the presence of CNT on the photopolymerization process was investigated by means of real-time FT-IR. The conversion curves as a function of irradiation time for the epoxy resin with and without CNT are presented in Figure 9.

The high reactivity of the epoxy groups results to a quite high initial rate of polymerization (slope of the curve). The epoxy groups' conversion levels off, after 2 minutes of irradiation, to a value of about 60%. This is due to the formation of a glassy polymer network, which hinders the mobility of the reactive species so that a large number of un-reacted epoxy groups remained trapped. Introduction of CNT leads to a slight decrease if the epoxy group photocuring rate compared to the neat epoxy system. In addition, the final conversion (after 120 seconds of irradiation) decreases from about 60% to 50%.

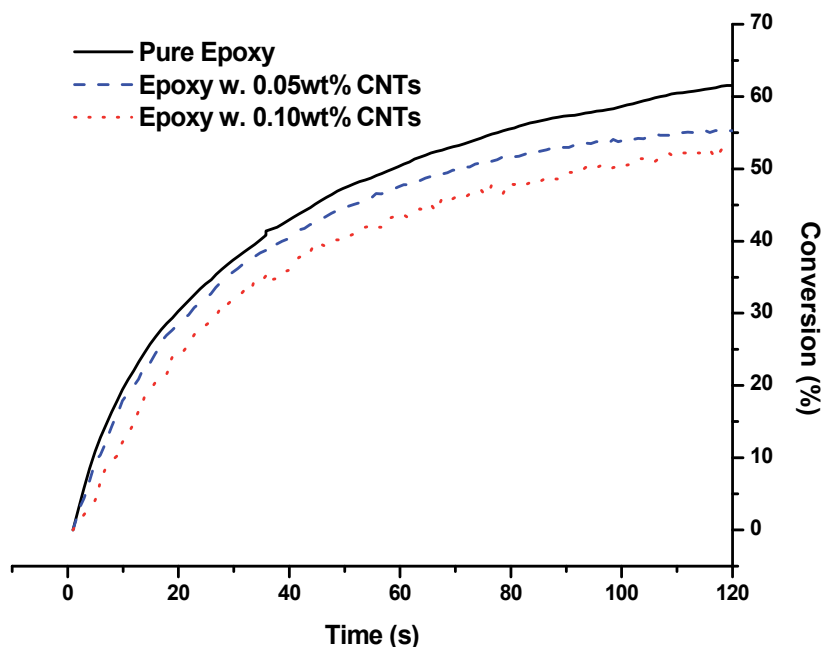


Fig. 9. RT-FTIR conversion curves as a function of irradiation time for dicycloaliphatic epoxy resin and in the presence of increasing amount of CNT. [Sangermano et al., 2008]

2.7 Thickness and photoinitiator concentration

In a clear formulation, UV radiation is absorbed mainly by the photoinitiator, so that the curing depth is directly controlled by its concentration. For each specific application, the best compromise must be found between curing speed and depth. Ideally, the initiation wavelength should be selected so that the initiator is the only absorbing specie.

By selecting an initiation wavelength where the monomer does not absorb, one can significantly increase the maximum photoinitiation rate and the rate of spatial propagation of the polymerization front. It is advantageous to use photobleaching initiators whose light absorption is higher than the one of the initiator products, thereby allowing more light to pass through the system.

Simulation results have confirmed that, at any given time, the initiation rate profile resembles a wave front, and the breadth of this front is determined by factors such as:

- Initial initiator concentration;
- Molar extension coefficient

Fouassier & Rabek, 1993, show that there is an optimum initiator concentration for the efficient photopolymerization of thick samples (Fig. 10). As the initiator concentration is increased, the initiation rate at the surface is increased, but the rate of propagation of the front through the sample is decreased.

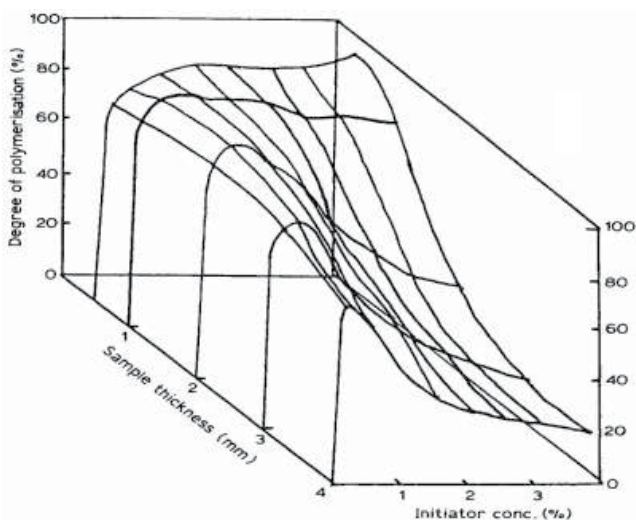


Fig. 10. RT-FTIR conversion curves as a function of sample thickness and concentration of the initiator [Fouassier & Rabek, 1993].

Low initiator concentration and/or photoinitiator of low extinction coefficient is required for the photocuring of thin films:

- A low molar absorptivity allows more efficient penetration of light into the sample; however, a higher molar absorptivity leads to higher rates of photon absorption and higher rates of bleaching.
- As the initiator molar absorptivity increases, so does the maximum initiation rate, the breadth of the propagating front decreases, and the rate of spatial propagation through the sample decreases.

2.8 Light Intensity

Lovell et al., 1999 investigated the photo-copolymerization of 50/50 BisGMA/TEGDMA at various light intensities (0.4, 1.5, and 2.9 mW/cm²). The effect of light intensity on the polymerization rate of the comonomer mixture at 25°C is depicted in Figure 11. The maximum rate of polymerization and the final conversion are both significantly affected by the differences in light intensity. Increasing the intensity of the UV light from 0.4 to 2.9 mW/cm² leads to an increase of the maximum rate to more than double. This is a clear investigation/result evidencing the effect of light intensity to photocuring reaction.

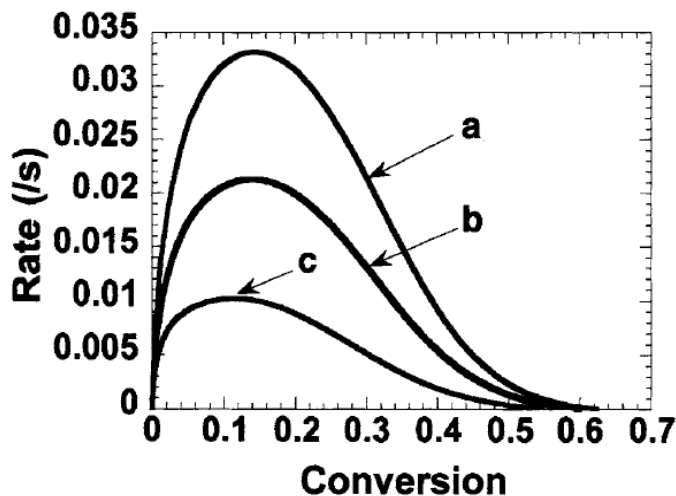


Fig. 11. Rate of polymerization of 50/50 BisGMA/TEGDMA (25°C) as a function of double-bond conversion for various light intensities of (a) 2.9 mW/cm², (b) 1.5 mW/cm², and (c) 0.4 mW/cm². [Lovelh et al., 1999]

3. Conclusion

Real-Time FTIR spectroscopy has been used extensively for the monitoring of UV-induced polymerization reactions. As shown in the present chapter starting from the pioneer work of Prof. Decker in the late 80s RT-FTIR has been proven to be a powerful technique, which allows following such reactions quantitatively, even if they occur in fraction of a second. Using this technique it is possible to calculate the conversion as a function of irradiation time during the progress of a reaction. From this data the polymerization rate can be calculated at any time, obtaining the true rate of photopolymerization and the amount of the residual reactive groups in the cured polymers. The efficiency of new photoinitiators as well as the reactivity of the different monomers can be studied in detail. Furthermore, the effect of experimental parameters on the photopolymerization rate and on the final conversion can be investigated in depth.

The RT-FTIR spectroscopy has a number of advantages over other existing methods:

- Real-Time monitoring, providing a species analysis of the quasi-instant liquid-solid phase change in a fraction of a second.
- The great sensitivity of IR spectroscopy allows very small changes in the monomer concentration to be detected.
- The kinetics of cure reactions can be studied over a very broad range of light intensity.

In spite of a number of advantages the RT-FTIR spectroscopy has also several limitations, such as:

- The sample thickness is limited to the range 1-100 μm .
- It is not possible to investigate samples containing black pigments and high concentration of other coloured pigments.
- The coatings support must be transparent to IR radiation.

4. References

- Amerio, E.; Sangermano, M.; Colucci, G.; Malucelli, G.; Messori, M.; Taurino, R. & Fabbri, P. (2008) Organic-inorganic hybrid coatings containing polyhedral oligomeric silsesquioxane (POSS) blocks: UV curing and characterization of methacrylic films *Macromol. Mater. Eng.*, 293, pp(700-707).
- Beyazit, S.; Aydogan, B.; Osken, I.; Ozturk, T. & Yagci, Y. (2011). Long wavelength photoinitiated free radical polymerization using conjugated thiophene derivatives in the presence of onium salts *Polym. Chem.*, 2 pp(1185-1189).
- Decker, C. & Bendaika T. (1984). Photopolymérisation de macromères multifonctionnels - I. Étude Cinétique Original Research *Europ. Polym. J.*, 20, pp(753-758).
- Decker, C. & Moussa, K. (1988). A new method for monitoring ultra-fast photopolymerizations by real-time infra-red (RTIR) spectroscopy *Makromol. Chem.*, 189, pp(2381-2394).
- Fouassier, J.P. & Rabek J.F. (1993). *Radiation Curing in Polym. Sci. Tech.*, Vol. I-IV, Elsevier, London.
- Lombardi, M.; Guerriero, A.; Kortaberria, G.; Mondragon, I.; Sangermano M. & Montanaro, L. (2011) Effect of the ceramic filler features on the properties of photo-polymerized BaTiO₃-acrylic composites *Polym. Compos.*, 32, pp (1304-1312).
- Lovelh, L.G.; Newman, S.M. & Bowman, C.N. (1999) The Effects of Light Intensity, Temperature, and Comonomer Composition on the Polymerization Behavior of Dimethacrylate Dental Resins *J Dent Res*, 78, pp (1469-1476).
- Sangermano, M.; Pegel, S.; Pötschke, P. & Voit B. (2008). Antistatic epoxy coatings with carbon nanotubes obtained by cationic photopolymerization *Macromol. Rap. Comm.*, 5 pp(396-400).
- Studer, K.; Decker, C.; Beck, E. & Schwalm, R. (2003) Overcoming oxygen inhibition in UV-curing of acrylate coatings by carbon dioxide inerting, Part I *Prog. Org. Coat.*, 48 pp(92-100).

Section 3

Materials Technology

Characterization of Compositional Gradient Structure of Polymeric Materials by FTIR Technology

Alata Hexig and Bayar Hexig*
*Department of Biomolecular Engineering,
Graduate School of Bioscience and Biotechnology,
Tokyo Institute of Technology, Nagatsuta-cho,
Midori-ku, Yokohama
Japan*

1. Introduction

Biomimetic and bioinspired optimal structures combining bioresorbable, bioactive and other advanced properties are expected for the next generation of biomaterials (Bruck et al., 2002, Hench et al., 2002, Akaike et al., 2005). Inspired by nature, to reveal the relationship between structure and functionality of biological materials has been emphasized in the biomaterials research field. In nature, gradient biological structures exist most commonly, such as the structure of bamboo (Amada et al., 1997), shells, teeth, bones, tendon and extracellular matrix (ECM) (Suresh et al., 2001). Man-made functionally gradient materials (FGMs) have been developed for combining irreconcilable properties within a single material and have been widely incorporated in metal/ceramic and organic/inorganic material fields for increasing the structural complexity and combining different functionality (Suganuma et al., 1983, Ishikawa et al., 2002, Czubarow et al., 1997). FGMs are spatial composites within which the composition or structure and thus the functions of the materials continuously or step-wisely vary along the specific coordinates. Examples of the structural change include those in crystal structure and orientation, porosity, particle size and so on.

The concept of FGMs first originated in Japan in 1984-1985 in the spacecraft project (Kawasaki et al., 1987). FGMs are developed to give two conflicting properties such as good thermal conductivity and good thermal resistance into one material. In general, we see uniformed functions and properties within the materials we use. However, in FGMs we see different functions between one part and the other of them. In a metal-ceramic FGM, the metal-rich side is placed in the region where mechanical performance, such as toughness, needs to be stronger; and the ceramic-rich side, which has better thermal resistance, is exposed to high temperatures, or placed in the region where there is a potentially severe temperature variation (Dao et al., 1997). In FGMs, the properties change gradually with position due to the spatial gradients in composition, density, microstructural arrangement or atomic-order, which

* Corresponding Author

contribute to distribute thermal stresses, to reduce mechanical stress, and to improve interfacial bonding between dissimilar materials. This kind of materials also provides other functional properties depending on their constituents of composites, such as gradient optical polymers and multifocal lenses (Zuccarello et al., 2002, Kryszewski et al., 1998, Ma et al., 2002).

Recently, there have been many efforts to develop polymeric FGMs with unique properties and advanced functions that are inaccessible in conventional uniform systems (Agari et al., 1996, Kano et al., 1997, Xie et al., 1998,). In particular, compositional gradient biodegradable polymeric materials have many potential applications for biomedical devices and tissue engineering, and we consider they may lead to a wide range of new generation of biomedical materials. Polymeric FGMs have great potential to be used in various fields such as separation membrane, adhesive, and biomedical materials including artificial skin, artificial bone and teeth, drug delivery system, and so on. However, the difference in structure, functional group, miscibility, solvent, and thermal treatment, induced a large complexity for designing, preparing, confirming, and characterizing polymeric FGMs. Many preparation approaches have been developed to generate a polymeric functionally gradient structure during homogenization or segregation processes. Despite these efforts made recently to generate polymeric FGMs, characterization of their gradient structure, physico-chemical properties and elucidation of formation mechanisms still remain to be explored. In this chapter, we will mainly discuss the confirming methods of compositional gradient structure of polymeric FGMs using FT-IR technology (such as ATR-FTIR, Mapping measurement of FTIR, and PAS-FTIR). FT-IR has been proven to be a powerful technique for characterizing the compositional differences of gradient film materials from surface to inside, and also on cross section. In our previous studies, four different compositional gradient polymeric materials have been prepared in miscible or immiscible blend systems, and in all these works, FT-IR has been applied as a main method for confirming the compositional gradient structure of the prepared materials (Hexig et al., 2005, 2010).

2. ATR-FTIR for confirming the compositional difference between two surfaces of polymeric FGM film

The consentaneous confirming standard for polymeric materials with gradient structure has not been established yet. In general, ATR-FTIR can give the information about chemical composition in the range from the top surface into a few μm deep. We have been utilizing ATR-FTIR for confirming the compositional difference between two surfaces of polymeric FGMs.

We successfully prepared a novel polymeric material with compositional gradient in a binary miscible biodegradable polymer blend system, that is, poly(butylene succinate)(PBS)/poly(ethylene oxide)(PEO) blend through controlling interdiffusion process at a temperature above the melting points of both components. The semicrystalline polymer PEO has attracted much attention and has been extensively investigated both experimentally and theoretically during recent decades (Allen et al., 1999). PEO is biocompatible, biodegradable, and water-soluble polymer (Dormidontova et al., 2002). These specific features of PEO make it applicable for drug delivery purposes, and it also has potential for other biomedical applications. PEO is miscible with several amorphous polymers through hydrogen bonding interaction (Miyoshi et al., 1996), and is also miscible with crystalline polymers, such as, poly(ethylene succinate)(PES) (Chen et al., 2000), and poly(3-hydroxypropionate) (PHP) (Na et al., 2002), while it is partly miscible or immiscible

with bacterial (PHB) (He et al., 2000). Poly(1,4-butylene succinate)(PBS) is a biodegradable aliphatic semi-crystalline polymer and flexible thermoplastic polyester (Uesaka et al., 2000). The miscibility and crystallization behavior in homogenous blends of PEO/PBS have been investigated by DSC and optical microscopy. PEO and PBS were found to be miscible in the amorphous phase (Qiu et al., 2003).

2.1 Sample preparation and creation of gradient film

The films of PBS, PEO and the binary blend of PBS/PEO were prepared by solution casting method. Pure PBS and PEO films with thickness of $200 \pm 10 \mu\text{m}$ were laminated together under pressure of 5 Mpa to obtain the bilayered film, and then used for preparation of gradient film. The laminated PBS/PEO film was annealed at $140 \text{ }^\circ\text{C}$ for 24 hours in an oven in the vacuum condition. By this way, we could generate a continuous gradient structure in the thickness direction, which is difficult to achieve by a conventional stepped multi-layer process.

2.2 Attenuated Total Reflectance Fourier Transform Infrared (ATR/FT-IR) spectroscopy

ATR-FTIR spectra were recorded on a AIM-8800 FT-IR spectrometer (Shimazu Co.Ltd. Japan) equipped with a Diamond EX'Press in order to analyze the chemical composition of the surfaces. The sum of 64 scans with a resolution of 4cm^{-1} was used to obtain the spectra.

2.3 Results of ATR-FTIR measurements

Figure 1 shows the ATR-FTIR spectra of the film surface of pure PBS, PEO and 50/50 (wt%/wt%) PBS/PEO blend. The peak centered at wavenumber 1724 cm^{-1} corresponding to

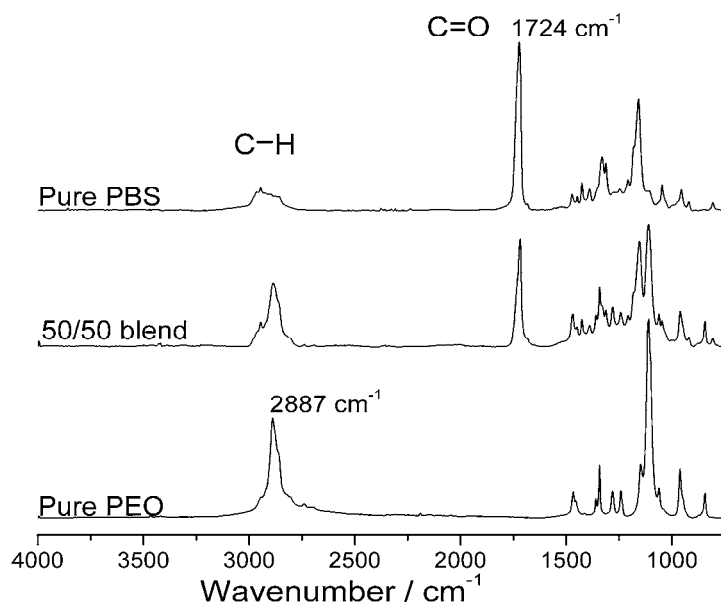


Fig. 1. ATR-FTIR spectra of pure PBS, PEO, and 50/50(wt%/wt%) PBS/PEO binary blend observed at room temperature.

the carbonyl vibration region of PBS and that at 2887cm^{-1} corresponding to the C-H stretching region of PEO were detected for the pure PBS and PEO films, respectively, at room temperature. Both of these characteristic peaks also appeared in the 50/50(wt%/wt%)PBS/PEO blend film. There are also some bands in the C-H stretching region in the spectrum of pure PBS, but they are very weak and broad. Therefore, the two peaks at 1724 cm^{-1} and 2887 cm^{-1} can be used to analyze qualitatively the contents of the PBS and the PEO components at the arbitrary position in the compositional gradient film. The difference of the chemical composition between the two surfaces of the compositional gradient film was examined by means of ATR-FTIR, as shown in Figure 2. It shows that the PBS has notably diffused to the PEO side while a comparatively small fraction of PEO diffused to the PBS side, implying that the composition varies from one side to the other side of the film.

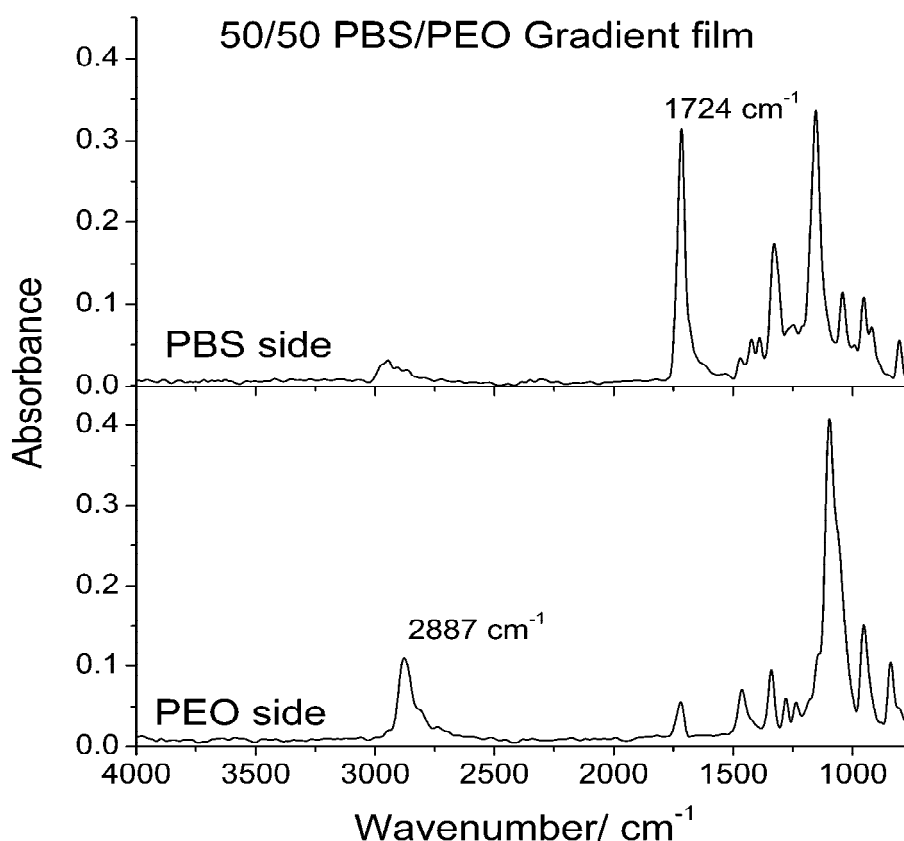


Fig. 2. ATR-FTIR spectra on both surfaces of the compositional gradient film observed at room temperature.

3. FT-IR mapping measurements for characterizing the compositional change along the thickness direction of polymeric FGMs

The fact that only a limited amount of miscible biodegradable polymer pairs are available constrains preparation of biodegradable polymeric gradient materials with high quality and

a wide range of applications. In the case of immiscible polymer system, the contributions from favorable intermolecular interactions are not enough to overwhelm the unfavorable contribution arising from the solubility parameters (Coleman et al., 1991). The addition of low molecular-weight agent is a well-known way to modify polymeric material properties and even improve the miscibility in case of immiscible polymer blends.

Our interest is to develop a new strategy for creation of functionally gradient polymeric composite materials in immiscible polymer blend system utilizing the miscibilization effect of low molecular-weight agent. Two kinds of commercially available biodegradable polymers, namely, a random copolyester, poly(butylene adipate-co-44 mol% butylenes terephthalate)[P(BA-co-BT)] and water-soluble poly(ethylene-oxide)(PEO) are chosen for this purpose, because P(BA-co-BT) and PEO are immiscible over the whole range of blend composition, but two components become miscible in the presence of optimum amount of low molecular-weight component 4,4'-thiodiphenol (TDP) as reported in our previous study (Hexig et al., 2004). It has been found that a suitable content of TDP has the ability to improve the miscibility between P(BA-co-BT) and PEO through intermolecular hydrogen bonding interaction, as revealed by DSC and FT-IR measurements (Figure 3). In this work, we demonstrate the generation of compositional gradient phase structure in the immiscible P(BA-co-BT)/PEO system through improving the miscibility between two components by the formation of TDP-mediated hydrogen bonds. The formation of compositional gradient was confirmed by FT-IR mapping measurement.

3.1 Sample preparation and creation of gradient film

The films of pure P(BA-co-BT), pure PEO, binary blends P(BA-co-BT)/TDP(92/8 wt%/wt%) and PEO/TDP (92/8 wt%/wt%), and the ternary blend of P(BA-co-BT)/PEO/TDP containing a constant composition(8wt%) of TDP with various P(BA-co-BT)/PEO ratios were prepared by conventional solution casting method. 5wt% Polymer solution in 1,4-dioxane was stirred for 6-8 h and cast on a Teflon dish. The solvent was allowed to evaporate slowly for 1 day at ambient temperature. The resulted films were then dried in a vacuum oven at 50 °C for 2 days to remove residual solvent and subsequently compression molded between Teflon sheets for 3 min at 160 °C under pressure of 5MPa by using laboratory press (Mini Test Press-10, Toyoseiki Co., Japan).

An *in situ* formation process that we used to create the gradient films is illustrated schematically in Figure 4. The low molecular weight TDP is expected to enhance the miscibility and induce the interdiffusion process. Firstly, the films of P(BA-co-BT)/TDP(92/8 wt%/wt%) and PEO/TDP (92/8 wt%/wt%) with thickness of 200 ± 10 μm were laminated together under pressure of 5 Mpa at room temperature to obtain a bilayered film, and then the laminated film was annealed at 140 °C in a vacuum oven to generate a gradient structure. In order to investigate the effect of gravity on the interdiffusion process, two laminated films were annealed in the same time, the one consists of P(BA-co-BT)/TDP(92/8 wt%/wt%) and PEO/TDP(92/8wt%/wt%) at the top and the bottom side, respectively, and the other one has the arrangement reverse to the first one. During the annealing process, the gradient structure of the resulted films was analyzed for several times and the best gradient phase in the whole thickness range was obtained after 12 hours annealing for both the films. The same process was also performed for the laminated film of P(BA-co-BT)/PEO without adding TDP.

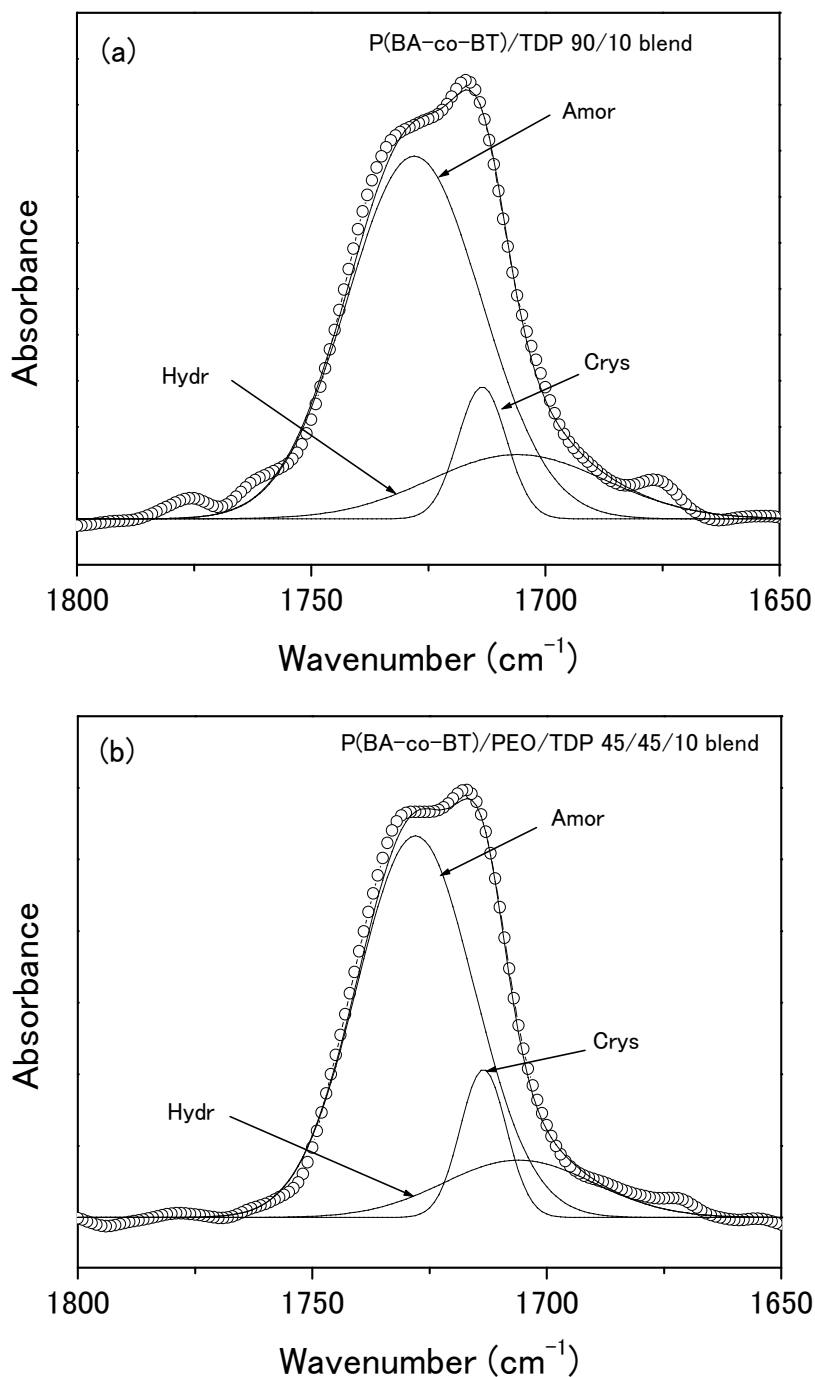


Fig. 3. Infrared spectra in the carbonyl stretching region for binary P(BA-co-BT)/TDP=90/10 blend (a) and ternary P(BA-co-BT)/PEO/TDP=45/45/10 blend (b) resolved by curve-fitting program; Amor.: amorphous component; Crys.: crystalline component; Hydr.: hydrogen-bonded component; Fitt.: curve-fitted; Exp.: experimental spectrum.

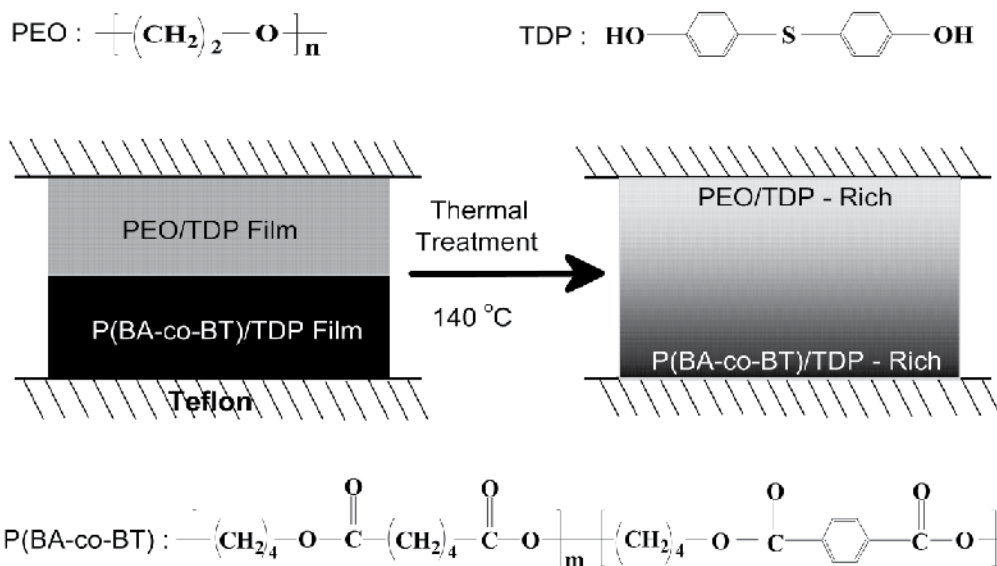


Fig. 4. Schematic illustration of the formation of P(BA-co-BT)/PEO/TDP compositional gradient film.

3.2 FT-IR microscopy and mapping measurements

The films of polymer blends used for the measurements of FT-IR were prepared by casting the polymer solution on the surface of a silicon wafer and dried under vacuum condition for 2 days. The film used in this study was thin enough to obey the Lambert-Beer law (<0.6 absorbance units). FT-IR spectra were recorded on a Perkin-Elmer Spectrum 2000 spectrometer using a minimum of 64 co-added scans at a resolution of 4cm⁻¹. Nitrogen was used to purge CO₂ and gaseous water in the detector and sample compartments prior to and during the scans.

The sample for FT-IR mapping measurement of the film cross-section was prepared by slicing the film with microtome. FT-IR mapping measurements of the compositional gradient films were carried out by using a AIM-8800 FT-IR microscope (Shimadzu Co.Ltd. Japan) equipped with a Diamond EX'Press. A square aperture of 30 x 30 μm was set on one side of the cross section and the aperture is automatically movable under a setting program. The 30 x 30 μm square aperture was displaced 50 times by a step of 10 μm. The sum of 64 scans with a resolution 4 cm⁻¹ was averaged at each step. The spectra were then accumulated together to make a mapping mode spectrum.

3.3 Results

Figure 5 shows the FT-IR spectra of pure TDP, pure PEO, pure P(BA-co-BT), and their blends of P(BA-co-BT)/TDP92/8(wt%/wt%), PEO/ TDP92/8(wt%/wt%), and P(BA-co-BT)/PEO/TDP46/46/8(wt%/wt%wt%). The peaks centered at wavenumber 1488cm⁻¹, 1596cm⁻¹ and 1612cm⁻¹ corresponding to the C=C stretching region of TDP were detected for the pure TDP at melting state and all its blends, indicating that TDP in the blends is in the amorphous state. The peak centered at wavenumber 1724 cm⁻¹ corresponding to the

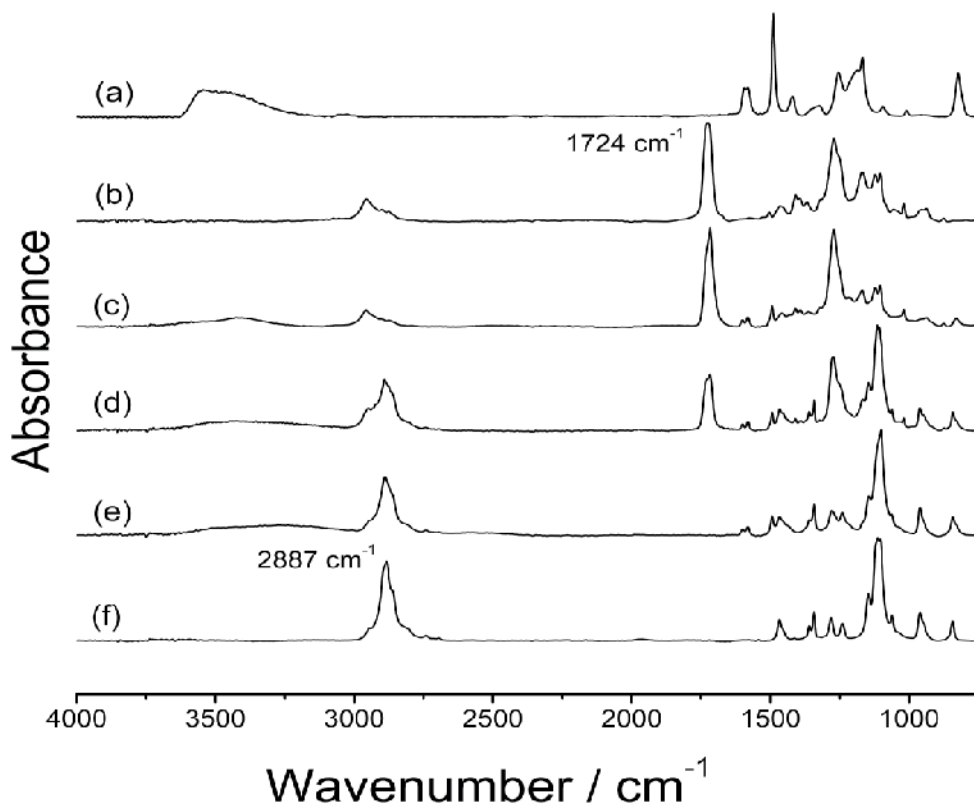


Fig. 5. FT-IR spectra of (a) pure TDP at 160°C, and (b) pure P(BA-co-BT), (c) 92/8 (wt%/wt%) P(BA-co-BT)/TDP binary blend (d) 46/46/8 (wt%/wt%/wt%) P(BA-co-BT)/PEO/TDP ternary blend (e) 92/8 (wt%/wt%) PEO/TDP binary blend, (f) pure PEO observed at room temperature.

carbonyl vibration region of P(BA-co-BT) and that at 2887 cm^{-1} corresponding to the C-H stretching region of PEO were detected for the pure P(BA-co-BT) and PEO films, respectively. Both of these characteristic peaks also appeared in the ternary 46/46/8 (wt%/wt%/wt%) blend film. There are some characteristic bands in the C-H stretching region in the spectrum of pure P(BA-co-BT), but they are very weak and broad. Therefore, the two peaks at 1724 cm^{-1} and 2887 cm^{-1} were used to analyze qualitatively the contents of the P(BA-co-BT) and PEO components, respectively, at the arbitrary position in the compositional gradient film.

The compositional change along the film thickness direction in the annealing process was investigated by FT-IR mapping measurements on the cross section of the resulted films after annealed for different times. In Figure 6, the intensities of the P(BA-co-BT) C=O, PEO C-H, and TDP C=C absorption peaks are plotted against the position in the film thickness direction. It reveals that the interdiffusion process begins from the interface between the P(BA-co-BT)/TDP and PEO/TDP blends, and develops towards the two outer surfaces of the film. Finally, a well-structured continuous compositional gradient along the film thickness direction was formed after 12 hours annealing.

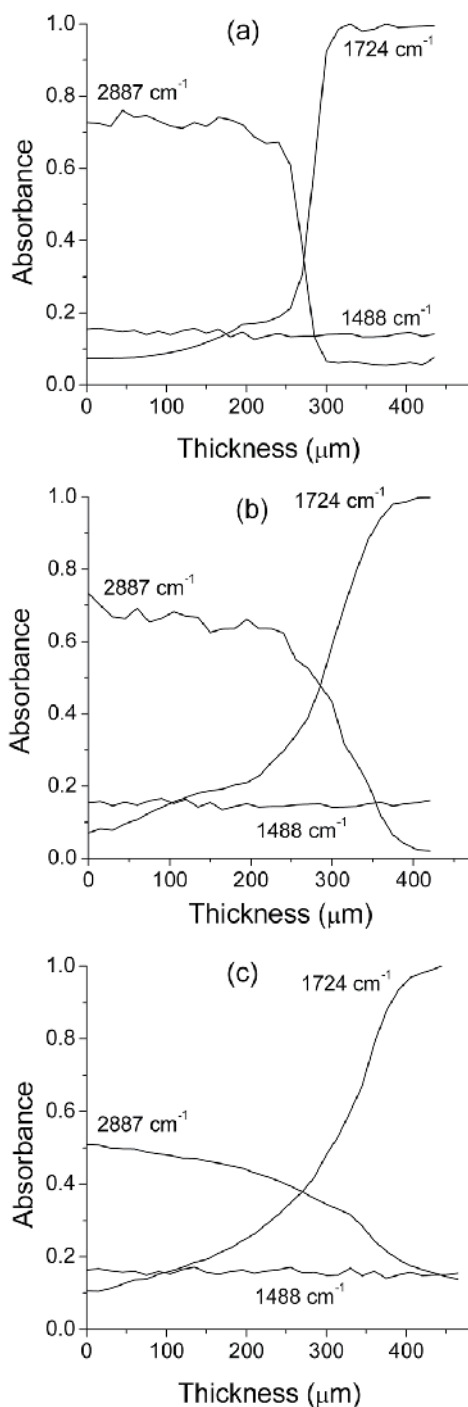


Fig. 6. Plots of the peak intensity of the P(BA-co-BT) C=O, PEO C-H, and TDP C=C absorptions along the thickness direction of the resulted films after annealed for (a) 4 hours, (b) 8 hours, and (c) 12 hours.

The results of FT-IR mapping measurements on the cross section of the resulted film are shown in Figure 7. It is clearly seen that the peak intensity of P(BA-co-BT) C=O vibration absorption at 1724cm^{-1} continuously increases along the thickness direction while that of the PEO C-H stretching absorption at 2887cm^{-1} decreases along the same direction. The weak bands centered at about 1600cm^{-1} and 1488cm^{-1} characteristic for TDP appear in all spectra and their peak intensities are almost constant over the whole thickness range, indicating that the TDP content is almost the same over the whole range in the thickness direction of the gradient film.

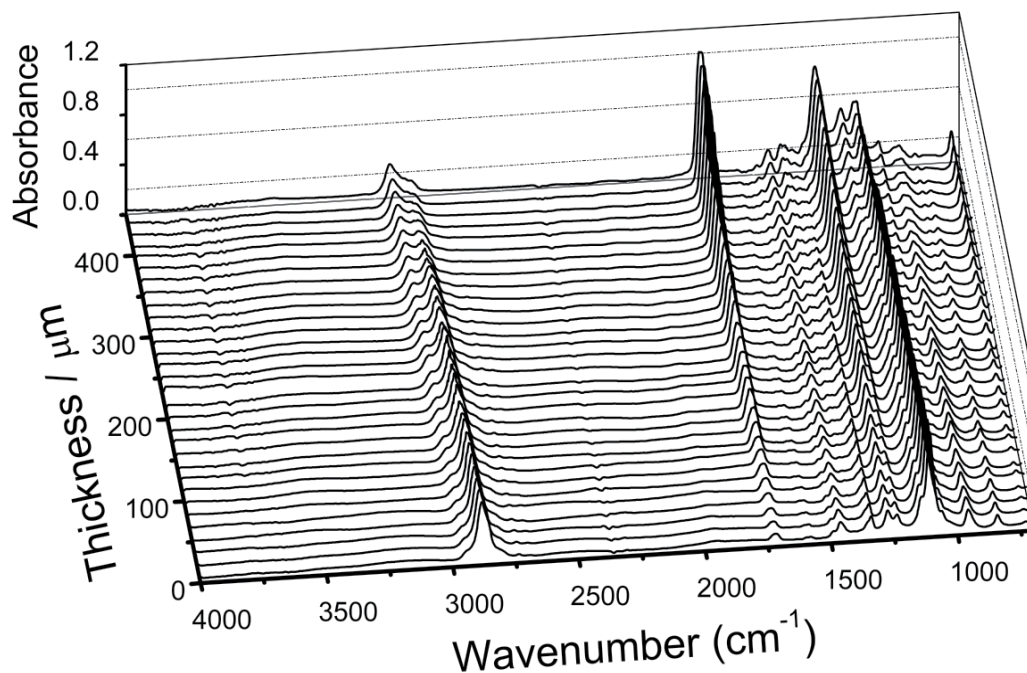


Fig. 7. Results of FT-IR mapping measurements on the cross section along the direction vertical to the sample surface.

The presence of a suitable content of TDP transformed the immiscible P(BA-co-BT)/PEO blend system into a miscible one through the intermolecular hydrogen bonding interactions, as experimentally demonstrated by DSC and FT-IR measurements (Hexig et al., 2004). In a miscible system, the favorable intermolecular interactions overwhelm the unfavorable intermolecular interactions and the free energy of the system decreases with mixing (Pines et al., 1972). As a result, the bilayered miscible polymer film shows a tendency towards homogeneous mixing. One more important factor is that the constant breaking and reforming of the hydrogen bond at a temperature above the glass transition (Coleman et al., 1991), especially at the high temperature used in this process provided the possibility and approach for the interdiffusion to occur. The optimal gradient structure can be obtained in the homogenizing process by controlling the interdiffusing time. The peak intensity of TDP C=C absorption is almost constant over the whole thickness range at all the annealing time, indicating that the motion of TDP is an isotropic thermal motion. The mapping measurements also revealed almost the same results for the films regardless that the upper

side in the annealing process was the PEO/TDP or the P(BA-co-BT)/TDP blend, indicating that the gravity has no effect on the gradation process.

4. PAS-FTIR as a non-destructive, non-contact confirming method of compositional gradient structure

Plasma technology can add functional groups to a surface of organic and inorganic materials at the molecular level, changing surface chemistries for increased bond strength, wettability, permeability, and activating and changing surfaces from hydrophobic to hydrophilic without affecting the bulk properties. The compositional gradient structure in hyaluronic acid (HA) and thermal responsible poly(N- isopropylacrylamide) (PIPAAM) blend film was self-organized during solvent evaporation process on the oxygen-plasma treated polystyrene dish (PTPSD), while on the non-treated polystyrene dish (NTPSD) nearly homogenous blend film was formed at ambient temperature. HA is a naturally occurring linear polysaccharide widely distributed in body as components of the extracellular matrix (ECM) of connective tissues, and HA-based biomaterials have been recently utilized for a variety of clinical application and tissue engineering of skin, cartilage tissue, and bone based upon its specific properties, excellent biocompatibility and bioactivity (Kano et al., 1997, Zacchi et al., 1998, Aigner et al., 1998, Solchaga et al., 1999). PIPAAm is a synthetic polymer which has a sharp and reversible phase transition at ~ 32 °C and applicable in tissue engineering fields as a functional hydrogel and a cell sheet (Park et al., 2002, Yoshida et al., 1995, Yamada et al., 1990, 1993).

4.1 Experiments

4.1.1 Plasma-treatment of polystyrene dish

The plasma treatment was performed with a SWP-101EX (NISSIN Co, Ltd. Japan), using low-pressure region output power of the microwave oscillator at 2.0KW. Polystyrene dishes were set on the sample stage which was 15cm below the reactor. The oxygen discharge was utilized and the oxygen was filled at a rate of 500 cc/min and a pressure of 70 Pa. Plasma irradiation was performed for 15 seconds.

4.1.2 Film preparation

1% HA solution was prepared by dissolving powder HA (weight average molecular weight 1680.000 by GPC, Life Core Biomedical Inc) in distilled water with stirring for 24 hours. 1% PIPAAm solution was prepared by diluting 15% PIPAAm (weight average molecular weight 220.000 by GPC, Kohjin Co. Ltd) aqueous solution by distilled water with stirring for 24 hours. After then 1% HA and 1% PIPAAm solutions were mixed together at the same weight ratios and stirred further for 24 hours before casting on the PTPSD and NTPSD at ambient and vacuum conditions, respectively. All resulted sample films were heated at 80 °C under vacuum condition for 5 hours before characterization.

4.1.3 PAS-FTIR spectroscopy measurements

PAS-FTIR spectroscopy measurements were carried out on the JIR-SPX200 FT-IR spectrometer (JEOL Co. Ltd. Japan) equipped with a MTEC 300 photoacoustic cell (MTEC

photoacoustic Ames USA). Prior to the start of penetration experiment the cell was purged with helium for 30 seconds.

4.2 Results

The step-scan PAS-FTIR is a non-destructive, non-contact method with controllable sampling depth and need little or no sample preparation. Figure 8 shows the results of PAS-FTIR spectroscopy measurements on the films cast on NTPSD and PTPSD in vacuum condition. PAS-FTIR spectra of increasing shallow-sampling depth corresponding to different mirror velocities of 1.0, 2.0 and 5.0 mm/s indicate that the fractions of HA and

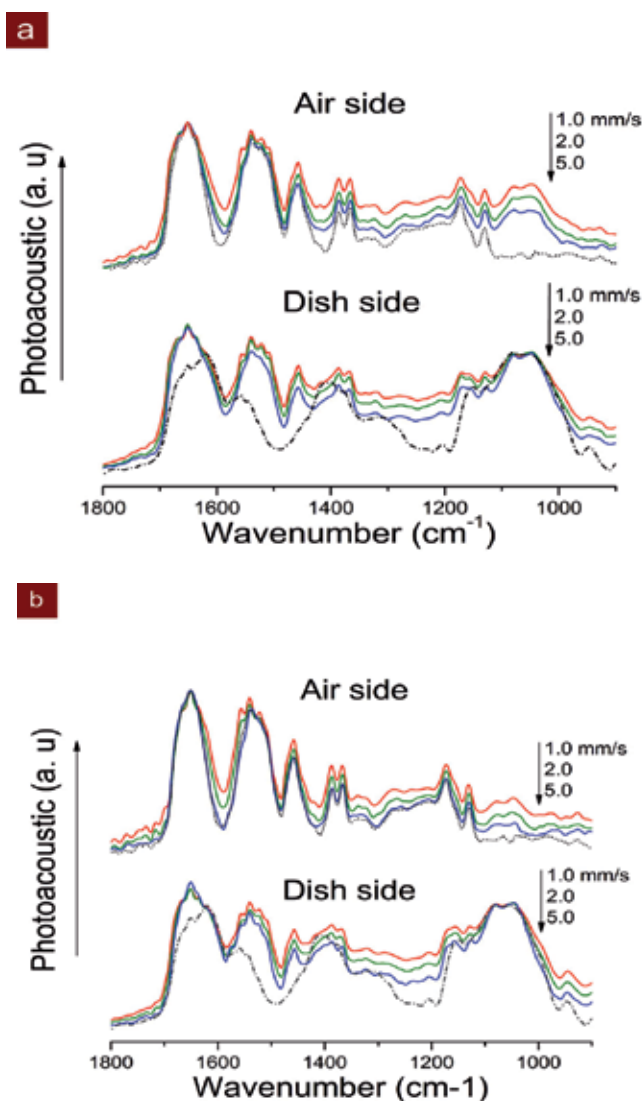


Fig. 8. Results of PAS-FTIR spectroscopy measurements on the films cast on NTPSD and PTPSD in vacuum condition.

PIPAAm gradually change from the surfaces to the inside of the film for both films cast on NTPSD and PTPSD. For the film cast on PTPSD in vacuum condition, more significant compositional difference was observed between the dish side and the air side than the film cast on NTPSD in vacuum. In combination with XPS and EDX mapping measurements on the films cast on NTPSD and PTPSD at ambient and vacuum conditions, respectively, it was revealed that both the oxidized hydrophilic surface and evaporation rate of water molecules contribute to the formation of an ideal gradient structure in the HA/PIPAAm blend system (Hexig et al., 2010).

5. Conclusions

Developing a methodology for characterizing the gradient structure is with the same importance as developing a method to generate the gradient structure. Utilizing ATR-FTIR spectroscopy, we can confirm the compositional difference between the two surfaces of the compositional gradient materials, while FT-IR mapping measurements can give a information of the compositional change on the cross section. The step-scan PAS-FTIR is a non-destructive, non-contact method reveals the compositional difference corresponding to the varying sampling depth. Thus, with a reasonable combination of these FT-IR spectroscopy measurements, we can characterized and confirm the compositional gradient of FGMs satisfactorily.

6. References

- [1] Bruck, H. A., Evans, J. J. & Peterson, M. L.. *Exp. Mech.* 42. 361-371 (2002).
- [2] Hench, L. L. & Polak, J. M. 295, 1014-1017 (2002).
- [3] Akaike, T. 35- 67 (Corona, Tokyo, Japan, 2005).
- [4] Amada, S., Ichikawa, Y., Munneka, T., Munekeata, T., Nagase, Y. & Shimizu, H. *Composites part B*, 28B, 13-20 (1997).
- [5] Suresh, S. *Science* 292. 2447- 2451 (2001).
- [6] Suganuma, K., Okamoto, T., Shimada, M. & Koizumi, M. *J. Amer. Ceram. Soc.* 66, c117-c118 (1983).
- [7] Ishikawa, T. *et al. Nature* 416, 64-67(2002).
- [8] Czubarow, P. & Seyferth, D. *J. Mater. Sci.* 32, 2121-2130 (1997).
- [9] Kawasaki, A. and Watanabe R., *J. Japan Inst. Merals*, 1987. 51. 525.
- [10] Ming Dao, Pei Gu, Akhilesh Maewal, and R. J. Asaro. *Acta mater.* 1997. 45. 3265
- [11] G. Zuccarello, D. Scribner, R. Sands, and L. J. Buckley, *Advanced Materials*. 2002, 14, 1261.
- [12] M. Kryszewski, *Polymers for Advanced Technologies*. 1998, 9, 244.
- [13] D. Ma, J. M. Lupton, R. Beavington, P.L. Burn, I. D. Samuel, *Adv, Funct, Mater.* 2002, 12, 507.
- [14] Y. Aragi, M. Shimada, A. Uede, *Macromol. Chem. Phys.* 1996, 197, 2017.
- [15] Y. Kano, S. Akiyama, H. Sano, *Polym. J.* 1997, 29, 158.
- [16] X. Xie, T. Xiao, Z. Zhang, A. Tanioka, *J. Colloid and Interface Sci.* 1998, 206, 189.
- [17] B. Hexig, H. Alata, N. Asakawa, Y. Inoue, *Sci. B Polym. Phys.* 2005, 43, 368.
- [18] B. Hexig, H. Alata, Y. Inoue, *J. Polym. Sci. B Polym. Phys.* 2005, 43, 3069.
- [19] B. Hexig, H. Alata, N. Asakawa, Y. Inoue, *Adv. Funct. Mater.* 2005, 15, 1630.

- [20] B. Hexig, K. Isama, Y. Haishima, T. Tsuchiya, Y. Inoue, T. Akaike, *Journal of Biomaterials Science* 2010, 21, 1957.
- [21] C. Allen, D. Maysinger, A. Eisenberg, *Colloids Surf. B* 1999, 16, 3.
- [22] E. E. Dormidontova, *Macromolecules*. 2002, 35, 987.
- [23] T. Miyoshi, K. Takegoshi, K. Hikichi, *Polymer*. 1996, 37, 11-18.
- [24] H-L. Chen, S-F. Wang, *Polymer*. 2000, 41, 5157.
- [25] Y-Ho. Na, Y, He. N. Asakawa, N. Yoshie, Y. Inoue, *Macromolecules*, 2002, 35, 727-735.
- [26] Y. He, N. Asakawa, Y. Inoue, *Polym Int*. 2000, 49, 609.
- [27] T. Uesaka, K. Nakane, S. Maeda T. Ogihara, N. Ogata, *polymer*, 2000, 41, 8449.
- [28] Z. B. Qiu, T. Ikehara, T. Nishi, *Polymer*. 2003, 44, 2799.
- [29] M. M. Coleman, J. F. Graf, P. C. Painter, *Specific Interaction and the Miscibility of Polymer Blends*, Technomic Publishing: Lancaster, PA, 1991.
- [30] B.Hexig, N. Asakawa, Y.Inoue, *J.Polym.Sci. Part B*, 2004, 42, 2971.
- [31] A. Pines, M. G. Gibby, and J. S. Waugh *J. Chem. Phys.* 1972. 56. 1776.
- [32] Kano, Y., Akiyama, S., Sano, H. & Yui, H. *Polym. J.* 29. 158-164 (1997).
- [33] Zacchi, V. *et al. J. Biomed. Mater. Res.* 40, 187-194 (1998).
- [34] Aigner, J. *et al. J. Biomed. Mater. Res.* 42, 172-181 (1998).
- [35] Solchaga, L. A., Dennis, J. E., Goldberg, V. M. & Caplan, A. I. *J. Orthop. Res.* 17, 205-213 (1999).
- [36] Park, J. U. & Tsuchiya, T. *J. Biomed. Mater. Res.* 60, 541-547 (2002).
- [37] Yoshida, R. *et al. Nature* 374, 240-242 (1995).
- [38] Yamada, N. *et al. Thermo-responsive polymeric surface; Makromol Chem Rapid Commun.* 11, 571-576 (1990). *J. Biomed. Mater. Res.* 27, 1243-1251 (1993).

Fourier Transform Infrared Spectroscopy – Useful Analytical Tool for Non-Destructive Analysis

Simona-Carmen Litescu¹, Eugenia D. Teodor¹,
Georgiana-Ileana Truica^{1,2}, Andreia Tache^{1,2} and Gabriel-Lucian Radu^{1,2}

¹Centre of Bioanalysis,

National Institute for Biological Sciences Bucharest

²Faculty of Applied Chemistry and Material Science,

University Polytechnica of Bucharest

Romania

1. Introduction

It is highly recognized that the use of Fourier Transform Infrared Spectrometry (FTIR) for chemical substances identification it is not a trivial task to be fulfilled by analytical chemists. The complexity of FTIR characterization comes mainly from the high degree of infrared absorption bands overlapping, that are difficult to be accurately ascribed, despite of the fact that up to date computer-searchable databases of spectra are currently available.

Regardless all these difficulties, FTIR analysis became the main used technique when specific analytical topics have to be addressed, mainly when non-destructive analysis is needed. In this respect, according to our opinion, challenging analytical issues are raised in two important cases; the first one is that when historic (archaeological) or artistic materials have to be analyzed while the second issue came from the analysis of highly- specific biomaterials. Starting from these points, the present chapter is addressing, as case studies, both issues: the FTIR assessment of peculiar archaeological samples, amber samples, and, respectively the FTIR assessment of a developed bio-mimetic system based on human lipoproteins immobilization on conductive solid supports. In both cases the restricted amount of samples and the emergent call for non-destructive analyses create constraints in the working procedure.

Consequently, we consider that the versatility of FTIR techniques (especially variable angle reflectance- FTIR, VAR-FTIR and attenuated transmittance-FTIR, ATR-FTIR) in solving these critical issues are presented and, moreover, supported with original experimental data.

2. Applicability of Fourier Transform Infrared technique in the assessment of archeological samples. Case study- Amber

Archaeology is a science dealing mainly with the reconstruction of past events by the mean of a cautious credentials and artefacts collection. Historical archaeologists usually encounter

on a list of so-called potential trace evidence, different items which require certain identification; the mentioned list may be formed by objects from various materials: paint, pottery, glass, bricks, liquid residues (oils, wines, and perfumes), fabrics, soil, metals etc. In order to rationalize on the evidences origin, source, transformation and historical age, the archaeologists need a deep analytical study, study that often has to be performed on irreplaceable pieces. Consequently, to accomplish these goals multiple analytical techniques, able to work as non-destructive techniques are used, such as: Fourier Transform Infrared Spectrometry (FTIR), scanning electron microscopy (SEM), polarized light microscopy (PLM) or X-photon spectrometry (XPS).

In our studies, in the amber analysis the main goal was to establish several criteria able to be useful in discrimination between different types of amber, the obtained FTIR information being used to ascribe the origin of the materials found in archaeological sites on the Romanian territory.

Amber is a fossil resin, extremely appreciated for its colour and beauty, and used as a gemstone from very early times. Natural amber deposits are found all around the world, the most famous being the ones from the Baltic sea, the Dominican republic, Sicily, Borneo, Spain, etc. Amber resources are documented in Romania since the late sixteenth century, around the village of Colți (Buzău County), but they have certainly been exploited only starting with the modern age, after 1828, in the same area (Ghiurcă, 1999; Wollmann, 1996).

The existence of a local amber exploitation on Romanian territory aroused the question of geological origin of amber artefacts found by Romanian archaeologists over time.

During recent years, analysts used mostly FTIR, mass spectrometry and pyrolysis-gas chromatography-mass spectrometry for the analytical study of geological or archaeological amber from different territories (Beck, 1972; 1986; Boon et al., 1993; Lambert & Poinar, 2002; Shedrinski et al., 2004; Angelini & Bellintani, 2005; Guiliano et al., 2007; Pakutinskiene et al., 2007; Tonidandel et al., 2008; Teodor ED et al., 2009; Virgolici et al., 2010a). In 2005, Angelini and Bellintani reviewed the analytical techniques used for the differentiation of amber types, dedicating special attention to the most suitable methods for archaeological materials (non-destructive methods).

There are a few comparative analytical studies of Romanian geological amber, referred to as Rumanite or Romanite, which conclude that Romanian amber is geologically younger, but chemically almost identical, to Baltic amber (Stout et al., 2000).

Regarding archaeological amber from Romanian territory, it was basically unstudied since we started our research project in 2007. Some studies by Nikolaus Boroffka on prehistoric amber (Boroffka, 2006) refer to chemical analyses of amber with an assumed Romanian origin; in another paper, Boroffka (2001) discusses the results published by Banerjee (Banerjee et al. 1999) for two prehistoric beads from Romania, both considered of Baltic origin.

As a hint for the archaeological output, in order to rationalize on the importance of non-destructive analysis, it should be mentioned that the quantity and quality of amber artefacts from Romania is lower than those found in territories placed on the track of the so-called Amber Route (Teodor ES et al, 2010). Nevertheless, from our studies, the Baltic amber is encountered very early, in Neolithic, i.e. only three isolated beads (not published), and only in southern Romania, as a clue that Danube may be considered as a secondary Amber Trail.

Local amber, Romanite, was also early used, as proved on some beads from the Middle Bronze Age from Pietroasa Mică, in a necropolis placed at the fringes of the Colți area. In our studies two types of amber have been investigated: artefacts from the largest amber deposit discovered in Romania, in Cioclovina cave (over 3000 beads, most of them in amber) (Teodor ES et al., 2010) and artefacts from Roman Age; discovered in cemeteries dug systematically, for instance in Tomis, Callatis, Beroe, or Carsium cemeteries (Virgolici et al. 2010b).

2.1 Assessment of amber origin based on FTIR analysis

Taking into account the lack of referential with respect to ascription of amber origin, and considering as critical issue the transformation occurring on amber samples during historical ages strongly influenced by the storing conditions in the deposits where were discovered, in the attempt of establishing few definite FTIR criteria to be useful for amber origin proper assignment we started the analysis not directly with archaeological samples but first, with geological amber, of controlled and certified origin, both from Baltic sources and from Romanian sources. Further obtained results are detailed.

2.1.1 FTIR method

FTIR assays of amber were performed using the FTIR-VAR technique with a beam incidence angle of 45°, on a Bruker TENSOR 27 instrument, using the OPUS software version 6.0. The samples were used without any pre-treatment, as whole pieces fixed on a gold mirror, and all the spectra were registered versus a background of clean gold foil between 4000 and 600 cm^{-1} . The spectral resolution was 4 cm^{-1} , and the co-added scans 96, with an aperture of 4 nm. The FTIR-VAR technique is able to provide the same information as FTIR in terms of transmittance, with a slight loss in signal intensity, but with the advantage of preserving samples integrity. In addition, the bounds between atom plans are not destroyed, and, as consequence, the amount of provided information increases.

2.1.2 Geological amber FTIR assessment

A large lot of samples from different controlled origins were analysed by FTIR-VAR, from Romania (Colti, Buzău County), from the Baltic region (Palanga and Kaliningrad), from Germany and Poland in order to settle a certain pattern to differentiate Romanian amber from other types of amber, especially the Baltic variety (the material was provided, mainly, from the National Geological Museum from Bucharest). In the case of unsure observations, to clarify some spectral zone from the fingerprint region (1300-900 cm^{-1}), or the region 1800-1450 cm^{-1} , the transmittance spectra of the samples were used for a better evaluation. Spectra were analysed and assigned on the three wave-numbers domains of significance for amber, namely those between 3600-2000 cm^{-1} , 1820-1350 cm^{-1} and the 1250-1045 cm^{-1} regions, which correlate with hydroxyl groups, carboxyl groups, carbonyl groups and with C=C instauration.

Subsequent data acquisition the following observations were drawn:

- a. There are no notable differences between Romanite spectra and Baltic spectra in the 3600-3000 cm^{-1} region mainly in case of geological samples. The noteworthy differences

appear (as in any IR technique) in the 'Baltic shoulder' region, 1250-1060 cm^{-1} , and in the 1161-1155 cm^{-1} region. For the Baltic amber, the shoulder appears in the region 1275-1155 cm^{-1} , while that of Romanite has a different shape and is shifted to about 1045-1020 cm^{-1} , as may be noticed from Fig. 1.

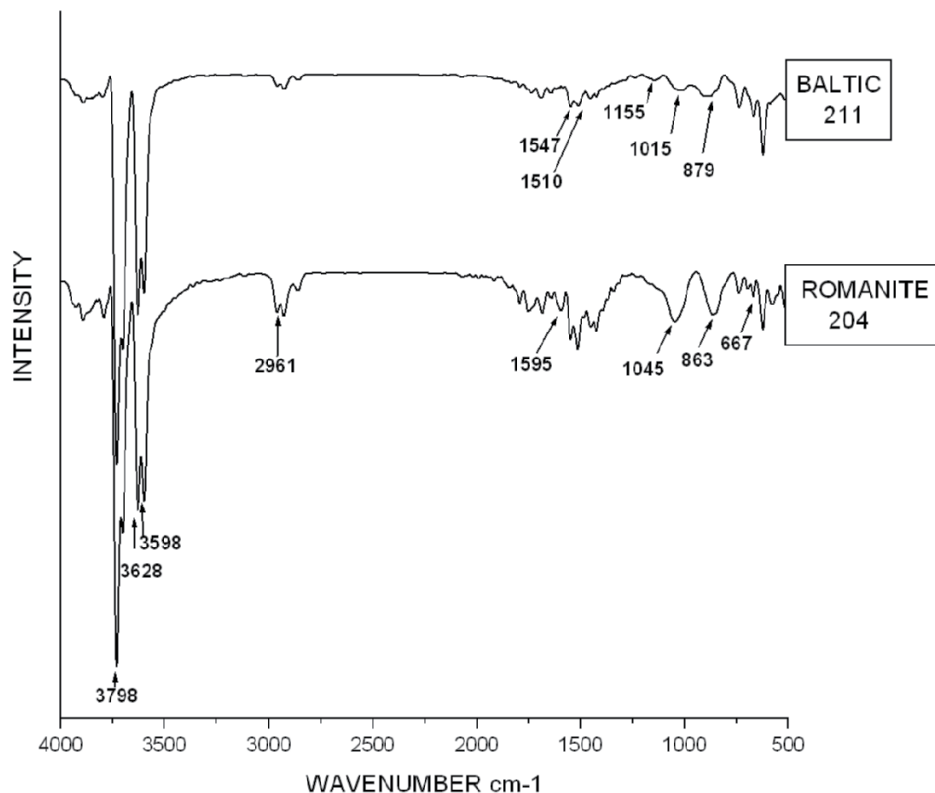


Fig. 1. The overlaid FTIR-VAR (reflectance) spectra, region 4000-600 cm^{-1} for geological reference Baltic amber (211) and reference Romanite (204)

- b. An important difference in Variable Angle Reflectance spectra is registered for absorption bands from 900-600 cm^{-1} region (Fig. 1); in this region two species can be differentiated, depending on the age of the polymer. The absence of some characteristic bands indicates that the contraction-reticulation of the polymeric chain is finished (connected with the older age of fossil resin); the absence of a double peak at 667 cm^{-1} in the Baltic amber spectra and the appearance of the shifted shoulder toward 1045 cm^{-1} , in the case of Romanite when compared to the Baltic shoulder, that occur at higher wavenumbers (demonstrated also by Fourier spectra de-convolution) provided evidence that Romanite was formed after Baltic amber (*i.e.*, it is younger), as it may be observed in Fig. 1.
- c. There are vibration frequency shifts determined by the degree of ethers and esters formation, correlated to the number of functional groups from the chain and showing evidence on the intramolecular bounds, which appear frequently in amber type resins with younger ages (for example the OH group, specific to Romanite, is slightly shifted

- due to intramolecular hydrogen bonds toward 1595 cm^{-1} , if compared to the Baltic amber where it occurs about 1640 cm^{-1}).
- d. The amber has an amorphous structure, and as consequence the reproducibility of determinations is affected by the heterogeneity of the sample, the obtained spectra depending on the analysed part of the sample. As a result of these observations, for each sample were registered two spectra, for different zones of sample, in order to observe if significant differences appear between the two, due to appearance/disappearance of certain absorption bands (specific vibration frequencies of interest). It was observed that difference between two spectra of the same sample appear only in the spectral region related to methyl, methylene, *etc.* ($-\text{CH}_3$, $-(\text{CH}_2)_n$ -, $-\text{CH}$, *etc.*) chains, namely $2962\text{--}2850\text{ cm}^{-1}$, and for the specific tensile bands of CH_3 from 1375 cm^{-1} . This led to the conclusion that the presence of functional groups (which are important because they correlate with the origin and the age of the sample, and giving the sample specificity) are equally distributed. Therefore it could be considered that the analytic information supplied by FTIR is acceptable, since the wavenumbers corresponding to carboxylic chains and hydroxy-carboxylic acids at $1547\text{--}1423\text{ cm}^{-1}$ for Romanite and, respectively, $1547\text{--}1300\text{ cm}^{-1}$ for Baltic amber are preserving their region for each duplicate recorded spectrum.

The differences appearing in the $1684\text{--}1642\text{ cm}^{-1}$ band of Baltic amber with respect to the 1547 cm^{-1} band of Romanite are determined by the shift of asymmetric vibration frequencies for the carboxylic type groups, as a function of the length of hydrocarbon chains. A strengthening-ageing of polymeric chains leads to shifts toward smaller wavenumbers. This can be observed also in $1046\text{--}900\text{ cm}^{-1}$ region, where the shifts toward the smaller wavenumbers are related to the better confirmation of the Baltic origin. The significant regions for each type of amber are summarised in Table 1, corresponding comment with respect to archaeological amber spectra being introduced at this point for a better understanding of the noticed differences.

2.1.3 Archaeological amber FTIR assessment

After analysis of geological specimens of amber, the next step was devoted to archaeological samples analysis. The investigated samples were originated from different times (Neolithic, Bronze Age, Roman Age, Byzantine period, etc) found on different archaeological sites from Romania.

Concerning the archaeological samples, the FTIR-VAR spectra pointed out some differences between the archaeological and geological material. Archaeological samples most generally presented a less intense signal in the $3600\text{--}3000\text{ cm}^{-1}$ region, which correlates with $-\text{OH}$ groups and influence the H bonds (Fig. 2); the presence of $-\text{OH}$ groups was confirmed by a signal of lower intensity for archaeological samples in the $746\text{--}736\text{ cm}^{-1}$ region, especially for Baltic amber, the relative dehydration of archaeological samples as compared to geological materials being the probable cause (Fig. 2).

The fingerprint zone is different in most of archaeological samples in comparison with geological ones. This region presents adsorption bands of higher intensity for the majority of archaeological samples and some shifts of the specific wavenumbers take place (Figs. 2-3).

Sample of controlled origin (geological)	Wavenumber domain (cm ⁻¹)	Signal Assignment	Comments regarding the differences between geological and archaeological spectra
Romanian amber (Colti, Buzău County)	3893-3200	OH frequencies, alcoholic (phenolic free OH and bound intramolecular OH) from hydroxy-acids; observed wavenumbers shifts characteristic of amorphous structures.	Less intense signals in this region for archaeological samples and slight shifts
	1684-1600	C=C; C=O frequencies of bond vibrations; out of plane vibration of bonded C-H-C. Plane vibration of H bonds (to O). Assignment confirmed by the peaks from 620-750 cm ⁻¹ domain. 1600-1604 -COO-unsaturated from carboxylic acids;	More intense signals in archaeological samples
	1617	OH group, specific to Romanite, that usually occurs as wide band at 1595 cm ⁻¹ , shifts and appears as shoulder toward 1617 or respectively 1625, due to H intramolecular bonds.	Not always present in archaeological samples
	1547-1423	Specific for carboxylic chains and hydroxy-carboxylic acids;	More intense signals in archaeological samples, shifts
	1046-doublet	Specific peak OH & C=O, slightly shifted due to intramolecular bonds.	
	750-620	Out of plane vibrations of C=O; combined bonds with those specific to C-C=O	
Baltic amber (Bitterfeld, Germany)	3893-3200	Same assignment as above, the differences appear in intensity and slight shifts, due to the different number of intramolecular bonds with respect to those of Romanite;	Less intense signals in this region for archaeological samples and slight shifts
	1684-1600	Same assignment as above, the differences appear in intensity and slight shifts, due to the different number of intramolecular bonds with respect to those of Romanite	More intense signals in archaeological samples, shifts
	1547-1300	Same functional groups, carboxylic chains and hydroxyl-carboxylic acids;	
	1155-1275	Baltic shoulder	Not always present in archaeological samples
	1046/1001	Very well defined peak of OH & C=O; compared to 1046-doublet of Romanite, has different shape and is shifted toward smaller wavenumbers in Baltic amber	More intense signals in archaeological samples, shifts
	750-620	Single peak, sharp, intense, specific for C-O, region slightly different in shape compared to Romanite	Not so well defined in archaeological samples

Table 1. The main characteristics of spectral domains in Baltic amber and Romanite and comparison between geological and archaeological samples)

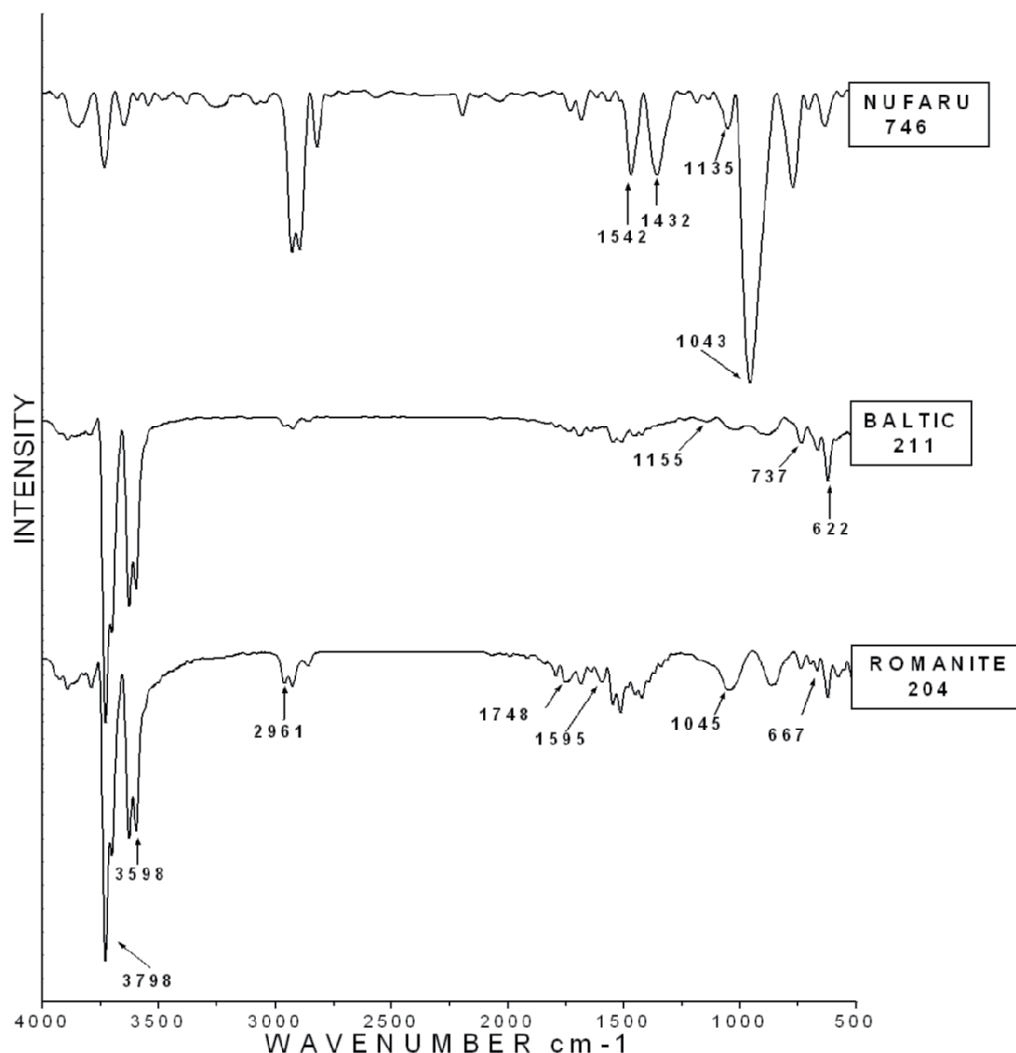


Fig. 2. The overlaid FTIR-VAR (reflectance) spectra, region 4000-600 cm^{-1} for geological reference Baltic amber (211), reference Romanite (204), and an archaeological sample from Nufăru (746)-Byzantine period- assigned by us to Baltic origin

Another difference in VAR spectra of geological origin is registered for absorption bands from 800-600 cm^{-1} region: 622-621 cm^{-1} are ascribed to C-O, C=O out of plane bands; 746-736 cm^{-1} are the confirmation of OH and H bonds; 676-666 cm^{-1} are the confirmation of CH_2 bonds. The absence of a double peak at 667 cm^{-1} in the Baltic amber spectra indicates that the contraction-reticulation of the polymeric chain is complete (an aspect related to the older age of the fossil resin, in our case the Baltic species). This region is not so well defined in archaeological samples, especially for Baltic amber (Figs. 2 and 3).

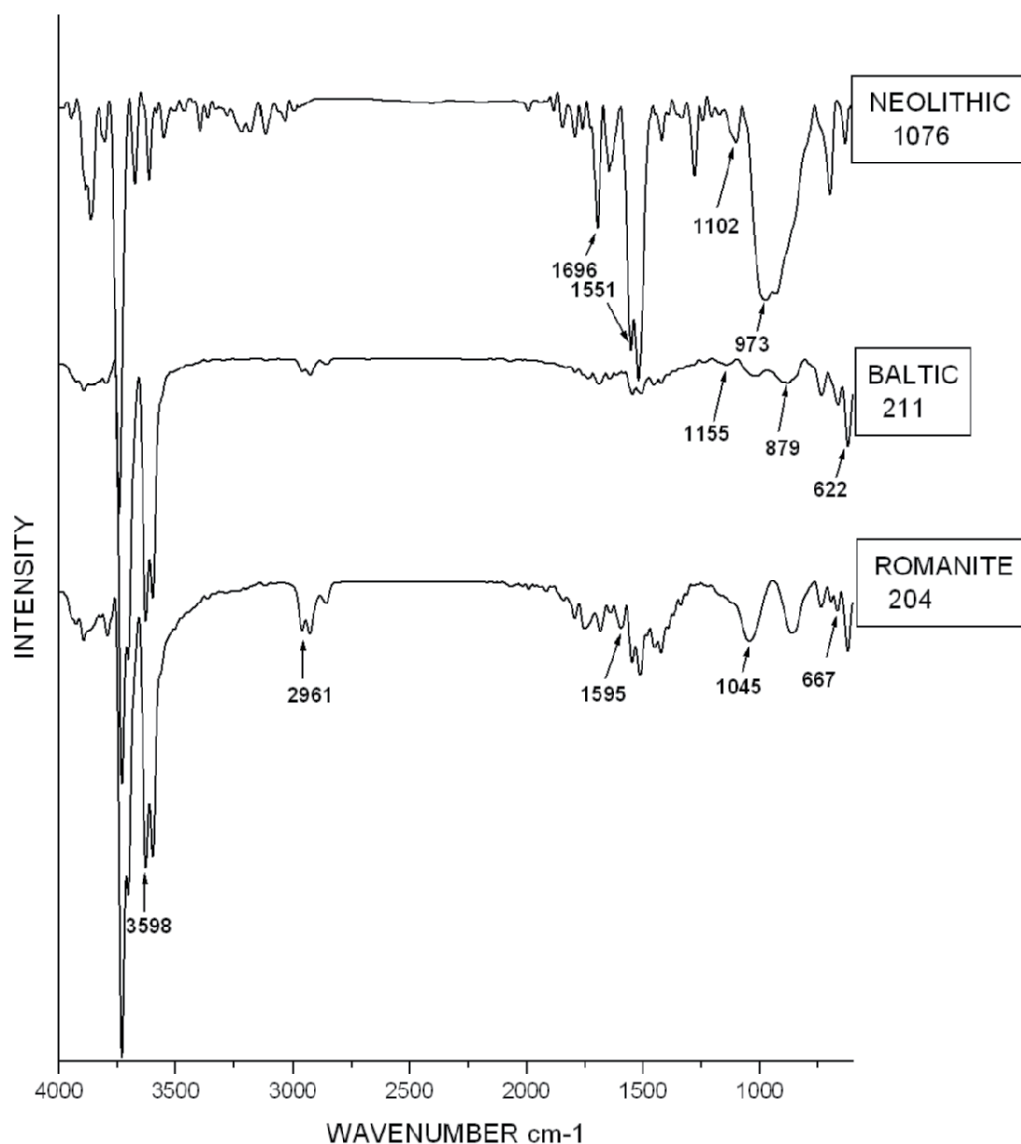


Fig. 3. The overlaid FTIR-VAR (reflectance) spectra, region 4000-600 cm^{-1} for geological reference Baltic amber (211), reference Romanite (204), and an archaeological sample from Pitesti (1076) –neolithic period- assigned by us to Baltic origin

Based on the relative comparison with the geological reference material (both Baltic and Romanian amber, see Table 1) and according to the FTIR-VAR bands of archaeological samples from the region 1820-1350 cm^{-1} , 1275-1020 cm^{-1} and 900-600 cm^{-1} , the classification of several archaeological samples is summarised in Table 2. Some spectra obtained for the samples from Nufăru (Roman Age), Cioclovina (Bronze Age) and a Neolithic bead are presented in Figs. 2, 3 and 4.

Sample origin	Age	FTIR-VAR assignment
Grădiştea-Cotlogeni, one bead Piteşti, one bead (2 samples)	Neolithic	Baltic amber (unpublished)
Cioclovina hoard, 12 beads (43 samples)	Late Bronze	10 beads Romanite 2 beads Baltic amber (Teodor ES et al., 2010)
Rosia Montană, statuette (6 samples)		Baltic amber
Dobrogea region (Tomis, Callatis, Beroe, Carsium, Noviodunum) 25 beads (85 samples)	Roman	16 beads Baltic amber 9 beads Romanite (Vîrgolici et al., 2010b)
Nufăru One pectoral cross, 2 beads (5 samples)	Byzantine	Baltic amber

Table 2. The main categories of archaeological samples analyzed by FTIR-VAR and the assignment of amber origin in comparison with geological samples

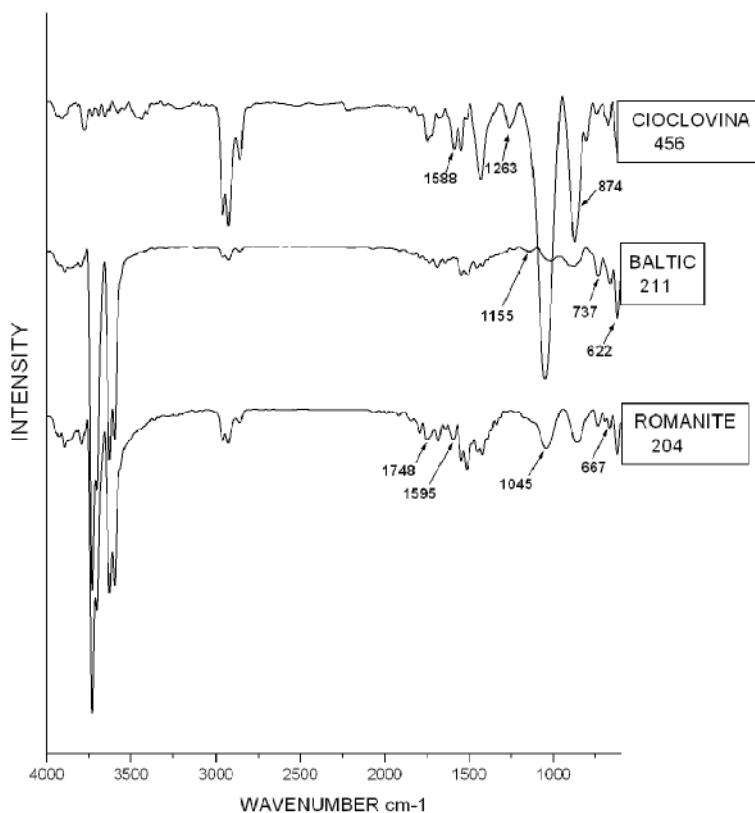


Fig. 4. The overlaid FTIR-VAR (reflectance) spectra, region 4000-600 cm⁻¹ for geological reference Baltic amber (211), reference Romanite (204), and an archaeological sample from Cioclovina (456)-Bronze period- assigned by us to Romanian origin

These results based on comparison of FTIR-VAR spectra about origin of amber artefacts were clarified and confirmed by other non-destructive analysis (Raman, statistical analysis) and supported by historical context, in some cases. In other cases, the assignment of samples to Baltic amber or local (Romanian) amber contributed to understanding of archaeological (historical) context.

FTIR-VAR is a reliable tool for non-destructive investigating of amber. The spectra are more complex than FTIR-transmittance spectra, the obtained signal are rather highly difficult to ascribe and the variability of results is high, but coupled with statistical analysis and corroborated with other techniques (Raman spectroscopy, X-rays fluorescence) is a consistent method to diagnose the origin of amber in archaeological artifacts.

3. Applicability of Fourier Transform Infrared technique in the assessment of bio-mimicking systems. Case study- Human low density lipoproteins

In order to sustain the assertion regarding the FTIR versatility as non-destructive analytical technique able to provide valuable information with respect to noteworthy molecular changes, the second exemplification is based on assessment of significant bio-markers used to indicate oxidative modifications occurring on cellular membrane. At the level of living organisms the cellular membranes are the main targets for reactive oxygen species (ROS) and reactive nitrogen species (RNS). Both ROS and RNS induce lipid peroxidation (LPO) of unsaturated fatty acids from membrane phospholipids. At the cellular level, reactive species are responsible for changes in the membrane properties, inducing modification on cell permeability and enzyme activities (Ahsan et al., 2003).

In our experiments we developed a bio-mimetic to be applied in assessment of lipoperoxidation processes using as significant oxidative substrate a component of the cellular membrane, low-density lipoproteins. The system development was based on system depositing a thin lipoproteic layer on the surface of conductive solid support, usually gold sheet, and quantification of the lipoprotein peroxidation degree by electrochemical measurements, the intensity of the registered intensity current at the lipoperoxides specific peak potential being proportional with the amount of formed lipoperoxides. At this point have to be mentioned the fact that we employed the VAR-FTIR in analysis of structural modifications occurring to low-density lipoprotein as result of the oxidative changes induced by free radicals (ROS) attack.

3.1.1 FTIR method

Starting from the important experimental issue which states that an appropriate development of a bio-mimetic system by immobilization of a compound to a support preserves the structure of the immobilized compound, the first FTIR study was performed on low-density lipoprotein layer deposited on gold support, the results being compared to those obtained for un-bound lipoprotein. For the deposited layer the reflectance mode was employed, while for free lipoprotein the transmittance mode was used. FTIR spectra were recorded at room temperature using a Bruker Tensor 27 Fourier Transform spectrometer. The spectra were collected and ascribed using Opus software. In transmittance mode the spectral range was 4000 – 400 cm^{-1} , the aperture 4 cm, the spectra resolution 4 cm^{-1} and 98 scans being acquired for each spectrum, 20 Hz. Samples were pressed into a potassium

bromide (KBr) pellet, the background spectrum being recorded against KBr pellet. In reflectance mode the spectral range was 4000 – 600 cm^{-1} , the background being recorded for an unmodified polycrystalline gold sheet after that being recorded the samples' spectrum. The optimum reflectance angle was 45 degrees, the aperture 6 cm, the spectra resolution 4 cm^{-1} , 98 scans being acquired for each spectrum, with 2.2 Hz.

3.1.2 FTIR assessment of native and oxidised low-density lipoprotein

As mentioned in the previous section, the first FTIR studies were performed to evaluate the suitable deposition of the low-density lipoprotein on the gold support in order to preserve the lipoprotein structural characteristics. This is an important experimental issue, because the protein structure and surface charging are the most important structural features necessary to be maintained to ensure feasible “ex-vivo” analytical information with respect to oxidative changes induced on cellular membrane by ROS.

The main regions corresponding to FTIR absorption bands and specific for native LDL are given in table 3. Absorption bands from 2800–3000 cm^{-1} corresponding to methyl groups are well defined, no matter the type of the sample, either free or deposited LDL.

Wavenumber domain (cm^{-1})	Signal assignment	Comments and observations
2800-3000	CH_2 – symmetric and asymmetric stretching vibration, CH_3 – asymmetric stretching vibration	2927 cm^{-1} ($\nu^{\text{as}}_{\text{CH}_2}$), 2854 cm^{-1} ($\nu^{\text{s}}_{\text{CH}_2}$), 2954 cm^{-1} ($\nu^{\text{as}}_{\text{CH}_3}$) and 2866 cm^{-1} ($\nu^{\text{s}}_{\text{CH}_3}$) are specific for lipid chains
1740	$\text{C}=\text{O}$ – stretching vibration for ester group of lipids	-
1630-1680	$\text{C}=\text{O}$ – stretching vibration for carbonyl group for protein, amide I	1656 cm^{-1} band correspond to amide I helix structure being the result of 60% vibration of $\text{C}=\text{O}$ group and 20% vibration of N-H
1541	N-H – deformation (scissoring)vibration for amine group of protein, amide II	Is due to 60 % vibration of N-H bound and the rest from -CO-NH-functional group
1466	CH_2 – deformation vibration for methylene group	-
1170-1245	PO_2^- – asymmetric stretching vibration for phosphate groups	-
1063-1100	PO_2^- – symmetric stretching vibration for phosphate groups $\text{CO}-\text{O}-\text{C}$ vibration for esters groups	Studies performed on incidence angles different of 45° proved that ester groups are oriented preferentially at 75°, the intensity of the corresponding band at 1099 cm^{-1} increasing suddenly

Table 3. Main IR absorption bands of low-density lipoprotein

As observable from figures 5 and 6, the amide specific band absorptions for proteins, amide I band around 1654 cm^{-1} and amide II band around 1541 cm^{-1} (Firth et al. 2008; Banuelos et al. 1995) are not changed when LDL was deposited on the gold support. This observation is important because it proved that the secondary structure of the protein is preserved subsequent deposition therefore it can be concluded that the deposition on solid support did not affect the LDL functionality, and, consequently, that deposited LDL is expected to react with free radicals according to the same pathway as free LDL. Moreover, it should be mentioned that this argument is consistent with the data published by Paker (Paker, 1991) where it is mentioned that LDL *ex vivo* peroxidation pathway is similar as *in vivo* peroxidation pathway.

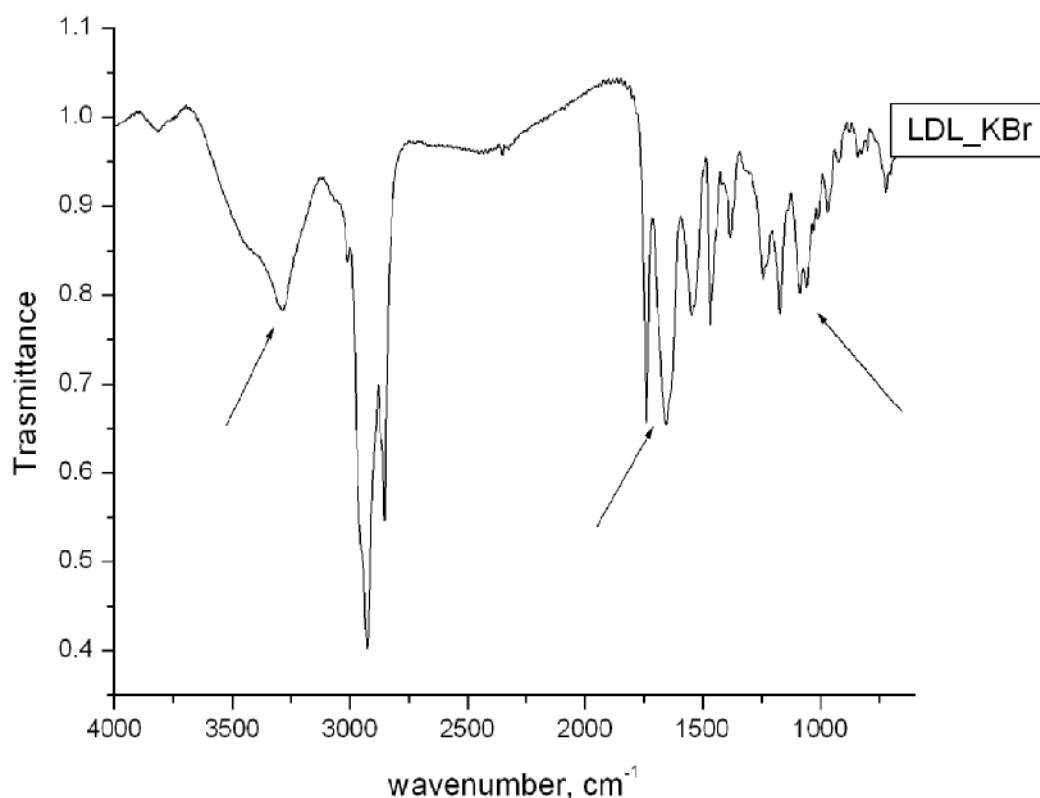


Fig. 5. FTIR spectra of LDL free, on transmittance (KBr pelleted)

When lipoprotein are subjected to the attack of peroxy radicals, thermally induced from aqueous solutions of azo-initiator 2,2'-azobis (2methylpropionamide).dihydrochloride (AAPH), the lipoperoxidation occurs according to a radical pathway (Litescu et al, 2002; Tache et al., 2011) leading to lipo-peroxides formation on the LDL layer. In our experiments the FTIR analysis was performed first on the LDL deposited on the solid support, then the LDL was subjected to free radicals attack for 10 minutes, allowed to dry on inert atmosphere and after that the oxidised LDL layer was once more assessed by FTIR.

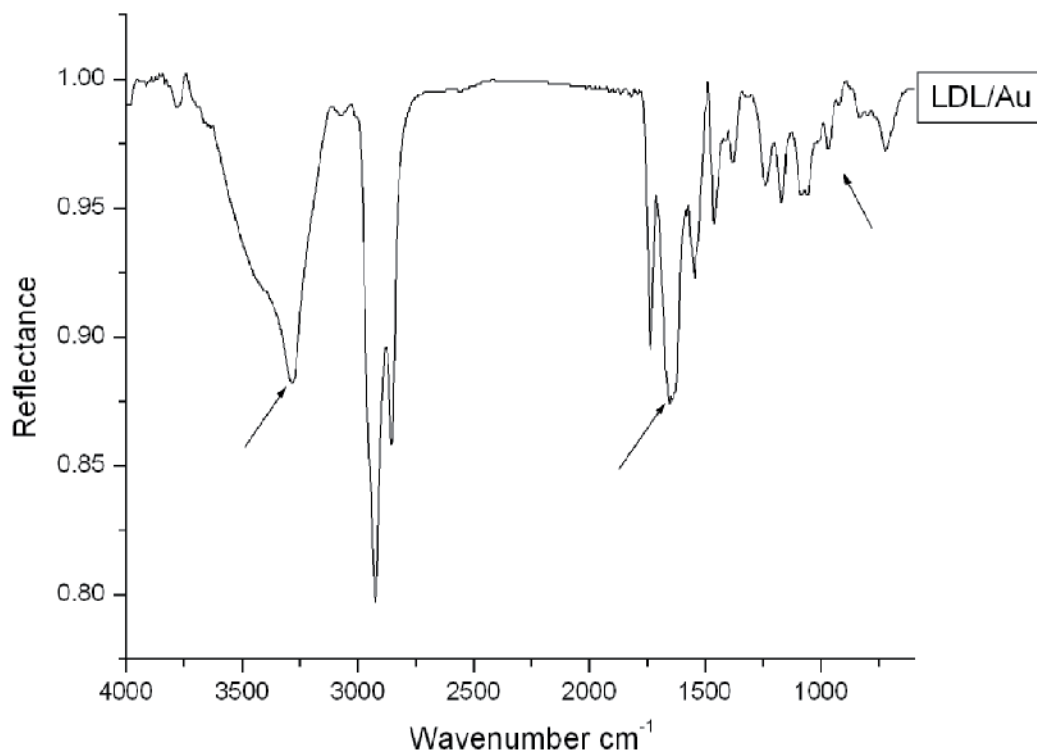


Fig. 6. FTIR spectra of LDL on Au support (variable angle reflectance, incidence angle 45°)

The performed studies proved that in the presence of free radicals (Fig. 7), the IR absorption bands corresponding to ester groups from lipid residues at 1740 cm⁻¹ were changed in intensity and shifted as wavenumber, thus proving the lipoperoxides formation.

Another proof of lipoperoxides existence was the presence of HO absorption bands from 3600–3700 cm⁻¹ and 917 cm⁻¹. In detail, the signal ascription are as follows: the band from 3278 cm⁻¹ increasing in intensity and shoulders rise at 3334 cm⁻¹, 3304 cm⁻¹, 3220 cm⁻¹ and 3197 cm⁻¹ assigned to O-H and N-H vibrations. The bands from 3072 cm⁻¹ are corresponding to hidroxil and amine groups involved in hydrogen bonds. In the same time, it is important to mention that several changes arose around 1717 cm⁻¹ indicating the formation of new C=O groups.

The changes observed on FTIR spectra of deposited LDL correlated perfectly with electrochemical and MALDI information (Litescu et al, 2011), proving the usefulness of non-destructive FTIR analysis in ascribing the oxidative modification occurring on lipoproteic components of the cellular membrane.

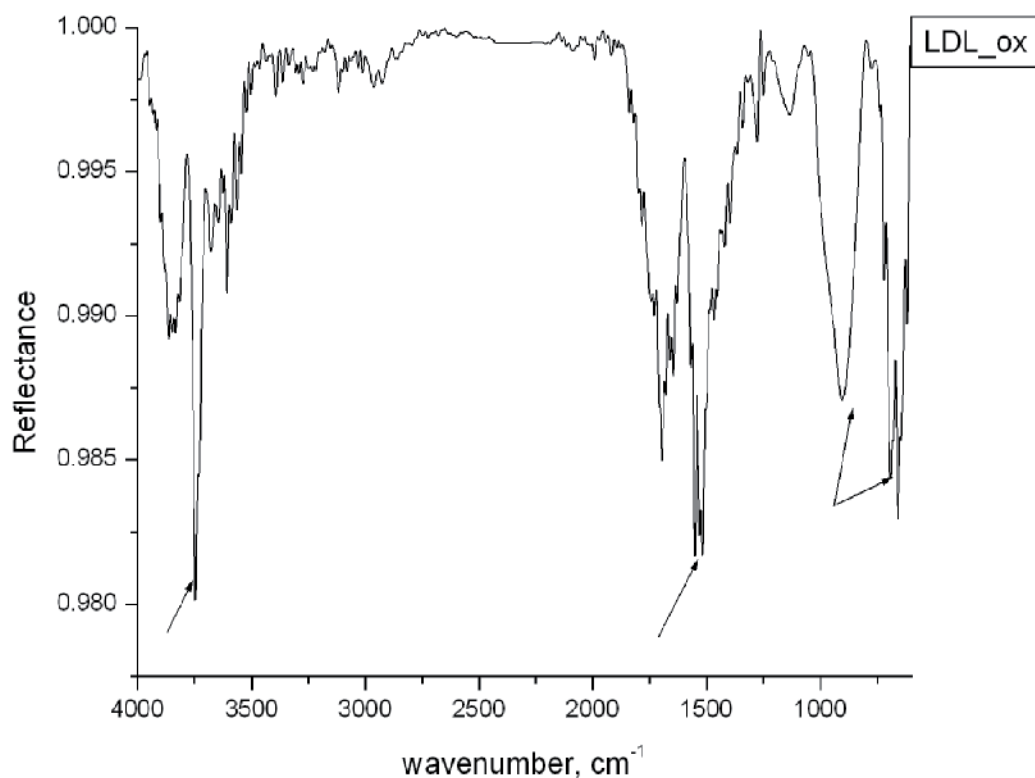


Fig. 7. FTIR spectra of native peroxidised LDL deposited on Au support

4. Conclusions

The use of FTIR, especially as variable angle reflectance technique, proved to be of crucial importance in two main types of applications where the critical issues are the importance to conserve the sample integrity and the limited amount of available sample.

Two examples of FTIR non-destructive analysis employment in two very different research domains, archaeology and modified surfaces are supporting the highest utility of the technique when the analysis is dealing with valuable samples, sometimes of patrimony value, which have to remain un-affected subsequent analysis, as it was the amber samples case study, or when the analysis have to provide arguments on sharp and specific structural changes, as it was the case of lipoprotein oxidation study.

It could be concluded that FTIR proved its efficiency in evaluation of the oxidative modifications on the level of one of the main components of the cellular membrane, oxidative process which plays, generally, as key-event in several age -related and degenerative pathologies.

In the same time, it should be emphasized that, in our opinion, FTIR-VAR technique use as non-destructive way to analyse archaeological artefacts is strongly recommended, especially when coupled with statistical analysis.

5. Acknowledgment

This work was partially supported by EU FP7-SME project Sensbiosyn, contract no 232522/2009.

6. References

- Angelini I. & Bellintani P. (2005). Archaeological ambers from northern Italy: an FTIR-DRIFT study of provenance by comparison with the geological amber database. *Archaeometry* 47, 441-54, ISSN: 0003-813X
- Ahsan, H., Ali, A. & Ali, R.(2003). Oxygen free radicals and systemic autoimmunity. *Clinical and Experimental Immunology* 131, 398-404, ISSN: 1365-2249
- Banuelos, S., Arrondo J. L. R., Goni F. M.& Pifat G.(1995). Surface-core relationships in human low density lipoproteins as studied by infrared spectroscopy. *Journal of Biology & Chemistry*, 270, 9192-9196, ISSN 0021-9258
- Banerjee A., Ghiurcă V., Langer B. & Wilhelm M. (1999). Determination of the provenance of two archaeological amber beads from Romania by FTIR- and Solid-State-Carbon-13 NMR spectroscopy. *Archäologisches Korrespondenzblatt* 29, 593-606, ISSN: 0342-734X
- Beck C. W. (1972). Amber in Archaeology. *Archaeology* 23, 7-11, ISSN: 0003-8113
- Beck C. W. (1986). Spectroscopic investigations of amber. *Applied Spectroscopy Review* 22, 57-200, ISSN: 0570-4928
- Boon J. J., Tom, A. & Pureveen, J. (1993). Microgram scale pyrolysis mass spectrometric and pyrolysis gas chromatographic characterisation of geological and archaeological amber and resin samples, in *Amber in archaeology: proceedings of the Second International Conference on Amber in Archaeology, Liblice, 1990* (eds. C. W. Beck and J. Bouzek), 9-27, Institute of Archaeology, Czech Academy of Sciences, Praha, ISBN: 8090102654 9788090102651
- Boroffka N. (2001). Bemerkungen zu einigen Bersteinfunden aus Rumänien. *Archäologisches Korrespondenzblatt* 31, 3, 395-409, ISSN: 0342-734X
- Boroffka N.(2006). Resursele minerale din România și stadiul actual al cercetărilor privind mineritul prehistoric. *Apulum* 43, 71-94, ISSN: 1013-428X
- Firth, C. A., Crone E. M., Flavall E. A., Roake J. A. & Gieseg S. P. (2008) Macrophage mediated protein hydroperoxide formation and lipid oxidation in low density lipoprotein are inhibited by the inflammation marker 7,8-dihydroneopterin. *Biochimica Biophysica Acta* 1783, 1095-101. ISSN 1570-9639
- Ghiurcă V. (1999). Chihlimbarul și alte resurse gemologice din județul Buzău. *Mousaios* 5, 389-407, ISSN: 1582-0688
- Guiliano M., Asia L., Onoratini G. & Mille G. (2007). Applications of diamond crystal ATR FTIR spectroscopy to the characterization of ambers. *Spectrochim. Acta A Mol. Biomol. Spectrosc.* 67, 1407-11, ISSN: 1386-1425
- Lambert, J. B. & Poinar, G. O. (2002). Amber: the organic gemstone. *Accounts of Chemical Research* 35, 628-36, ISSN: 0001-4842

- Litescu, SC, Cioffi, N, Sabbatini L, Radu G.L. (2002), Study of Phenol-Like Compounds Antioxidative Behavior on Low- Density Lipoprotein Gold Modified Electrode, *Electroanalysis*, 14(12), 858-865, ISSN 1040-0397
- Litescu SC, Eremia SAV, Diaconu M., Tache A., Radu G.L. (2011) Biosensor applications on Assessment of Reactive Oxygen Species and Antioxidants, in *Environmental Biosensors*, Ed. Vernon Sommerset, Intech, ISBN: 978-953-307-486-3, Riejsda Croatia
- Paker, L., (1991). Protective role of vitamin E in biological systems, *American Journal of Clinical Nutrition*, 53, 1050S-1055S, ISSN 0002-9165
- Pakutinskiene I., Kiuberis J., Bezdicika P., Senvaitiene J. & Kareiva A. (2007). Analytical characterization of Baltic amber by FTIR, XRD and SEM. *Canadian J. Anal. Sci. Spectrosc.* 52, 287- 94, ISSN: 1205-6685
- Shedrinsky A. M., Wampler T. P. & Chugunov K. V. (2004). The examination of amber beads from the collection of the state hermitage museum found in Arzhan-2 burial memorial site. *J. Anal. Appl. Pyrolysis* 71, 69–81, ISSN: 0165-2370
- Stout E. C., Beck C. W. & Anderson, K. B. (2000). Identification of rumanite (Romanian amber) as thermally altered succinite (Baltic amber). *Physics and Chemistry of Minerals* 27, 665–78, ISSN: 0342-1791
- TacheA, Cotrone S, Litescu SC, Cioffi N., Torsi L.; Sabbatini L & Radu GL (2011) Spectrochemical Characterization of Thin Layers of Lipoprotein Self-Assembled Films on Solid Supports Under Oxidation Process, *Analytical Letters*, 44 (5), 747 – 760, ISSN 00032719
- Teodor E.D., Lițescu S. C., Neacșu A., Truică G. & Albu C. (2009). Analytical methods to differentiate Romanian amber and Baltic amber for archaeological applications, *Cent. Eur. J. Chem.* 7, 560-68, ISSN: 1895-1066
- Teodor E.S., Teodor E.D., Virgolici M., Manea M.M., Truica G. & Litescu S. C. (2010). Non-destructive analysis of amber artefacts from Prehistoric Cioclovina Hoard. *J. Arch. Sci.* 37, 2386-96, ISSN: 0305-4403
- Tonidandel L., Ragazzi E., Roghi G. & Traldi P. (2008). Mass spectrometry in the characterization of ambers I. Studies of amber samples of different origin and ages by laser desorption ionization, atmospheric pressure chemical ionization and atmospheric pressure photoionization mass spectrometry. *Rapid Commun. Mass Spectrom.* 22, 630-38, ISSN: 0951-4198
- Virgolici M., Ponta C., Manea M., Neagu D., Cutrubinis M., Moise I., Șuvăilă R., Teodor E. S., Sârbu C. & Medvedovici A. (2010a). Thermal Desorption/Gas Chromatography/Mass Spectrometry Approach for Characterization of the Volatile Fraction from Amber Specimens: a Possibility of Tracking Geological Origins, *J. Chrom. A* 1217, 1977–1987, ISSN: 0021- 9673
- Virgolici M., Petroviciu I., Teodor E. D., Lițescu S. C., Manea M. M., Ponta C., Niculescu G., Sarbu C. & Andrei Medvedovici A. (2010b). TD/CGC/MS and FT-IR characterization of archaeological amber artefacts from Romanian collections (Roman age), *Rev. Roum. Chim.* 55, 349-55, ISSN: 0035-3930
- Wollmann V. (1996). Der Bernsteinbergbau von Colti, in *Bernstein - Tränen der Götter. Katalog des Ausstellung des Deutschen Bergbau-Museums Bochum in Zusammenarbeit mit dem Ostpreußischen Landesmuseum Lüneburg und dem Siebenbürgischen Museum Gundelsheim*, M. Ganzelewski, R. Slotta (eds), 369-377, Bochum, ISBN: 3-921533-57-0

Infrared Spectroscopy in the Analysis of Building and Construction Materials

Lucia Fernández-Carrasco¹, D. Torrens-Martín¹,
L.M. Morales¹ and Sagrario Martínez-Ramírez²

¹Escola Tècnica Superior d'Arquitectura (UPC), LiTA, Barcelona

²Instituto de Estructura de la Materia (CSIC), IEM-CSIC, Madrid
Spain

In memorial of Prof. Tomás Vázquez

1. Introduction

In the characterization of building and construction materials, the most frequently analytical tool performed have been X-ray diffraction but also, thermal analysis and microscopic techniques. Nowadays, infrared and other spectroscopic techniques have become as a useful, non-destructive and easy technique to study the phase composition of initial but also the evolved materials due to their exposure to the climatic conditions. Moreover, by using this tool is possible the detection of crystalline but also the amorphous phases very frequently developed on certain cementitious materials, mainly at early ages. The infrared spectroscopy is used both to gather information about the structure of compounds and as analytical tool to assess in qualitative and quantitative analysis of mixtures.

The infrared spectra are quick and easy to achieve and refers to the spectrum region between the visible and microwave regions. In theory, infrared radiation is absorbed by molecules and converted into energy of molecular vibration; when the radiant energy matches the energy of a specific molecular vibration, absorption occurs. The frequencies at which a molecule absorbs radiation give information on the groups present in the molecule. As an approximation, the energy of a molecule can be separated into three additive components associated with the motion of the electrons in the molecule, the vibration of the constituent atoms, and the rotation of the molecule as a whole. The absorption in the infrared region arises predominantly from excitation of molecular vibrations. Then, if a molecule is placed in an electromagnetic field, a transfer of energy from the field to the molecule will occur when Bohr's frequency condition is satisfied.

$$\Delta E = h\nu$$

Where ΔE is the difference in energy between two quantized states, h is the Planck's constant and ν is the frequency of the light. Then the molecule "absorbs" ΔE when it is excited from E_1 to E_2 and "emits" ΔE when it reverts from E_2 to E_1 . The infrared absorption spectra originate in photons in the infrared region that are absorbed by transitions between two vibrational levels of the molecule in the electronic ground state.

The application of infrared spectroscopy to the inorganic compounds started as a more frequent technique during the 60's with Lawson. This author made a first attempt to compile the work done in the relatively new field-Inorganic Infrared Spectroscopy since 1952 where 1171 references were reported. Farmer, in 1964, studied the silicates and Nakamoto in relation to the coordinated compounds prepared a helpful atlas of these compounds. Afremow (1966) presented for an important research of inorganic pigments and extenders in the mid-infrared region from 1500 cm^{-1} to 200 cm^{-1} . The study of surface chemistry and the nature of surface functional groups was also advanced by Basila (1968).

In the first decade of infrared research on the study of Portland cements, Vázquez (1969), was a lead the way in the study by infrared spectroscopy the main present compounds in the Portland cement but also later, made some research about the carbonation processes of calcium aluminate cements. Also, the hydration of Portland cement and its constituents was developed by Bensted (1974).

After that initial period, several reports have been done in the study on cementitious materials by infrared. More recent studies in relation with the calcium aluminates cements were reported by Vázquez (1993). Later on, different papers have present some characterization of materials and evolution over several exposition conditions using the infrared spectroscopy as a complementary technique join to mainly XRD and SEM analytical tools.

Without doubt, the infrared spectroscopy has not been really used in the qualitative and quantitative analysis of these materials; the main uses have rather been in identification of compounds and few structural studies. The main objective of this chapter will be to present a revision of infrared spectra useful in the study of the building and construction materials, mainly cements, from the point of view of characterization.

2. Characterization of cementitious systems by infrared spectroscopy

As a general rule, as it is easier to bend a bond than to stretch or compress it, in the spectra the stretching frequencies are higher than the corresponding bending frequencies; bonds to hydrogen have higher stretching frequencies than those to heavier atoms; and double bonds have higher stretching frequencies than single bonds (Figure 1).

2.1 Portland cement

The ordinary Portland cement is made by firing raw materials - limestone, clay minerals, sand and iron minerals- at around 1500°C in a rotary kiln. At this temperature a series of chemical reaction take place and the clinker synthesized. Clinker is cooled, mixed with setting regulators (e.g. gypsum) grounded to a fine powder to obtain the cement. The common phases present in the cement clinkers are: alite ($3\text{CaO} \cdot \text{SiO}_2$, C_3S^1), belite ($2\text{CaO} \cdot \text{SiO}_2$, C_2S^1), tricalcium aluminate ($3\text{CaO} \cdot \text{Al}_2\text{O}_3$, C_3A^1), and tetracalcium aluminate ferrite ($4\text{CaO} \cdot \text{Al}_2\text{O}_3 \cdot \text{Fe}_2\text{O}_3$, C_4AF^1). One typical composition of cement consists of: $\text{C}_3\text{S} = 55\text{-}60\%$ (wt); $\text{C}_2\text{S} = 15\text{-}20\%$ (wt); $\text{C}_3\text{A} = 5\text{-}10\%$ (wt); $\text{C}_4\text{AF} = 5\text{-}8\%$ (wt) and $\text{C}\bar{\text{S}}\text{H}_2 = 2.6\%$ (wt). In this chapter, synthetic silicates and aluminates phases have been used to identify infrared vibrations bands previous to study the more complicated commercial cement.

¹ Cement chemistry nomenclature is used: $C = \text{CaO}$; $S = \text{SiO}_2$; $A = \text{Al}_2\text{O}_3$; $F = \text{Fe}_2\text{O}_3$; $H = \text{H}_2\text{O}$; $\bar{S} = \text{SO}_3$

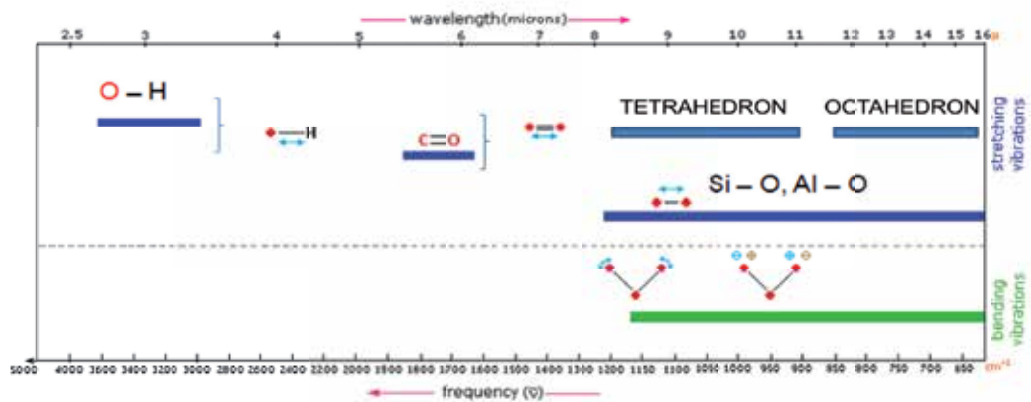


Fig. 1. General rules in the interpretation of building cementing material IR spectra.

As a resume, the vibrations can be divided in stretching and bending: vibrations can involve either a change in bond length (stretching) or bond angle (bending); some bonds can stretch in-phase (symmetrical stretching) or out-of-phase (asymmetric stretching). The main structure elements in building the crystal lattice of silicates are tetrahedral SiO_4 groups, with may be either isolated as in the orthosilicates or connected with one another by common O atoms as in building an Si_2O_7 group from two connected tetraheda [Matossi]. Connection of SiO_4 groups so as to form a ring of tetrahedral occurs in the crystal of alite (C_3S) or belite (C_2S). The infrared spectra of all silicates [Matossi] contain two reflection maxima near 1000 and 500 cm^{-1} , which have been interpreted as a two active frequencies of a tetrahedral point group. In addition to these, there may occur other maxima corresponding to other particular features of the crystal lattice.

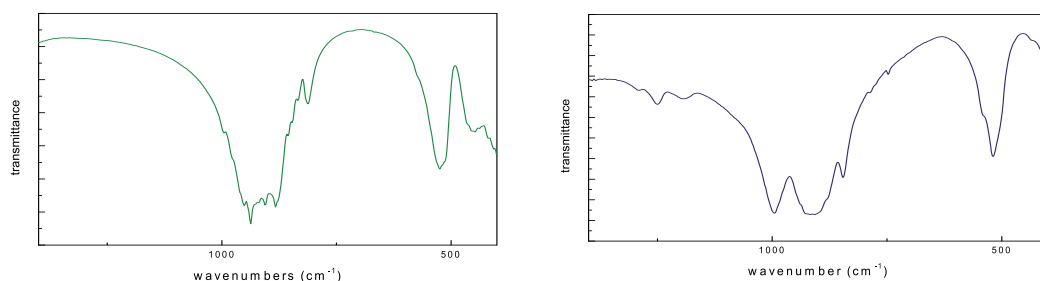
The spectrum of the main constituent of OPC, C_3S , shows two regions dominated by the internal modes of SiO_4^{4-} tetrahedral units, with to broad absorption bands centred between 890 and 955 cm^{-1} , solved in to maxima near to 870 and 940 cm^{-1} due to the symmetric and antisymmetric stretching of Si-O bonds within tetrahedral SiO_4 groups, ν_1 and ν_3 , respectively. Another absorption band of medium intensity appears close to 525 cm^{-1} and a lower intense band sited near to 450 cm^{-1} due to the symmetric and antisymmetric bending of the O-Si-O bonds, ν_2 and ν_4 , respectively (see details of maxims in Table 1 and Figure 2). The other calcium silicate phase spectra, C_2S , exhibits strong bands in the area 1000-800 cm^{-1} with maximums at 990 and 840 cm^{-1} due the stretching Si-O bond of the silicon tetrahedron and the bending vibration absorption band appear at lower frequencies, 520 cm^{-1} and a shoulder at 538 cm^{-1} .

The C_3A -cubic tricalcium aluminate polymorph spectra (Figure 3), shows a well-defined spectra with two dominant absorption areas with very broad bands. The first ones appear in the area between 950-650 cm^{-1} and the second ones appearing between 500-380 cm^{-1} , respectively. The main observed maxima appear near to 900, 865, 820, 780, 720 and 705 cm^{-1} of AlO_4 -tetrahedral groups, and close to 520, 510, 460 and 414 cm^{-1} due to AlO_6 -octahedral groups. The Ca-O bands appear at lower frequencies.

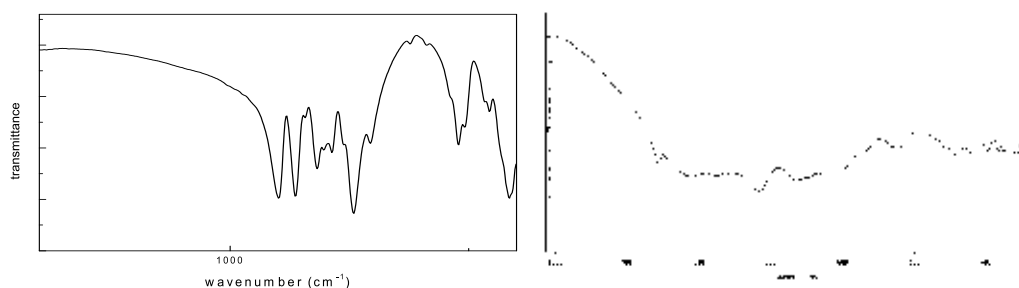
The grey colour of Portland cements is due to the presence of the names ferrite phases; in absence of elements other than calcium, aluminium, iron and oxygen, calcium

phase	Fundamental vibrations (cm ⁻¹)	
C_3S	935	521
$\beta - C_2S$	991, 879, 847	509
C_3A	900, 865, 820, 780, 720, 705	520, 510, 460, 414
C_4AF	700 - 500	

Table 1. Characteristic absorbance bands for cement Portland phases

Fig. 2. Infrared spectra of pure C_3S (left) and C_2S (right).

aluminoferrite forms a solid solution series of formula $Ca_2(Al_xFe_{1-x})_2O_5$ for all values of x in the range 0-0.7, compositions with $x > 0.7$ do not exist at ordinary pressures. The spectrum of C_4AF presents as significant absorption bands the sited between 800-830 cm⁻¹ with maxima close to 720 cm⁻¹ due to ν_1 [(Fe,Al)O₄⁵⁻]; moreover, a broad and less intense band with several maximums between 620 and 670 cm⁻¹ is also present (Figure 3).

Fig. 3. Infrared spectra of C_3A (left) and C_4AF (right).

In a real cement the main phases are alite (C_3S -base solid solutions i.e. MgO, Na₂O) and belite (C_2S -base solid solutions i.e.- Al₂O₃, Fe₂O₃). The presence of these impurities prompts a change in the crystalline structure of the silicate phases that may cause modifications in the Infrared spectra compared to the pure phases. Figure 4 present the infrared spectra of the ordinary Portland cement. In this spectrum, it is possible to identify different vibrations bands from the calcium silicates, calcium aluminates, and gypsum, the last one added as setting regulator.

The gypsum can lose part of the structure water and the sulfates can be present as bassanite and/or anhydrite. In the IR spectras, the strongest peak is presented at 1102, 1111, and 1094

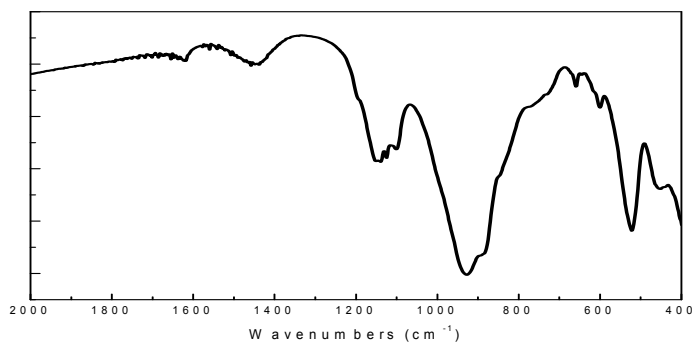


Fig. 4. IR Spectrum of ordinary Portland cement.

cm^{-1} , for the gypsum, bassanite, and anhydrite, respectively. They are ν_3 antisymmetric stretch vibration modes of SO_4 tetrahedra. The gypsum, bassanite, and anhydrite present two absorption bands ($669, 604 \text{ cm}^{-1}$), three ($660, 629, 600 \text{ cm}^{-1}$) and three ($677, 615, 600 \text{ cm}^{-1}$), anti-symmetric bending vibrations, respectively. The peaks at 595 cm^{-1} in gypsum and 594 cm^{-1} in bassanite split into two peaks (610 and 591 cm^{-1}) in anhydrite, which indicates a lowering of symmetry in anhydrite. The shift of frequency from 677 cm^{-1} in anhydrite to 660 cm^{-1} in bassanite indicates that the sulfate ions in bassanite are linked with water molecules by hydrogen bonding, because in general the hydrogen bonding will lower the frequency of the absorption band. In addition, there is a very weak peak at 1140 cm^{-1} in gypsum, 1150 cm^{-1} in bassanite, and 1150 cm^{-1} in anhydrite, which should be the ν_1 symmetric stretch vibration modes of SO_4 tetrahedral. The Table 2 present the characteristics absorption bands of sulfate compounds. For gypsum and bassanite presence it will be also possible to analyze $4000\text{-}3000 \text{ cm}^{-1}$ region were ν_1 O-H absorptions can be observed (3553 and 3399 cm^{-1} for gypsum and 3611 and 3557 cm^{-1} for bassanite).

Sulfates	FUNDAMENTALS			OVERTONES	OH-STRECHT	OH-BEND
	ν_1	ν_3	ν_4			
gypsum	1140	1117	669, 604	2500 - 1900	3553, 3399	1686, 1618
Bassanite	1150	1117, 1098	660, 629, 600	2500 - 1900	3611, 3557	1618
anhydrite	1150	1120	677, 615, 600	2500 - 1900	---	---

Table 2. Absorption bands of sulfate compounds (cm^{-1})

2.2 Calcium aluminate cement

The calcium aluminate cement (CAC) was developed as a solution to the sulphates attack in OPC, and was patented in France in 1908. The CACs are cements consisting predominantly of hydraulic calcium aluminates: mainly monocalcium aluminate, CA , but also contains minor amounts of C_{12}A_7 , CA_2 and C_4AF .

According to Tarte, in the interpretation of IR spectra of inorganic aluminates, the characteristic frequency ranges are "condensed" AlO_4 tetrahedral in the $900\text{-}700 \text{ cm}^{-1}$, "isolated" AlO_4 tetrahedral $800\text{-}650 \text{ cm}^{-1}$, "condensed" AlO_6 octahedral in the $680\text{-}500 \text{ cm}^{-1}$,

“isolated” AlO_6 octahedral $530\text{-}400\text{ cm}^{-1}$. In the spectra of the main present phase of CAC, the CA, the most relevant signals are presented in the two region $850\text{-}750\text{ cm}^{-1}$ and $750\text{-}500\text{ cm}^{-1}$ due to the mentioned groups, with maxima near to $840, 805, 780$ and 720 cm^{-1} of AlO_4 tetrahedral and close to $680, 640, 570, 540, 450$ and 420 cm^{-1} of AlO_6 groups (Figure 5).

The infrared spectrum of C_{12}A_7 contains absorption bands mainly in two regions: a very broad absorption region between $680\text{-}900\text{ cm}^{-1}$ of tetrahedral groups and another area in the $650\text{-}400\text{ cm}^{-1}$ range with very sharp and intense bands due to octahedral groups. The maxima appear close to $850, 780, 610, 575, 460$ and 410 cm^{-1} (Figure 5).

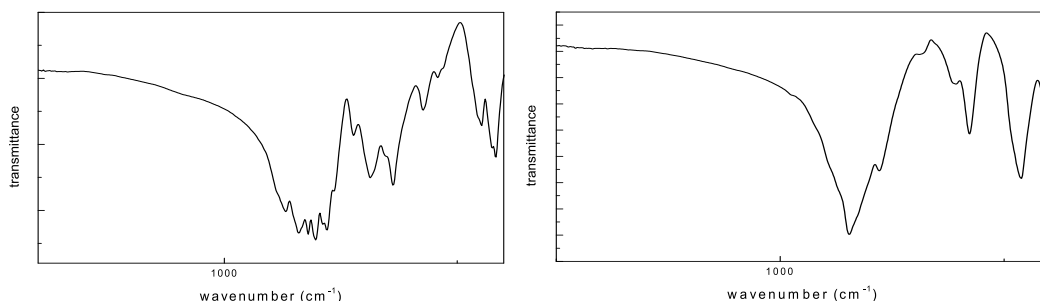


Fig. 5. Infrared spectra of CA (left) and C_{12}A_7 (right).

The minor phases present in the CAC are the CA_2 aluminate with the two absorption in the areas $950\text{-}700\text{ cm}^{-1}$ and $690\text{-}410\text{ cm}^{-1}$ with maxima at $945, 920, 860, 840, 810$ and 745 cm^{-1} of AlO_4 groups and near to $680, 660, 640, 575, 540, 440$ and 422 cm^{-1} of AlO_6 groups. The C_2AS mineral presents the AlO_4 vibration area between 920 and 720 cm^{-1} while the AlO_6 groups give absorption bands between $720\text{-}400\text{ cm}^{-1}$. At higher frequencies, in this spectra appear the signals due to the Si-O vibrations, 1020 and 973 cm^{-1} . The IR spectra of CA_2 and C_2AS are presented in Figure 6.

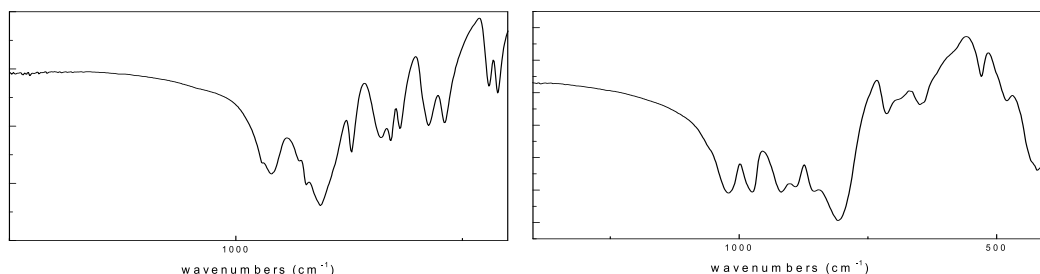


Fig. 6. Infrared spectra of CA_2 (left) and C_2AS (right).

Then, the most relevant signals on the FTIR spectrum for CAC are the absorption bands in the region between 850 and 650 cm^{-1} – the bands at around $840, 805$ and 780 cm^{-1} – attributed to AlO_4 groups; the bands between 750 and 400 cm^{-1} – with bands at about $720, 685, 640$ and 570 cm^{-1} , ascribed to AlO_6 groups; and the bands at under 400 cm^{-1} owing to Ca-O bonds [15, 16]. The Figure 7 shows the IR spectra of the commercial cement. The Table 3 presents the characteristics absorption bands of CAC mineral compounds.

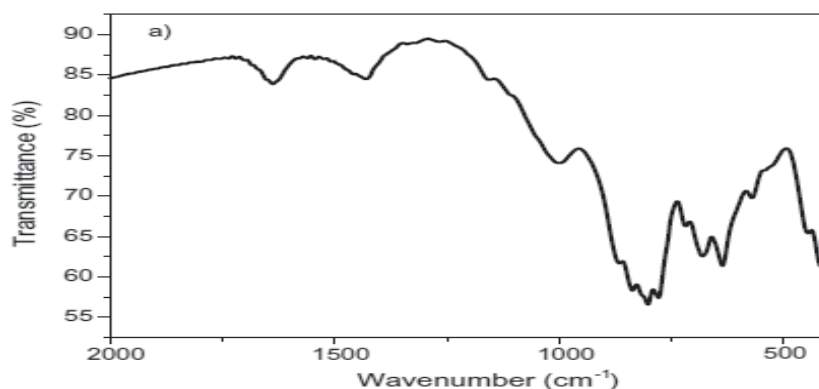


Fig. 7. IR spectra of commercial calcium aluminate cement.

phase	Fundamental vibrations (cm ⁻¹)	
<i>CA</i>	840, 805, 780, 720	680, 640, 570, 540, 450, 420
<i>C₁₂A₇</i>	850, 780,	610, 575, 460, 410
<i>CA₂</i>	945, 920, 860, 840, 810, 745, 680,	660, 640, 575, 540, 440, 422
<i>C₂AS</i>	920, 720, 710, 1020, 973	650, 530, 480, 420

Table 3. Characteristic absorbance bands for calcium aluminate cement phases.

2.3 Calcium sulfoaluminate cement

From the sustainability point of view new cement production has been developed in the past decades. One of these new cements is calcium sulfoaluminate (*CSA*) that was first developed in China in 1980's. Industrial production requires essentially gypsum, bauxite and limestone as raw materials, which are burnt at 1,300°C in a conventional rotary kiln. These starting materials lead to a final clinker based on the quinary system $\text{CaO-SiO}_2\text{-Al}_2\text{O}_3\text{-Fe}_2\text{O}_3\text{-SO}_3$ and formed by three main minerals: tetracalcium trialuminate sulphate or yeelimite ($\text{C}_4\text{A}_3\bar{\text{S}}$); dicalcium silicate or belite (C_2S) and calcium sulphate or anhydrite ($\text{C}\bar{\text{S}}$). Minor phases such as C_3A , C_4AF , C_{12}A_7 and (C_2AS) can also be present. The infrared spectra of main mineral phase of calcium sulfoaluminate cement can be described as follow: yeelimite has two absorption bands due to vibrational modes of sulphate $[\text{SO}_4]^{2-}$ groups at 1110 cm^{-1} , a very intense absorption band due to silicate groups near to 800 cm^{-1} , the third band at 620 cm^{-1} is due to vibrational modes of $[\text{AlO}_4]^{5-}$ tetrahedra; ii) belite, anhydrite, C_{12}A_7 and C_2AS spectras have been described previously. Then, the infrared spectrum of the *CSA* cement presents the most intense bands located at 1110 and 800 cm^{-1} , in the region where stretching vibrations of $[\text{SO}_4]^{2-}$ groups lie. A broadened signal appears between 900 and 800 cm^{-1} , centered at 857 cm^{-1} . This feature is strongly asymmetrical: this is probably the result of the convolution of the two bands of C_2S , that appear unresolved or as a consequence of lower crystal perfection caused by the presence of foreign ions in the lattice or because of the small particle size of minerals of *CSA* clinker. But it is also possible to highlight the presence of the three anhydrite bands at 677, 615, and 600 cm^{-1} , respectively. The Figure 8 displays the IR spectra of yeelimite.

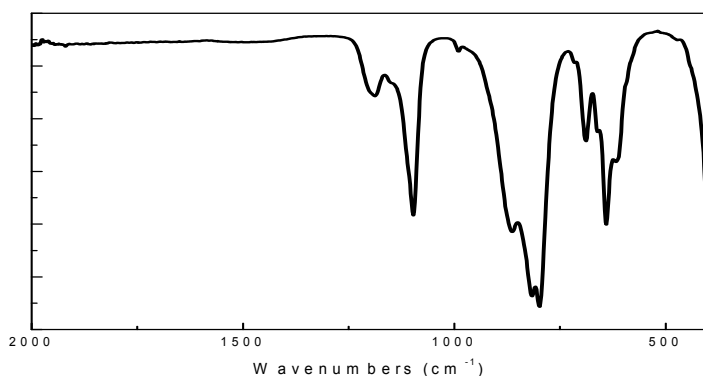


Fig. 8. Infrared spectra of yeelimite.

3. Infrared analysis of hydrated cementitious materials

The hydration of Portland cement give rise both, amorphous phase calcium silicate hydrated (C-S-H gel) and two crystalline phases, ettringite ($\text{Ca}_6\text{Al}_2(\text{OH})_{12} \cdot (\text{SO}_4)_3 \cdot 26\text{H}_2\text{O}$) and portlandite. The C-S-H gel is the primary binding phase in Portland cement but poorly crystalline. The Figure 9 presents the infrared spectra of a hydrated commercial Portland cement.

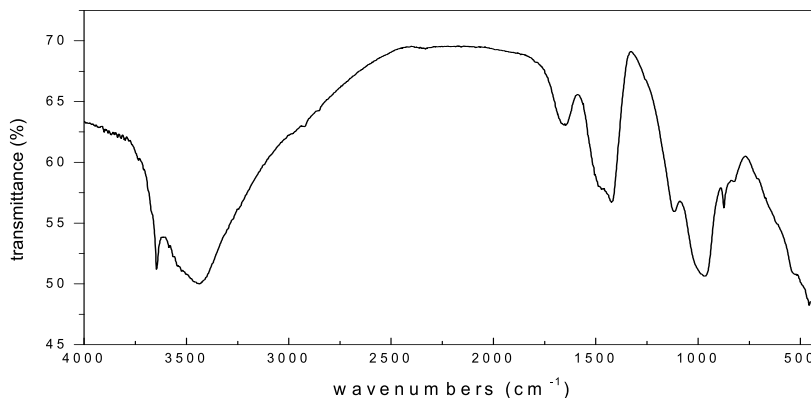


Fig. 9. IR spectra of hydrated Portland cement.

The ettringite ($\text{C}_6\text{A}\bar{3}\text{H}_{32}$) is the first developed phase due to the reaction of aluminates with sulfates of Portland cement. According to the structure model by Taylor [76], the crystals are based on columns of cations of the composition $\{\text{Ca}_3[\text{Al}(\text{OH})_6]_{12} \cdot 12 \text{H}_2\text{O}\}^{3+}$. In there, the $\text{Al}(\text{OH})_6^{3-}$ -octahedral are bound up with the edgesharing CaO_8 -polyhedra, that means each aluminum-ion, bound into the crystal, is connected to Ca^{2+} -ions, with which they share OH-ions. The intervening channels contain the SO_4^{2-} -tetrahedral and the remaining H_2O molecules (fig. 2). The H_2O molecules are partly bound very loose into the ettringite structure. According to Bensted, the infrared spectra of ettringite $\text{C}_3\text{A} \cdot 3\text{CS} \cdot \text{H}_{32}$ or

$\text{Ca}_6[\text{Al}(\text{OH})_6]_2(\text{SO}_4)_3 \cdot 26\text{H}_2\text{O}$ presents a very strong anti-symmetrical stretching frequency of the sulphate ion ($\nu_3 \text{SO}_4$) centred towards 1120 cm^{-1} ; this band is indicative of relative isolation of this ion in the hexagonal prism structure. The water absorption bands appear in the region $1600\text{-}1700 \text{ cm}^{-1}$ (1640 and 1675 cm^{-1} $\nu_2 \text{H}_2\text{O}$) and above 3000 cm^{-1} (3420 due to $\nu_1 \text{H}_2\text{O}$ and 3635 cm^{-1} from $\nu \text{OH}_{\text{free}}$). The presence of aluminate bands are near to 550 cm^{-1} (νAlO_6) due to stretching Al-O groups, and 855 cm^{-1} (Al-O-H bending). The Figure 10 shows the structure and the infrared spectra of ettringite compound.

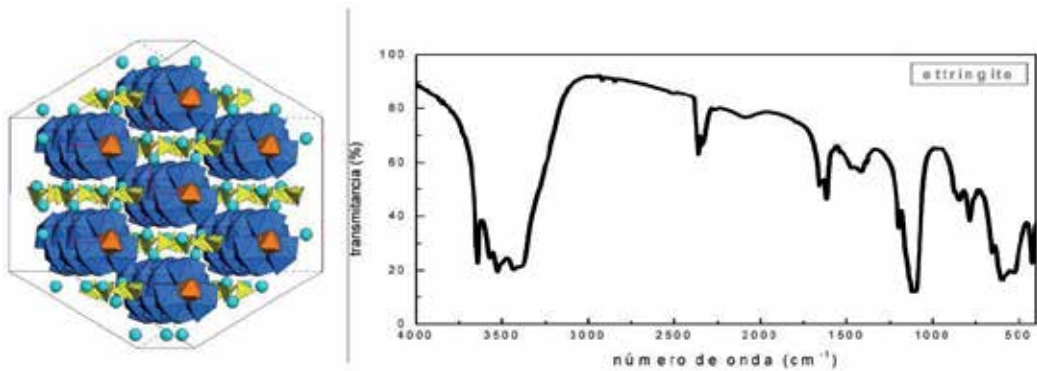


Fig. 10. Structure model of ettringite (according to Dr. J. Neubauer/University Erlangen/Germany) (left), infrared spectra of ettringite (right).

The other crystalline phase present in cement hydration, *portlandite*, $\text{Ca}(\text{OH})_2$, shows two prominent sharp peaks, the first one at 3645 cm^{-1} due to the presence of OH stretching and the second one at 353 cm^{-1} assigned to Ca-O lattice vibrations (Figure 11).

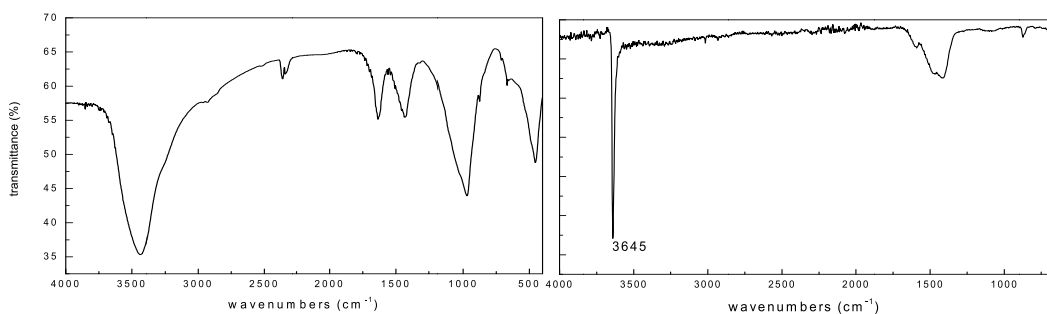


Fig. 11. Infrared spectra of gel C-S-H (left) and portlandite (right)

While crystalline materials give sharp well-defined bands and the glasses give broad, poorly defined bands, the C-S-H samples lie between these two extremes. The distribution function, which describes the line shape of the bands, is strongly dependent upon the

distribution of bond angles and bond lengths within common environments, and the broad half-width of the absorption bands of the C-S-H samples reflect their low symmetry and crystallinity. This distribution is assumed to be symmetry for glasses; hence, any asymmetry of the shape of the bands is due to a superimposition of several symmetrically shaped bands. The infrared spectra of synthetic *C-S-H gel* samples show a broad band in the 3800-3000 cm^{-1} region attributed to OH stretching vibrations of water molecules with maxima close to 3420 and 3626 cm^{-1} , 1428 and 666 cm^{-1} (Figure 11). According to Martinez-Ramirez, depending on the C/S ratio of the C-S-H gel the frequency of the maximum can be different.

With respect to the CACs, the normal CAC hydration with water gives up to the development of hydrated calcium aluminates, CAH_{10} at low temperatures but C_2AH_8 and C_3AH_6 at intermediate and high temperatures joint to AH_3 according to the following reactions:



High early strength, good chemical resistance and high temperature resistance of calcium aluminate cement (CAC) products had encouraged the use of CAC in certain applications. However, conversion of hexagonal phases, CAH_{10} and/or C_2AH_8 to cubic C_3AH_6 and AH_3 in hydrated CAC cement under certain temperature conditions has been the major consequence in limiting its use to special applications. The presence of a minor amount of C_2ASH_8 (strätlingite) in CAC at later ages may be responsible of some strength recovery after conversion process.

The IR spectra of CAH_{10} have a very broad and intense band due to hydroxyl vibration in the 3400-3550 cm^{-1} region, with maxima near to 3500 cm^{-1} . A very weak band at 1650 cm^{-1} is associated to the H-O-H deformation vibration. The 1200-400 cm^{-1} region is a very poor resolution area due to the complexity and associated vibrations sometimes indicating a low crystalline grade; but some absorption bands at 1,024, 774 (shoulder) 699 and a doublet close to 573-528 cm^{-1} . The IR spectra of the CAH_{10} phase are depicted in Figure 12. *The β - C_2AH_8 hexagonal phase presents in the 3400-3700 cm^{-1} region absorption bands at 3,465 and 3,625 cm^{-1} due to OH vibrations of the molecular water. In the 1100-400 cm^{-1} region there is a very complex vibration area with difficulties in the interpretation.*

The C_3AH_6 and the gibbsite are the stable phases in this system. The C_3AH_6 structure can be described as $[\text{Al}(\text{OH})_6]^{2-}$ octahedrals connected by Ca^{2+} cations. The IR spectra presents a very intense OH-free band at 3670 cm^{-1} . This compound do not presents water molecular in the structure so, in the area between 3,400 and 3,600 cm^{-1} , there is not the presence of the deformation H-O-H band. Others fundamental bands due to the stretching and bending vibrations of the Al-O in the octahedral AlO_6 groups, appear at 802, 525 and 412 cm^{-1} (Figure 12).

Different AH_3 polymorphs can be identified by FTIR (Table 4). Although the differences in the strength of OH bond are reflected mainly by the numerous absorption maxima in the

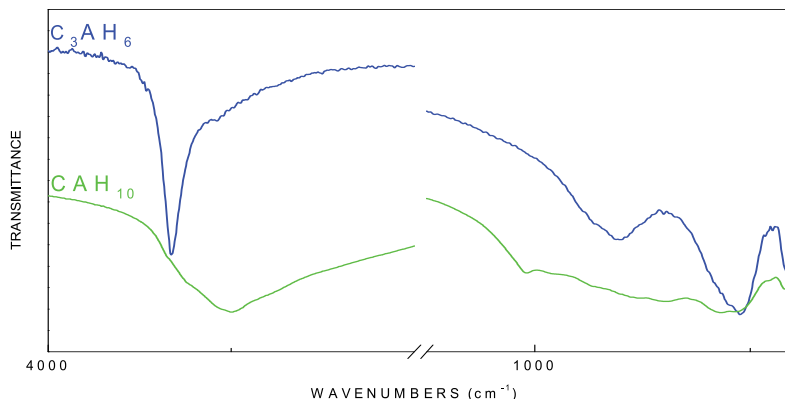


Fig. 12. Infrared spectra of main CAC hydrates, CAH_{10} and C_3AH_6 .

area of $3000\text{--}3700\text{ cm}^{-1}$ of the various polymorphs of the aluminium hydroxide (Fig. 13), the spectroscopy of the calcium aluminate cement does not specify clearly the difference between the three forms of the $Al(OH)_3$. However and as guidance that can help in the interpretation, the bayerite has a band in 3550 cm^{-1} , a shoulder in 3430 cm^{-1} and one other shoulder in 3660 cm^{-1} ; these are not observed in the spectrum of gibbsite. Table 4 shows the bands of greater interest in the three polymorphisms, according to some authors (Fernández, Frederickson, Van der Marel).

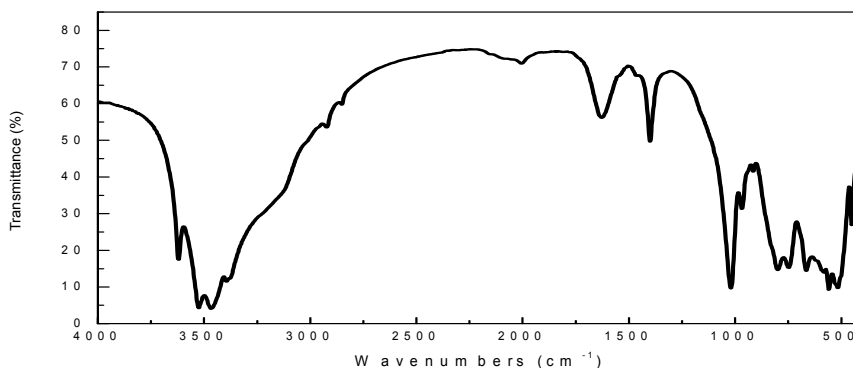


Fig. 13. Aluminium hydroxide, gibbsite, infrared spectra.

	Absorption bands (cm^{-1})	references
Gibbsite	3620, 3524, 3468, 3395 1025, 969	Fernández
Bayerite	3360, 3620, 3540, 3420, 3401, 3454, 3533 1024, 975	Frederickson
Nordstrandite	3660, 3558, 3521, 3490, 3455, 3380, 3360 1060, 1030, 823, 770, 461	Van der Marel

Table 4. Characteristic frequencies of aluminium hydroxides.

4. Carbonated compounds

The infrared spectroscopy is very sensitive to detect the presence of carbonates. The bands more features and more valid for its identification are those indicated in Table 5. The *Calcium carbonate* phases formed after portlandite carbonation, calcite, aragonite or/and vaterite; although vaterite is the least thermodynamically stable of the three crystalline calcium carbonate polymorphs. Indeed, vaterite has been observed following exposure of C-S-H gels to carbon dioxide (accelerated carbonation). The formation of vaterite may occur upon carbonation of pastes with high lime contents, and is favoured by the presence of imperfectly crystalline portlandite. The observed absorptions bands for calcium carbonate phases are due to the planar CO_3^{2-} ion. There are four vibrational modes in the free CO_3^{2-} ion: i) the symmetric stretching, $\nu_1[\text{CO}_3]$; ii) the out-of-plane bend, $\nu_2[\text{CO}_3]$; iii) the asymmetric stretch, $\nu_3[\text{CO}_3]$; and iv) the split in-plane bending vibrations $\nu_4[\text{CO}_3]$; and Ca-O lattice vibrations. Depending on the calcium carbonate polymorph the vibration of the bands appears at different wavenumber. Figure 14 shows the spectra of calcite, vaterite and aragonite.

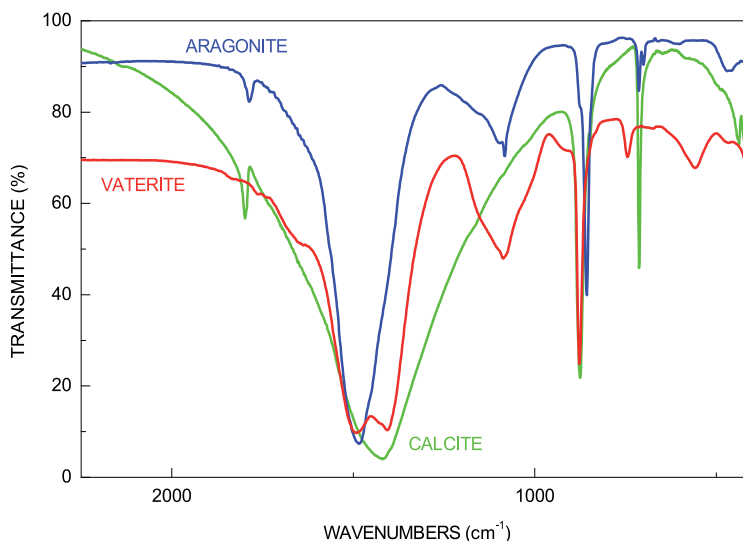


Fig. 14. Infrared spectra of calcite, vaterite and aragonite.

	calcite	vaterite	aragonite
ν_1	1063	1085	
ν_3	1420	1482	1492-1404
ν_4	875, 848	856	877
ν_2	712	713, 700	744

Table 5. Calcium carbonate polymorphs infrared bands

5. Acknowledgments

Special thanks to Tomás Vázquez to teach and pass on to us his enthusiasm for the infrared spectroscopy techniques. The authors also thank the support by the MICINN (Ministerio de Ciencia e Innovación) with the BIA00767- 2008 project.

6. References

- A. S. Povaennykh "The use of infrared spectra for the determination of minerals" American Mineralogist, Volume 63, pages 956-959, 1978.
Academic Press, New York., 1971.
- Afremow L. "High resolution spectra of inorganic pigment and extenders in the mid-infrared region from 1500 cm⁻¹ to 200 cm⁻¹" Journal of paint technology vol. 28 issue 34 (1966).
- Basila M. R. "Infrared Spectra of Adsorbed Molecules", 1968.
- Bensted J, Varna SP. Some applications of IR and Raman. Spectroscopy in cement chemistry, Part III: Hydration of Portland cement and its constituents. *Cement Technology*, (5):440-450, 1974.
- Farmer, V. C. (Ed.) The Infrared Spectra of Minerals. Mineralogical Society, London, 1974.
- Fernandez, L., Vazquez, T. "Aplicación de la espectroscopia infrarroja al estudio de cemento aluminoso" *Materiales de Construcción* 46(241):53-65, 1996.
- Frederickson, L.D.: Analytical Chemistry, vol. 26, p. 1883, die., 1954.
- Ghosh, S. N. "Infrared and Raman spectral studies in cement and concrete" *Cement and Concrete Research* 10(6):771-782 (1980).
- Ghosh, S. N., Chatterjee, A. K. "Absorption and reflection infrared spectra of major cement minerals, clinkers and cements" *Journal of Materials Science* 9(10):1577-1584, 1974.
- Hughes, T.L., Methven, C.M., Jones, T.G.J., Pelham, S.E., Fletcher, P., Hall, C. "Determining cement composition by Fourier Transform infrared spectroscopy" *Advanced Cement Based Materials* 2(3):91-104, 1995.
- Lawson, K. E. "Infrared Absorption of Inorganic Substances", Reinhold Publishing Corp., New York, 1961.
- Matossi, F. "Vibration Frequencies and Binding Forces in Some Silicate Groups" *The Journal of Chemical Physics* Vol. 17, n 8, 1949.
- Nakamoto, K. *Infrared Spectra of Inorganic and Coordination Compounds*. Wiley, New York., 1970.
- Nyquist, R. P. and R. O. Kagel "Infrared spectra of inorganic compounds (3800 - 45 cm⁻¹).
Schaefer, C., Matossi, F., Wirtz, K., *Zeits. F. Physik* 89, 210, 1934.
- Tarte, P. "Infrared spectra of inorganic aluminates and characteristic vibrational frequencies of AlO₄ tetrahedra and AlO₆ octahedra" *Spectrochimica Acta: Part A Molecular Spectroscopy* 23A(7):2127-2143, 1967.
- Tarte, P. Etude infra-rouge des orthosilicates et des ortho-germanates. Une nouvelle method d'interpretation des spectres. *Spectrochim. Acta*, I 8, 467 -483, 1962.
- Taylor, H. F. W.: *Cement Chemistry*. Reedwood Books, Trowbridge, 2nd Edition, 1997.
- Van der Marel and Beutelspacher, H.: *Atlas of Infrared Spectroscopy of Clay Minerals and Their Admixtures*. Ed. ELSEVIER. New York. 1976.

Vázquez, T. "Espectroscopía Infrarroja de algunos compuestos de interés en la química del cemento". Cuadernos de Investigación del Instituto Eduardo torroja de la Construcción y del Cemento, 1969.

Infrared Spectroscopy Techniques in the Characterization of SOFC Functional Ceramics

Daniel A. Macedo et al.*

*Material Science and Engineering Post Graduate Program, UFRN
Brazil*

1. Introduction

Infrared spectroscopy is certainly one of the most important analytical techniques available nowadays for scientists. One of the greatest advantages of infrared spectroscopy is that virtually any sample in any physical state can be analyzed. The technique is based on the vibrations of atoms of a molecule. An infrared spectrum is obtained by passing infrared radiation through a sample and determining what fraction of the incident radiation is absorbed at a particular energy. The energy at which any peak in an absorption spectrum appears corresponds to the frequency of a vibration of a part of a sample molecule (Stuart, 2004).

Fourier transform infrared spectroscopy (FTIR) has been widely used for *in situ* analysis of adsorbed species and surface reactions. Infrared spectroscopy techniques have been used for the characterization of solid oxide fuel cells (SOFCs). FTIR is utilized to identify the structure of the SOFC electrode and electrolyte surface (Resini et al., 2009; Guo et al., 2010). Liu and co-workers (Liu et al., 2002) were pioneers in the *in situ* surface characterization by FTIR under SOFC operating conditions.

The development of high-performance electrode and electrolyte materials for SOFC is an important step towards reducing the fuel cell operation temperature to the low and intermediate range (500 – 700 °C). As the operating temperature is reduced, many cell parts, such as the auxiliary components can be easily and cost-efficiently produced. To meet long operational lifetime, material compatibility and thermomechanical resistance would be less critical as the range of possibilities for lower temperature increases. To that end, recent research at UFRN, Natal, Brazil has successfully focused on novel synthesis processes based on microwave-assisted combustion and modified polymeric precursor methods in order to synthesize high performance cobaltite-based composite cathodes for low-intermediary-temperature SOFCs.

* Moisés R. Cesário², Grazielle L. Souza³, Beatriz Cela⁴, Carlos A. Paskocimas¹, Antonio E. Martinelli¹, Dulce M. A. Melo^{1,2} and Rubens M. Nascimento¹

¹Material Science and Engineering Post Graduate Program, UFRN, Brazil

²Chemistry Pos Graduate Program, UFRN, Brazil

³Chemical Engineering Department, UFRN, Brazil

⁴Forschungszentrum Jülich GmbH, Central Department of Technology (ZAT), Germany

This book chapter reviews how powerful infrared spectroscopy techniques play a fundamental role in the novel synthesis approaches developed during the last 5 years (2007 – 2011) by this research group. Synthesized high performance cathode powders had their features investigated using different materials characterization techniques, such as Fourier Transform Infrared Spectroscopy (FTIR), FAR and MID-Infrared spectroscopy.

2. Solid oxide fuel cells and its components

Fuel cells are highly efficient power generation devices which convert chemical energy of gaseous fuels (hydrogen, fossil fuels and ethanol among others) directly into electric power in a silent and environmentally friendly way. These electrochemical devices are promising alternatives to traditional mobile and stationary power sources, such as internal combustion engines and coal burning power plants. Among the various types of fuel cells, solid oxide fuel cells (SOFCs) have advantages linked to high energy conversion efficiency and excellent fuel flexibility because of their high operating temperature compared to other types of fuel cells. Fig. 1 depicts a typical SOFC single cell produced by our research group. It consists of three basic components: two porous electrodes (anode and cathode) and a solid electrolyte. Each one of these components must fulfil specific performance requirements such as microstructural stability during preparation and operation; chemical and physical compatibility, i.e., similar thermal expansion coefficients; adequate porosity and catalytic activity to achieve the highest performance (Minh & Takahashi, 1995; Singhal, 2000).

The SOFC electrolyte material, typically yttria stabilized zirconia (YSZ) or rare earth doped ceria, must be an electronic insulating but ion-conducting ceramic that allows only protons or oxygen ions to pass through. Furthermore, the electrolyte material must be dense to separate the air and fuel, chemically and structurally stable over a wide range of partial pressures of oxygen and temperatures. The cathode (air electrode) material, typically lanthanum manganites and cobaltites, has to be electrocatalyst for oxygen reduction into oxide ions. When an oxygen ionic conducting oxide is adopted as electrolyte, these ions diffuse through the material to the anode (fuel electrode), driven by the differences in oxygen chemical potential between fuel and air constituents of the cell, where they electrochemically oxidize fuels such as hydrogen, methane, and hydrocarbons. The released electrons flow through an external circuit to the cathode to complete the circuit. The complete mechanism of electric power production in a SOFC is also shown in Fig. 1.

SOFCs have attracted significant attention in the last 20-30 years due to their high efficiency, fuel flexibility and environmental advantages (Minh, 2004; Molenda et al., 2007; McIntosh & Gorte, 2004). However, typical SOFCs operate at 1000 °C. Elevated operating temperatures introduce a series of difficulties such as sintering of the electrodes and high reactivity between cell components. For these reasons, there is a considerable research interest in reducing the operating temperature of these devices down to the range between 500 and 800 °C, which characterizes intermediate temperature solid oxide fuel cells (IT-SOFCs) or even lower, which would imply the use of inexpensive metallic materials, rapid start-up and shut-down, minimization of thermal degradation and reactions between cell components, and longer operational lifetime. Furthermore, as the operation temperature is reduced, system reliability increases, increasing the possibility of using SOFCs for a wide variety of applications, including residential and automotive devices. On the other hand, reduced operating temperatures reduces the overall electrochemical performance due to increased

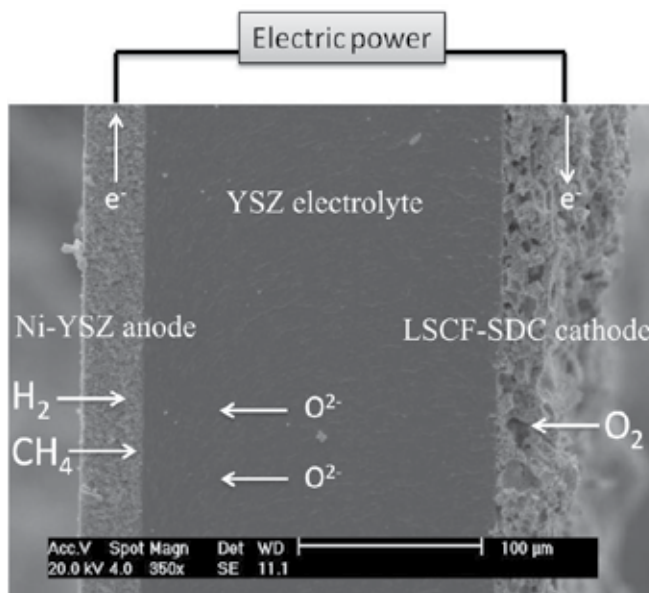


Fig. 1. A typical SOFC single cell with its basic components (anode, cathode and electrolyte) and the mechanism of energy production.

ohmic losses and electrode polarization losses associated with thermally activated processes of both ionic transport and electrode reactions. In special, the electrochemical activity of the cathode dramatically deteriorates with decreasing temperature for typical strontium-doped lanthanum manganite (LSM) based electrodes (Singhal 2000; Steele, 2000; Steele & Heinzel, 2001).

Thus, to achieve acceptable performance of IT-SOFCs, reducing the electrolyte resistance and electrode polarization losses are two key points. Losses attributed to electrolytes can be minimized by decreasing the thickness of electrolyte layers or substituting traditional YSZ by other electrolytes, such as doped ceria and apatite-like materials. The overall electrochemical limitation would then be ruled by electrode polarization losses. Due to the higher activation energy and lower reaction kinetics for oxygen reduction at the cathode compared with those of the fuel oxidation at the anode, the polarization loss from the air electrode (cathode) that limits the overall cell performance (Ivers-Tiffée et al., 2001; Tsai & Barnett, 1997). Therefore, the development of new cathode materials with high electrocatalytic activity for oxygen reduction becomes a critical issue for the development of IT-SOFCs.

2.1 Development of cathode materials

The development of high performance cathodes is based on reducing its thickness from hundreds to few micrometers associated with the addition of an electrolyte material in the formation of composite cathodes. These are interesting approaches that can improve electrode performance for the reduction of oxygen. The latter allows the extension of the triple phase boundaries (TPB) from the electrolyte/cathode interface deep into the bulk of the electrode, permitting electrochemical reactions to take place within the electrode. The

preparation of composite cathodes by the combination of strontium-doped lanthanum manganite (LSM) with yttria stabilized zirconia (YSZ) or even samarium oxide-doped ceria (SDC) has been intensively studied in the last years. Whereas rare earth doped ceria, both samarium (SDC) and gadolinium doped ceria (CGO), have higher ionic conductivity than YSZ. Thus, composite cathodes such as LSM-SDC or LSM-CGO have better electrochemical performance than LSM-YSZ, and are particularly indicated for IT-SOFCs (Zhang et al., 2007; Chen et al., 2008; Wang et al., 2007).

2.1.1 Lanthanum manganite and cobaltite based cathodes

Lanthanum manganites (LaMnO_3), particularly strontium-doped lanthanum manganites ($\text{La}_{1-x}\text{Sr}_x\text{MnO}_3$ - LSM), are widely used as cathode materials in SOFCs operating at high temperatures (800 - 1000 °C), which is the temperature range where yttria-stabilized zirconia (YSZ) is commonly used as electrolyte. Doping Sr into LaMnO_3 considerably increases electrical conductivity because of the increased number of holes. LSM cathodes present high stability, electro-catalytic activity for O_2 reduction at high temperatures and thermal expansion coefficient reasonably similar to YSZ electrolyte (Escobedo et al., 2008; Jiang, 2003; Minh, 1993). Even though LSM cathodes have been successfully used as functional materials in high temperature SOFCs, they have been replaced for more efficient lanthanum strontium cobaltite ferrites (LSCF). LSMs are poor ionic conductors and the electrochemical reactions are limited to the region close to triple phase boundaries (TPB). On the other hand, LSCF is a mixed electronic/ionic conductor (MEIC) with appreciable ionic conductivity. The exchange of oxygen ions occurs at the electrode surface with the diffusion of oxygen through the mixed conductor (Liu et al., 2007; Shao et al., 2009).

Due to low ionic conductivity and high activation energy to oxygen dissociation at low temperatures, cathodes made of LSM and LSCF are normally combined with the electrolyte material forming a composite cathode. The composite cathodes containing ceria are more attractive to low and intermediate temperatures (500 - 700 °C) than the ones containing YSZ, which has lower ionic conductivity in such temperatures (Yang et al., 2007; Xu et al., 2006; Xu et al., 2005; Chen et al., 2007; Zhang et al., 2008; Lin et al., 2008).

Among the extensive number of chemical synthesis routes available for the preparation of LSM and LSCF powders, the polymeric precursor method (Pechini method), solid state reaction, spray pyrolysis and combustion synthesis have been successfully used (Conceição et al., 2009; Cela et al., 2009; Grossin & Noudem, 2004; Guo et al., 2006; Macedo et al., 2009; Conceição et al., 2011). In spite of the proved efficiency of the polymeric precursor method to produce monophasic nanometric powders, alternative synthesis methods mainly using microwave technology have been implemented in an attempt to minimize energy consumption and total powder production time (Liu et al., 2007). An alternative method for preparing nanoparticles with particle sizes of order of nanometers using low annealing temperatures has been developed using commercial gelatin as a polymerizing agent. This method has been named by the authors as *soft chemical route* (Medeiros et al., 2004; Maia et al., 2006).

Regarding the development of LSM based composite cathodes, several works have reported the preparation of LSM-SDC cathodes from the powders obtained by different synthesis methods (Ye et al., 2007; Chen et al., 2007; Xu et al., 2009). However, no reports on the

preparation of LSM-SDC films from powders synthesized using commercial gelatin have been encountered. This chapter presents recent results in obtaining cathodes based on LSM and SDC powders obtained by the modified Pechini method using commercial gelatin as polymerizing agent. LSM-SDC films were prepared using different amounts of ethyl cellulose as pore former. Among the many methods which can be used to produce SOFC cathodes, slurry spin coating was selected due to its fast processing time and high uniformity over the surface. In this technique, a high spin rotation quickly lays the slurry on the substrate which dries in short times, hindering particle agglomeration, which also contributes to the uniform distribution of particles along the green film. The characteristics of not only LSM, SDC and LSCF powders, but also LSM-SDC spin-coated and LSCF-SDC screen-printed films have been investigated by different techniques.

3. Infrared spectroscopy techniques applied in the SOFC research

The fundamental studies of the catalytic reactions mechanisms that occur near the three-phase boundary in the anode of a solid oxide fuel cell still deserving attention and investigation. Many in situ spectroscopies such as Raman and infrared spectroscopy are routinely used in catalysis research to characterize surface intermediates and reaction mechanisms. It is very difficult to apply in situ spectroscopy techniques to an operating SOFC anode (Atkinson et al., 2004). Recently research groups (Liu et al., 2002; Guo et al., 2010) presented their methodologies on the possible ways to apply the infrared emission spectroscopy to characterize working SOFC anodes.

Guo and co-workers (Guo et al., 2010) worked recently developing a novel experimental technique to measure in situ surface deformation and temperature on the anode surface of a SOFC button cell, along with cell electrochemical performance under operating conditions. An adaptation of a SOFC button cell test apparatus was integrated with a Sagnac interferometric optical setup and IR thermometer. This optical technique was capable of in situ, noncontact, electrode surface deformation, and temperature measurement under SOFC operating conditions. The surface deformation measurement sensitivity is half-wavelength and is immune to temperature fluctuation and environmental vibration. The experimental data can be used for the validation and further development of SOFC structural and electrochemical modeling analyses (Guo et al., 2010).

Other application of infrared spectroscopy techniques, for example FTIR, is for functional ceramic, electrodes and electrolyte, characterization. Through analyze of the absorption bands in low wave number region the oxygen-metal linkage are associated; the enlarged bands are attributed to the stretching vibration of hydrogen-bonded OH groups present. Moreover, the residual carbon from the synthesis not eliminated in the thermal treatment processes, can also be observed in some bands, for example associated to carboxylate anion (COO⁻) stretching and the C-O groups or to stretching vibration of the C-O bonds.

4. Experimental

4.1 Preparation and characterization of functional materials for SOFC

During the last years the research of the group on SOFC development has been focused on the synthesis of LaSrMnO₃ (LSM), SmCeO₂ (SDC) and LaSrCoFeO₃ (LSCF) powders by two different methods. LSM and SDC powders have been prepared by the modified Pechini

method using gelatin as a polymerizing agent. LSCF powder has been synthesized by microwave-assisted combustion. The electrochemical performance of a single electrolyte-supported SOFC containing LSCF-SDC composite cathode film has also been investigated.

The raw materials used to synthesize LSM and SDC powders by the modified Pechini method, in which gelatin replaces ethylene glycol, were lanthanum, strontium, manganese (VETEC, Brazil), samarium and cerium (Sigma-Aldrich, Germany) nitrates. For synthesizing LSM, a solution of manganese citrate was firstly prepared from manganese nitrate and citric acid with a molar ratio of 1:3 (metal/citric acid) under stirring for 2 h at 70 °C. Stoichiometric amounts of the other citrates were added one by one at 1 hour intervals. The temperature was slowly increased up to 80 °C and then gelatin was added at a weight ratio of 40:60 (gelatin/citric acid). The solution was stirred on a hot plate, which allowed the temperature to be controlled until a polymeric resin was formed. This resin was pre-calcined at 300 °C for 2 h, forming a black solid mass which was grounded into a powder and calcined at 500, 700 or 900 °C for 4 h to obtain the LSM perovskite structure. SDC powder was obtained following the same procedure but calcined between 700 and 900 °C.

To further understand the synthesis mechanism used in this work, which uses gelatin instead of ethylene glycol, it is necessary to review the traditional polymeric precursor method proposed by Pechini (Pechini, 1967). The Pechini method involves the formation of stable metal-chelate complexes with certain alpha-hydroxycarboxyl acids, such as citric acid, and polyesterification in the presence of a polyhydroxy alcohol, such as ethylene glycol, to form a polymeric resin. The metal cations are homogeneously distributed in the polymeric resin, which is then calcined to yield the desired oxides. The most common materials used as source of cations are nitrate salts since they can be fully removed at low temperatures (400 - 500 °C). The synthesis mechanism of the modified Pechini method used in this work can be explained in three basic steps, as shown in Fig. 2. It stands out by its simplicity and low cost, using only citric acid, gelatin and metal nitrates as reagents.

In the first step, a solution of metallic citrate is prepared from the mixture of deionized water, citric acid and the salts of each metal ion. The citric acid acts as a chelating agent to remove metal ions from the solution. Chelation is the ability that a chemical substance has to form a ring-like structure with a metal ion, resulting in a compound with different chemical properties compared to the original metal, which prevents it from following different chemical routes. The chelating agent acts as a crayfish which traps the metal in its claws. When metal ions are in solution, they are surrounded by water molecules which avoid the establishment of new bonds. Thus, the chelating agent replaces such water molecules (bonds) and forms a ring-like structure, resulting in the phenomenon known as chelation. The number of binding sites that can form coordination bonds in the metal determines the number of rings formed.

The second step of this synthesis mechanism is the gelatin hydrolysis. Gelatin is a natural polymer, composed of a mixture of high molecular weight polypeptides (proteins) obtained by controlled hydrolysis of collagen fiber. Therefore, it can be used for cheap aqueous polymeric precursor synthesis in order to attain nanocrystalline powders. As illustrated in Fig. 2, the gelatin hydrolysis corresponds to the breaking of peptide bonds in the presence of water. For easier understanding, the second step reaction, in this illustration, is taking place in a low molecular weight peptide. An extra hydrogen ion is necessary to react with the -NH₂ group on the left-hand end of the peptide, the one not involved in the peptide bond. By

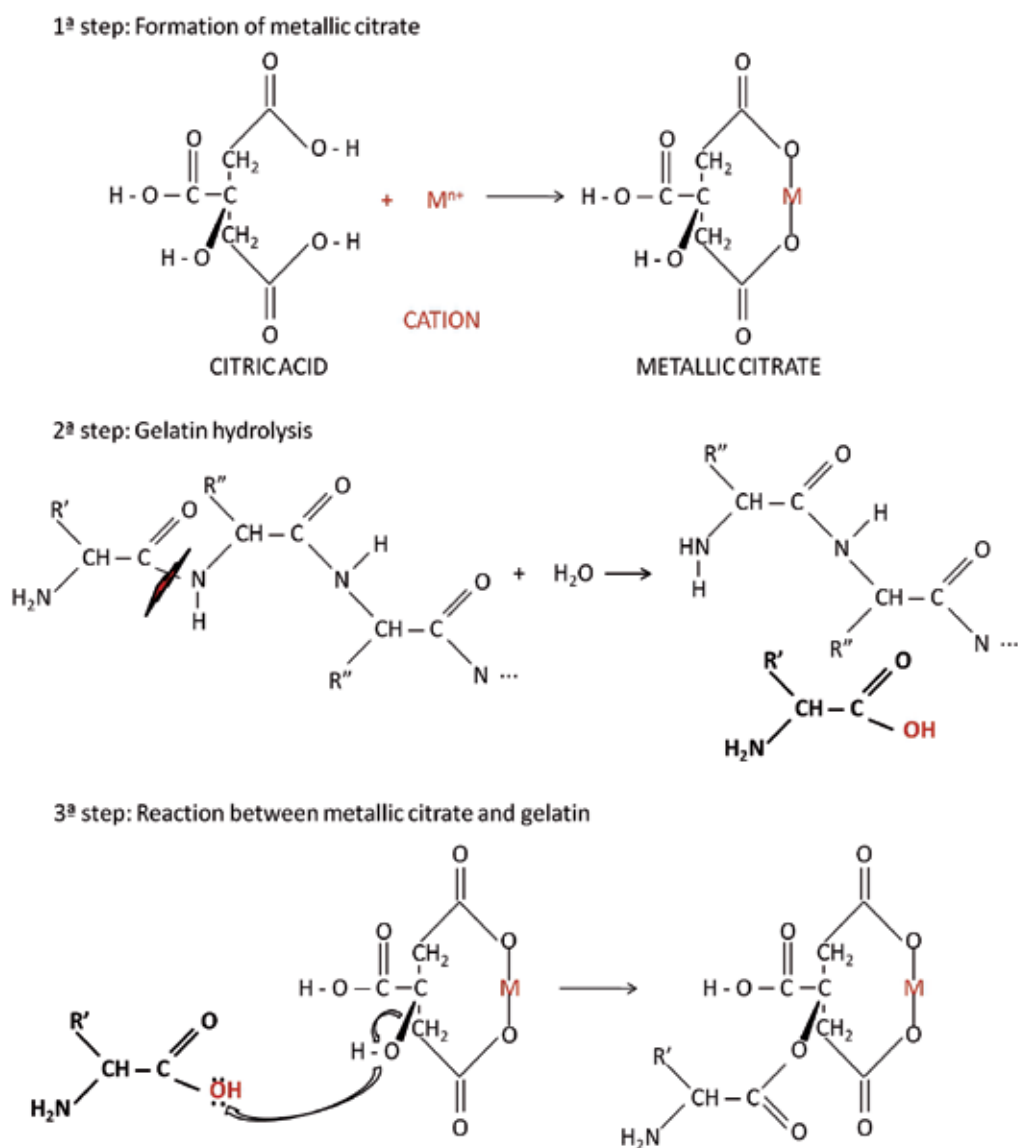


Fig. 2. Synthesis mechanism of the modified Pechini method.

scaling this up to a polypeptide (a protein chain), each of the peptide bonds will be broken in exactly the same way. This means that a mixture of the amino acids that makes up the protein will form, although in the form of their positive ions because of the presence of hydrogen ions from the citric acid. The presence of positive ions (not shown in Fig.2) is due to the fact that an amino acid has both a basic amine group and an acidic carboxylic acid group. There is an internal transference of a hydrogen ion from the -COOH group to the -NH_2 group to grant both a negative and positive charge to the ion. This is called a zwitterion. This is how amino acids exist even in the solid state. After being dissolved in water, the gelatin forms a simple solution which also contains this ion. A zwitterion is a compound with no overall electrical

charge, but which contains separate parts, positively and negatively charged. As the pH decreases by adding an acid to a solution of an amino acid, the $-\text{COO}^-$ side of the zwitterion picks up a hydrogen ion, forming the desirable compound.

In the third step, proteins act as amides and react with the free hydroxyl of the citric acid. The hydroxyl of the citric acid reacts like the hydroxyl of an alcohol in a standard esterification process. During the reaction of the amide with the citric acid, the substitution of the amide hydroxyl by an alkoxy radical ($-\text{OR}$) takes place. At the end of the process, the oxygen in the $-\text{OH}$ group of the citric acid remains in the chain whereas the hydroxyl oxygen in the amino acids is eliminated in the form of water. This mechanism results in long chains containing metal cations tightly bond and evenly distributed.

To synthesize LSCF powders, an aqueous solution of $\text{La}(\text{NO}_3)_3$, $\text{Sr}(\text{NO}_3)_2$, $\text{Co}(\text{NO}_3)_2$, and $\text{Fe}(\text{NO}_3)_3$ (VETEC, Brazil) and urea as fuel was heated up to $100\text{ }^\circ\text{C}$ under stirring for 10 minutes. Afterwards, the becker was placed in a microwave oven set to 810 W and 2.45 GHz. Self-ignition takes place in about 1 minute. The resulting powder was then calcined at $900\text{ }^\circ\text{C}$ for 4 h in order to remove carbon residues remaining in the ash and to convert the powder to the desired LSCF phase with a well-defined crystalline perovskite structure.

LSM, SDC and LSCF powders were characterized by XRD using a Shimadzu XDR-7000 diffractometer and scanning electron microscopy (SEM-SSX 550, Shimadzu). Infrared spectra were also recorded with FTIR (IR Prestige-21, Shimadzu) in the $400 - 4600\text{ cm}^{-1}$ spectral range. Specific surface area measurements were performed only for the LSM powders. An infrared reflectance spectrum of a LSM pellet prepared from a powder calcined at $900\text{ }^\circ\text{C}$ was recorded with a Fourier-transform spectrometer (Bomem DA 8-02) equipped with a fixed-angle specular reflectance accessory (external incidence angle of 11.5°).

4.1.1 Preparation and characterization of composite cathodes

Composite powders consisted of 50 wt.% cathode (LSM or LSCF) and 50 wt.% SDC were prepared by mixing in a ball mill for 24 h in order to deposit LSM-SDC and LSCF-SDC composite films by spin coating (LSM-SDC) and screen printing (LSCF-SDC). Prior to spin coating deposition, ceramic suspensions of LSM-SDC composite powders were prepared using ethanol and different amounts of ethyl cellulose as pore-forming material. Ethyl cellulose was added in the weight ratios of 4, 8 and 10 wt.% with respect to the total solid weight. With the purpose of studying the influence of the milling process on the particle size distribution, another mixture was prepared without milling and without the addition of ethyl cellulose. Before coating, the ceramic suspensions were ultrasonically treated and then deposited by spin coating onto YSZ substrates. Commercially available YSZ powder (Tosoh Corporation, Japan) was compressed into pellets (13 mm in diameter) under uniaxial pressure (74 MPa) and then sintered in air at $1450\text{ }^\circ\text{C}$ for 4 h to increase its mechanical strength for application as ceramic substrate. In the deposition process, 25 layers were applied using initial and final rotation speeds of 500 rpm for 15 seconds and 5000 rpm for 30 seconds, respectively. The composite films were attained after sintering at $1150\text{ }^\circ\text{C}$ for 4 h. LSCF-SDC cathodes were screen-printed onto YSZ electrolytes and sintered at $950\text{ }^\circ\text{C}$ for 4 h. The morphological characterization of the surface and cross section of LSM-SDC composite cathodes was performed using a field emission gun scanning electron microscope (FEG-SEM, Zeiss-Supra 35) and a scanning electron microscope (SEM-SSX 550, Shimadzu).

4.2 Preparation and characterization of a SOFC single cell

A preliminary performance test was carried out to qualitatively evaluate the prepared LSCF-SDC composite cathode. A single SOFC supported on commercial, 200 μm thick, YSZ electrolyte (Kerafol, Germany) with Ni-YSZ anode and LSCF-SDC composite cathode screen printed was used. To assemble the single cell, first the anode suspension was printed and the half cell was sintered at 1300 $^{\circ}\text{C}$ for 4 h. The anode was reduced during cell operation. Later on, the LSCF-SDC cathode was printed on the other electrolyte side and sintered at 950 $^{\circ}\text{C}$ for 4 h to avoid undesirable reactions. An in-house test station was used in the performance evaluation. The single cell was tested using dry hydrogen as fuel and oxygen as oxidant, in the ratio of 40ml/min H_2 and 40ml/min O_2 . The current-voltage characteristic of the cell was measured using linear sweep voltammetry (LSV) over a temperature range of 800 to 950 $^{\circ}\text{C}$. The microstructure of the cathode/electrolyte interface after the performance test was examined by SEM.

5. Results and discussion

5.1 Characterization of functional materials for SOFC

XRD patterns of the calcined LSM powders can be observed in Fig. 3. The as-synthesized material depicts the main diffraction peaks characteristic of the rhombohedral structure with space group $R\bar{3}c$ (Konyshva et al., 2009) and the respective JCPDS (Joint Committee on Powder Diffraction Standards) chart number 53-0058. Secondary phases were found and identified as SrCO_3 and Mn_3O_4 . The presence of SrCO_3 was identified at 500 and 700 $^{\circ}\text{C}$ by comparison with JCPDS pattern number 84-1778. The formation of strontium carbonate is due to the reaction between SrO and CO_2 produced during organic compound decomposition. Mn_3O_4 is present only in the powder calcined at 900 $^{\circ}\text{C}$ and was identified by comparison with pattern JCPDS 89-4837. It probably came from the change of oxidation state of the Mn ion. Vargas and co-workers (Vargas et al., 2008) have reported that

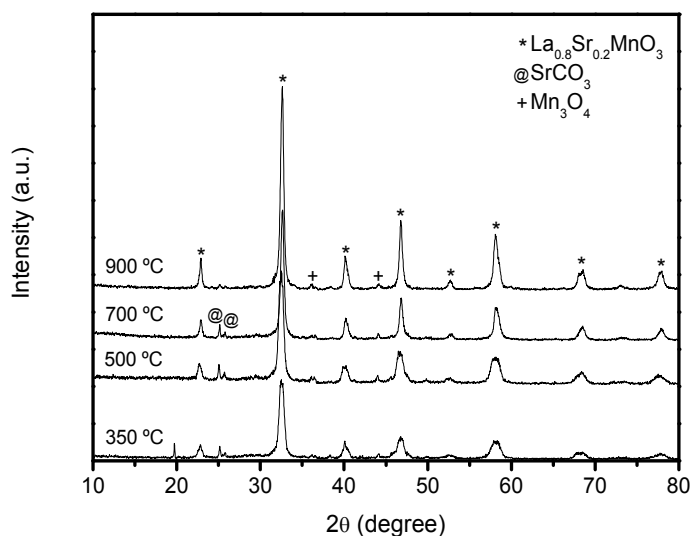


Fig. 3. XRD patterns of LSM powders calcined at different temperatures.

temperatures higher than 1000 °C are necessary to remove all the carbon present in the LSM powders. Lower calcination temperatures result in free carbon or as carbonates from the degradation of citrates.

Table 1 lists the specific surface area (S_{BET}), average crystallite size (D_{XRD}), average particle size (d_{BET}), microstrain and the $d_{\text{BET}}/D_{\text{XRD}}$ ratio for LSM powders calcined at 700 and 900 °C. There is a clear dependency between the average crystallite size and the calcination temperature. The thermal treatment temperature is directly proportional to the crystallite size, because of the crystallization process that occurs in high temperatures. Therefore, the specific surface area decreases with the onset of particle sintering. High particle sizes promote lower surface area to volume ratio, which results in small deformations in the crystalline structure parameters.

Calcination temperature (°C)	S_{BET} (m ² /g)	d_{BET} (nm)*	D_{XRD} (nm)**	Microstrain (%)	$d_{\text{BET}}/D_{\text{XRD}}$
700	18.79	48.9	22.80	0.004869	2.1
900	8.46	108.7	25.21	0.003917	4.3

*Calculated from specific surface area

*Theoretical density: LSM= 6.521 g/cm³

**Calculated by Rietveld refinement

Table 1. Specific surface area (S_{BET}), average particle size (d_{BET}), average crystallite size (D_{XRD}), microstrain and crystalline degree of LSM powders.

The $d_{\text{BET}}/D_{\text{XRD}}$ ratio, which indicates the degree of particle agglomeration, increases with the calcination temperature. In a previous study (Cela et al., 2009), $d_{\text{BET}}/D_{\text{XRD}}$ equal to 12 was established for the LSM powder synthesized with ethylene glycol as the polymerizing agent and calcined at 900 °C. This result shows that the substitution of ethylene glycol for gelatin reduces powder agglomeration, improving the potential to prepare ceramic suspensions to be deposited as cathode films with good adherence to the substrate.

LSM powders were observed by scanning electron microscopy (Fig. 4). SEM micrographs revealed the presence of soft particles agglomerates. Fig. 4(d) displays a FEG-SEM high magnification image of the LSM powder calcined at 900 °C. As it can be seen, this powder reveals strong agglomeration of particles with an estimated size lower than 100 nm. Results from SEM analyses are in good agreement with specific surface area measurements.

In the FTIR spectra of the LSM powders calcined between 500 and 900 °C, displayed in Fig. 5, a band located at 603 cm⁻¹ is attributed to M - O (metal - oxygen) stretching, and is characteristic of the perovskite structure. On the other hand, bands corresponding to carbon bonds, particularly carboxyl groups are visible in 1000 - 2500 cm⁻¹ interval. The two absorption bands at 1460 cm⁻¹ and 2360 cm⁻¹ are due to C=O vibration and can be related to traces of carbonate. In the range of 3300 - 3670 cm⁻¹ a band corresponding to O - H bond can be attributed to adsorbed water due to the contact of the sample with the environment. With this information and the XRD analyses, it became clear that the carbonate content of the synthesized powders decreases and even vanishes at higher calcination temperatures.

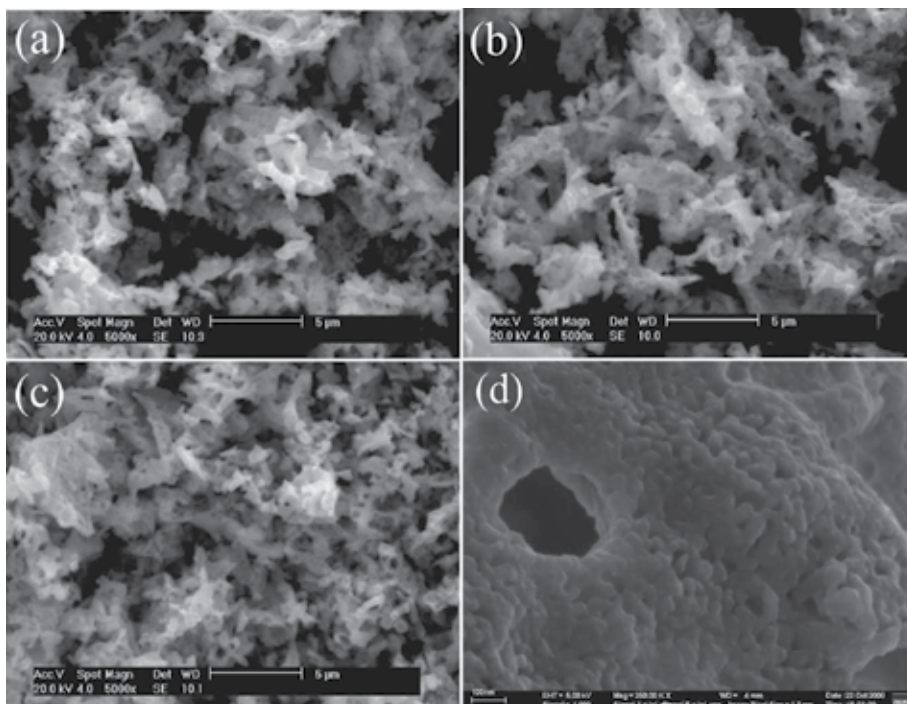


Fig. 4. SEM micrographs of LSM powders calcined at: (a) 500 °C, (b) 700 °C and (c) 900 °C for 4 h. FEG-SEM high magnification image of powder calcined at 900 °C (d).

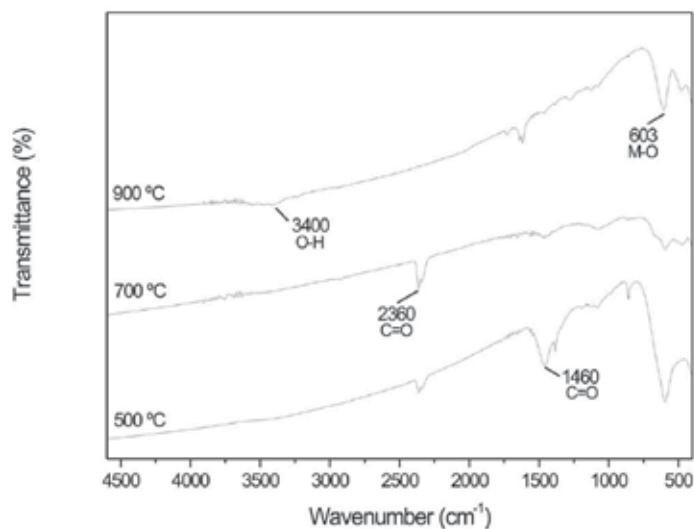


Fig. 5. FTIR spectra of LSM powders calcined at different temperatures.

The infrared reflectance spectrum in the FAR and MID ranges is presented in Fig. 6. The almost continuous decrease of the reflectivity as a function of the wave number shows that this spectrum is dominated by a conduction mechanism (Gosnet et al., 2008). Moreover, first

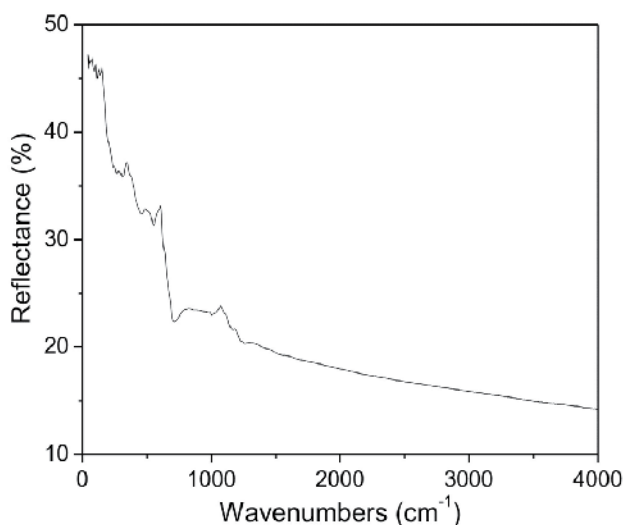


Fig. 6. Infrared reflectance spectrum in the FAR and MID ranges for LSM powder calcined at 900 °C.

order phonon features characteristic of the crystal lattice are clearly superposed on the decreasing reflectivity curve below 700 cm^{-1} . The reflectivity line shape of these phonons is rather characteristic of conducting materials and denotes possibly electron-phonon coupling in the LSM powder calcined at 900 °C, as also observed in $\text{La}_{0.7}\text{Ca}_{0.3}\text{MnO}_3$ ceramics (Kim et al., 1996). On the other hand, the two modes above 1000 cm^{-1} are likely to be defect modes from impurities due to unreacted materials, probably Mn_3O_4 , as observed by XRD.

The XRD patterns of SDC powders, as synthesized by the modified Pechini method and after calcination from 700 to 900 °C, are shown in Fig. 7. XRD results revealed no peaks corresponding to secondary phases, i.e., there are no obvious peaks from phases other than SDC (JCPDS 75-0158) until the detection limit of the X-ray diffraction. The Rietveld refinement of the diffraction data using Maud program indicates that SDC powders exhibit cubic structures with space group Fm-3m and crystallite sizes in the range of 7-38 nm. Typical particle morphology of the SDC powder calcined at 900 °C is shown in Fig. 7(b), from which it can be seen that the particles are nearly spherical and strongly agglomerated, as expected for nanoparticles synthesized by the polymeric precursor method. FEG-SEM images also showed that the spherical particles are lower than 50 nm.

The FTIR spectra of SDC powders synthesized by the modified Pechini method and calcined at different temperatures are shown in Fig. 8. The peaks at around 3400 and 1640 cm^{-1} correspond to the H-O stretching and H-O-H bending vibration, respectively. They indicate that water or hydroxyl groups still existed not only in the as-prepared, but also in all calcined samples. A low intensity band at 1380 cm^{-1} in the as-prepared powder might indicate the physical adsorption of CO_2 or be caused by residual NO_3^- (Chen et al., 2006). However, this band is eliminated after heat treatment. Therefore, although a synthesis temperature as low as 350 °C was sufficient to produce the SDC phase, powders with higher purity were obtained by calcining above 700 °C.

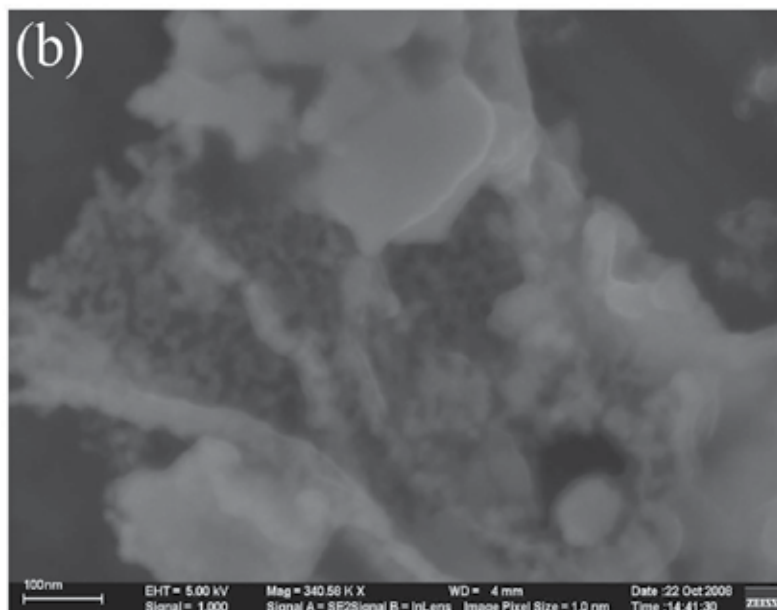
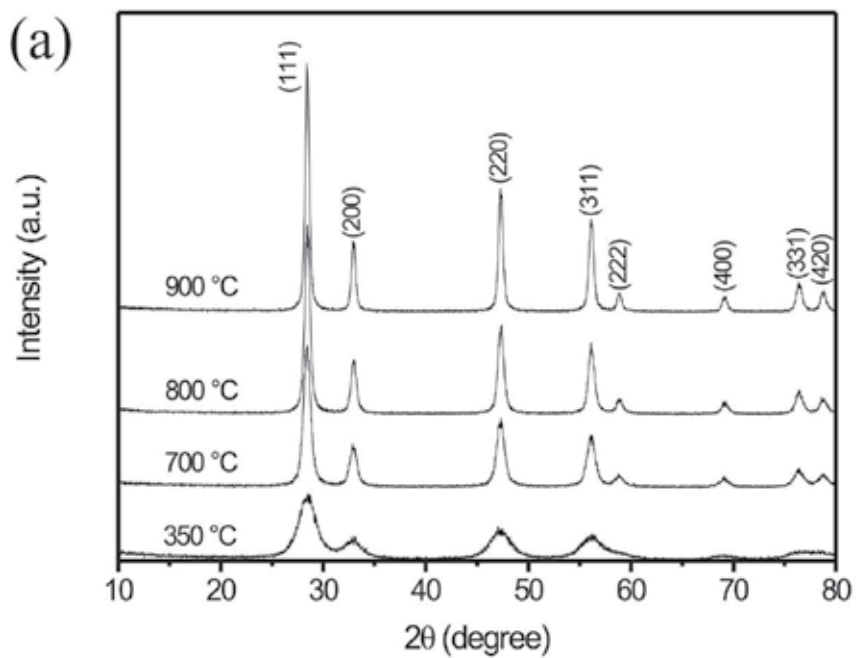


Fig. 7. XRD patterns of SDC powders calcined at different temperatures (a) and FEG-SEM image of the SDC powder calcined at 900 °C (b).

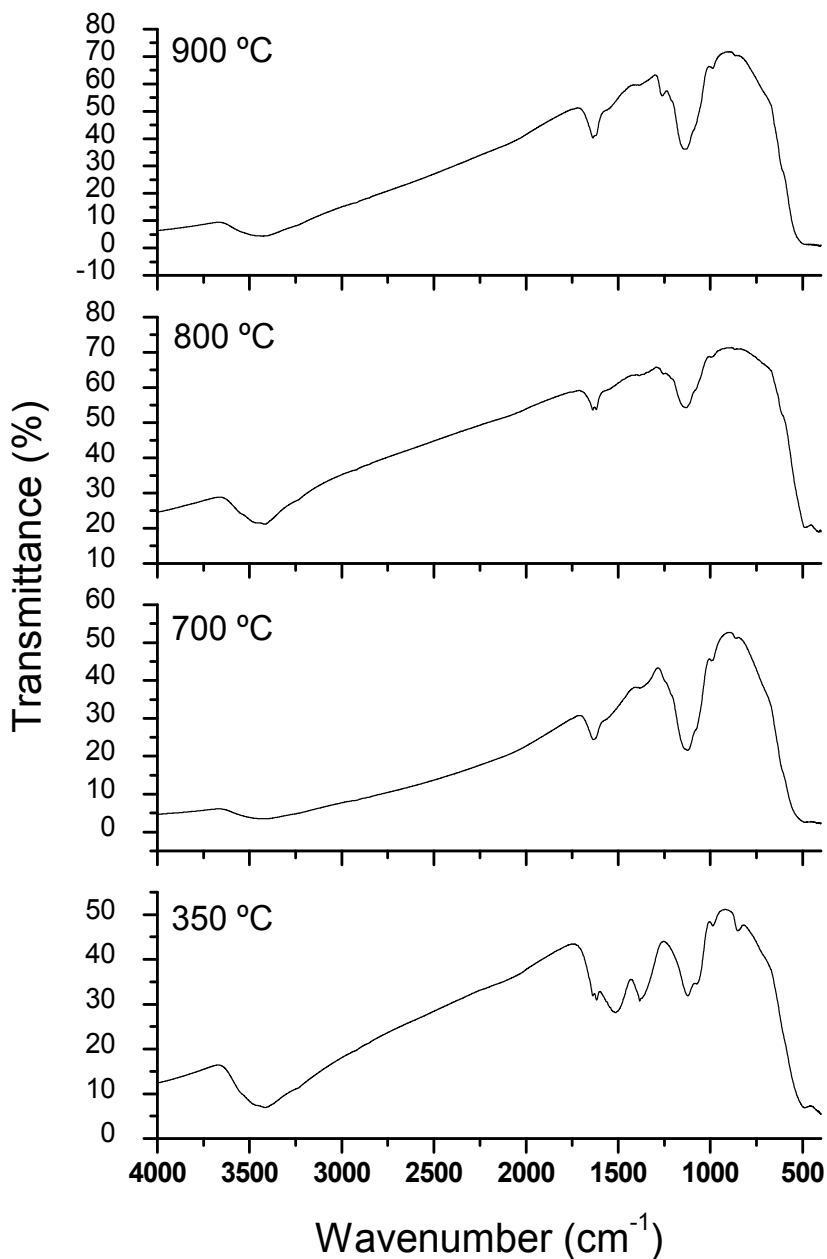


Fig. 8. FTIR spectra of SDC powders at different temperatures.

Fig. 9 shows the XRD patterns of LSCF powder both as-prepared and calcined at 900 °C for 4 h. Prior to calcination and after only 1 minute of microwave irradiation, the powder already exhibited mainly the perovskite-type structure. In addition, some peaks of deleterious phases (LaCoO_4 and SrCO_3) were detected before calcination. The formation of SrCO_3 can be attributed to the reaction of $\text{Sr}(\text{NO}_3)_2$ and CO_2 . Compared with the as-prepared powder, the LSCF powder after calcination displayed higher crystallization. Since carbonaceous phases

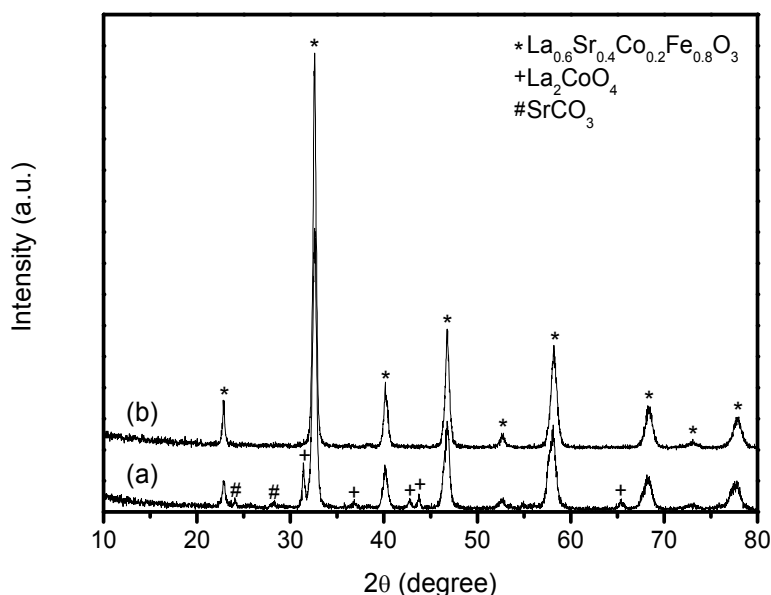


Fig. 9. XRD patterns of LSCF powder: (a) as-prepared and (b) calcined at 900 °C.

may dramatically deteriorate the cathode performance for SOFCs due to its poisoning effect on the cathode surface, further calcination at 900 °C under air for 4 h was carried out in order to eliminate the SrCO_3 impurity, driving its decomposition to CO_2 . Accompanied by the formation of SrCO_3 , another K_2NiF_4 -structured phase with many small peaks was identified in the as-prepared LSCF powder. This phase was ascribed as La_2CoO_4 , based on JCPDS card 34-1296. It is important to mention that it has good electronic and oxygen ionic conductivity and activity for oxygen reduction, being therefore, expected to have negligible effect on the cathode performance of LSCF (Borovskikh et al., 2003; Vashook et al., 2000). In any case, it is observed that both secondary phases decomposed completely after calcination.

Fig. 10 shows SEM images of the LSCF powder after calcination at 900 °C. As expected for ceramic materials synthesized by the combustion method, the powder presents a porous microstructure consisting of small uniform particles. The porous structure of this material can be attributed to significant gas evolution during the combustion reaction.

Fig. 11 shows the FTIR spectra for the as-prepared and calcined LSCF powders. The strong absorption bands in the low wave number region ($\sim 595 \text{ cm}^{-1}$) are associated with metal-oxygen (M-O) bonds characteristic of the perovskite structure. The similar absorption intensity of this band confirms that the perovskite-type structure is almost completely obtained after the combustion reaction, as observed by X-ray diffraction. The band at 1620 cm^{-1} corresponds to the stretching vibration frequency of coordinated H_2O (δ_{HOH}). The bands related to absorbed water (3400 cm^{-1}) were also present in both samples. Before calcination at 900 °C for 4 h, the LSCF powder exhibited strong absorption bands at 1381 cm^{-1} and 1454 cm^{-1} , which indicate the characteristic vibration of NO_3^{-1} and the stretching of the CO_3^{2-} , respectively. Based on these results, it is possible to conclude that during LSCF synthesis, some nitrates can react with carbon dioxide to form carbonaceous phases which decompose after further calcination at 900 °C for 4 h. Therefore, FTIR results are consistent with XRD analyses.

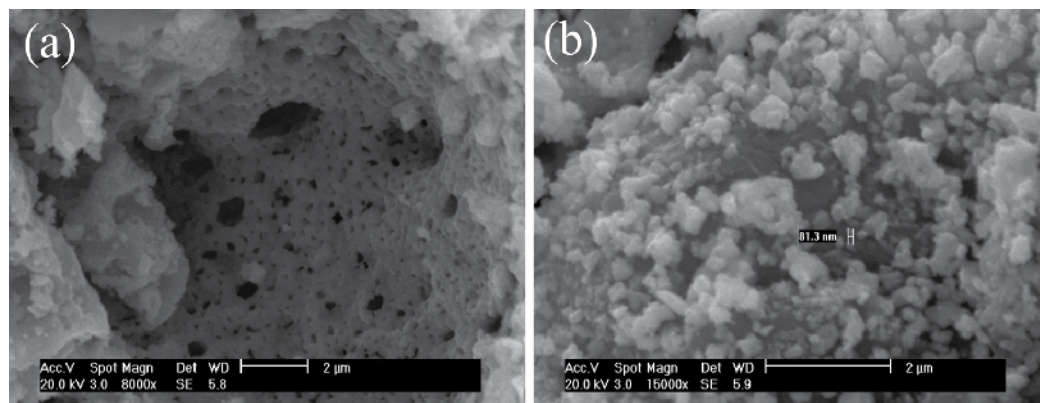


Fig. 10. SEM images of LSCF powder calcined at 900 °C: (a) porous structure and (b) typical small particles.

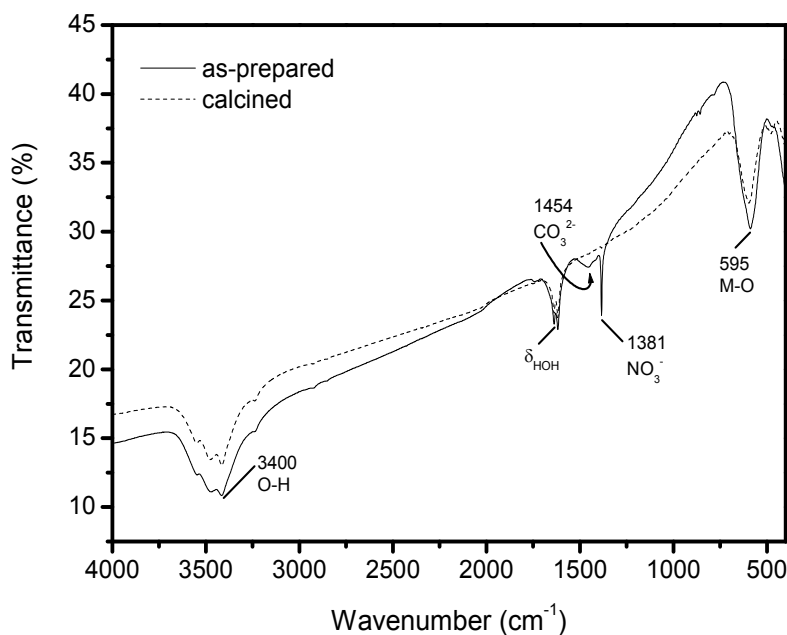


Fig. 11. FTIR spectra for the as-prepared and calcined LSCF powders.

5.1.1 Characterization of composite cathodes

LSM, SDC and LSCF powders synthesized by the above mentioned methods were used to prepare LSM-SDC and LSCF-SDC composite films onto YSZ substrates. A previous study performed by Ye and co-workers (Ye et al., 2007) demonstrated that the amount of ethyl cellulose in LSM-SDC slurries is restricted by cracking of the surface of the films. These authors observed that cracking took place when the amount of pore former reached 15 wt.% and is caused by the large amount of organics which evaporates during sintering. Therefore, in the present study, LSM-SDC slurries with a maximum of 10 wt.% ethyl cellulose were used. Fig. 12 shows FEG-SEM images of the porous structure of LSM-SDC composite

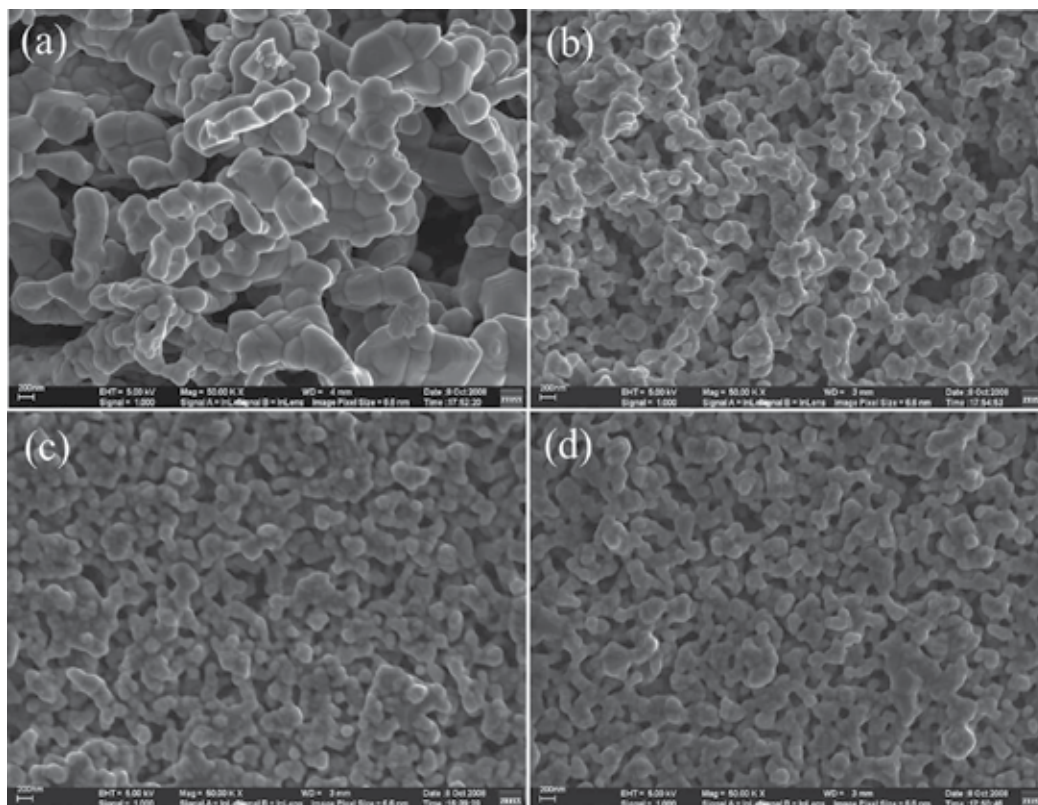


Fig. 12. FEG-SEM images of the surface of LSM-SDC composite cathodes containing different amounts of ethyl cellulose: (a) 0 wt.%, (b) 4 wt.%, (c) 8 wt.%, (d) 10 wt.%.

cathodes containing different amounts of ethyl cellulose. In these images, it is possible to observe the effects of the milling process and the addition of ethyl cellulose in the final microstructure of composite cathodes. The film obtained without addition of ethyl cellulose and without prior milling treatment of powders (Fig. 12a) depicted particle sizes of about 200 nm. On the other hand, in the films obtained with the powders previously milled for 24 h (Figure 12b-d) it can be observed that both particle agglomeration and pore size decrease as the ethyl cellulose content increases. Moreover, the particle size is lower than 200 nm. Typically, if the slurry contains 10 wt.% ethyl cellulose (Fig. 12d), the film exhibits a highly porous surface morphology and uniform pore structure, which are essential conditions for obtaining high-performance cathodes. The electrochemical evaluation of these composite cathodes are currently under way.

Fig. 13 shows cross-sectional SEM images of the LSM-SDC cathodes containing 0 and 10 wt.% ethyl cellulose after milling LSM and SDC powders. The film without addition of ethyl cellulose (Fig. 13a) is tightly adhered to the substrate and shows few pores. However, the film containing 10 wt.% ethyl cellulose ($\sim 10 \mu\text{m}$ thick) is also well adhered to the YSZ substrate and exhibits higher pore uniformity than that in Fig. 13a. Such a porous microstructure fulfils the need for a SOFC cathode, which possess high active surface area, while permitting rapid diffusion of oxygen through the porous cathode film.

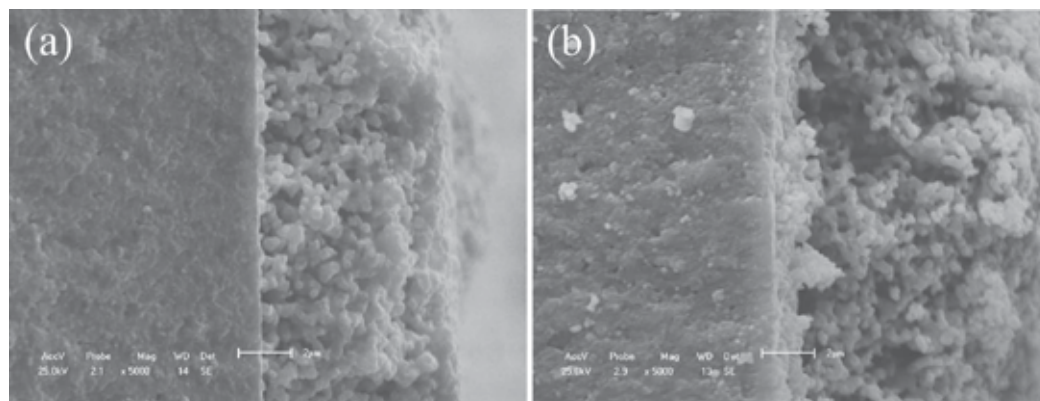


Fig. 13. Cross-sectional SEM images of LSM-SDC cathodes containing different amounts of ethyl cellulose: (a) 0 wt.% and (b) 10 wt.%.

5.2 Characterization of a SOFC single cell

A SEM micrograph of the cathode/electrolyte interface and preliminary results on the electrochemical activity of YSZ electrolyte-supported SOFCs containing Ni-YSZ anode and a LSCF-SDC composite cathode are shown in Fig. 14. As it can be seen in Fig. 14(a), the composite film not only has good adhesion to the electrolyte, but also possesses a porous microstructure which is required for the oxidant electrochemical reduction. It indicates that such a composite film can have a good performance as SOFC cathode. By the LSV technique, qualitative information about electrochemical activity of this SOFC was acquired. The power density curves (Fig. 14b) revealed that maximum power densities were 19, 26, 36 and 46 mW/cm^2 at 800, 850, 900 and 950 $^{\circ}\text{C}$. It is possible to compare these first results with literature data and safely state that the LSCF-SDC cathode composite is qualitatively better than other plain standard materials or cathode composites already reported. It should also be mentioned that the result obtained at 800 $^{\circ}\text{C}$ is similar to that reported by Muccillo et al (Muccillo et al., 2006) for a SOFC single cell with LSM-YSZ cathode, Ni-YSZ anode and 70 μm

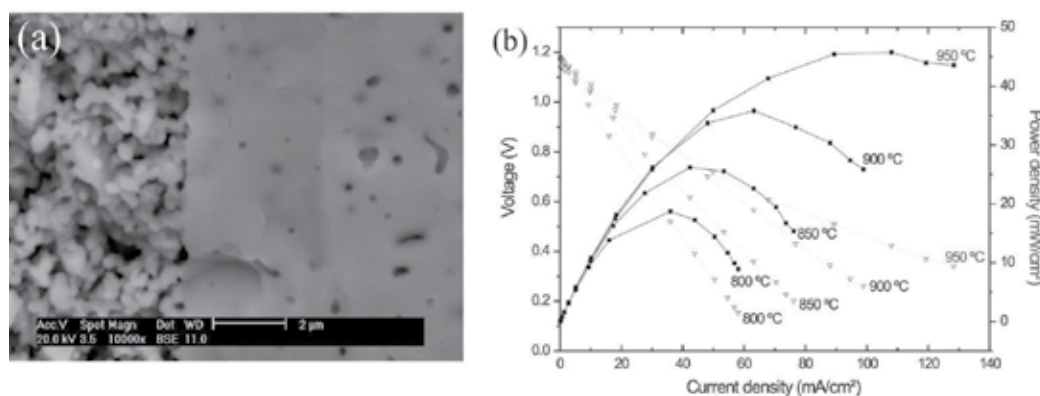


Fig. 14. Electrolyte-supported SOFC: (a) SEM micrograph of the cathode (LSCF-SDC)/electrolyte (YSZ) interface, (b) I-V and power density curves at different temperatures.

thick YSZ electrolyte. Nonetheless, voltage and power density values cannot be compared to literature data because of the thick (200 μm) electrolyte used as cell support, which is responsible for high ohmic polarization. The improvement in cell performance is attributed to the good catalytic activity of the novel LSCF-SDC composite film prepared from the powders obtained by different synthesis methods.

6. Conclusions

Results showed that LSM, SDC and LSCF powders were successfully synthesized by modified Pechini and microwave-assisted combustion methods. The milling process of the LSM-SDC composite powders and the addition of ethyl cellulose to the slurries seem to reduce particle agglomeration and pore size, that could improve the triple phase boundary (TPB) and, consequently, the electrochemical efficiency of the cathode. According to the results gathered herein, LSM-SDC films containing 10 wt.% ethyl cellulose (maximum concentration in order to avoid surface cracks) exhibited uniform and continuous pore structure and excellent adhesion to the YSZ substrate. The composite films produced presented porous microstructures desirable for the electrochemical reduction of the oxidant. Homogeneity and agglomeration absence or phase segregation were also characteristics found in the composite films prepared.

FTIR technique was successfully applied for powder characterization. Results were in agreement with XRD data, demonstrating that the FTIR is also a powerful tool for evaluating the crystalline structure evolution after a chemical synthesis. Moreover, the data could also indicate that water or hydroxyl groups still existed for some calcinated samples as well as physical adsorption of CO_2 , giving a qualitative information of purity of the samples.

7. Acknowledgments

The authors acknowledge PPGCEM-UFRN, PPGQ-UFRN, PRH-ANP 14, CAPES (PRÓ-ENGENHARIAS and PDEE program - BEX 6775/10-1), CAPES-PROCAD, and CNPq (477294/2006-5, 502238/2007-0 and 554576/2010-4) for their financial support.

8. References

- Atkinson, A.; Barnett, S.; Gorte, R. J.; Irvine, J. T. S.; McEvoy, A. J.; Mogensen, M.; Singhal, S. C.; Vohs J. (2004). Advanced anodes for high-temperature fuel cells. *Nature Materials*, Vol. 3, pp. (17-27), ISSN 1476-1122
- Borovskikh, L.; Mazo, G.; Kemnitz, E. (2003). Reactivity of oxygen of complex cobaltates $\text{La}_{1-x}\text{Sr}_x\text{CoO}_{3-\delta}$ and LaSrCoO_4 . *Solid State Sciences*, Vol. 5, No. 3, (23 March 2003), pp. (409-17), ISSN 1293-2558
- Cela, B.; Macedo, D. A.; Souza, G. L.; Nascimento, R. M.; Martinelli, A. E.; Paskocimas, C. A. (2009). Strontium-doped lanthanum manganite synthesis for solid oxide fuel cells cathode. *Journal of New Materials for Electrochemical Systems*, Vol. 12, No. 2-3, (1 April 2009), pp. (109-113), ISSN 1480-2422
- Chen, K.; Lü, Z.; Ai, N.; Chen, X.; Hu, J.; Huang, X.; Su, W. (2007). Effect of SDC-impregnated LSM cathodes on the performance of anode-supported YSZ films for SOFCs. *Journal of Power Sources*, Vol. 167, No. 1, (1 May 2007), pp. (84-89), ISSN 0378-7753

- Chen, M.; Kim, B. H.; Xu, Q.; Nam, O. J.; Ko, J. H. (2008). Synthesis and performances of Ni-SDC cermet for IT-SOFC anode. *Journal of the European Ceramic Society*, Vol. 28, No 15, (November 2008), pp. (2947-2953), ISSN 0955-2219
- Chen, W.; Li, F.; Yu, J. (2006). Combustion synthesis and characterization of nanocrystalline CeO₂-based powders via ethylene glycol-nitrate process. *Material Letters*, Vol. 60, No. 1, (January 2006), pp. (57-62), ISSN 167-577X
- Conceição, L.; Silva, A. M.; Ribeiro, N. F. P.; Souza, M. M. V. M. (2011). Combustion synthesis of La_{0.7}Sr_{0.3}Co_{0.5}Fe_{0.5}O₃ (LSCF) porous materials for application as cathode in IT-SOFC. *Materials Research Bulletin*, Vol. 46, No. 2, (February 2011), pp. (308-314), ISSN 0025-5408
- Conceição, L.; Silva, R. C. B.; Ribeiro, N. F. P.; Souza, M. M. V. M. (2009). Influence of the synthesis method on the porosity, microstructure and electrical properties of La_{0.7}Sr_{0.3}MnO₃ cathode materials. *Materials Characterization*, Vol. 60, No. 12, (December 2009), pp. (1417-1423), ISSN 1044-5803
- Escobedo, C. A. C.; Saldaña, J. M.; Miró, A. M. B.; Jesús, F. S. (2008). Determination of strontium and lanthanum zirconates in YPSZ-LSM mixtures for SOFC. *Journal of Power Sources*, Vol. 180, No. 1, (15 May 2008), pp. (209-214), ISSN 0378-7753
- Gosnet, A. M. H.; Koubaa, M.; Santander-Syro, A. F.; Lobo, R. P. S. M.; Lecoeur, P.; Mercey, B. (2008). Metallic nature of strained thin single-crystal La_{2/3}Sr_{1/3}MnO₃ films. *Physical Review B*, Vol. 78, No. 11, (September 2008), Article Number 115118, pp. (1-5), ISSN 1098-0121
- Grossin, D.; Noudem, J. G. (2004). Synthesis of fine La_{0.8}Sr_{0.2}MnO₃ powder by different ways. *Solid State Sciences*, Vol. 6, No. 9, (September 2004), pp. 939-944, ISSN 1293-2558
- Guo, H.; Iqbal, G.; Kang, B. S. (2010). Development of an In Situ Surface Deformation and Temperature Measurement Technique for a Solid Oxide Fuel Cell Button Cell. *International Journal of Applied Ceramic Technology*, Vol. 7, No. 1, (January/February 2010), pp. (55-62), ISSN 1744-7402
- Guo, R. S.; Wei, Q. T.; Li, H. L.; Wang, F. H. (2006). Synthesis and properties of La_{0.7}Sr_{0.3}MnO₃ cathode by gel combustion. *Materials Letters*, Vol. 60, No. 2, (January 2006), pp. 261-265, ISSN 0167-577X
- Ivers-Tiffée, E.; Weber, A.; Herbristrit, D. (2001). Materials and technologies for SOFC-components. *Journal of the European Ceramic Society*, Vol. 21, No. 10-11, (22 August 2001), pp. (1805-1811), ISSN 0955-2219
- Jiang, S. P. (2003). Issues on development of (La,Sr)MnO₃ cathode for solid oxide fuel cells. *Journal of Power Sources*, Vol. 124, No. 2, (24 November 2003), pp. (390-402), ISSN 0378-7753
- Kim, K. H.; Gu, J. Y.; Choi, H. S.; Park, J. W.; Noh, T. W. (1996). Frequency Shifts of the Internal Phonon Modes in La_{0.7}Ca_{0.3}MnO₃. *Physical Review Letters*, Vol. 77, No. 9, (26 August 1996), pp. (1877 - 1880), ISSN 0031-9007
- Konyshева, E.; Irvine, J. T. S.; Besmehn, A. (2009). Crystal structure, thermochemical stability, electrical and magnetic properties of the two-phase composites in the La_{0.8}Sr_{0.2}MnO_{3±δ}-CeO₂ system. *Solid State Ionics*, Vol. 180, No. 11-13, (22 June 2009), pp. (778-783), ISSN 0167-2738
- Lin, H.; Ding, C.; Sato, K.; Tsutai, Y.; Ohtaki, H.; Iguchi, M.; Wada, C.; Hashida, T. (2008). Preparation of SDC electrolyte thin films on dense and porous substrates by modified sol-gel route. *Materials Sciences and Engineering B*, Vol. 148, No. 1-3, (25 February 2008), pp. (73-76), ISSN 0921-5107

- Liu, S.; Qian, X.; Xiao. (2007). Synthesis and characterization of $\text{La}_{0.8}\text{Sr}_{0.2}\text{Co}_{0.5}\text{Fe}_{0.5}\text{O}_{3\pm\delta}$ nanopowders by microwave assisted sol-gel route, *Journal of Sol-Gel Science and Technology*, Vol. 44, No. 3, (3 October 2007), pp. (187-193), ISSN 0928-0707
- Liu, X.; Faguy, P. W.; Liu, M. (2002). In Situ Potential-Dependent FTIR Emission Spectroscopy. *Journal of The Electrochemical Society*, Vol. 149, No. 10, 2002, pp. (1293-1298), ISSN 1945-7111 (online)
- Macedo, D. A.; Cela, B.; Martinelli, A. E.; Nascimento, R. M.; Melo, D. M. A.; Paskocimas, C. A.; Rabelo, A. A. (2009) Synthesis, processing and characterization of $\text{ZrO}_2\text{-8Y}_2\text{O}_3$, $\text{ZrO}_2\text{-8CeO}_2$ and $\text{La}_{0.78}\text{Sr}_{0.22}\text{MnO}_3$ powders. *Journal of New Materials for Electrochemical Systems*, Vol. 12, No. 2-3, (1 April 2009), pp. (103-108), ISSN 1480-2422
- Maia, A. O. G.; Meneses, C. T.; Menezes, A. S.; Flores, W. H.; Melo, D. M. A.; Sasaki, J. M. (2006). Synthesis and X-ray structural characterization of NiO nanoparticles obtained through gelatin. *Journal of Non-Crystalline Solids*, Vol. 352, No. 32-35, (15 September 2006), pp. (3729-3733), ISSN 0022-3093
- McIntosh S.; Gorte R. J. (2004). Direct Hydrocarbon Solid Oxide Fuel Cells. *Chemical Reviews*, Vol. 104, No. 10, (21 July 2004), pp. (4845-4866), ISSN 0009-2665
- Medeiros, A. M. L.; Miranda, M. A. R.; Menezes, A. S.; Jardim, P. M.; Silva, L. R. D.; Gouveia, S. T.; Sasaki, J. M. (2004). Synthesis and Characterization of Cr_2O_3 Nanoparticles Obtained by Gelatin. *Journal of Metastable and Nanocrystalline Materials*, Vol. 20-21, pp. (399-406), ISSN 1422-6375
- Minh, N. Q. & Takahashi T (1995). Science and Technology of Ceramic Fuel Cell, Elsevier Science, ISBN 0-444-89568-X, Amsterdam, The Netherlands.
- Minh, N. Q. (1993). Ceramic fuel cells. *Journal of the American Ceramic Society*, Vol. 76, No. 563, (March 1993), pp. (563-588), ISSN 1551-2916
- Minh, N. Q. (2004). Solid oxide fuel cell technology – features and applications. *Solid State Ionics*, Vol. 174, No. 1-4, (29 October 2004), pp. (271-277), ISSN 0167-2738
- Molenda, J.; Swierczek, K.; Zajac, W. (2007). Functional materials for the IT-SOFC. *Journal of Power Sources*, Vol. 173, No. 2, (15 November 2007), pp. (657-670), ISSN 0378-7753
- Muccillo, R.; Muccillo, E. N. S.; Fonseca, F. C.; França, Y. V.; Porfírio, T. C.; Florio, D. Z.; Berton, M. A. C.; Garcia, M. C. (2006). Development and testing of anode-supported solid oxide fuel cells with slurry-coated electrolyte and cathode. *Journal of Power Sources*, Vol. 156, No. 2, (1 June 2006), pp. (455-460), ISSN 0378-7753
- Pechini, M. P. (1967). Method of preparing lead and alkaline earth titanates and niobates and coating method using the same to form a capacitor. US Patent No. 3,330,697 (11 July 1967)
- Resini, C.; Venkov, T.; Hadjiivanov, K.; Presto S.; Riani, P.; Marazza, R.; Ramis, G.; Busca, G. (2009). An FTIR study of the dispersed Ni species on Ni-YSZ catalysts. *Applied Catalysis A: General*, Vol. 353, No. 1, (January 2009), pp. (137-143), ISSN 0926-860X
- Shao, J.; Tao, Y.; Wang, J.; Xu, C.; Wang, W. G. (2009). Investigation of precursors in the preparation of nanostructured $\text{La}_{0.6}\text{Sr}_{0.4}\text{Co}_{0.2}\text{Fe}_{0.8}\text{O}_{3-\delta}$ via a modified combined complexing method. *Journal of Alloys and Compounds*, Vol. 484, No. 1-2, (18 September 2009), pp. (263-267), ISSN 0925-8388
- Singhal, S. C. (2000). Advances in solid oxide fuel cell technology. *Solid State Ionics*, Vol. 135, No. 1-4, (1 November 2000), pp. (305-313), ISSN 0167-2738

- Steele B. C. H.; Heinzl, A. (2001). Materials for fuel-cell technologies. *Nature*, Vol. 414, (15 November 2001), pp. (345-352), ISSN 0028-0836
- Steele, B. C. H. (2000). Appraisal of $Ce_{1-y}Gd_yO_{2-y/2}$ electrolytes for IT-SOFC operation at 500°C. *Solid State Ionics*, Vol. 129, No. 1-4, (April 2000), pp. (95-110), ISSN 0167-2738
- Stuart, B. H. (2004). Infrared Spectroscopy: Fundamentals and Applications (Analytical Techniques in the Sciences (AnTs) *), John Wiley and Son's Ltd. England.
- Tsai, T.; Barnett, S. A. (1997). Effect of LSM-YSZ cathode on thin-electrolyte solid oxide fuel cell performance. *Solid State Ionics*, Vol. 93, No. 3-4, (January 1997), pp. (207-217), ISSN 0167-2738
- Vargas, R. A.; Chiba, R.; Andreoli, M.; Seo, E. S. M. (2008). Synthesis and characterization of $La_{1-x}Sr_xMnO_{3\pm\delta}$ and $La_{1-x}Sr_xCo_{1-y}Fe_yO_{3-\delta}$ used as cathode in solid oxide fuel cells. *Cerâmica*, Vol. 54, No. 331, (July - September 2008), pp. (366-372), ISSN 0366-6913
- Vashook, V. V.; Ullmann, H.; Olshevskaya, O. P.; Kulik, V. P.; Lukashevich, V. E.; Kokhanovskij, L. V. (2000). Composition and electrical conductivity of some cobaltates of the type $La_{2-x}Sr_xCoO_{4.5-x/2\pm\delta}$. *Solid State Ionics*, Vol. 138, No. 1-2, (4 December 2000), pp. (99-104), ISSN 0167-2738
- Wang, K.; Ran, R.; Shao, Z. (2007). Methane-fueled IT-SOFCs with facile in situ inorganic templating synthesized mesoporous $Sm_{0.2}Ce_{0.8}O_{1.9}$ as catalytic layer. *Journal of Power Sources*, Vol. 170, No. 2, (10 July 2007), pp. (251-258), ISSN 0378-7753
- Xu, X.; Cao, C.; Xia, C.; Peng, D. (2009). Electrochemical performance of LSM-SDC electrodes prepared with ion-impregnated LSM. *Ceramics International*, Vol. 35, No. 6, (August 2009), pp. (2213-2218), ISSN 0272-8842
- Xu, X.; Jiang, Z.; Fan, X.; Xia, C. (2006). LSM-SDC electrodes fabricated with an ion-impregnating process for SOFCs with doped ceria electrolytes. *Solid State Ionics*, Vol. 177, No. 19-25, (15 October 2006), pp. (2113-2117), ISSN 0167-2738
- Xu, X.; Xia, C.; Xiao, G.; Peng, D. (2005). Fabrication and performance of functionally graded cathodes for IT-SOFCs based on doped ceria electrolytes. *Solid State Ionics*, Vol. 176, No. 17-18, (31 May 2005), pp. (1513-1520), ISSN 0167-2738
- Yang, K.; Shen, J. H.; Yang, K. Y.; Hung, I. M.; Fung, K. Z.; Wang, M. C. (2007). Characterization of the yttria-stabilized zirconia thin film electrophoretic deposited on $La_{0.8}Sr_{0.2}MnO_3$ substrate. *Journal of Alloys and Compounds*, Vol. 436, No. 1-2, (14 June 2007), pp. (351-357), ISSN 0925-8388
- Ye, F.; Wang, Z.; Weng W.; Cheng, K.; Song, C.; Du, P.; Sheng, G.; Han, G. (2007). Spin-coating derived LSM-SDC films with uniform pore structure. *Thin Solid Films*, Vol. 516, No. 16, (30 June 2008), pp. (5206-5209), ISSN 0040-6090
- Zhang, L.; Zhao, F.; Peng, R.; Xia, C. (2008). Effect of firing temperature on the performance of LSM-SDC cathodes prepared with an ion-impregnation method. *Solid State Ionics*, Vol. 179, No. 27-32, (30 September 2008), pp. (1553-1556), ISSN 0167-2738
- Zhang, Y.; Huang, X.; Lu, Z.; Liu, Z.; Ge, X.; Xu, J.; Xin, X.; Sha, X.; Su, X. (2007). Ni- $Sm_{0.2}Ce_{0.8}O_{1.9}$ anode-supported YSZ electrolyte film and its application in solid oxide fuel cells. *Journal of Alloys and Compounds*, Vol. 428, No. 1-2, (31 January 2007), pp. (302-306), ISSN 0925-8388

Infrared Spectroscopy of Functionalized Magnetic Nanoparticles

Perla E. García Casillas,
Claudia A. Rodríguez Gonzalez and Carlos A. Martínez Pérez
*Universidad Autónoma de Ciudad Juárez,
Instituto de Ingeniería y Tecnología,
Ciudad Juárez Chihuahua
México*

1. Introduction

Nanotechnology development has allowed that nanomaterials can be used in biomedical applications, and nanometer sized objects can interact with biological entities like cells, virus, protein, enzyme, etc. For this reason, many research projects has been focused in the development of nanosystems, nanoparticles and nanodevices for this applications. This area is relatively new, according to the ISI web of knowledge, the publications of the nanoparticles for biomedical applications started on 2000 year, and since that time they have increased exponentially (Figure 1). The nanoparticles (NPs) used for biomedical purposes generally include zero-dimensional nanospheres and one-dimensional nanowires and nanotubes.

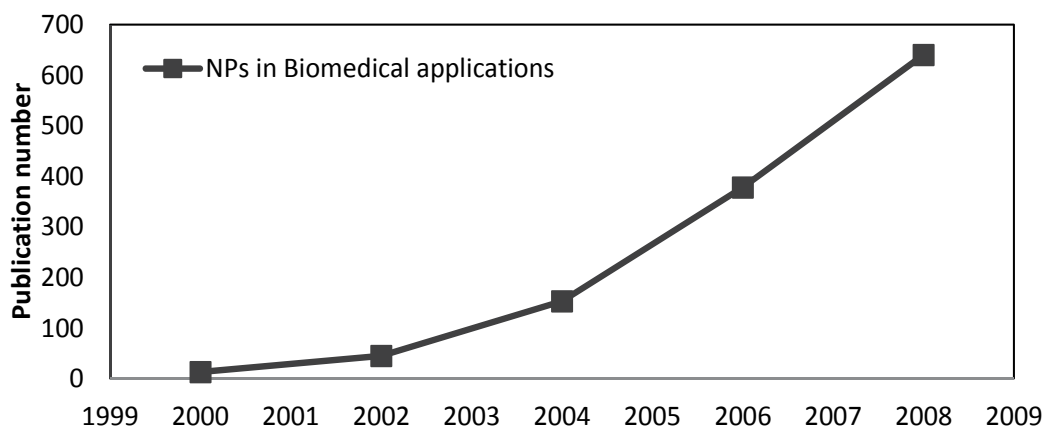


Fig. 1. Trends of Nanoparticles (NPs) in Biomedical application, information extracted from ISI Web of Knowledge.

Figure 2, extracted from ISI Web of Knowledge, shows the publications related to gold, silver, iron and magnetic nanoparticles for biomedical application. Magnetic nanoparticles

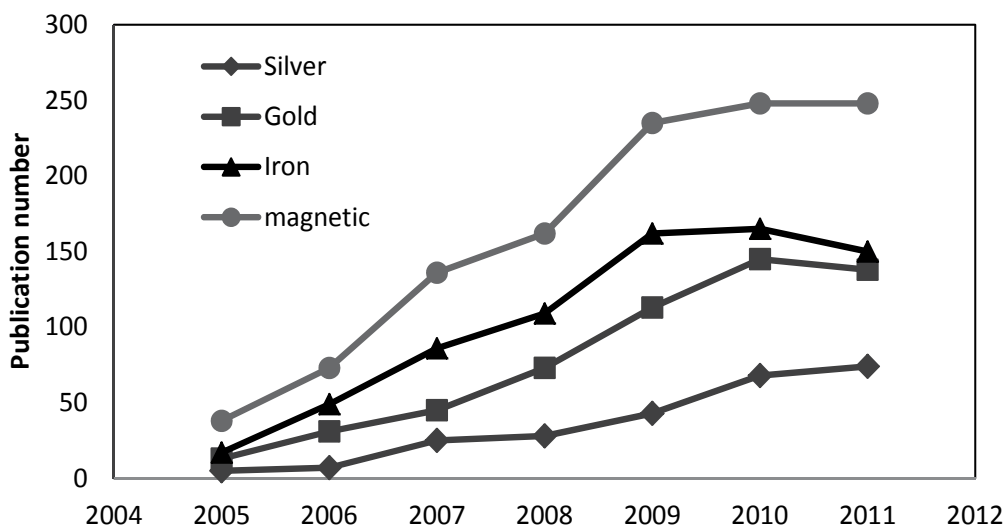


Fig. 2. Trends of silver, gold, iron and magnetic nanoparticles used in Biomedical applications, information extracted from ISI Web of Knowledge

are at the forefront as the most promising materials for clinical diagnostic and therapeutic applications. Magnetic nanoparticles (MNPs) are widely used for labeling and manipulating biomolecules, targeting drugs and genes, magnetic resonance imaging, as well as hyperthermia treatment (Varadan et al., 2008; Cornell and Schwertmann, 2003). Magnetite Nanoparticles (Fe_3O_4) are the most used magnetic material for biomedical applications because they have a high enough saturation magnetization to allow its manipulation with an external field, superparamagnetic behavior and ability to bond with different molecules to surface functionalized (Cullity and Graham, 2009; Neuberger et al., 2005). In biomedical applications, the characteristics of the magnetite nanoparticles have a significant advantage when they interact with biological molecules, therefore, many methods of synthesis have been developed in order to control surface morphology, particle size, particle distribution, and chemical stability among others (An-Hui et al., 2007; Gao and Gu, 2009).

2. Magnetic nanoparticles

Many magnetic nanoparticles such as magnetite, strontium and cobalt ferrites, lanthanum-zinc ferrites, nickel, iron and some compounds with a rare earth like SmCo_5 have been developed (Pankhurst et al., 2003). Magnetite, Fe_3O_4 is the magnetic material most used in biomedical application due to its several interesting properties such as great chemical stability, low toxicity, and its magnetic saturation mentioned above for being manipulated with an external field, biocompatibility and the heating ability in presence of a field, which made it an interesting candidate for hyperthermia treatment (Sun et al., 2004) for this reason in recent years, much effort has been focused in the design and controlled synthesis of this material with certain shape and particle size. Many methods for synthesis of magnetite nanoparticles have been developed like co-precipitation, microemulsion, sol-gel, sputtering,

thermal decomposition, etc. With this variety of methods particles with different morphologies such as spheres, rods, wires and tubes has been obtained (Palla et al, 1999; Joralemon et al, 2005; Terrazas et al, 2010). However, the coprecipitation method is still the most popular method for their simplicity and easy way to manipulate the size and morphology of the particles by the use of templates, besides being a method whose raw materials are relatively inexpensive.

Recent publications have been emphasized on the particle size control of magnetite nanoparticles, because under some critical value, the material exhibits a superparamagnetic behavior, this means that there is no hysteresis in the magnetization curves, which implies that the retentivity and coercivity are close to zero (Cullity and Graham, 2009). Biomedical applications involve strict requirements on particle size, and it can be by using a chemical coprecipitation through the control of nucleation and growth process. Magnetite nanoparticles obtained by chemical coprecipitation method are produced by the precipitation of divalent (Fe^{+2}) and trivalent (Fe^{+3}) iron salts in an alkaline medium. The size and the number of nucleus are influenced by the alkaline medium and the addition velocity, which results in a nucleation and growing process; a fast nucleation will form high concentration of nuclei and small particles, while a slow nucleation will form low nuclei concentration generating larger nanoparticles (figure 3).

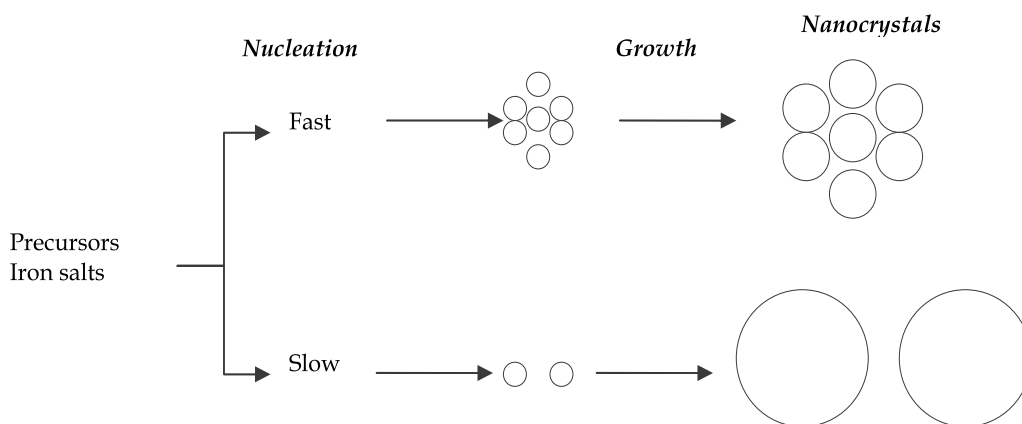


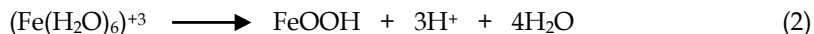
Fig. 3. Schematic representation of nucleation and growth kinetics.

2.1 Chemical coprecipitation

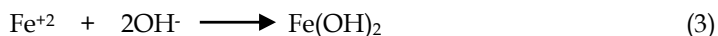
As mentioned above, chemical co-precipitation consists in the precipitation of divalent (Fe^{+2}) and trivalent (Fe^{+3}) iron salts in an alkaline medium, maintaining a molar ratio of 1:2, by using ammonium hydroxide, ammonia or some other alkaline solution to increase pH reaction that is required to magnetite formation. Commonly the addition of alkaline solution to divalent and trivalent iron solution is made slowly, drop by drop (titration) under vigorous agitation using a magnetic agitator. The initial solution of divalent and trivalent iron cations had acidic pH and after the titration is close to 12, a black precipitate is formed which indicates that the reaction has been completed. The chemical reaction that takes place during magnetite formation from iron salts solutions by increasing the pH can be represented in the following overall chemical equation (Cornell et al, 2003; Gnanaprakash et al, 2007):



In general, the solubility of trivalent iron oxide (Fe^{+3}) is smaller than the one observed on divalent iron oxides (Fe^{+2}). The trivalent iron hydrolyzes and forms hydroxide species. The hydrolysis can be induced by heating up the solution. The complete hydrolysis corresponds to the formation of a trivalent iron oxide-hydroxide and it is represented according to the following chemical reaction:



The divalent iron cation in solution (Fe^{+2}) reacts to form the divalent iron oxide in basic conditions (presence of hydroxyl ion OH^-), which is presented in equation 3:



Under the reaction conditions, divalent iron hydroxide and trivalent iron oxide-hydroxide species were likely to be formed. This being established, it is suggested that the following chemical reaction mechanism occurred: trivalent iron cation hydrolyzes forming (FeOOH) as pH increases; under alkaline conditions divalent iron cation forms $\text{Fe}(\text{OH})_2$. Both chemical species reacted to each other at pH values of around 10 to 11, forming magnetite according to equation 4:



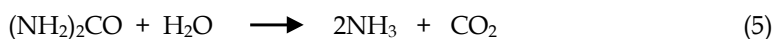
2.2 Chemical coprecipitation with fast injection

The chemical coprecipitation with fast injection differs from conventional coprecipitation in the speed at pH of the reaction pH solution is increased; in order to favor magnetite formation abruptly. Divalent and trivalent iron salt solutions have an initial pH of 0 to 1. On the conventional coprecipitation method, the pH of the solution is increased by the addition of an alkaline solution drop by drop, which is considered slow speed; while on the rapid injection method, the pH of the solution is increased by adding the salt solution directly to ammonium hydroxide solution, speed to be considered rapid and explosive. The difference between both methods is schematically shown in figure 4.

2.3 Chemical coprecipitation with reflux and aging conditions

A trivalent iron solution is placed into a bowl flask and heated up to 80 °C under refluxing conditions for a period of time of 2 hours. A precipitate is formed and separated from supernatant. Trivalent iron cation is hydrolyzed due to an increment of temperature promoting the hydrolysis and forming a trivalent iron oxide-hydroxide (FeOOH). After the 2 hours of hydrolysis reaction, a yellowish precipitate is obtained.

Another solution is prepared with divalent iron and urea. This solution is mixed with the previous precipitate and heated up to 90°C-96°C for 20 hours under refluxing conditions. The required pH condition is obtained through the slow decomposition of the urea when the temperature increases above 90°C, this condition will increase the pH uniformly favoring a more slower nucleation in the solution (Terrazas et al., 2010).



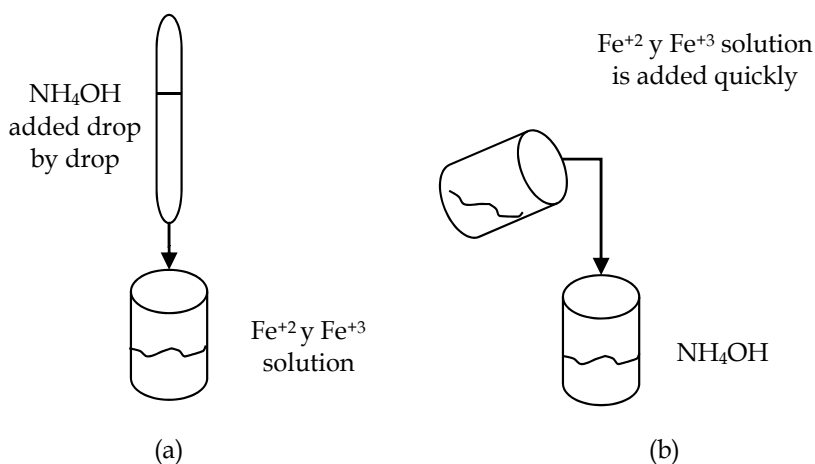
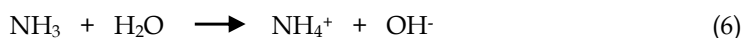


Fig. 4. Difference between conventional coprecipitation (a) and coprecipitation with fast injection (b).



By the use of urea in the chemical coprecipitation with reflux and aging conditions method, the speed of pH increment is considerably slower than the one observed in the slow injection and rapid injection co-precipitation methods. The condition of slow and uniform pH increment and the reacting time of 20 hours under favorable conditions for magnetite formation, affect the nucleation and particle growth process making it very slow, which is reflected in the formation of bigger particles than those promoted in slow injection and rapid injection methods.

The difference of these methodologies lies in the particle size and its distribution as is shown in figure 5. Magnetite obtained by coprecipitation with reflux and aging shows higher particle size and a wide particle size distribution. According to these results, magnetite obtained by coprecipitation with fast injection shows the smallest average particle size and the closest particle size distribution; differing from magnetite obtained by common coprecipitation, Table 1.

The magnetite obtained using these three methodologies have a spherical particle shape with a superparamagnetic behavior, and their saturation magnetization is influenced by the particle size. Values of 55.9, 64.3 and 78.2 emu/g were obtained from nanoparticles with an average particle size of 16 nm, 27 nm and 200 nm respectively. The saturation magnetization increases when the particle sizes are larger. Hysteresis loops of the synthesized nanoparticles are shown in figure 6.

Magnetite structure is an inverse spinel with a face center cubic unit based on 32 O²⁻ ions with a regularly cubic close packed along the [111] direction. There are eight formula units per unit cell. Magnetite differs from other iron oxides in that it contains both divalent and trivalent iron. Its formula is written as Fe^{III}[Fe^{II}Fe^{III}]O₄ and the brackets denote octahedral sites, tetrahedral Fe spins are directed antiparallel to octahedral Fe³⁺ and Fe²⁺ spins so

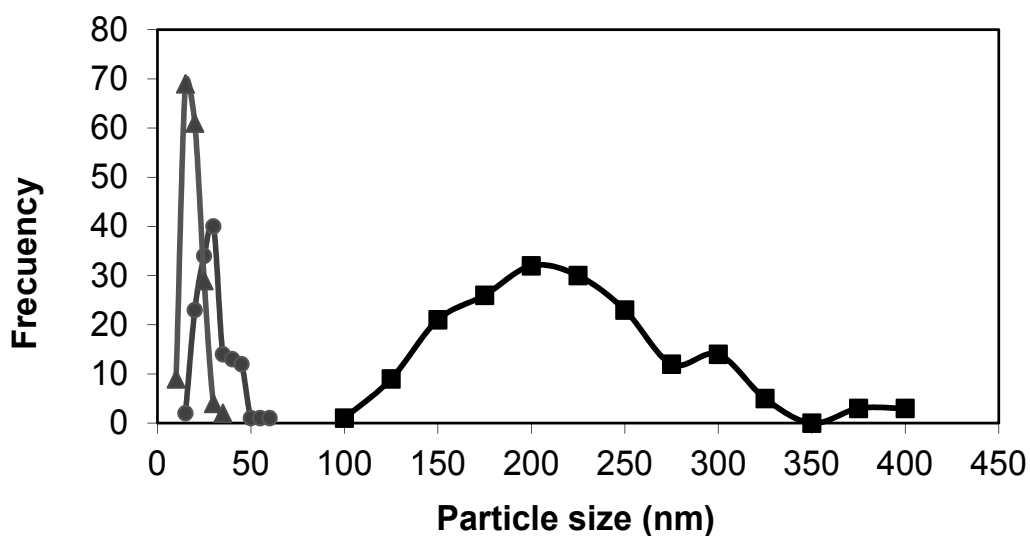


Fig. 5. Comparison of magnetite particle sizes and their distribution obtained by common coprecipitation (●), coprecipitation with fast injection (▲) and coprecipitation with reflux and aging (■)

	Common coprecipitation	Coprecipitation with fast injection	Coprecipitation with aging and reflux
Average particle size (nm)	27.6	16.2	206.9
Standard Deviation (nm)	8.2	4.4	58.9

Table 1. Average particle size of magnetite obtained by different methodologies

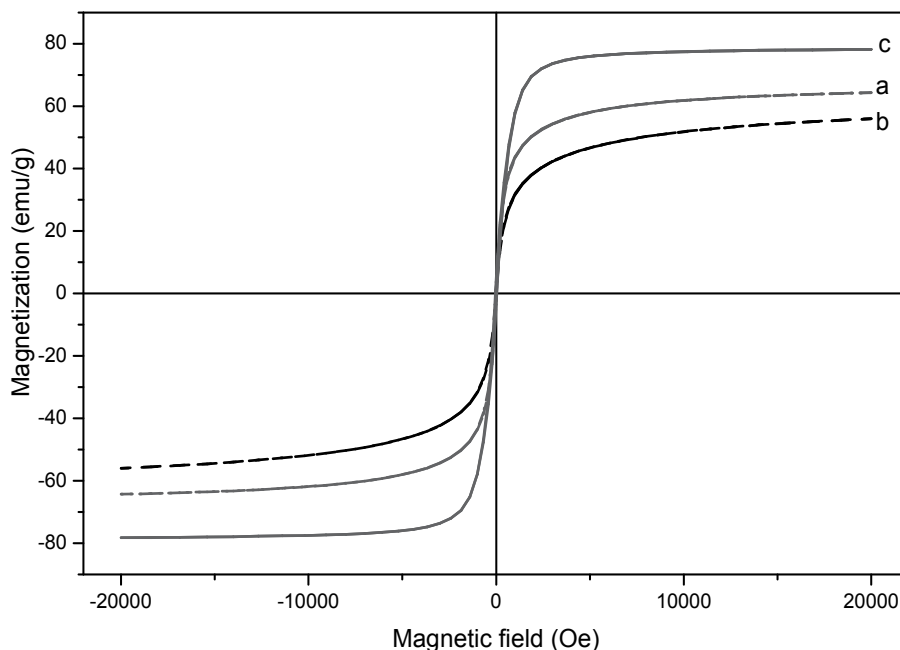


Fig. 6. Hysteresis loops of magnetite obtained by common coprecipitation (a), with a fast injection (b) and aging and reflux(c)

that the Fe^{3+} moments cancel, leaving a spontaneous magnetization equivalent to one Fe^{2+} moment per molecule, eight tetrahedral sites are occupied by trivalent iron, and the divalent and trivalent cations occupies the sixteen octahedral sites (Cornell and Schwertmann, 2003). X-ray diffraction is the most widely used technique to determine the crystalline structure of a material. However in the case of magnetite it can be confusing because the magnetite has the same crystalline structure that maghemite, but this one has a interstitial voids, therefore by using XRD is not conclusive. The difference between the two materials is that some of the interstitial atomic positions of the maghemite are not fully occupied, and consequently having atomic holes. In the case of magnetite, the infrared spectroscopy is very useful because this technique arises as a result of divalent and trivalent cations interaction with electromagnetic radiation, this interaction involves excitation for vibration or rotation of molecules in their ground electronic state, and they are associated with stretching deformation of the interatomic bonds and bending deformation of the interbond angles. FTIR spectroscopy provides a fast mean of identification.

Infrared spectra of the magnetite shows the chareacteristic bands at 590 and 450cm^{-1} approximately due to the Fe-O bond in tetrahedral and octahedral positions. Figure 7 shows the infrared spectra of the magnetite with a different particle size, the band at 600cm^{-1} approximately is broadening when the particle size decreases. According to Nasrazadani (1993) this effect indicates an increment of cation vacancy in the lattice, this behavior corroborated with the decreased value of the lattice parameter, which is shown in table 2. These values are minor than the lattice parameter of defect free magnetite (8.396 \AA), this small reduction is assumed to be due to the prevalence of a small amount of cation deficiency.

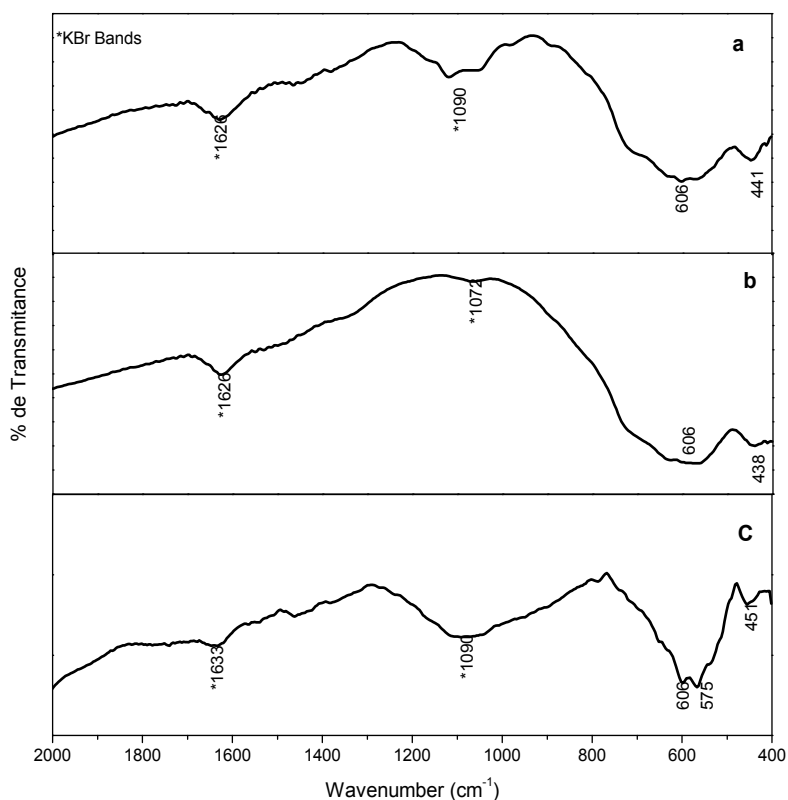


Fig. 7. Infrared spectra of the magnetite obtained by common coprecipitation (a), with a fast injection (b) and aging and reflux(c).

Sample	Method of Synthesis	Particle size (nm)	Lattice cell (Å)
Magnetite	Coprecipitation with aging and reflux	206.9 ± 58.9	8.34468
Magnetite	Common coprecipitation	27.6 ± 8.2	8.34270
Magnetite	Coprecipitation with fast injection	16.2 ± 4.4	8.33475

Table 2. Variation of the magnetite lattice cell with a determined particle size

Substitution of the cation on magnetic structures has been studied in order to improve the magnetic properties and FTIR spectroscopy is one of the techniques used in this kind of studies. In magnetite structure, the divalent iron is totally or partially replaced for strontium, cobalt, copper, nickel, manganese, cadmium, aluminum and gadolinium (Brabers et al., 1998). Figure 8 shows the infrared spectra of magnetite doped with cobalt; this cation occupies octahedral sites without changing inverse spinel crystal structure of magnetite.

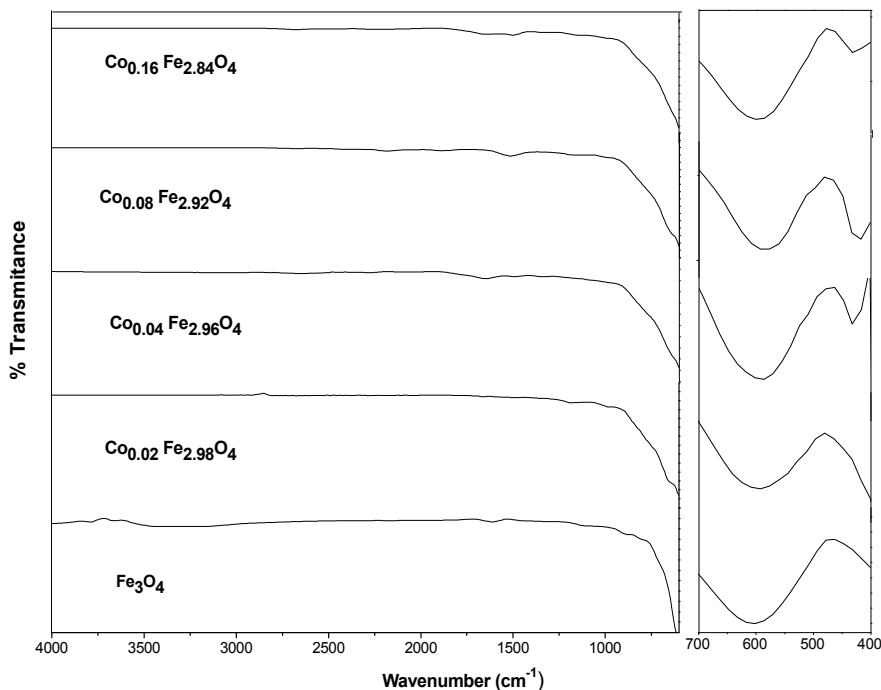


Fig. 8. Infrared spectra of cobalt doped magnetite.

3. Functionalization of magnetic nanoparticles

One of the most important aspects of the nanoparticles for biomedical applications is the surface preparation of the nanoparticles in order to improve their biocompatibility with biological entities and provide chemical stability. The nanoparticles surfaces can be modified with a biocompatible or/and biodegradable polymeric coating. The polymer can be natural such as chitosan ($C_6H_{13}NO_5$), collagen, folic acid ($C_{19}H_{19}N_7O_6$) or synthetic as dextran ($H(C_6H_{10}O_5)_x(OH)$), tetraethyl orthosilicate ($SiC_8H_{20}O_4$), N-(2-aminoethyl-3-aminopropyl) trimethoxysilane ($C_8H_{22}N_2O_3Si$), poly-lactic-co-glycolic acid (PLGA), polyethylene glycol ($C_{2n}H_{4n+2}O_{n+1}$), etc. This surface modification needs to have a functional groups like: carboxyl ($-COOH$), hydroxyl ($-OH$), amine ($-NH_2$), etc, with the capability to bond with a biological molecules. Table 3 shows a summary of recent publications of the most used coating materials for magnetite nanoparticles.

One of the most used techniques to ensure that the functionalization of magnetic nanoparticles has occurred, is the Fourier infrared spectroscopy (FTIR) because of its simplicity and availability. This technique provides the information about the excitation of vibration or rotation of molecules in their ground electronic State. In magnetite structure, these vibration, are associated with the stretching deformation of the interatomic bond of the iron with other molecules. Magnetite with a silica (figure x, MS sample) shell is confirmed by the characteristic adsorption band at 1090 cm^{-1} due to silane group presence. When a aminosilane is used like a coating, the spectra (figure, MA sample) show the band at 2943 cm^{-1} due to the stretching of C-H from methyl group ($-CH_2$, $-CH_3$), the band at 1072 cm^{-1} is due to the Si-O bond and the bands at 3309 and 1654 cm^{-1} are attributed to the amine

Material	Particle size (nm)	Application	Reference
Silica	20-300	DNA separation, Drug delivery, Metal separation in waste	Schweoger et al, 2011; Chen et al, 2011; Del Campo et al, 2001; Ajay and grupta, 2005
Dextran	10-200	Drug delivery NMR imagines	Liu et al, 2011; Quin et al, 2011; Catherine et al, 2003; Zhang et al ,2007
Polyethylene glycol (PET)	10-50	NMR imagines, Gen delivery	Kami et al, 2011; Phadatare et al, 2011; Zang et al, 2008;
Polyvinyl alcohol (PVA)	10-50	NMR imagines, Drug delivery,	Pardoe et al, 2001; Morteza et al, 2009.
Polyvinyl Pyrrolidone (PVP)	10-20	Drug delivery	Young-Lee et al, 2006
poly-lactic-co-glycolic acid (PLGA)	250	Tissue engineering, Cell targeting	Schliehe et al, 2011; Chih-Hang et al, 2011; Mu andFeng,2001; Yoshida and. Babensee, 2006;
Polystyrene (PS)	10-20	NMR imagines DNA separation	McCarthy et al, 2011; Ramirez et al, 2003
Methyl polymethacrylate	10-50 o	NMR imagines, Entities separation	Gao et al, 2010;
Polypyrrole	20-100	Protein separation, Metal separation	Madhumita et al, 2011; Ammar et al, 2004; Andrevia et al, 2006;
Cellulose	20-50	Drug delivery	Huixia et al, 2011
Chitosan	20-100 o	Cell targeting, Tissue engineering, Drug delivery, hyperthermia	Coroto et al, 2011; Arami et al, 2011; Del campo et al, 2001;
Gelatin	50-100	DNA separation, drug delivery	Gaihre et al, 2009
Starch	10-20	Cell Separation	Dong-Hyun et al, 2009

Table 3. Materials used in functionalization of magnetite nanoparticles.

group (-NH₂). A sample with a double coating silica-aminosilane (Figure 9, MSA sample) shows the band of both materials, and a new band is shown at 802 cm⁻¹ due to Si-O-Si bond. Using this information, a suggested mechanism of coated particles can be proposed (Scheme 1) in magnetite-aminosilane shell, the silicon is bonded with the iron through the deprotonation of magnetite; when a silica shell is added before the aminosilane groups, the silicon is bonded in the same way with the magnetite and the silicon bonded with aminosilane trough S-O-S bond.

Chitosan is a natural polymeric material widely used in biomedical applications as coating in magnetic nanoparticles for biomedical applications. The spectra of this material, Figure 10 show bands at 1400 cm^{-1} due to C-O of the primary OH groups; at 1600 cm^{-1} due to the N-H; at 2943 cm^{-1} due to the stretching of C-H from methyl group (-CH₂, -CH₃) and the band at 1100 cm^{-1} of the hydroxyl group of the pyranosic ring of the chitosan beside the Fe-O bond due to octahedral sites of the magnetite. The band at 2250 cm^{-1} is due to carbon dioxide air.

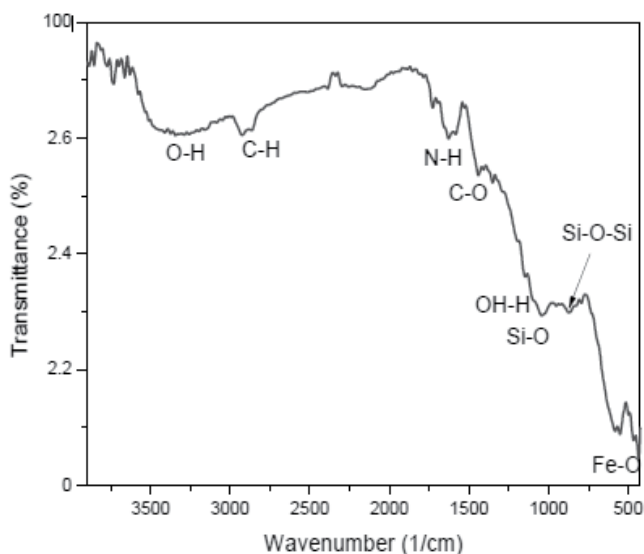


Fig. 10. FT spectra of magnetite coated with a chitosan shell.

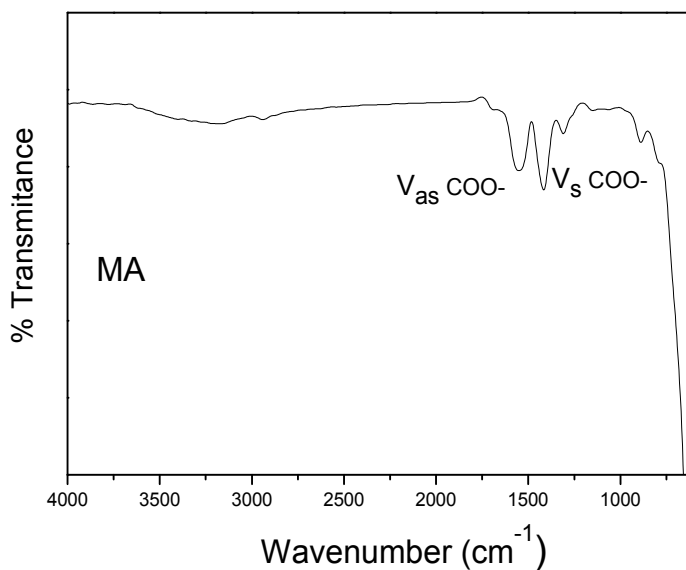


Fig. 11. FT spectra of magnetite coated with an adipic acid shell.

On the other hand adipic acid is a materials that has not been widely studied like a coating shell on magnetic nanoparticles; however, these materials have been widely used in drug delivery systems. In figure 11, the spectrum of the magnetite coated with this polymer shows the bands at 1415 y 1550 cm^{-1} due to the symmetric and asymmetric carboxylate ion (COO^-) and approximately at 600 cm^{-1} the band due to the Fe-O bond in octahedral sites of the magnetite.

4. Conclusions

One of the most important aspects of nanoparticles in biomedical applications is their surface functionalization in order to improve their biocompatibility with biological entities, and Fourier infrared spectroscopy (FTIR) is very useful technique that provides information about iron oxides in their ground electronic state, and when this material is bonding with a polymeric coating provides information about mechanism of functionalized magnetic nanoparticles. This technique is widely used in characterization nanoparticles due to its simplicity and availability. In magnetite structure it provides information about the excitation of vibration or rotation of the trivalent and divalent iron cations and allows knowing the occupied sites when the divalent iron is replaced with other cations.

5. References

- An-Hui Lu, Salabas E. L., Schüth Ferdi. (2007). Magnetic Nanoparticles: Synthesis, Protection, Functionalization, and Application, *Angewandte Chemie-International*, Volume 46, Issue 8, pp 1222-1244.
- Ammar Azioune, Amel Ben Slimane, Lobnat Ait Hamou, Anne Pleuvy, Mohamed M. Chehimi, Christian Perruchot, and Steven P. Armes.(2004). Synthesis and Characterization of Active Ester-Functionalized Polypyrrole-Silica Nanoparticles: Application to the Covalent Attachment of Proteins, *Langmuir*, Volume 20, Issue 8, pp 3350-3356.
- Babita Gaihre, Myung Seob Khil, Douk Rae Lee, Hak Yong Kim. (2009). Gelatin-coated magnetic iron oxide nanoparticles as carrier system: Drug loading and *in vitro* drug release study, *International Journal of Pharmaceutics*, Volume 365, Issues 1-2, pp 180-189.
- Berry Catherine, C, Stephen Wells , Stuart Charles, Adam S.G. Curtis. (2003) Dextran and albumin derivatised iron oxide nanoparticles: influence on fibroblasts in vitro, *Biomaterials*, Volume 24, Issue 25, pp 4551-4557.
- Brabers V. A. M., Walz F.and Kronmüller H. (1998) Impurity effects upon the Verwey transition in magnetite, *Phys. Rev. B*, Volume 58, pp 14163-14166.
- Chen Yuwei and Wang Jianlong (2011). Preparation and characterization of magnetic chitosan nanoparticles and its application for Cu(II) removal, *Chemical Engineering Journal*, Volume 168, Issue 1, 15,pp 286-292.
- Chih-Hang Chu, Yu-Chao Wang, Hsin-Ying Huang, Li-Chen Wu and Chung-Shi Yang. (2011). Ultrafine PEG-coated poly(lactic-co-glycolic acid) nanoparticles formulated by hydrophobic surfactant-assisted one-pot synthesis for biomedical applications, *Nanotechnology*, Volume 22, Number 18, DOI:10.1088/0957-4484/22/18/185601.
- Cornell R. M. and Schwertmann Udo (2003). *The iron oxides: Structure, properties, reactions, occurrences, and uses*, wiley publisher, ISBN 3-527-30274-3.

- Cullity Bernard Dennis and Graham Chad D. (2009), *Introduction to magnetic materials*, wiley publisher, ISBN 978-0-471-47741-9.
- Daisuke Kami, Shogo Takeda, Yoko Itakura, Satoshi Gojo, Masatoshi Watanabe and Masashi Toyoda. (2011). Application of Magnetic Nanoparticles to Gene Delivery *Int. J. Mol. Sci* , Volume 12, Issue 6, pp 3705-3722.
- Daria V. Andreeva, Dmitry A. Gorin, Dmitry G. Shchukin, Gleb B. Sukhorukov. (2006). Magnetic Microcapsules with Low Permeable Polypyrrole Skin Layer, *Macromolecular Rapid Communications*, Volume 27, Issue 12, pp 931-936.
- De Campos Angela, M, Alejandro Sánchez, María J. Alonso. (2001). Chitosan nanoparticles: a new vehicle for the improvement of the delivery of drugs to the ocular surface. Application to cyclosporin A, *International Journal of Pharmaceutics*, Volume 224, Issues 1-2, 14 August 2001, pp 159-168.
- Di Corato Riccardo, Bigall Nadja C, Ragusa Andrea, DorfsDir, Genovese Alessandro, Marotta Roberto, Manna Liberato, and Pellegrino Teresa (2011). Multifunctional Nanobeads Based on Quantum Dots and Magnetic Nanoparticles: Synthesis and Cancer Cell Targeting and Sorting, *ACS Nano*, Volume 5, Issue 2, pp 1109-1121.
- Dong-Hyun Kim, Kyoung-Nam Kim, Kwang-Mahn Kim, Yong-Keun Lee (2009). Targeting to carcinoma cells with chitosan- and starch-coated magnetic nanoparticles for magnetic hyperthermia, *Journal of Biomedical Materials Research Part A*, Volume 88, Issue 1, pp 1-11.
- Gao J, Gu H. (2009). Multifunctional magnetic nanoparticles: design, synthesis, and biomedical applications, *Acc. Chem. Res.*, Volume 42, Issue 8, pp 1097-1107.
- Gnanaprakash G., Mahadevan S., Jayakumar T., Kalyanasundaram P., Philip J., Baldev R. (2007). Effect of initial pH and temperature of iron salt solutions on formation of magnetite nanoparticles. *Materials chemistry and Physics* Volume 103, Issue 1, pp 168-175.
- Gupta Ajay Kumar and Mona Gupta. (2005). Synthesis and surface engineering of iron oxide nanoparticles for biomedical applications, *Biomaterials*, Volume 26, Issue 18, pp 3995-4021.
- Hamed Arami, Zachary Stephen, Omid Veisheh and Miqin Zhang. (2011). Chitosan-Coated Iron Oxide Nanoparticles for Molecular Imaging and Drug Delivery, Chitosan for biomaterials I, *Advances in Polymer Science*, Volume 243/2011, 163-184, DOI: 10.1007/12_2011_121.
- Huixia Zhu, Shiru Jia, TongWan, Yuanyuan Jia, Hongjiang Yang, Jing Li, Lin Yan, Cheng Zhong. (2011). Biosynthesis of spherical Fe₃O₄/bacterial cellulose nanocomposites as adsorbents for heavy metal ions, *Carbohydrate Polymers*, Volume 86, Issue 4, pp 1558-1564.
- Heath Pardoe, Wanida Chua-anusorn^a, Timothy G. St. Pierre, Jon Dobson. (2001). Structural and magnetic properties of nanoscale iron oxide particles synthesized in the presence of dextran or polyvinyl alcohol, *Journal of Magnetism and Magnetic Materials*, Volume 225, Issues 1-2, pp 41-46.
- Huan Qin, Dong Xu and Sihua Yang. (2011). Dextran-coated Fe₃O₄ magnetic nanoparticles as a contrast agent in thermoacoustic tomography for hepatocellular carcinoma detection, *Journal of Physics: Conference Series*, Volume 277, Number 1, doi:10.1088/1742-6596/277/1/012028.

- Joralemon MJ and Rachel KOR. (2005). Shell click-crosslinked (SCC) nanoparticles: a new methodology for synthesis and orthogonal functionalization, *J. Am. Chem. Soc.*, Volume 127, Issue 48, pp 16892-16899.
- Liu G., Hong R.Y., Guo L., Li Y.G, Li H.Z. (2011). Preparation, characterization and MRI application of carboxymethyl dextran coated magnetic nanoparticles, *Applied Surface Science*, Volume 257, Issue 15, pp 6711-6717.
- Madhumita Bhaumik, Arjun Maity, V.V. Srinivasu, Maurice S. Onyango. (2011) Enhanced removal of Cr(VI) from aqueous solution using polypyrrole/Fe₃O₄ magnetic nanocomposite, *Journal of Hazardous Materials*, Volume 190, Issues 1-3, pp 381-390.
- McCarthy Joseph E, Prina-Mello Adriele, Rakovich Tatsiana, Volkov Yuri and K. Gun'ko Yurii. (2011) Fabrication and characterization of multimodal magnetic - fluorescent polystyrene nanowires as selective cell imaging probes, *J. Mater. Chem.*, DOI: 2011, 21, 14219-14225.
- Morteza Mahmoudi, Abdolreza Simchi and Mohammad Imani. (2009). Cytotoxicity of Uncoated and Polyvinyl Alcohol Coated Superparamagnetic Iron Oxide Nanoparticles, *J. Phys. Chem. C*, volume 113, Issue 22, pp 9573-9580.
- Mutsumi Yoshida and Julia E. Babensee (2006). Differential effects of agarose and poly(lactic-co-glycolic acid) on dendritic cell maturation, *Journal of Biomedical Materials Research Part A*, Volume 79A, Issue 2, pp 393-408.
- Mu L and Feng S.S.(2001). Fabrication, characterization and in vitro release of paclitaxel (Taxol®) loaded poly (lactic-co-glycolic acid) microspheres prepared by spray drying technique with lipid/cholesterol emulsifiers, *Journal of Controlled Release*, Volume 76, Issue 3, pp 239-254.
- Nasrazadani S. adn Raman A. (1993). The application of infrares spectroscopy to the study of rust systems: Study of cation deficiency in magnetite produced during its transformation to maghemite and hematite, *Corrosion Science*, Volume 34, No. 8, pp. 1355-1365.
- Neuberger Tobias, Schöpf Bernhard, Hofmann Heinrich, Hofmann Margarete and von Rechenberg Brigitte. (2005). Superparamagnetic nanoparticles for biomedical applications: Possibilities and limitations of a new drug delivery system, *J. Magn. Mater.*, Volume 293, Issue 1, pp 483-496.
- Qiang Gao, Dan Luo, Jun Ding, Yu-Qi Feng. (2010). Rapid magnetic solid-phase extraction based on magnetite/silica/poly(methacrylic acid-co-ethylene glycol dimethacrylate) composite microspheres for the determination of sulfonamide in milk samples, *Journal of Chromatography A*, Volume 1217, Issue 35, pp 5602-5609.
- Palla B.J., Shah D.O, Garcia Casillas P., Matutes-Aquino J.(1999) Preparation of nanoparticles of barium ferrite from precipitation in microemulsions, *J. Nanoparticle Res.*, Volume 2, Issue 1, pp 215-221.
- Phadatare M.R., Khot V.M., Salunkhe A.B., Thorat N.D., Pawar S.H. (2011). Studies on polyethylene glycol coating on NiFe₂O₄ nanoparticles for biomedical applications, *Journal of Magnetism and Magnetic Materials*, doi:10.1016/j.jmmm.2011.09.020.
- Pankhurst Q A, Connolly J, Jones S K and Dobson J. (2003). Applications of magnetic nanoparticles in biomedicine *J. Phys. D: Appl. Phys*, Volume 36, Issue 13, pp 167-172.

- Ramírez Liliana P. and Landfester Katharina. (2003). Magnetic Polystyrene Nanoparticles with a High Magnetite Content Obtained by Miniemulsion Processes, *Macromolecular Chemistry and Physics*, Volume 204, Issue 1, pp 22–31.
- Schliehe Christopher, Schliehe Constanze, Thiry Marc, I. Tromsdorf Ulrich, Hentschel Joachim, Weller Horst, Marcus Groettrup.(2011). Microencapsulation of inorganic nanocrystals into PLGA microsphere vaccines enables their intracellular localization in dendritic cells by electron and fluorescence microscopy, *Journal of Controlled Release*, Volume 151, Issue 3, pp 278-285.
- Schweiger Christoph, Pietzonka Clemens, Heverhagen Johannes, Kissel Thomas.(2011). Novel magnetic iron oxide nanoparticles coated with poly(ethylene imine)-g-poly(ethylene glycol) for potential biomedical application: Synthesis, stability, cytotoxicity and MR imaging, *International Journal of Pharmaceutics*, Volume 408, Issues 1-2, 15, pp 130-137.
- Sidhu P.S., Gilkes R.J., Posner A.M. (1978). The synthesis and some properties of Co, Ni, Zn, Cu, Mn and Cd substituted magnetites, *Journal of Inorganic and Nuclear Chemistry*, Volume 4, Issue 3, pp 429-435.
- Sun Yong-kang, Ming Ma, Zhang Yu, Ning Gu.(2004) Synthesis of nanometer-size maghemite particles from magnetite, *Colloids and Surfaces A: Physicochemical and Engineering Aspects*, Volume 245, Issues 1-3, pp 15-19.
- Terrazas Reza R., Martinez Perez C. A., Rodriguez Gonzalez C.A. Romero Monreal H. T and Garcia Casillas P. E.(2010). Effect of the polymeric coating over Fe₃O₄ particles used for magnetic separation, *Cent. Eur. J. Che*, 2010, Volume 8, Issue 5, pp 1041-1046.
- Varadan V. K, Linfeng Chen and Jining Xie. (2008). *Nanomedicine: design and applications of magnetic nanomaterials, nanosensors*, wiley publisher, ISBN 978-0-470-03351-7.
- Young Lee Ha Hyun Lim Nak. Seo Jin A Soon Hong Yuk Byung Kook Kwak Gilson Khang Hai Bang Lee Sun Hang Cho (2006). Preparation and magnetic resonance imaging effect of polyvinylpyrrolidone-coated iron oxide nanoparticles, *Journal of Biomedical Materials Research Part B: Applied Biomaterials*, Volume 79B, Issue, pp 142–150.
- Zhang J. L., Srivastava R. S, and Misra R. D. K. (2007). Core–Shell Magnetite Nanoparticles Surface Encapsulated with Smart Stimuli-Responsive Polymer: Synthesis, Characterization, and LCST of Viable Drug-Targeting Delivery System, *Langmuir*, Volume 23, Issue 11, pp 6342–6351.
- Zhang J., Rana S., Srivastava R.S., Misra R.D.K. (2008). On the chemical synthesis and drug delivery response of folate receptor-activated, polyethylene glycol-functionalized magnetite nanoparticles, *Acta Biomaterialia*, Volume 4, Issue 1, pp 40-48.

Determination of Adsorption Characteristics of Volatile Organic Compounds Using Gas Phase FTIR Spectroscopy Flow Analysis

Tarik Chafik

*Laboratory of Chemical Engineering and Resources Valorisation (FST/L01),
University Abdelmalek Essaadi,
Faculty of Sciences and Techniques of Tangier, Tangier
Morocco*

1. Introduction

Adsorption is an important operation for gas mixture separation and purification (Yang et al.1987). Thus, measurement of adsorption capacity is crucial for correct designing and operating of adsorption facilities. The heat of adsorption is also an important adsorption characteristic usually needed if adsorbent regeneration and/or adsorbate recovery is targeted (Do, 1998). Accurate knowledge of this thermodynamic parameter is of interest because the heat effects involved during adsorption and/or desorption may induce significant local warming to start combustion of either the adsorbate or the adsorbent itself, particularly, when activated carbon is used (EPA, 1998).

In case of physical adsorption, the involved heat effects might be determined with the isosteric method based on Clausius–Clapeyron equation using adsorption isotherms data at various temperatures (Sircar et al.1999). However, it is to be noted that the isosteric method is limited only to physisorption processes involving relatively low heat of adsorption and for equilibrium reached within accessible range of pressure and temperature (Ranke et al.2002). Under equilibrium, the physically adsorbed species are trapped in different potential wells predisposed within the accessible porosity. During desorption, the species adsorbed in more easily accessible porosity desorbs first. As for those adsorbed in the less accessible porosity, one has to supply required thermal energy for their transfer into gas phase. This energy could be estimated by TPD method using a relatively inexpensive and simple experiment to set up and to run (Cvetanovic et al.1967).

This chapter is devoted to the description of an easy and efficient method based on the application of gas phase Flow FTIR spectroscopy analysis for determination of adsorption characteristics of volatile organic compounds. As adsorbent beds are usually operated under dynamic conditions, the adopted analytical approach is based on gas phase composition monitoring at reactor outlet during adsorption/ desorption experiments carried out under dynamic regime. This method permits further simultaneous detection of new IR bands that may originate from adsorbate dissociation during adsorption or desorption.

Although, Infra Red (IR) spectroscopy is generally used for compounds identification based on measurement of IR radiation resulting from molecular vibration perturbation. The application of Beer's law allows quantitative exploitation of IR spectra using preliminary calibration with known composition. Therefore, the technique was found to be adequate for transient signals monitoring and quantification owing to faster response to instantaneous change in IR bands positions and intensities due to rapid spectra acquisitions allowed by FTIR instrumentation (Chafik et al, 1998). In addition, the high transparency of gases and the low background values achieved, allows detection of lower species concentration in the gas stream. Further increase of analytical sensitivity might be obtained with multiple-pass gas cell.

In the present study, we show an example of the application of this experimental methodology to the investigation of adsorption characteristic of local bentonite clay. Adsorption / desorption experiment were performed at laboratory scale with model-contaminated gaseous stream containing *o*-xylene that has been selected as representative VOC because it is environmentally relevant regarding industrial concern. The work aimed to help further development of low cost materials involved in environmental engineering control.

2. Experimental

2.1 Adsorbent

The clay tested in the present work comes from deposits located in the north of Morocco (Nador area). The results corresponding to its textural and mineralogical composition have been published (Harti et al, 2007). The clay was found to be a mixture of phases, namely, opal, montmorillonite, kaolinite, muscovite, topaz, rutile, calcite, dolomite, suggesting a bentonite type clay. Textural studies performed with N₂ adsorption-desorption at 77 K have shown a BET specific surface area of 79 m² g⁻¹, and a negligible micropore volume of 0.002 cm³ g⁻¹ as compared with total pore volume of 0.205 cm³ g⁻¹. The pore size distribution obtained following BJH method revealed the presence of a wide pore size distribution in the mesopore range with a significant contribution of pores widths between 8 and 50 nm.

2.2 Adsorption and desorption experiments

Adsorption/desorption experiments were performed under dynamic conditions at atmospheric pressure using the experimental apparatus as reported elsewhere (Zaitan et al.2005). The bentonite adsorptive properties were investigated with respect to *O*-xylene vapour. Prior to adsorption, a model mixture with a given concentration of *o*-xylene vapour in nitrogen flow, was prepared by means of a saturator connected to a condenser that was immersed in a thermostatically controlled bath. This temperature was carefully checked so as to maintain constant *o*-xylene vapour pressure and consequently keep the *o*-xylene concentration unchanged. The resulting concentration is expressed as molar fraction (or partial pressure; P/P_0), where P is the vapour pressure of *o*-xylene obtained from Antoine equation and P_0 the atmospheric pressure taken as 760 Torr. Hence, fixing condenser temperature between -8 and 40°C permitted obtaining a value of concentration at reactor inlet (C_{in}) in a range of 700 - 11000 ppm (Zaitan et al, 2006).

2.3 Determination of adsorbed and desorbed amounts

The *o*-xylene concentrations at reactor outlet during adsorption and desorption were monitored with a FTIR spectrometer (Jasco 410, resolution 4 cm^{-1}), using a Pyrex gas cell equipped with CaF_2 windows. The quantitative analysis is facilitated by FTIR instrumentation and programs that allows high frequency spectra acquisition and manipulation (subtraction, multiplication, smoothing). This operation is particularly easy when there are no IR bands overlapping and the application of Beer-Lambert law permits relating IR bands area to concentration. In the present work, the quantitative treatment was achieved by integrating *o*-xylene IR bands located between 2600 and 3200 cm^{-1} . Preliminary calibration with *o*-xylene/ N_2 mixtures of known composition was carried out using reactor by pass, in order to correlate bands area with concentration. Figure 1 shows the calibration curve representing the integral of *o*-xylene IR bands area between 2600 and 3200 cm^{-1} as function of concentration. The FTIR response was found to produce linear plot in the studied concentration range and its accuracy was checked over 3 experiments and represented as mean value.

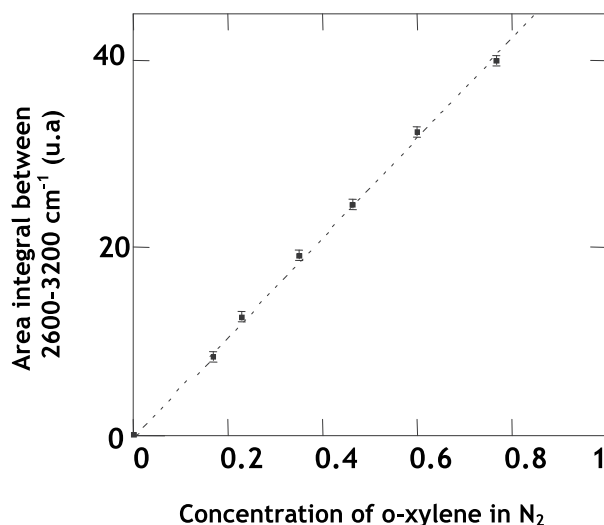


Fig. 1. Calibration curve *o*-xylene IR band area integral (2600-3200 cm^{-1}) versus its concentration in N_2 (molar fraction %)

The sample pre-treatment as well as adsorption and desorption experiments were performed with a flow rate of 100 $\text{cm}^3 \text{min}^{-1}$ that was passed through a quartz reactor (U-type) containing 1 g of bentonite meshes. The sample was first pre-treated under N_2 flow at 473 K for 30 minutes than adsorption was carried out using the model mixture flow until saturation was reached in order to obtain breakthrough curves. The gas mixture was switched again to pure N_2 flow, to proceed with isothermal desorption until *o*-xylene concentration at the reactor outlet reached zero. This step was followed by a subsequent linear heating in order to perform Temperature Programmed Desorption (TPD) experiment.

The monitoring of *o*-xylene IR bands during adsorption at 300 K shows gradual increase of IR bands until equilibrium was reached, which corresponds to adsorbent saturation (Fig2, part A). Following this step, the gas mixture was switched to pure nitrogen flow (0.36 % *o*-xylene/ $\text{N}_2 \rightarrow \text{N}_2$), to perform isothermal desorption giving rise to gradual decrease of IR

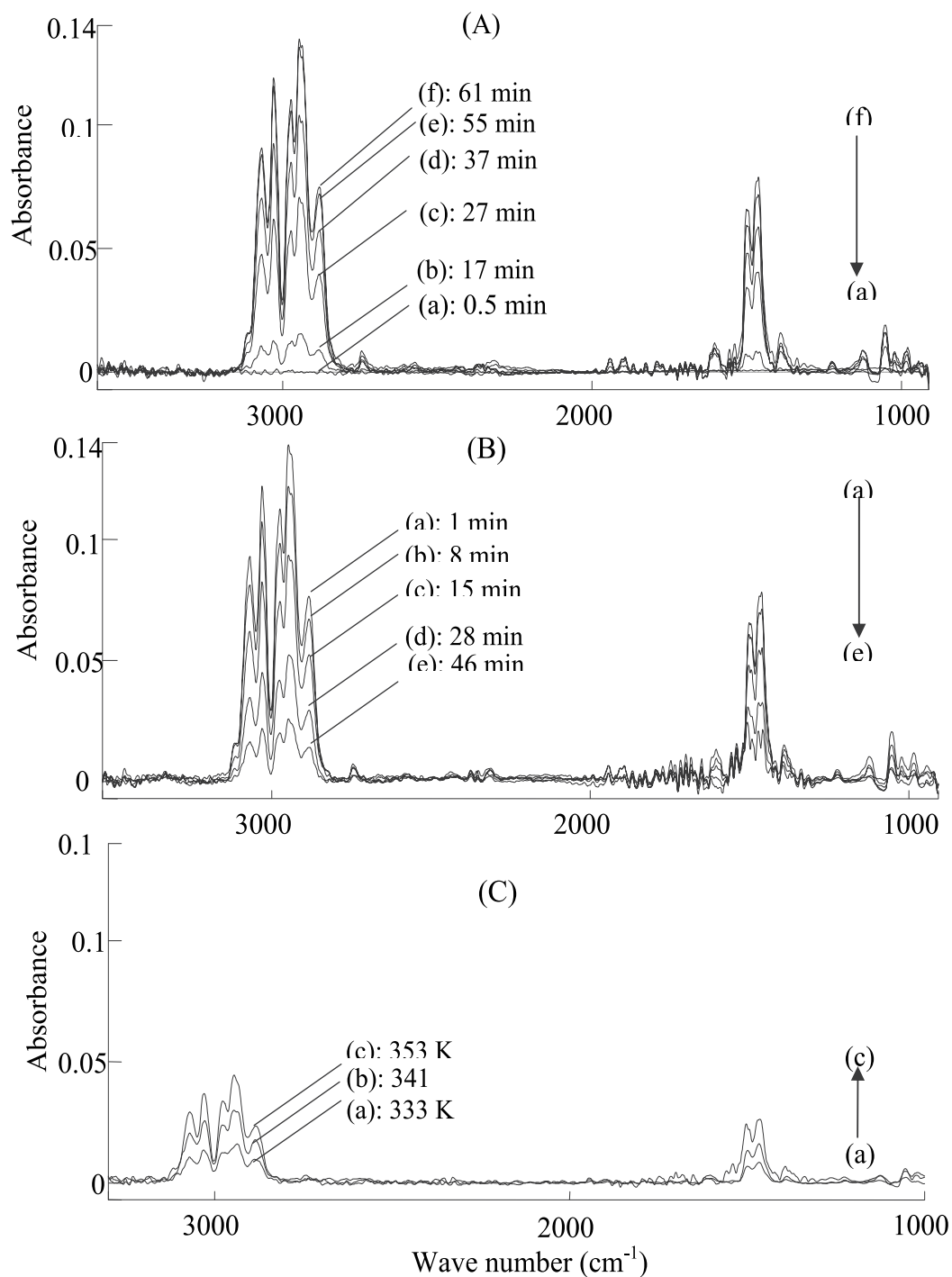


Fig. 2. Evolution of o-xylene IR bands during the following successive experiments: A; Isothermal adsorption at 300K, B; isothermal desorption and TPD under N_2 at linear heating rate of 5K/min.

bands with time, as shown in part B. The sample was, then, linearly heated up to 473K to carry out TPD experiment under N_2 flow (part C of Figure 2). It is to be noted, that the recorded FTIR spectra do not reveal any new species formation originating from *o*-xylene transformation due to catalytic activity. This information provided by the use of FTIR analysis technique can be considered as an advantage of the experimental approach.

The evolution of *o*-xylene concentration at the reactor outlet (C_{out}) obtained from FTIR spectra, permitted the monitoring of adsorbent loading as function of time during adsorption (i.e. breakthrough curve) and desorption processes.

Figure 3 shows the profile of the variation of *o*-xylene concentration in the gas flow at reactor outlet, represented as relative values (C_{out}/C_{in}), during the aforementioned cycle of successive steps (adsorption at 300K until saturation followed by isothermal desorption than Desorption with Programmed Temperature).

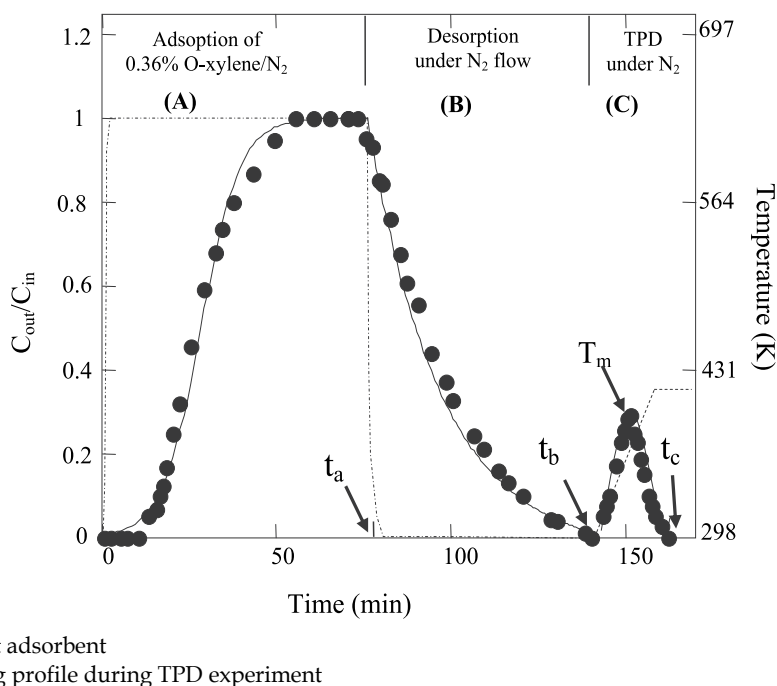


Fig. 3. Profile of the variation of *o*-xylene concentration in the gas flow at reactor outlet, represented as relative values (C_{out}/C_{in}), during a cycle of successive steps; adsorption performed with a mixture of 0.36% xylene in N_2 at 300K until saturation followed by isothermal desorption than Temperature Programmed Desorption carried out with a linear heating rate of 5K/min

It is to be noted that the adsorption/ desorption experiments carried out in the present work with samples of 1g of bentonite compressed as small meshes contained in a quartz microreactor (type U with an internal volume $\approx 1 \text{ cm}^3$). The experiments carried out under atmospheric pressure (760 torr) using total flow rate of $100 \text{ cm}^3/\text{min}$ resulted in a residence time $< 1 \text{ sec}$. Under these conditions the flow pass through the sample in mode 'plug flow' and since small amounts are involved in adsorption or desorption experiments, the reactor

could be considered operating under differential mode as Continuous flow Stirred Tank Reactor (CSTR). This approach permit creation of appropriate and accurate conditions that avoid limitation due to mass and heat transfer within the adsorbent particles in the reactor bed (Zaitan et al, 2008). Consequently, the experiments could be considered as occurring under isothermal conditions in which the pressure drop as well as the variation in fluid velocity between the reactor inlet and outlet were considered negligible. Thus, the adsorbed amount can be calculated using the mass balance equation (Ruthven, 1984).

$$n_{ads} = \frac{FC_{in}}{m} \left[t_a - \int_0^{t_a} \frac{C_{out}}{C_{in}} dt \right] \quad (1)$$

Where n_{ads} is the adsorbed mole number of toluene at saturation (adsorption capacity in mol/g), C_{in} and C_{out} the molar fractions of toluene at reactor inlet and outlet, m is the adsorbent mass, t_a the saturation time and F the gaseous molar flow rate.

The adsorbed amount measured from breakthrough curve is generally used to indicate adsorbent performance in terms of a given constituent removal from a flowing stream. In the present study, the adsorption capacity is obtained by integration of the breakthrough curve, according to the equation (1) and considering the curve corresponding to the reactor response in the absence of solid. Accordingly, the numerical integration of the breakthrough curve using MathCAD software yields to a total adsorbed amount of $420 \mu\text{mol g}^{-1}$, for adsorption carried out with a flow containing 0.36% *o*-xylene in N_2 (Fig. 3 part A). This amount is lower than the adsorption capacity of $1958 \mu\text{mol g}^{-1}$ reported in our previous work for SiO_2 Degussa ($200 \text{ m}^2\text{g}^{-1}$) (Zaitan et al 2005). In comparison with the literature, substantially higher values of 4666, 2800, 1800 and $2050 \mu\text{mol g}^{-1}$ are reported for xylene adsorption, respectively, for activated carbon AC40 ($1300 \text{ m}^2\text{g}^{-1}$) (Benkhedda et al, 2000) and zeolites (Al-Meso 100 ($915 \text{ m}^2\text{g}^{-1}$) UL-ZSM5-100-2 ($840 \text{ m}^2\text{g}^{-1}$), UL-ZSM5-100-6 ($780 \text{ m}^2\text{g}^{-1}$) (Huang et al, 2000)

The numerical integration of the desorption curve (part B of Figure 3) using equation (2) and considering the curve in the absence of solid, permitted quantification of loosely adsorbed fraction (n_{1ads}) of $370 \mu\text{mol.g}^{-1}$ released during isothermal desorption.

$$n_{1ads} = \frac{FC_{in}}{m} \left[\int_{t_a}^{t_b} \frac{C_{out}}{C_{in}} dt \right] \quad (2)$$

Where t_a and t_b correspond to starting and ending time of isothermal desorption.

It is to be noted that although the *o*-xylene desorption curve reached zero, the calculated weakly adsorbed fraction represents 88% of the total adsorbed amount. The remaining *o*-xylene adsorbed amount corresponds to the more strongly adsorbed fraction. The removal of the latter fraction requires thermal treatment with linear heating rate according to TPD method. The integration of the corresponding curve, shown in part C of Figure 3 using equation (3), permits obtaining an irreversible amount of $60 \mu\text{mol.g}^{-1}$.

$$n_{2ads} = \frac{FC_{in}}{m} \left[\int_{t_b}^{t_c} \frac{C_{out}}{C_{in}} dt \right] \quad (3)$$

(where t_b and t_c correspond to the starting and the ending of TPD curve).

Therefore, the data corresponding to total adsorbed amount (n_{ads}) were found to fit the mass balance equation ($n_{ads} \approx n_{1ads} + n_{2ads}$) with a precision around 2%, corresponding to the accuracy of the used analytical methodology. It is to be noted that the n_{ads} values do not suffer major changes during successive cycles of adsorption desorption experiments carried out with the same benonite samples and the precision remains at worst around 5%. However, for bentonite sample used for more than 3 successive cycles of adsorption/desorption experiments, a treatment under N_2 flow at 473 K for 30 min, is enough for recovering its initial performances.

Another important information given by TPD experiment concerns the desorption performance indicated by the temperature at the peak maximum. The T_m value of 353 K shown by Figure 3, is slightly, lower than the T_m value of 368 K given by TPD peak obtained using the same heating rate for SiO_2 Degussa ($200 \text{ m}^2\text{g}^{-1}$) (Zaitan et al 2005).

The obtained results reveals adsorptive properties of bentonite clay such as larger reversibly adsorbed fraction, lower temperature for complete thermal desorption and absence of catalytic activity that might be of interest for adsorbent regeneration and adsorbate recovery. Even though its lower BET surface area, Bentonite's potential use as adsorbent material deserves to be investigated because adsorbent with higher specific surface area; such as active carbons is not usually the best (Brasseur et al, 2004). Thus, investigation of adsorption energies is also needed for selection of efficient adsorbent material, particularly, if collecting and reusing VOCs is targeted.

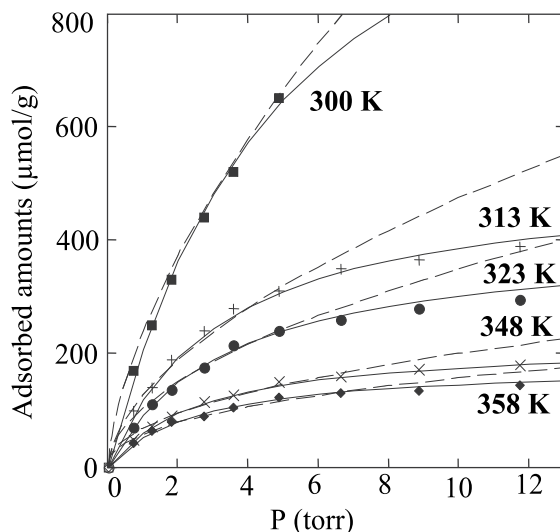
2.4 Isothermic heat of adsorption

The amounts adsorbed at equilibrium corresponding to adsorption capacity obtained from breakthrough curves, were determined for different adsorption temperatures and for different xylene pressures, yields to isotherms shown in Figure 4. The isotherms are represented in the form of $N = f(P)$ where N is the adsorbed amount per adsorbent weight at equilibrium and P the O-xylene partial pressure in the mixture flow. The experimental isotherms were modeled with Langmuir and Freundlich equations using a nonlinear regression method (MathCAD software). The corresponding fitting curves are shown as solid and dashed lines, respectively, for Langmuir and Freundlich models (Fig. 4). Apparently, the experimental data were well represented by Langmuir model while Freundlich equation deviates at pressures higher than 4 torr.

The adsorption isotherms presented in Figure 4 were used for determination of isosteric heat (Q_{st}) of adsorption by extrapolation at different temperatures and for a given coverage according to Clausius-Clapeyron equation (Rouquerol, 1999):

$$Q_{st} = -R \left(\frac{\partial \ln P}{\partial \left(\frac{1}{T} \right)} \right) \quad (4)$$

Where R is the perfect gas constant, P and T correspond, respectively; to partial pressure and temperature at equilibrium.



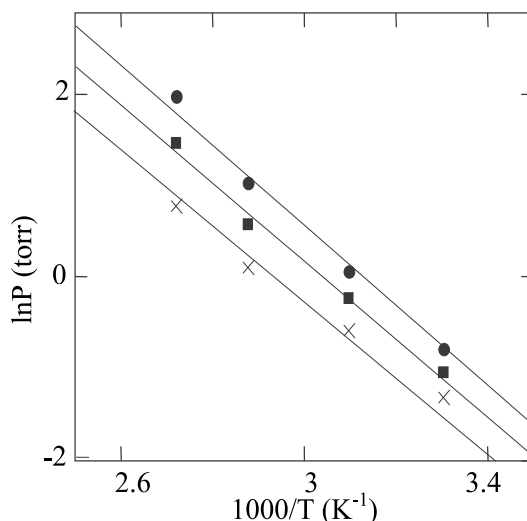
— Langmuir equation

- - - Freundlich model

Fig. 4. Experimental and Modeled adsorption isotherms of O-xylene at different temperatures

This approach do not requires an assumption on model fitting with experimental data even though we have shown that Langmuir equation described well the adsorption process in the studied T, P ranges. Thus, (Q_{st}) values were extracted from the slops of isosteres (Figure 5)

representing the plot of $\ln(P) = f\left(\frac{1}{T}\right)$. One has to check very carefully whether the resulting



●, 206; ■, 133; ×, 100 $\mu\text{mol g}^{-1}$

Fig. 5. Plot of isostere corresponding to $\ln(P)$ versus $1/T$ corresponding to the following adsorbed amounts

isosteres correspond to straight lines, which depends strongly on the accuracy of experimental conditions. So far, a temperature measurement error of ± 2 K may yield to an uncertainty of ± 8 kJ/mol for the isosteric heat calculation (Bülow et al, 2002 and Dulaurent et al 2000).

For temperatures ranging from 300 to 363 K, values of isosteric heat of adsorption in range of 40 to 44 kJ/mol were obtained for o-xylene loading between 100 and 250 $\mu\text{mol/g}$ corresponding to a coverage between $0.05 \leq \theta \leq 0.125$ ($\theta = n_{\text{ads}}/n_{\text{ads m}}$, where n_{ads} is the adsorbed amount and $n_{\text{ads m}}$ is the adsorbed amount at monolayer). Nevertheless, these values do not exceed the heat of vaporization (55 kJ/mole) (CRC Handbook, 1985) indicating a weak physisorption adsorption.

2.5 Estimation of the desorption energy with TPD method

In the following section, the part C of the cycle (Figure 3), corresponding to TPD experiment carried out after adsorbent saturation followed by isothermal desorption, will be used for the determination of the desorption energy. The TPD method proposed by Cvetanovic and Amenomiya (Cvetanovic et al., 1967) was also validated under various experimental conditions by several authors (Yang et al.1999; Joly et al.2000; Kanervo et al.2006, Yoshimoto et al.2007). The method allows an easier estimation of the binding energy between the adsorbate and the adsorbent by plotting the desorption rate of the adsorbate as function of temperature. Although, a criticism is reported concerning the assumption related with experimental conditions permitting to achieve TPD measurement free of the influence of diffusion and readsorption (Gorte et al.1996).

The analysis of TPD curves collected at different linear heating rates (β), is based on exploitation of the shift of temperature at desorption peak maximum (T_m) as a function of β . Hence the activation energy for desorption E_d is extracted from the slope of the line obtained from the following equation:

$$2\ln T_m - \ln \beta = E_d/RT_m + \text{constant} \quad (5)$$

Where T_m is the desorption temperature at peak maximum (K), β is the linear rate of temperature rise (K/min), E_d is the desorption energy (kJ/mol) and R is the perfect gas constant (kJ/molK).

Therefore, in order to provide reliable data on the desorption energy, the TPD curves have to be well defined, with clearly detectable T_m positions. This was the case of our experiment as shown in part C of Figure 3.

Table 1 gives the T_m positions obtained with different heating rates β during the TPD (part C of the cycle). For this purpose additional experiments set of adsorption and desorption cycles at 300K were carried out with the same adsorption pressure of 2.72 Torr of O-xylene (molar concentration of 0.36% in N_2) but with the TPD experiment performed using different linear heating rate β (curves not shown).

B (K/min)	4	5	7	10	12
T_m (K)	350	353	356	361	364

Table 1. Linear heating rate β used for TPD experiments and its corresponding Temperature at Peak maximum T_m (K)

As observed in Figure 6, a linear and positive relationship was observed between $2\ln T_m - \ln \beta$ and $1/T_m$, and a value for the heat of desorption of 75 kJ/mol is obtained from the slope of this plot. This value is higher than those obtained using isosteric method. As stated above, the analytical procedure adopted in the present work permitted quantification of weakly and strongly adsorbed fractions occurring within the predisposed porosity of the clay. Moreover, previous work on textural characterisation revealed that the studied clay is mainly mesoporous and presents wider pore sizes distribution with a significant contribution of pores widths around 9 nm and 40nm (Harti et al, 2007). It is known that the efficiency of an adsorbent depends on its pore structure and the size of adsorbate molecules which affect their diffusion and interaction within the pores. Thus, adsorption in larger pores is associated with lower heats of adsorption corresponding to the weakly adsorbed fraction (n_{ads}) which represents about 88% of the total adsorbed. While the remaining adsorbed fraction corresponds to the more strongly adsorbed physisorbed species trapped in deeper potentials of predisposed micropores and narrowest mesopores. The resulting heat of adsorption values might be enhanced by "confinement effect", particularly, in case of physisorption of molecules disposing with size similar to those of adsorbent pores (Yoshimoto et al.2007). As shown in the present work, these species will need supplying thermal energy for their transfer to the gas phase, corresponding to the desorption energy which is equal to the heat of adsorption in case of physisorption.

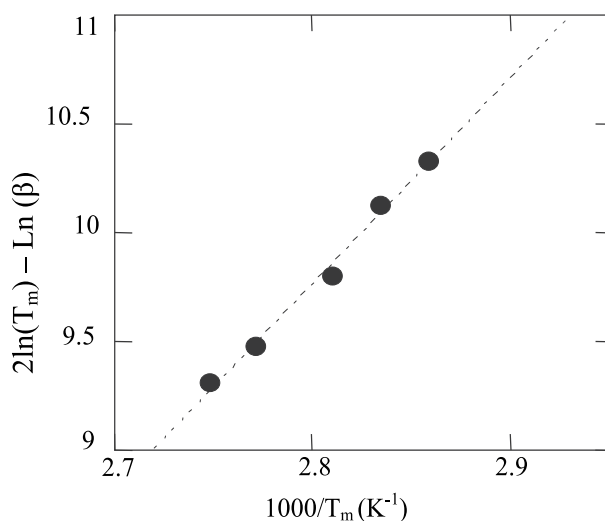


Fig. 6. Cvetanovic curve obtained with TPD experiments performed with β and T_m values presented in table 2 for an adsorption test performed with a flow containing 3600 ppmv of xylene

On the other hand, it is to be noted that the use of Clausius Clapeyron for the estimation of the heat of adsorption, is efficient and accurate when the adsorption process is essentially reversible. This approach is no longer valid for stronger adsorption. As shown in the present work, significant difference might be obtained in the values of the heat of physisorption depending on the nature of the involved porosity. Thus, the analytical method must be able to quantify different adsorbed fractions (i.e. weakly and strongly physisorption) or else, at best, only an average of the heats of adsorption is obtained, as it is the case of integral or

differential heat of adsorption provided by microcalorimetric methods (Simonot-Grange et al, 1997, Cardona-Martinez and Dumesic, 1997).

3. Conclusion

The use of FTIR spectroscopy was found to permit accurate quantitative analysis that allows determination of adsorbent saturation loading from breakthrough curves and differentiation between weakly and strongly physisorption. The experimental methodology allows, also, the possibility of simultaneous detection of further adsorbate dissociation through appearance of new IR bands. The data obtained using this analytical approach have been used to derivate useful thermodynamic parameters related to the heat involved during adsorption and/or desorption processes. It was shown that significant difference might be obtained for the values of the heat of adsorption depending on to the nature of the involved porosity. This aspect need to be considered for designing and operating of adsorption facilities.

4. References

- Benkhedda, J., Jaubert, J. N., Barth, D., Perrin, L., Bailly, M., J. Chem. Thermodyn. (2000) 32 (3) 411
- Brasseur, A.; Gambin, A.; Laudet, A.; Marien, J.; Pirard, J.P. Elaboration of new formulations to remove micropollutants in MSWI flue gas. *Chemosphere* 2004, 56, 745-756.
- Bülow, M.; Shen, D.; Jale, S. Measurement of sorption equilibria under isosteric conditions The principles, advantages and limitations. *Appl. Surf. Sci.* 2002, 196,157-172
- Cardona-Martinez, N.; Dumesic, J.A.; Microcalorimetric measurements of differential heats of adsorption on reactive catalyst surfaces. *Thermochimica Acta.* 1997, 1,3, 43-53 .
- Chafik T., Dulaurent O., Gass J.L., and Bianchi D.,(1998), Heat of adsorption of carbon monoxide on Pt/Rh/CeO₂/Al₂O₃ Three way catalyst using in-situ Infrared Spectroscopy at high temperatures, *J. Catal.*, 179(2) 503
- Cvetanovic, R. J. and Amenomiya, Y. (1967) Application of a Temperature-Programmed Desorption Technique to Catalyst Studies. In *Advances in Catalysis*; Eley, D. D., Pines, H. and Weisz, P. B. Eds.; Academic Press: New York, Vol. 17, p. 103.
- CRC Handbook, 65 th ed.; CRC Press Inc, Boca Ratton, FL, 1985
- Do, D. D. Adsorption Analysis: Equilibria and kinetics; Series on Chemical Engineering 2; Imperial College Press: London, 1998.
- Dulaurent, O.; Bianchi, D. Adsorption isobars for CO on a Pt/Al₂O₃ catalyst at high temperatures using FTIR spectroscopy: isosteric heat of adsorption and adsorption model. *Appl. Catal. A: General* 2000, 196, 271-280
- EPA,(May 1998) Chemical Emergency Preparedness and Prevention Office. *Fire hazard from carbon adsorption deodorizing systems. EPA 550-F-97-002-e.*
- Joly, J.P. and Perrard, A. (2000) Determination of the heat of adsorption of ammonia on zeolites from temperature-programmed desorption experiments. *Langmuir* 1538-42.
- Harti, S.; Cifredo; G.; Gatica J.M; Vidal H, and Chafik, T. Physicochemical characterization and adsorptive properties of some Moroccan clay minerals extruded as lab-scale monoliths. *Applied Clay Science* (2007) 36, 287-296

- Huang, Q., Vinh-Thang, H., Melekian, A., Eic, M., Trong-On, D., Kaliaguine, S., Micropor. Mesopor. Mater., 87 (2006) 224
- Kanervo, J.M., Keskitalo, T.J., Slioor, R.I. and Krause, A.O.I.(2006) Temperature-programmed desorption as a tool to extract quantitative kinetic or energetic information for porous catalysts, Journal of Catalysis 382-393
- Gorte, R. J. (1996) Temperature-programmed desorption for oxide catalysts. Catalysis Today 405-414.
- Simonot-Grange, M.H.; Bertrand, O.; Pilverdier, E.; Bellat, J.P.; Paulin, C. Differential calorimetric enthalpies of adsorption of p-xylene and m-xylene on Y faujasites at 25°C. J. Therm. Anal. 1997, 48, 741-754.
- Sircar, S. , Mohr, R., Ristic, C. and Rao, M. B. (1999) Isosteric Heat of Adsorption: Theory and Experiment. *J. Phys. Chem. B* 103 ,6539–6546.
- Ranke, W. and Josephy, Y. (2002) Determination of Adsorption Energies and Kinetic Parameters by Isosteric Methods. *Phys. Chem. Chem. Phys.* 4 ,2483–2498.
- Rouquerol, F. , Rouquerol, J. and K.S.W. Sing, *Adsorption by Powders and Porous Solids*, Academic Press (Eds.), Harcourt Brace & Company, London, (1999) pp. 47–49.
- Yang R.T., Long Q., Padin J., Takahashi A., Takahashi T., Adsorbents for Dioxins (1999) A New Technique for Sorbent Screening for Low-Volatile Organics. *Ind. Eng. Chem. Res.* 38, 2726-2731.
- Yoshimoto R., Hara K., Okumura K., Katada N., M. Niwa M., (2007) Analysis of Toluene Adsorption on Na-Form Zeolite with a Temperature-Programmed Desorption Method. *J. Phys. Chem.* 111, 1474-1479.
- Yang R.T., Long Q., Padin J., Takahashi A., Takahashi T., Adsorbents for Dioxins (1999) A New Technique for Sorbent Screening for Low-Volatile Organics. *Ind. Eng. Chem. Res.* 38, 2726-2731.
- Zaitan H., Chafik T., FTIR Determination of Adsorption Characteristics for Volatile Organic Compounds Removal on Diatomite Mineral Compared to Commercial Silica (2005) *C.R. Chimie* 8, 1701–1708.
- Zaitan, H.; Feronnato, C.; Bianchi, D.; Achak, O.; Chafik, T. Etude des propriétés texturales et adsorbantes d'une diatomite marocaine: Application au traitement D'air chargé d'un polluant de type composé organique volatil. *Ann. Chim. Sci. Mat.* 2006, 31(2), 183-196.
- Zaitan H., Bianchi D., Ouafae Achak O., and Chafik T., A comparative study of the adsorption and desorption of o-xylene onto bentonite clay and alumina. *Journal of Hazardous Materials* 153 (2008) 852–859

Identification of Rocket Motor Characteristics from Infrared Emission Spectra

N. Hamp, J.H. Knoetze, C. Aldrich* and C. Marais
*University of Stellenbosch
South Africa*

1. Introduction

The prediction of infrared (IR) emission spectra from the exhaust gases of rocket plumes finds numerous applications in the strategic identification of rockets. These rocket fingerprints could be classified, thus allowing for the distinction between friend and foe. Likewise, the plume radiation intensity could also be reduced for stealth purposes, where accurate prediction of the spectra could be used to determine whether rockets have the required stealth characteristics during their design phase already. This would reduce the high manufacturing and testing costs involved in later stages.

The challenge of predicting the plume radiance is describing the thermodynamic combustion process within the rocket chamber, the plume structure and the rocket plume chemical composition. The factors guiding these processes are the rocket motor design parameters, as well as the rocket motor fuel chemistry. In addition, environmental conditions have a significant impact on the plume structure and the plume chemical composition.

Previously, attempts were made to model the middle IR band emission spectra (2 to 5.5 μm) from the rocket fuel chemistry and the physical properties during combustion by making use of techniques such as quantum mechanics and computational fluid dynamics. These methods proved to be too time consuming and the accuracies of the predictions were not acceptable (Roodt, 1998).

More recently, Roodt (1998) was the first to show that the IR spectra could be modelled with a multilayer perceptron neural network using the elemental composition and other physical properties of the rocket motor fuel as input. Although these models were successful, there were some indications that they were not optimal and in this investigation the use of multilayer perceptrons similar to the ones used by Roodt (1998), as well as linear partial least squares (PLS) and neural network PLS (with and without weight updating) are considered.

In addition, the modelling problem is considered in terms of a forward mapping, i.e. prediction of the emission spectra of the rockets from their design parameters, as well as a reverse mapping, where the rocket design parameters are predicted from the middle-IR spectral absorbances of the rocket plume.

* Corresponding Author

2. Partial least squares (PLS) and neural network models

2.1 Linear PLS

The advantage of PLS lies in the fact that a multivariate regression problem can be decomposed into a number of uncorrelated univariate or SISO (single input, single output) data mappings. This is especially useful when the available data are sparse, such as when dealing with relatively small sets of samples across many highly correlated input, as well as output variables.

The linear PLS algorithm has various forms like the one given by Lorber et al. (1987). The nonlinear iterative partial least squares (NIPALS) algorithm for training PLS models was pioneered by H. Wold (1966). The NIPALS algorithm may be computationally less efficient, but it is well understood and serves as the basis for nonlinear neural network PLS algorithms. The objective of the NIPALS algorithm is to project input and output matrices \mathbf{X} and \mathbf{Y} (consisting of rows corresponding to data sample points $i = 1, 2, \dots, n$) onto a subset of latent variables, \mathbf{T} and \mathbf{U} , which are referred to as the input and output scores, respectively. The dimensionalities of variable spaces of \mathbf{X} and \mathbf{Y} are denoted by $k = 1, 2, \dots, m$ and $j = 1, 2, \dots, l$ respectively. The output scores can then be fitted to the input scores by linear least squares regression in order to obtain the so-called inner linear relationship coefficients, b_a for $a = 1, 2, \dots, h$:

$$\mathbf{u}_a = \mathbf{t}_a b_a + \mathbf{e}_a \quad (1)$$

Here the h primary latent dimensions explaining most of the model variance are retained. The decompositions of \mathbf{X} and \mathbf{Y} can be defined using the loading vectors \mathbf{p} and \mathbf{q} such that PLS outer models become:

$$\mathbf{X} = \sum_{a=1}^h \mathbf{t}_a \mathbf{p}_a^T + \mathbf{F} \quad (2)$$

$$\mathbf{Y} = \sum_{a=1}^h \hat{\mathbf{u}}_a \mathbf{q}_a^T + \mathbf{E} \quad (3)$$

The matrices, \mathbf{F} and \mathbf{E} are the resulting residual matrices when a model with $h \leq \min(n, m)$ latent dimensions is used for the approximation of \mathbf{X} and the prediction of \mathbf{Y} . The remaining latent dimensions usually explain random noise that may be present in the data. The predicted scores of \mathbf{u} are calculated using the inner model

$$\hat{\mathbf{u}}_a + \mathbf{t}_a b_a \quad (4)$$

The linear projections constituting the NIPALS algorithm (see Appendix A) are described in Baffi et al. (1999a), where it is further shown that the $n \times h$ score matrix, \mathbf{T} can be related to the input matrix, \mathbf{X} by

$$\mathbf{T} = \mathbf{X}\mathbf{R} \quad (5)$$

where \mathbf{R} is obtained from

$$\mathbf{R} = \mathbf{W}(\mathbf{P}^T \mathbf{W}) \tag{6}$$

This is a useful expression, since \mathbf{T} can be expressed in terms of \mathbf{W} , the PLS input weights, without having to break down \mathbf{X} into its residuals for each latent dimension. A matrix of linear inner model regression parameters on the diagonal and zero-values off the diagonal, \mathbf{B} can now be defined. Equations (5) and (4) can further be used to obtain

$$\hat{\mathbf{Y}} = \hat{\mathbf{U}}\mathbf{Q}^T = \mathbf{X}\mathbf{R}\mathbf{B}\mathbf{Q}^T = \mathbf{X}\mathbf{B}_{PLS} \tag{7}$$

where \mathbf{B}_{PLS} is the $m \times 1$ matrix of overall regression coefficients which converges to multiple linear regression coefficients for $h = m$.

2.2 Multilayer perceptron neural networks

Artificial neural networks (ANNs) are a non-linear function mapping technique that was initially developed to imitate the brain from both a structural and computational perspective. Its parallel architecture is primarily responsible for its computational power. The multilayer perceptron network architecture is probably the most popular and is used here.

A multilayer perceptron neural network (Bishop, 1995; Haykin, 1999) consists of an input and an output layer of nodes, which may be separated by one or more layers of hidden nodes (see figure 1 below). Each node links to another node with a weighted connection, ω .

Considering a network with a single hidden layer, where the hidden and output layers are denoted by superscripts (1) and (2) respectively, then for $r = 1, 2, \dots, H$ hidden nodes the nonlinear functional relationship is represented by equation (8):

$$f_{ij}(\mathbf{x}_i, \boldsymbol{\Omega}^{(1)}, \boldsymbol{\omega}_j^{(2)}, \boldsymbol{\beta}^{(1)}, \beta_j^{(2)}) = \sum_{r=1}^H \omega_{jr}^{(2)} \phi_{ir} \left\{ \sum_{k=1}^m (\omega_{rk}^{(1)} x_{ik}) + \beta_r^{(1)} \right\} + \beta_j^{(2)} \tag{8}$$

Here $\boldsymbol{\Omega}^{(1)}$ is the $H \times m$ matrix of weights (ω_{rk}) in the hidden layer, $\boldsymbol{\omega}$ represents a vector of weights for a single node and β is a bias value associated with each node. The function ϕ is a sigmoidal activation function, typically of the form:

$$\phi(z) = \tanh(z) = \frac{1 - \exp(-2z)}{1 + \exp(-2z)} \tag{9}$$

The advantage of this form of the function is that its derivative is simple to calculate, i.e.

$$\phi'(z) = 1 - \phi^2(z) \tag{10}$$

This derivative form becomes useful when calculating the Jacobian matrix used when the weights of the network are updated within the neural network PLS algorithm below.

The performance of an ANN is measured by the root-mean-square error (RMSE) which is also the function to be minimised. The Levenberg-Marquardt optimization algorithm (Marquardt, 1963) and resilient propagation algorithm (RPROP) (Riedmiller & Braun, 1993) were used to train the neural networks in this study.

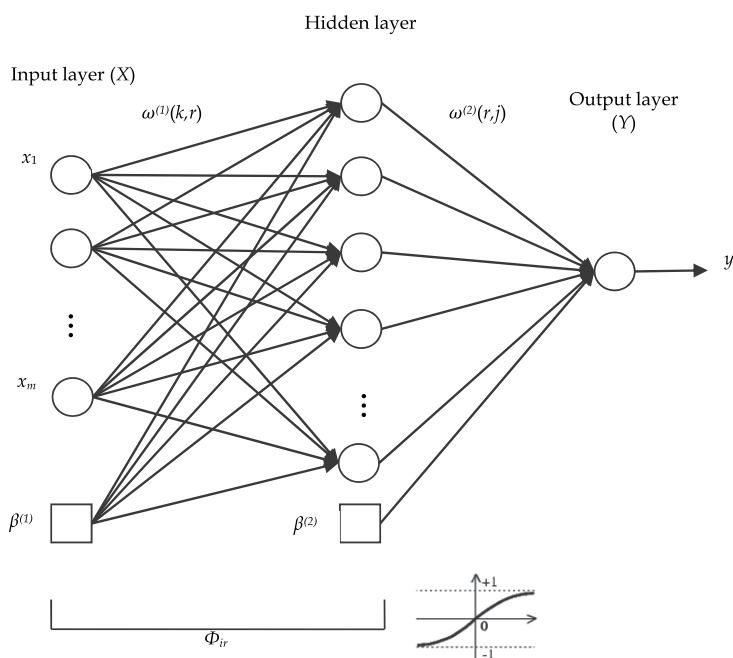


Fig. 1. Multi-layered perceptron neural network with one hidden layer.

$$RMSE = \sqrt{\frac{\sum_{i=1}^n SSE_i}{nl}} \quad (11)$$

n refers to the training vector number (i.e. observation) and SSE_i is the sum-square error of the i^{th} training vector for all l output nodes:

$$SSE_i = \sum_{j=1}^l (y_{true,j}^i - y_{pred,j}^i)^2 \quad (12)$$

The weight matrices are initially randomised. A subset of the input dataset is applied to the network input nodes and the outputs of the hidden and output nodes are calculated. The SSE is calculated as in equation 12 upon which the weight matrices are updated using the optimisation framework. The procedure is repeated for the remaining input dataset to calculate the $RMSE$ which completes a single iteration. A number of these iterations are necessary to minimise the $RMSE$.

2.3 Neural network PLS

When applying linear PLS to nonlinear problems, it may not be sensible to discard the minor latent dimensions, as they may contain valuable information with regard to the mapping. It may therefore be advantageous to derive a nonlinear relationship for the PLS inner model. This can be accomplished by use of a multilayer perceptron neural network such as described above and illustrated in figure 2.

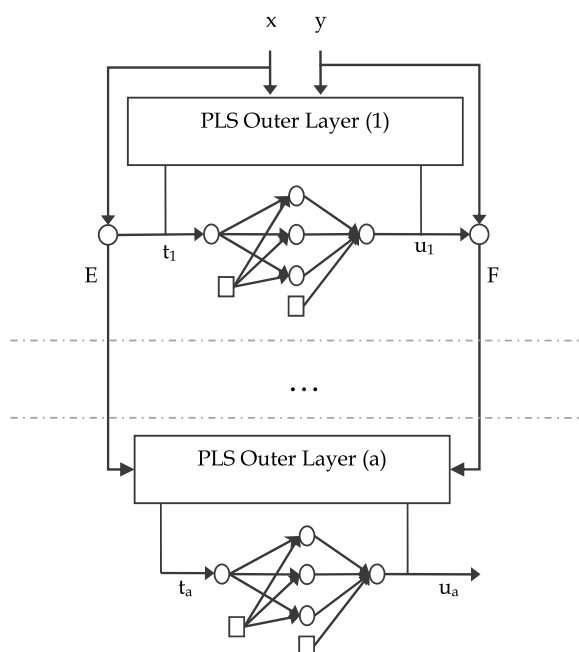


Fig. 2. Diagram illustrating the NNPLS algorithm wherein data are transformed to latent scores, then neural networks used to learn the scores (adapted from Qin & McAvoy, 1992).

A neural network has the advantage that it is a universal approximator and the inner PLS model is therefore not limited to some predefined functional form. In Qin & McAvoy (1992) the neural network PLS (NNPLS) algorithm is introduced by replacing the linear inner relationship in equation (4) with a feed-forward multilayer perceptron neural network, such that

$$\hat{u}_a = f(t_a, \boldsymbol{w}^{(1)}, \boldsymbol{w}^{(2)}, \boldsymbol{\beta}^{(1)}, \boldsymbol{\beta}^{(2)}) \tag{13}$$

The NIPALS algorithm now replaces the inner linear regression coefficient calculation (Appendix A, step x) by a neural network training step. The use of a nonlinear function as inner PLS relationship influences both the inner and outer mappings of the PLS algorithm. If the inner mapping is highly nonlinear, this approach may no longer be acceptable. This problem was addressed by S. Wold et al. (1998) by updating the PLS weights, \boldsymbol{w} using a complicated, non-intuitive Taylor series linearization method. More recently, Baffi et al. (1999b) proposed an error-based (EB) input weight (\boldsymbol{w}) updating procedure using a Taylor series expansion to improve the weight updating procedure originally suggested by S. Wold et al. (1998).

3. Experimental data

The data set of rocket motor features consisted of 14 elemental rocket propellant compositions and 4 rocket motor design parameters. The elemental compositions were molar values calculated from a 100 kg basis and included the elements C, H, O, N, Al, K, F, Cu, Pb, S, Cl, Si, Ti and Fe. The design parameters consisted of the nozzle throat temperature (T_C), pressure (P_C), nozzle diameter (D_T) and the expansion ratio of the outlet nozzle diameter to the nozzle throat diameter (E_C).

The data set of IR emission spectra consisted of radiometer absorbance values at 146 different wavelengths in the middle-IR band (2 to 5.5 μm).

Two types of rocket motor propellants were used, namely a composite (C) and a double-base (DB) type. The C-type propellants consisted of heterogeneous grains where the fuel and oxidiser were held together in a synthetic rubber matrix. The DB-types had homogeneous grains containing small amounts of dispersed additives. There were 12 C-type and 6 DB-type rocket motor propellants.

Each rocket motor type was fired a number of times (see table 1) and the IR emission spectra were recorded for each test as replicate measurements. The total set of recorded IR emissionspectra thus comprised 420 measurements. The spectra were recorded by Roodt (1998) using a spectral radiometer at varying distances, i.e. 500 m, 350 m, 250 m and 200 m. The data were preprocessed in order to compensate for the varying absorbance path lengths and atmospheric conditions (Bouguer's law) as described in Roodt (1998).

DB1	DB2	DB3	DB4	DB5	DB6	C1	C2	C3	C4	C5	C6	C7	C8	C9	C10	C11	C12
39	21	31	20	20	22	15	24	24	17	18	26	44	15	25	14	23	22

Table 1. The number of middle-IR emission spectra repeat measurements taken from tests for each of the rocket motor types.

A principal components analysis was done on a standardised IR emission spectrum data set including all 420 data samples. Results showed that 86.7% of the total variance of the wavelength variables could be explained by the first two principal components. The map of squared correlation coefficients in figure 3 confirms this result.

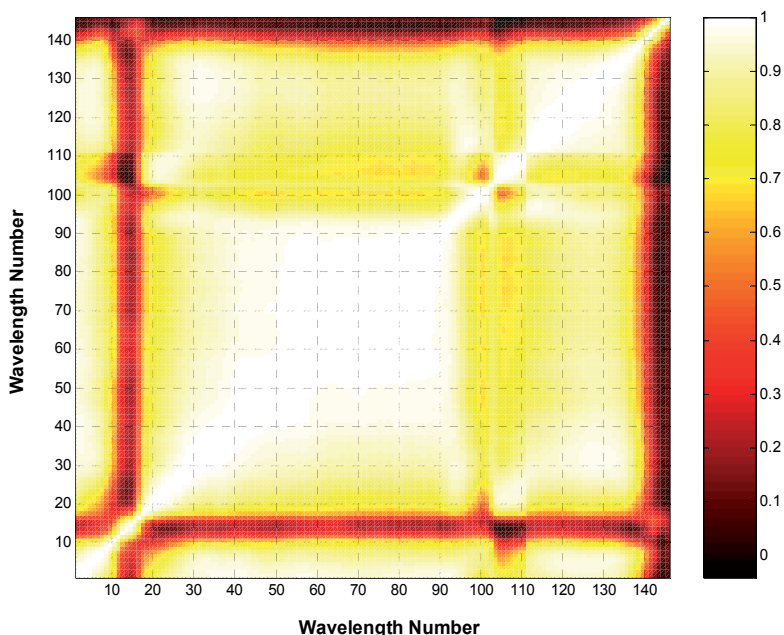


Fig. 3. A map of squared correlation factors of the IR emission spectral absorbance values to investigate the presence of potentially redundant correlated information in the variable space.

A correlation map of the rocket motor design features in figure 4 shows that there is very little correlation between the variables representing the rocket motor parameters.

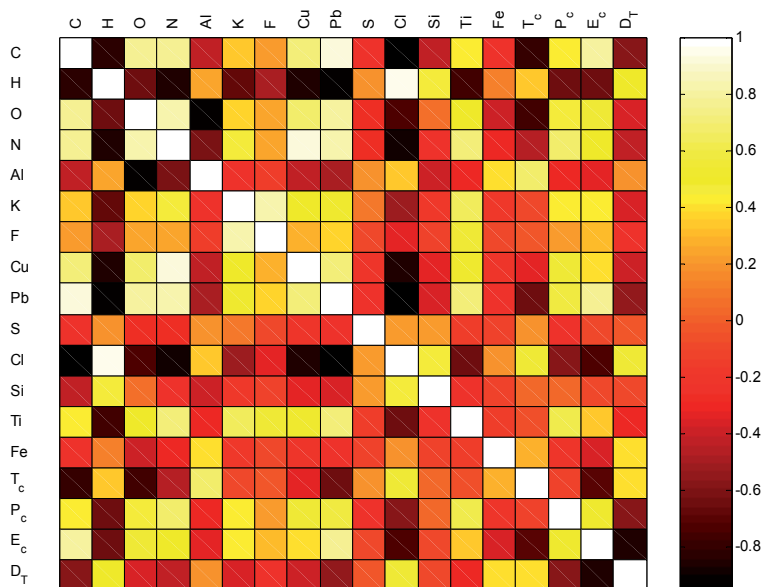


Fig. 4. A map of correlation factors of the rocket motor design parameters and chemistry to investigate the presence of potentially redundant correlated information in the underlying structure.

4. Construction of models

All data in the forward mappings (prediction of emission spectra) were mean-centred and scaled to unit variance during the training of the models.

4.1 Model validation

Although the complete data set consisted of 417 measured IR spectra, it covered only 18 different rockets, i.e. it contained 399 replicates. These replicates were not used in the validation of the models. Instead, leave-one-out cross-validation (Hjorth, 1994) was used to assess the quality of the models, i.e. the set of n ($= 18$) independent samples was split into $n-1$ training samples, while the n^{th} point was reserved for model validation. The training-validation split was repeated n times until each data point had been omitted once for validation. A validation set of n predictions on the 'unseen' data was therefore derived from all the available data and a predicted residual estimate sum of squares (PRESS) was calculated on the validation set.

$$PRESS_j = \sum_{i=1}^n e_{ij}^2 \quad (14)$$

The PRESS-values calculated for the output variables normally passed through a minimum with increased model complexity, as the model started to map random noise in the data and was used to guide the complexity of the constructed models. A residual score defined as SSP, which had the same form as equation (12), except that it was calculated on all n data points was used when training on the overall model.

The fraction of the variance (R^2 -value) of an output variable explained by the model is defined as the variance explained by the model over the total variance using the prediction error, SSE (SSEP_{*j*} or PRESS_{*j*}):

$$R^2 = \left(\frac{\sum_{i=1}^n (f(x_i, \theta) - \bar{y})^2}{\sum_{i=1}^n (y_i - \bar{y})^2} \right) = SSM/SST = 1 - SSE/SST \quad (15)$$

In the case of both the forward and reverse mappings there are a large number of output variables. In order to be able to compare the performances of the candidate models, the PRESS_{*j*} and SSEP_{*j*}-values were summed over all $j = 1, 2, \dots, l$ output variables to yield single PRESS- and SSEP-values for each model. The model yielding the lowest PRESS-score was expected to best predict validation data and therefore best generalize the input-output relationships.

During cross-validation of the linear PLS model, model fitting was therefore repeated 18 times (once for each of the 18 rockets) for each latent dimension as the overall complexity increased. In the case of the feed-forward multilayer perceptron neural network, 18 training sessions were required each time a node was added to the hidden layer.

4.2 Degrees of freedom

In the case of the forward mapping where the IR emission spectra were to be predicted by a given set of rocket motor features, there were 18 input and 146 output variables. Clearly, for a simple linear least squares model, the model requires 19 degrees of freedom (18 input variables plus the bias). However, the situation is more complicated when nonlinear models are fitted to the data.

Statistical theory requires that a regression model has to be built from an overdetermined system. For this reason it is required that there should be at least 3 to 5 lack-of-fit degrees of freedom (n_{lof}) available as a check on the suitability of the model (Brereton, 1992; Draper & Smith, 1981). Hence in this case, for the simplest linear regression model using a total number of n sample points of which there are n_r replicates, the maximum required number of model degrees of freedom, df , excluding bias, becomes: $df = n - n_r - n_{lof} - 1 = 420 - 402 - 3 - 1 = 14$.

For m input variables the pseudo-dimension for prediction by a multilayer perceptron neural network requires that at least $m+1$ independent samples are available per node for building a model (Sontag, 1998; Schmitt, 2001). It therefore appears that a larger set of data points is required to fit nonlinear models, such as neural networks that generally have a large number of parameters (weights) to fit.

Lawrence et al. (1997) have shown an example of a single-layer perceptron neural network, where the optimal model built on 200 independent data points consisted of 661 parameters. Justification for this result is given by the fact that the nonlinear optimization algorithm for a neural network does not reach a global optimum. Lawrence et al. (1997) further stated that the Vapnik-Chervonenkis (VC) dimension is somewhat conservative in estimating the lower bound for the required number of data points.

Partial least squares and principal components regression can be used to reduce the dimensionality of the input space, in this case attempting to reduce the degrees of freedom of the models to 14 or less without losing the most important information in the input data.

The evaluation of the degrees of freedom of a nonlinear model built on a data set so close to full rank can only be possible if the degrees of freedom associated with each model can be estimated reliably. Van der Voet (1999) suggested a method of defining pseudo-degrees of freedom (pdf) based on the performance of a model, as in (14)

$$pdf = n(1 - \sqrt{MSEP_{rs}/MSECV}) \quad (16)$$

Here $MSEP_{rs}$ is the mean square error of resubstitution for the entire data set per output variable and $MSECV$ is the mean square error of leave-one-out cross-validation. This method has been developed mainly to help with the estimation of the degrees of freedom of complex models and results are consistent with $df = m+1$, for m input variables, in the case of linear regression models.

5. Results

The regression models, cross-validation cycles and statistical analyses were programmed using the MATLAB® Release 12 software package. The neural network toolbox available in this package was used for the training of the multilayer perceptron neural networks.

5.1 Forward mapping

The results in table 2 show that the NNPLS model was the most parsimonious. The NNPLS model yielded the lowest PRESS-value, SSEP-value and average pseudo-degrees of freedom.

	Linear PLS	MLP	NNPLS
Complexity	11 LD	2 H	11 LD
PRESS	688.50	613.23	258.10
SSEP	76.28	52.74	45.41
X-Block $\% \eta^2$	99.69	NA	99.76
Y-Block $\% \eta^2$	90.52	93.43	94.34
Y-Block max $\% \eta^2$	94.98	98.31	98.98
Average R_{cv}^2	0.461	0.417	0.626
Average $R_{cv,max}^2$	0.541	0.548	0.746
Average R^2	0.876	0.803	0.825
Average R_{max}^2	0.957	0.907	0.954
Average pdf	12.42	12.91	12.33
Parameters	220	476	307

Table 2. A summary of performance scores of each candidate model for the forward mapping problem. The Y-block variances are calculated on the overall optimised models.

The Y-block variance (η^2) is the percentage of the output variance explained by the model over all output variables. This is analogous to the R^2 -values calculated for the individual output variables. The values indicated by maxima were those where the pure error component had been subtracted. Only the linear PLS model was able to perform better than the NNPLS model on the R^2 -scores calculated for the overall model. The reason for this is the fact that except for C5, the C-class rocket motor irradiance spectra were most accurately predicted using the linear PLS model.

Furthermore, the NNPLS model appeared not only to retain the linear latent projections, but also introduced nonlinearity in the inner models to compensate for the shortcomings of the linear PLS algorithm. This is shown in figure 5, where the PLS inner model scores are plotted to show the shape of the curve fitted by the neural network. The output scores after the first latent dimension seem to have near linear relationships with the input scores.

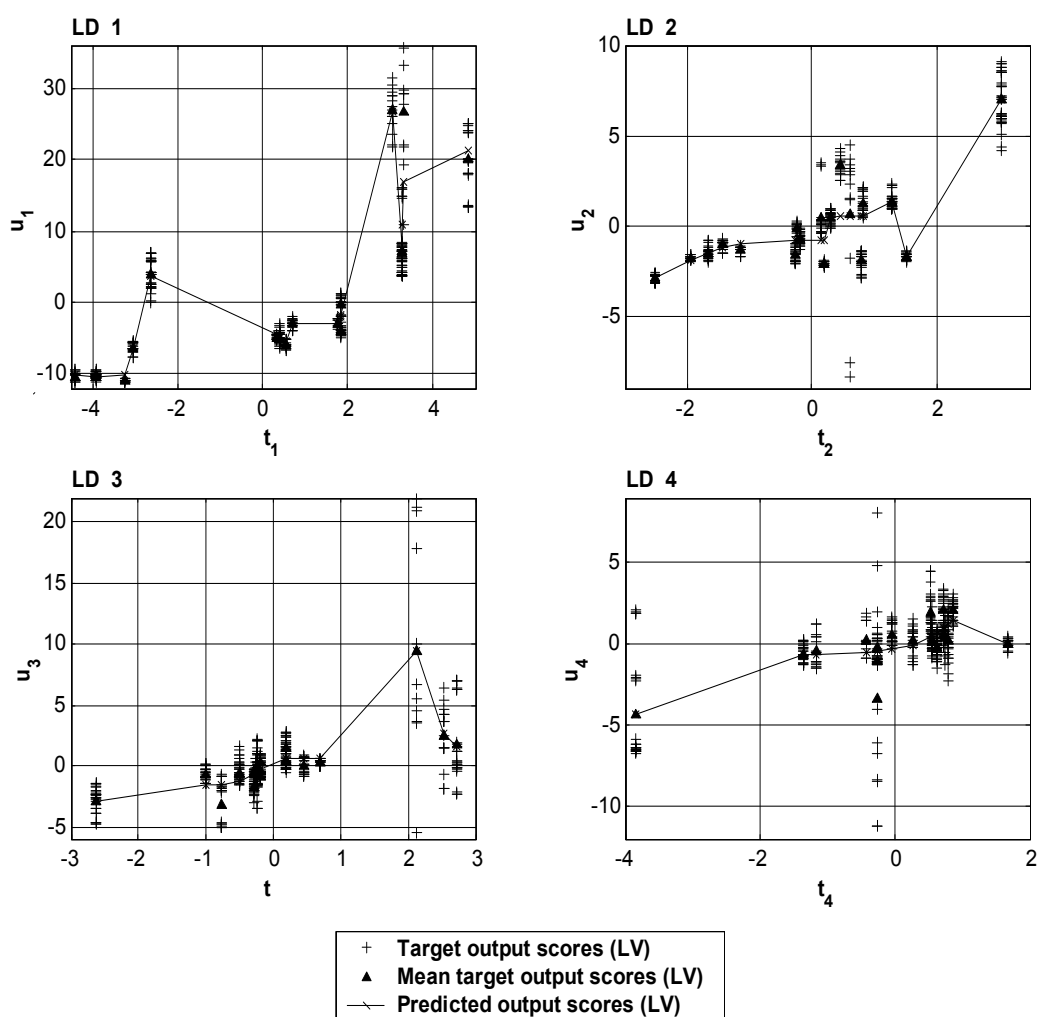


Fig. 5. The target and predicted PLS output scores vs. the input scores for the first 4 latent dimensions using the overall NNPLS model.

The advantage of linear PLS can be seen in figure 6. The regression coefficients can be collapsed into a single coefficient per input variable, as shown in equation 7. In this way the input variables with the most significant leverages could be determined for certain ranges of wavelengths in the spectrum. The improved predictions using nonlinear PLS could be attributed to the distinctions made between DB- and C-class rocket motor designs. This suggests that with the availability of more data, it may be useful to build separate linear PLS models for each of the DB- and C-class rocket motor types.

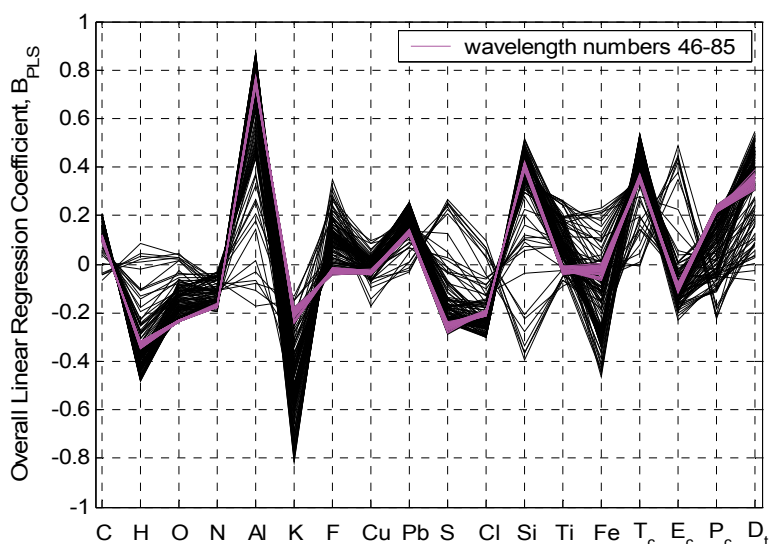


Fig. 6. A plot of the regression coefficients of the linear PLS model for all 146 output variables.

The NNPLS model appears to be the best, owing to its better generalization ability. The low average R_{CV}^2 -values and the relatively poor prediction on DB2 (figure 7) were not entirely unexpected, since the model had to extrapolate, as a result of the lack of data similar to DB2. The linear tendency in input-output relationships shows that some predictions on unseen data can be fairly accurate, such as that for C4 (figure 8). The overall model predictions for DB2 and C4 (trained on all data), together with their 95% confidence intervals are shown in figures 9 and 10.

As a note of interest, Qin & McAvoy (1992) have shown that NNPLS models can be collapsed to multilayer perceptron architectures. In this case it was therefore possible to represent the best NNPLS model in the form of a single layer neural network with 29 hidden nodes using tan-sigmoidal activation functions and an output layer of 146 nodes with purely linear functions.

Moreover, it is interesting to note that the optimal models (PLS, neural network and NNPLS) yielded similar average pseudo-degrees of freedom (MSECV/MSEP_{rs}-ratios). The large numbers of parameters (as shown in table 2) support the conclusions by Lawrence et al. (1997) that there can be more variables than independent data points in nonlinear modelling. The pseudo-degrees of freedom appear to be a more consistent way of measuring model complexity than simple comparison of the number of parameters of each model.

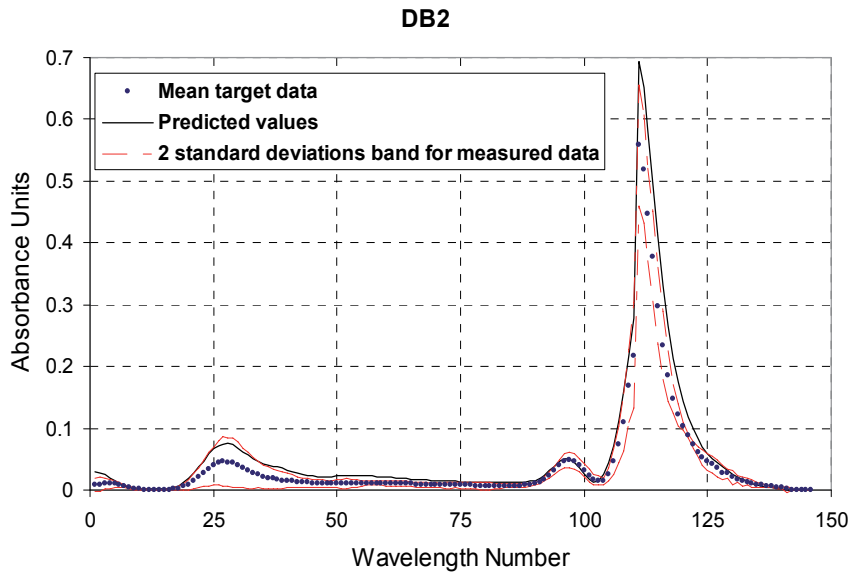


Fig. 7. Examples of plume irradiance predictions for 'unseen' DB-class rocket motors obtained during leave-one-out cross-validation of NNPLS with 11 latent dimensions.

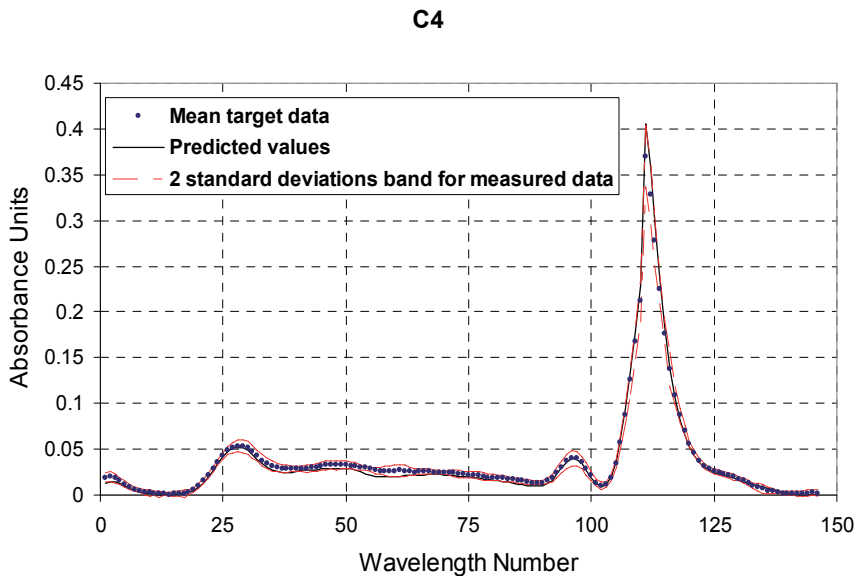


Fig. 8. Examples of plume irradiance predictions for 'unseen' C-class rocket motors obtained during leave-one-out cross-validation of NNPLS with 11 latent dimensions.

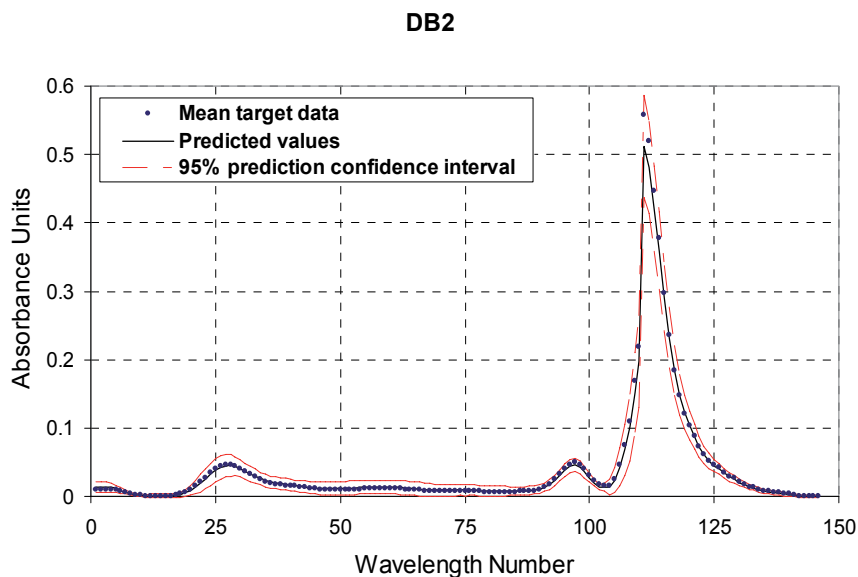


Fig. 9. Examples of plume irradiance predictions for DB-class rocket motors obtained for the overall NNPLS model using 11 latent dimensions.

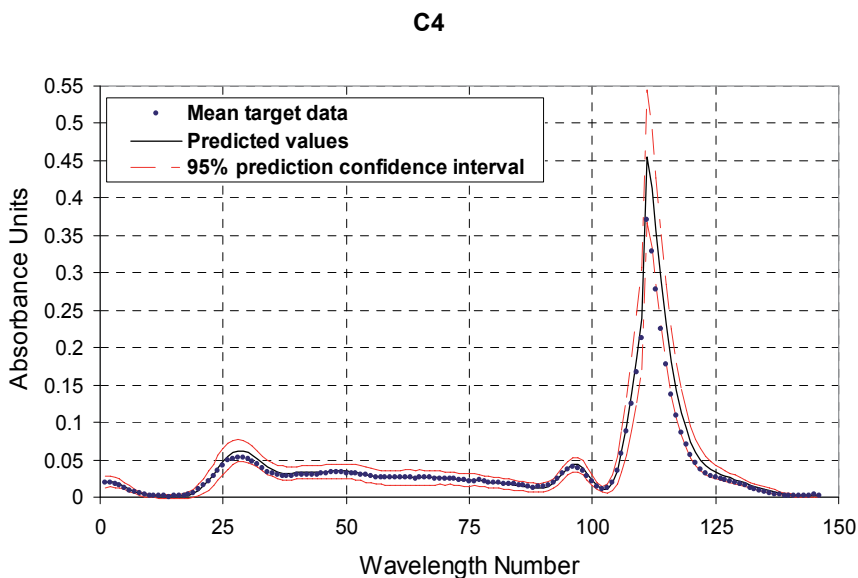


Fig. 10. Examples of plume irradiance predictions for C-class rocket motors obtained for the overall NNPLS model using 11 latent dimensions.

5.2 Reverse mapping

The optimal scores of the prediction abilities for each of the candidate models are shown in table 3. In the reverse problem it would be possible to find the optimal model complexity for each individual output variable. However, for the sake of simplicity, it is more sensible to compare the models by pooling the results for all output variables. Except for the R^2 -scores, the average performance scores over all output variables did not differ much from the results shown in table 3.

	Linear PLS	MLP	NNPLS
Complexity	2 LD	2 H	3 LD
PRESS	475.6	329.1	273.8
SSEP	307.08	245.61	171.18
X-Block $\% \eta^2$	95.3	NA	99.84
Y-Block $\% \eta^2$	26.9	41.49	59.22
Average R_{CV}^2	0.183	0.351	0.322
Average R^2	0.351	0.615	0.615
Average pdf	3.75	7.07	6.19
Parameters	296	297	462

Table 3. A summary of performance scores of each candidate model for the reverse mapping problem. The Y-block variances are calculated on the overall optimised models.

Even though the relatively low average R_{CV}^2 -value is a poor result, it does not necessarily reflect adversely on the true performance of the NNPLS model. This is owing to the data of output variables K, F, S, Si, Ti and Fe consisting of numerous zero entries and the inability of the model to handle these irregularities. The R_{CV}^2 -values for C, H, O, N, Al, Cu, Pb, Cl and E_C range between 0.6 and 0.8.

It was difficult to exactly determine the optimal model for linear PLS. In table 4 it is shown that a linear PLS model with 3 or 4 latent dimensions could have been chosen to increase the Y-block explained variance. This would have moved the average pdf-values closer to larger values of the other models. These results show that there is a requirement for nonlinear structures in the model building.

A few of the predictions for unseen data obtained from leave-one-out cross-validation are shown in figures 11 and 12. The square root of MSEC_V (RMSEC_V) is calculated for each individual output variable in order to obtain a measure of the standard deviation of the error of prediction. The same predictions made from the overall model built on all the available data are shown in figures 13 and 14.

LD	X-Block $\% \eta^2$	Y-Block $\% \eta^2$	Avg pdf	PRESS	SSEP
1	92.44	13.57	1.87	466.1	362.83
2	95.25	26.85	3.75	475.6	307.08
3	98.63	32.61	4.91	551.1	282.89
4	99.60	43.81	7.45	664.3	235.89
5	99.85	60.05	8.66	632.3	167.72
12	99.99	88.47	15.35	1971.9	48.42

Table 4. The sum-squared residuals obtained from building a linear PLS model for the reverse modelling problem.

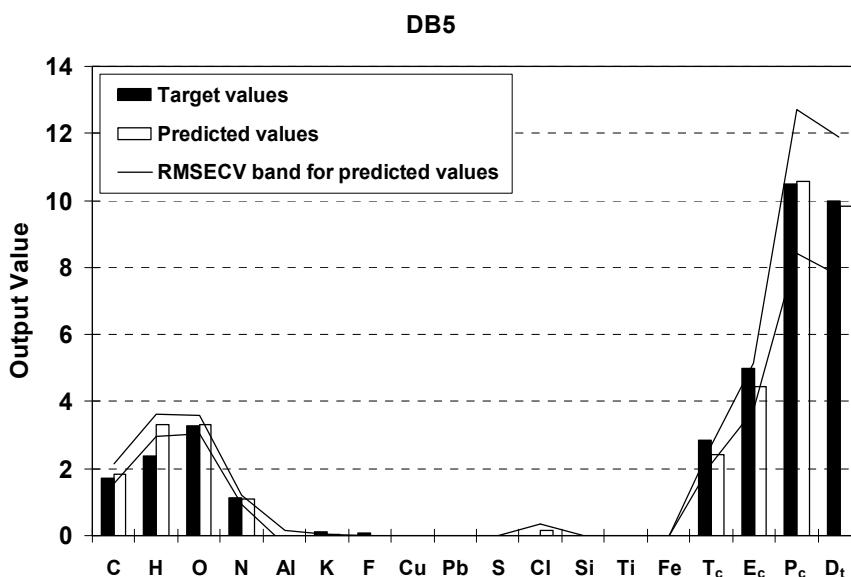


Fig. 11. Examples of rocket motor parameter predictions for 'unseen' rocket motors in the DB-class obtained during leave-one-out cross-validation of the NNPLS model (3 latent dimensions).

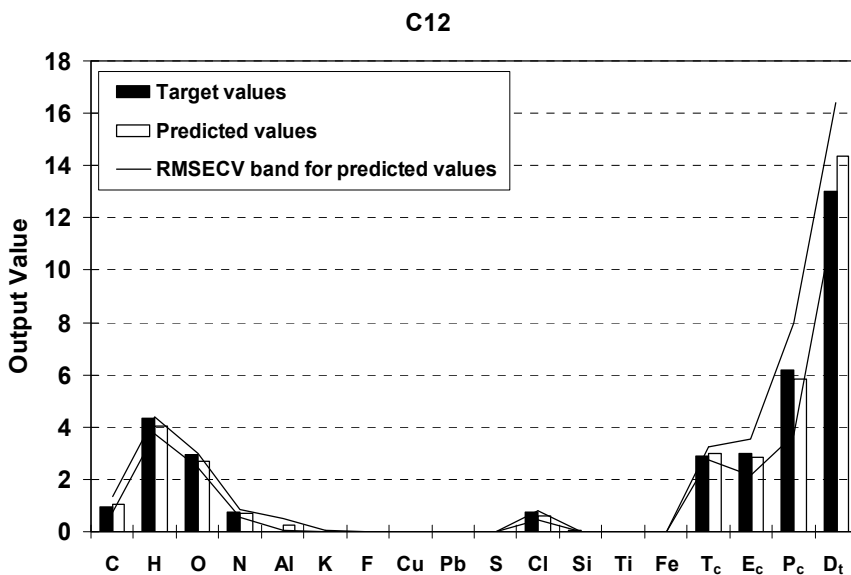


Fig. 12. Examples of rocket motor parameter predictions for 'unseen' rocket motors in the C-class obtained during leave-one-out cross-validation of the NNPLS model (3 latent dimensions).

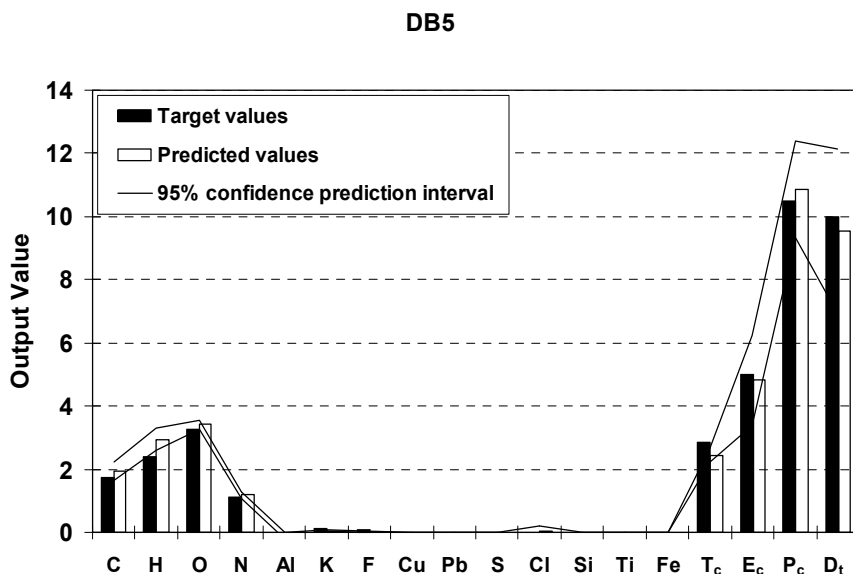


Fig. 13. Examples of rocket motor parameter predictions DB-class rockets obtained for the overall optimum NNPLS model trained with 3 latent dimensions on all data points.

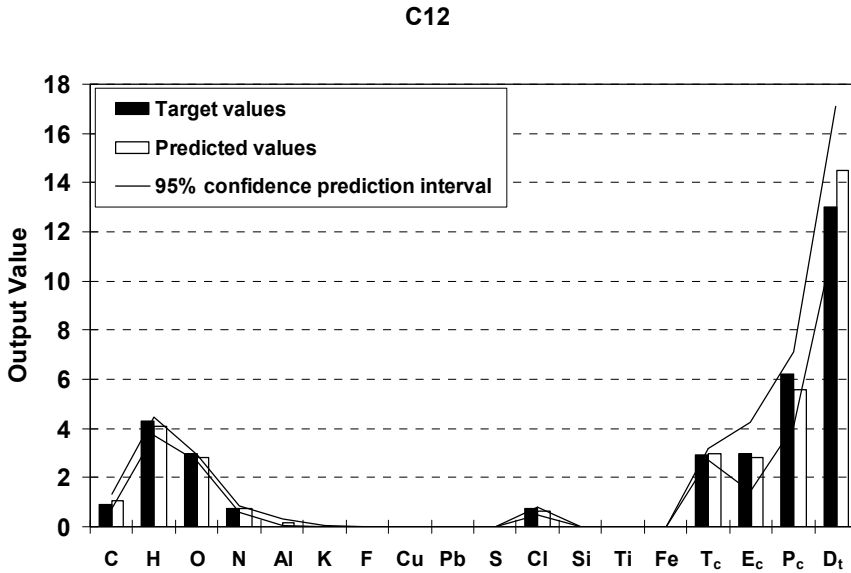


Fig. 14. Examples of rocket motor parameter predictions for C-class rockets obtained for the overall optimum NNPLS model trained with 3 latent dimensions on all data points.

Similarly to the forward problem the better predictions are obtained for the C-class rocket motors due to the more data available in this class of rocket designs. The physical design parameters, E_c , P_c and D_t show the largest confidence intervals. Even so, the predictions on unseen data are better than expected given the small amount of available data.

6. Appendix

The NIPALS algorithm for PLS according to Baffi et al, (1999a):

- i. Mean centre or standardise the inputs and outputs, X and Y . Initialise the algorithm by setting the output scores, u equal to a column of Y . For each latent dimension, $a = 1, 2, \dots, h$ follow steps ii to xiii below:
- ii. Calculate the input weights, w , by regressing X on u :

$$w^T = u^T X / u^T u \tag{A1}$$

- iii. Normalise w to unit length:

$$w = w / \|w\| \tag{A2}$$

- iv. Calculate the input scores:

$$t = Xw / w^T w \tag{A3}$$

- v. Calculate output loadings by regressing Y on t :

$$\mathbf{q}^T = \mathbf{t}^T \mathbf{Y} / \mathbf{t}^T \mathbf{t} \quad (\text{A4})$$

vi. Normalise \mathbf{q} to unit length:

$$\mathbf{q} = \mathbf{q} / \|\mathbf{q}\| \quad (\text{A5})$$

vii. Calculate new output scores \mathbf{u} :

$$\mathbf{u} = \mathbf{Y} \mathbf{q} / \mathbf{q}^T \mathbf{q} \quad (\text{A6})$$

viii. Check for convergence on \mathbf{w} : If not return to step ii

ix. Calculate the input loadings, \mathbf{p} by regressing \mathbf{X} on \mathbf{t} :

$$\mathbf{p}^T = \mathbf{t}^T \mathbf{X} / \mathbf{t}^T \mathbf{t} \quad (\text{A7})$$

x. Calculate the inner linear regression coefficient b :

$$b = \mathbf{t}^T \mathbf{u} / \mathbf{t}^T \mathbf{t} \quad (\text{A8})$$

xi. Calculate the input residual matrix:

$$\mathbf{F} = \mathbf{X} - \mathbf{t} \mathbf{p}^T \quad (\text{A9})$$

xii. Calculate the output residual matrix:

$$\mathbf{E} = \mathbf{Y} - \hat{\mathbf{u}} \mathbf{q}^T \quad (\text{A10})$$

xiii. If additional PLS latent dimensions are required replace \mathbf{X} and \mathbf{Y} with \mathbf{F} and \mathbf{E} respectively and return to step ii for calculation of latent dimension $a + 1$.

7. Conclusions

The building of data-driven models in this study was constrained by the sparsity of the available data, as there were only 18 independent samples (rocket motor designs) available. In addition the input and output data were highly multivariate with 18 rocket motor design parameters and 146 spectral wavelengths in the middle IR band. One advantage is that the IR spectral measurements were repeated a number of times (4 to 44 repeats per rocket motor).

The variables (wavelengths) associated with the IR emission spectra were highly correlated. Principal components analysis (PCA), linear and nonlinear PLS showed that at least 86% of the total variance could be explained by the two primary latent dimensions. The forward and reverse modelling results showed that dimensional reduction with a linear model (PLS) produced better models than a nonlinear model (multilayer perceptron neural network trained with the back propagation algorithm) without dimensional reduction.

The NNPLS algorithm with Levenberg-Marquardt training of the inner feed forward neural network models produced the best predictions of the forward models. The average R_{CV}^2 -value of 0.63 (0.75 for maximum R_{CV}^2) for all 146 output variables on unseen data was satisfactory when considering the lack of available data. The average R^2 -value of more than 0.80 obtained for the overall model trained on all data was also an encouraging result. The average pseudo-dimension for the NNPLS model with 11 latent dimensions was 12.33. This left about 5 lack-of-fit degrees of freedom as a check for the model complexity.

Despite these promising results, the best candidate models for both the forward and reverse problems cannot be regarded as adequate for practical applications. However, considering the lack of available data, the results can be regarded as acceptable to motivate funding for the collection of more data and rigorous testing. The fact that the input-output relationships appear to have almost linear relationships in some latent dimensions is promising, as this could lead to the development of robust models.

8. References

- Baffi, G., Martin, E.B. & Morris, A.J. (1999a). Non-linear projection to latent structures revisited: The quadratic PLS algorithm, *Computers and Chemical Engineering*, Vol. 23, pp. 395-411.
- Baffi, G., Martin, E.B. & Morris, A.J. (1999b). Non-linear projection to latent structures revisited (the neural network PLS algorithm), *Computers and Chemical Engineering*, Vol. 23, pp. 1293-1307.
- Bishop, C.M. (1995). *Neural Networks for Pattern Recognition*, Oxford University Press, Oxford, UK.
- Brereton, R.G. (1992). *Multivariate Pattern Recognition in Chemometrics*, Elsevier Science Publishers, Amsterdam.
- Draper, N.R. & Smith, H. (1981). *Applied Regression Analysis* (2nd ed), John Wiley and Sons, NY, USA.
- Haykin, S. (1999). *Neural Networks - A Comprehensive Foundation*, (2nd ed), Prentice-Hall, Upper Saddle River, NJ, USA.
- Lawrence, S., Giles, C.L. & Tsoi, A.C. (1997). Lessons in neural network training: Overfitting may be harder than expected, *Fourteenth National Conference on Artificial Intelligence*, AAAI Press, Menlo Park, CA, USA.
- Lorber, A., Wangen, L.E. & Kowalski, B.R. (1987). A theoretical foundation for the PLS algorithm. *Journal of Chemometrics*, Vol. 1, pp. 19-31.
- Marquardt, D.W. (1963). An algorithm for least-squares estimation of non-linear parameters, *Journal of the Society for Industrial and Applied Mathematics*, Vol. 11, pp. 431-441.
- Qin, S.J. & McAvoy, T.J. (1992). Nonlinear PLS Modeling using neural networks. *Computers and Chemical Engineering*, Vol. 16, pp. 379-391.
- Riedmiller, M. & Braun, H. (1993). A Direct adaptive method for faster backpropagation learning: The RPROP algorithm, *Proceedings of the IEEE International Conference on Neural Networks*, Vol. 1, pp. 586-591.
- Roodt, J.H.S. The Prediction of the Emission Spectra of Solid Rocket Propellants. (1998). *Ph.D. dissertation*, University of Stellenbosch, Stellenbosch, South Africa.
- Schmitt, M. (2001). *Neural Networks with local receptive fields and superlinear VC dimension*, Ruhr University of Bochum, Germany, Retrieved from www.ruhr-uni-bochum.de/lmi/mschmitt.
- Sontag, E.D. (1998). *VC Dimension of Neural Networks*, State University of New Jersey, NJ, USA, Retrieved from www.math.rutgers.edu/~sontag
- Urban Hjorth, J.S. (1994). *Computer Intensive Statistical Methods*, Chapman and Hall, London, UK.
- Van der Voet, H. (1999). Pseudo-degrees of freedom for complex predictive models: The example of partial least squares, *Journal of Chemometrics*, Vol. 13, pp. 195-208.

Wold, H. (1966). Estimation of principal components and related models by iterative least squares, In: *Multivariate Analysis*, Academic Press, NY, USA.

Wold, S., Kettaneh-Wold, N. & Skagerberg, B. (1998). Nonlinear PLS modeling, *Chemometrics and Intelligent Laboratory Systems*, Vol. 7, pp. 53-65.

Optical Technologies for Determination of Pesticide Residue

Yankun Peng, Yongyu Li and Jingjing Chen
China Agricultural University
China

1. Introduction

Pesticides are essential for agricultural and horticultural crops production. Pesticides are commonly classified as insecticide, fungicide, herbicide, rodenticide, etc. These pesticides act against insects, rodents, weeds which are harmful in agricultural or horticultural planting. Normally, farmers use the pesticides following the instruction written in the package. In most cases, the pesticides are mixed with water and sprayed over the plants. Basically, after spraying fruits or vegetables with pesticide, a period of 10 to 14 days is required to allow the chemical to degrade. However, the full degradation of pesticide is not always achieved. In recent years, some farmers ignored to use the pesticide correctly and rationally. In order to chase a better insecticidal effect and the economic interests, the phenomenon of using pesticide excessively, or selling the fruits or vegetables just after spraying the pesticide in few days are not difficult to see. Moreover, the pesticides overdosing also have the potential to contaminate the soil, air, and river.

Currently, several different technologies such as gas chromatography (GC), high-performance liquid chromatography (HPLC), thin-layer chromatography, supercritical fluid chromatography, chromatography-mass spectrometry, capillary electrophoresis, enzyme inhibition method, immunoassay method, and bio-sensor method are used to determine the concentration of pesticide residue. The accuracy of these technologies such as GC and HPLC is best (Gambacorta et al., 2005). However, these analysis methods have limitations of time and labor for controlling individual products. Normally, at least hours are needed to measure the pesticide concentration in a single sample because of the complication in the testing process. These instrument analysis methods as such, can be used only in laboratory for accurate analysis and statutory inspection (Luypaert et al., 2003). Biological and chemical analysis methods were developed in recent years, but there are also some flaws, such as the pre-treatments are needed and the demanding of experimental conditions.

Compare with the growing public requirement of food security, the traditional pesticide detection technologies are not competent because of the shortcomings such as longer detection cycle, complex testing process, testing process, lagged nature of nature of detection results, etc. Therefore, development of fast, reliable detection method or equipment of pesticides residue is imperative. And it is vital to control the pesticide concentration on agricultural products for maintaining public health conditions and protecting the entire environment.

Development of safe, fast, reliable and low-cost analytical methods for the determination of pesticide residue that avoids the use of organic solvents, and reduces the contact of operator with the toxic substances is growing interest at present. In recent years, spectroscopy based procedures is regarded as a potential method which could solve the above problems. Spectroscopy analysis methods have been widely used in chemical industry, agriculture, medicine and other areas (Peng et al., 2008, 2009; ElMasry et al., 2007).

A NIR spectroscopic method and an optical imaging technology for prediction of organophosphorus pesticide are introduced as follows.

2. NIR spectroscopy for pesticide determination

Among the optical analysis methods, near-infrared (NIR) spectroscopy is the most popular method because of its non-destructive nature, the low operating cost and the fast response times (Armenta et al., 2007), and it also has been successfully applied to quality control in food (Pi et al., 2009; Leroy et al., 2003; Subbiah et al., 2008), petrochemical, pharmaceutical, clinical and biomedical and environmental sectors (Ripoll et al., 2008). Near-infrared (0.7-2.5 μm ; 12900-4000 cm^{-1}) spectroscopy is further classified into NIR reflectance spectroscopy and NIR transmission spectroscopy. NIR can be non-dispersive (filter-based instrumentation), dispersive and use Fourier transform-based instrumentation. Table 1 lists some NIR spectroscopic applications suitable for pesticides determination. All these researches have shown the possibility and reasonability for determination of pesticide concentration using NIR spectroscopy.

Instrumental method	Determination attribute	Reference
Mid- and near-infrared	Metribuzin in agrochemicals	Khanmohammadi et al., 2008
NIR	Pesticide determination in commercially formulations	Armenta et al., 2007
Fourier transform infrared spectroscopy	Propamocarb in emulsifiable pesticide concentrate formulations	Quintás et al., 2008
NIR	Pesticide phoxim residues	Shen et al., 2009
IR spectroscopy	Classification of Pesticide Residues in the Agricultural Products	Makio et al., 2007
Mid- and near-infrared	Describing diuron sorption in soils	Forouzanhoar et al., 2009
NIR/ Dry extracts	Determination of acephate, dichlofluanid and tetrachloro-isophthalonitrile	Sarawong et al., 2007
NIR	Determination of soil content in chlordecone	Brunet et al., 2009
NIR-Raman	Quantitative analysis of methyl-parathion pesticide	Ysacc Sato-Berrú et al., 2004
NIR	Detecting the chlorpyrifos content	Liu et al., 2009
NIR	Determination of active ingredient of agrochemicals	Xiong et al., 2010

Table 1. Near-infrared spectroscopy to determinate pesticides concentration.

The following example presents the methodology for determination of chlorpyrifos based on NIR.

Samples

Pesticide solution: A commercial pesticide, containing 40% chlorpyrifos (Noposion, China) was used. Chlorpyrifos is an organophosphorus pesticide, normally used in the paddy, wheat, cotton, fruit trees, and vegetables. Distilled water was prepared in order to provide the solutions with different concentrations. A total of 24 concentration levels, from 1 mg/kg to 400 mg/kg of active ingredient were diluted based on the amount of chlorpyrifos. After preparation, the solutions were kept in conical flasks and preserved in a cool place in order to prevent chemical degradation and contamination.

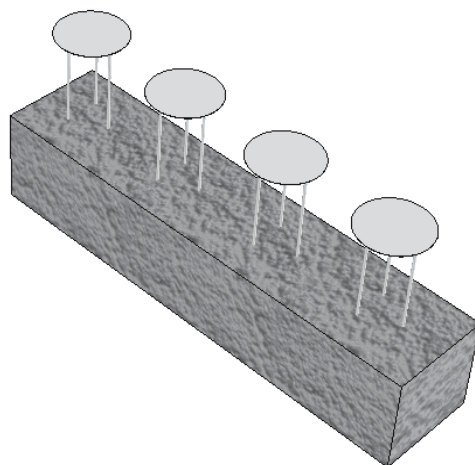


Fig. 1. Platform for filter paper.

Filter paper samples: It is well known that the control level of pesticide residue does not lie at the percent level but at the 10^{-6} level, even 10^{-9} level. It is hard to obtain a satisfactory result by the use of NIR spectroscopy to determine the concentration of pesticide solution. The reason being that water has several strong absorption peaks in near-infrared bands; as a result it is difficult to get the information of pesticide compared to water in the solution. In order to obtain the absorption of trace chemicals, a special method to concentrate the amount of chemicals on samples was developed. Filter paper was used as substrate, water was removed from wet substrate by drying, and then the NIR measurement was performed on the dried substrate.

Normal filter papers (Shuangquan, China), 9 cm diameter were selected. Initially, every piece of 9 cm filter-papers were sheared into four pieces each 30 mm diameter by using a special mold. Then the filter paper were kept into a special platform, which was made of polystyrene foam and pins (Figure 1). Each platform were almost 20 cm long and 5 cm wide, and four pieces of filter paper could be placed on each platform. After putting the filter papers onto the platform, 200 μ L of pesticide solution was gently pipetted onto each filter paper (the amount of 200 μ L is the volume absorbable by filter paper without any overflow). Several pieces of filter paper samples were prepared for each concentration level. A total of 99 filter paper samples were prepared.

Drying filter paper samples: Platform with filter paper samples were carefully moved into the vacuum drying oven, at room temperature for 1 hour. After drying, samples were stored into vacuum packing bags immediately and marked with different concentrations.

Spectrum acquisition

An Antaris FT-NIR spectrometer (Thermo Nicolet, Waltham, Massachusetts, USA), equipped with an InGaAs detector was used. The filter paper sample was placed in a specially modified sample cell. The spectra were acquired in the range of 4000 cm^{-1} to 10000 cm^{-1} at 8 cm^{-1} interval. For each sample, three points were chosen randomly for the NIR measurement, and 32 scans were co-added for each point. The sample was then removed, and the spectra were collected again in the same manner. Three spectra were obtained for each sample at the same state, and averaged spectra were calculated for further evaluation. To prevent the interference of water vapor in the air, the spectra of samples were acquired immediately after taking out from the vacuum packing bags.

Pre-processing method and data analysis

The Matlab 7.0 software (MathWorks, USA) was used for all calculations. A total of 99 filter paper samples were divided into two groups, 75 samples were selected as calibration set; the left 24 samples in each concentration level were put into validation sample set. Partial least squares regression (PLSR) was used to develop a prediction model. Multiplicative scatter correction (MSC) and standard normal variate (SNV) were used in PLSR for pre-processing of spectral data. MSC efficiently eliminates the base line drift of the spectra which in turn reflects the more detailed characteristics of the spectra, and also removes additive and/or multiplicative signal effects (Brunet et al., 2009). The main advantage of SNV is to avoid attributes in greater numeric ranges dominate those in smaller numeric ranges. The PLSR model basing on all variables of the spectra is complex, thus a special algorithm uninformative variable elimination (UVE) was used as a method for variables selection of NIR spectral data in order to develop the effective PLSR prediction model for determination of pesticide the concentrations in each sample.

UVE is an algorithm based on the regression coefficient b of PLSR (Chen et al., 2005; Wu et al., 2009). In the PLSR-NIR prediction model, there is a relationship between X (spectral matrix) and Y (concentration matrix):

$$Y = Xb + e \quad (1)$$

where b is the regression coefficient vector, e is the error vector. The following five steps were taken to get a new spectral matrix with fewer wave bands:

1. PLSR was used to develop a prediction model in the entire wave range from 4000 cm^{-1} to 10000 cm^{-1} . Cross validation was applied to the calibration set. Each time, one sample was taken out from the calibration set. A calibration model was established for the remaining samples and the model was then used to predict the sample left out. Thereafter, the sample was placed back into the calibration set and a second sample was taken out. The procedure was repeated until all samples have been left out once. The root mean square error of cross validation (RMSE_{cv}) was calculated for each of all wavelength combinations. The best principal component (PC) number with the highest R_{cv} (correlation coefficient of cross validation) and lowest RMSE_{cv} value was selected.

2. A random matrix was developed which has the same dimension size as spectral matrix X . Then X and R_a were joined together to be a new matrix XR_a .
3. Partial least squares regression (PLSR) was used again. Leave one out cross validation was carried between the new matrix XR_a and concentration matrix Y . After each step of leave one out cross validation, a regression coefficient b was obtained.
4. Analyzing the stability of C value which is the ratio of the mean value of vector b and the standard deviation of vector b :

$$C_i = \frac{\text{mean}(b_i)}{\text{std}(b_i)} \quad (2)$$

5. Absolute value of C_i was used to discriminate if each spectra variable is effective or not. All effective variables were selected to create a new independent variable matrix, and then this new matrix and Y were used to establish a new PLSR prediction model.

NIR spectra

Original NIR spectra of total 99 filter samples are shown in figure 2, and the spectra of samples after pre-processing with MSC are shown in figure 3. It is obviously seen that the base line drift of the spectra is reduced in the figure 3 compared to figure 2 by the application of MSC.

Results of PLSR in full bands

For the total sets, two spectrum pre-processing methods MSC and SNV were used. Figure 4 illustrates the results of the cross validation when MSC and SNV were used as the spectrum pre-processing method.

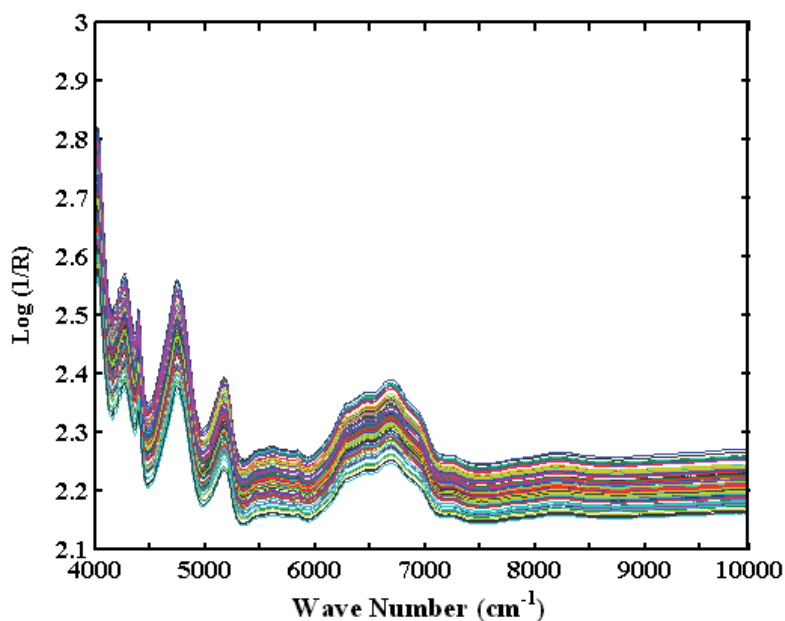


Fig. 2. NIR transmittance spectra of filter-paper samples with different chlorpyrifos content.

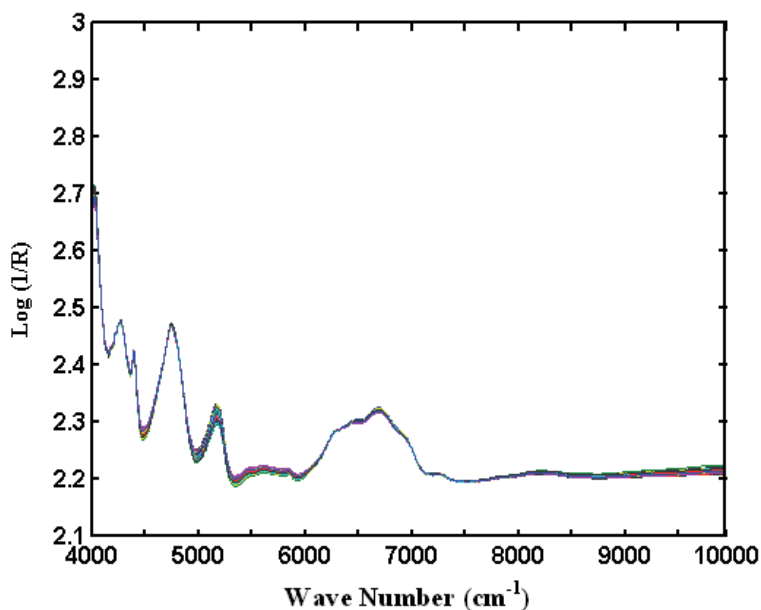


Fig. 3. NIR transmittance spectra of filter-paper samples after MSC.

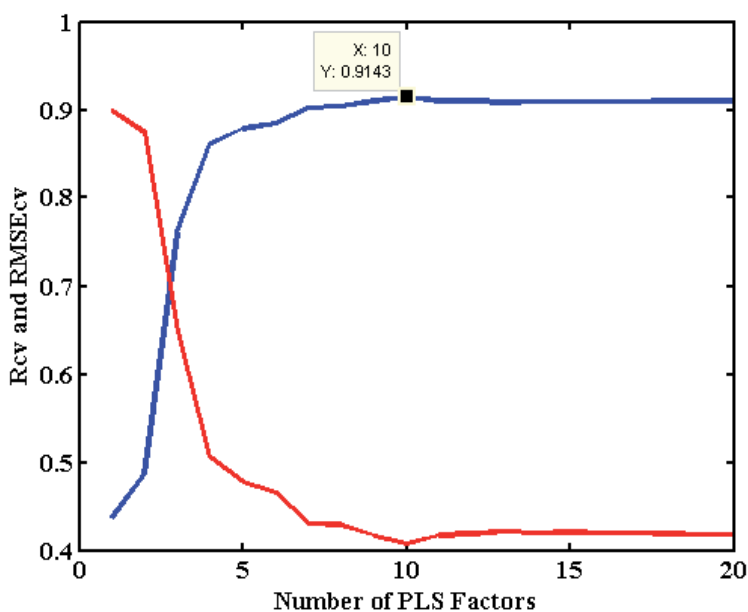


Fig. 4. Optimal PC number of prediction model for filter-paper samples.

The total sample sets were separated into calibration set and validation set. Cross validation was first used in calibration sample set to find the optimal principle component number. From figure 4 we can see the best principle component number to be 10 with corresponding highest Rcv of 0.91 and lowest RMSEcv of 0.41. Model accuracy was then evaluated on the validation set using the root mean square error of prediction (RMSEP), correlation

coefficient (R) between predicted and actual data. The results obtained are shown in table 2 corresponding to $R = 0.95$ and $RMSEP = 0.32$ mg/kg.

Results of UVE-PLSR

From table 2 we can see that PLSR method do get satisfied prediction results. However, PLSR method using full bands of the spectra for developing calibration model are time-consuming while running the computer program. Some variables in the full bands of samples' spectra are effective while some are not. As such determining effective spectra from the full band spectra is very essential. A special algorithm, namely uninformative variable elimination (UVE) was used in this research to find out the effective variables. The variables with useless information were eliminated.

Pre-processing method	LV	Rcv	RMSEcv (mg/kg)	R	RMSEP (mg/kg)
MSC + SNV	10	0.91	0.41	0.95	0.32

LV: the optimal principal component (PC) number used in cross-validation

Rcv: correlation coefficient of cross validation

RMSEcv: root mean square error of cross validation

R: correlation coefficients in validation set

RMSEP: root mean square error of prediction

Table 2. Calibration and validation results for chlorpyrifos concentration by using PLSR method.

MSC and SNV were used as the pre-processing method. According the result in table1, the optimal principal component number was chosen as 10. Then UVE algorithm was used to select the effective variables. The results are shown in figure 5.

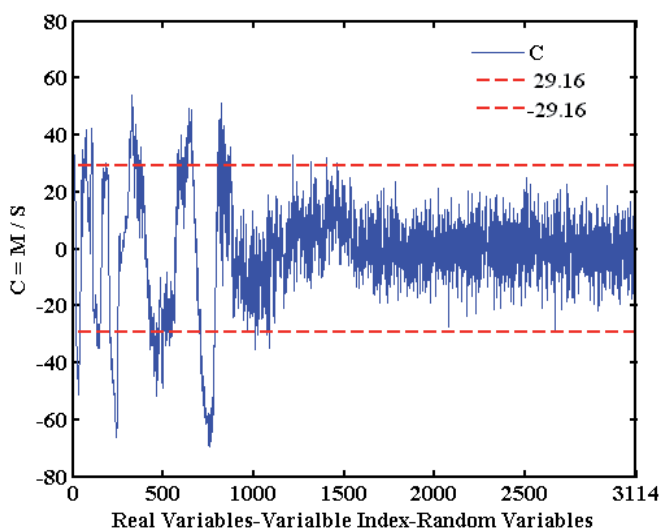


Fig. 5. Variables selected by UVE.

In figure 5, the dotted line indicates the threshold of variables selection. In the range of [1, 1557], the variables corresponding the C value within the threshold range are not effective,

and 368 variables left after ineffective variables were eliminated. A new PLSR prediction model was developed by using these 368 variables. The results showed that the correlation coefficient (Rcv) in cross validation is 0.91, the root mean square error of cross validation (RMSEcv) is 0.42 mg/kg, and the correlation coefficient (R) in validation set is 0.94, the root mean square error of prediction (RMSEP) is 0.36 mg/kg. Compared with the results of the PLSR used in full bands, the UVE-PLSR could get similar results but using fewer wave bands. In the UVE algorithm, the random matrix which was added into the original matrix was different each time, so the results would be different in every prediction model. In order to prove the stability of UVE algorithm, another 4 times of UVE-PLSR was used. The results of a total of five times UVE-PLSR are shown in table 3.

Model	Number of Variables	LV	Rcv	RMSEcv (mg/kg)	R	RMSEP (mg/kg)	Variables Thresholds
UVE-PLSR-1	368	7	0.91	0.42	0.94	0.36	±29.16
UVE-PLSR-2	281	7	0.90	0.47	0.94	0.37	±31.31
UVE-PLSR-3	395	7	0.90	0.43	0.94	0.36	±27.61
UVE-PLSR-4	379	7	0.90	0.43	0.94	0.37	±28.23
UVE-PLSR-5	330	7	0.90	0.43	0.94	0.36	±30.27

LV: the optimal principal component (PC) number used in cross-validation

Rcv: correlation coefficient of cross validation

RMSEcv: root mean square error of cross validation

R: correlation coefficients in validation set

RMSEP: root mean square error of prediction

Table 3. Prediction results of UVE-PLSR methods.

Figure 6 shows the variables selection results by the use of another 4 times UVE-PLSR based on different random matrix. As the results shown in table 3, the differences between each UVE-PLSR are small. The number of variables ranged from 281 to 395, and the prediction results were almost identical to each other. Considering the different random matrix, the Rcv (correlation coefficient of cross validation) range from 0.90 to 0.91, RMSEcv (cross validation) range from 0.42 to 0.47 mg/kg, R (validation set) is 0.94, RMSEP range from 0.36 to 0.37mg/kg which MSC and SNV were used as the pre-processing method. It could be concluded that the differences of random matrix have very weak affection in the process of developing a prediction model, and the numbers of variables used in UVE-PLSR could be declined by more than 70%. These results indicated that the prediction capability of UVE-PLSR is similar as the PLSR used in full bands. So, it can be concluded that NIR determination of pesticide is a low cost, an environment friendly and a potential method compared to the traditional methods, and the UVE-PLSR algorithm is an efficient method to select the effective variables of spectra and develop a prediction model of pesticide concentration with fewer wave bands.

3. Optical imaging technology for pesticide determination

In recent years, optical imaging technology has become popular. Hyperspectral imaging as one of optical imaging technology has been used in agriculture, biomedicine, food industry

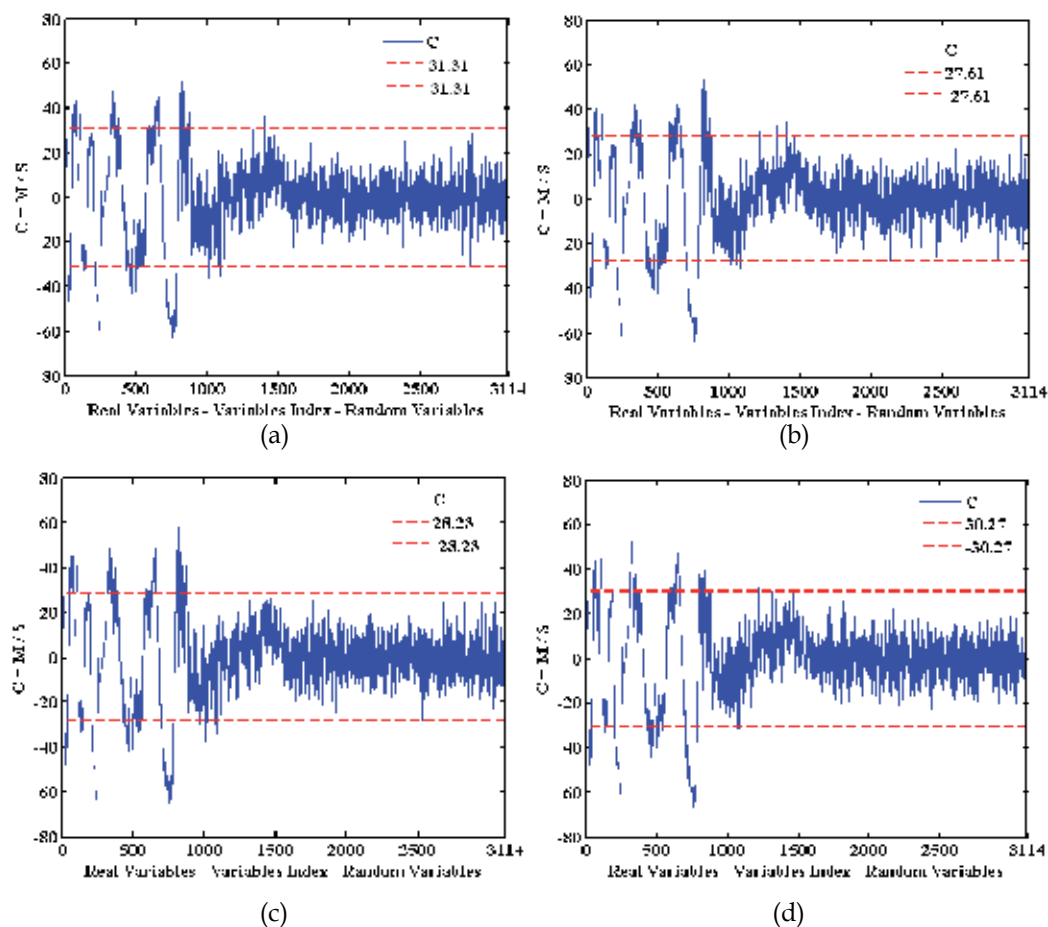


Fig. 6. Variables selected by UVE with different random matrix.

etc. Hyperspectral imaging is a powerful tool for acquiring both spectral and spatial information from an object at contiguous wavelengths over a wide spectral range. According to determination of pesticide, hyperspectral imaging combined with fluorescence stimulate technology could acquire a satisfactory result.

The following example presents the methodology to determinate chlorpyrifos based on hyperspectral fluorescence imaging technology.

Samples

Pesticide solution: A commercial pesticide, containing 40% chlorpyrifos (Noposion, China) was used. Methanol was prepared in order to provide the solutions with different concentrations. Five concentration levels, 0.5, 1, 2, 8 and 16 mg/kg of active ingredient were diluted based on the amount of chlorpyrifos.

Vegetable samples: Pollution-free rapes bought from local market were used. After washing up all the surface of rape samples by the use of distilled water, pesticide solutions were sprayed evenly on dry rape samples' surface.

Data acquisition

A hyperspectral fluorescence imaging system (Figure 7) was used which mainly consisted of a high-performance back-illuminated charge coupled device (CCD) camera (Sencicam QE Germany), an imaging spectrograph (ImSpector V10E, Spectral Imaging Ltd., Finland), and a light unit with fluorescence lamps as the light source (Foshan, China). The camera, with spatial resolution of 1376×1040 , was fitted with a 25mm lens (Computar, Japanese), the spectrograph had an effective spectral region from 400 to 1100nm with a 2.8 nm spectral resolution. The light source used in this study was a pair of fluorescence lamps which had the spectral region from 340 to 600nm. The whole system was shielded with a close chamber avoiding the interferences of external lights from outside. Hyperspectral fluorescence images were acquired and ENVI 4.3 software was used for data analysis.

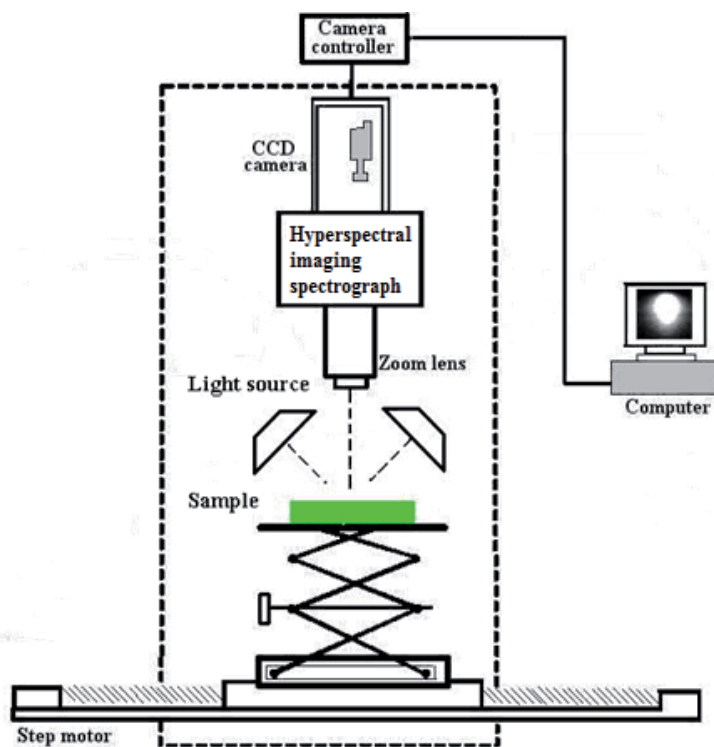


Fig. 7. Hyperspectral fluorescence imaging system.

Data analysis

Figure 8 shows the hyperspectral fluorescence image of 8mg/kg sample which was composed by the use of ENVI 4.3 software. In this picture, the white regions are the fluorescence of chlorpyrifos solutions. Threshold segmentation method was used to acquire the Region of Interest (Figure 9, red regions). Then average spectral curves of different samples in Region of Interest were calculated in whole wave bands (Figure 10). According to figure 10, chlorpyrifos has strong fluorescence characteristic when methanol is used as solvent. The emission spectrum of chlorpyrifos indicates that it has the peak emission at the wavelength of 437 nm, and chlorpyrifos samples with different concentration have different fluorescence

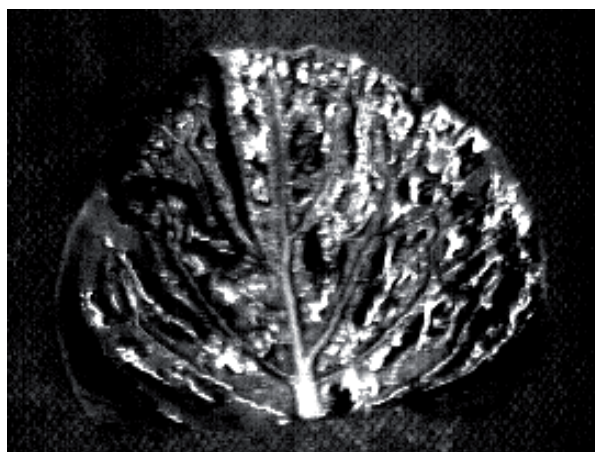


Fig. 8. Hyperspectral fluorescence image of 8mg/kg sample.



Fig. 9. ROI image of the sample with the chlorpyrifos concentration of 8mg/kg sample.

emission spectral intensity at the peak. It can also be seen in figure 10 that the fluorescence emission peak value reduces when the concentration of chlorpyrifos decreases. The peak emission at the wavelength 524nm might be the effect of other organic elements present in the commercial composite pesticide used in this research. The results can be used as theoretical basis for developing rapid detection instrument for vegetable pesticide residue.

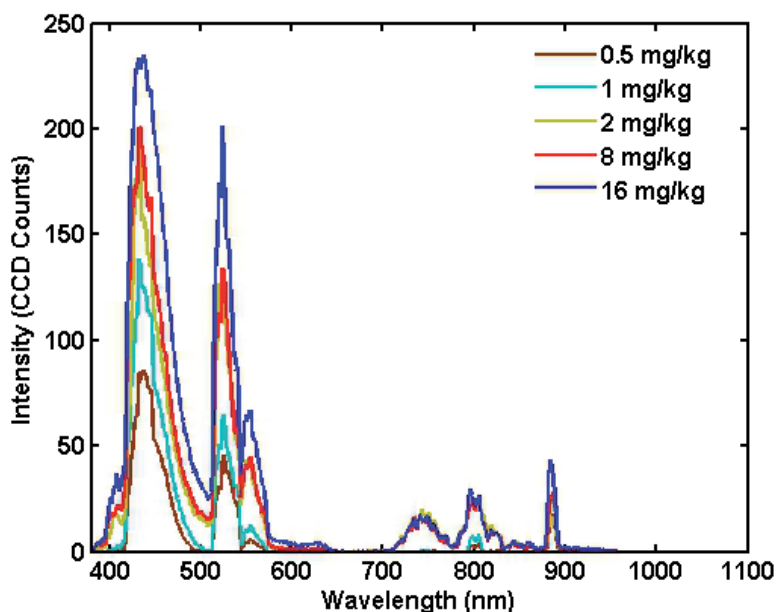


Fig. 10. Emission spectrum of samples with different chlorpyrifos concentration.

4. Conclusion

Pesticide concentration can be readily measured with NIR spectroscopy and optical imaging technology. However the accuracy and precision could be improved. There is a need to develop rapid optical techniques for pesticide determination which could be used in the future for agro-food safety assurance. The optical technique could be one of the most useful tools along with the advancement of spectral instrument for determination of pesticide residue.

5. References

- Armenta, S., S. Garrigues, and M. de la Guardia. 2007. Partial least squares-near infrared determination of pesticides in commercial formulations. *Journal of Vibrational Spectroscopy*. 44: 273-278.
- Brunet, D., T. Woignier, M. Lesueur-Jannoyer, R. Achard, L. Rangon, and B.G. Barthes. 2009. Determination of soil content in chlordecone (organochlorine pesticide) using near infrared reflectance spectroscopy (NIRS). *Environmental Pollution*. 157: 3120-3125.
- Chen, B., and D. Chen. 2005. The application of uninformative variables elimination in near-infrared spectroscopy. *Spectronic Instruments and Analysis*. 04: 26-30.
- ElMasry, G., N. Wang, A. ElSayed, and M. Ngadi. 2007. Hyperspectral imaging for nondestructive determination of some quality attributes for strawberry. *Journal of Food Engineering*. 81: 98-107.
- Gambacorta, G., M. Faccia, C. Lamacchia, A. Di Luccia, and E. La Notte. 2005. Pesticide residues in tomato grown in open field. *Food control*. 16: 629-632.

- Khanmohammadi M., S. Arment, S. Garrigues and M. de la Guardia. 2008. Mid-and near-infrared determination of metribuzin in agrochemicals. *Journal of Vibrational Spectroscopy*. 46: 82-88.
- Leroy, B., S. Lambotte, O. Dotreppr, H. Lecocq, L. Istasse, and A. Clinquart. 2003. Prediction of technological and organoleptic properties of beef longissimus thoracis from near-infrared reflection and transmission spectra. *Meat Science*. 66: 45-54.
- Luybaert, J., M.H. Zhang, and D.L. Massart. 2003. Feasibility study for the use of near infrared spectroscopy in the qualitative and quantitative analysis of green tea, *Camellia sinensis* (L.). *Analytica Chimica Acta*. 478: 303-312.
- Peng, Y., and R. Lu. 2008. Analysis of spatially resolved hyperspectral scattering images for assessing apple fruit firmness and soluble solids content. *Postharvest Biology and Technology*. 48: 52-62.
- Peng, Y., and J. H. Wu. 2008. Hyperspectral scattering profiles for prediction of beef tenderness. ASABE Paper No. 080004. Rhode Island convention center, Rhode, USA.
- Peng, Y., J. Zhang, and J.H. Wu. 2009. Hyperspectral scattering profiles for prediction of the microbial spoilage of beef. SPIE Paper No. 7315-25, Orlando, Florida, USA.
- Ripoll, G., P. Alberti, B. Panea, J.L. Olleta, and C. Sanudo. 2008. Near-infrared reflectance spectroscopy for predicting chemical, instrumental and sensory quality of beef. *Meat Science*. 80: 697-702.
- Saranwong, S., and S. Kawano. 2005. Rapid determination of fungicide contaminated on tomato surface. *Journal of Near infrared spectrosc.* 13 : 169-175.
- Subbiah, J., C.R. Calkins, A. Samal, and G.E. Meyer. 2008. Visible/near-infrared hyperspectral imaging for beef tenderness prediction. *Journal of Computers and Electronics in Agriculture*. 64: 225-233.
- Wu, D., H.X. Wu, J.B. Cao, Z.H. Huang, and Y. He. 2009. Classifying the species of *exopalaemo* by using visible and near infrared spectra with uninformative variable elimination and successive projections algorithm. *Journal of Infrared and Millimeter Waves*. 28(6): 423-427.
- Li Shuqian, Lu Lei, Chen Fusheng, et al. Rapid detection techniques of organophosphorus pesticide residue in fruits and vegetables [J]. *Hubei Agricultural Science*, 2004, (4): 58-59. (in Chinese with English abstract)
- Zhao Siqi, Yan Su. The detection technologies of pesticide residue [J]. *Anhui Agricultural Sciences*, 2008, 36(10): 4176-4178. (in Chinese with English abstract)
- Zhu Chunyan, Li Weikai, Li Yanmei. Detection of organophosphorus pesticide residues on vegetables by using FTIR/ATR method [J]. *Science and Technology Innovation Herald*, 2008, (2): 108-108. (in Chinese with English abstract)
- Lai Suichun, Wang Fuhua, Deng Yicai. Research situation and development of pesticide residues analysis technology [J]. *Guangdong Agricultural Science*, 2006, (1): 76-77. (in Chinese with English abstract)
- ReneeD. Jiji, GaryA. Cooper, KarlS. Booksh. Excitation- emission matrix fluorescence based determination of carbamate pesticides and polycyclic aromatic hydrocarbons [J]. *Analytica Chimica Acta* · 1999, (397): 61-72.
- Shengye Jin, Zhaochao Xu, Jiping Chen, Xinmiao Liang, Yongning Wu, Xuhong Qian. Determination of organophosphate and carbonate pesticides based on enzyme

- inhibition using a pH-sensitive fluorescence probe [J]. *Analytica Chimica Acta*, 2004, (523): 117-123.
- Salan Hassoon, Israel Schechter. A sensitive fluorescence probe for DDT-type pesticides [J]. *Analytica Chimica Acta*, 1998, (368): 77-82.
- Salan Hassoon, Israel Schechter. In situ fluorimetric determination of pesticides on vegetables [J]. *Analytica Chimica Acta* · 2000, (405): 9-15.
- Harald Hake, Ravid Ben-Zur, Israel Schechter, Angelika Anders. Fast optical assessment of pesticide coverage on plants [J]. *Analytica Chimica Acta* · 2007, (596): 1-8.
- Bengt Danielsson, Ioana Surugiu, Anatoli Dzgoev, Michael Mecklenburg, Kumaran Ramanathan. Optical detection of pesticides and drugs based on chemiluminescence-fluorescence assays [J]. *Analytica Chimica Acta* · 2001, (426): 227-234.
- Xiangying Sun, Kaihao Xia, Bin Liu. Design of fluorescent self-assembled multilayers and interfacial sensing for organophosphorus pesticides [J]. *Talanta*, 2008, (76): 747-751.
- J.F.Garcia Reyes, E.J.LlorentMart Mnez, P.Ortega Barrales, A.Molina Diaz. Multiwavelength fluorescence based optosensor for simultaneous determination of fuberidazole, carbaryl and benomyl [J]. *Talanta* · 2004, (64): 742-749.
- Atanasse Coly, Jean-Jacques Aaron. Fluorimetric analysis of pesticides: Methods, recent developments and applications. *Talanta*, 1998, (46) : 815-843.
- Munoz de la Pena, M.C. Mahedero, A.Bautista-Sanchez. High-performance liquid chromatographic determination of phenylureas by photochemically-induced fluorescence detection [J]. *Journal of Chromatography A*, 2002, (950): 287-291.
- Wang Yutian, Wang Zhongdong. Study on fluorescence spectrometer for monitoring pesticide residues on vegetables [J]. *Journal of Applied Optics*, 2005, 26(5): 10-13. (in Chinese with English abstract)
- Wang Zhongdong, Wang Yutian. Theoretical and experimental study on fluorescence characteristics of common pesticides [J]. *Chinese Journal of Luminescence*, 2005, 26(1): 59-65. (in Chinese with English abstract)
- Lou Zhizai, Huang Shihua. Detecting of pesticide residue in vegetable using fluorescence technique [J]. *Acta Laser Biology Sinica*, 2008, 17(6): 657-660. (in Chinese with English abstract)
- Chen Jingjing, Li Yongyu, Wu Jianhu, Peng Yankun. Rapid determination of ppm-order concentration of organophosphorus pesticide based on near-infrared spectroscopy[C]. *The 3rd international symposium on sustainability in food production, agriculture and the environment in Asia, Japan*, 2009: 103-107.
- Chen Jingjing, Li Yongyu, Wu Jianhu, et al. Rapid determination of ppm-order concentration of organophosphorus pesticide based on near-infrared spectroscopy[J]. *Food safety & Quality Detection Technology*, 2009, 1(1): 45-50. (in Chinese with English abstract)
- Y. Peng, R. Lu. Prediction of apple fruit Firmness and soluble solids content using characteristics of multispectral scattering images [J]. *Journal of Food Engineering*, 2006, (82): 142-152.

High Resolution Far Infrared Spectra of the Semiconductor Alloys Obtained Using the Synchrotron Radiation as Source

E.M. Sheregii
*University of Rzeszow, Rzeszów
Poland*

1. Introduction

It is known that far-infrared (FIR) spectra give direct information on phonon modes and impurity levels in the crystal lattices. Infrared spectroscopy enable us also to obtain information about real crystalline microstructure and interior interactions of the semiconductor solid solutions (Barker & Sievers, 1975; Robouch et al.,2001).

A role of the semiconductor alloys in electronics and optoelectronics increases constantly. Since the electron-phonon interaction is main mechanism of the current carriers scattering in semiconductors it is important to recognize deeply the phonon spectra of the semiconductors solid solutions. The results on the semiconductor alloy FIR-spectra collected during 70, 80 and 90 decades have not been explained satisfactorily on base of simple "two-mode behavior" for ternary and "three-mode behavior" for quaternary alloys. The previous reviews and books dedicated to the phonon spectra of semiconductor's compounds (Barker & Sievers, 1975; Tylor,1988; Adachi,1999; Kosevich,1999) give not a reasonable answers on the questions concerning: whether the vibrations of different dipole pairs in the solid solution are connected in the alloy lattice and form a running wave (phonons) or on the contrary: they are disseminated on great number of local modes? Another one concerning of the solid solutions microstructure - geometry of chaos: whether this geometry factor is sufficient or thermodynamic one is necessary to add. The adequate describing of this geometry factor applying to the phonon spectra interpretation should be developed both for ternary alloys and quaternary also.

In order to give answers on these principally important question we need the credible experimental results and for this purpose in years 2001-2006 were performed in Laboratory Nazionale di Frascati the six TARI (Transnational Access to the Research Infrastructure) Projects concerning the FIR-spectra of the semiconductor solid solutions obtained by measuring of optical reflectivity using synchrotron radiation as source. The brilliant properties of synchrotron radiation enable us to obtain FIR-spectra of comparably high resolution: about 1 cm^{-1} whereas nature sources provided 2.5 cm^{-1} at better case. The results on FIR-spectra obtained by this way for mercury contained semiconductor alloys - ternary as $\text{Hg}_{1-x}\text{Cd}_x\text{Te}$ as well as quaternary like $\text{Zn}_y\text{Cd}_x\text{Hg}_{1-x-y}\text{Te}$ - will be presented in this Chapter. There is third principally important question concerning Hg-contained solid solutions:

additional lines arising constantly in the region of frequencies lower than main HgTe-like modes. The cause of appearing of these additional lines was not explained (Baars & Sorgers, 1972; Amirtharaj et al., 1990; Biao, 1996; Rath et al., 1995). The new results as well as previous published ones (Sheregii et al., 2006; Cebulski, et al., 2008; Polit et al., 2010; Sheregii et al., 2009; Sheregii et al., 20011) but with new interpretation, will be presented here and allow us partly to respond on the formulated above questions.

2. Experiment

2.1 Experimental technique

The optical reflection spectra in the region from 10 to 10 000 cm^{-1} where the phonon frequency values (30 – 400 cm^{-1}) of semiconductor's compounds are located, were measured in the wide temperature interval and composition region. Experiments were performed at the DAFNE-light laboratory at Frascati (Italy) using the experimental set-up described in (Cesteli Guidi et al., 2005). A BRUKER Equinox 55 FT-IR interferometer modified to collect spectra in vacuum and both the synchrotron radiation light emitted by the DAFNE storage ring as well as a mercury lamp were used as IR sources (Marcelli et al., 2005). The measurements were performed in the temperature range of 20-300 K at the spectral resolution of 1 cm^{-1} (2 cm^{-1} in some cases) collecting typically 200 scans within 600 s of acquisition time with a bolometer cooled down to 4.2 K.

The reflectivity was measured by using as a reference a gold film evaporated onto the surface of the investigated samples. This method enabled us to measure the reflectivity coefficient with an accuracy of about 0.2 %. The imaginary part curves of the dielectric function $\text{Im}[\epsilon(\omega, T)]$ were calculated, from reflectivity spectrum, by means of the Kramers-Kronig (KK) procedure with uncertainty less than 1.5%.

2.2 Experimental results for ternary alloys

In our previous published works were presented results obtained by the same way on the ternary solid solutions $\text{Hg}_{1-x}\text{Cd}_x\text{Te}$ and $\text{Hg}_{1-x}\text{Zn}_x\text{Te}$ (Cebulski, et al., 2008; Polit et al., 2010; Sheregii et al., 2009; Sheregii et al., 2011). It was shown in these works that observed subtle structure of the two phonon sub-bands in case of ternary alloys can be successfully explained on base of the five structural cells model of H.W. Verleur and A.S. Barker (V-B model) (Verleur & Barker, 1966) thought the additional phonon lines were observed. Last one required the new hypothesis – the two wells potential model for Hg-atoms in lattice (Polit et al., 2010) – for explanation the experimental spectra. The V-B model will be presented in next sub-chapter. In this sub-chapter are exposed the FIR-spectra concerning ternary alloys in order to illustrate the fact of multi-mode behaviour – main statement of the random version of the V-B model which is necessary to interpret of the experimental FIR-spectra.

The high-resolution reflection FIR-spectra obtained for the ternary $\text{Hg}_{1-x}\text{Cd}_x\text{Te}$ for compositions from $x=0.06$ to $x=0.7$ at the temperature 300K and in the spectral range 100 cm^{-1} to 200 cm^{-1} are shown in Fig.1 as reflectivity curves $R(\omega)$. Two bands which shift weakly with the composition are observed: first one around 118-128 cm^{-1} and second one around 145-155 cm^{-1} . The amplitude of first band increases when the content of HgTe increases and amplitude of second band increases when the CdTe content increases. The first band

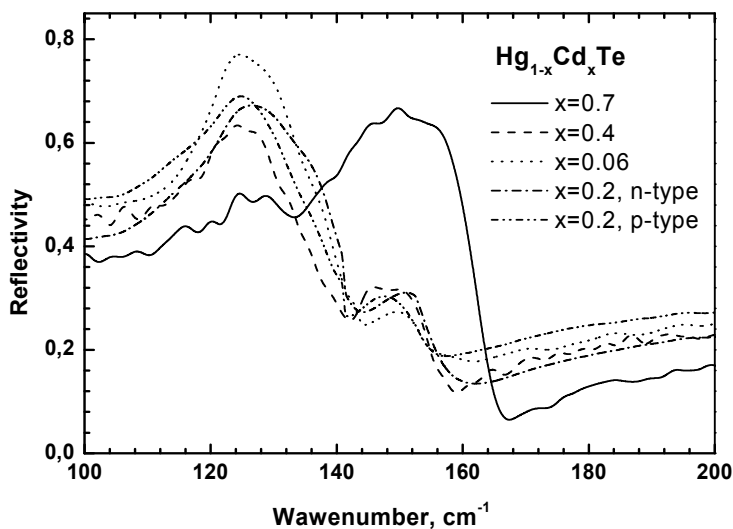


Fig. 1. Reflectivity spectra $Cd_xHg_{1-x}Te$ (x is changing from 0.06 to 0.7) obtained at 300K.

corresponds to the $HgTe$ -like sub-band and second one - to the $CdTe$ -like sub-band.. This type of reflectance spectrum again shows according to previous work (Baars & Sorgers, 1972; Amirtharaj et al.,1990; Biao,1996; Rath et al., 1995) two-mode behavior of the optical phonons in the $Hg_{1-x}Cd_xTe$ alloys. Whereas, the subtle structure of both sub-bands is clearly observed too what undoubtedly indicates on multi-mode character of phonon spectra (above two modes). Authors (Kozyrev et al.,1998) interpreted these subtle structure in frame of the V-B model but they limited consideration of the FIR-spectra in the spectral region 118 – 160 cm^{-1} . Whereas, in the region 90 – 116 cm^{-1} are observed additional lines registered earlier (Talwar, 1984; Amirtharaj et al., 1990;Biao,1996;Rath 1995). The line amplitudes of main sub-bands ($HgTe$ -like at 118 – 130 cm^{-1} as well as $CdTe$ -like at 140 – 170 cm^{-1}) decrease when the temperature increases for both samples. Contrary, the line amplitudes of additional lines (we can call them as Additional Phonon Modes (APM) whereas the main sub-bands we can called as Canonical Phonon Modes (CPM)) increase when the temperature increases. That is clearly shown on the temperature dependence of FIR-spectra presented in Fig. 2 and 3.

In Fig.2 are shown the FIR-spectra as reflectivity curves $R(\omega)$ for the n-type $Hg_{0.8}Cd_{0.2}Te$ alloy in the temperature region 30 K – 300 K. The temperature dependence of reflectivity curves $R(\omega)$ for p- $Hg_{0.8}Cd_{0.2}Te$ alloy is presented in Fig. 3. We may see the shift of the $HgTe$ -like band towards the higher frequency side with increase of the temperature and shift of the $CdTe$ -like band to the lower frequency side when the temperature increases similarly to results obtained in (Roth et al.,1995). The main TO - phonon mode frequency of $HgTe$ -like sub-band increases from 118 cm^{-1} at 30K to 121 cm^{-1} at 300 K for n-type alloy. We have inferred from the FIR-spectra that the sings of the temperature induced shifts of the $HgTe$ - like and $CdTe$ -like mode frequencies in the MCT alloy are opposite to each other for the composition range $x \leq 0.3$. The $CdTe$ -like mode frequency decrease from 154.2 cm^{-1} to 152 cm^{-2} with the increase in temperature from 30K to 300K and the intensity of the $HgTe$ -like and $CdTe$ -like TO mode decreases and higher background is observed for the p-type $Hg_{0.8}Cd_{0.2}Te$ in the spectral range 90 cm^{-1} - 115 cm^{-1} .

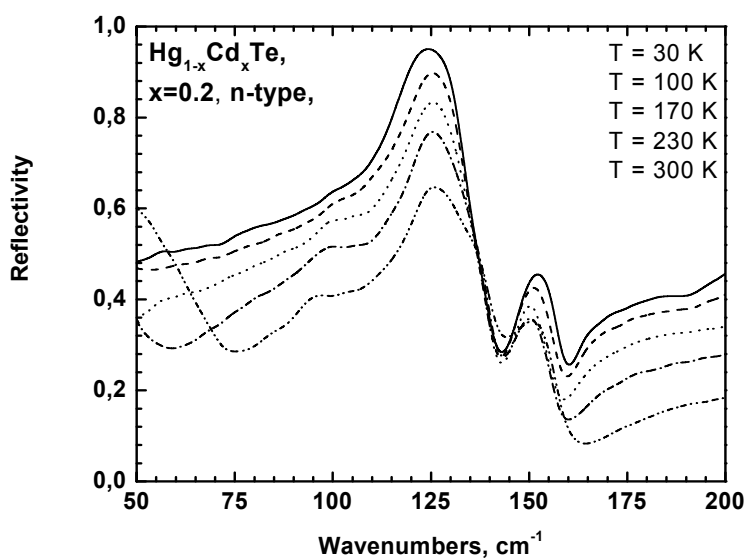


Fig. 2. Reflectivity spectra of n- $\text{Cd}_{0.2}\text{Hg}_{0.8}\text{Te}$ in the temperature range 30 K – 300 K.

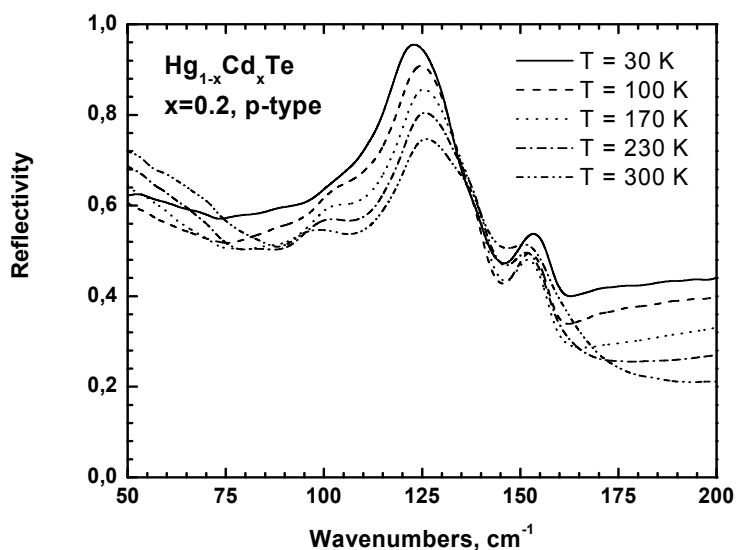


Fig. 3. Reflectivity spectra of p- $\text{Cd}_{0.2}\text{Hg}_{0.8}\text{Te}$ in the temperature range 30 K – 300 K.

In case of p-type $\text{Cd}_{0.2}\text{Hg}_{0.8}\text{Te}$ alloy the main TO - phonon mode frequency of HgTe -like sub-band increases from 118 cm^{-1} at 30K to approximately 122 cm^{-1} at 300 K.

2.3 Experimental results for quaternary alloys

The introduction of low amounts of Zn stabilizes the weak Hg–Te bonds, in crystal lattice of the MCT solid solution, while Cd destabilizes them (Sher et al.,1985). The introduction of a third metal cation (Zn for example), by substitution of matrix cations (Hg or Cd) in solid

solution lattices with a common anion ($Zn_xCd_yHg_{1-x-y}Te$ or ZMCT in our case), enables us to control the material parameters with one extra degree of freedom (Cebulski et al., 1998). The bulk quaternary layers of $Zn_xCd_yHg_{1-x-y}Te$ were obtained by liquid phase epitaxial technique on the CdTe substrates in A.F. Joffe Physical-Technical Institute (St.Petersbourg, Russian), the compositions of samples are shown in Table 1. The thickness of the homogeneous layer was 4 μm . The surface of samples was natural (110) plane of grown layer and was ideal for optical measurements.

Number of sample	x, mol %	y, mol. %
I	0.020	0.200
II	0.070	0.21
III	0.120	0.17
IV	0.127	0.117
V	0.180	0.120
VI	0.050	0.230
VII	0.120	0.130

Table 1. Compositions of the $Zn_xCd_yHg_{1-x-y}Te$ samples investigated.

Optical reflectivity from surface of nine $Zn_xCd_yHg_{1-x-y}Te$ samples of seven compositions in the far-infrared region was measured using the synchrotron radiation as source (high resolution FIR-spectra - the reflectivity experiment is described above)). Some of results were published earlier (Sheregii et. al., 2006). The measurements of reflectivity were performed in temperature region from 30 K to 300 K. In Fig. 4 and 5 are presented reflectivity FIR-spectra obtained for two compositions of $Zn_xCd_yHg_{1-x-y}Te$ for three temperatures: 30 K, 100K and 300 K.

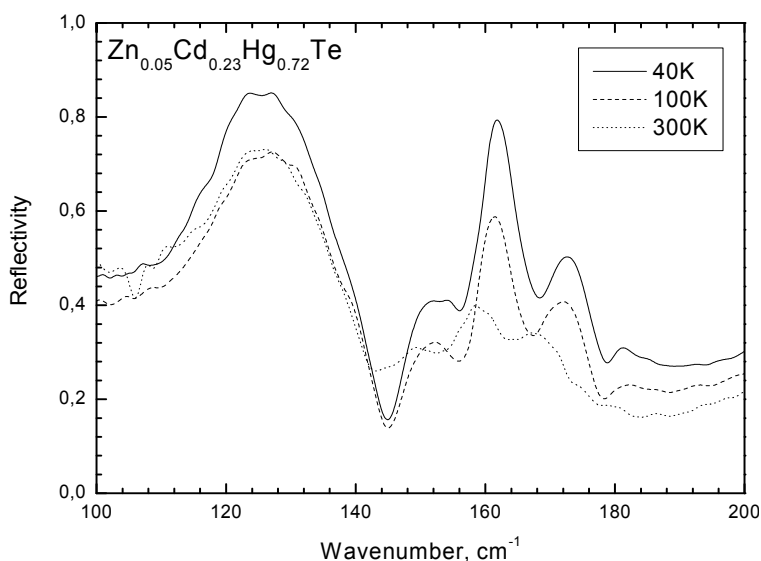


Fig. 4. Reflectivity Spectra of $Zn_{0.05}Cd_{0.23}Hg_{0.72}Te$ (sample VI).

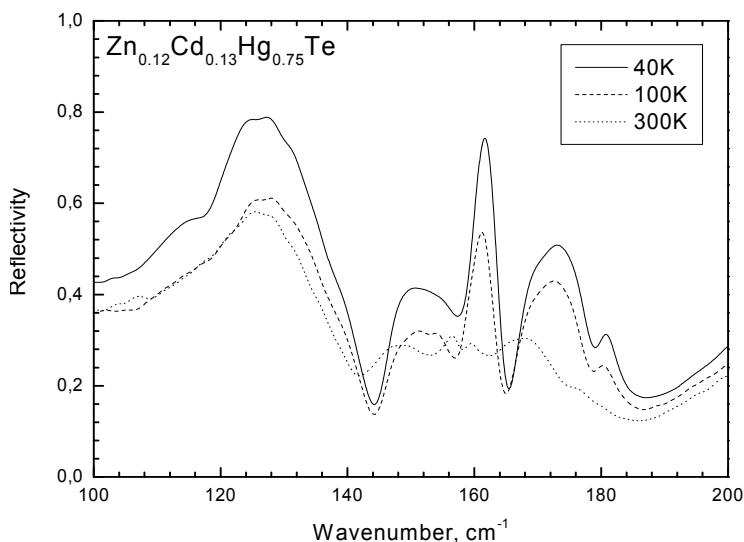


Fig. 5. Reflectivity Spectra of $\text{Zn}_{0.12}\text{Cd}_{0.13}\text{Hg}_{0.75}\text{Te}$ (sample VII).

These curves are similar to typical reflection spectra but these curves have a much richer structure of spectra, as were observed for ternary alloys. It is seen three main bands at 130 cm^{-1} , 160 cm^{-1} and 180 cm^{-1} can be point out in the reflective spectra. However, each of these sub-bands has additional subtle structures, which point to the superposition of a greater number of lines. With increasing of temperature from 30 K to 300 K the subtle structure of observed sub-bands became more smooth.

3. Discussion

3.1 Spectral analyses of the ternary alloy FIR-spectra

The lines corresponding to phonon modes are clearly observed on the $\text{Im}[\varepsilon(\omega)]$ curves calculated by Kramers-Kronig analyses from the experimental FIR reflectivity curves $R(\omega)$. In Fig.6 and 7 are shown $\text{Im}[\varepsilon(\omega)]$ -curves for $p\text{-Hg}_{0.8}\text{Cd}_{0.2}\text{Te}$ obtained for temperature 300 K and 30 K, respectively. In Fig. 6 we can see considerable asymmetry of HgTe-bands caused by additional lines in the range of 90 cm^{-1} – 115 cm^{-1} . That are the additional lines origin of which is discussed during last two decades. The dispersion analysis of the CPMs and APMs was performed by approximating the $\text{Im}[\varepsilon(\omega, T)]$ curves by the Lorentzian sum

$$\text{Im} \varepsilon(\omega) = \sum_{i=1}^k \frac{S_i \gamma_i \omega}{(\omega_{TOi}^2 - \omega^2)^2 + \omega^2 \gamma_i^2} \quad (1)$$

where S_i , ω_{TOi} and γ_i are the oscillator strength, frequency and damping parameters of the i -phonon mode, respectively. The results of spectral analysis for $p\text{-Hg}_{0.8}\text{Cd}_{0.2}\text{Te}$ are presented in Fig.6 and for $n\text{-Hg}_{0.8}\text{Cd}_{0.2}\text{Te}$ in Fig. 7. Parameters of Lorentzian's oscillators used for fitting the $\text{Im}[\varepsilon(\omega, T)]$ -curves are shown in Table 2.

In Table 3 the oscillator strengths sum for APM are shown separately as $(\sum S_{\text{HgTe}})_{\text{add}}$. There are nine well-resolved oscillators for p -type $\text{Hg}_{0.8}\text{Cd}_{0.2}\text{Te}$ at 30 K and eleven for this sample at

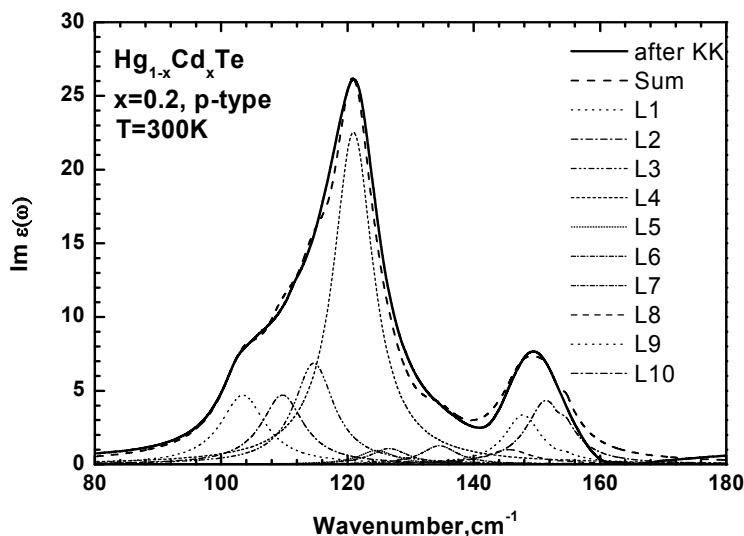


Fig. 6. Imaginary part of the dielectric function of $Hg_{0.8}Cd_{0.2}Te$ p -type in the temperature 300K.

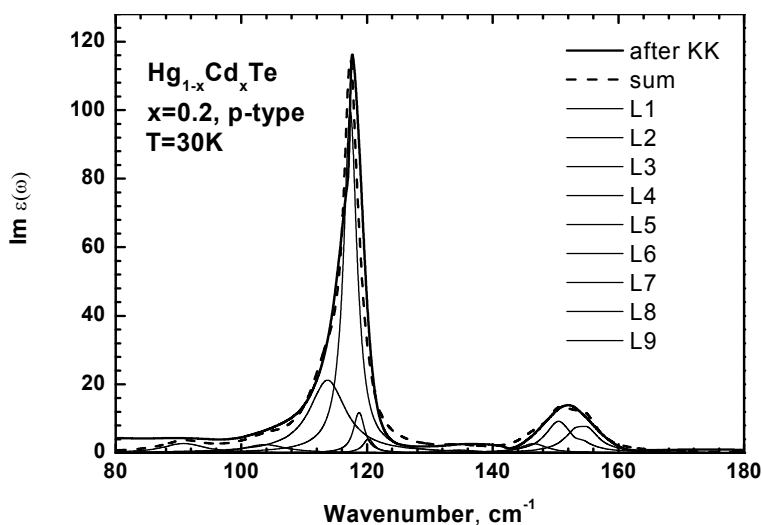


Fig. 7. Imaginary part of the dielectric function of $Hg_{0.8}Cd_{0.2}Te$ p -type in the temperature 30K.

300 K. The position of main $HgTe$ -line for p -type is 118 cm^{-1} at 30 K and is the same as for n -type sample while the oscillator strengths of these lines for n - and p -type samples are drastically different: 62500 cm^{-2} for n -type and 39000 cm^{-2} for p -type, respectively. The damping factor is nearly two times larger for p -type $Hg_{0.8}Cd_{0.2}Te$ because the line shape is much asymmetric and wider in comparison with the n -type $Hg_{0.8}Cd_{0.2}Te$.

It is interesting to consider in details the temperature behavior of the observed phonon modes for both n - and p -type $Hg_{0.8}Cd_{0.2}Te$. In Figures 8 and 9 are shown the temperature dependences of frequencies for observed phonon lines of the $HgTe$ -like and $CdTe$ -like subbands (CPMs) of n - and p -type samples. It is seen that only one $HgTe$ -like mode is observed at 30K and two $CdTe$ -like mode for n - $Hg_{0.8}Cd_{0.2}Te$ (see Fig.7).

Temperature [K]	Number of Line	S	ω	γ	$\sum S_{HgTe}$		$\sum S_{CdTe}$	
					CPM	AVM	CPM	AVM
30	1	600	91,00	5.0		6200		
	2	1500	107.0	4.0				
	3	4700	112.4	4.0				
	4	48000	118.0	3.5	48000			
	5	500	135.0	7.0				500
	6	1300	148.0	5.0			15800	
	7	5800	151.0	5.0				
	8	8700	154.2	6.2				
300	1	4200	103.7	8.6		11400		
	2	4200	110.0	8.1				
	3	6100	115.0	7.7				
	4	21100	121.3	7.7	31300			
	5	830	125.0	7.0				
	6	1000	127.0	7.0				
	8	1200	135.0	7.0				1000
	9	1300	146.1	8.9			9690	
	10	3500	148.3	7.0				
	11	4890	152.0	7.4				

Table 2. Parameters of Lorentzian's oscillators used for fitting the $Im[\epsilon(\omega, T)]$ -curves of the p - $Hg_{0.8}Cd_{0.2}Te$ for the temperatures 30 K and 300K.

Temperature [K]	$s_{HgTe}^i = \frac{S_{HgTe}^i}{\omega^2}$	$\left(\sum_j^j S_{HgTe}^j \right)_{add}$
30	2.8	0.5
300	1.54	1.19

Table 3. The oscillator's sums of the CPM and AVM for p - $Hg_{0.8}Cd_{0.2}Te$ at 30 K and 300K.

When the temperature is higher than 100K the splitting on two $HgTe$ -like modes takes place and at last at 300 K the three $HgTe$ -like CPMs are displayed in case of n -type sample. Whereas in the region 90 – 115 cm^{-1} , one weak line is observed at 108 cm^{-1} which amplitude increases with increasing of temperature and after 230 K this line is splitted on three ones in the range 106 – 118 cm^{-1} .

We can see a considerably larger number of lines for p -type sample in comparison with n -type sample but the temperature shift of the phonon mode frequencies is similar. These results obtained for the n - and p - $Hg_{0.8}Cd_{0.2}Te$ at 30 K agree generally with data presented in (Rath et al., 1995) but in this work was not performed a comparison for n - and p -type

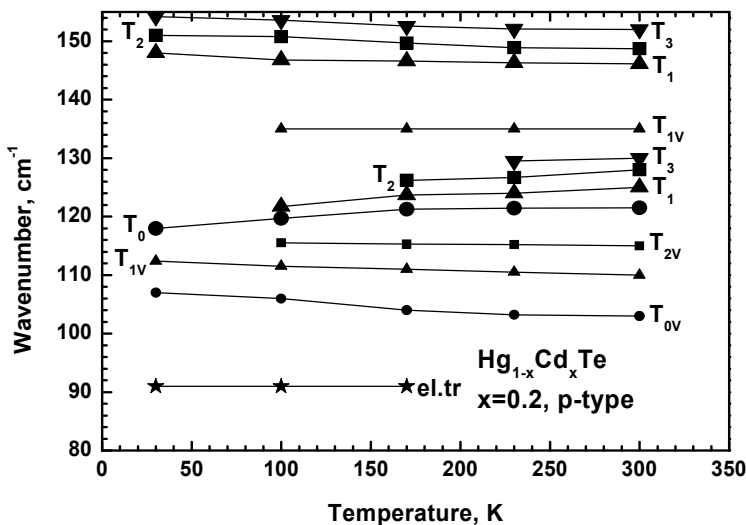


Fig. 8. The temperature dependencies of the phonon mode frequencies for the *p*- type The $Hg_{0.8}Cd_{0.2}Te$, shown in Fig. 2 and 3 as well as in Table II and III. T_0 , T_1 and T_2 are tetrahedra generated the corresponding CPM modes. The T_{nV} are tetrahedra generated by the corresponding APM modes.

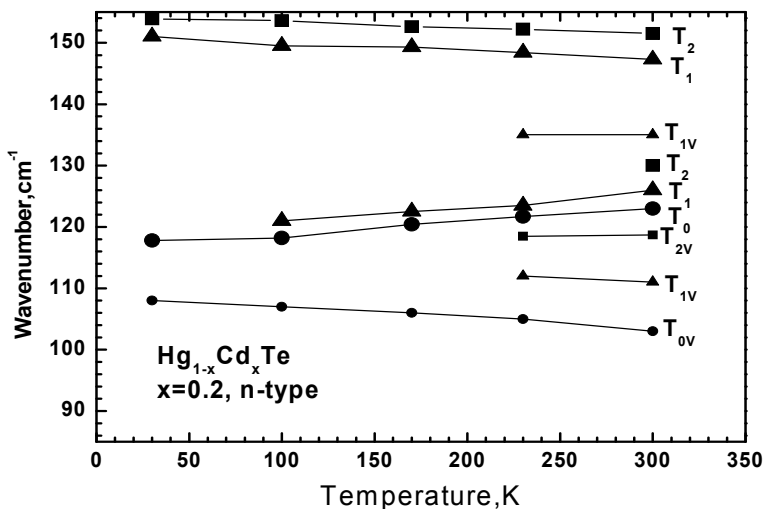


Fig. 9. The temperature dependencies of the phonon mode frequencies for the *n*- type $Hg_{0.8}Cd_{0.2}Te$.

samples. Moreover, in previous works was not shown such drastic difference between the phonon spectra of the *n*- and *p*- $Hg_{0.8}Cd_{0.2}Te$.

The composition frequency dependencies for all observed phonon modes in *p*-type MCT-system at the temperature of 300K is presented on Figure 10. It is seen that these dependencies are similar to that one obtained in (Kozyrev et al., 1998) but the APMs observed in the spectral region 104 - 116 cm^{-1} are presented here also (are absented in work

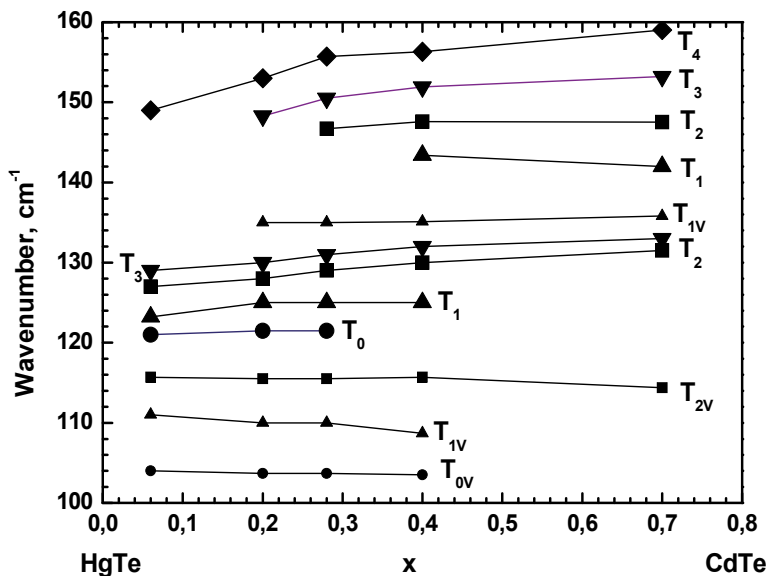


Fig. 10. The composition dependencies of the phonon mode frequencies for $p\text{-Hg}_{1-x}\text{Cd}_x\text{Te}$, at temperature 300K.

of these authors). The amplitudes of these lines decrease with increasing of the CdTe-contains. That are the same lines which temperature behavior were described above for the n - and p -type $\text{Hg}_{0.8}\text{Cd}_{0.2}\text{Te}$. It is undoubtedly that these lines are related to the HgTe -pairs oscillations. It is possible to state that the APMs reproduce the CPM of HgTe -like band but are shifted to lower frequencies.

3.2 The random V-B model for ternary alloys

To understand and interpret the experimental data on the phonon spectra of the solid solutions it is necessary to describe mathematically the non-regular distribution of atoms in its lattices. It occurs that such description is possible in case of the strongly chaotically (stochastically) homogenous distribution what require a very great number of atoms and a very carefully mixed alloys. These conditions are fulfilled generally in case of the high quality homogenous semiconductor solid solutions of the III-V and II-VI semiconductor compounds. In this case we can use the Bernoulli equation (Ziman, 1979) describing a probability to occur a one from n equivalent events what can be apply to the probability to find one from n configurations in the solid solution lattice.

The crystalline structure of the most III-V and II-VI compounds (possessed zinc-blend or wurzit structure as was mentioned above) is characterized by basic cell – tetrahedron – each with a central ion surrounded in the first coordination shell by four nearest neighbours (NN) at the vertices. In a $A_xB_{1-x}Z$ ternary solid solution with substitution of the cation B by cation A, different tetrahedron configurations T_n (n is the number of B-atoms in the tetrahedron) coexist simultaneously: 2 strictly-binary ones corresponding to the AZ and the BZ compounds, whose lattices are characterized by the tetrahedron units T_0 and T_4 (configurations), respectively and 3 strictly-ternary ones actually characterized by the configurations T_1 , T_2 and T_3 . The similar configurations exist in a AY_xZ_{1-x} solid solution

where anions Z are substituted by anions Y – the tetrahedra will be looked at similarly because in zinc-blend lattice we can represent a basic unit as tetrahedron in two versions: centred by anion and surrounded by four cations or oppositely: four anions surround cation in centre.

The probability to find the T_n configuration in ideal lattice of the $A_xB_{1-x}Z$ or $AY_{1-y}Z_y$ ternary solid solution can be calculated using the Bernoulli polynomial (Ziman, 1979):

$$P_n(x) = \binom{4}{n} (1-x)^{4-n} x^n \quad (2)$$

where $\binom{4}{n} = \frac{4!}{n!(4-n)!}$ is the number of combinations with n elements in the fourth set:

$\binom{4}{0} = \binom{4}{4} = 1$, $\binom{4}{1} = \binom{4}{3} = 4$, $\binom{4}{2} = 6$, x is a mol composition of BZ compound in the solid solution what is equal to the ratio of the $B-Z$ ion pairs per whole number of ion pairs in lattice.

It is obvious that probability $P_n(x)$ must be function of composition x because increasing of x means increasing of the B -atoms number in lattice what leads to increasing of the tetrahedron's number with high value of n (not higher then 4). The sum of probabilities to find all configurations in lattice of alloy with composition x must be equal to 1:

$$\sum_n^4 P_n(x) = 1 \quad (3)$$

The probabilities to find a some of cation A or B in tetrahedron T_n in lattice respectively are:

$$P_n^A(x) = \frac{4-n}{4} \binom{4}{n} (1-x)^{4-n} x^n \quad (4)$$

$$P_n^B(x) = \frac{n}{4} \binom{4}{n} (1-x)^{4-n} x^n \quad (5)$$

The same equations there are for the probabilities to find the certain of anions Z or Y respectively in the alloys $AY_{1-y}Z_y$:

$$P_n^Z(y) = \frac{n}{4} \binom{4}{n} (1-y)^{4-n} y^n \quad (4')$$

$$P_n^Y(y) = \frac{4-n}{4} \binom{4}{n} (1-y)^{4-n} y^n \quad (5')$$

It is easy to determine that

$$\sum_n^4 P_n^A(x) = 1 - x \quad (6)$$

$$\sum_n^4 P_n^B(x) = x \quad (7)$$

The same one takes place for the $AY_{1-y}Z_y$ alloys:

$$\sum_n^4 P_n^Z(y) = 1 - y \quad (6')$$

$$\sum_n^4 P_n^Y(y) = y \quad (7')$$

It is necessary to note that (4) and (5) are simultaneously the probabilities to find in the solid solution lattice the ion pairs $A-Z$ and $B-Z$, respectively (in case of the $AY_{1-y}Z_y$ alloys, the probabilities to find the ion pairs $A-Z$ and $A-Y$ according Eqns. (4') and (5'), respectively).

The oscillator strength of the vibrational mode generated by a $A-Z$ -dipole in the T_n configuration is (Robouch et al., 2001):

$$S_n^{A-Z}(x) = f_{AZ} N_0 P_n^A(x) \quad (8)$$

where f_{AZ} is the oscillator strength of the single dipole $A-Z$ -pair, N_0 is total number of dipole pairs in the solid solution crystal, probability $P_n^A(x)$ is determined by (4).

It is important to remember that three assumption are introduced in this consideration:

1. the role of defects is negligible;
2. the alloy lattice is ideally homogenous and a random distribution of atoms in lattice takes place (stochastic homogeneity);
3. the oscillator strengths of the single dipole pairs for different configurations T_n are the same e.g. f_{AZ} or f_{BZ} depends not on index n .

If these conditions are fulfilled, the oscillator sum rule

$$\sum_n S_n^{A-Z}(x) = \sum_n f_{AZ} N_0 P_n^A(x) = f_{AZ} N_0 \sum_n P_n^A(x) = f_{AZ} N_0 (1 - x) \quad (9)$$

has to be satisfied.

Similarly for $B-Z$ dipole pairs:

$$S_n^{B-Z}(x) = f_{BZ} N_0 P_n^B(x) \quad (10)$$

and the oscillator sum rule

$$\sum_n S_n^{B-Z}(x) = \sum_n f_{BZ} N_0 P_n^B(x) = f_{BZ} N_0 \sum_n P_n^B(x) = f_{BZ} N_0 x \quad (11)$$

In case of the $AY_{1-y}Z_y$ alloys the similar oscillator strengths sums must be fulfilled:

$$\sum_n S_n^{A-Z}(y) = f_{AZ} N_0 y \quad (10')$$

$$\sum_n S_n^{A-Y}(y) = f_{AY} N_0 (1-y) \quad (11')$$

Therefore, within this approximation the experimental $\text{Im } \varepsilon(\omega)$ -curves (obtained by Kramers-Kronig transformation from experimentally measured $R(\omega)$ -curve) enable us to find the S_i values, to identify that with certain S_n^{A-Z} or S_n^{B-Z} and to verify the sums (10) or (11) what means the proportionality of the oscillator sum to the contain of the each component in alloy ($N_0 x$ is equal to molar percent of the BZ component and $N_0(1-x)$ – to the molar percent of the component AZ).

Some deviations of experimental data from the dependences (10) or (11) indicate evidently on considerable role of defects or others structural factors (non-random distribution).

3.3 Identification of observed lines in case of the n-Hg_{0.2}Cd_{0.8}Te alloys

The probability to find the atoms Hg and Cd in the particular tetrahedra T_n (n is number of the Cd-atoms in tetrahedral) in the $Hg_{0.8}Cd_{0.2}Te$ lattice should be taken into account using formulas (4) and (5). If $x=0.2$ the values of $P_n^{Hg}(x)$ for different n are equal to: 0.410 ($n=4$), 0.307 ($n=2$), 0.077 ($n=3$) and 0.006 ($n=4$) while the $P_n^{Cd}(x)$ values are: 0.102 ($n=1$), 0.077 ($n=2$), 0.192 ($n=3$) and 0.002 ($n=4$). At $T=30$ K all HgTe-like CPMs oscillate at the same frequency because tetrahedra with different number n are not deformed and we observed a degeneration of vibrational modes (Hg-Te and Cd-Te bonds have the same length). If $T=300$ K the splitting of the mode frequency takes place (see Fig.9): the most strong line at 122.6 cm^{-1} should be generate by Hg-Te dipoles in the T_0 tetrahedron while the line at 125.0 cm^{-1} – by this dipoles in the T_1 one and very small line at 128.6 – in the T_2 . So, the frequency consequence takes place for HgTe-like modes: $\text{HgTe}\omega_0 < \text{HgTe}\omega_1 < \text{HgTe}\omega_2 < \text{HgTe}\omega_3$ according with work (Kozyrev et al., 1998). Analogical analyses for CdTe-like modes shown that the line at 151.5 cm^{-1} is generated by Cd-Te dipoles in T_1 tetrahedron and the line at 147.3 cm^{-1} – by the same dipoles in T_2 one. The frequency consequence for CdTe-like modes is: $\text{CdTe}\omega_1 > \text{CdTe}\omega_2 > \text{CdTe}\omega_3 > \text{CdTe}\omega_4$ what agree with the data of work (Kozyrev et al., 1998) also. It allow to find to what basic cells (tetrahedra) belongs each observed vibrational mode generating by Hg-Te and Cd-Te dipoles: corresponding tetrahedra are shown in Fig. 9 for CPM (T_n) as well as for APM (T_{nv}).

3.4 Identification of observed lines in case of the p-Hg_{0.2}Cd_{0.8}Te alloys

The dissipation of the $\text{Im}[\varepsilon(\omega, T)]$ -curves on the Lorentzians was carried out for the p -type $Hg_{0.8}Cd_{0.2}Te$ sample (see Fig. 6). The parameters of these oscillators are presented in Tables 2 and 3. There are eight well-resolved oscillators for p -type $Hg_{0.8}Cd_{0.2}Te$ at 30 K and eleven for this sample at 300 K. The temperature dependencies of the phonon mode frequencies for p - $Hg_{0.8}Cd_{0.2}Te$ are presented in Fig. 8. We can see a considerably larger number of lines here in comparison with n -type sample but the temperature shift of the phonon mode frequencies is similar. Analogically was fined for what basic cells (tetrahedra) belongs each observed

vibrational mode generating by Hg-Te and Cd-Te dipoles: corresponding tetrahedra are shown in Fig. 8 for CPM (T_n) as well as for APM (T_{no}).

3.5 Additional phonon modes

There are important guiding principles that the lines in the region 104 cm^{-1} - 116 cm^{-1} are related to the Hg-vacancies (Cebulski et al., 2008). This hypothesis can be verified by temperature dependences of the specific oscillator strength sum (SOSS) of the lines observed in this region. These temperature dependences are presented in Fig. 11 for n - $\text{Hg}_{0.8}\text{Cd}_{0.2}\text{Te}$ and Fig. 12 for p - $\text{Hg}_{0.8}\text{Cd}_{0.2}\text{Te}$. It is shown in Fig.11 that temperature dependences of the SOSS of APM for p -type $\text{Hg}_{0.8}\text{Cd}_{0.2}\text{Te}$, have the exponential character described by function

$$\sum s_{\text{HgTe}}^{\text{add}} = 0.5 + 12 \exp(-0.075 / kT) \quad (12)$$

with activation energy equal to 75 meV. It is too small energy in comparison with the Hg-vacancy activation energy to be equal to about 1eV (Chandra et al., 2003).

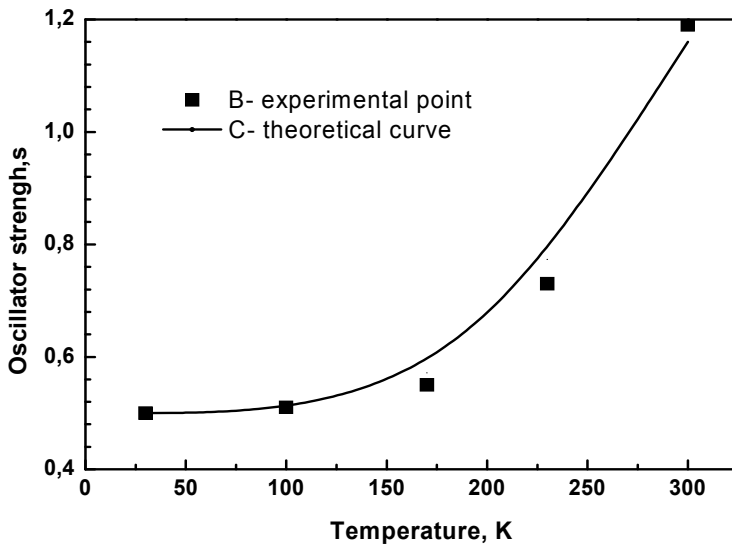


Fig. 11. The temperature dependence of the sum of the additional modes oscillator strengths for the p -type $\text{Hg}_{0.8}\text{Cd}_{0.2}\text{Te}$, B- experimental points, C is approximated curve calculated according the Equation $s=0,5+12\exp(-0,075/kT)$.

The Fig.12 presents the temperature dependence of the SOSS of the same lines for n -type $\text{Hg}_{0.8}\text{Cd}_{0.2}\text{Te}$. This dependence is described by exponential function similar to (12):

$$\sum s_{\text{HgTe}}^{\text{add}} = 0.04 + 12 \exp(-0.09 / kT) \quad (13)$$

with activation energy equal to 90 meV, which is larger than for p -type but is too small to be an activation energy for Hg-vacancies.

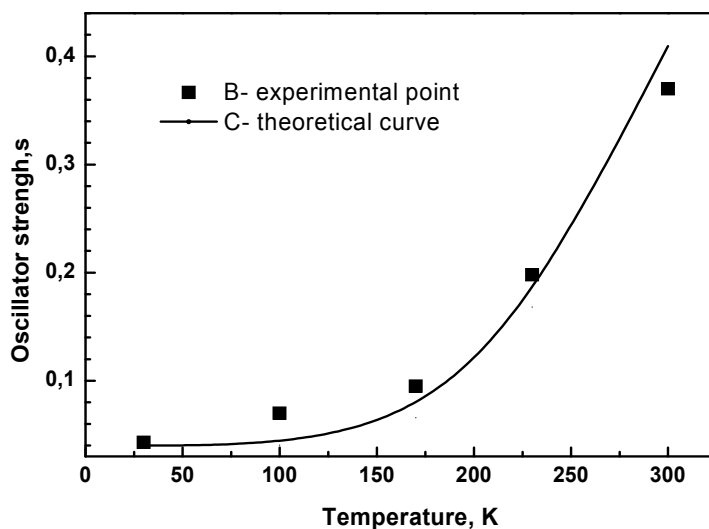


Fig. 12. The temperature dependence of the sum of the additional modes oscillator strengths for the *n*-type $Hg_{0.8}Cd_{0.2}Te$, B- experimental points, C is approximated curve calculated according the Equation $s=0,04+12\exp(-0,09/kT)$.

It is clear that the temperature dependencies of the oscillator strength sum of the lines observed in the region of the 104 – 116 cm^{-1} , presented here, do not confirm the hypothesis that these lines are related to the Hg-vacancies. There are others doubtful circumvents, namely: in case of *n*-type $Hg_{0.8}Cd_{0.2}Te$ the single very weak line at 107 cm^{-1} is observed at 30 K also.

If we assume that this line is caused by Hg- vacancies it is necessary to agree that the vacancy density must be not less than $10^{18} cm^{-3}$. While the data of the positron annihilation for *n*-type $HgCdTe$ shown values of the Hg-vacancy concentration closer to $10^{15} cm^{-3}$ (Krause et al., 1990). It is necessary to note that method of the positron annihilation, seems to be direct method of the vacancy concentration measurement, in case of HgCdTe use the data of Hall-effect (in determination of the specific positron trapping rate) identifying the hole concentration to the concentration of Hg-vacancies. It is not completely correct because in $HgCdTe$ there is always background of the electrically native compensated Hg-vacancies and real level of the Hg-vacancies is naturally higher than the hole concentration. Nevertheless, the Hg-vacancy density over $10^{18} cm^{-3}$ in the *n*- $Hg_{0.8}Cd_{0.2}Te$ Te of high quality (very high electron mobility of $2.5 \times 10^5 V/ms$) is absolutely impossible.

The temperature dependences of the SOSS for discussed lines lead to the activation energy of process to be equal to 75 – 90 meV what could be as substantial argument for the model of two potential wells (Hg-atoms in lattice of HgCdTe) applying by J.A. Sussman (Sussman, 1967).

3.6 Two valley potential model and quasi quaternary alloys

J.A. Sussman (Sussman, 1967) proposed this model for the binary compounds. From this theory arise that a cation in the crystal lattice could have the two positions: first stable

position energetically more deep, second one is metastable state with higher energy and suitably with more long bond. This model related to HgTe and HgCdTe means that the Hg atoms can be shifted from the vertex position in tetrahedra (stable position) to a non centered position (metastable position). According to Sussman's theory such transition from stable to metastable state, means that the Hg-Te bonds become longer. The probability for such transition is described by

$$W = w \exp(-\Delta E / \kappa T) \quad (14)$$

where ΔE is the energy difference between the two states – stable and metastable one and w is the assumed probability at the absolute zero.

The temperature dependences of SOSS for APM shown in Figures 11 and 12 and described by relations (12) and (13) enable us to determine the ΔE . Therefore, in the case of *p*-type $Hg_{0.8}Cd_{0.2}Te$ the energy transition from the stable position of the Hg atoms to the metastable position is 75 meV and 90 meV for the *n*-type one. This difference can be explained by the fact that for *p*-type material where the considerable path of the crystal lattice is non relaxed, the density of metastable states is large than in *n*-type what could change the deep of the energy minimum (value E_2) for stable position. The ratio of the SOSSs of additional lines (104 -116 cm^{-1}) for *p*- and *n*-type materials is about one order. Therefore, the density of the metastable states and stable ones should differ with the same value. Simultaneously, the length of the Hg-Te bonds is longer for the metastable states in comparison with stable one. This difference have been appeared in X-ray analyses (Polit et al., 2010): 6.4604 Å for *n*- $Hg_{0.8}Cd_{0.2}Te$ and 6.4648 Å for *p*- $Hg_{0.8}Cd_{0.2}Te$ - the density of metastable states is larger of one order in *p*-type material and that causes statistically more long bonds Hg-Te.

3.7 General description of the HgCdTe phonon spectra

The general description of the phonon spectra is based on three Figures: 4, 5 and 6. These Figures present the temperature dependences of the HgTe-like and CdTe-like mode frequencies for *n*- and *p*-type $Hg_{0.8}Cd_{0.2}Te$ (Fig. 4 and 5) as well as the composition dependences of the same modes at the room temperature (Fig. 6). If temperature increases, the number of Hg-atoms occupied the meta-stable positions (Hg^{II}) increases also and the deformation of crystal lattice rises, respectively. The last factor can cause the removing of degeneracy of the HgTe-like CPMs in *n*- $Hg_{0.8}Cd_{0.2}Te$ when the temperature increases over the 100 K (see Fig. 5): the AVMs appear simultaneously, too. Indeed, the AVM at 112 cm^{-1} (beside very weak from 30 K at 108 cm^{-1}) take place after 100 K in *n*-type $Hg_{0.8}Cd_{0.2}Te$ and after 200 K appear additionally one AVM at 115-116 cm^{-1} . The presence of Hg^{II} in a tetrahedron leads to the stretching of bonds which in its turn causes the shift of the Hg-Te oscillation frequency towards smaller frequencies. This effect can occur in three kinds of tetrahedra: 1) containing 3 Hg-atoms in stable position (Hg^I) and one Hg^{II} ; 2) containing two Hg^I , one Cd-atom and one Hg^{II} ; 3) containing one Hg^I , two Cd-atoms and one Hg^{II} . The frequencies of Hg-Te oscillations in these tetrahedra should be arranged in the next sequence: the lowest frequency corresponds to the Hg-Te oscillations in the tetrahedron of first type and most higher corresponds to the oscillations in the tetrahedron of third type.

The lines in the range of 135 -137 cm^{-1} are generated as could be assumed, by the oscillation of Cd-Te pair in the tetrahedra containing two Hg^I , one Cd-atom and one Hg^{II} . Therefore, the Figures 9,10 and 11 enable us to assume that the phonon spectra in MCT are reproduced in

two versions: first one is realized in the lattice consisted only from the Hg^I -atoms (that are CPM) and second one occurs in the lattice included the Hg^{II} -atoms too (that are APM). The theory of the quasi-quaternary alloys contained the two kind of Hg -atom position developed in (Cebulski et al., 2008) enable us to determine the Hg^{II} concentration on base of phonon spectra. The details of such consideration will be presented in next sub-chapter. As arise from this consideration, the sum of the specific oscillator strengths of AVM observed in the range 104 – 116 cm^{-1} is equal to

$$S_{(n-1),Hg^{II}}^{Hg^{II}Te}(y) = f_{HgTe}y \quad (15)$$

This simple expression enable us to determine experimentally (using the phonon spectra according to the the Eqn. (10)) the y - molar part of the Hg^{II} -atoms, assuming that: i) the lines corresponding to the AVM generating by tetrahedra bearing by Hg^{II} are identified correctly, ii) the specific oscillator strength of the Hg^{II} -Te oscillations in tetrahedra with Hg^{II} -atoms are the same as in tetrahedra without Hg^{II} atoms as was mentioned above. We assume that these conditions are fulfill in case of measured materials of n - and p -type $Hg_{0.8}Cd_{0.2}Te$. The calculated values of the molar fraction y of the Hg^{II} -Te obtained from phonon spectra (sum of the specific oscillator strength) are presented in Table IV for 30 K and 300 K.

Material	Sum of the specific oscillator strength for AVM		y , mol. %	
	30 K	300 K	30 K	300 K
n -type $Hg_{0.8}Cd_{0.2}Te$	< 0.043	0.37	< 0.7	6.3
p -type $Hg_{0.8}Cd_{0.2}Te$	0.50	1.1987	9.7	20.67

Table 4. Molar fraction of the Hg^{II} -atoms determine from phonon spectra

Reassuming we can affirm that in case $HgCdTe$ of the p -type it consists of two sublattices: one sublattice contains the atoms of mercury in the stable state with the shorter length bonds of $HgTe$, second sublattice contains atoms Hg in the metastable state with the longer bond of $HgTe$. The phonon spectra of $HgTe$ -like modes are reproduced for each above mentioned sublattices. Increase of the temperature leads to the increase of the number of Hg^{II} atoms (metastable state) and the same to the enlargement of tensions in the lattice what leads to splitting $HgTe$ -like mod CPM in the n -type the material. Because of that differences between phonon spectra of n and p type in the room temperature are disappeared.

One can also affirm, that in the temperature 30K in the material n - $Cd_{0.2}Hg_{0.8}Te$ is observed one $HgTe$ -like mode and two $CdTe$ - like of the mode (CPM) would confirm the percolation model of authors (Pages et al., 2009). It indicates (non directly) that the bond percolation thresholds x_c for the $HgCdTe$ alloys is larger then 0.19, namely $x_c \geq 0.2$. Nevertheless, generally the V-B model developed for random case is confirmed completely for the $HgCdTe$ solid solutions.

In Fig. 13 are shown the values of the oscillator strengths sums (OSS) for the Hg-Te dipoles and for Cd-Te dipoles for each samples investigated. The data are presented in two way: i) only OSS for CPMs are included (open circles and squares), for $x=0.2$ there are two open circles because first one (upper open circle) is regarded to $n\text{-Cd}_{0.2}\text{Hg}_{0.8}\text{Te}$ and lower open circle - to $p\text{-Cd}_{0.2}\text{Hg}_{0.8}\text{Te}$; ii) in the OSS are included the APM OSS also (filled circles and squares). That enable us to obtain the dependencies of the OSS on composition. As follow from Fig. 13 if the oscillator strengths of APM are included in the sum of the oscillator strengths for the modes generated by Hg-Te dipoles as well as Cd-Te dipoles the OSS are proportional to the contain of correspond compound: to the x in case of Cd-Te dipoles and to the $1-x$ in case of Hg-Te ones. As was mentioned above (see Eqns. (9) and (11)) these dependences are considered as a criterion of applying the random V-B model to the phonon spectra interpretation of the ternary solid solutions. Therefore, the random version of the V-B model satisfactorily explains the high resolution FIR-spectra of ternary HgCdTe solid solutions if APM are included into consideration.

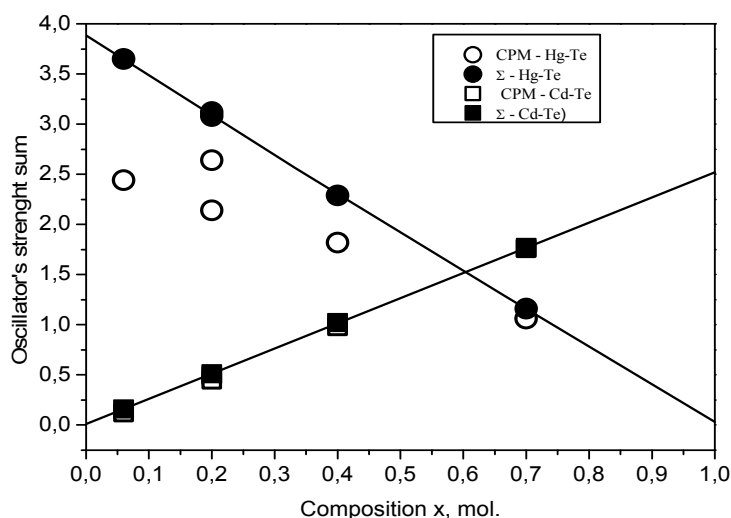


Fig. 13. The oscillator strength sum dependence on composition for the HgCdTe alloys

3.8 Spectral analyses of the FIR-spectra for quaternary alloys

The Kramers – Kronig analysis was applied to determine the position of observed lines. In Fig. 14 and 15 are shown the curves of imaginary part of dielectric function $\text{Im } \varepsilon(\omega, x, y)$ for compositions VI and VII (see Table 1) respectively, obtained by Kramers-Kronig transformation from the reflectivity curves presented in Fig. 4 and 5 at 30 K. The imaginary part of dielectric function for $\text{Zn}_x\text{Cd}_y\text{Hg}_{(1-x-y)}\text{Te}$ solid solution can be presented as the superposition of Lorentzians as it is follow from Eqn. (1). The fittings by the Lorentzian sums are presented in Fig.14 and 15 too. The parameters of Lorentzians are presented in Tab. 5 and 6 respectively.

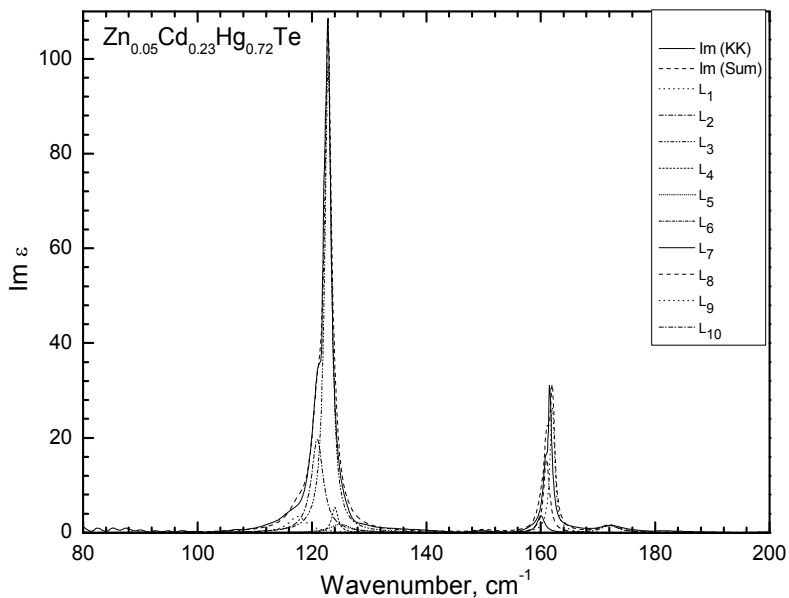


Fig. 14. Spectral analysis for Sample $Zn_{0.05}Cd_{0.23}Hg_{0.72}Te$ (sample VI).

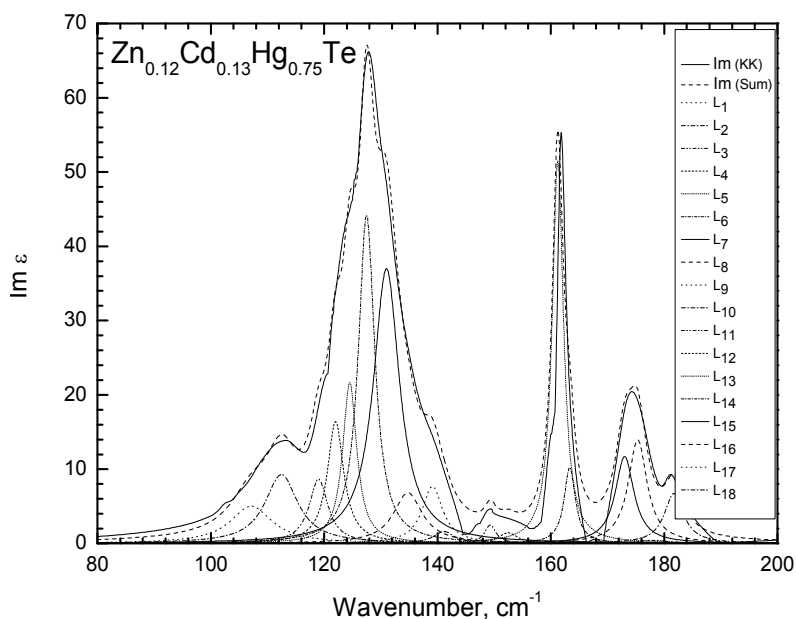


Fig. 15. Spectral analysis for sample $Zn_{0.12}Cd_{0.13}Hg_{0.75}Te$ (sample VII).

The present analysis shows that the investigated quaternary ZMCT has larger number of the resonance frequencies in the observed spectra compared to the ternary solid solutions of the binary HgTe, CdTe and ZnTe (118 to 180 cm^{-1}) and extends the frequency region of the phonon modes - from 108 to 190 cm^{-1} .

Frequency (cm ⁻¹)	Oscillator strength (cm ⁻²)	Damping factor (cm ⁻¹)
107,20	4847	9,02
112,50	7341	7,02
119,00	4130	4,00
122,00	7000	3,50
124,50	8090	3,00
127,47	19700	3,50
131,00	27000	5,57
134,80	5700	6,20
139,10	4700	4,40
141,10	1000	4,40
149,30	900	2,40
152,40	890	4,10
160,20	4410	2,40
163,30	4000	2,40
173,00	8100	4,00
175,30	9800	4,00
178,00	483	6,40
181,70	5000	4,10

Table 5. Parameters of Lorentzians presented in Fig.10 for sample VII

Frequency (cm ⁻¹)	Oscillator strength (cm ⁻²)	Damping factor (cm ⁻¹)
117,52	1600	4,02
120,92	6000	2,52
122,80	17041	1,41
124,00	860	1,30
125,00	1000	4,50
150,00	200	3,00
160,00	900	1,57
161,00	3000	1,20
162,00	4300	1,00
172,00	1000	3,80

Table 6. Parameters of Lorentzians presented in Fig.9 for sample VI.

It is necessary to use 10 oscillators to fit the $\text{Im } \varepsilon(\omega, x, y)$ curve ($x=0.05, y=0.23$) – sample VI, and 18 ones to fit the $\text{Im } \varepsilon(\omega, x, y)$ curve ($x=0.12, y=0.13$) – sample VII. The identification of observed lines in obtained spectra will be performed in the frame of the V-B model developed for random distribution of atoms in the lattice for quaternary solid solutions.

3.9 The random V-B model for quaternary alloys

We consider here the four-component solid solution $A_x B_y C_{1-x-y} Z$ with three kinds of cations A, B and C and with the same anion Z . The lattice of quaternary alloy contents 15 basic units (tetrahedra): three binary AZ, BZ, CZ , nine strictly ternary ABZ, ACZ, BCZ and three strictly quaternary $ABCZ$. If quaternary alloy have x mol part of AZ compound and y mol part of BZ we can determine the probability to find in lattice the tetrahedron T_{nm} with n A-cations and m B-cations. This probability is equal to:

$$P_{n,m}(x, y) = \binom{4-n}{m} \binom{4}{n} (1-x-y)^{4-n-m} x^n y^m \quad (16)$$

where matrixes $\binom{4-n}{m}$ and $\binom{4}{n}$ are the same number of combinations as in Eqn. (2).

It is seen that if $y=0$ and $m=0$, the Eqn.(16) is:

$$P_n(x) = 1 \cdot \binom{4}{n} (1-x)^{4-n} \cdot x^n \cdot 1 \quad (17)$$

and the Eqn. (2) takes place for an alloy $A_x C_{1-x} Z$.

At least, it is possible to consider when $1-x-y = 0, 4-n-m = 0$. In this case $y = 1-x$ and $m = 4-n$, therefore

$$P_{n,m}(x, y) = \binom{4-n}{m} \binom{4}{n} \cdot 1 \cdot x^n \cdot y^m \quad (18)$$

and we obtain the probability to find a tetrahedron T_n for an alloy $A_x B_y Z$. It means that Eqn. (16) really correctly described the random distribution of atoms in the quaternary solid solutions $A_x B_y C_{1-x-y} Z$. The correspond probabilities to find particular cations in tetrahedron $T_{n,m}$ in lattice are:

$$P_n^A(x) = \frac{n}{4} \binom{4-n}{m} \binom{4}{n} x^n y^m (1-x)^{4-n-m}, \quad (19)$$

for cation A ;

$$P_n^B(x) = \frac{m}{4} \binom{4-n}{m} \binom{4}{n} x^n y^m (1-x)^{4-n-m}, \quad (20)$$

for cation B , and

$$P_n^C(x) = \frac{4-n-m}{4} \binom{4-n}{m} \binom{4}{n} x^n y^m (1-x)^{4-n-m} \quad (21)$$

for cation C.

By this way the Eqns. (2, 4, 5, 16, 19 – 21) represent the complete description of the random atom distribution in the ternary $A_xB_{1-x}Z$ and quaternary $A_xB_yC_{1-x-y}Z$ solid solutions with substitution of cations. The four-component solid solution $A_xB_yC_{1-x-y}Z$ in ideally random case described by relations (16) and (19-21) consists from fifteen structural units – tetrahedra – which can generate 66 optically active phonon (vibrational) modes. These number of modes arose by next way: three strictly binary tetrahedra generate three vibrational modes AZ-like, BZ-like and CZ-like, nine (3x3) strictly ternary tetrahedra generate $9 \times 6 = 54$ vibrational modes and three strictly quaternary tetrahedra generate $3 \times 3 = 9$ vibrational modes: in sum 66 vibrational modes. In practice the most of these modes are degenerated (have the same frequencies): for example, the AZ-like modes generated in tetrahedra ABZ could have the same frequencies as AZ-like modes in tetrahedra ACZ. The same concerns the BZ-like and CZ-like modes. By this way the number of distinguished modes should be 30.

The expression for the oscillator strengths are similar as for ternary alloys:

$$S_{n,m}^{A-Z}(x,y) = f_{AZ} N_0 P_{n,m}^A(x,y) \quad (22)$$

where probability $P_{n,m}^A(x,y)$ is determined by (19). Similarly are given the expression for $S_{n,m}^{B-Z}$ and $S_{n,m}^{C-Z}$. The corresponding oscillator sum rule are:

$$\sum S_{n,m}^{A-Z} = N_0 f_{AZ} (1-x-y) \quad (23)$$

$$\sum S_{n,m}^{B-Z} = N_0 f_{BZ} x \quad (24)$$

$$\sum S_{n,m}^{C-Z} = N_0 f_{CZ} y \quad (25)$$

The role of these oscillator sum rules would be the same as in ternary alloys but in the practice it is more difficult to relies the verification of the random distribution of atoms because the number of theoretically possible modes is very large and this factor prevent calculation of the oscillator sum rule.

3.10 Identification of observed lines in case of the $Zn_xCd_yHg_{1-x-y}Te$ alloys

An oscillator strength of particular mode enables us to determine the fraction of basic tetrahedral cells and interpret observed lines in phonon spectra. The attempt to interpret the spectra for sample VI (Fig. 9) and sample VII (Fig.10) is presented in Table 7. Here are presented results of the probabilities to find one of three dipole pairs (Hg-Te, Cd-Te, Zn-Te) in corresponding tetrahedron in lattice calculated according Eqn. (19-21) practically for all possibilities configurations in lattice of the $Zn_xCd_yHg_{1-x-y}Te$ alloys. There are observed modes generated by dipoles in cells probabilities to find of which in lattice is not less than 0.02. Summarizing the above mentioned results on the quaternary $A_{1-x-y}B_xC_yZ$ alloys, it is

Tetraedra	Dipole-pairs	Probabilities	Composition VI, n-type	Composition VII, p-type	Nr of line
2Hg ^{II} 2Cd 1Zn 1Cd 2Hg ^{II}	Hg - Te	0,002 - 0,007		107,2 cm ⁻¹	1
1Hg ^{II} 3Cd 1Zn 2Cd 1Hg ^{II}	Hg - Te	8 · 10 ⁻³ - 2 · 10 ⁻³		112,5 cm ⁻¹	2
4 Hg	Hg - Te	0,37 - 0,24	117,5 cm ⁻¹	119,0 cm ⁻¹	3
1Zn 1Cd 2Hg	Hg - Te	0,06 - 0,01	120,92 cm ⁻¹	122,3 cm ⁻¹	4
2Hg 2Cd	Hg - Te	0,05 - 7 · 10 ⁻⁴		124,5 cm ⁻¹	5
3Hg 1Zn	Hg - Te	0,18 - 2 · 10 ⁻²	122,8 cm ⁻¹	127,5 cm ⁻¹	6
3Hg 1Cd	Hg - Te	0,28 - 0,13	124,0 cm ⁻¹	131,0 cm ⁻¹	7
2Hg 2Zn	Hg - Te	0,05 - 7 · 10 ⁻⁴	125,0 cm ⁻¹	134,8 cm ⁻¹	8
1Zn 1Cd 1Hg	Hg - Te	0,07 - 0,02		139,1 cm ⁻¹	9
1Hg 3Cd	Hg - Te	6 · 10 ⁻³ - 1,2 · 10 ⁻³			
1Hg 3Zn 2Zn 1Cd 1Hg	Hg - Te	4 · 10 ⁻³ - 6 · 10 ⁻⁶			
4Cd	Cd - Te	0,02 - 2 · 10 ⁻⁴		141,1 cm ⁻¹	10
1Hg 3Cd	Cd - Te	0,02 - 0,004	150,0 cm ⁻¹	149,3 cm ⁻¹	11
2 Hg 2Cd	Cd - Te	0,07 - 0,02	160 cm ⁻¹	152,4 cm ⁻¹	12
1Zn 2Cd 1Hg	Cd - Te	0,015 - 0,004	161,5 cm ⁻¹	160,2 cm ⁻¹	13
3Hg 1Cd	Cd - Te	0,09 - 0,04			
3Hg 1Zn	Zn - Te	0,056 - 9 · 10 ⁻³	162,0 cm ⁻¹	163,0 cm ⁻¹	14
1Zn 3Cd	Cd - Te	1,9 · 10 ⁻³ - 4,8 · 10 ⁻⁴			
2Hg 2Zn	Zn - Te	0,05 - 7 · 10 ⁻⁴			
2Zn 2Cd	Cd - Te	1,4 · 10 ⁻³ - 5 · 10 ⁻⁵			
1Hg 3Zn	Zn - Te	1,2 · 10 ⁻² - 1,9 · 10 ⁻⁵			
3Zn 1Cd	Cd - Te	7 · 10 ⁻⁴ - 2 · 10 ⁻⁶			
1Zn 1Cd 2Hg	Cd - Te	0,032 - 0,007			
1Zn 3Cd	Zn - Te	1,6 · 10 ⁻⁴ - 6,5 · 10 ⁻⁴			
2Zn 1Cd 1Hg	Cd - Te	8 · 10 ⁻³ - 2 · 10 ⁻⁴			

Tetraedra	Dipole-pairs	Probabilities	Composition VI, n-type	Composition VII, p-type	Nr of line
2Zn 2Cd	Zn - Te	$5 \cdot 10^{-5} - 1,4 \cdot 10^{-3}$			
3Zn 1Cd	Zn - Te	$2 \cdot 10^{-3} - 5 \cdot 10^{-6}$			
1Zn 1Cd 2Hg	Zn - Te	0,032 - 0,007	172,0 cm⁻¹	173,0 cm⁻¹	15
2Zn 1Cd 1Hg	Zn - Te	$0,02 - 4 \cdot 10^{-4}$		175,3 cm⁻¹	16
1Zn 2Cd 1Hg	Zn- Te	$7 \cdot 10^{-3} - 2 \cdot 10^{-3}$		178,0 cm⁻¹	17
4Zn	Zn - Te	$1 \cdot 10^{-3} - 2 \cdot 10^{-6}$		181,7 cm⁻¹	18

Table 7. Interpretation of observed lines in FIR spectra of $Zn_xCd_yHg_{1-x-y}Te$

possible to conclude that 21 different modes are distinguished among the high resolution FIR-spectra of the seven composition of the $Zn_xCd_yHg_{1-x-y}Te$ alloys measured. By this way, the V-B random model developed for the quaternary alloys enable us to identify the observed structure of the sub-bands in the high resolution FIR-spectra for the $Zn_xCd_yHg_{1-x-y}Te$ alloys.

The next step is calculation of the OSS for certain dipole pairs. It is reason to consider the dependence on composition of the OSS for Zn-Te dipoles (the ZnTe contain is changed from 0.05 to 0.18). In Table 8 are shown calculated OSS for this dipoles.

Number of sample	x, mol	OSS for Zn-Te
I	0.02	0.065
VI	0.05	0.197
II	0.07	0.211
VII	0.12	0.769
V	0.18	0.907

Table 8. The oscillator strength sum for Zn-Te dipoles in measured samples of $Zn_xCd_yHg_{1-x-y}Te$

From Table 8 follow that OSS for Zn-Te dipoles is really approximately proportional to contain of ZnTe (values of x) in the $Zn_xCd_yHg_{1-x-y}Te$ alloys. Therefore, this important consequence of the V-B random model (Eqn.25) is fulfilled for the semiconductor quaternary alloys also.

4. Conclusion

Those, the high resolution FIR-spectra of the ternary HgCdTe and quaternary HgZnCdTe alloys obtained by using of the synchrotron radiation as source enable us to decipher the tangled phonon spectra in these kinds of the semiconductor solid solutions applying the random version of the V-B model for its interpretation.

The results described above can give affirmative answer on the question: whether geometry of chaos e.g. the Bernoulli equation is enough to describe the oscillator strengths of observed lines in FIR-spectra if the Additional Phonon Modes will be involved in sums of the oscillator strengths.

Presented here cycle of researches dedicated to the ternary $\text{Hg}_{1-x}\text{Cd}_x\text{Te}$ cannot confirm but allow us to assume that the HgTe-like CPMs for $x \leq 0.2$ are extending and dispersion relation should be exist for them (as was shown the data on Magnetophonon Resonance confirm this assumption (Sheregii & Ugrin, 1992)).

5. References

- Adachi Sadao, *Optical Properties of Crystalline Solids and Amorphous Semiconductors. Materials and Fundamental Principles*, Kluwer Academic Publishers, Boston, 1999
- Amirtharaj P.M., Dhart N.K, Baars J. and Seelewind H., *Semicond. Sci. Technol.* 5, S68 (1990)
- Baars J. and Sorgers F., *Solid State Commun.* 10, 875 (1972)
- Barker A.S. and Sievers J., *Rev. Modern Phys.* 47, S1 (1975)
- Biao Li., Chu J.H, Ye H.J., Guo S.P., Jiang W., Tang D.Y., *Appl.Phys.Lett.* 68, 3272 (1996)
- Cebulski J., Ge bicki W., Ivanov-Omskii V.I., Polit J., Sheregii E.M., *J. Phys.: Cond. Matter* 10, 8587 (1998)
- Cebulski J., Sheregii E. M., Polit J., Marcelli A., Piccinini M., Kisiel A., Kucherenko I., Triboulet R., *Appl. Phys. Lett.* 92, 121904 (2008)
- Cestelli Guidi M., Piccinini M., Marcelli A., Nucara A., Calvani P., Burattini E., *Journal of the Optical Society of America*, A22, 2810 (2005)
- Chandra D., Schaake H.F., Kinch M.A., *J. Electronics Materials*, 32, 810, (2003).
- Kosevich A.M., *The crystal lattice*, WILEY-VCH, Berlin-NewYork, (1999)
- Kozyrev S.P., L.K. Vodopyanov, R.Triboulet, *Phys. Rev. B*, 58, 3, 1374 (1998).
- Krause R., Klimakow A., Kiessling F.M., Polity A., Gille P., Schenk M., *J. Cryst.Growth.*, 101, 512 (1990)
- Marcelli A., Cesteli Guidi M., Piccinini M., Innocenzi P., Malfatti L., Xu W., *Phys. Stat. Sol.C*, 6, 1999 (2009)
- Pagès O., Souhabi J., Postnikov A. V., and Chafi A., *Phys. Rev. B* 80, 035204 (2009)
- Polit J., E.M. Sheregii, J. Cebulski, A. Marcelli, B. Robouch, A. Kisiel, A. Mycielski, *Phys. Rev. B*, 82, 014306 (2010)
- Rath S., Jain K.P., Abbi S.C., Julien C., Balkanski M., *Phys. Rev. B* ,52, 24, 17172 (1995)
- Robouch B., Kisiel A. and Sheregii E. M., *Phys. Rev B.*, 64, 073204 (2001)
- Sher A., Chen A.B., Spicer W.E. and Shih C.K., *J. Vac. Sci. Technol.* A3, 105 (1985)
- Sheregii E. M. and Ugrin Yu. O., *Sol. State Comm.*, 83, 1043 (1992)
- Sheregii E. M., J. Cebulski, A. Marcelli, M. Piccinini, *China J. Phys.*, 102, 045504 (2011)
- Sheregii E.M., Cebulski J., Marcelli A. and Piccinini M., *Phys. Rev. Lett.* 102, 045504 (2009)
- Sheregii E.M., J. Polit , J. Cebulski, A. Marcelli, M. Castelli Guidi, B. Robouch, P. Calvani, M. Piccinini,, A. Kisiel, I. V. Ivanov-Omskii, *Infrared Physics & Technology* 49, 13 (2006)
- Sussmann J.A. *J.Phys.Solids* ,28,1643,(1967)
- Talwar D.N., *J.Appl.Phys.* 56, 1601 (1984)
- Taylor D.W. in: Elliot R.J., Ipatova I.P. (Eds), *Optical properties of mixed crystals*, Elsevier Science Publishers, Amsterdam, pp. 35-131, (1988)

Verleur H.W. and Barker A.S., *Phys. Rev.* 149,715 (1966).

Ziman J.M., *Models of disorder*, Cambridge University Press, Cambridge, England, 1979

Effective Reaction Monitoring of Intermediates by ATR-IR Spectroscopy Utilizing Fibre Optic Probes

Daniel Lumpi and Christian Braunschier
Vienna University of Technology
Brenntag CEE GmbH
Austria

1. Introduction

The use of reaction monitoring in order to determine operation parameters in organic synthesis and pharmaceutical chemistry still commonly relies on off-line approaches. However, application of on-line or in particular in-line methodologies provides highly valuable data with respect to process optimization and scale-up (Bakeev, 2005; Rubin et al., 2006). This statement is especially true for time-resolved spectroscopic *in-situ* techniques, which allow to gain insights into key intermediate formation or structures, and therefore also provide valuable information for mechanistic considerations (Minnich et al., 2007; Wiss et al., 2006).

One of the major advantages of in-line techniques (both *in-situ* and real-time) over off-line approaches is that the investigation occurs inside the reaction system, thus eliminating sample alterations prior to analysis. These alterations during probing, including the loss of inertness or changes of reaction conditions, may result in erroneous readings; especially when directly compared to the (batch) process. This dramatically affects investigations at low temperatures. Both sampling and standard bypass approaches, which do not ensure constant thermal conditions in the course of analysis, potentially lead to incorrect results. For obtaining real-time information on chemical composition of samples in gas, liquid or solid phase, mid-infrared (IR) spectroscopy proved to be highly versatile, especially when performed with the attenuated total reflectance (ATR) technique (Grunwaldt & Baiker, 2005; Marziano et al., 2000; Minnich et al., 2007; Zogg et al., 2004).

In this chapter, we focus on in-line monitoring of both highly sensitive and reactive organic key intermediates (reagents) by mid-IR fibre probes based on the ATR technique (Fig. 1). At first, we give a short introduction to mid-IR spectroscopy (also briefly commenting on alternative spectroscopic methods), outline advantages of IR fibre optics as well as ATR technologies and provide a brief overview of fibres suitable for mid-IR fibre applications. The last part is intended to introduce the interested reader to fibre-optic probes available and typical characteristics, referring to literature about chemical and physical properties of modern IR fibre materials, showcasing potential areas of application.



Fig. 1. Mid-IR fibre and ATR probe (left) and IR probe focused on the ATR element (right).

In the second part, we report on recent results of in-line investigations successfully utilizing mid-IR fibres on organometallic species. Hence, explorations on the formation of sodium alkoxy intermediates (performed in our group, Lumpi et al.) and their impact on reaction optimizations towards monodisperse oligo (ethylene glycols) are outlined. Subsequently, we switch to monitoring of organolithium compounds. In these projects Weymeels et al. as well as Gupta et al. were able to demonstrate ATR-IR fibre probe applications on metallation reactions and Lumpi et al. on metal halogen exchange reactions under cryogenic conditions.

2. Monitoring by mid-infrared spectroscopy

Spectroscopy in the mid-infrared of a spectral range from approximately 4000 cm^{-1} to 400 cm^{-1} ($2.5\text{ }\mu\text{m}$ to $25\text{ }\mu\text{m}$) emerged as an effective tool for both qualitative and quantitative analysis. Within this range most of the fundamental molecular vibrations, the first overtones and combination frequencies occur. These typically relatively sharp absorption bands generally possess high absorption coefficients. Not only do these desirable spectroscopic properties facilitate an identification of molecules by its specific spectral “fingerprint”, but also comprise valuable structural information (e.g. functional groups, substitution patterns, etc.) (Melling & Thomson, 2002).

The distinctive absorption bands associated with individual molecules enable the analysis of individual components in even complex mixtures by either evaluating isolated bands or by applying modern chemometric methods (e.g. Principal compound analysis), which process the entire spectral information. As a consequence, mid-IR spectroscopy represents a widely applicable tool for investigations of dynamic processes (e.g. chemical reactions, phase transitions, sedimentations, etc.). Moreover, information about interactions of the analyst with the surrounding media can be acquired because vibrational modes tend to be affected by the molecule’s environment (Raichlin & Katzir, 2008).

Therefore, from many perspectives, mid-IR spectroscopy provides clearly more information than spectroscopy in other regions of the spectrum, such as the visible or the near-infrared range (Raichlin & Katzir, 2008).

2.1 Mid-infrared optical fibre probes

Modern-technology fibre optics offers important and versatile tools in spectroscopy. In the field of vibrational spectrometry fibre optics had a great influence on near-IR and Raman spectroscopy. The development of mid-IR transparent fibres (discussed in chapter 2.3) in the last decades had a significant impact on IR methods (Lendl & Mizaikoff, 2002). The fibre application makes it possible to overturn the established method of analyzing samples

within the typically stationary IR spectrometer by enabling the direct placement of the fibre-optic probe inside the reaction system of interest (Melling & Thomson, 2002).

The technologies of mid-IR spectroscopy providing highly relevant physico-chemical information, and the flexibility of fibre-optic probes offering new possibilities of application to measure samples in gas, liquid and solid phase, result in a breakthrough in molecular spectroscopy. Nowadays, spectroscopy utilizing IR fibre probes is routinely used in research laboratories, process development facilities and industrial quality control. This routine application can be explained by the fact that data, often not available by other methods, can be conveniently acquired (Melling & Thomson, 2002).

Additionally, ATR-based mid-IR fibre optic probes represent an entirely non-invasive technique, which has recently been shown to be a promising tool e.g. for biotechnological applications (Mazarevica, 2004) and, even more impressively, for obtaining spectroscopic information *in vivo* (Brancaleon et al., 2000).

In principle, the sensor constructions rely on five basic sensing schemes: transmission, reflection, grazing angle reflection, attenuated total reflection (ATR), and a variant of the ATR effect known as the fibre-evanescent wave sensor (FEWS) (Melling & Thomson, 2002). The investigations described in chapters 3 and 4 are based on the use of the ATR technique, focusing on its advantageous properties, especially in terms of mechanical robustness.

2.2 Attenuated total reflection

The majority of reported mid-IR fibre probes rely on the well-established attenuated total reflection (ATR) technique, revealing many advantages in the general applicability over e.g. absorption measurements in short pathway flow cells. In the ATR method only a thin film (a few micrometers) at the proximity of the ATR element is subject to the measurement. The thickness of the analyzed film is defined by the penetration depth of the evanescent field (Fig. 2).

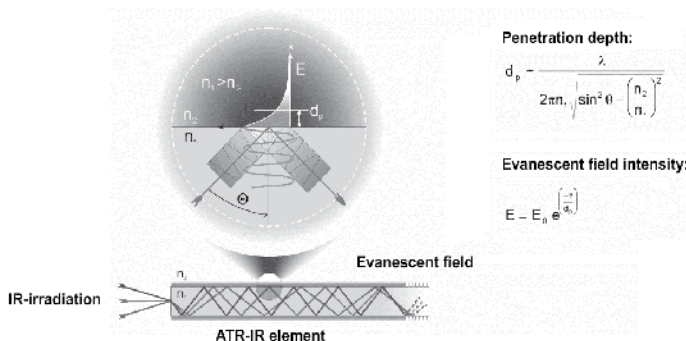


Fig. 2. Principle of total reflection of an infrared beam at the boundary of the ATR element to a medium with lower refractive index $n_2 < n_1$ (n_1 , n_2 , refractive indices; θ , angle of incidence; E , exponentially decaying evanescent field; d_p , penetration depth; λ , wavelength of incident radiation). Figure reproduced from Mizaikoff & Lendl, 2002.

The interactions of the incident and the internally reflected electromagnetic waves generate an exponentially decaying evanescent field, which penetrates the adjacent medium to a

certain depth. The depth of penetration depends on the irradiation wavelength, the incident angle and the refractive indices of both the ATR element and the contact medium. The equations describing this behavior are given in Fig. 2 (Mizaikoff & Lendl, 2002).

2.3 Infrared transparent fibres

This chapter gives a brief insight into the most important, for the main part commercially available, IR fibre optics. Detailed reviews on IR fibres are given in the literature by J.A. Harrington (Harrington, 2010) and, with a special focus on mid-IR applications by B. Lendl and B. Mizaikoff (Lendl & Mizaikoff, 2002).

The basic requirements for mid-IR fibres include physical properties such as transparency over the spectral range requested for the intended investigations, robustness (mechanically), stability (thermally and chemically) as well as adequate flexibility (Lendl & Mizaikoff, 2002). The characteristic of the optical transparency is typically evaluated by focusing on relevant loss mechanisms. The most important losses include intrinsic and extrinsic losses, Fresnel losses and bending losses (Sanghera & Aggarwal, 1998, as cited in Lendl & Mizaikoff, 2002). Available mid-IR fibre optics meet these challenges to different extents.

First developments on non-silica based IR transparent fibres from chalcogenide glasses, mainly arsenic sulphide, were published in 1965, exhibiting losses higher than 10 dB/m (Kapany & Simms, 1965, as cited in Harrington, 2010). Due to an elevated demand for IR fibres in short-haul applications increased research efforts were reported from the mid-1970s onwards (Harrington, 2010). Up to date, both optical and mechanical characteristics of IR fibres cannot compete with silica fibres (which are not applicable in the mid-IR region due to a transmission only up to approximately 2.5 μm). Losses in the range of a few decibels per meter still limit these to short-haul applications. Nevertheless, modern mid-IR fibres for short-haul have already enabled a broad variety of developments in spectroscopy and important usage in practical (e.g. medical) applications (Minnich et al., 2007, and references therein).

A logical categorization of the most important IR fibres can be illustrated as follows: glass, crystalline and hollow waveguides. Table 1 outlines this categorization also providing further subdivision based on materials and structures (Harrington, 2010).

Main	Subcategory	Examples
Glass	Heavy metal fluoride (HMFG)	ZrF ₄ -BaF ₂ -LaF ₃ -AlF ₃ -NAF (ZBLAN)
	Germante	GeO ₂ -PbO
	Chalcogenide	AsS ₃ and AsGeTeSe
Crystal	Polycrystalline (PC)	AgBrCl
	Single crystal (SC)	Sapphire
Hollow waveguide	Metal/dielectric film	Hollow glass waveguide
	Refractive index <1	Hollow sapphire at 10.6 μm

Table 1. Categories of the most important of IR fibers; data reproduced from Harrington, 2010.

A graphical comparison of attenuation losses of the most relevant mid-IR fibres is given in Fig. 3. Among these, materials suitable for optic chemical sensor applications in liquid phase

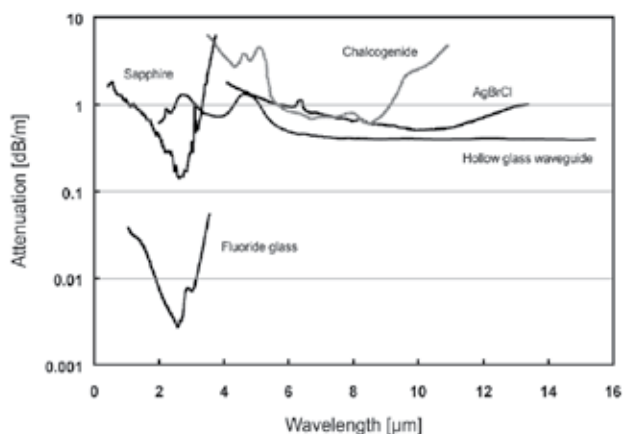


Fig. 3. Composite loss spectra for some common IR fibre optics: ZBLAN fluoride glass, SC sapphire, chalcogenide glass, PC AgBrCl, and hollow glass waveguide; plot reproduced from Harrington, 2010.

(e.g. reaction mixtures), relying on the evanescent wave principle, are AgBrCl, sapphire, chalcogenide and HFMG (Harrington, 2004). Polycrystalline silver halide fibres have been shown to be a promising candidate for mid-IR (ATR) fibre probes, especially for measurements at wavelength $> 10 \mu\text{m}$ (Brandstetter, 2009).

The combination of the flexible structure and IR transmission of AgBrCl fibres ensures a convenient analytical approach; thus, also being applied in investigations presented later in this chapter.

2.4 Alternative spectroscopic methods for reaction monitoring

Besides IR spectroscopy, RINMR (rapid injection nuclear magnetic resonance) experiments also received considerable attention in the field of spectroscopic investigations of highly reactive species, especially under cryogenic conditions. The RINMR methodology, often based on the developments of J. F. McGarrity (McGarrity, 1981), C. A. Ogle and H. R. Loosli was successfully applied by several research groups to investigate reactive intermediates also at low temperatures and short time scales. In contrast to conventional NMR studies the rapid injection design relies on a piston-driven syringe injection assembly above the vessel inside the bore of the spectrometer magnet. This setup simultaneously provides turbulent mixing in the sample. In their first studies McGarrity et al. could establish that butyllithium in THF exists in equilibrium of the tetramer and the dimer complex with the proportion of dimer increasing as the temperature is decreased (McGarrity, 1985a). Moreover, kinetic examination proved that the dimeric butyllithium is more reactive toward the applied electrophiles than the tetramer by a factor of 10 (McGarrity, 1985b). Improved designs of RINMR systems implementing features such as multiple reactant and faster rapid injection were developed in the last decade by P. J. Hore et al., H. J. Reich et al. and S. E. Denmark et al.

In conclusion, RINMR is a powerful tool for monitoring reactive intermediates, directly providing highly relevant structural data. However, the experimental complexity of this technique, in contrast to ATR-IR fibre probe applications, certainly limits its versatility.

2.5 Reaction monitoring of organometallic compounds

As mentioned before, the scientific results discussed in this contribution focus on monitoring of reactive organometallic species by ATR-IR spectroscopy utilizing mid-IR fibre probes. While alkoxide species, the conjugated base of an alcohol, are rather generally applied in synthetic chemistry (e.g. bases, nucleophiles and ligands) organolithium compounds require further introduction.

Since W. Schlenk and J. Holtz reported on the first syntheses of organolithium species in 1917 these powerful reagents or intermediates have gained enormous importance in the field of synthetic and pharmaceutical chemistry (Rappoport & Marek, 2004; Wu & Huang, 2006). Synthetic operations are generally carried out at low temperatures as a consequence of the high reactivity of lithium reagents; in some specific examples even below $-100\text{ }^{\circ}\text{C}$ (Rappoport & Marek, 2004). Nowadays, modern lithiation chemistry represents a well-established technique also receiving considerable attention in industrial processes (Rathman & Bailey, 2009; Wu & Huang, 2006). Despite the broad application of cryogenic temperature reactions dynamic analysis in order to monitor reactive lithium species remains a challenging task.

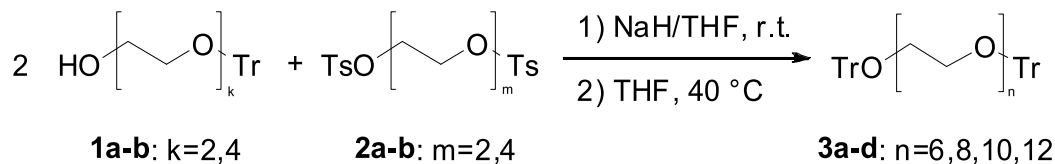
3. *In-situ* IR monitoring of alkoxides

In this chapter, we focus on monitoring the formation of alkoxides, as this is an important intermediate for the synthesis of ether and ester containing substances. The conventional approach is to transform deprotonated moieties, followed by classical analytical methods (e.g. thin layer chromatography, HPLC or NMR spectroscopy). There are only limited descriptions of in-line methods in the literature, therefore an investigation is of high interest.

3.1 Introduction

A study (Lumpi et al., 2009) is presented in detail, where the usage of in-line ATR-IR was demonstrated in order to optimize the synthesis of monodisperse oligo(ethylene glycols) (OEG). This substance class has a wide range of applications in many fields of science and industry. They can be used as synthons for crown ether-type derivatives, as non-ionic surfactants, as templates for the synthesis of porous inorganic materials, and, more recently, functional mono-layers were applied to develop biocompatible material. The physical and chemical properties of these modified materials often depend to a large extent on the number of repetition units of the OEG moiety. For a systematic investigation of the influence of chain length, novel polystyrene-oligo(oxyethylene) graft copolymers containing monodisperse OEG units have been synthesized (Braunshier et al., 2008). For the preparation of these resins, access to well-defined oligo(ethylene glycols) of up to 12 units was required. Despite the widespread utility of OEGs, their synthesis remains a challenging task. The published synthetic methods for commercially unavailable or expensive representatives ($n > 4$) are usually time-consuming and/or include extensive purification procedures. The most efficient strategy for synthesis of OEGs is based on bidirectional chain elongation (Keegstra et al., 1992).

Based on this approach, the key steps should be optimized in order to shorten reaction times from periods as long as several days to more acceptable values. The formation of corresponding alkoxides by deprotonation of mono-trityl protected glycols **1a-b** (first



Scheme 1. Synthesis of glycols **3a-d**. Scheme reproduced from Lumpi et al., 2009.

reaction step shown in Scheme 1) is reported to take at least 18 h to reach completion. To prove this information, it was necessary to monitor the conversion in an inert, anhydrous reaction medium. Due to the lack of other proper methods of analysis, a mid-IR fibre optic probe was chosen for fast in-line monitoring of the chemical reaction under investigation.

3.2 Technical details

The ATR fibre system was built up by a FT-IR spectrometer Bruker Matrix F® in connection with an ATR fibre probe (A.R.T. Photonics, Berlin; Ø 12 mm) and a MCT (mercury cadmium telluride) detector (Belov Technology, Co., Inc.). The probe was directly inserted through the ground neck of the reaction vessel and comprised two 1 m silver halide fibres (Ø 1 mm) connected to a conical two bounce diamond ATR element housed in a rod of hastelloy. Using this set-up it was possible to follow the reactions to be studied in real-time covering a spectral range from 600 to 2000 wavenumbers.

3.3 Inline monitoring

Two possibilities for the analysis of the obtained data have been applied. Single band analysis on the one hand, and multivariate curve resolution on the other hand.

3.3.1 Single band analysis

Determination of reaction progress by tracking changes in absorbance values at selected wavenumbers is described. Absorbance values at characteristic wavenumbers for the substrate and the product respectively are plotted against reaction times in Figure 4.

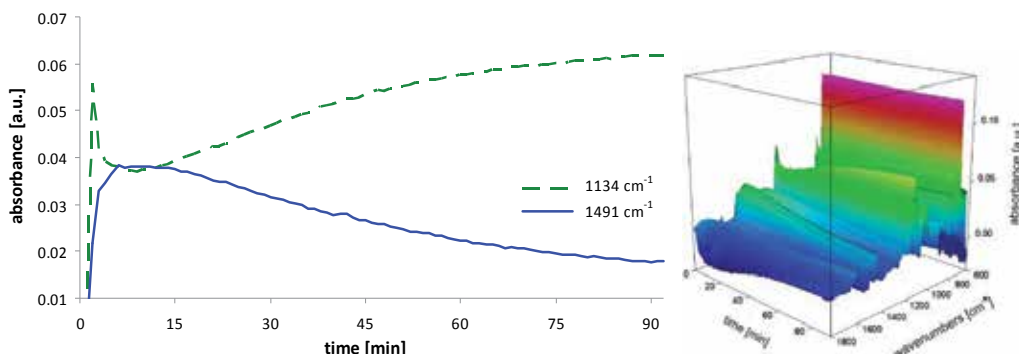


Fig. 4. (a) Left: ATR-IR in-line monitoring for the deprotonation of 13,13,13-triphenyl-3,6,9,12-tetraoxatridecanol (substance **1b**). Distortions for $t \leq 10$ min are attributed to equilibration effects (temperature and concentration). (b) Right: Representative 3-D example of measurement. Figure reproduced from Lumpi et al., 2009.

The blue curve derives from the starting alcohol; the green graph originates from the deprotonated moiety. The graph clearly shows that after 90 min no significant changes of absorption values can be observed, thus being an indication for the end of the reaction.

3.3.2 Multivariate curve resolution

Multivariate curve resolution – alternating least squares (MCR-ALS) – was additionally applied for the analysis of the IR data set. MCR-ALS is a modern chemometric method for the resolution of multiple component responses in unknown unresolved reaction mixtures (Tauler, 1995). This technique decomposes the recorded data set into smaller matrices containing information on the spectra and the concentration profiles of each component involved in the reaction. MCR-ALS can be applied to the analysis of a global instrumental response such as a set of mid-IR spectra recorded from a chemical reaction over time. In this case a matrix D ($n \times w$) is obtained with n being the number of spectra and w representing the number of wavelengths. The MCR technique has the target to decompose D into the pure contributions of the components of the reaction according to the equation:

$$D = CS^T + E \quad (1)$$

C contains the concentration profiles for all involved compounds and S^T represents the corresponding spectra. MCR-ALS solves this equation in an iterative, alternating least squares manner by minimizing the residual matrix E . For the MCR analysis the data matrix D may be augmented with pure component spectra. Furthermore, several data sets may be analyzed simultaneously. During calculation meaningful constraints may be applied with the aim to guide the iteration process toward a mathematically as well as chemically meaningful solution.

Despite all advantages, MCR-ALS algorithms written in MATLAB have the disadvantage of how the selected constraints are implemented in the execution of the MATLAB routine. This process can be troublesome and sophisticated, particularly in complex cases where several data matrices are simultaneously analyzed and/or different constraints are applied. In order to overcome these difficulties and taking advantage of the better MATLAB tools to create graphical user interfaces, an improved MCR-ALS toolbox with a user-friendly graphical interface was presented by Jaumont et al., 2005.

Examples for meaningful constraints in the chemical system under investigation in the paper by Lumpi et al., 2009 are non-negativity of concentrations and spectral intensities as well as unimodality. As a result, quantitative information on the amount of spectral contribution of each component in every spectrum of the data set is obtained. 99.72 % of the spectral variance of the recorded data could be explained with two components. Therefore it was concluded that the two components needed to be considered in modeling the data set, as shown in Figure 5. The reaction under study came to completion after 90 minutes.

3.4 Results and discussion

Both techniques for IR data analysis presented, showed clearly that time for deprotonation is much shorter than described in the literature. The subsequent nucleophilic reaction of the alkoxides with the tosylated glycols **2a-b** lead to substances **3a-d**.

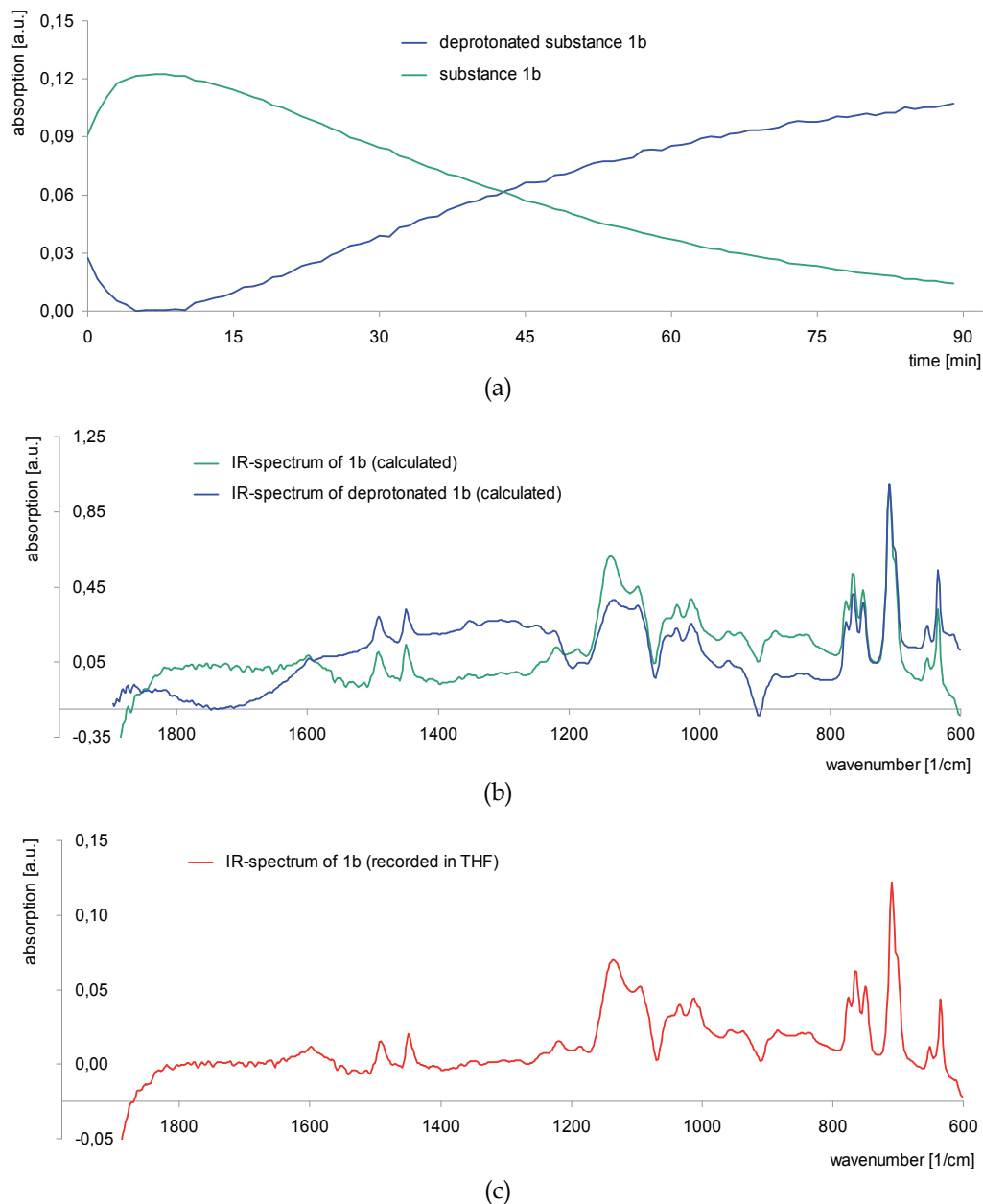
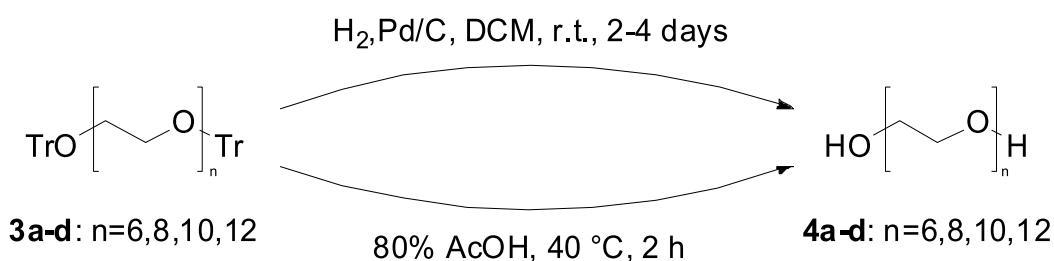


Fig. 5. MCR-ALS calculations of the deprotonation of trityl-protected 1b; (a) calculated absorption profiles, (b) spectra calculations, (c) pure substance 1b spectrum. MCR-ALS-Parameters: [efa_matrix]=efa(dep10,90); min value of log efa plot=1; number of factors=2; als2004; Data matrix=dep10; Init estimate=efa_matrix; Non negative Concentration nnls; number of spec with non neg=2; spec equal height; Plots are optimum in the iteration Nr. 935 Std.dev of residuals vs. exp. data=0.0011238 Fitting error (lack of fit, lof) in %(PCA)=2.8319e-014 Fitting error (lack of fit, lof) in %(exp)=4.881 Percent of variance explained at the optimum is=99.7618. Figure reproduced from Lumpi et al., 2009.

Entry	Glycol	Tosylate	Time	Product	Yield
	1	2	h ^a	3	%
1	1a	2a	4/84	3a	98
2	1a	2b	4/84	3b	97
3	1b	2a	2/60	3c	98
4	1b	2b	2/60	3d	95

Table 2. Reaction times and yields for the preparation of substances **3a-d**. ^aTimes given refer to deprotonation and overall reaction time respectively. Modified from Lumpi et al., 2009.

To obtain the target compounds (OEGs **4a-d**), the protecting groups have to be cleaved off. Virtually all published procedures use hydrogenolysis under high-pressure conditions in the presence of palladium for several days to achieve this final transformation. Apart from long reaction time, this procedure suffers from some more disadvantages. The most serious one is the need for equipment allowing to perform gas reactions under high pressure, which might be a limiting factor. Moreover, the use of halogenated organic solvents, e.g. dichloromethane and transition metal catalysts, might become troublesome, if the final product is intended to be used in the field of pharmaceuticals or biology, especially when the procedure is performed on industrial scale.



Scheme 2. Synthesis of glycols **4a-d**; hydrogenolysis *vs.* acidic cleavage. Scheme reproduced from Lumpi et al., 2009.

In the work presented, this deprotection step was substituted for a safe, fast and inexpensive procedure. Acidic cleavage by acetic acid in water for only 2 h was performed to obtain the pure OEGs. Comparing this new protocol to hydrogenolysis, the advantages are the following: dramatically shortened reaction times (2 h *vs.* 4 days), easier work-up and higher product quality. In summary, an optimized protocol for the synthesis of monodisperse OEGs up to 12 units has been reported. In contrast to other approaches described in the literature, neither special equipment for high pressure hydrogenolysis nor any chromatographic purification is needed for the key steps of the sequence. In-line ATR-IR spectroscopy was shown to be a powerful analytical tool for the effective monitoring of such “problematic” processes.

4. *In-situ* monitoring in organolithium chemistry

4.1 Introduction

In this chapter, we describe monitoring in organolithium chemistry, one of the most important fields within organic synthesis, especially for the functionalization of

heteroaromatic substances. They are applied in many fields of chemistry, either for pharmaceuticals or as building blocks for various applications within materials science, e.g. in Organic Light Emitting Transistors (OLET). As a matter of fact, extensive efforts have been applied to a variety of synthetic methodologies. The most prominent strategy is based on lithium moieties, formed through deprotonation, which allows multiple functionalizations. Organolithium chemistry is known to be highly sophisticated due to the fact that analytical methods for the monitoring of reactive intermediates, often only stable at low temperatures, are rare. Furthermore, side reactions related to the aggregation state and structures of the reactive species are common. Over the last years, only a few studies on monitoring of metallation by in-situ infrared spectroscopy have been carried out (Kondo et al., 1999; Sun & Collum, 2000; Pippel et al., 2001; Zhao & Collum, 2003). One reason might be that IR spectroscopy is preferred mostly for strong absorbing groups, like carbonyl moieties, which are often missing in heteroaromatics. Some of the most important reagents for lithiation are *n*-butyllithium (BuLi), lithium tetramethylpiperidine (LTMP) and lithium diisopropylamide (LDA), which have been selected in the following examples.

4.2 *In-situ* infrared studies applying BuLi and LTMP

Here, the work of Weymeels et al., 2005, in which the kinetics and mechanism of the deprotonation of 3,5-dichloropyridine by lithium tetramethylpiperidine (LTMP) and *n*-butyllithium (BuLi) were investigated.

4.2.1 Technical details

The IR spectra were recorded with a ReactIR4000 equipped with a DiComp ATR probe (ASI Applied Systems, Mettler Toledo). The following steps of the experiments have been performed: (1) THF was cooled to -75°C ; (2) the spectral baseline was reset to zero and the spectra recording was started; (3) the substrate was added; (4) the base was added dropwise; and (5) the reaction was quenched by deuterium oxide.

4.2.2 Results and discussion

The absorption bands of 3,5-dichloropyridine instantly decreased upon the addition of the base. As a result, the absorbance values associated with the aryllithium species appeared. By comparing the absorbance bands obtained using LTMP (Fig. 6(a)) and BuLi (Fig. 6(b)), it is clearly visible that two values (753 and 1007 cm^{-1}) out of the three attributed to 3,5-dichloro-4-pyridyllithium are identical, while the third (1139 cm^{-1} using LTMP and 1143 cm^{-1} using BuLi) is different. A possible explanation was that lithium bears different ligands, which is even more sophisticated due to the presence of the ring nitrogen atom. Studies comparing the consumption of LTMP and BuLi respectively for achieving quantitative protonation have been applied. It was assumed that a competitive formation of a complex between the generated aryllithium and LTMP could be responsible for different consumptions (1,25 equiv. LTMP *vs* 1,0 equiv. BuLi). To sum up, transition structures between the substrate and the lithio derivative could be detected by using IR in-situ monitoring. Moreover, IR monitoring assured that reaction conditions (time, temperature, number of equivalents) had been selected in a right way. This is a crucial requirement to circumvent overestimation, which can be a source of degradation and/or competitive reactions.

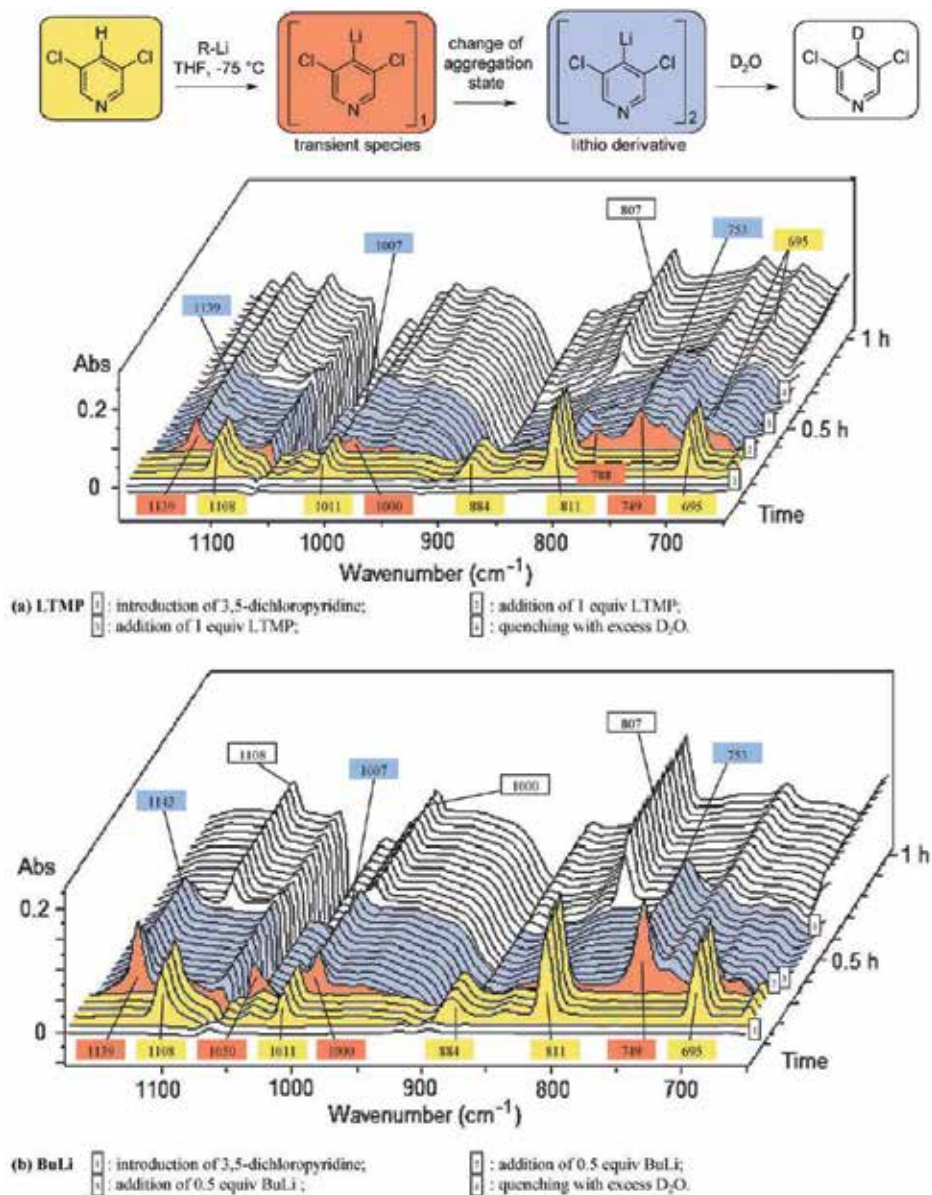


Fig. 6. Progression of the reaction between 3,5-dichloropyridine and (a) LTMP or (b) BuLi, and subsequent deuteration. Figure reproduced from Weymeels et al., 2005.

4.3 In-situ studies applying LDA

Lithium diisopropylamide (LDA) is the most prominent and preferred reagent for reactions requiring a strong non-nucleophilic base, therefore being one of the most important reagents in organic chemistry (Collum et al., 2007). The central importance of LDA motivated several research teams to examine mechanism and transition state as well. Based on ATR-IR spectroscopy Collum et al. presented some studies on lithiation reaction.

The topic of the presented contribution (Gupta et al., 2008) is ortholithiation on a range of arenes mediated by LDA in combination with catalytic amounts of LiCl (0.5% relative to LDA). The lithiation reactions were monitored using in-situ IR spectroscopy following both the disappearance of the arene and the formation of the resulting aryllithium moiety. In addition, ^{19}F NMR spectroscopic analysis was performed, providing comparable results. The challenge was to monitor the Li-species as sensitive key intermediate, only stable at cryogenic temperatures. Therefore classical analytical methods could not be applied.

4.3.1 Technical details

The spectra were recorded by applying an in-situ IR spectrometer fitted with a 30-bounce, silicon-tipped probe. The spectra were acquired in 16 scans, and a representative reaction was carried out as follows: The IR probe was inserted into an oven-dried, cylindrical flask fitted with a magnetic stir bar and a T-joint. The T-joint was equipped with a septum for injections and a nitrogen line for inertness.

4.3.2 Results and discussion

Reaction rate studies investigating the effect of the LiCl and other lithium salts as catalyst were performed. Furthermore, the effect of the influence of the substrate was part of the study. In conclusion, despite some detected irregularities, the obtained results might be important for industrial application. Rate variations that go undetected in the lab could give way to unexpected and potentially costly variations on production scales. A representative example of in-situ monitoring is shown in Figure 7. A significant difference in the half-lives ($t_{1/2}$) can be identified, indicating an acceleration of the lithiation by addition of LiCl.

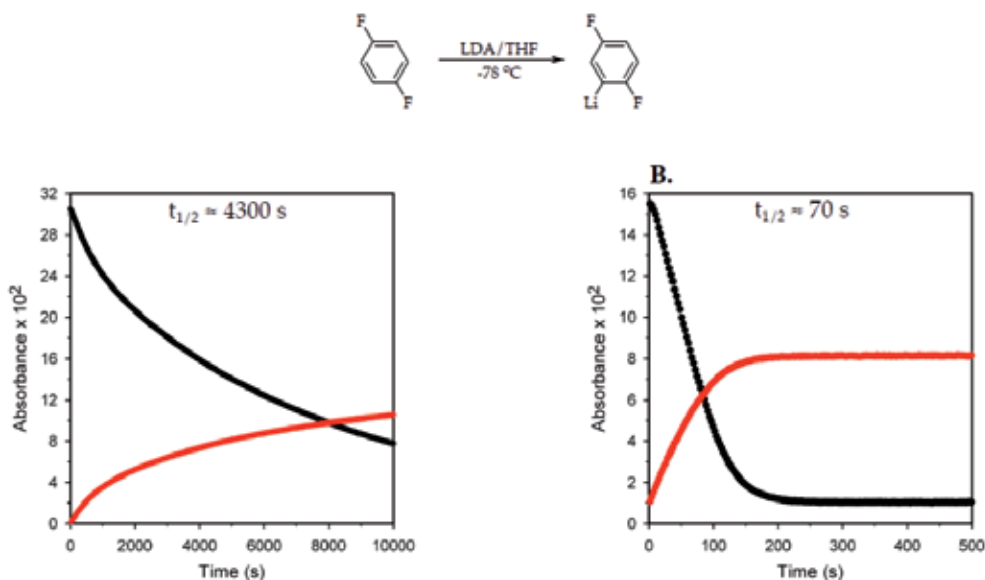


Fig. 7. Plot of IR absorbances (black – 1507 cm⁻¹, red – 1418 cm⁻¹) versus time for the ortholithiation of 1,4-difluorobenzene (0.10 M) with LDA (0.12 M) in THF at -78 °C: (A) no added LiCl; (B) 0.5 mol% LiCl. Figure reproduced from Gupta et al., 2008.

4.4 Investigations of metal halogen exchange reactions

In contrast to the previous chapters dealing with the deprotonation (metallation) of the substrate this chapter focuses on metal halogen exchange reactions towards the desired organolithium intermediates using BuLi. This type of reaction is of particular importance for the selective synthesis of certain substitution patterns (Rappoport & Marek, 2004).

The outlined contribution (Lumpi et al., 2012) presents investigations on metal halogen exchange reactions by inline monitoring of organolithium species under both inert and cryogenic conditions. Starting from relatively simple substrates the exploration of a complex Halogen Dance reaction sequence was realized, which allows the convenient synthesis of precursors for e.g. thiophene ring-opening reactions (Bobrovsky et al., 2008). In order to acquire reliable spectroscopic data *via* an optical ATR-IR fibre probe a procedure to correct the effects of (co-)sine type fringes, which are observed during the fast and exothermic metal halogen exchange reactions, has been developed.

4.4.1 Technical details

The instrumental setup was identical to the setup described in chapter 3.2. The fibre probe was mounted through a ground neck into a 4-neck round bottom flask, which was subsequently charged with dry solvent and cooled *via* a cooling bath. After a steady temperature in the vessel was reached a background spectrum was recorded, the measurement started and the lithium species added. Finally, the respective reactant was rapidly added *via* a syringe.

4.4.2 FFT correction procedure

Temperature deviations between the sample spectra and the background acquired during dynamic reaction processes represent one of the major challenges in IR spectroscopy at cryogenic temperatures. During these investigations the application of an ATR-IR fibre probe to relatively fast and exothermic metal halogen exchange reactions resulted in spectra heavily overlaid with (co-)sine-type artifacts. The introduced fringes lead to spectral data not utilizable for further interpretation.

To overcome these limitations a correction procedure based on fast Fourier transformation (FFT) was implemented to the data evaluation process. This high pass filter significantly reduced the fringes (attributed to differing thermal expansion coefficients of the probe materials) and rendered it possible to achieve a reliable monitoring of metal halogen exchange reactions at temperatures even below $-80\text{ }^{\circ}\text{C}$.

4.4.3 Results and discussion

An application of the developed methodology to simple substrates for metal halogen exchange reactions but also to metallation procedures afforded reliable results. Thus, the technique was utilized for a detailed kinetic investigation of a double-sided Halogen Dance (Fig. 8, A) reaction towards 4,4'-dibromo-2,2'-bithiophene (Bobrovsky et al., 2008).

In this multi-step sequence (Fig. 8, A) the first metallation could be shown to proceed faster than the second lithiation towards **3** leading to an accumulation of intermediate **2** (Fig. 8, B). This assumption of the first reaction step exclusively consuming LDA to form **2** and the second Halogen Dance being realized in a next step leading to **3** could be verified by a

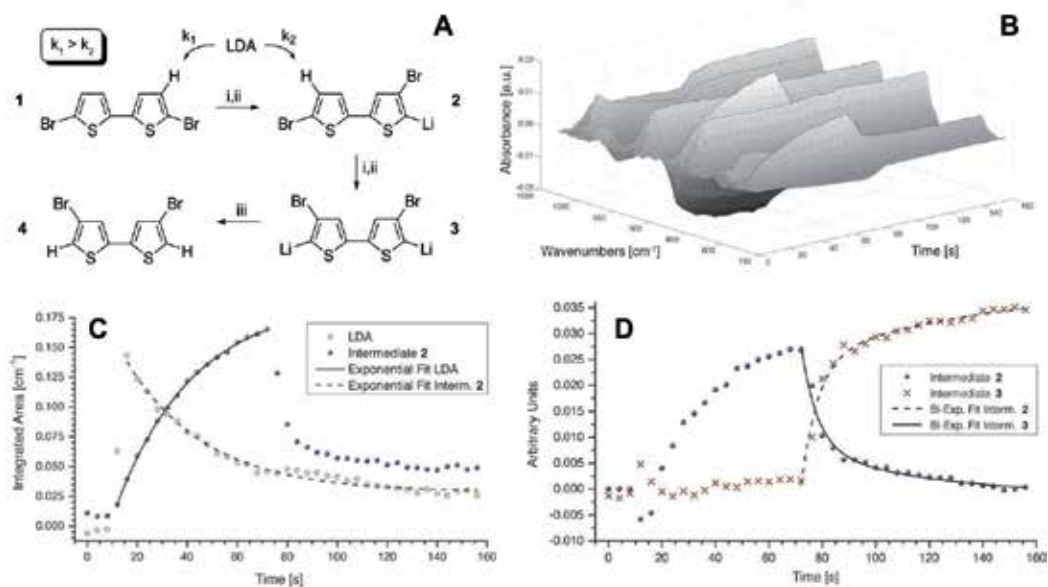


Fig. 8. Double-sided Halogen Dance reaction; A: reaction scheme; LDA (2.5 equiv.), $-40\text{ }^{\circ}\text{C}$. i: metallation reaction, ii: Halogen Dance reaction, iii: excess of methanol; B: 3D plot of spectra ($750 - 1050\text{ cm}^{-1}$) recorded during reaction progress (0 - 160 s); C: monitoring of Li-species LDA and intermediate 2; D: intermediate 3 formation as extracted from the spectral data set via MCR-ALS algorithm. Figure reproduced from Lumpi et al., 2012.

good agreement of kinetic parameters of LDA consumption and intermediate formation (Fig 8, C).

Due to overlapping absorption bands the MCR-ALS algorithm (chapter 3.3.2.) was applied to the spectral data set prior to analysis in order to compare the consumption of intermediate 2 and the formation of product 3 (Fig 8, D). The results again disclose a good agreement of kinetic data supporting the aforementioned conclusion, being highly valuable for potential application of this reaction (e.g. sequential Halogen Dance).

In summary, a methodology utilizing an FFT based correction procedure for a convenient monitoring of metal halogen exchange (but also metallation) reactions is presented. By applying this technique a mechanistic investigation of a complex double-sided Halogen Dance reaction could be realized.

5. Conclusion

In conclusion, it has been demonstrated that mid-infrared (ATR) spectroscopy utilizing modern optical fibre probes is an effective methodology for in-line monitoring of highly reactive species. Therefore, this non-invasive technique has emerged as a versatile tool for direct reaction monitoring, which was outlined using the example of organometallic intermediates.

6. References

- Bakeev, K. A. (Ed.). (2005). *Process Analytical Technology - Spectroscopic tools and implementation strategies for the Chemical and Pharmaceutical Industries*, Blackwell Publishing Ltd., ISBN 9781405121033, Oxford/UK
- Bobrovsky, R.; Hametner, C.; Kalt, W. & Froehlich J. (2008). Selective Halogen Dance Reactions at 5,5'-Dibromo-2,2'-bithiophene. *Heterocycles* Vol.76, No.2, pp. 1249-1259, ISSN: 0385-5414
- Brancaleon, L.; Bamberg, M. P. & Kollias, N. (2000). Spectral differences between stratum corneum and sebaceous molecular components in the mid-IR. *Applied Spectroscopy*, Vol.54, No.8, pp. 1175-1182, ISSN 0003-7028
- Brandstetter, M. (2009). Ultrasonically enhanced in-line Attenuated Total Reflection (ATR) infrared absorption spectroscopy of suspensions, Diploma Thesis, Institute of Chemical Technologies and Analytics, Vienna University of Technology, Vienna
- Braunshier, C.; Hametner, C.; Froehlich, J.; Schnoeller, J. & Hutter, H. (2008). Novel monodisperse PEG-grafted polystyrene resins: synthesis and application in gel-phase ¹³C NMR spectroscopy. *Tetrahedron Letters* Vol.49, pp. 7103-7105, ISSN: 0040-4039
- Collum, D. B.; McNeil, A. J. & Ramirez, A. (2007). Lithium Diisopropylamide: Solution Kinetics and Implications for Organic Synthesis. *Angewandte Chemie International Edition* Vol.46, pp. 3002 - 3017, ISSN 1521-3773
- Grunwaldt, J. -D. & Baiker, A. (2005). In situ spectroscopic investigation of heterogeneous catalysts and reaction media at high pressure. *Physical Chemistry Chemical Physics*, Vol.7, No.20, 3526-3539, ISSN 1463-9084
- Gupta, L.; Hoepker, A. C.; Singh, K. J. & Collum, D. B. (2008). Lithium Diisopropylamide-Mediated Ortholithiations: Lithium Chloride Catalysis. *Journal of Organic Chemistry* Vol.74, pp. 2231-2233, ISSN 0022-3263
- Harrington, J. A. (2004). Introduction to Infrared Fiber Optics, In: *Infrared Fibers and Their Applications*, J. A. Harrington, SPIE Press, Bellingham, ISBN 978-0819452184
- Harrington, J. A. (2010). Infrared Fibres, In: *Handbook of Optics* (3rd Ed.), M. Bass (Ed.), 12.1-12.13, The McGraw-Hill Companies, ISBN 978-0-07-163314-7
- Jaumot, J.; Gargallo, R.; de Juana, A. & Tauler, R. (2004). A graphical user-friendly interface for MCR-ALS: a new tool for multivariate curve resolution in MATLAB. *Chemometrics and Intelligent Laboratory Systems* Vol.76, pp. 101-110, ISSN 0169-7439
- Keegstra, E. M. D.; Zwikker, J. W.; Roest, M. R. & Jennekens, L. W. (1992). A highly selective synthesis of monodisperse oligo(ethylene glycols). *Journal of Organic Chemistry* Vol.57, pp. 6678-6680, ISSN 0022-3263
- Lendl, B. & Mizaikoff, B. (2002). Optical Fibers for Mid-infrared Spectrometry, In: *Handbook of Vibrational Spectroscopy*, J. M. Chalmers & P. R. Griffiths (Eds.), John Wiley & Sons Ltd., ISBN 0471988472, Chichester
- Lumpi, D.; Braunshier, C.; Hametner C.; Horkel, E.; Zachhuber, B.; Lendl, B. & Froehlich J. (2009). Convenient multigram synthesis of monodisperse oligo(ethylene glycols): effective reaction monitoring by infrared spectroscopy using an attenuated total reflection fibre optic probe. *Tetrahedron Letters* Vol.50, pp. 6469-6471, ISSN: 0040-4039
- Lumpi, D.; Wagner, C.; Schoepf, M.; Horkel, E.; Ramer, G.; Lendl, B. & Froehlich J. (2012). Fibre optic ATR-IR spectroscopy at cryogenic temperatures: in-line reaction

- monitoring on organolithium compounds. *Chemical Communications* Vol.48, pp. 2451–2453, ISSN: 1359-7345
- Marziano, I.; Sharp, D. C. A.; Dunn, P. J. & Hailey, P. A. (2000). On-Line Mid-IR Spectroscopy as a Real-Time Approach in Monitoring Hydrogenation Reactions, *Organic Process Research & Development*, Vol.4, No.5, pp. 357-361, ISSN 1520-586X
- Mazarevica, G.; Diewok, J.; Baena, J. R.; Rosenberg, E. & Lendl, B. (2004). On-Line Fermentation Monitoring by Mid-infrared Spectroscopy. *Applied Spectroscopy*, Vol.58, No.7, pp. 804-810, ISSN 1943-3530
- McGarrity, J. F.; Ogle, C. A.; Brich, Z.; Loosli, H. R. (1985b). A rapid-injection (RI) NMR study of the reactivity of butyllithium aggregates in tetrahydrofuran. *Journal of the American Chemical Society*, Vol.107, No.7, 1810-1815, ISSN 0002-7863
- McGarrity, J. F.; Prodolliet, J. & Smyth, T. (1981). Rapid injection NMR: a simple technique for the observation of reactive intermediates. *Organic Magnetic Resonance*, Vol.17, No.1, pp. 59-65, ISSN 0030-4921
- McGarrity, John F.; Ogle, Craig A. (1985a). High-field proton NMR study of the aggregation and complexation of n-butyllithium in tetrahydrofuran. *Journal of the American Chemical Society*, Vol.107, No.7, 1805-1810, ISSN 0002-7863
- Melling P. J. & Thomson M. (2002). Fiber-optic Probes for Mid-infrared Spectrometry, In: *Handbook of Vibrational Spectroscopy*, J. M. Chalmers & P. R. Griffiths (Eds.), John Wiley & Sons Ltd., ISBN 0471988472, Chichester
- Minnich, C. B.; Buskens, P.; Steffens, H. C.; Bäuerlein, P. S.; Butvina, L. N.; Küpper, L.; Leitner, W.; Liauw, M. A. & Greiner, L. (2007). Highly Flexible Fibre-Optic ATR-IR Probe for Inline Reaction Monitoring. *Organic Process Research & Development*, Vol.11, No.1, pp. 94-97, ISSN 1520-586X
- Mizaikoff, B. & Lendl, B. (2002). Sensor Systems Based on Mid-infrared Transparent Fibers, In: *Handbook of Vibrational Spectroscopy*, J. M. Chalmers & P. R. Griffiths (Eds.), John Wiley & Sons Ltd., ISBN 0471988472, Chichester
- Pippel, D. J.; Weisenburger, G. A.; Faibish, N. C. & Beak, P. (2001). Kinetics and Mechanism of the (–)-Sparteine-Mediated Deprotonation of (E)-N-Boc-N-(p-methoxyphenyl)-3-cyclohexylallylamine. *Journal of the American Chemical Society* Vol.123, pp. 4919–4927, ISSN 0002-7863
- Raichlin Y. & Katzir A. (2008). Fiber-Optic Evanescent Wave Spectroscopy in the Middle Infrared. *Applied Spectroscopy*, Vol.62, No.2, pp. 55A-72A, ISSN 1943-3530
- Rappoport, Z. & Marek, I. (2004). *The chemistry of organolithium compounds*, Wiley, ISBN 0-470-84339-X, Chichester
- Rathman, T. L. & Bailey, W. F. (2009). Optimization of Organolithium Reactions. *Organic Process Research & Development*, Vol.13, No.2, pp. 144-151, ISSN 1520-586X
- Rubin, A. E.; Tummala, S.; Both, D. A.; Wang, C. & Delany, E. J. (2006). Emerging Technologies Supporting Chemical Process R&D and Their Increasing Impact on Productivity in the Pharmaceutical Industry. *Chemical Reviews (Washington, DC, U. S.)*, Vol.106, No.7, pp. 2794-2810, ISSN 1520-6890
- Sun, X. & Collum, D. B. (2000). Lithium Diisopropylamide-Mediated Enolizations: Solvent-Dependent Mixed Aggregation Effects. *Journal of the American Chemical Society* Vol.122, pp. 2452–2458, ISSN 0002-7863
- Tauler, R. (1995). Multivariate curve resolution applied to second order data. *Chemometrics and Intelligent Laboratory Systems* Vol.30, pp. 133-146, ISSN 0169-7439

- Weymeels, E.; Awad, H.; Bischoff, L.; Mongin, F.; Trécourt, F.; Quéguiner, G. & Marsais, F. (2005). On the deprotonation of 3,5-dichloropyridine using lithium bases: in situ infrared spectroscopic studies. *Tetrahedron* Vol.61, pp. 3245-3249, ISSN 0040-4020
- Wiss, J.; Fleury, C. & Onken, U. (2006). Safety Improvement of Chemical Processes Involving Azides by Online Monitoring of the Hydrazoic Acid Concentration. *Organic Process Research & Development*, Vol.10, No.2, pp. 349-353, ISSN 1520-586X
- Wu, G. & Huang, M. (2006). Organolithium Reagents in Pharmaceutical Asymmetric Processes. *Chemical Reviews (Washington, DC, U. S.)*, Vol.106, No.7, pp. 2596–2616, ISSN 1520-6890
- Zhao, P. & Collum, D. B. (2003). Lithium Hexamethyldisilazide/Triethylamine-Mediated Ketone Enolization: Remarkable Rate Accelerations Stemming from a Dimer-Based Mechanism. *Journal of the American Chemical Society* Vol.125, pp. 4008–4009, ISSN 0002-7863
- Zogg, A.; Fischer, U. & Hungerbuehler, K. (2004). Identification of kinetic and thermodynamic reaction parameters from online calorimetric and IR-ATR data using a new combined evaluation algorithm. *Chemical Engineering Science*, Vol.59, No.24, 5795-5806, ISSN 0009-2509



Edited by Theophile Theophanides

The present book is a definitive review in the field of Infrared (IR) and Near Infrared (NIR) Spectroscopies, which are powerful, non invasive imaging techniques. This book brings together multidisciplinary chapters written by leading authorities in the area.

The book provides a thorough overview of progress in the field of applications of IR and NIR spectroscopy in Materials Science, Engineering and Technology. Through a presentation of diverse applications, this book aims at bridging various disciplines and provides a platform for collaborations among scientists.

Photo by LuFeeTheBear / iStock

IntechOpen

